EFFECTS OF SUPERCOOLED LARGE-DROPLET ICING ON AIRFOIL AERODYNAMICS

BY

SAM LEE

B.S., Cornell University, 1994
M.S., University of Illinois, 1997

THESIS

Submitted in partial fulfillment of the requirements
for the degree of Doctor of Philosophy in Aeronautical and Astronautical Engineering
in the Graduate College of the
University of Illinois at Urbana-Champaign, 2001

Urbana, Illinois

Abstract

An experimental study was conducted at the University of Illinois to understand the effect of supercooled large droplet (SLD) ice accretion on airfoil aerodynamics. The study consisted of a sensitivity analysis of airfoil lift, drag, pitching moment, and hinge moment to different chordwise locations, sizes, and shape of the ridge-ice simulations. Two airfoils were used in this investigation: the NACA 23012m and the NLF 0414.

The forward-facing quarter round (used as SLD ridge-ice simulation) severely altered the flowfield around the two airfoils tested. A small separation bubble formed upstream of the ice-shape simulation, and a much longer separation bubble formed downstream of the ice-shape simulation. The longer bubble grew rapidly with increasing angle of attack and failed to reattach at an angle of attack much lower than that at which the clean model stalled. This led to severe reduction in maximum lift and a large increase in drag. The pitching and hinge moments were severely altered as well.

The most critical ice-shape location on the NACA 23012m was around 10% chord. This corresponded to the location of the maximum adverse pressure gradient of the clean airfoil, just aft of the large leading-edge pressure peak where most of the lift was generated. When the ice shape was located in this region, the bubble that formed downstream had to reattach in a very adverse pressure gradient. This led to a very long bubble and a severely altered pressure distribution, with the elimination of the leading-edge suction peak.

The effects of simulated ice shape on the NLF 0414 were quite different from the NACA 23012m. There was little variation of lift when the simulated ice-shape location was varied from 2% to 20% chord. The large losses in lift occurred when the ice shape was located downstream of 30% chord, and the separation bubble formed over the adverse pressure gradient of the clean airfoil, which started at 75% chord. The effect of the ice shape on the NLF 0414 was not as severe as on the NACA 23012m because the lift was much more aft loaded.

Increasing the ice-shape height decreased lift and increased drag. Streamlining the ice shape increased lift and decreased drag. The presence of surface roughness in the

vicinity of the shape did not have large effects on lift, drag, pitching moment, and hinge moment. The presence of gaps in the spanwise ridge ice simulation significantly increased maximum lift when compared to the full span case. There was little effect on ice-airfoil aerodynamics as the Reynolds number was varied from 1 to 1.8 million.

Acknowledgements

I would first like to thank my dissertation advisor Dr. Michael Bragg for his guidance. His patience and understanding during the numerous crises in this study were invaluable. I also wish to thank the other members of my dissertation committee, Professors S. Balachandar, Eric Loth, Michael Selig, and John Walker for the review of the manuscript. This work was funded under grant DTFA 96-G-023 from the FAA. I wish to thank Dr. Jim Riley and Mr. Gene Hill of the FAA for their technical support.

During the years working at the University of Illinois Subsonic Aerodynamics Laboratory, I had the pleasure of working with many exceptional graduate and undergraduate students. I would like to thank Andy "the Skipper" Broeren, Chad Henze, Holly Gurbacki, Darren Jackson, Han Kim, Andy Anderson, Kris Engelson, and Jason "Skippy" Merret for their support. I would also like to thank all my friends at the University of Illinois who made my stay in Champaign-Urbana so enjoyable.

Finally, I wish to thank my family, especially my parents for their love and support during this endeavor. I dedicate this thesis to them.

Table of Contents

List of Figures

List of Tables

Nomenclature

A_{SS}	Settling section cross sectional area
A_{TS}	Test section cross sectional area
C_d	Drag coefficient
C_h	Hinge-moment coefficient
C_l	Lift coeffecient
$C_{l,\alpha}$	Lift curve slope
$C_{l,sep}$	Lift coefficient at separation
$C_{l,max}$	Maximum lift coefficient
$C_{l,\delta f}$	Rate of change in lift coefficient with change in flap deflection
C_m	Pitching moment coefficient
C_p	Pressure coefficient
$C_{p,min}$	Minimum pressure coefficient
c	Model chord
c_f	Distance between flap hinge line and trailing edge
D	Drag
D'	Drag per unit span
FA	Axial force
FN	Normal force
g_w	Wake total pressure
g_∞	Freestream total pressure
H	Hinge moment
H'	Hinge moment per unit span
h	Test section height
k	Protuberance height
L	Lift
L'	Lift per unit span
M	Pitching moment, Mach number
M'	Pitching moment per unit span
P_{amb}	Ambient pressure
P_{SS}	Settling section static pressure
P_{TS}	Test section static pressure
p	Static pressure
p_∞	Freestream static pressure
q_∞	Freestream dynamic pressure
R	Universal gas constant
Re	Reynolds number
r	Horn radius
s	Model coordinate in surface length
T_{amb}	Ambient temperature

U_w	Wake velocity
U_∞	Freestream velocity
V_{TS}	Test section velocity
w	Horn base width
x	Model coordinate in chordwise direction
x_r	Bubble reattachment location
y	Model coordinate normal to chorline
z	Model coordinate in spanwise direction
α	Angle of attack
$\alpha_{c_\ell,max}$	Angle of attack at maximum lift
α_{stall}	Angle of attack at stall
ΔC_d	Iced drag coefficient – clean drag coefficient
ΔC_h	Clean hinge moment coefficient – iced hinge moment coefficient
ΔC_l	Clean lift coefficient – iced lift coefficient
$\Delta C_{l,max}$	Clean maximum lift – iced maximum lift
ΔC_m	Clean pitching moment coefficient – iced pitching moment coefficient
δ	Boundary-layer thickness
δ_f	Flap deflection angle
μ	Viscosity
ρ	Density
ρ_{amb}	Ambient density

Chapter 1

Introduction

In-flight ice accretion on aircraft has been recognized since the early days of aviation as a source of potential threat to safety. Ice on aircraft aerodynamic surfaces can lead to loss in lift, increase in drag, and early stall. It can also severely alter the stability and control characteristics of the aircraft. Although major advancements in aircraft ice protection systems have been made over the years due to increased understanding of the ice-accretion process and its effect on aerodynamics, accidents due to icing are still occurring. Between 1975 and 1988, there were 803 aircraft accidents due to icing-related problems.[1] Furthermore, snow and ice accumulation was determined to be the leading cause of 9% of all fatal aircraft accidents that occurred in the United States between 1987 and 1996.[2]

1.1 Ice-Accretion Physics

The current understanding of the ice-accretion process comes from the early analysis by Messinger.[3] Aircraft can accrete ice on its aerodynamic surfaces when flying through clouds of supercooled water droplets. When these droplets impact the surface of the airfoil (usually near the leading-edge stagnation region), they will either freeze on contact or run downstream in liquid state. Depending on the surface temperature of the airfoil, this flow will either freeze as it runs back or may simply run off the airfoil entirely.

The size and shape of the ice accretion depend on numerous factors: aircraft configuration, airfoil geometry, angle of attack, airspeed, temperature, water droplet size, liquid water content, and the duration the aircraft has operated in icing condition. An experiment by Hansman, et al.[4] has identified four distinct types (as shown in Fig. 1.1) into which most ice accretions can be categorized. This experiment was conducted on a cylinder, but the results are applicable to airfoils as well. The rime ice was characterized by a conformal white ice and was observed at temperatures well below freezing. Mixed-ice and the two glaze-horn accretions were observed at temperatures near freezing. The mixed-ice accretions had a smooth, clear glaze near the stagnation zone with a rime-like accretion downstream. The horn A growth was characterized by glaze ice in the stagnation region surrounded by a closely spaced white-ice horns that grew into the flow. The horn B growth was similar to the horn A growth except the horns were spread farther apart and grew out radially. The horns also consisted of clear, glaze ice instead of white, rime ice.

1.2 Aircraft Deicing Systems

Aircraft remove in-flight ice accretion by activating ice protection systems. Most systems in use today can be categorized into two general types: thermal and pneumatic. Thermal systems melt the ice accretion or prevent the ice from forming by application of heat on the protected surface of the wing. This is done either through use of electric heaters or by ducting hot bleed air from the jet engine. Pneumatic deicing systems usually consist of an inflatable rubber boot located at the leading edge of the wing. This boot is inflated with air, causing the ice accreted over it to break and shed off the surface. The bleed-air thermal system is common on jet-powered aircraft. The pneumatic deicing system is common on piston-engine aircraft (which cannot generate any bleed air) and turbo-prop powered aircraft (which cannot generate sufficient bleed air). The deicing system typically covers the region of the wing leading edge where the ice is likely to accrete during standard icing encounters prescribed by FAA Part 25, Appendix C icing envelopes used in aircraft certification.

1.3 Supercooled Large Droplet Icing

The term supercooled large droplets (SLD) is used to describe droplets larger than 50 micron. This is larger than those prescribed in the FAA Part 25, Appendix C. It was originally thought that SLD arise from the classic melting of snow as it falls through a warm layer, becoming rain or drizzle drops. These then fall through a subfreezing layer and become freezing rain or drizzle. More recently, however, it was discovered that SLD could also form entirely in a liquid state, without the classic process of freezing and then melting.[5] It has been recognized that icing clouds with droplets the size of SLD can pose significant threat to the safety of aircraft. However, because SLD encounters do not occur very often (and when they do, only briefly) they were not part of the FAA Part 25, Appendix C icing envelope, and aircraft manufactures were not required to test their aircraft in SLD conditions as part of the certification process. Pilots were simply told to avoid encounters with SLD icing clouds.

SLD icing encounters are especially dangerous because aircraft deicing systems are not specifically designed for them. This is because the ice accretion from SLD can be significantly different from that of standard icing condition due to the differences in the trajectory of the droplets. The trajectory of the small droplets (found in standard icing clouds) tends to follow the streamlines around the airfoil very closely. Only the droplets near the stagnation point streamline will impinge on the airfoil surface. The droplets away from the stagnation streamline will follow the streamlines around the airfoil and will not impinge. However, the trajectory of the larger droplets (SLD) is less likely to follow the streamlines around the airfoil due to the higher inertia of the droplets. Thus, as the droplet size gets larger, the impingement limit moves further down the chord.[6] This is illustrated in Fig. 1.2. The impingement limits of SLD icing may be further downstream than the active portion of the deicing system. When the deicing system is activated, only the ice over the active portion is removed. This can lead to a spanwise-step type of ice accretion protuberance that forms behind the leading-edge deicing system.[7,8] An example of simulated SLD icing on an ATR-72 wing is shown in Fig. 1.3.[9] This type of accretion can present both a forward and aft facing step to the flow and is essentially 2-D, extending spanwise on the wing. This can also partially shed in flight, leaving large spanwise gaps.

1.4 Effect of SLD Icing on Performance and Control

The crash of an ATR-72 aircraft near Roselawn, IN on October 21, 1994 was thought to have been a result of SLD ice accretion. Tests following the crash suggested that there was significant ridge-type ice accretion immediately behind the deicing boot, which led to severe control degradation.[7,9] The severity of the aerodynamic degradation due to ridge ice that formed aft of the leading-edge ice protection system has been recognized as far back as 1940. Johnson[10] reported that the ridge ice that formed aft of the deicer resulted in a larger lift loss and drag increase than when the leading edge was completely iced over. In 1952, Morris[11] reported the effect of ridge ice on elevator hinge moment and effectiveness.

However, most of the studies concerning the effects of SLD-type ice accretion were conducted after the Roselawn accident in 1994. A study at the University of Wyoming, which examined the effects of various types of icing conditions on a King Air aircraft, found that the freezing drizzle exposure resulted in the most severe performance degradation.[12] Under this icing condition, a spanwise-step ice accretion was observed. In low-Reynolds number wind tunnel tests with simulated ice shapes, Ashenden, Lindberg and Marwitz[13] found that a freezing drizzle ice shape with a simulated deicing boot operation resulted in a more severe performance degradation than one without the de-icing boot operation. When the deicing boot is not in use (in SLD icing condition), the ice accretion occurs around the leading edge of the wing and tends to conform to the geometry of the wing. No spanwise step is formed. However, when the de-icing system is in use, the spanwise-step shape forms immediately downstream of the boot, which typically extends to 5 - 10% chord on the upper surface. Bernstein et al.[14] reported a reduction in $C_{l,max}$ of 30% and increase in drag of up to 200% (with a substantial reduction in the flight envelope) during one SLD encounter with a Twin Otter research aircraft.

All of the aircraft used in studies discussed above were commuter-sized aircraft that were expected to spend significant amount of flight time in icing conditions during their normal operations. There is little information in the literature concerning the effects of SLD ice accretion on large, jet powered commercial transports. Cook[15] reported the

results of limited flight tests on the Boeing 777 in SLD conditions, which did not show any severe effect on performance and handling qualities.

In 1996 Bragg[16,17] reviewed the aerodynamic effects of the SLD ice accretion based on literature in existence at the time. The review showed that the SLD accretion not only severely degraded lift and drag, but also could also adversely affect the aileron hinge moment. This was thought to be the result of a large separation bubble that formed downtream of the ice accretion, which severely altered the pressure distribution over the aileron. A large change in the aileron hinge moment could lead to an uncommanded aileron deflection, causing the loss of aircraft control.

1.5 Research Objective

The studies described above showed SLD ice accretion can cause degradation in aircraft performance and control that were more severe than what is encountered in normal icing conditions. It was still not clear exactly why the SLD accretion had such a severe effect because the understanding of the effects of SLD ice accretion on aircraft aerodynamics and control was still rather limited. Aircraft icing research up until now has primarily been concentrated on ice accretion that forms near the leading edge of the wing and can easily be removed by conventional deicing systems.

The objective of the current research was to understand the effect SLD ice accretion on airfoil aerodynamics. The study consisted of the following:

- Sensitivity analysis of airfoil lift, drag, pitching moment, and hinge moment to different chordwise locations, sizes, and shape of the ridge-ice simulations.
- Identify location, size, and geometry of ridge ice that results in the most severe performance and control degradation and determine why these are most severe.
- Investigate the effect of SLD icing on flap effectiveness.
- Investigate the importance of airfoil geometry on the sensitivity to SLD icing by testing two airfoils with very different aerodynamic characteristics.

The study presented in this dissertation was conducted experimentally at the University of Illinois. Preliminary results were presented in several conference papers[18,19,20] and a journal article.[21] A parallel study was conducted by Dunn[22,23] using

numerical methods and looked at SLD effects on a number of other airfoils and at higher Reynolds number than that could be obtained experimentally at Illinois. A better understanding of the effects of SLD ice accretion will improve aircraft operational safety by helping to identify the types of airfoils that are most susceptible to dangerous performance and control degradation when operating in SLD conditions. The knowledge can also be used to design airfoils and wings with ice protection systems that are less sensitive to SLD ice accretions.

This dissertation is organized into five major sections: Introduction, Review of Literature, Experimental Methods, Results and Discussion, and Summary, Conclusions, and Recommendations. The Review of Literature contains a survey of existing technical publications relevant to this dissertation. The area where the current knowledge is lacking will be identified and will be used as the motivation for this research. The Experimental Methods section describes the data acquisition and reduction methods used in this experiment. An uncertainty analysis of the reduced data will be presented. The experimental apparatus will also be discussed in detail. The Results and Discussion section contains the presentation and analysis of the data from this experiment. Finally, the Summary, Conclusions, and Recommendation section contains a summary of important findings and conclusions derived from this study and recommendations for further research.

Chapter 2

Review of Literature

This chapter will provide a summary of existing literature relevant to this study. The effects of a particular ice accretion on aircraft aerodynamics are dependent on several factors: the ice-accretion geometry, size and location, the airfoil geometry, flap configuration, Mach number, and the flight Reynolds number. As stated in the Introduction, a major objective in this investigation was to perform a sensitivity study on these factors. Because of this, it is important to review the findings of previous studies on some of these factors. Also, because the separation bubble that forms downstream of the ice shape plays such an important role, factors that influence its length will be reviewed.

2.1 Flowfield About an Airfoil With Ice Accretion

Before the effects of various factors on iced-airfoil aerodynamics are discussed, it is important to understand the flowfield about an airfoil with ice accretion. As stated earlier, the severe effect of the SLD ice shape was thought to be due, in large part, to the large separation bubble that forms downstream of the ice shape. The bubble is a complex region of unsteady recirculating flow, with a flow structure that is analogous to the laminar separation bubble that forms on clean airfoils.[24] An example of this is shown on Fig. 2.1. Laminar separation on a clean airfoil occurs when an adverse pressure gradient of sufficient strength is imposed on an approaching laminar boundary layer and the flow

near the surface is forced to zero velocity at the point of separation. When sufficient pressure recovery is achieved some distance downstream, the flow reattaches, forming the separation bubble. Flow separation leads to the formation of a shear layer, which divides the recirculating flow within the bubble and the external freestream flow. Before the laminar shear layer transitions to turbulent flow, the static pressure in the bubble remains fairly constant and the speed of the reverse flow is very slow. This area of the bubble is commonly termed the "dead-air" region. The end of the constant-pressure plateau indicates transition. Entrainment of high-energy external flow by the turbulent shear layer allows for adequate pressure recovery and results in flow reattachment.

Separation bubbles are classified on the basis of their effect on the flowfield. Tani[24] referred to them as short or long, but contrary to what the names may indicate, the classification is not based on the actual bubble length. A short bubble describes a separation region what has a minimal effect on airfoil performance since it only influences the pressure distribution locally. A long bubble describes a separation region that has a global effect on the pressure distribution of the entire airfoil. A sufficiently large long bubble can result in a significantly altered airfoil pressure distribution in which the leading-edge suction peak, which normally occurs, is replaced by a suction plateau of reduced magnitude. This helps to reduce the pressure recovery required by the approaching boundary layer. The pressure plateau lengthens and decreases in magnitude as angle of attack is increased. In the case of a short bubble, the suction peak is preserved and continues to increase with increasing angle until stall is reached. If the long separation bubble cannot recover the pressure, it bursts and results in complete separation, leading to stall.

Bragg, Khodadoust and Spring[25,26] studied the formation of a separation bubble behind a simulated leading-edge glaze ice accretion and found remarkable similarities to conventional laminar separation bubbles. A surface pressure distribution plot with the glaze ice is shown on Fig. 2.2. In this case, the ice accretion imposed a severe pressure gradient on the flow, causing the flow to separate at the horn. A separation bubble formed to reduce the necessary pressure recovery. Since there was a horn on both the upper and lower surface, a separation bubble was present on both surfaces. A region of constant pressure was followed by recovery, which marked shear-layer transition and eventually reattachment of the flow. The authors showed that the reattachment point

moved downstream with increasing angle of attack because of the increasing adverse pressure gradient. Since the ice-induced separation bubble had a global effect on the flowfield, it was classified as a long bubble. Thus, it was very clear that the large changes in the iced-airfoil performance were directly related to these separation bubbles.

2.2 Effects of Ice-Shape Height

Brumby[27] provided a generalized summary of the effects of roughness (including icing) on the airfoil maximum lift, as shown in Fig. 2.3. It showed the relationship between the airfoil maximum lift and the surface disturbance height/location as derived from existing wind-tunnel data at the time. The figure shows that increasing the protuberance height and moving it towards the leading edge resulted in the most severe performance degradations. The relationship shown in the Fig. 2.3 was derived primarily from roughness and leading-edge ice simulations. Recent investigations and new analysis of past studies have revealed that some modifications to this relationship are required for ice accretions where the protuberance height is much larger than the local boundary-layer height.

In 1932**,** Jacobs[28] reported the effects of various spanwise spoiler heights and locations on the NACA 0012 airfoil, as shown in Fig. 2.4. Although these were not tested as ice-shape simulations, the effects on airfoil performance degradation would have been similar to that of ridge ice. The effect of the protuberance height on $C_{l,max}$ exhibited a strong dependence on the ice shape location, as Fig. 2.5 shows. When the protuberance was at locations other than the leading edge, the $C_{l,max}$ decreased with increasing protuberance height. When the protuberance was located at the leading edge, the $C_{l,max}$ decreased with increasing protuberance height until k/c = 0.005. When the size of the protuberance was further increased, it had little additional effect on $C_{l,max}$.

Papadakis et al.[29] tested spanwise spoilers (k/c = 0.0625 and 0.125) similar to that of Jacob on the NACA 0011 airfoil. The spoilers were tested at x/c = 0.02 and 0.04. Clearly defined $C_{l,max}$ was not observed with these large spoilers. However, increasing the spoiler height decreased the angle of attack at which the lift curve became nonlinear (from -1° to -4° for x/c = 0.02 and from -2° to -6° for x/c = 0.04). Increasing the spoiler height also increased drag at all angles of attack.

Kim and Bragg[30] tested leading-edge glaze-horn shapes of various heights, location, and geometry on the NLF 0414, as shown on Fig. 2.6. Figure 2.7 shows the C_l and C_m curves with the simulated glaze ice at the leading edge and Fig. 2.8 shows the same at s/c = 0.034. The height variations at the leading edge did not cause any appreciable change in $C_{l,max}$ which remained near 1.1 regardless of height variations ($C_{l,max}$ = 1.12 for k/c = 0.02, $C_{l,max}$ = 1.09 for k/c = 0.0433, $C_{l,max}$ = 1.10 for k/c = 0.0667). The same was true for α_{stall} which remains at α = 9° - 10°. However, it can be seen that there was a large incremental change in C_m caused by the variation in height, with the moment increasing as the ice height increased for 0° < α < 10°. Near α = 9° the k/c = 0.0667 shape shows C_m = -0.005, k/c = 0.0433 shows C_m = -0.013, and k/c = 0.02 shows C_m = -0.031. This was probably due to the changes in the flowfield and the effective lengthening of the airfoil chord due to the presence of the ice shape. Extending the leading edge increases the ice-shape moments and this coupled with the larger force on the larger shape increased the C_m about the quarter-chord location. This was also unusual since changes in C_m generally indicate changes in the flowfield, which are also reflected in C_l. However, this was not the case here as seen in the two figures.

At s/c = 0.034, the height made a significant difference in $C_{l,max}$ and α_{stall} as shown in Fig. 2.8a. With k/c = 0.0667, the $C_{l,max}$ = 0.43 and α_{stall} = 1°, which was only about 32% of the clean $C_{l,max}$ and 12° less than the clean α_{stall}. The k/c = 0.0433 and k/c = 0.02 shapes show $C_{l,max}$ values of 0.56 and 0.72, respectively and α_{stall} values of 3° and 5°, respectively. Figure 2.9 shows the summary of $C_{l,max}$ as a function of the ice-shape height for the four ice shape locations tested on the NLF 0414.

All of the data showed that increasing the ice shape height generally resulted in more severe performance degradations. The exception to this was when the ice shape was located at the leading edge of the airfoil. After a critical height was reached, further increases in the height did not significantly worsen the performance degradation.

2.3 Effects of Ice-Shape Geometry

Trunov and Ingelman-Sundberg[31] tested ice shapes of various geometries on the leading edge of a horizontal tailplane. They observed that the glaze-horn accretions

resulted in the greatest degradation of aircraft performance and stability. The conformal rime ice accretion resulted in the least degradation.

Kim and Bragg[30] examined the effects of variations of the glaze-horn geometry on iced-airfoil aerodynamics. The glaze horn shapes tested on the NLF 0414 had varying horn radii, as shown in Fig. 2.6. All of the cases tested had a constant height to base ratio of 3.12. For these shapes, the leading-edge radius had very little effect on the iced-airfoil performance. Figure 2.10 shows the effects of the $k/c = 0.0433$ glaze-ice horn radius on $C_{l,max}$. It shows that rounding the horn increased $C_{l,max}$ only slightly. The effects became slightly more pronounced, as the ice shape was located further away from the leading edge. When the ice shape was located at the leading edge, the $C_{l,max}$ actually decreased by 0.02 as r/w was increased from 0 to 0.50. The largest increase in $C_{l,max}$ occurred when the ice shape was located furthest from the leading edge (at $s/c = 0.034$), but this was only a 0.07 increase.

Figure 2.11 shows the effects of the glaze-ice horn radius at $s/c = 0.017$ with varying ice-shape heights. Again, it shows increasing $C_{l,max}$ with increasing horn radius, but it was not very large. Also, the effects appeared to be relatively insensitive to the ice shape height. For the smallest shape ($k/c = 0.02$), as the r/w was increased from 0 to 0.50, the $C_{l,max}$ increased by 0.07. For the largest shape ($k/c = 0.0667$), as the r/w was increased from 0 to 0.50, the $C_{l,max}$ increased by 0.08.

The magnitude of the ice simulation leading-edge radius effect varied slightly with position and height. Ice horn radius effects were most pronounced for positions further away from the leading edge of the airfoil. It also appeared to be relatively insensitive to the ice shape heights.

As Fig. 2.6 showed, varying the chordwise location of the simulated horn shape on the NLF varied the angle of the horn with respect to the chordline because the horn was placed normal to the surface of the model. Papadakis, et al.[29] examined the effect of the protuberance angle at fixed chorwise locations. The results showed that the maximum lift loss occurred when the spoiler was perpendicular to the flow, which coincided with the highest protuberance height with respect to the model surface.

Wright and Chung[32] presented findings from a statistical analysis of computational results of an airfoil with various leading-edge glaze horn ice accretions. The results showed that the maximum lift did not vary significantly with the horn height.

However, there was a strong correlation between the horn angle and the maximum lift. Increasing the horn angle (so that it was more perpendicular to the flow) decreased the maximum lift, which supported the findings of Pakadakis, et al.[29]

2.4 Reynolds Number Effects

When the Reynolds number of a clean airfoil is increased, the $C_{l,max}$ typically increases as well. However, on an airfoil with surface contamination, this does not occur once a critical Reynolds number is reached, as $C_{l,max}$ becomes relatively insensitive to increases in the Reynolds number.

This is evident from Fig. 2.12 (from Hoerner[33]), which shows the effect of Reynolds number on maximum lift on the NACA 0012 airfoil with leading-edge roughness of various heights. On the clean airfoil, increasing the Reynolds number from 0.1 million to 10 million increased the $C_{l,max}$ from 0.8 to nearly 1.5. When the leading-edge roughness was present on the airfoil, the $C_{l,max}$ only increased up to a certain Reynolds number, after which it became fairly insensitive to increases in *Re*. This critical Reynolds number also decreased with increasing roughness size. For $k/c = 0.00005$, the critical Reynolds number was between 1 and 2 million. For $k/c = 0.0009$ (typical size of a small ice accretion) the critical Reynolds number was below 0.1 million, as the $C_{l,max}$ was insensitive to *Re* even at this value. Morgan, Ferris, and McGhee[34] tested frost and ice shape on a high lift airfoil in cruise configuration, with the Reynolds numbering varying from 2.8 to 12 million. They observed that the maximum lift of the iced airfoil varied by less than 10% even in this wide range of Reynolds number (shown in Fig. 2.13).

Kim and Bragg[30] observed similar results, although the range of Reynolds number tested was much lower. Figure 2.14 shows the clean airfoil data for the NLF 0414 at Reynolds numbers of $0.5\text{x}10^6$, $1.0\text{x}10^6$, $1.8\text{x}10^6$. It can be seen from Fig. 2.14a that $C_{l,max}$ varied greatly with Reynolds number even in this limited range. The $C_{l,max}$ for $0.5\text{x}10^6$ case was 1.12 whereas $C_{l,max}$ for $1.8\text{x}10^6$ case was 1.35; a difference of 0.23. It can also be seen from Fig. 2.14b that the break in the C_m curve occurred at $\alpha = 11°$ at $Re = 0.5$ million and at $\alpha = 15°$ for $Re = 1.8$ million.

With the addition of the simulated glaze ice, these Reynolds number effects were greatly reduced. This can be seen in Fig. 2.15 that C_l and C_m among the three Reynolds numbers tested were virtually identical. The $C_{l,max}$ for $Re = 0.5 \times 10^6$ case was 1.10, $Re = 1.0 \times 10^6$ case was 1.12, and for $Re = 1.8 \times 10^6$ case was 1.09 (a maximum difference of 0.03). Therefore, $\Delta C_{l,max}$ between clean and iced configurations may vary with Reynolds number, but the actual $C_{l,\max}$ of the airfoil with the glaze ice shape remained consistent at least within this Reynolds number range.

Figure 2.16 shows the Reynolds number effect on the lift curve of the NACA 0011, as reported by Papadakis, et al.[29] using spanwise spoilers. The results show that as the Reynolds number was increased from 1.36 to 2.46 million, the effect on the lift curve was minimal.

An implication of the insensitivity of the 2-D iced-airfoil to the increases in the Reynolds number is that the wind-tunnel data generated at relatively low Reynolds number (less than 2 million) can be applied to flight Reynolds number (over 6 million) since the results will not vary significantly. Also, this indicates that when the full size ice shape/airfoil is to be scaled down to be tested using a smaller airfoil at lower Reynolds number, the proper ice shape scaling is the k/c (direct geometric scaling). The ice shape should not be scaled by k/δ (the local boundary layer thickness).

2.5 Effect of Ice Shape Location

Brumby[27] provided a generalized summary of the effects of ice accretion (including roughness) on the airfoil maximum lift, as shown in Fig. 2.3. The figure shows that moving the ice towards the leading edge caused the effects to become more severe. As stated previously, recent investigations have revealed that this relationship is only valid for small roughness (with $k < \delta$).

Figure 2.17 shows the effect of surface roughness ($k/c = 0.0004$) location on the $C_{l,\max}$ of the NACA 0012 as reported by Gregory.[35] It shows that the most critical location for the start of the roughness was at the leading edge, with a loss in $C_{l,\max}$ of 27%. In fact, there was not a large loss in $C_{l,\max}$ until the leading edge of the roughness was upstream of $x/c = 0.05$.

However, for larger protuberances (those much larger than the local boundary-layer thickness), the most critical location is not necessarily the leading edge. Calay, Holdo and Mayman[36] tested 3 different small simulated runback ice shapes (k/c = 0.0035) at 5, 15 and 25% chord on a NACA 0012 airfoil. The shapes at 5% chord had the largest effect on lift and drag. Because the simulated ice shapes were only tested at three chordwise locations, the authors could not precisely pinpoint the most critical location. Figure 2.18 shows the effect of spanwise protuberance location on the maximum lift on the NACA 0012 (as reported by Jacobs[28]). It shows that the most critical protuberance location depended greatly on the size. For protuberances of $k/c \leq 0.001$(typical size of roughness), the most critical location was the leading edge. For larger protuberances, the most critical location appears to be near x/c = 0.05. However, because the tests were only conducted at five chordwise locations, the precise location could not be determined. There also appears to be a trend of the most critical location moving upstream with the decreasing protuberance height. Again, this is not conclusive from this figure because of the sparseness of the data.

In 1956, Bowden[37] speculated that the most critical ice accretion location, in terms of drag increase, was the location of the maximum local air velocity (or $C_{p,min}$) of the clean airfoil. This was possibly due to ice accretion extracting the greatest amount of boundary-layer momentum at this location. As explained by Bragg,[16,17] the large performance degradations due to ice accretion are primarily due to the large separation bubble that forms downstream of the ice, causing large performance degradations and earlier stall. It was believed that the largest separation bubbles would form when the ice accretion was located near the location of $C_{p,min}$ and the maximum adverse pressure gradient.

A new analysis of the Jacobs[28] data showed that for the NACA 0012 airfoil, the critical ice accretion location was often related to the location of $C_{p,min}$ and the maximum adverse pressure gradient. Figure 2.19 shows the ΔC_l (lift loss due to the k/c = 0.0125 protuberance/ice-shape when compared to the clean airfoil at the same angle of attack) on the NACA 0012.[28] Each curve represents a fixed angle of attack, and the spanwise protuberance location is depicted on the x-axis. Also shown on the figure by the solid arrows are the locations of maximum local air velocity (or $C_{p,min}$) of the clean airfoil for each angle of attack and the open arrows are the location of the maximum adverse

pressure gradient (also of the clean airfoil). At angles of attack of greater than 2°, these were located upstream of x/c = 0.02 and are difficult to see on the plot. Figure 2.19 shows that of the five chordwise locations tested, the 15% chord location usually resulted in the largest loss in lift. In fact, placing the protuberance at the leading edge usually resulted in the least lift loss at these angles of attack. The most critical protuberance locations were downstream of the suction peak and the maximum adverse pressure gradient.

The increase in the drag due to the presence of k/c = 0.0125 spanwise protrusion (ΔC_d) on the NACA 0012 is shown on Fig. 2.20.[28] A cursory look at the figure might indicate that the most critical location in terms of drag increase was not related to the location of the maximum local air velocity. However, there were no data taken at the location of maximum adverse gradient due to the limited number of chordwise locations at which the protuberance was tested. At angles of attack of greater than 2°, the most critical location was likely between the leading edge and x/c = 0.05. This could have put it near the location of the maximum local air velocity. Because of this, it was possible that the most critical location in terms of drag increase coincided with the location of the maximum local air velocity.

The studies described above strongly indicated that for protrusions much larger than the local boundary layer thickness, the most critical chordwise location is not the leading edge, as previously thought. It is located somewhere downstream of the leading edge, with the exact location a function of airfoil geometry and protrusion height. None of the studies described identified the precise chordwise location where the protrusion had the most severe effect, primarily due to the limited number of locations tested.

2.6 Flap Effects

It has generally recognized that ice accretion can severely degrade the effectiveness of aircraft control surfaces, such as flaps, elevators, rudders, and aileron.[31] These devices (the common term flap is often used to describe any of these) work by altering the airflow and the pressure distribution around the airfoil, thereby increasing (or decreasing) the lift generated without having to alter the angle of attack. Ice accretion on an airfoil can degrade the flap effectiveness in two ways. The first is the reduction in

C_{l,δ_f}, which is associated with the decrease in the $C_{l,\alpha}$ in the linear region of the lift curve before the airfoil is stalled. Another is the sudden decrease in C_{l,δ_f} due to early stall, as the stall angle of attack decreases with increasing flap deflection. This typically occurs at high angles of attack. Although the rapid drop in C_{l,δ_f} due to stall occurs on clean airfoil, it occurs at a lower angle of attack for iced airfoils due to the decrease in α_{stall}.

The degradation in flap effectiveness due to ice accretion is important for elevator, aileron, and rudder. Johnson[10] reported that leading-edge ice accumulation ahead of the aileron could result in substantial reduction in rolling moment. However, it is especially critical for elevators. The ice accretion on the horizontal tail tends to be more severe than on the wing. This is because of its smaller chord and thinner airfoil. Because of this, the tail usually experiences greater performance degradation. Ice accretion on the aircraft wing can cause large changes in the aircraft pitching moment, which must be trimmed out using elevator deflection. This is compounded when the wing flap is deployed, causing further change in the pitching moment. Under certain condition, even a slight degradation in elevator effectiveness may prevent the aircraft from being trimmed.[31,38,39]

2.7 Effect of Pressure Gradient on Bubble Reattachment

Because the long separation bubble plays such an important role in iced-airfoil performance degradation, it is important to understand the aerodynamic factors that govern its development. There have been numerous studies on the separation bubble downstream of a backward-facing step. Keuhn[40] experimentally studied the effects of pressure gradient on the reattachment length of the separation bubble. The adverse pressure gradient is important because the separation bubble downstream of an SLD ice shape is usually forced to reattach in an adverse pressure gradient. In the experiment the step was located at the floor of the test section. There was no step present at the ceiling. However, the ceiling was hinged above the step and could be rotated to adjust the pressure gradient downstream of the step. When the ceiling angle was set at zero degree, Keuhn[40] observed reattachment 6 step heights downstream of the step. When the ceiling was not deflected, there was still an adverse pressure gradient as the flow diverged over

the step. When the pressure gradient was varied by deflecting the ceiling, the reattachment length was observed to vary between 4 and 20 step heights.

Driver and Seegmiller[41] presented detailed boundary-layer measurements of the separation bubble downstream of the backward step with varying pressure gradient. They showed that as the pressure gradient became more adverse, the displacement and the momentum thickness increased even after reattachment. The significance of this was that increasing the adverse pressure gradient not only increased the separation bubble length but also the drag.

Eaton et al.[42], Adams and Johnston[43], and Yoo and Baik[44] studied the effect of the boundary-layer state and the Reynolds number on the separation length downstream of the backward step. They showed that when the boundary layer upstream of the step was fully turbulent, the separation bubble was up to 30% longer than when the flow was laminar. In fact, the longest separation bubble occurred when the flow upstream of the step was transitional. Adams and Johnston speculated that this was due to a larger initial free-shear-layer entrainment in a laminar flow separation. The separation bubble length was also not observed to vary significantly with the Reynolds number as long as the flow did not transition.

2.8 Summary of Literature Review

A review of relevant technical literature revealed that there may be several reasons why SLD ice accretions have much more severe affect on aircraft performance and control than the standard leading-edge ice accretion. One major reason may be the location of the ice accretion. SLD ice accretion forms immediately downstream of the active portion of the deicing system, usually between 5-10% chord. A careful analysis of past studies have shown that the most critical protuberance location is somewhere in this vicinity and is related to the adverse pressure gradient in the recovery region.[28,37] The geometry of the SLD accretion may also be important. Studies with glaze horn ice[20,29,32] showed that the largest reduction in performance was observed when the horn was perpendicular to the flow. The ridge ice that forms in SLD encounters often has a vertical, forward facing step similar to a glaze horn perpendicular to the flow.

Although the studies described in this chapter provided the initial insight into the effect of SLD ice accretion on airfoil aerodynamics, some important question remained unanswered. Why is the most critical ice accretion location not the leading edge of the airfoil but further downstream? How do parameters, such as ice accretion geometry and height, airfoil geometry, and Reynolds number affect the critical ice shape location? In order to determine this, the most critical ice accretion location must be precisely identified and the flowfield about the iced airfoil must be known. However, there has been no study to date where a dense array of protuberance locations were systematically tested in order to accurately identify the most critical ice shape location. Also, few studies described in this chapter contained high-resolution surface pressure measurements from which the flowfield could be studied.

The study presented in this dissertation answered these questions. Because a dense test matrix of various ice shape locations, size, and geometry was implemented, the most critical ice shape location was accurately determined for various ice shape size and geometry. High-resolution surface pressure measurements as well as flow visualization provided for flowfield analysis. The tests were also conducted on two airfoils with very different clean-model characteristics, allowing the effect of airfoil geometry to be studied. The results of this study contributed to the understanding of the effects of SLD ice accretion on airfoil aerodynamics by providing answers to the questions posed above.

Chapter 3

Experimental Methodology

The experiment was conducted in the low-turbulence subsonic wind tunnel in the Subsonic Aerodynamics Laboratory at University of Illinois at Urbana-Champaign. The general laboratory layout is shown in Fig. 3.1. The overall schematic of the experimental setup is shown in Figs 3.2 and 3.3. The airfoil model was mounted in the test section on a 3-component force balance, which was also used to set the model angle of attack. A traverseable wake rake was mounted downstream of the model and was used to measure drag. The airfoil models were instrumented for surface pressure measurements. The models were also flapped so that hinge moments could be measured and measurements could be taken with the flap deflected. A single IBM-compatible Pentium computer was used for all data acquisition and was used to control the all of the experimental hardware.

3.1 Wind Tunnel and Facility

The wind tunnel used was a conventional, open-return type and is shown in Fig. 3.4. The inlet settling chamber contained a 4-inch honeycomb, which was immediately followed downstream by 4 stainless steel anti-turbulence screens. The test section measured 2.8 ft x 4.0 ft x 8.0 ft and the side walls expanded 0.5 inch over its length to accommodate the growing boundary layer. The inlet had a 7.5:1 contraction ratio. The test section turbulence intensity was measured to be less than 0.1% at all operating speeds.[45] The tunnel contained a 5-bladed fan that was driven by a 125-hp AC motor controlled by a variable frequency drive. The maximum speed attainable in the test

section was 160 mph (235 ft/sec), which corresponded to a Reynolds number of 1.5 million per foot under standard conditions. The tunnel speed was controlled by an ABB ACS-600 frequency drive that was connected to the data acquisition computer by a serial RS-232 interface. During the data acquisition, the tunnel velocity was iterated until the desired Reynolds number was obtained within 2%.

There were wall static ports in the inlet settling section just behind the last screen that were pneumatically averaged by connecting them to a single output port. This provided the static pressure in the inlet settling section of the tunnel. Four wall static ports (also pneumatically averaged) just ahead of the test section provided the test section freestream static pressure. The tunnel velocity was obtained by measuring the difference in the static pressures in these two locations and applying the Bernoulli's equation.

The ambient temperature was measured using an Omega type-T thermocouple that was mounted on the inlet of the tunnel. The output signal was gained by factor of 1,000 using Measurement Group model 2210 signal conditioning amplifier before it was read by the data acquisition computer. The laboratory ambient pressure was measured using a Setra model 270 barometric pressure transducer. The temperature and the ambient pressure were used to determine the Reynolds number.

3.2 Airfoil Models

There were two airfoils studied in this investigation, a modified NACA 23012m model (built for this study) and a NLF 0414 model (borrowed from NASA/AGATE tests).[46] The nature of the NACA 23012m modification (and its impact on the airfoil aerodynamics) will be discussed later in the Validation section 4.1. The NACA 23012 airfoil was chosen because it has aerodynamic characteristics that are typical of the current commuter aircraft fleet. The NLF 0414 airfoil was chosen because, as a natural laminar flow airfoil, it has aerodynamic characteristics that are quite different from the NACA 23012. The differences will be explained in more detail in the Results and Discussion section.

Table 3.1: Model tap locations and pressure transducer used.

3.1a) NACA 23012m

Main Element Taps				
Tap	x/c	y/c	z/c	ESP Module
1	0.750	0.0371	1.0579	1 PSID
3	0.680	0.0456	1.0472	1 PSID
4	0.640	0.0502	1.0365	1 PSID
5	0.600	0.0545	1.0258	1 PSID
6	0.560	0.0585	1.0151	1 PSID
7	0.520	0.0622	1.0043	1 PSID
8	0.480	0.0656	1.0043	1 PSID
9	0.440	0.0687	1.0151	1 PSID
10	0.400	0.0713	1.0258	1 PSID
11	0.380	0.0724	1.0311	1 PSID
12	0.360	0.0734	1.0365	1 PSID
13	0.340	0.0742	1.0418	1 PSID
14	0.320	0.0749	1.0472	1 PSID
15	0.300	0.0755	1.0526	5 PSID
16	0.280	0.0758	1.0579	5 PSID
17	0.260	0.0760	1.0633	5 PSID
18	0.240	0.0759	1.0686	5 PSID
19	0.220	0.0756	1.0740	5 PSID
20	0.200	0.0750	1.0794	5 PSID
21	0.180	0.0741	1.0847	5 PSID
22	0.160	0.0728	1.0901	5 PSID
23	0.140	0.0707	1.0954	5 PSID
24	0.120	0.0678	1.1008	5 PSID
25	0.100	0.0638	1.1062	5 PSID
26	0.080	0.0585	1.1115	5 PSID
27	0.060	0.0514	1.1169	5 PSID
28	0.050	0.0471	1.1195	5 PSID
29	0.040	0.0421	1.1222	5 PSID
30	0.030	0.0362	1.1249	5 PSID
31	0.020	0.0291	1.1276	5 PSID
32	0.010	0.0199	1.1303	5 PSID
33	0.009	0.0055	1.1319	5 PSID
34	0.006	0.0152	1.1334	5 PSID
35	0.003	0.0106	1.1349	5 PSID
36	0.000	0.0000	1.1364	5 PSID
37	-0.001	-0.0054	1.2007	5 PSID
38	-0.004	-0.0100	1.1992	5 PSID
39	-0.010	-0.0141	1.1973	5 PSID
40	-0.025	-0.0195	1.1932	5 PSID
41	-0.050	-0.0240	1.1865	5 PSID
42	-0.075	-0.0271	1.1798	5 PSID
43	-0.100	-0.0298	1.1731	5 PSID
44	-0.200	-0.0397	1.1463	5 PSID
45	-0.300	-0.0446	1.1195	5 PSID
46	-0.400	-0.0448	1.0928	1 PSID
47	-0.500	-0.0419	1.0660	1 PSID
48	-0.600	-0.0368	1.0392	1 PSID
49	-0.700	-0.0300	1.0124	1 PSID
50	-0.750	-0.0261	0.9990	1 PSID

Flap Taps				
Tap	x/c	y/c	z/c	ESP Module
1	1.000	0.0000	1.1329	1 PSID
2	0.975	0.0053	1.1262	1 PSID
3	0.950	0.0092	1.1195	1 PSID
4	0.900	0.0167	1.1062	1 PSID
5	0.850	0.0238	1.0928	1 PSID
6	0.825	0.0273	1.0861	1 PSID
7	0.800	0.0306	1.0794	1 PSID
8	0.779	0.0335	1.0736	1 PSID
9	0.767	0.0312	1.0705	1 PSID
10	0.758	0.0250	1.0675	1 PSID
11	0.752	0.0158	1.0645	1 PSID
12	0.750	0.0049	1.0616	1 PSID
13	-0.758	-0.0151	1.0006	1 PSID
14	-0.779	-0.0237	1.0066	1 PSID
15	-0.800	-0.0218	1.0124	1 PSID
16	-0.850	-0.0172	1.0258	1 PSID
17	-0.900	-0.0123	1.0392	1 PSID
18	-0.950	-0.0070	1.0526	1 PSID

Spanwise Taps				
Tap	x/c	y/c	z/c	ESP Module
1	0.900	0.0167	0.0139	1 PSID
2	0.900	0.0167	0.0440	1 PSID
3	0.900	0.0167	0.0910	1 PSID
4	0.900	0.0167	0.1549	1 PSID
5	0.900	0.0167	0.2357	1 PSID
6	0.900	0.0167	0.3333	1 PSID
7	0.900	0.0167	1.5313	1 PSID
8	0.900	0.0167	1.6289	1 PSID
9	0.900	0.0167	1.7097	1 PSID
10	0.900	0.0167	1.7736	1 PSID
11	0.900	0.0167	1.8206	1 PSID
12	0.900	0.0167	1.8507	1 PSID

3.1b) NLF 0414

Main Element Taps				
Tap	x/c	y/c	z/c	ESP Module
1	0.7600	0.0391	1.0686	1 PSID
3	0.7400	0.0460	1.0633	1 PSID
4	0.7200	0.0522	1.0579	1 PSID
5	0.7000	0.0574	1.0526	1 PSID
6	0.6806	0.0615	1.0474	1 PSID
7	0.6500	0.0668	1.0392	1 PSID
8	0.6306	0.0697	1.0340	1 PSID
9	0.6000	0.0734	1.0258	1 PSID
10	0.5500	0.0781	1.0124	1 PSID
11	0.5000	0.0810	0.9990	1 PSID
12	0.4500	0.0824	1.0124	1 PSID
13	0.4000	0.0826	1.0258	1 PSID
14	0.3667	0.0819	1.0347	1 PSID
15	0.3333	0.0807	1.0436	1 PSID
16	0.3000	0.0788	1.0526	5 PSID
17	0.2667	0.0763	1.0615	5 PSID
18	0.2333	0.0731	1.0704	5 PSID
19	0.2000	0.0692	1.0794	5 PSID
20	0.1800	0.0665	1.0847	5 PSID
21	0.1600	0.0635	1.0901	5 PSID
22	0.1400	0.0601	1.0954	5 PSID
23	0.1200	0.0565	1.1008	5 PSID
24	0.1000	0.0523	1.1062	5 PSID
25	0.0800	0.0476	1.1115	5 PSID
26	0.0600	0.0419	1.1169	5 PSID
27	0.0500	0.0387	1.1195	5 PSID
28	0.0400	0.0350	1.1222	5 PSID
29	0.0300	0.0309	1.1249	5 PSID
30	0.0200	0.0261	1.1276	5 PSID
31	0.0100	0.0194	1.1303	5 PSID
32	0.0061	0.0155	1.1317	5 PSID
33	0.0030	0.0110	1.1332	5 PSID
34	0.0008	0.0058	1.1347	5 PSID
35	0.0000	0.0004	1.1362	5 PSID
36	0.0010	-0.0050	1.2031	5 PSID
37	0.0045	-0.0093	1.2016	5 PSID
38	0.0100	-0.0125	1.1999	5 PSID
39	0.0200	-0.0165	1.1973	5 PSID
40	0.0400	-0.0221	1.1919	5 PSID
41	0.0600	-0.0264	1.1865	5 PSID
42	0.0800	-0.0301	1.1812	5 PSID
43	0.1000	-0.0333	1.1758	5 PSID
44	0.1250	-0.0369	1.1691	5 PSID
45	0.1500	-0.0400	1.1624	5 PSID
46	0.1750	-0.0428	1.1557	5 PSID
47	0.2000	-0.0454	1.1490	5 PSID
48	0.2500	-0.0497	1.1356	5 PSID
49	0.3000	-0.0533	1.1222	1 PSID
50	0.3500	-0.0561	1.1088	1 PSID
51	0.4000	-0.0582	1.0954	1 PSID
52	0.4500	-0.0594	1.0820	1 PSID
53	0.5000	-0.0600	1.0686	1 PSID
54	0.5500	-0.0598	1.0552	1 PSID
55	0.6000	-0.0586	1.0418	1 PSID
56	0.6306	-0.0572	1.0337	1 PSID
57	0.6611	-0.0552	1.0255	1 PSID
58	0.6806	-0.0534	1.0203	1 PSID
59	0.7000	-0.0509	1.0150	1 PSID
60	0.7200	-0.0474	1.0097	1 PSID
61	0.7400	-0.0433	1.0043	1 PSID
62	0.7600	-0.0394	0.9990	1 PSID

Flap Taps				
Tap	x/c	y/c	z/c	ESP Module
1	1.0000	-0.0273	1.1329	1 PSID
2	0.9750	-0.0220	1.1262	1 PSID
3	0.9500	-0.0176	1.1195	1 PSID
4	0.9250	-0.0124	1.1129	1 PSID
5	0.9000	-0.0065	1.1062	1 PSID
6	0.8750	0.0002	1.0995	1 PSID
7	0.8500	0.0076	1.0928	1 PSID
8	0.8250	0.0158	1.0861	1 PSID
9	0.8000	0.0246	1.0794	1 PSID
10	0.7830	0.0308	1.0748	1 PSID
11	0.7704	0.0281	1.0713	1 PSID
12	0.7597	0.0209	1.0679	1 PSID
13	0.7525	0.0102	1.0644	1 PSID
14	0.7500	-0.0024	1.0609	1 PSID
15	0.7544	-0.0189	0.9959	1 PSID
16	0.7665	-0.0310	1.0005	1 PSID
17	0.7830	-0.0356	1.0051	1 PSID
18	0.8000	-0.0334	1.0097	1 PSID
19	0.8250	-0.0306	1.0164	1 PSID
20	0.8500	-0.0285	1.0231	1 PSID
21	0.8750	-0.0271	1.0298	1 PSID
22	0.9000	-0.0263	1.0365	1 PSID
23	0.9250	-0.0263	1.0432	1 PSID
24	0.9500	-0.0268	1.0499	1 PSID
25	0.9750	-0.0276	1.0566	1 PSID

Spanwise Taps				
Tap	x/c	y/c	z/c	ESP Module
1	0.6500	0.0668	0.0278	1 PSID
2	0.6500	0.0668	0.0579	1 PSID
3	0.6500	0.0668	0.1049	1 PSID
4	0.6500	0.0668	0.1688	1 PSID
5	0.6500	0.0668	0.2496	1 PSID
6	0.6500	0.0668	1.3611	1 PSID
7	0.6500	0.0668	1.6151	1 PSID
8	0.6500	0.0668	1.6958	1 PSID
9	0.6500	0.0668	1.7597	1 PSID
10	0.6500	0.0668	1.8067	1 PSID
11	0.6500	0.0668	1.8368	1 PSID

Both of the models had 18-inch chord with 25% chord simple flaps. The leading edge of the flap was located at $x/c = 0.75$ on both of the models. The flap hinge line was located at $x/c = 0.779$ and $y/c = 0.0049$ on both of the models. The models were constructed of a carbon fiber skin surrounding a foam core. Two rectangular steel spars were located at $x/c = 0.25$ and 0.60 and were supported by wooden ribs. The spars extended 4" past one end of the model. This allowed it to be attached to the metric force plate of the 3-component force balance using custom-built mounting supports. The flap gap was sealed on the model lower surface using a 1" wide Mylar strip that was taped only on the main element side. At positive angles of attack, the high pressure on the lower surface of the model pushed the Mylar strip against the flap gap, effectively sealing it without adversely affecting the measurements from the flap hinge balance. A 1/16"-thick plywood span extender was attached to the ceiling end of the model in order to minimize the gap between the model and the ceiling.

The airfoil models were equipped with surface pressure taps in order to measure the surface pressure distribution. The NACA 23012m model had 50 surface pressure taps on the main element and 30 taps on the flap (including 12 spanwise taps). The NLF 0414 had 72 taps on the main element (including 11 spanwise taps) and 25 taps on the flap. This arrangement is shown in Fig. 3.5 and Table 3.1. The main tap line was angled at 15 degrees with respect to the direction of the flow in order to put the pressure taps out of a possible turbulent wedge generated by the taps preceding them. The spanwise taps were used to measure spanwise flow non-uniformity near the walls.

3.3 Force and Moment Balance

An Aerotech 3-component force and moment balance (shown in Fig. 3.6) was primarily used to set the model angle of attack. However, it was also used to measure the lift, drag, and pitching moment for comparisons to the pressure and wake measurements. The model was mounted on the metric force plate of the balance with mounting supports. The signals from the load cells on the balance were gained by a factor of 250, low-pass filtered at 1Hz and converted to normal, axial, and pitching moment components. These three measurements (in voltages) were read by the data acquisition board on the computer. The balance did not directly measure lift and drag because the load cells turned with the model. The force balance was equipped with a position encoder that

precisely measured the angle of attack. The turntable portion of the balance (including the encoder) was interfaced to the data acquisition computer through the RS-232 serial connection. A more detailed description of the force balance can be found in Noe.[47]

3.4 Flap Actuator and Balance

The flap was actuated by a two-arm linkage system, which was driven by a Velmex linear traverse, as shown in Fig. 3.7. An Omega LCF-50 load cell with 50lb range was attached to one of the arms and was used to measure the flap hinge moments. The traverse was mounted on the metric force plate of the force balance. Thus, the entire load on the flap was eventually transferred to the force balance.

The flap load cell was calibrated by directly applying loads to the flap by using weights and pulley as shown in Fig. 3.8. The flap was calibrated up to 20 ft-lbs (which was 50% over the maximum moment it was expected to encounter) with 15 points and was linearly curve fit. The flap was calibrated at five flap deflection angles (-10°, -5°, 0°, 5°, and 10°), providing a separate calibration curve for each flap angle that was to be tested.

3.5 Wake Survey System

The primary drag measurements were recorded using a wake rake system (Fig. 3.9). It contained 59 total pressure probes aligned horizontally. The wake rake was traversed by a Velmex traverse system, which allowed it to span the entire width of the test section. The outer 6 ports on each side of the wake rake were spaced 0.27” apart and the inner 47 ports were spaced 0.135” apart. The total width of the wake rake was 9.75”. This was wide enough to capture the entire wake when the flow over the model was attached. However, when there was a very large wake due to flow separation, two or three spans of the wake rake were needed to capture the entire wake. There was a 0.27” overlap between the successive spans in order to not to leave any gaps in the wake. The pressures from the wake rake were measured using two PSI ESP-32 units with 0.35 psid range. The total pressures measured from the wake rake were referenced to the atmosphere.

3.6 Digital Pressure Acquisition System

The PSI 8400 digital pressure system was used to measure all of the pressures except for the ambient pressure. The schematic of the pressure measurement system is shown in Fig. 3.10. Five electronically scanned pressure (ESP) modules with 32 ports each were used in this investigation. Two 0.35 psid ESP modules were used to measure the drag from the wake rake with the reference ports (labeled 'ref') open to the ambient pressure in the control room. Two 1 psid and one 5 psid modules were used to measure the surface pressures on the airfoil models and were referenced to the tunnel static pressure port. The pressure taps near the leading edge of the models were connected to the 5 psid module as these were expected to have the highest differential pressure. Table 3.1 shows the pressure tap locations and the ESP modules that they were connected to. A port on the 1 psid module also measured the tunnel settling section static pressure from which the test section dynamic pressure was derived.

The PSI 8400 system had two built in pressure calibration units (PCU). During the calibration, pneumatic valves on each ESP module switched the positive pressure side of the transducers from the 32 run ports to the single calibration port (labeled 'cal' in Fig. 3.10). The PCU applied predetermined pressures to the calibration port of the ESP module. The PCUs were referenced to the ambient pressure. During the calibration, the reference port on the 5 and 1 psid ESP modules were opened to the ambient pressure as well, through the use of a solenoid valve. During the runs, the reference ports were open to the tunnel test section static ports. During the calibration, the reference ports were open to the ambient pressure. The 0.35 psid modules were calibrated by the 1 psid PCU and the 1 psid and 5 psid modules were calibrated by the 5 psid PCU. The calibration employed a three-point (2^{nd} order) curve fit, using three predetermined pressures. The ESP modules were calibrated before each run and during the runs when the temperature drifted by more than 2° F.

3.7 Ice Simulation

The spanwise step-ice accretions were simulated using several basic geometries as shown in 3.11. The baseline SLD ice accretions were simulated with wooden forward-facing quarter-round shapes of 0.10", 0.15", and 0.25" heights (with corresponding k/c =

0.0056, 0.0083, 0.0139). This geometry was used because it has a vertical step facing the flow, which is consistent with the shape of the residual ice that forms just aft of the wing ice protection system under an SLD encounter. The forward facing quarter round is also the geometry used by the FAA during aircraft certification. Finally, a simple geometry, such as the forward-facing quarter round, allowed a much easier implementation for the numerical modeling aspect of this investigation.[22,23]

The other geometries tested consisted of backward-facing quarter round, half-round, and forward-facing ramp (all with 0.25" height). The ramp shape was had a base-length-to-height ratio of 3. The quarter and half rounds were cut from wooden dowels, and the ramp shape was machined from aluminum. The 0.25" forward-facing quarter round was also tested with spanwise gaps (the detailed geometry of the spanwise gaps is provided in the results and discussions section). The simulated ice shapes were attached to the model using clear Scotch™ tape.

Roughness was also used in place of, and in addition to, the simulated ice shape. When it was used in place of the ice shape, the roughness had a 0.5" chordwise extent. When used with the ice shape, the roughness extended upstream and/or downstream from the ice shape. The chordwise extent of the upstream roughness varied from 0.25" to 2", and the extent of the downstream roughness was 2". The roughness was simulated using 16-grit aluminum carbide attached to a double-sided tape. This resulted in 0.025" roughness height, with $k/c = 0.0014$. The roughness density in terms of the coverage area was visually estimated to be about 30%.

The 0.25" height of the baseline shapes was obtained from scaling the actual 0.75" SLD ice accretion observed during the tanker and icing wind tunnel tests.[9] A survey of various commuter-type aircraft[48] by the authors showed that the average chord over the aileron section was roughly 5 feet. The airfoil models used in the current investigation had 1.5-ft chord. Thus, when the actual 0.75" ice accretion was scaled by the ratio of the UIUC airfoil model and the full size chord (1.5/5), a scaled height of 0.225" resulted. This was rounded up to 0.25" to provide a convenient number. Two other heights (0.10" and 0.15") were also tested in order to determine the effects of ice accretion height.

For most of the cases tested, the boundary layer was tripped at $x/c = 0.02$ on the upper surface and at $x/c = 0.05$ on the lower surface. The trip consisted of 0.012-inch

diameter microbeads that were applied onto a 0.003-inch thick and 0.25 inch wide double-sided tape. The models were tripped for two reasons. When the leading-edge-deicing boot is activated, it usually does not remove all of the ice accretion. Instead, a residual ice roughness is usually left behind, which causes the flow to be turbulent (or at least transitional) from the leading edge. Another reason for the trip was to provide a fixed transition location for the CFD simulations. Figure 3.12 shows the NACA 23012m model with the baseline 0.25" forward-facing quarter round at $x/c = 0.10$.

3.8 Data Acquisition Computer

A single Pentium 133MHz IBM compatible computer was used to control all of the hardware in this experiment and to acquire the data. Data acquisition software was specifically written for this experiment using National Instruments LabWindows/CVI. The raw data were reduced online during the runs and displayed on the computer monitor to ensure that everything was working properly.

The wind tunnel variable frequency drive, the force balance, and the Velmex stepper motor controller (which controlled the movement of the wake rake and flap) were controlled through the three RS-232 ports on the computer. The PSI 8400 system was controlled through a National Instruments General Purpose Interface Bus (GPIB) IEE-488 board. The voltages from the force balance load cells, the laboratory ambient pressure transducer, and the thermocouple were obtained using a 16-bit National Instruments AT-MIO-16XE50 analog to digital (A/D) conversion board.

3.9 Flow Visualization

Surface fluorescent oil flow visualization was performed on the two models for flow diagnostics. It was also used to accurately determine the size of the separation bubbles that formed upstream and downstream of the ice simulations.

The method comprised of spraying a coat of fluorescent dyed mineral oil on the surface of the model. The oil would then coalesce into tiny beads, which ran in the direction of the airflow on the surface of the model, leaving streaks. When the flow was attached to the model, the beads flowed in the direction of the freestream. When the flow

was separated and there was reverse flow, the beads moved in the opposite direction of the freestream. The relative magnitude of surface shear can also be ascertained using the surface oil method. If there is very little oil remaining on a particular region on the surface of the model, it is an indication of high surface shear stress in that region. If the oil remains beaded (instead of streaked) on a particular region, it is due to low surface shear stress. This is typically found in the "dead-air" region of separated flow.

After the tunnel has been run for 3 to 5 minutes, the tunnel was turned off and the lab was darkened. Ultraviolet lights were shined on the surface of the model, causing the dye in the oil to fluoresce. The flowfield on the surface of the model were then obtained by interpreting the streak patterns left by the oil. A more though description of the surface fluorescent oil flow visualization method can be found in Winkler.[49]

Because of the surface pressure taps, the fluorescent oil was not directly applied to the model surface. A sheet of black Ultracote (a self adhesive plastic sheet with a glossy surface) was applied to the entire upper surface of the model. The oil was then sprayed on the Ultracote, which kept the pressure taps on the model free of oil. A yellow reflective tape was placed chordwise on the model and was marked off every 5% chord using a black permanent marker. This was used as the chordwise location indicator.

3.10 Data Acquisition and Reduction

A typical run consisted of sweeping the angle of attack from negative stall to a few degrees past positive stall in 1° increments. At each angle of attack, the flap was swept from -10° to 10° in 5° increments. Before each run, the digital pressure system was calibrated and the force and hinge-moment balance tares were measured. All measurements were taken at 50 Hz and averaged over 2 seconds. The force balance data were low-pass filtered at 1Hz. None of the other measurements were filtered.

The lift coefficient (C_l) and pitching moment coefficient (C_m) measurements were derived from both the force balance and the surface pressure measurements. In this report, the C_l and C_m data were taken from the pressure measurements unless indicated otherwise. This was because the pressure measurements were considered more 2-dimensional in nature, which would lead to greater accuracy. The primary drag coefficient (C_d) measurements were taken with the wake rake and confirmed with the force balance. The flap hinge-moment coefficients (C_h) were measured with the surface-

pressure measurements and confirmed with the flap-hinge load cell. The surface pressure measurements and fluorescent oil flow visualization were used for flow diagnostics. The C_l, C_m, C_d, and C_h measurements were calculated using standard methods with conventional definitions:

$$C_l = \frac{L'}{q_\infty c} \tag{3.1a}$$

$$C_d = \frac{D'}{q_\infty c} \tag{3.1b}$$

$$C_m = \frac{M'}{q_\infty c^2} \tag{3.1c}$$

$$C_h = \frac{H'}{q_\infty c_f{}^2} \tag{3.1d}$$

The surface pressure coefficients were defined as:

$$C_p = \frac{p - p_\infty}{q_\infty} \tag{3.2}$$

All of the aerodynamic coefficients were corrected for wall effects using the method described by Rae and Pope.[50] In the equations below, subscript (u) denotes uncorrected values. The corrected values for the angle of attack and aerodynamic coefficients are given by

$$\alpha = \alpha_u + \frac{57.3\sigma}{2\pi}\left(C_{\ell,u} + 4C_{m,u}\right) \tag{3.3a}$$

$$C_\ell = C_{\ell,u}\left(1 - \sigma - 2\varepsilon\right) \tag{3.3b}$$

$$C_d = C_{d,u}\left(1 - 3\varepsilon_{sb}\sigma - 2\varepsilon_{wb}\right) \tag{3.3c}$$

$$C_m = C_m\left(1 - 2\varepsilon\right) + \frac{\sigma C_\ell}{4} \tag{3.3d}$$

where,

$$\sigma = \frac{\pi^2}{48}\left(\frac{c}{h}\right)^2 \tag{3.4a}$$

$$\varepsilon = \varepsilon_{sb} + \varepsilon_{wb} \tag{3.4b}$$

$$\varepsilon_{wb} = \frac{c}{2h} C_{d,u} \tag{3.4c}$$

In the equations above, (σ) is 0.0289. ε_{sb} is the solid blockage coefficient and ε_{wb} is the wake blockage coefficient.

The test section dynamic pressure was obtained by measuring the difference between the static pressure at the test section and the tunnel settling section ($P_{SS} - P_{TS}$) and applying the Bernoulli's equation and conservation of mass. The dynamic pressure in the test section freestream is defined as

$$q_\infty = \tfrac{1}{2}\rho V_{TS}^2 \tag{3.5}$$

The Bernoulli's equation for the incompressible flow in the tunnel settling and test section is given by:

$$\tfrac{1}{2}\rho V_{SS}^2 + P_{SS} = \tfrac{1}{2}\rho V_{TS}^2 + P_{TS} \tag{3.6}$$

The conservation of mass is given by:

$$V_{SS} A_{SS} = V_{TS} A_{TS} \tag{3.7}$$

A manipulation of the equations (3.6 and 3.7) yields

$$\tfrac{1}{2}\rho V_{TS}^2 = \frac{\left(P_{SS} - P_{TS}\right)}{\left(1 - \left(A_{TS} / A_{SS}\right)^2\right)} \tag{3.8}$$

Thus, the freestream dynamic pressure is given by

$$q_\infty = \frac{\left(P_{SS} - P_{TS}\right)}{\left(1 - \left(A_{TS} / A_{SS}\right)^2\right)} \tag{3.9}$$

The dynamic pressure obtained from the wall static ports was compared with a survey of the test section dynamic pressure obtained from a pitot static probe. These two measurements agreed favorably, and the differences were within the measurement uncertainties. The ambient density ρ_{amb} of the test section was obtained by applying the ideal gas law

$$\rho_{amb} = \frac{P_{amb}}{T_{amb} R} \tag{3.10}$$

where R is the universal gas constant (1716 lb-ft/(R-slug)). The viscosity was obtained using the Sutherland law

$$\mu \approx \mu_0 \left(\frac{T_{amb}}{T_0}\right)^{1.5} \frac{\left(T_0 + Su\right)}{\left(T + Su\right)} \tag{3.11}$$

where μ_0 is the known viscosity value at temperature T_0. In this study, $\mu_0 = 3.58404 \times 10^{7}$ lb-s/ft^2 and T_0 = 491.6 R were used. Su is the Sutherland constant (199.8 R). The Reynolds number was then calculated using

$$Re = \frac{\rho V_{TS} c}{\mu} \tag{3.12}$$

3.10.1 Pressure Measurements

The pressure coefficient C_p is defined as

$$C_p = \frac{P_s - P_\infty}{q_\infty} \tag{3.13}$$

Substituting equation (3.9) into (3.13) results in

$$C_p = \frac{\left(P_s - P_\infty\right)\left(1 - \left(\frac{A_{TS}}{A_{SS}}\right)^2\right)}{P_{SS} - P_{TS}} \tag{3.14}$$

Because model surface pressure taps were referenced to the test section static ports, the (P_s-P_∞) term was obtained from a single measurement.

The model lift (using the surface pressure method) was calculated by integrating the surface pressures over the model using the trapezoidal method. The force on the model was broken into the normal and axial components. The normal component was perpendicular to the chord line while the axial component was parallel to the chord line. The incremental normal and axial forces per unit span was given by:

$$\Delta FN_i' = \frac{P_i + P_{i+1}}{2}\left(x_{i+1} - x_i\right) \tag{3.15a}$$

$$\Delta FA_i' = \frac{P_i + P_{i+1}}{2}\left(y_{i+1} - y_i\right) \tag{3.15b}$$

Here, the subscript (i) denotes the i-th pressure tap on the model. The pressure taps were numbered sequentially in a loop around the airfoil as shown in Table 3.1. As stated earlier, the surface pressure measurements were referenced to the tunnel static pressure. However, it does not matter what the reference pressure is, as long as they are same for all the pressure taps.

The incremental loads were then summed to get the total normal and axial forces per unit span:

$$FN' = \sum_{i=1}^{N} \Delta FN_i' \tag{3.16a}$$

$$FA' = \sum_{i=1}^{N} \Delta FA_i' \tag{3.16b}$$

The main element and the flap were treated as two separate airfoils and the forces integrated separately before they were added. The normal and the axial forces were transformed into lift using the following equation:

$$L' = FN'\cos(\alpha) - FA'\sin(\alpha) \tag{3.17}$$

The pitching moment was calculated by integrating the incremental pitching moment about the airfoil surface. The incremental pitching moment was derived from the moments about the model ¼ chord due to the incremental normal and axial forces:

$$\Delta FM'_i = \Delta FN'_i \left(x_{\frac{1}{4}c} - \frac{(x_i + x_{i+1})}{2} \right) + \Delta FA'_i \frac{(y_i + y_{i+1})}{2} \tag{3.18}$$

The incremental loads were then summed to get the total pitching moment:

$$M' = \sum_{i=1}^{N} \Delta FM'_i \tag{3.19}$$

As before, the main element and the flap were integrated separately before they were added.

The flap hinge moment was obtained in a manner similar to that of the pitching moment, with the moment that causes the flap to be deflected downward defined as being positive. However, the moment was taken about the flap hinge-line location, and only the flap surface pressures were integrated. The incremental hinge-moment was given by:

$$\Delta FH'_i = \Delta FN'_i \left(x_h - \frac{(x_i + x_{i+1})}{2} \right) + \Delta FA'_i \left(\frac{(y_i + y_{i+1})}{2} - y_h \right) \tag{3.20}$$

This Iwas then integrated to obtain the total flap-hinge moment per unit span:

$$H' = \sum_{i=1}^{N} \Delta F H_i' \tag{3.21}$$

The drag from the wake rake was determined using the method described in Jones.[51] In order to use this method, the wake rake had to be far enough downstream of the model so that the static pressure in the wake was equal to the freestream static pressure upstream of the model. The drag per unit span was calculated using the following equation:

$$D' = \int \left(\sqrt{q_w q_\infty} - q_w \right) dy \tag{3.22}$$

It was necessary to modify the above equation to use terms that were directly measured in the experiment. First, the equation above was rearranged into

$$D' = \int \rho U_w (U_\infty - U_w) dy \tag{3.23}$$

The total pressures in the free stream (g_∞) and in the wake (g_w) are given by

$$g_\infty = P_\infty + \tfrac{1}{2} \rho U_\infty^2 = P_\infty + q_\infty \tag{3.23a}$$

$$g_w = P_w + \tfrac{1}{2} \rho U_w^2 = P_w + q_w \tag{3.23b}$$

A manipulation of the equation (3.18) using (3.19) resulted in

$$D' = \int 2\sqrt{g_w - P_w} \left(\sqrt{g_\infty - P_\infty} - \sqrt{g_w - P_w} \right) dy \tag{3.24}$$

Since $P_w = P_\infty$, the equation above could be manipulated into

$$D' = \int 2\sqrt{q_\infty - (g_\infty - g_w)} \left(\sqrt{q_\infty} - \sqrt{q_\infty - (g_\infty - g_w)} \right) dy \tag{3.25}$$

The term (g_∞ - g_w) was not directly measured in the experiment. The value that was measured was (g_w - P_{amb}) since the total pressure probes in the wake rake was referenced to the atmosphere. This value will be referred to as $P_{0,W}$. The (g_∞ - P_{amb}) value was obtained by averaging the first and the last six (g_w - P_{amb}) measurements of the wake profile since these should have been in the freestream. This averaged value will be referred to as $P_{0,\infty}$. Thus, changing the equation above into

$$D' = \int 2\sqrt{q_\infty - \left(P_{0,\infty} - P_{0,w}\right)}\left(\sqrt{q_\infty} - \sqrt{q_\infty - \left(P_{0,\infty} - P_{0,w}\right)}\right)dy \tag{3.26}$$

resulted in an equation that only contains terms which were directly measured.

The integral above was calculated using the trapezoidal method. Thus, the incremental sectional drag was

$$\Delta D' = \left[\begin{array}{l}\sqrt{q_\infty - \left(P_{0,\infty} - P_{0,w(i)}\right)}\left(\sqrt{q_\infty} - \sqrt{q_\infty - \left(P_{0,\infty} - P_{0,w(i)}\right)}\right) + \\ \sqrt{q_\infty - \left(P_{0,\infty} - P_{0,w(i+1)}\right)}\left(\sqrt{q_\infty} - \sqrt{q_\infty - \left(P_{0,\infty} - P_{0,w(i+1)}\right)}\right)\end{array}\right] dy_{(i)} \tag{3.27}$$

where $dy_{(i)}$ was the distance between the probe (i) and (i+1). The total sectional drag was then

$$D' = \sum_{i=1}^{N} \Delta D_i' \tag{3.28}$$

3.10.2 Force Balance Measurements

The force balance was pre-calibrated by the manufacturer using a second order fit. Because all three components were coupled, a 3x6 calibration matrix was required and is shown below:

$$\begin{Bmatrix} FN(kg) \\ FA(kg) \\ FM(kg \cdot m) \end{Bmatrix} = \begin{bmatrix} 37.7 & 0.03159 & -0.2095 & 0.01094 & 0 & -0.0008465 \\ -0.1607 & 8.3125 & -0.01638 & 0.007084 & 0 & -0.0007660 \\ -0.01299 & -0.005521 & 1.247 & -0.002122 & 0 & 0.0001497 \end{bmatrix} \cdot \begin{Bmatrix} V_N - V_{N,0} \\ V_A - V_{A,0} \\ V_M - V_{M,0} \\ (V_N - V_{N,0})^2 \\ (V_A - V_{A,0})^2 \\ (V_M - V_{M,0})^2 \end{Bmatrix} \quad (3.29)$$

The calibration matrix shown above does not contain any 0th order term. Thus, the zero-load voltage values were subtracted from the raw voltages before they were sent through the calibration matrix. Before each run, the zero load voltages were obtained for every 2 degrees angles of attack from -16° to 16°. The actual zeroes for a particular angle of attack were linearly interpolated from these values.

As with the pressure measurements, the normal and the axial forces were transformed into lift and drag using the following equations:

$$L = FN\cos(\alpha) - FA\sin(\alpha) \quad (3.30a)$$

$$D = FN\sin(\alpha) + FA\cos(\alpha) \quad (3.30b)$$

The airfoil pitching moment could not be directly taken from the balance moment because the model chordline ¼ chord location was not at the center of the balance. Thus, the moment output from the balance was transformed using the following equation in order to obtain the moment about the model ¼ chord.

$$M = FM + FN \cdot x_{offset} - FA \cdot y_{offset} \quad (3.31)$$

In the equitation above, x_{offset} and y_{offset} are the distances (in x and y coordinates) between the model ¼ chord location and the center of the turntable.

The flap hinge moment was calculated using the hinge-moment load cell calibration coefficients (k_h).

$$H = k_h \cdot \left(V_h - V_{h,0}\right) \tag{3.32}$$

As with the force balance, the flap load cell was tared before the runs. Table 3.2 shows the hinge-moment load cell coefficients used in the experiment. A different calibration coefficient was used for each flap deflection angle.

Table 3.2: Hinge-moment load-cell calibration coefficients.

δ_f (deg)	k_h (ft-lb/V)
-10	-0.601
-5	-0.592
0	-0.584
5	-0.574
10	-0.566

3.11 Uncertainty Analysis

An analysis was performed to estimate the uncertainties in the reduced data presented in this study. The purpose of this analysis was not to determine the absolute statistical uncertainty, but rather to provide a reasonable estimate of the uncertainty in the data. As such, where possible, complicated equations were simplified when in doing so, the results were not significantly altered. Also, uncertainty analysis was not done for wind-tunnel wall correction.

A common method for calculating experimental uncertainties is described in Coleman and Steele.[52] The method assumes equations of the following form:

$$r = r\left(X_1, X_2, ..., X_J\right) \tag{3.33}$$

In the equation above, the value of r is calculated from the values of X_i, which are measured in the experiment. If the values X_i are independent of one another, then the uncertainty in r (denoted by U_r) is given by,

$$U_r = \left[\left(\frac{\partial r}{\partial X_1} U_{x_1} \right)^2 + \left(\frac{\partial r}{\partial X_2} U_{x_2} \right)^2 + \cdots + \left(\frac{\partial r}{\partial X_J} U_{x_J} \right)^2 \right]^{1/2} \tag{3.34}$$

where U_{x_i} are the uncertainties in the measured values of X_i.

The freestream dynamic pressure was derived using equation 3.9. The value (P_{SS}-P_{TS}) was derived from a single pressure measurement since the pressure port at the settling section was referenced to the test section. Thus, the uncertainty in the dynamic pressure is given by

$$U_{q_\infty} = \frac{1}{\left(1 - (A_{TS} / A_{SS})\right)} U_{(P_{SS} - P_{TS})} \tag{3.35}$$

The uncertainty in the (P_{SS}-P_{TS}) measurement was 0.001 psi.

3.11.1 Pressure Measurements

Because the surface pressure measurements on the models were referenced to the test section static pressure, the term (P_s-P_∞) in equation (3.14) was obtained directly from a single measurement. Thus, the uncertainty in C_p can be expressed as

$$U_{C_p} = \left[\left(\frac{\partial C_p}{\partial (P_s - P_\infty)} U_{(P_s - P_\infty)} \right)^2 + \left(\frac{\partial C_p}{\partial q_\infty} U_{q_\infty} \right)^2 \right]^{1/2} \tag{3.36}$$

Substituting the following partial derivatives

$$\begin{aligned} \frac{\partial C_p}{\partial (P_s - P_\infty)} &= \frac{1}{q_\infty} \\ \frac{\partial C_p}{\partial q_\infty} &= -\frac{(P_s - P_\infty)}{q_\infty^2} \end{aligned} \tag{3.37}$$

results in

$$U_{C_p} = \left[\left(\frac{1}{q_\infty} U_{(P_s - P_\infty)} \right)^2 + \left(\frac{(P_s - P_\infty)}{q_\infty^2} U_{q_\infty} \right)^2 \right]^{1/2} \tag{3.38}$$

as the uncertainty of the pressure coefficient. The uncertainty in the (P_s-P_∞) measurement was 0.001 psi.

Equation (3.16a) shows the equation used in the data reduction code to calculate the normal force per unit span (FN') from the pressure measurements. However, for uncertainty analysis, it can be simplified even further. Expanding equation (3.16a) results in

$$\begin{aligned} FN' = \frac{1}{2}(P_1 + P_2)(x_2 - x_1) + \frac{1}{2}(P_2 + P_3)(x_3 - x_2) + \\ \frac{1}{2}(P_3 + P_4)(x_4 - x_3) + \cdots \frac{1}{2}(P_{N-1} + P_N)(x_N - x_{N-1}) \end{aligned} \tag{3.39}$$

Further expanding and then factoring out the pressure terms results in

$$\begin{aligned} FN' = P_1(x_2 - x_1) + P_2(x_3 - x_1) + P_3(x_4 - x_2) + P_4(x_5 - x_3) + \cdots \\ P_i(x_{i+1} - x_{i-1}) + \cdots P_N(x_N - x_{N-1}) \end{aligned} \tag{3.40}$$

Ignoring the first and last terms for simplicity results in the following approximation:

$$FN' \approx \sum_{i=2}^{N-1} P_i (x_{i+1} - x_{i-1}) \tag{3.41}$$

Similarly, the axial force per unit span (FA') shown in equation (3.16b) can be simplified and approximated to

$$FA' \approx \sum_{i=2}^{N-1} P_i (y_{i+1} - y_{i-1}) \tag{3.42}$$

If equation (3.17) is expanded using the equations (3.41) and (3.42),

$$\begin{aligned} L' \approx & \frac{1}{2}P_2(x_3 - x_1)\cos\alpha + \frac{1}{2}P_3(x_4 - x_2)\cos\alpha + \cdots \frac{1}{2}P_{N-1}(x_N - x_{N-2})\cos\alpha \\ & \frac{1}{2}P_2(y_3 - y_1)\sin\alpha + \frac{1}{2}P_3(y_4 - y_2)\sin\alpha + \cdots \frac{1}{2}P_{N-1}(y_N - y_{N-2})\sin\alpha \end{aligned} \tag{3.43}$$

The uncertainty in *L'* is given by

$$U_{L'} = \left[\sum_{i=2}^{N-2} \left(\frac{\partial L'}{\partial P_i} U_{p_i} \right)^2 + \left(\frac{\partial L'}{\partial \alpha} U_\alpha \right)^2 \right]^{1/2} \tag{3.44}$$

Substituting the following partial derivatives

$$\begin{aligned} \frac{\partial L'}{\partial P_i} &= \frac{1}{2}(x_{i+1} - x_{i-1})\cos\alpha + \frac{1}{2}(y_{i+1} - y_{i-1})\sin\alpha \\ \frac{\partial L'}{\partial \alpha} &= -\sum_{i=2}^{N-2} P_i(x_{i+1} - x_{i-1})\sin\alpha + \sum_{i=2}^{N-2} P_i(y_{i+1} - y_{i-1})\cos\alpha \end{aligned} \tag{3.45}$$

results in

$$U_{L'} = \left[\sum_{i=2}^{N-2} \left(\left(\frac{1}{2}(x_{i+1} - x_{i-1})\cos\alpha + \frac{1}{2}(y_{i+1} - y_{i-1})\sin\alpha \right) U_{p_i} \right)^2 + \left(\left\{ -\sum_{i=2}^{N-2} P_i(x_{i+1} - x_{i-1})\sin\alpha + \sum_{i=2}^{N-2} P_i(y_{i+1} - y_{i-1})\cos\alpha \right\} U_\alpha \right)^2 \right]^{1/2} \tag{3.46}$$

as the uncertainty in the sectional lift value. Using the definition of the lift coefficient (3.1a), the uncertainty can be expressed as

$$U_{C_l} = \left[\left(\frac{\partial C_l}{\partial L'} U_{L'} \right)^2 + \left(\frac{\partial C_l}{\partial q_\infty} U_{q_\infty} \right)^2 + \left(\frac{\partial C_l}{\partial c} U_c \right)^2 \right]^{1/2} \tag{3.47}$$

Applying the following partial derivates

$$\begin{aligned} \frac{\partial C_l}{\partial L'} &= \frac{1}{q_\infty c} \\ \frac{\partial C_l}{\partial q_\infty} &= -\frac{L'}{q_\infty^2 c} \\ \frac{\partial C_l}{\partial c} &= -\frac{L'}{q_\infty c^2} \end{aligned} \tag{3.48}$$

results in

$$U_{C_l} = \left[\left(\frac{1}{q_\infty c} U_{L'} \right)^2 + \left(\frac{L}{q_\infty^2 c} U_{q_\infty} \right)^2 + \left(\frac{L}{q_\infty c^2} U_c \right)^2 \right]^{1/2} \tag{3.49}$$

as the uncertainty in the lift coeffcient.

The uncertainty for the pitching moment coefficient was derived in a similar fashion. Expanding the moment equation (3.19) results in

$$\begin{aligned} M' = {} & \frac{1}{2}(P_1 + P_2)(x_2 - x_1)\left(x_{c/4} - \frac{x_1 + x_2}{2} \right) + \frac{1}{2}(P_1 + P_2)(y_2 - y_1)\left(\frac{y_1 + y_2}{2} \right) \\ & + \frac{1}{2}(P_2 + P_3)(x_3 - x_2)\left(x_{c/4} - \frac{x_2 + x_3}{2} \right) + \frac{1}{2}(P_2 + P_3)(y_3 - y_2)\left(\frac{y_2 + y_3}{2} \right) \\ & + \frac{1}{2}(P_3 + P_4)(x_4 - x_3)\left(x_{c/4} - \frac{x_3 + x_4}{2} \right) + \frac{1}{2}(P_3 + P_4)(y_4 - y_3)\left(\frac{y_3 + y_4}{2} \right) \\ & + \frac{1}{2}(P_3 + P_4)(x_4 - x_3)\left(x_{c/4} - \frac{x_3 + x_4}{2} \right) + \frac{1}{2}(P_3 + P_4)(y_4 - y_3)\left(\frac{y_3 + y_4}{2} \right) \\ & + ... \\ & + \frac{1}{2}(P_{N-1} + P_N)(x_N - x_{N-1})\left(x_{c/4} - \frac{x_{N-1} + x_N}{2} \right) + \frac{1}{2}(P_{N-1} + P_N)(y_N - y_{N-1})\left(\frac{y_{N-1} + y_N}{2} \right) \end{aligned} \tag{3.50}$$

Expanding the equation above further and factoring out the pressure terms results in

$$\begin{aligned} M' = \frac{1}{4}\Big[& P_1(....) + P_2\left(x_1^2 - x_3^2 - 2x_1x_{c/4} + 2x_3x_{c/4} - y_1^2 + y_3^2\right) \\ & + P_3\left(x_2^2 - x_4^2 - 2x_2x_{c/4} + 2x_4x_{c/4} - y_2^2 + y_4^2\right) \\ & + P_4\left(x_3^2 - x_5^2 - 2x_3x_{c/4} + 2x_5x_{c/4} - y_3^2 + y_5^2\right) \\ & + ... + P_N(....)\Big] \end{aligned} \tag{3.51}$$

If the P_1 and P_N terms are ignored for simplicity, then the moment can be approximated by

$$M' \approx \frac{1}{4}\sum_{i=2}^{N-1} P_i\left(x_{i-1}^2 - x_{i+1}^2 - 2x_{i-1}x_{c/4} + 2x_{i+1}x_{c/4} - y_{i-1}^2 + y_{i+1}^2\right) \tag{3.52}$$

The uncertainty in the sectional moment is given by

$$U_{M'} = \left[\sum_{i=2}^{N-2}\left(\frac{\partial M'}{\partial P_i}U_{P_i}\right)^2\right]^{1/2} \tag{3.53}$$

Substituting the following partial derivative

$$\frac{\partial M'}{\partial p_i} = \frac{1}{4}\left(x_{i-1}^2 - x_{i+1}^2 - 2x_{i-1}x_{c/4} + 2x_{i+1}x_{c/4} - y_{i-1}^2 + y_{i+1}^2\right) \tag{3.54}$$

results in

$$U_{M'} = \left[\sum_{i=2}^{N-1}\left(\frac{1}{4}\left(x_{i-1}^2 - x_{i+1}^2 - 2x_{i-1}x_{c/4} + 2x_{i+1}x_{c/4} - y_{i-1}^2 + y_{i+1}^2\right)U_{P_i}\right)^2\right]^{1/2} \tag{3.55}$$

as the uncertainty in the pitching moment per unit span. Using the definition of the pitching moment coefficient (3.1b), the uncertainty can be expressed as

$$U_{C_m} = \left[\left(\frac{\partial C_m}{\partial M'} U_{M'} \right)^2 + \left(\frac{\partial C_m}{\partial q_\infty} U_{q_\infty} \right)^2 + \left(\frac{\partial C_m}{\partial c} U_c \right)^2 \right]^{1/2} \tag{3.56}$$

Applying the following partial derivates

$$\begin{aligned} \frac{\partial C_m}{\partial M'} &= \frac{1}{q_\infty c^2} \\ \frac{\partial C_m}{\partial q_\infty} &= -\frac{M'}{q_\infty^2 c^2} \\ \frac{\partial C_m}{\partial c} &= -\frac{2M'}{q_\infty c^3} \end{aligned} \tag{3.57}$$

results in

$$U_{C_m} = \left[\left(\frac{1}{q_\infty c^2} U_{M'} \right)^2 + \left(\frac{M'}{q_\infty^2 c^2} U_{q_\infty} \right)^2 + \left(\frac{2M'}{q_\infty c^3} U_c \right)^2 \right]^{1/2} \tag{3.58}$$

as the uncertainty in the pitching-moment coefficient.

The uncertainty for the hinge-moment coefficient was derived similarly. Expanding the hinge moment equation (3.21) results in

$$\begin{aligned} H' = {} & \frac{1}{2}(P_1 + P_2)(x_2 - x_1)\left(x_h - \frac{x_1 + x_2}{2} \right) + \frac{1}{2}(P_1 + P_2)(y_2 - y_1)\left(\frac{y_1 + y_2}{2} - y_h \right) \\ & + \frac{1}{2}(P_2 + P_3)(x_3 - x_2)\left(x_h - \frac{x_2 + x_3}{2} \right) + \frac{1}{2}(P_2 + P_3)(y_3 - y_2)\left(\frac{y_2 + y_3}{2} - y_h \right) \\ & + \frac{1}{2}(P_3 + P_4)(x_4 - x_3)\left(x_h - \frac{x_3 + x_4}{2} \right) + \frac{1}{2}(P_3 + P_4)(y_4 - y_3)\left(\frac{y_3 + y_4}{2} - y_h \right) \\ & + ... \\ & + \frac{1}{2}(P_{N-1} + P_N)(x_N - x_{N-1})\left(x_h - \frac{x_{N-1} + x_N}{2} \right) + \frac{1}{2}(P_{N-1} + P_N)(y_N - y_{N-1})\left(\frac{y_{N-1} + y_N}{2} - y_h \right) \end{aligned} \tag{3.59}$$

Expanding the equation above further and factoring out the pressure terms results in

$$\begin{aligned} H' = \frac{1}{4}\big[& P_1(....) + P_2\left(x_1^2 - x_3^2 - 2x_1x_h + 2x_3x_h - y_1^2 + y_3^2 + 2y_1y_h - 2y_3y_h\right) \\ & + P_3\left(x_2^2 - x_4^2 - 2x_2x_h + 2x_4x_h - y_2^2 + y_4^2 + 2y_2y_h - 2y_4y_h\right) \\ & + P_4\left(x_3^2 - x_5^2 - 2x_3x_h + 2x_5x_h - y_3^2 + y_5^2 + 2y_3y_h - 2y_5y_h\right) \\ & + ... + P_N(....)\big] \end{aligned} \tag{3.60}$$

If the P_1 and P_N terms are ignored for simplicity, then the moment can be approximated by

$$F' \approx \frac{1}{4}\sum_{i=2}^{N-1} P_i\left(x_{i-1}^2 - x_{i+1}^2 - 2x_{i-1}x_h + 2x_{i+1}x_h + 2y_{i-1}x_h + 2y_{i+1}y_h - y_{i-1}^2 + y_{i+1}^2\right) \tag{3.61}$$

The uncertainty in the sectional moment is given by

$$U_{H'} = \left[\sum_{i=2}^{N-1}\left(\frac{\partial H'}{\partial P_i}U_{P_i}\right)^2\right]^{1/2} \tag{3.62}$$

Substituting the following partial derivative

$$\frac{\partial H'}{\partial P_i} = \frac{1}{4}\left(x_{i-1}^2 - x_{i+1}^2 - 2x_{i-1}x_h + 2x_{i+1}x_h - y_{i-1}^2 + y_{i+1}^2 + 2y_{i-1}y_h - 2y_{i+1}y_h\right) \tag{3.63}$$

results in

$$U_{H'} = \left[\sum_{i=2}^{N-1}\left(\frac{1}{4}\left(x_{i-1}^2 - x_{i+1}^2 - 2x_{i-1}x_h + 2x_{i+1}x_h - y_{i-1}^2 + y_{i+1}^2 + 2y_{i-1}y_h - 2y_{i+1}y_h\right)U_{P_i}\right)^2\right]^{1/2} \tag{3.64}$$

as the uncertainty in the pitching moment per unit span. Using the definition of the pitching moment coefficient (3.1b), the uncertainty can be expressed as

$$U_{C_h} = \left[\left(\frac{\partial C_h}{\partial H'} U_{M'} \right)^2 + \left(\frac{\partial C_h}{\partial q_\infty} U_{q_\infty} \right)^2 + \left(\frac{\partial C_h}{\partial c_f} U_{c_f} \right)^2 \right]^{1/2} \tag{3.65}$$

Applying the following partial derivates

$$\begin{aligned} \frac{\partial C_h}{\partial M'} &= \frac{1}{q_\infty c_f^2} \\ \frac{\partial C_h}{\partial q_\infty} &= -\frac{H'}{q_\infty^2 c_f^2} \\ \frac{\partial C_h}{\partial c} &= -\frac{2H'}{q_\infty c_f^3} \end{aligned} \tag{3.66}$$

results in

$$U_{C_h} = \left[\left(\frac{1}{q_\infty c_f^2} U_{H'} \right)^2 + \left(\frac{H'}{q_\infty^2 c_f^2} U_{q_\infty} \right)^2 + \left(\frac{2H'}{q_\infty c_f^3} U_{c_f} \right)^2 \right]^{1/2} \tag{3.67}$$

as the uncertainty in the pitching-moment coefficient. In the lift, pitching moment, and hinge moment uncertainty equations shown above, the uncertainty in the individual surface pressure tap term was 0.001 psi if the 1 psid ESP module was used and 0.005 psi if the 5 PSID module was used.

The uncertainty in the drag measured from the wake was obtained first by reworking equation (3.28) into

$$D' = \sum_{i=1}^{N} \left[\begin{array}{l} \sqrt{q_\infty^2 - q_\infty \left(P_{0,\infty} - P_{0,w(i)} \right)} - \left(q_\infty - \left(P_{0,\infty} - P_{0,w(i)} \right) \right) + \\ \sqrt{q_\infty^2 - q_\infty \left(P_{0,\infty} - P_{0,w(i+1)} \right)} - \left(q_\infty - \left(P_{0,\infty} - P_{0,w(i+1)} \right) \right) \end{array} \right] dy_{(i)} \tag{3.68}$$

Expanding the equation above results in

$$
\begin{aligned}
D' = & \left[\begin{array}{l} \sqrt{q_\infty^2 - q_\infty\left(P_{0,\infty} - P_{0,w(1)}\right)} - q_\infty + P_{0,\infty} - P_{0,w(1)} + \\ \sqrt{q_\infty^2 - q_\infty\left(P_{0,\infty} - P_{0,w(2)}\right)} - q_\infty + P_{0,\infty} - P_{0,w(2)} \end{array} \right] dy_{(1)} \\
& + \left[\begin{array}{l} \sqrt{q_\infty^2 - q_\infty\left(P_{0,\infty} - P_{0,w(2)}\right)} - q_\infty + P_{0,\infty} - P_{0,w(2)} + \\ \sqrt{q_\infty^2 - q_\infty\left(P_{0,\infty} - P_{0,w(3)}\right)} - q_\infty + P_{0,\infty} - P_{0,w(3)} \end{array} \right] dy_{(2)} \\
& + \left[\begin{array}{l} \sqrt{q_\infty^2 - q_\infty\left(P_{0,\infty} - P_{0,w(3)}\right)} - q_\infty + P_{0,\infty} - P_{0,w(3)} + \\ \sqrt{q_\infty^2 - q_\infty\left(P_{0,\infty} - P_{0,w(4)}\right)} - q_\infty + P_{0,\infty} - P_{0,w(4)} \end{array} \right] dy_{(3)} \\
& + \cdots \\
& + \left[\begin{array}{l} \sqrt{q_\infty^2 - q_\infty\left(P_{0,\infty} - P_{0,w(N-1)}\right)} - q_\infty + P_{0,\infty} - P_{0,w(N-1)} + \\ \sqrt{q_\infty^2 - q_\infty\left(P_{0,\infty} - P_{0,w(N)}\right)} - q_\infty + P_{0,\infty} - P_{0,w(N)} \end{array} \right] dy_{(N-1)}
\end{aligned}
\tag{3.69}
$$

Because $dy_{(i)}$ are constant across the wake rake except at the ends, where the distance between the ports doubles, $dy_{(i)} = dy_{(i+1)}$ everywhere except at two location. Thus, for simplicity, it was assumed that $dy_{(i)} = dy_{(i+1)}$ everywhere, and the equation above can be rearranged into

$$
\begin{aligned}
D' = & \left(\sqrt{q_\infty^2 - q_\infty\left(P_{0,\infty} - P_{0,w(1)}\right)} - q_\infty + P_{0,\infty} - P_{0,w(1)} \right) dy_{(1)} \\
& + 2\left(\sqrt{q_\infty^2 - q_\infty\left(P_{0,\infty} - P_{0,w(2)}\right)} - q_\infty + P_{0,\infty} - P_{0,w(2)} \right) dy_{(2)} \\
& + 2\left(\sqrt{q_\infty^2 - q_\infty\left(P_{0,\infty} - P_{0,w(3)}\right)} - q_\infty + P_{0,\infty} - P_{0,w(3)} \right) dy_{(3)} \\
& + \cdots \\
& + \left(\sqrt{q_\infty^2 - q_\infty\left(P_{0,\infty} - P_{0,w(N)}\right)} - q_\infty + P_{0,\infty} - P_{0,w(N)} \right) dy_{(N)}
\end{aligned}
\tag{3.70}
$$

Ignoring the first and the Nth term for simplicity, the equation above can be approximated into

$$
D' = \sum_{i=2}^{N-1} 2\left(\sqrt{q_\infty^2 - q_\infty\left(P_{0,\infty} - P_{0,w(i)}\right)} - q_\infty + P_{0,\infty} - P_{0,w(i)} \right) dy_{(i)} \tag{3.71}
$$

Substituting equation (3.71) into (3.1b) results in

$$C_d = \frac{1}{q_\infty c}\sum_{i=2}^{N-1} 2\left(\sqrt{q_\infty^2 - q_\infty\left(P_{0,\infty} - P_{0,w(i)}\right)} - q_\infty + P_{0,\infty} - P_{0,w(i)}\right)dy_{(i)} \tag{3.72}$$

which can be rearranged into

$$C_d = \frac{2}{c}\sum_{i=2}^{N-1}\left(\sqrt{1 - \frac{\left(P_{0,\infty} - P_{0,w(i)}\right)}{q_\infty}} - 1 + \frac{P_{0,\infty} - P_{0,w(i)}}{q_\infty}\right)dy_{(i)} \tag{3.73}$$

The uncertainty for the drag coefficient is expressed as

$$U_{C_d} = \left[\sum_{i=2}^{N-1}\left(\frac{\partial C_d}{\partial P_{0,w(i)}}U_{p_{0,w(i)}}\right)^2 + \left(\frac{\partial C_d}{\partial P_{0,\infty}}U_{p_{0,\infty}}\right)^2 + \left(\frac{\partial C_d}{\partial q_\infty}U_{q_\infty}\right)^2\right]^{1/2} \tag{3.74}$$

Using the following derivatives

$$\frac{\partial C_d}{\partial P_{0,w(i)}} = \frac{2}{c}\left(\frac{1}{2\sqrt{q_\infty^2 + q_\infty\left(P_{0,w(i)} - P_{0,\infty}\right)}} - \frac{1}{q_\infty}\right)dy_{(i)} \tag{3.75a}$$

$$\frac{\partial C_d}{\partial P_{0,\infty}} = \frac{2}{c}\sum_{i=2}^{N-1}\left(-\frac{1}{2\sqrt{q_\infty^2 + q_\infty\left(P_{0,w(i)} - P_{0,\infty}\right)}} + \frac{1}{q_\infty}\right)dy_{(i)} \tag{3.75b}$$

$$\frac{\partial C_d}{\partial q_\infty} = \frac{2}{c}\sum_{i=2}^{N-1}\left(\frac{\left(\frac{P_{0,\infty} - P_{0,w(i)}}{q_\infty^2}\right)}{\sqrt{1 + \frac{\left(P_{0,w(i)} - P_{0,\infty}\right)}{q_\infty}}} + \frac{P_{0,w(i)} - P_{0,\infty}}{q_\infty}\right)dy_{(i)} \tag{3.75c}$$

results in the following expression for the uncertainty of the drag coefficient:

$$U_{C_d} = \left[\begin{array}{l} \sum_{i=2}^{N-1} \left(\frac{2}{c} \left(\frac{1}{2\sqrt{q_\infty^2 + q_\infty \left(P_{0,w(i)} - P_{0,\infty} \right)}} - \frac{1}{q_\infty} \right) dy_{(i)} U_{p_{0,w(i)}} \right)^2 \\ + \left(\frac{2}{c} \sum_{i=2}^{N-1} \left(- \frac{1}{2\sqrt{q_\infty^2 + q_\infty \left(P_{0,w(i)} - P_{0,\infty} \right)}} + \frac{1}{q_\infty} \right) dy_{(i)} U_{p_{0,\infty}} \right)^2 \\ + \left(\frac{2}{c} \sum_{i=2}^{N-1} \left(\frac{\left(\frac{P_{0,\infty} - P_{0,w(i)}}{q_\infty^2} \right)}{\sqrt{1 + \frac{\left(P_{0,w(i)} - P_{0,\infty} \right)}{q_\infty}}} + \frac{P_{0,w(i)} - P_{0,\infty}}{q_\infty} \right) dy_{(i)} U_{q_\infty} \right)^2 \end{array} \right] \tag{3.76}$$

In the drag uncertainty equation above, the uncertainty of individual wake pressure port measurement was 0.00035 psi.

3.11.2 Force Balance Measurements

The aerodynamic coefficients derived from the force balance are given by

$$\begin{aligned} C_\ell &= \frac{L}{q_\infty bc} \\ C_d &= \frac{D}{q_\infty bc} \\ C_m &= \frac{M}{q_\infty bc^2} \\ C_h &= \frac{H}{q_\infty bc_f^2} \end{aligned} \tag{3.77}$$

Applying equation (3.29) to the equation above yields

$$
\begin{aligned}
U_{C_\ell} &= \left[\left(\frac{1}{q_\infty bc}U_L\right)^2 + \left(\frac{L}{q_\infty^2 bc}U_{q_\infty}\right)^2 + \left(\frac{L}{q_\infty b^2 c}U_b\right)^2 + \left(\frac{L}{q_\infty bc^2}U_c\right)^2\right]^{1/2} \\
U_{C_d} &= \left[\left(\frac{1}{q_\infty bc}U_D\right)^2 + \left(\frac{D}{q_\infty^2 bc}U_{q_\infty}\right)^2 + \left(\frac{D}{q_\infty b^2 c}U_b\right)^2 + \left(\frac{D}{q_\infty bc^2}U_c\right)^2\right]^{1/2} \\
U_{C_m} &= \left[\left(\frac{1}{q_\infty bc^2}U_M\right)^2 + \left(\frac{M}{q_\infty^2 bc^2}U_{q_\infty}\right)^2 + \left(\frac{M}{q_\infty b^2 c^2}U_b\right)^2 + \left(\frac{2M}{q_\infty bc^3}U_c\right)^2\right]^{1/2} \\
U_{C_h} &= \left[\left(\frac{1}{q_\infty bc_f^2}U_H\right)^2 + \left(\frac{H}{q_\infty^2 bc_f^2}U_{q_\infty}\right)^2 + \left(\frac{H}{q_\infty b^2 c_f^2}U_b\right)^2 + \left(\frac{2H}{q_\infty bc_f^3}U_c\right)^2\right]^{1/2}
\end{aligned}
\tag{3.78}
$$

From equation (3.30a), the uncertainty in L is derived as,

$$
U_L = \left(\left(\frac{\partial L}{\partial FN}U_{FN}\right)^2 + \left(\frac{\partial L}{\partial FA}U_{FA}\right)^2 + \left(\frac{\partial L}{\partial \alpha}U_\alpha\right)^2\right)^{1/2} \tag{3.79}
$$

Using the following partial derivatives

$$
\begin{aligned}
\frac{\partial L}{\partial FN} &= \cos(\alpha) \\
\frac{\partial L}{\partial FA} &= -\sin(\alpha) \\
\frac{\partial L}{\partial \alpha} &= -FN\sin(\alpha) - FA\cos(\alpha)
\end{aligned}
\tag{3.80}
$$

the uncertainty in lift can be expressed as

$$
U_L = \left((\cos(\alpha)U_{FN})^2 + (\sin(\alpha)U_{FA})^2 + \left((-FN\sin(\alpha) - FA\cos(\alpha))^2 U_\alpha\right)^2\right)^{1/2} \tag{3.81}
$$

From equation (3.30b), the uncertainty in D is derived as,

$$U_D = \left(\left(\frac{\partial D}{\partial FN} U_{FN} \right)^2 + \left(\frac{\partial D}{\partial FA} U_{FA} \right)^2 + \left(\frac{\partial D}{\partial \alpha} U_{\alpha} \right)^2 \right)^{1/2} \tag{3.82}$$

Using the following partial derivatives

$$\begin{aligned} \frac{\partial D}{\partial FN} &= \sin(\alpha) \\ \frac{\partial D}{\partial FA} &= \cos(\alpha) \\ \frac{\partial D}{\partial \alpha} &= FN\cos(\alpha) - FA\sin(\alpha) \end{aligned} \tag{3.83}$$

the uncertainty in drag can be expressed as

$$U_D = \left((\sin(\alpha) U_{FN})^2 + (\cos(\alpha) U_{FA})^2 + \left((FN\cos(\alpha) - FA\sin(\alpha))^2 U_{\alpha} \right)^2 \right)^{1/2} \tag{3.84}$$

From equation (3.26), the uncertainty in M is derived as,

$$U_M = \left(\begin{array}{l} \left(\frac{\partial M}{\partial FM} U_{FM} \right)^2 + \left(\frac{\partial M}{\partial FN} U_{FN} \right)^2 + \left(\frac{\partial M}{\partial FA} U_{FA} \right)^2 \\ + \left(\frac{\partial M}{\partial x_{offset}} U_{x_{offset}} \right)^2 + \left(\frac{\partial M}{\partial y_{offset}} U_{y_{offset}} \right)^2 \end{array} \right)^{1/2} \tag{3.85}$$

Using the following partial derivatives

$$\begin{aligned}
\frac{\partial M}{\partial FM} &= 1 \\
\frac{\partial M}{\partial FN} &= x_{offset} \\
\frac{\partial M}{\partial FA} &= -y_{offset} \\
\frac{\partial M}{\partial x_{offset}} &= FN \\
\frac{\partial M}{\partial y_{offset}} &= -FA
\end{aligned} \tag{3.86}$$

the uncertainty in the pitching moment can be expressed as

$$U_M = \begin{pmatrix} (U_{FM})^2 + (x_{offset} U_{FN})^2 + (y_{offset} U_{FA})^2 \\ + (FN \cdot U_{x_{offset}})^2 + (-FA \cdot U_{y_{offset}})^2 \end{pmatrix}^{1/2} \tag{3.87}$$

From equation (3.32), the uncertainty in H is derived as,

$$U_H = \left(\left(\frac{\partial H}{\partial k_h} U_{k_h} \right)^2 + \left(\frac{\partial H}{\partial V_h} U_{V_h} \right)^2 + \left(\frac{\partial H}{\partial V_{h,0}} U_{V_{h,0}} \right)^2 \right)^{1/2} \tag{3.88}$$

Using the following partial derivatives

$$\begin{aligned}
\frac{\partial H}{\partial k_h} &= V_h - V_{h,0} \\
\frac{\partial H}{\partial V_h} &= k_h \\
\frac{\partial H}{\partial V_{h,0}} &= -k_h
\end{aligned} \tag{3.89}$$

the uncertainty in the hinge moment can be expressed as

$$U_H = \left(\left(\left(V_h - V_{h,0}\right)U_{k_h}\right)^2 + \left(k_h U_{V_h}\right)^2 + \left(k_h U_{V_{h,0}}\right)^2\right)^{1/2} \tag{3.90}$$

Equations (3.81, 3.84, 3.87, 3.90) can be substituted into equation (3.78) in order to calculate the uncertainty in the aerodynamic coefficients from the force balance. The uncertainty in the FN, FA, and FM terms were 0.09 lb, 0.027 lb, and 0.0675 ft-lb, respectively. The uncertainty in V_h and $V_{h,0}$ terms were both 0.075 ft-lb. The uncertainty in k_h term was 0.018 ft-lb/V.

3.11.3 Summary of Uncertainties

Shown in this section is a sample of the experimental uncertainty for a typical case. These values were obtained from the case with the ¼" forward-facing quarter round at x/c = 0.10 on the NACA 23012m. The Reynolds number was 1.8 million and the angle of attack was 5°.

Table 3.3 shows the uncertainties for the variables that have constant absolute uncertainties for all of the runs. Table 3.4 shows the uncertainties of the pressure-based measurements, including the drag measured with the wake rake. Table 3.5 shows the uncertainties of the force balance and flap hinge-moment balance measurements.

Table 3.3: Variables with constant uncertainties.

Variable	Reference Value	Absolute Uncertainty	Relative Uncertainty (%)
α	5°	0.02°	0.4
q_∞	0.329 psi	0.001 psi	0.3
c	18 in	0.01 in	0.06
b	33.375 in	0.05 in	0.15
c_f	3.978 in	0.01 in	0.25

Table 3.4: Pressure-based measurement uncertainties.

Variable	Reference Value	Absolute Uncertainty	Relative Uncertainty (%)
C_p	-0.712	0.0037	0.52
L'	20.04 lb/ft	0.09 lb/ft	0.449
D'	11.23 lb/ft	N/A	N/A
M'	-8.389 lb	0.0681 lb	0.812
H'	-0.317 lb	0.00214 lb	0.675
C_l	0.282	0.00153	0.543
C_d	0.158	0.00147	0.93
C_m	-0.0787	0.000687	0.873
C_h	-0.0612	0.000543	0.887

Table 3.5: Force balance-based measurement uncertainties.

Variable	Reference Value	Absolute Uncertainty	Relative Uncertainty (%)
L	58.31 lb	0.235 lb	0.403
D	25.1 lb	0.919 lb	3.66
M	-23.45 ft-lb	0.0825 ft-lb	0.352
H	-0.724 ft-lb	0.065 ft-lb	8.98
C_l	0.295	0.00155	0.525
C_d	0.127	0.00463	3.65
C_m	-0.0791	0.0003927	0.496
C_h	-0.05	0.00447	8.94

The uncertainty in the wake drag (D') was not calculated because (D') term was never calculated and the equation was extremely complicated. The absolute uncertainty in the wake-drag coefficient (C_d) appears rather high. However, this was due to a very large value of C_d since the uncertainty was directly related to the value of C_d. The uncertainty of the clean model was much lower. The uncertainty of the hinge moment obtained from the pressure measurement was an order of magnitude lower than that of the balance. However, this does not take into consideration of the fairly sparse pressure tap distribution on the flap. Because of this, it does not mean the hinge moment value from the pressure measurements was 10 times as accurate as that from the force balance.

Chapter 4

Results and Discussion

4.1 NACA 23012 modification

As stated in the previous section, the NACA 23012 airfoil that was used in this experiment had coordinates were generated through XFOIL by selecting the standard NACA 23012 configuration. However, XFOIL generated thickness normal to the chord line instead of the mean camber line, producing small differences when compared to a conventional NACA 23012. This was especially noticeable near the leading edge where the airfoil has the greatest amount of camber. The result was a slightly drooped leading edge with a maximum vertical coordinate shift of 0.4% chord as compared to the conventional NACA 23012. In addition, because of errors in the manufacture of the model, the maximum thickness was 12.2% instead of the standard 12%. The coordinates for the standard NACA 23012 and the modified NACA 23012 (as measured using a digital coordinate measurement machine) are shown in Tables 4.1 and 4.2. These are plotted and compared in Fig. 4.1. Figure 4.1a shows that, overall, these two airfoils were nearly identical. The largest differences were found near the leading edge, as Fig. 4.1b shows. Because of these differences, the airfoil model used in this study was called NACA 23012m.

The slight change in the airfoil geometry did not significantly alter the airfoil aerodynamic characteristics. Figure 4.2a shows the lift curve comparison between the two airfoils. The results were obtained from XFOIL[53] with both of the airfoils at a Reynolds number of 1.8 million. It shows nearly identical values of C_l in the linear

region of the lift curve, with very similar lift curve slope, as Table 4.3 shows. The NACA 23102m had a slightly higher $C_{l,max}$ (1.61) when compared to the standard NACA 23012 (1.57) due to increased camber.

Table 4.1: Standard NACA 23012 coordinates.

Upper Surface			
x/c	y/c	x/c	y/c
0.00000	0.00000	0.30824	0.07530
-0.00052	0.00241	0.32252	0.07489
-0.00065	0.00491	0.33707	0.07440
-0.00036	0.00751	0.35187	0.07380
0.00035	0.01019	0.36691	0.07312
0.00148	0.01295	0.38220	0.07234
0.00304	0.01580	0.39773	0.07148
0.00503	0.01871	0.41349	0.07052
0.00747	0.02169	0.42947	0.06948
0.01035	0.02471	0.44567	0.06834
0.01368	0.02778	0.46208	0.06713
0.01747	0.03087	0.47870	0.06583
0.02170	0.03397	0.49552	0.06445
0.02639	0.03706	0.51253	0.06299
0.03154	0.04013	0.52973	0.06145
0.03713	0.04316	0.54711	0.05983
0.04317	0.04612	0.56466	0.05814
0.04966	0.04901	0.58238	0.05637
0.05658	0.05181	0.60026	0.05453
0.06393	0.05449	0.61829	0.05263
0.07170	0.05705	0.63647	0.05065
0.07987	0.05946	0.65479	0.04861
0.08844	0.06172	0.67324	0.04650
0.09738	0.06381	0.69181	0.04433
0.10669	0.06573	0.71050	0.04209
0.11635	0.06746	0.72931	0.03979
0.12635	0.06901	0.74821	0.03743
0.13665	0.07038	0.76721	0.03501
0.14724	0.07156	0.78631	0.03253
0.15812	0.07257	0.80548	0.02999
0.16924	0.07342	0.82472	0.02739
0.18060	0.07411	0.84404	0.02473
0.19218	0.07467	0.86341	0.02201
0.20395	0.07512	0.88283	0.01923
0.21597	0.07547	0.90230	0.01639
0.22829	0.07573	0.92180	0.01349
0.24090	0.07590	0.94133	0.01053
0.25381	0.07597	0.96089	0.00750
0.26700	0.07594	0.98045	0.00441
0.28047	0.07582	1.00000	0.00126
0.29422	0.07561		

Lower Surface			
x/c	y/c	x/c	y/c
0.00000	0.00000	0.30559	-0.04469
0.00091	-0.00229	0.31988	-0.04491
0.00219	-0.00444	0.33443	-0.04506
0.00383	-0.00646	0.34924	-0.04512
0.00582	-0.00834	0.36430	-0.04510
0.00815	-0.01009	0.37961	-0.04500
0.01083	-0.01172	0.39516	-0.04482
0.01383	-0.01324	0.41094	-0.04456
0.01715	-0.01465	0.42696	-0.04422
0.02080	-0.01597	0.44319	-0.04381
0.02475	-0.01721	0.45964	-0.04332
0.02900	-0.01837	0.47630	-0.04275
0.03356	-0.01946	0.49317	-0.04211
0.03841	-0.02050	0.51023	-0.04141
0.04355	-0.02149	0.52748	-0.04063
0.04899	-0.02245	0.54491	-0.03978
0.05471	-0.02338	0.56252	-0.03886
0.06073	-0.02428	0.58030	-0.03788
0.06704	-0.02518	0.59824	-0.03683
0.07364	-0.02608	0.61634	-0.03572
0.08055	-0.02698	0.63459	-0.03455
0.08776	-0.02789	0.65298	-0.03332
0.09528	-0.02881	0.67150	-0.03203
0.10312	-0.02976	0.69016	-0.03068
0.11129	-0.03072	0.70893	-0.02927
0.11980	-0.03171	0.72781	-0.02780
0.12866	-0.03272	0.74681	-0.02628
0.13788	-0.03375	0.76590	-0.02470
0.14748	-0.03480	0.78508	-0.02306
0.15745	-0.03585	0.80434	-0.02137
0.16782	-0.03690	0.82369	-0.01962
0.17860	-0.03794	0.84310	-0.01782
0.18979	-0.03895	0.86257	-0.01596
0.20141	-0.03991	0.88210	-0.01404
0.21340	-0.04079	0.90167	-0.01206
0.22569	-0.04159	0.92128	-0.01003
0.23829	-0.04231	0.94093	-0.00793
0.25118	-0.04295	0.96059	-0.00577
0.26436	-0.04351	0.98028	-0.00355
0.27782	-0.04398	1.00000	-0.00126
0.29157	-0.04438		

Table 4.2: Modified NACA 23012m coordinates.

Upper Surface			
x/c	y/c	x/c	y/c
0.00001	0.00037	0.26005	0.07687
0.00011	0.00182	0.27779	0.07666
0.00094	0.00555	0.31478	0.07576
0.00170	0.00756	0.35461	0.07419
0.00358	0.01142	0.37689	0.07311
0.00381	0.01181	0.40376	0.07162
0.00765	0.01738	0.42647	0.07021
0.01109	0.02136	0.49844	0.06467
0.01512	0.02536	0.55317	0.05977
0.01961	0.02926	0.58462	0.05673
0.02902	0.03613	0.60356	0.05479
0.03470	0.03971	0.62187	0.05284
0.03892	0.04217	0.63299	0.05162
0.04236	0.04404	0.63913	0.05094
0.05899	0.05188	0.64566	0.05020
0.06478	0.05419	0.65571	0.04906
0.07189	0.05679	0.66687	0.04778
0.08701	0.06153	0.68282	0.04592
0.09457	0.06356	0.70686	0.04307
0.10486	0.06598	0.71858	0.04166
0.11263	0.06757	0.72607	0.04075
0.12141	0.06912	0.73215	0.04000
0.12857	0.07023	0.74520	0.03839
0.15473	0.07333	0.74881	0.03794
0.16089	0.07388	0.80000	0.03117
0.16252	0.07402	0.85000	0.02425
0.18336	0.07541	0.90000	0.01698
0.19975	0.07612	0.95000	0.00933
0.22696	0.07678	1.00000	0.00128
0.24468	0.07691		

Lower Surface			
x/c	y/c	x/c	y/c
0.00008	-0.00141	0.10523	-0.03148
0.00017	-0.00227	0.11551	-0.03262
0.00054	-0.00414	0.11988	-0.03309
0.00117	-0.00584	0.12680	-0.03383
0.00206	-0.00752	0.13376	-0.03457
0.00337	-0.00933	0.14312	-0.03553
0.00448	-0.01055	0.15183	-0.03641
0.00567	-0.01164	0.16268	-0.03747
0.00662	-0.01239	0.18158	-0.03923
0.00716	-0.01280	0.20329	-0.04105
0.00851	-0.01371	0.23507	-0.04322
0.00989	-0.01454	0.26035	-0.04451
0.01142	-0.01535	0.33481	-0.04608
0.01308	-0.01613	0.35556	-0.04612
0.01486	-0.01689	0.40086	-0.04572
0.01584	-0.01728	0.44020	-0.04486
0.02046	-0.01888	0.47542	-0.04373
0.02497	-0.02017	0.56559	-0.03970
0.03150	-0.02166	0.59802	-0.03789
0.03617	-0.02253	0.62621	-0.03614
0.04206	-0.02352	0.66851	-0.03318
0.04908	-0.02456	0.69886	-0.03087
0.05754	-0.02572	0.73450	-0.02800
0.05988	-0.02603	0.75000	-0.02672
0.06545	-0.02676	0.80000	-0.02234
0.07327	-0.02773	0.85000	-0.01762
0.07788	-0.02829	0.90000	-0.01256
0.08615	-0.02928	0.95000	-0.00712
0.08891	-0.02961	1.00000	-0.00128
0.09796	-0.03066		

Table 4.3: Lift curve slopes of the modified NACA 23012m and the standard NACA 23012 airfoils; results from XFOIL, Re = 1.8×10^6.

Airfoil	$C_{l,\alpha}$ **(/deg)**
Modified NACA 23012m	0.1092
Standard NACA 23012	0.1099

Figure 4.3 shows the surface pressure distribution comparisons (again obtained using XFOIL at *Re* = 1.8 million). It shows nearly identical surface pressure distributions at angles of attack of 0° and 5°. At α = 5°, both the modified and the standard NACA

23012 surface pressure distributions contained a discontinuity between 15% and 20% chord which was caused by a laminar separation bubble (this will be explained in more detail in Section 4.3). At $\alpha = 10°$ (where the lift curve started to become nonlinear), there were greater differences in the surface pressure distributions. The modified NACA 23012m airfoil had a $C_{p,min}$ of -4 while the standard NACA 23012 had a $C_{p,min}$ of -4.8. Also, the laminar separation bubble on the modified NACA 23012m was located near x/c = 0.10 while on the standard NACA 23012, it was located near x/c = 0.06. Figures 4.2 and 4.3 show that although the modification of the airfoil geometry caused some changes in aerodynamic characteristics, they were not large and the distinctive aerodynamic characteristics of the NACA 23012 were maintained.

4.2 Experimental Methods Validation

The clean baseline measurements were taken and compared to previously published data in order to validate the experimental apparatus and data reduction methods. The measurements were also compared to the results from XFOIL.

4.2.1 NACA 23012m Validation

Figure 4.4 shows the comparison of the Illinois measurements at Re = 1.8 million (M = 0.18) with that of Stuttgart[54] and Abbot and von Doenhoff.[55] Also shown are the results from XFOIL.[53] The previously published experimental data were obtained with the standard NACA 23012 without a flap. However, the XFOIL results were generated with the NACA 23012m coordinates for a more direct comparison (although still without a flap). The Stuttgart data were for Re = 2 million and the Abbot and von Doenhoff data were for Re = 3 million. The XFOIL results were generated at Re = 1.8 million, M = 0.20.

Figure 4.4a shows the lift curve comparisons, which indicated good agreement between the present Illinois experiment and Stuttgart data. The data of Abbott and von Doenhoff showed a $C_{l,max}$ that was approximately 8 percent higher which was largely due to higher Reynolds number (Re = 3 million). All of the experimental data showed a sudden, sharp drop in lift after $C_{l,max}$ was attained. This was indicative of leading-edge

stall, as expected for the NACA 23012 airfoil. XFOIL, which was not designed to predict large separated flow regions, incorrectly showed a more gradual stall and a higher $C_{l,max}$. A more detailed explanation of various airfoil stall types can be found in Appendix A, as well as in Broeren.[56]

Table 4.4 shows the lift curve slope comparisons. The pressure data had a lift curve slope that was 2% higher than that the of the balance data. This was probably due to the loss in lift near the ends of the model due to wall interference. The balance data were derived from the lift over the entire span of the model and included the forces at the ends of the span. The pressure data only measured the lift at the center of the span and were not as influenced by the flow at the ends of the span. The Illinois lift curve slopes compared favorably with that of Stuttgart[54] and were slightly lower than that of Abbot and von Doenhoff.[55]

Table 4.4: Lift curve slopes of the clean NACA 23012m airfoil. Comparisons of the present Illinois data with existing data and XFOIL results.

Data	**$C_{l,\alpha}$ (/deg)**
Illinois - Pressure	0.1027
Illinois - Balance	0.1003
Abbott	0.1132
Stuttgart	0.1005
XFOIL	0.1092

Figure 4.4b shows the comparisons of the drag polars. Its shows a large discrepancy between the balance and the wake pressure measurements everywhere except at zero lift, with the balance measurements exhibiting much higher drag. Noe[47]observed similar behavior with the S809 wind turbine airfoil a using similar experimental setup. This was thought to be the result of flow leakage through the gaps between the model and the ceiling/floor. Minimizing the gap between the model and floor/ceiling using wooden span extension lessened this effect. However, it could not be completely eliminated because in order for the force balance to work properly, the model could not touch the floor/ceiling. Thus, in this experiment, the balance drag was not used, although it was measured. Good agreement in drag was observed between the Illinois wake measurements and the existing experimental data. The Illinois measurements were

generally a few percent higher than the other data. This was thought to be the result of the discontinuity in the model surface at the flap gap location.

Figure 4.4c shows the comparisons for the pitching moment. The pitching moment data from Stuttgart[54] was not shown because they were too sparse and scattered. There was a good agreement between the Illinois pressure and balance measurements. However, the C_m's from the Illinois data were generally more positive (or leading-edge up) than Abbott and von Doenhoff[55] with a more positive C_m-α slope. It was speculated that this was due to the loss in lift near the trailing edge of the model due to the flap gap discontinuity. This will be explained in greater detail when the surface pressures are compared.

No previous experimental results were found for flap-hinge moment comparisons. Also, XFOIL[53] cannot handle multi-elements and typically loses accuracy when predicting the thick boundary layer near the trailing edge; therefore it was not used to generate C_h. Thus, Fig. 4.4d shows only the comparison between the Illinois pressure and hinge-balance data.

Figure 4.5 shows the comparison between the experimental surface pressures and those predicted by XFOIL. The angles of attack for the experimental data and XFOIL were different by as much as 1°. This was done in order to match C_l because XFOIL overpredicted lift, as shown in Fig. 4.4a. Figure 4.5a shows that at matched lift coefficients, the surface pressure agreed reasonably well, including the location of the laminar separation bubble at C_l = 0.65 and 1.18 (located at x/c = 0.19 and 0.07, respectively). Figure 4.5b shows the C_p distributions at C_l = 0.62 isolated and zoomed in, in order to highlight the subtle differences between XFOIL and experimental data. The experimental C_p's were generally more negative than the XFOIL prediction, with an offset of around 0.05. The largest differences were observed near the trailing edge, over the flap. The pressure differences between the upper and lower surfaces were much smaller in the experimental data when compared to XFOIL results. This resulted in decreased lift near the trailing edge of the airfoil, where there was a large moment arm about the quarter chord of the airfoil. This resulted in a more nose up (or positive) pitching moment when compared to XFOIL results. This explained the more positive C_m of the Illinois experimental results, as shown in Fig. 4.4c. The loss in lift near the trailing

edge of the model was likely due to the discontinuity in the surface due to the flap gap. Although the flap gap was sealed, a surface discontinuity still existed.

4.2.2 NLF 0414 Validation

Figure 4.6 shows the comparisons of the clean-model Illinois measurements to existing experimental data and XFOIL.[53] Again, the clean-model Illinois data, as well as the XFOIL results, were obtained at Re = 1.8 million. The McGhee, et al.[57] data were taken at Re = 3.0 million. Figure 4.6a shows that the lift from the pressure and the balance measurements compared favorably at all angles of attack. Both sets of data show similar breaks in the lift curve slope at $\alpha = 2°$. However, the McGhee data had slightly higher lift (when compared to the Illinois data) at most angles of attack. This offset was most likely due to an offset error in angle of attack (either in Illinois data or McGhee). The Illinois data reached a $C_{l,max}$ at $\alpha = 13°$ while the maximum lift was not achieved even at $\alpha = 18°$ in McGhee's data. This was most likely due to a higher Reynolds number in McGhee's data. The XFOIL results did not compare very well to either sets of experimental data. Although the XFOIL results show a break in the lift curve slope at $\alpha = 2°$, it was much more gradual. Because of this, at an angle of attack greater than 2°, the lift values became significantly higher than the experimental results. XFOIL results showed a $C_{l,max}$ of 1.56 at $\alpha = 15°$, while the Illinois pressure data showed a $C_{l,max}$ of 1.38 at $\alpha = 13°$.

Table 4.5 shows the lift curve slope comparisons. These were measured at the linear region of the lift curve ($-5° < \alpha < 0°$) before the break in the curve at $\alpha = 2°$. Again, the Illinois pressure data showed a slightly higher slope than the balance data due to the end wall interference effects described previously. However, they agreed favorably to that of McGhee.

Figure 4.6b shows the comparisons of the clean-model drag polars. As with the NACA 23012m model, the drag values obtained from the balance and the wake rake coincided only at zero lift. At all other lift values, the drag from the force balance was significantly higher. Again, this was probably to due the flow leakage through the gaps between the model and the floor/ceiling as well as the juncture flow interference. At $C_l < 0.7$ (before the break in the lift curve slope), the Illinois wake drag was slightly higher

than McGhee (possibly due to the surface discontinuity at the flap gap), but otherwise compared favorably, including the edge of the drag bucket at $C_l = 0.7$.

Table 4.5: Lift curve slopes of the clean NLF 23012m airfoil. Comparisons of the present Illinois data with existing data and XFOIL results.

Data	$C_{l,\alpha}$ (/deg)
Illinois - Pressure	0.1111
Illinois - Balance	0.1067
McGhee	0.1147
XFOIL	0.1236

Figure 4.6c shows the comparisons of the clean-model pitching moment. Both the pressure and balance measurements show the same trends, including a break in the slope at $\alpha = 2°$, due to the formation of a leading-edge suction and trailing edge separation (this will be explained in more detail later). However, the pitching moment from the pressure measurements was more negative than the balance measurements, with the largest difference (0.02) occurring at $\alpha = 2°$. The McGhee data and XFOIL results agreed much more favorably with the balance measurements.

The flap hinge-moment comparisons are shown in Fig. 4.6d. As with the NACA 23012m model, the hinge-moment data are not compared with any existing experimental data because they do not exist. Also, they are not compared with XFOIL because it does not accurately handle the thick boundary layer/separated flow that exists over the flap. Thus, the only comparison provided is that between the pressure measurements and the hinge-balance measurements. Figure 4.6d shows that the pressure and the balance measurements agreed reasonably well. As with the pitching moment, the largest discrepancy occurred at $\alpha = 2°$, which coincided with the start of trailing-edge separation.

Figure 4.7 shows the comparisons of experimental surface pressure distribution to the XFOIL results at matched lift coefficients. The pressure distribution from the experimental data compared favorably to XFOIL at $C_l = 0.027$ and 0.484. This was also indicated by the closeness of the angles of attack; at $C_l = 0.027$, the angles of attack were identical and at $C_l = 0.484$, they differed by 0.42. However, at $C_l = 0.964$, there were large discrepancies in the pressure distribution, especially near the trailing edge. In the experimental data, the upper surface C_p was nearly constant from $x/c = 0.75$ to the trailing edge, with a value of -0.20. This indicated that the pressure recovery was not taking

place and the flow in this region had separated. The C_p values from the XFOIL results were significantly higher in the same region, with the values increasing from -0.3 to 0.1. This indicated that the flow, at least for the most part, was attached in this region. As before, this discrepancy was probably due to XFOIL's inability to accurately calculate thick boundary layers and separation.

4.2.3 Effect of Flap Seal

All of the experimental data shown above were acquired with the flap gap sealed, as described in the Experimental Methods section. However, it was not known whether or not the gap seal was really necessary. Thus clean-model measurements were taken with and without the flap-gap seal and compared in order to determine the effect of the flow leakage through the gap. For the comparison, the NACA 23012m model was used at Re = 1.8 million. The spanwise gap insert was not used for both sealed and unsealed cases for this comparison.

Figure 4.8a shows the effect of the flap gap seal on lift at three flap setting (-10°, 0°, and 10°). It shows that the effect of the unsealed gap was minimal at flap settings of -10° and 0°. However, there was a significant effect at 10° flap deflection, with the unsealed model exhibiting lower lift values at most angles of attack. However, the differences became smaller as stall was approached, resulting in nearly identical lift values. In fact, the gap seal appeared to have decreased the stall angle of attack by 1 degree, resulting in a lower maximum lift value. Table 4.6 shows the lift curve slope comparisons. Again, it shows that only the 10° flap deflection produced large changes in the lift curve slopes, with a 10% reduction when the gap was sealed

Table 4.6: Effect of flap-gap seal on lift-curve slope. NACA 23012m, Re = 1.8x10^6.

Gap Seal	δ_f (deg)	$C_{l,\alpha}$ (/deg)
Not Sealed	-10	0.1017
Not Sealed	0	0.1028
Not Sealed	10	0.094
Sealed	-10	0.101
Sealed	0	0.1019
Sealed	10	0.0883

Figure 4.8b shows the effect of the flap gap seal on drag. The comparisons are shown only for $\delta_f = 0°$ case. It shows that at C_l of less than 0.7, the gap-sealed case had a higher drag, due to the Mylar tape used to seal the gap acting as a surface discontinuity. There was little leakage through the gap in the unsealed case, thus the drag remained low. At higher lift, the gap leakage in the unsealed case became more significant which led to a drag that was larger than the sealed case.

The comparison in the pitching moment is shown in Fig. 4.8c. The trends were nearly identical to that of the lift (shown in Fig. 4.8a). The two $\delta_f = -10°$ cases were nearly identical at positive angles of attack. The $\delta_f = 0°$ cases were identical up to $\alpha = 12°$, after which the C_m for the unsealed case became more positive due to loss in lift near the flap gap region. The $\delta_f = 10°$ cases showed significant discrepancies at nearly all angles of attack.

Figure 4.8d shows the comparisons of the flap hinge moment. It shows that the results for the $\delta_f = 0°$ cases agreed very closely at all angles of attack. However, there were some discrepancies in $\delta_f = -10°$ and 10° cases. At $\delta_f = -10°$, the magnitude of the hinge moment was generally lower when the gap was sealed. However, at $\delta_f = 10°$, the magnitude of the hinge moment was higher when the gap was left unsealed.

The effect of the flap gap seal on the aerodynamic coefficients was better understood when its effect on the flowfield (through surface pressure distribution) was analyzed. Figure 4.9 shows the effect of the flap seal on the pressure distribution at $\alpha = 5°$. Figure 4.9a shows that with $\delta_f = -10°$, the flap seal had little effect as the two pressure distributions were nearly identical. This occurred because with -10° flap deflection, the pressure at the upper surface of the model was higher than at the lower surface of the model at the flap gap location. Since the flap gap seal required a higher pressure on the lower surface of the model than on the upper surface, the flap gap seal was not effective.

Figure 4.9b shows the effect of the flap gap seal with zero flap deflection. It shows nearly identical pressure distribution on the main element of the airfoil. The largest difference was at the farthest aft pressure tap location on the upper surface, just ahead of the flap gap (with the unsealed case having a slightly higher C_p value). Over the upper surface of the flap however, the C_p values were slightly higher for the unsealed case, likely due to the energized boundary layer caused by the airflow through the flap gap. This led to a discontinuity in the upper surface pressure distribution between the

main element and the flap when the gap was not sealed. When the gap was sealed, the transition was much smoother. Overall, the flap gap seal created little difference in the surface pressure distribution other than in the immediate vicinity of the gap.

Figure 4.9c shows the effect of the flap gap seal on the pressure distribution with 10° flap deflection. It shows significant differences even on the main element. Although the lower surface pressures were very similar, the gap-sealed case had lower C_p (by approximately 0.05) throughout the entire upper surface. The discrepancy was largest immediately upstream of the gap, with 0.10 difference in C_p. This led to significant changes in lift and pitching moment, as Figs. 4.8a and 4.8b shows. However, the flow about the flap compared much more favorably, resulting in closer C_h values, as Fig. 4.8d shows. However, there was slightly less pressure recovery at the trailing edge when the flap gap was not sealed. At high angles of attack near stall, the flow in the flap region became separated and the influence of the flap gap seal became much smaller, resulting in the convergence of the lift values as shown in Fig. 4.8.

The results shown above demonstrated that the flap gap seal was required in order to minimize the flow leakage through the gap. This leakage cause significant effect on the surface pressure distribution when there were large differences in the pressure between the upper and lower surfaces in the vicinity of the gap. The seal used in this experiment was not effective for negative flap deflections because it required a higher pressure on the lower-surface side of the gap when compared to the upper-surface side. With negative flap deflection, this did not occur.

4.2.4 Effect of Spanwise-Gap Insert

Figure 4.10 shows the effect of the spanwise-gap insert. As stated in Section 3.2, this was a 1/16" thick wooden model extension placed on the ceiling end in order to reduce the gap between the model and the ceiling from 1/8" to 1/16". Figure 4.10 shows that the insert had a minimal effect on lift at all flap settings. Table 4.7 shows that the insert increased the lift curve slope by about 1%. The only significant difference was the $C_{l,max}$. At $\delta_f = 0°$, the use of the insert increased the $C_{l,max}$ from 1.48 to 1.50.

Table 4.7: Effect of spanwise-gap insert on lift-curve slope. NACA 23012m, Re = 1.8×10^6.

Gap Insert	δ_f (deg)	$C_{l,\alpha}$ (/deg)
Not Present	-10	0.1010
Not Present	0	0.1019
Not Present	10	0.0893
Present	-10	0.1019
Present	0	0.1027
Present	10	0.0909

4.3 Clean-Model Aerodynamics

In order to properly understand the effects of simulated ice accretion on airfoil aerodynamics, the characteristics of the clean, un-iced airfoil had be determined. One reason for this was to provide a baseline from which to compare the iced-arfoil aerodynamics. Another was to determine how the characteristics of the clean airfoil influenced its behavior when it had simulated ice. Thus in this section, the clean-model characteristics of the two airfoils examined in this experiment (NACA 23012m and NLF 0414) will be discussed.

4.3.1 NACA 23012m

The NACA 23012 (from which the NACA 23012m was derived) was a analytically defined airfoil, which shares the same thickness distribution with the NACA 0012. However, unlike the NACA 0012, it was a cambered airfoil and was designed to have nearly zero pitching moment about the ¼ chord.

4.3.1.1 NACA 23012m Baseline

The baseline condition used in this experiment was Re = 1.8 million with $\delta_f = 0°$ with the airfoil undergoing a natural boundary-layer transition. Figure 4.11 shows the integrated aerodynamic coefficients for the NACA 23012m at this condition. These are the same data that were shown in Fig. 4.4. However, they are shown here again without

the validation data in order to describe the NACA 23012m characteristics in more detail. The most important feature in the lift curves of Fig. 4.11a was the sudden stall which occurred between α = 15° and 16°. The C_l derived from the pressure data decreased from 1.50 to 0.92 while the C_l on the balance data decreased from 1.43 to 1.08. There was also a slight discontinuity in the lift curve slope at α = 0°. The drag polar of Fig. 4.11b shows a "bucket" of substantially lower drag between C_l = 0 and 1. Figure 4.11c shows a discontinuity in C_m at α = 1°, while Fig. 4.11d shows a discontinuity in C_h at α = 0°. All of these discontinuities were attributed to the laminar bubbles (or transition) that were present on the NACA 23012m undergoing natural boundary-layer transition. This will be explained in more detail in Section 4.3.1.3.

Figure 4.12 shows the comparisons of the surface fluorescent oil flow visualization with the surface pressure distribution on the clean NACA 23012m. The surface pressure distribution was obtained at *Re* = 1.8 million. The flow visualization was obtained at *Re* = 2.0 million. However, at such close Reynolds numbers, the differences in the flow characteristics were not significant and allowed a direct comparison between the flow visualization and surface pressures.

Figure 4.12a shows the comparisons at α = 0°. The first item to note on the flow visualization picture is the bright vertical line at x/c = 0.77. This was caused by the fluorescent oil pooling at the flap gap discontinuity, which can also be seen on the surface pressure distribution. The boundary-layer transition location is indicated at the x/c = 0.27 location on the flow-visualization picture. Upstream of this location, there was still a large amount of oil present on the model (indicated by bright color), while downstream of this location, very little oil was present (indicated by dark color). This was because upstream of this location, the flow was laminar, and the surface shear stress was low as transition was approached. Downstream of this location, the flow was turbulent with much higher surface shear stress, which caused most of the oil to be scrubbed off. This transition location was indicated by the slight discontinuity in the surface pressures as shown by the arrow. It was not clear from the surface pressure or flow visualization if there was a laminar bubble at transition, as described by Tani.[24]

Figure 4.12b shows the flow visualization and the surface pressure comparisons at α = 5°. At this angle of attack, the flow visualization indicated that the transition was induced by a laminar separation bubble which formed at x/c = 0.07. A close examination

of the model surface showed a thin pool of oil (not visible in the picture) at x/c = 0.04. This was the location of the start of the separation bubble, as the oil from the laminar boundary layer that flow downstream merged with the oil from the separation bubble that flowed upstream. The wider band of oil seen between x/c = 0.05 and 0.07 was the laminar bubble. The start of the turbulent boundary layer (at x/c = 0.07) was indicated by the start of the dark region on the model, where most of the oil had scrubbed off die to high surface shear stress. Again, this was indicated by the discontinuity in the surface pressure distribution.

Figure 4.13 shows the summary of the measured clean-airfoil pressure distribution from α = -3° to 16°. It shows that the NACA 23012m was a forward-loaded airfoil, with most of the lift generated near the leading edge. This was purposely done to generate very low (nearly zero) pitching moment about the 1/4 chord at nearly all angles of attack. However, this required that the pressure recovery start near leading edge. At higher angles of attack, the pressure recovery became very severe. As the angle of attack was increased, the location of the laminar bubble moved upstream as the adverse pressure gradient increased. Between α = 15° and 16°, the bubble burst, leading to a rapid and sudden stall. This is shown on Fig. 4.13e. Between α = 15° and 16°, the $C_{p,min}$ increased from -6.35 to -3.80, while the C_p at the trailing edge decreased from -0.12 to -0.55. At α = 16°, the C_p was nearly constant from x/c = 0.15 to the trailing edge, indicating that the flow was separated in this region. All of the above were characteristic of a stalled airfoil. The stall process described above was consistent with that of an airfoil with a leading-edge stall, as described in Appendix A.

4.3.1.2 Flap Deflection

Figure 4.14 shows the effect of flap deflection on the clean-airfoil aerodynamics. Again, the Reynolds number was 1.8 million with natural boundary-layer transition. Figure 4.14a shows that each 5° flap deflection resulted in a 0.20 vertical shift in the lift curve. Table 4.8 shows the effect of the flap deflection on the lift curve slopes, maximum lift, and stall angle of attack. These lift curve slopes were obtained over a linear portion of the lift curve slopes and varied with flap deflection (α = -1° to 4° for δ_f = 10° and 5°, α = 2° to 6° for δ_f = 0° and -5, α = 4° to 8° for δ_f = -10°). The largest lift

curve slopes were observed for the -5° and 0° flap deflections. The lowest lift curve slope was observed for the 10° flap deflection case. The surface pressure distribution (to be shown later) showed that it was the result of flow separation over the upper surface of the flap. Increasing the flap deflection increased $C_{l,max}$ but decreased the stall angle of attack. A note of interest on Fig. 4.14a is the large discontinuity in the lift curve slope at α = 2° for the -10° flap deflection. It will be shown later that this was due to flow separation over the lower surface of the flap.

Table 4.8: Effect of flap deflection on lift curve slope, $C_{l,max}$, and α_{stall}. Clean NACA 23012m, Re = 1.8 million.

δ_f (deg)	$C_{l,\alpha}$ (/deg)	$C_{l,max}$	α_{stall} (°)
-10	0.1019	1.1899	16
-5	0.1027	1.2984	15
0	0.1027	1.5025	15
5	0.1003	1.5776	14
10	0.0909	1.6791	14

Figures 4.14b and 4.14c show the effect of flap deflection on the drag. The lowest drag at positive lift occurred with -5° and 0° flap deflections, which also had the highest lift curve slopes. The 10° flap deflection had the highest drag at positive lift values, as well as the lowest lift curve slope. At -10° flap deflection, there was a sudden large change in the drag coefficient at C_l = -0.2. This is the same angle of attack that the discontinuity in the lift curve slope was observed.

Figure 4.14d shows the effect of flap deflection on the pitching moment. Increasing the flap deflection by 5° resulted in approximately a 0.04 vertical shift in the C_m curve. With -10° flap deflection, there was a sharp break in the C_m curve at α = 1°. Figure 4.14e shows the effect of flap deflection on the flap hinge moment. As with the pitching moment, increasing the flap deflection by 5° resulted in approximately a 0.04 vertical shift in the C_h curve. Again, with -10° flap deflection, there was a sharp break in the C_h curve at α = 1°.

The effect of flap deflection on the surface pressure distribution is shown on Fig. 4.15. Increasing the flap deflection moved the location of the upper surface suction peak and the transition/laminar bubble location upstream. In the cases where the flap was

deflected, there were sharp negative and positive C_p spikes near the leading edge of the flap. This was due to the flow accelerating over (negative C_p spikes) and stagnating (positive C_p spikes) on the flap leading edge. Fig. 4.15b shows that at $\alpha = 5°$ and $\delta_f = 10°$, the C_p on the upper surface of the flap was constant at -0.20 from $x/c = 0.90$ to the trailing edge. This indicated that the flow over the flap was separated even at this low angle of attack and explained the low lift curve slope and high drag shown in Fig. 4.14.

Figure 4.16 shows the pressure distributions with $\delta_f = -10°$ as α was varied between -1° and 4°. It is important to note that at this flap deflection, the pressures on the upper surface of the flap was higher than on the lower surface and is indicated as such on Fig. 4.16. At angles of attack of -1° to 1°, the flow over the lower surface of the flap was separated, as indicated by a nearly constant C_p from $x/c = 0.85$ to the trailing edge. However, at $\alpha = 1°$, the flow became reattached. This coincided precisely with the discontinuities in the lift, drag, pitching and hinge moments, as shown in Fig. 4.14.

4.3.1.3 Boundary-Layer Trip

Contrary to popular belief, the boundary layer-trip used on airfoils does not cause the boundary layer to be turbulent at the location of the trip. Instead, it merely starts the transition process, which may not yield a fully turbulent boundary layer for another 10 to 20% chord.[45] Figure 4.17 shows the effect of the boundary-layer trip on the NACA 23012m using the method described in Section 3.7. The trip consisted of 0.012-inch diameter microbeads that were applied onto a 0.003-inch thick and 0.25 inch wide double-sided tape. The trip was placed at $x/c = 0.02$ on the upper surface and $x/c = 0.05$ on the lower surface.

Figure 4.17a and Table 4.9 shows the effect of the boundary-layer trip on lift. It shows that the boundary-layer trip decreased the $C_{l,max}$ by 17%, lift curve slope by 5% and α_{stall} from 15° to 13°. Also, the trip eliminated the slight discontinuity in the lift curve slope present at $\alpha = 0°$. Figure 4.17b shows that the boundary-layer trip eliminated the drag bucket and increased the drag at all lift values. Figures 4.17c and 4.17d show that the trip smoothed out the C_m and C_h curves by eliminating the discontinuities. The breaks in the C_m and C_h also occurred at a lower angle of attack due to early stall. Tripping the boundary may have smoothed out the aerodynamic coefficients by

eliminating the separation bubble and keeping the transition location fixed at 2% chord. When the model underwent natural transition, the transition location on the upper surface varied from x/c = 0.50 at α = -3° to x/c = 0.10 at α = 11°. Turbulent boundary layers have larger displacement thickness than laminar boundary layers. Thus, when the transition location varied with angle of attack (for the untripped case), the effective geometry of the airfoil changed slightly as well, producing the slight bumps in the aerodynamic coefficients.

Table 4.9: Effect of boundary-layer trip on lift curve slope, $C_{l,max}$, and α_{stall}. Clean NACA 23012m, Re = 1.8 million.

Trip	$C_{l,\alpha}$ (/deg)	$C_{l,max}$	α_{stall} (°)
No	0.1027	1.5025	15
Yes	0.0977	1.2464	13

Figure 4.18 shows the effect of the boundary-layer trip on the surface pressure distribution. It shows that the boundary-layer trip eliminated the separation bubble and the surface pressure discontinuity associated with it. This, however, was the only significant effect.

4.3.1.4 Reynolds Number

In this experiment, the NACA 23012m model was tested with simulated ice accretions at Re = 1 million and 1.8 million, with the latter being the maximum attainable for this series of tests in the University of Illinois Subsonic Wind Tunnel. These Reynolds numbers were much lower than those typically found in actual flight conditions, which range between 6 and 10 million. However, studies[33,34] have shown that iced-airfoil aerodynamics is relatively insensitive to Reynolds number variations between 1 and 16 million. The clean airfoil aerodynamics at Re = 1 million and 1.8 million were compared on Fig. 4.19. Figure 4.19a and Table 4.10 shows the effect of the Reynolds number on lift. They show that increasing the Reynolds number from 1 million to 1.8 million increased $C_{l,max}$ and α_{stall}, as well as lift in the nonlinear regions. However, the lift in the linear regions was very similar, with nearly identical lift curve slopes.

Table 4.10: Effect of Reynolds number on lift curve slope, $C_{l,max}$, and α_{stall}. Clean NACA 23012m, Re = 1.8 million.

Re	$C_{l,\alpha}$ (/deg)	$C_{l,max}$	α_{stall} (°)
1 million	0.1025	1.3754	14
1.8 million	0.1027	1.5025	15

Figure 4.19b shows that increasing the Reynolds number resulted in decreased drag. Figures 4.19c and 4.19d show that increasing the Reynolds number had little effect on C_m and C_h. The discontinuities in C_m and C_h were slightly reduced, and the angle of attack where the breaks (due to stall) occurred increased.

Figure 4.20 shows the effect of Reynolds number on the surface pressure distribution. It shows that increasing the Reynolds number caused a slight vertical shift in C_p. Also, the transition/laminar bubble location moved upstream.

4.3.2 NLF 0414

The NLF 0414 was designed to achieve laminar flow over a significant portion of its chord. This was done by delaying the onset of the adverse pressure gradient as much as possible at operating angles of attack. This was quite different from the NACA 23012m, where the adverse pressure gradient started almost from the leading edge. The result was an airfoil with significantly different aerodynamics characteristics.

4.3.2.1 NLF 0414 Baseline

Figure 4.21 shows the integrated aerodynamic coefficients for the clean NLF 0414 model. There was a break in the slope at α = 2°, which was due to the onset of boundary-layer separation on the aft part of the model. (This will be described in more detail later with surface pressures.) The stall was also much more gradual than that observed with the NACA 23012m, with a $C_{l,max}$ of 1.34 at α = 13°. Figure 4.21b shows the drag polar. The drag increased rapidly at C_l = 0.7 (α = 2°) due to the flow separation at the aft portion of the model. Figures 4.21c and 4.21d showed that there were similar breaks in C_m and C_h at α = 2°.

Figure 4.22 shows the pressure distribution on the clean NLF 0414. At $\alpha = 0°$ and 1° (its operating angles of attack), the pressure gradient was nearly constant from the leading edge to $x/c = 0.75$. At this location, the pressure gradient became very adverse as the pressure recovery started. This adverse gradient extended to the trailing edge. Because the pressure recovery (and the associated adverse gradient) was delayed until $x/c = 0.75$, the boundary layer remained laminar up to this point. However, a negative side effect to this was a very large negative pitching moment, as shown in Fig. 4.21c.

As the angle of attack was increased, a very narrow suction peak formed at the leading edge. This led to a very severe adverse gradient near the leading edge. However, this region was very narrow and a significant portion of the chord was still at nearly constant C_p. At $\alpha = 2°$, the flow over the trailing edge started to separate, causing loss in lift, and led to a severe change in the pitching moment. The effect of this can be seen in Fig. 4.21. As the angle of attack was increased further, the point of separation gradually moved upstream eventually leading to stall. This gradual stall mechanism is clearly shown on Fig. 4.21a and was characteristic of an airfoil with a trailing-edge stall.

4.3.2.2 Boundary-Layer Trip

The boundary-layer trip caused significant differences in the NLF 0414 airfoil aerodynamics. Figure 4.23 shows that the trip eliminated the kink in the lift curve that was present at $\alpha = 2°$. The drag was also doubled at positive lift values. As with the NACA 23012m, the boundary-layer trip significantly smoothed out the C_m and C_h curves. Figure 4.24 shows the pressure distribution comparisons. At $\alpha = 0°$, the C_p with the trip was much higher (by almost 0.1) on the upper surface while that of the lower surface was nearly identical. When the boundary layer was tripped, there appeared to be a trailing edge separation, which accounted for the smoothing of the curves shown in Fig. 4.23. At $\alpha = 5°$, the offset on the upper surface was much smaller at 0.04.

4.4 Iced-Airfoil Results

Unless stated otherwise, the C_l and C_m and C_h data in this section were taken from the integrated surface pressures and the C_d measurements were taken from the wake pressure data.

4.4.1 Effect of Simulated Ice Shape on Flowfield

The effect of the simulated ice accretion on the airfoil flowfield will be discussed first in order to provide a better understanding of the integrated results that will be shown later. For this discussion, the case with the 0.25" forward-facing quarter round at x/c = 0.10 on the NACA 23012m at Re = 1.8 million and M = 0.18 was chosen. The boundary layer was not tripped for this particular case. Figure 4.25 shows the result of the fluorescent oil flow visualization and the surface pressure distribution at $\alpha = 0°$. (Note that the chordwise location markers on the picture do not always line up with the x/c locations on the surface pressure plot. This was because the flow visualization picture was taken at an angle and the image was digitally manipulated in order to give the appearance that it was taken straight on.) The vertical pool of oil near x/c = 0.06 was due to the flow separating upstream of the simulated ice shape. There was another pool of oil near x/c = 0.08 due to separation of the reverse flow, generating a secondary recirculation region. The separation bubble that formed downstream of the simulated ice shape reattached at x/c = 0.45 as indicated by the discontinuity in the oil streak pattern. The pressure distribution plot shows that the turbulent mixing and pressure recovery started at x/c = 0.23, as indicated by the end of the constant pressure region in the bubble. However, this could not be ascertained from the flow visualization. There was another pool of oil at x/c = 0.15 possibly due to separation of the reverse flow in the bubble, generating a secondary recirculation.

The reattachment location was uniform in spanwise direction except at the first and last 15% of the span due to the wall-interference effect. Near the model-wall juncture, the reattachment location moved upstream towards the ice shape. This was due to the horse-shoe vortex system[58,59] that formed at the model-wall juncture, which energized the boundary layer, decreasing the momentum loss due to the ice shape. This caused the separation bubble to be much smaller near the wall.

The features described above can be seen in the surface pressure distribution plot in Fig. 4.25. On the upper surface, the flow initially accelerates from the leading edge stagnation line until x/c = 0.05. The flow then encounters an adverse pressure gradient due to the simulated ice shape, which caused the flow to separate upstream of the ice shape at x/c = 0.10. There was a sudden large drop in the C_p at x/c = 0.10 as the flow

accelerated over the simulated ice shape. The flow then separated downstream of the ice shape, which was indicated by a nearly constant C_p between x/c = 0.10 and 0.23. The pressure started to increase again at x/c = 0.23, where the turbulent mixing and pressure recovery started to occur. This continued until the C_p approached the value of the clean model at x/c = 0.45, where reattachment occurred. The flow characteristics described above was very similar to that of leading edge ice accretion as described by Bragg, et al.[25], shown on Fig. 2.2.

Figure 4.26 shows the flow visualization and pressure distribution at $\alpha = 2°$. It shows that the onset of separation upstream of the ice shape remained at x/c = 0.06. However, the reattachment of the bubble downstream of the ice shape moved to x/c = 0.63. There was also significantly more spanwise variation in the reattachment location, with spanwise uniformity in existence for only the mid 50% span. The surface pressure distribution plot showed again that the reattachment location coincided with the location where the iced airfoil C_p approached the clean airfoil value.

Figure 4.27 shows the flow visualization and pressure distribution at $\alpha = 3°$. It shows that the onset of separation upstream of the ice shape moved to x/c = 0.05. The reattachment of the bubble downstream of the ice shape moved downstream to x/c = 0.83. Again, there was spanwise uniformity for only the mid 50% span. The surface pressure distribution plot showed that the C_p downstream of the simulated ice shape did not approach the clean values. However, the reattachment location appeared to be where the C_p distribution started to match the clean case, albeit shifted vertically.

Figure 4.28 shows the flow visualization and pressure distribution at $\alpha = 5°$. The onset of separation upstream of the ice shape remained at x/c = 0.05. However, the bubble that formed aft of the simulated ice shape failed to reattach, resulting in a separated flow over the airfoil. The pressure distribution plot showed that the C_p downstream of the simulated ice shape did not approach the clean-airfoil values nor have similar shape. This clearly shows that C_p alone cannot determine the reattachment location for very large bubbles near stall.

Figure 4.29 summarizes the boundary-layer state observed on the model using fluorescent oil flow visualization. The figure shows the progression of the separation bubbles upstream and downstream of the ice shape simulation as the angle of attack was increased. The primary separation bubble upstream of the simulated ice shape formed at

x/c = 0.06 at α = 0°. The separation point moved gradually upstream to x/c = 0.05 at α = 3° and remained at this location to α = 5°. Evidence of a secondary separation bubble upstream of the simulated ice shape was observed but was not shown because it could not be accurately measured. The primary downstream bubble reattachment region was located between x/c = 0.42 and x/c = 0.44 at α = 0°. It was not clearly defined because the reattachment of the ice-induced bubble was seen in the oil flow as a band of relatively stagnant oil on the surface. The stagnant oil band was probably an indication of an unsteady reattachment process. The region moved downstream as α was increased and at α = 3.25° was located between x/c = 0.88 and the trailing edge. Thus, for the 0.25" quarter round at x/c = 0.10, the stall was initiated by a rapidly growing separation bubble that eventually reached the trailing edge, which is characteristic of a thin-airfoil stall.

The large separation bubble caused by the simulated quarter round severely altered the aerodynamic coefficients of the NACA 23012m, as Fig. 4.30 shows. Figure 4.30a shows that the lift coefficient of the iced airfoil rapidly deviated from the clean values at α = 2° with rapidly decreasing lift-curve slope. At α = 5°, the lift coefficient stopped increasing with increasing α and remained relatively constant. This resulted in a substantially lower $C_{l,max}$ of 0.32 (when compared to 1.51 of the clean model) derived from the pressure measurements. The balance measurements showed a nearly identical lift curve, which indicated that the spanwise flow variations shown in Fig. 4.28 did not cause significant differences between the pressure data (which is taken only at the center of the span) and the balance data (which was integrated over the entire span). This was also the case for pitching (Fig. 4.30c) and flap hinge moment (Fig. 4.30d). Figure 4.30b shows that the simulated ice shape substantially increased the drag at all angles of attack. Figure 4.30c shows the effect of the ice shape on the pitching moment. It shows that the ice shape altered the pitching moment at all angles of attack. However, at α < -1°, the effects were less significant, resulting only in a slightly more positive pitching moment. However, at α = -1°, the pitching moment started to break and rapidly became more negative as it deviated from the clean values. This break in the pitching moment was due to the rapidly growing separation bubble that formed downstream of the ice shape. Similar trends were observed for the flap hinge moment. At α < 2°, the C_h values did not change greatly with increasing angles of attack. As with the pitching moment, they were slightly more positive than the clean values. However, at α = 2°, the C_h rapidly became

more negative and deviated from the clean values. The boundary-layer state plot of Fig. 4.29 shows that this was the approximate angle of attack that the separation bubble reached the leading edge of the flap, which was located at $x/c = 0.75$. Thus, the break in the flap hinge moment was caused by the separation bubble reaching the flap. The reason for these sudden changes with increasing angles of attack will be discussed in the sections to follow.

4.4.2 Effect of Simulated Ice-Shape Location

The location of the simulated ridge ice had a significant effect on the NACA 23012m aerodynamic coefficients. Figure 4.31 shows the effect of the 0.25" (k/c = 0.0139) forward-facing quarter round ice simulation on lift as the location was varied from the leading edge to the mid-chord. The boundary layer was tripped (at 2% chord upper and 5% lower surface) for the cases with the simulated ice shapes at, and downstream of, $x/c = 0.04$. All of the simulated-ice cases showed reduced lift curve slopes in the linear regions ($-5° < \alpha < 1°$) when compared to the clean case. Varying the ice-shape location from x/c = 0.00 to 0.50 had large effects on the lift of the NACA 23012m.

When the simulated ice shape was located at $x/c = 0.00$, the airfoil stalled at α = 11°, with a clearly defined $C_{l,max}$ of 0.95. The stall process was very gradual, with the lift becoming nonlinear at $\alpha = 4°$. Moving the ice shape downstream to $x/c = 0.02$ and 0.04 further decreased the $C_{l,max}$ with lower stall angles of attack. The $C_{l,max}$ also became less well defined. When the simulated ice shape was located at $x/c = 0.06$ a clearly defined $C_{l,max}$ was not present. The lift became nonlinear at $\alpha = 3°$ and reached a maximum value at $\alpha = 4°$. However, instead of decreasing at higher angles of attack, the lift remained nearly constant This type of lift curve was observed until the ice shape was located at $x/c = 0.12$. When the ice shape was located between $x/c = 0.06$ and 0.12, the lift curves looked nearly identical. When the ice shape was located at $x/c = 0.14$, the $C_{l,max}$ in the traditional sense was not observed. The lift curve became nonlinear at α = 2° as the slope began to rapidly decrease. However, instead of leveling off to a maximum lift value, an inflection in the lift curve was observed at $\alpha = 5°$, after which the lift curve started to increase again. When the ice shape was located at $x/c = 0.30$ and 0.50, the

inflection in the curve was not present. However, there did appear to be a $C_{l,max}$ associated with these two cases (0.93 for x/c = 0.30 and 1.05 for x/c = 0.50). It will be shown later that the flow downstream of the simulated ice ridge was fully separated at α = 2°, where the lift curve started to diverge from the clean case. This was well before the $C_{l,max}$ was reached for these cases.

Figure 4.32 shows the drag polars with the 0.25" simulated ice shape at various chordwise locations. Location of the simulated ice shape had a significant effect on drag. The lowest drag was observed when the simulated ice shape was located at the leading edge. Moving the ice shape downstream resulted in increased drag until x/c = 0.10. When the simulated ice shape location was varied between x/c = 0.10 and 0.20, there was not a large change in drag. The drag decreased significantly when the ice shape was located at x/c = 0.30. It decreased further at x/c = 0.50. This was probably due to a large portion of the airfoil being upstream of the ice shape, outside of the direct influence of the separation bubble. Both the x/c = 0.30 and 0.50 cases showed a break in the drag polar (at C_l = 0.93 for x/c = 0.30 and C_l = 1.05 for x/c = 0.50), which corresponded to the $C_{l,max}$ shown on Fig. 4.32.

The pitching moments with the three simulated ice shape locations are shown in Fig 4.33. When the simulated ice shape was moved downstream from the leading edge, the angle of attack at which the break in the pitching moment occurred decreased. At x/c = 0.00, the pitching moment exhibited a large break in the slope at α = 12°. When the simulated ice shape was located at x/c = 0.02, the pitching moment diverged at α = 5°. As the simulated ice shape was moved downstream, these breaks became somewhat less severe, with decreases in the magnitude of $C_{m,\alpha}$. When the simulated ice ridge was located at x/c = 0.50, the break in the C_m did not occur until α = 13°. The pitching moment coefficient was lower than the clean airfoil at all angles of attack before this break. Before the break in the pitching moment occurred, the C_m values were generally more positive than the clean airfoil values. The exceptions to this were the cases with the simulated ice ridge located at x/c = 0.30, and 0.50. At these two locations, the C_m values were lower than the clean case at all angles of attack. There was also a sharp drop in C_m (at α = 15° for x/c = 0.30 and α = 14° for x/c = 0.50) that was similar to that of the clean case.

Figure 4.34 shows the flap hinge moments with the simulated ice shape at various x/c locations. The results were very similar to that of the pitching moment. When the simulated ice shape was moved downstream from the leading edge, the angle of attack at which the break in the flap-hinge moment occurred decreased. This change was very significant when the simulated ridge ice was located between x/c = 0.00 and 0.06. However, when the simulated ice ridge was moved from x/c = 0.08 to 0.30, the angle of attack that the C_h break occurred changed by only 1 degree. When the simulated ice ridge was moved to x/c = 0.50, a completely different C_h curve resulted, the break occurring before α = -5°. As with the pitching moment, the flap-hinge moment before the break was more positive than the clean case.

Figure 4.35 shows the summary of maximum lift versus the chordwise location of the simulated ice accretion (0.25" forward facing quarter round) as well as the clean airfoil $C_{l,max}$ with natural transition. Figure 4.31 showed that the classically defined $C_{l,max}$ only existed when the ice shape was located ahead of x/c = 0.12 chordwise location. When the ice shape was located between x/c = 0.12 and 0.30, a traditional $C_{l,max}$ was not observed. The reason for this will be explained later with the surface pressure measurements. Thus, in addition to the $C_{l,max}$, the lift coefficient when the separation bubble reached the trailing edge (referred to as $C_{l,sep}$) are also shown on Fig. 4.35. The $C_{l,sep}$ was determined by examining the plot of C_p vs. α of the trailing edge pressure tap. Comparison of this plot to the flow visualization results showed that the angle of attack when the separation bubble reached the trailing edge coincided with the location of the inflection in the C_p vs. α curve. This is discussed in more detail in Appendix B.

Figure 4.35 shows that when the simulated ice ridge was located between x/c = 0.02 and 0.06, the $C_{l,max}$ and the $C_{l,sep}$ values were identical. When the ice ridge was located between x/c = 0.08 and 0.12, the $C_{l,max}$ values were approximately 0.04 higher than the $C_{l,sep}$ values. This was because α at $C_{l,max}$ was 1° higher than α at $C_{l,sep}$ when the ice ridge was at these locations. The lowest $C_{l,max}$ for the 0.25" shape (k/c = 0.0139) was 0.25 and occurred at x/c = 0.12. The $C_{l,max}$ increased rapidly as the simulated ice was moved forward of this location, reaching 0.97 at the leading edge. The $C_{l,max}$ value also increased when the ice shape moved downstream of the x/c = 0.12 location, reaching 1.07 at x/c = 0.50. However, when the ice shape was at x/c = 0.50, the maximum lift was

reached at an angle of attack 12 degrees higher than that of $C_{l,sep}$. This indicated that the airfoil continued to generate more lift even after the bubble was completely blown off the surface. Thus, it is clear from Fig. 4.35 that in terms of maximum lift loss, the most critical location for this simulated ice shapes was in the region between x/c = 0.08 and 0.16. When the ice shape was located further downstream, more lift could be generated, but only at the expense of severely increased drag.

Figure 4.36 shows the ΔC_l ($C_{l,clean} - C_{l,iced}$), or the lift loss compared to the clean airfoil, due to the 0.25" ice shape simulation. Each curve represents a fixed angle of attack, and the simulated ice shape location is depicted on the x-axis. Also shown on the figure by the solid arrows are the locations of maximum local air velocity, $C_{p,min}$, (of the clean airfoil) for each angle of attack and by the open arrows are the location of the maximum adverse pressure gradient (also of the clean airfoil). Figure 4.36 shows that ΔC_l remained relatively small and did not vary significantly with the ice-shape location at angles of attack below 1°. The ΔC_l values remained approximately at 0.04 at all x/c locations except at the leading edge where it was nearly zero. The lift loss also remained relatively insensitive to changes in angle of attack. However, at α = 1°, the lift loss started to vary significantly with the ice shape location as well as angle of attack. Increasing angle of attack increased the lift loss at all ice shape location. The largest lift loss occurred when the ice shape was located at x/c = 0.12 and did not change with angle of attack until α = 7° where it moved upstream to x/c = 0.10. This clearly showed that for ice shapes of this size, the leading edge is not the most critical location in terms of lift loss. The simulated ice-shape location for maximum lift loss was well downstream of the maximum local air velocity and slightly upstream of the maximum adverse pressure gradient. The x/c = 0.12 ice-ridge location was the same x/c location that produced the lowest $C_{l,max}$ as shown in Fig. 4.35. This is in disagreement with earlier results[27,35] that showed that the most critical location was the leading edge. This discrepancy was likely due to the much smaller protuberances used in the previous studies. As stated in the Section 2.5, a detailed analysis of Jacobs data[28] by the author also showed that for the large (k/c = 0.0125) protuberance, the largest lift loss also occurred when it was located well downstream of the maximum local air velocity in the adverse pressure region.

Figure 4.37 shows the drag increase ΔC_d ($C_{d,iced} - C_{d,clean}$) compared to the clean airfoil due to the 0.25" ice shape simulation. Please note that for drag, the clean values

were subtracted from the iced values in order to obtain positive values. It shows that there was significant variation ΔC_d with the ice shape location even at angles of attack as low as -3°. At this angle of attack, the largest increase in the drag was observed when the ice shape was located at $x/c = 0.16$. As the angle of attack was increased, ΔC_d increased as well. However, as the angle of attack was increased, the ice shape location where the largest drag increase occurred moved upstream as well. At $\alpha = 0°$, this occurred at $x/c = 0.12$ and at $\alpha = 8°$, this occurred at $x/c = 0.06$. The most critical location in terms of drag increase appeared to coincide with the location of maximum local air velocity. This was identical to what Bowden[37] had observed. A possible explanation for this is that the protuberance would extract the greatest amount of boundary-layer momentum when placed at that location, which would thicken the boundary layer and increase drag.

Figure 4.38 shows ΔC_m ($C_{m,clean} - C_{m,iced}$), the change in the pitching moment due to the 0.25" ridge ice simulation on the NACA 23012m. At $\alpha = -3°$, the ice shape did not have any effect on C_m when it was located at the leading edge. As it was moved downstream, the ΔC_m became more negative, which indicated that the pitching moment became more nose up than the clean case. However, at $x/c = 0.10$, ΔC_m started to increase, reaching a value of 0.023 when the ice shape was located at $x/c = 0.50$. As the angle of attack was increased, the x/c location at which the ΔC_m started to increase moved upstream. The ΔC_m values downstream of this location increased with increasing angle of attack. The ΔC_m values upstream of this location did not change significantly with angle of attack. At $\alpha = 0°$, the ΔC_m value leveled off at $x/c = 0.12$ and remained nearly constant until $x/c = 0.50$. At $\alpha = 1°$, the ΔC_m value reached a peak (or a maxima) at $x/c = 0.12$ and started to decrease as the ice shape was moved downstream. The location where the ΔC_m peak occurred remained constant at $x/c = 0.12$ at angles of attack between 1° and 4°. At $\alpha = 5°$, the x/c location where ΔC_m peak started to move upstream with increasing angle of attack. Also, downstream of the ΔC_m peak, increasing the angle of attack did not significantly increase the ΔC_m values. It shows that the largest changes in C_m occurred when the simulated ice shape was located between the locations of the maximum local air velocity and the maximum adverse pressure gradient. This is identical to what was observed on the NACA 23012m for lift (Fig. 4.36).

Figure 4.39 shows the effect of the simulated ridge ice on ΔC_h ($C_{h,clean} - C_{h,iced}$). The results were very similar to that of ΔC_m shown in Fig. 4.37. At $\alpha = -3°$, the ice shape

did not have any effect on C_h when it was located at the leading edge. As it was moved downstream, the ΔC_h became more negative, which indicated that the hinge moment became more trailing-edge up than the clean case. However, at $x/c = 0.10$, ΔC_h started to become more positive, reaching a value of 0.023 when the ice shape was located at $x/c = 0.50$. As the angle of attack was increased, the x/c location at which the ΔC_h started to increase moved upstream. The ΔC_h values downstream of this location increased with increasing angle of attack. The ΔC_h values upstream of this location did not change significantly with angle of attack. At $\alpha = 0°$, the ΔC_h value leveled off at $x/c = 0.12$ and remained nearly constant until $x/c = 0.50$. At $\alpha = 1°$, the ΔC_h value reached a peak (or a maxima) at $x/c = 0.12$ and started to decrease as the ice shape was moved downstream. The location where the ΔC_h peak occurred remained constant at $x/c = 0.12$ at angles of attack between 1° and 4°. At $\alpha = 5°$, the x/c location where ΔC_h peak started to move upstream with increasing angle of attack. Also, downstream of the ΔC_h peak, increasing the angle of attack did not significantly increase the ΔC_h values. Largest changes in C_h were observed when the simulated ice shapes were located between the locations of the maximum local air velocity and the maximum adverse pressure gradient. However, at $\alpha = 8°$, the ΔC_h was nearly constant when the ice shape was located at and downstream of $x/c = 0.02$. This occurred because at this angle of attack, the flow over the flap was completely separated when the ice shape was located at and downstream of $x/c = 0.02$.

The large change in the flowfield around the airfoil can be seen in the pressure distribution plots of Figs. 4.40 - 4.42. Figure 4.40 shows the surface pressure distribution with the $k = 0.25$" quarter-round ridge-ice simulation placed at various chordwise locations at $\alpha = 0°$ and compared to the clean case. The clean case showed the stagnation point at the leading edge with a suction peak at $x/c = 0.12$ on the upper surface and at $x/c = 0.02$ on the lower surface. There was a discontinuity in the C_p at $x/c = 0.78$ due to the flap gap. On a clean NACA 23012m airfoil, over 50% of the lift is generated in the first 25% of the chord.

It is first important to note that the surface pressure was not measured over the simulated ice shape. Thus, the C_p from the last pressure tap upstream of the simulated ice shape is connected to the first pressure tap downstream of the simulated ice shape by a straight line. When the simulated ice shape location was at the leading edge of the model, the pressure distribution was nearly identical to that of the clean model. The only

major difference was the elimination of the laminar separation bubble, as the ice shape likely caused the flow to transition. The flowfield started to become significantly altered when the simulated ice shape was at x/c = 0.02. There was a large suction peak (C_p = -1.18) immediately downstream of the simulated ice shape as the flow accelerated over it and separated. However, the simulated ice shape was located in a very favorable pressure gradient and the bubble was able to reattach quickly at x/c = 0.10. This allowed another suction peak (due primarily to the airfoil geometry and not the simulated ice shape) to form at x/c = 0.18 with a C_p value of -0.51.

When the simulated ice shape was located at x/c = 0.06, the flow on the upper surface initially accelerated from the leading-edge stagnation point. However, the flow started to decelerate as it approached the simulated ice shape and experienced an adverse pressure gradient and flow separation. This resulted in a local $C_{p,min}$ of 0.62 located ahead of the simulated ice shape at x/c = 0.03, followed by a $C_{p,max}$ of 0.70 at x/c = 0.05. Immediately downstream of the simulated ice shape, a longer separation bubble was formed, and the C_p was nearly constant at -1.15 until x/c = 0.15, where it started to increase as the reattachment process began. Near x/c = 0.32, the C_p approached the clean model value and indicated that the flow had reattached. Although the simulated ice shape was located in a favorable pressure gradient, it was so close to the location of the onset of adverse pressure gradient that the separation bubble was forced to reattach in an adverse pressure gradient. Thus, the separation bubble for this simulated ice shape location was much larger than when the simulated ice shape was located at x/c = 0.02.

With the simulated ice shape located at x/c = 0.10 (Fig. 4.40b), the local $C_{p,\min}$ and $C_{p,max}$ upstream of the simulated ice shape became more clearly defined as there was a greater surface length along the model for the flow to first accelerate and decelerate upstream of the simulated ice shape. In this case, the simulated ice shape was located near the clean airfoil suction peak and all of the separation bubble was located in the clean-airfoil adverse pressure gradient region. This resulted in a very large separation bubble that did not reattach until near x/c = 0.60. (This is quite different from what was shown in Fig. 4.29 because there was a significant difference in the bubble length between the tripped and untripped cases. The tripped cases generally had about 20% longer separation bubble length and subsequently the effects of the ice shape were more severe. In the fluorescent oil flow visualization, the boundary layer was not tripped.

However, in the pressure distribution plot of Fig. 4.40 to 4.42, as well as in all of the other figures, the boundary layer was tripped.) When the simulated ice shape was moved downstream to x/c = 0.12 both the simulated ice shape and the separation bubble were located in a region of adverse pressure gradient. It is interesting to note that when the ice shape was located between x/c = 0.12 and 0.20, the pressure distribution in the separated regions appeared nearly identical. In those cases, the C_p value in the constant pressure region downstream of the simulated ice shape was approximately -0.80, and reattachment occurred near x/c = 0.75. Thus, the separation bubble length actually decreased when the simulated ice shape was moved from x/c = 0.12 to 0.20.

As Fig. 4.41 shows, similar trends in the pressure distributions were observed for $\alpha = 5°$. This was approximately the angle of attack at which $C_{l,max}$ occurred for many of the cases with a simulated ice shape. The pressure distribution for the clean case shows a suction peak (C_p = -1.7) at x/c = 0.06. Well over half of the lift occurred in the first 25% chord due to the large leading-edge suction. When the simulated ice shape was placed at the leading edge, a very small separation bubble formed that reattached at x/c = 0.02. The extremely small separation bubble was due to the very favorable pressure gradient in which the simulated ice shape was located. Downstream of the reattachment location, the pressure distribution was similar to the clean case. However, the suction peak (due to the airfoil geometry) was not as large. When the simulated ice shape was at x/c = 0.02, the C_p in the separation bubble downstream of the simulated ice shape was even more negative than that of the clean model suction peak. The simulated ice shape was still located in a favorable pressure gradient and, although the resulting separation bubble was longer than the case with the simulated ice shape located at the leading edge, it was still relatively short.

When the simulated ice shape was located at x/c = 0.06, a very long separation bubble formed downstream of the simulated ice shape. In fact, the large suction peak that normally forms near x/c = 0.08 was completely replaced by this separation bubble. This was the case where the simulated ice shape was located near the suction peak of the clean model and almost all of the resulting separation bubble was located in the adverse pressure region. It was difficult to determine from the surface pressure values whether or not the separation bubble reattached. However, it was likely that the bubble was unsteady and was intermittently attached at the trailing edge. When the simulated ice

shape was located at, and downstream, of x/c = 0.06, the resulting separation bubbles were completely separated, with nearly identical C_p values. In these cases all of the separation bubble was located in the adverse pressure gradient of the clean model. This was also observed at α = 0°, as Fig. 4.40 shows. As the simulated ice shape was moved downstream from the leading edge to x/c = 0.50, the local suction peak upstream of the simulated ice shape grew, since there was a greater surface length along the model for the flow to first accelerate and decelerate upstream of the simulated ice shape. Thus, as the ice shape was moved further downstream, more lift was recovered near the leading edge. As the ice shape was moved downstream, the percentage of the chord that could be set under the separation bubble decreased, leaving more of the airfoil free of the direct influence of the separation bubble.

Figures 4.40 and 4.41 clearly showed why the most sensitive ice-shape location in terms of lift loss was in the region near 10% chord. When the ice shape was located near the leading edge, the ice shape, and the resulting separation bubble, were in a favorable pressure gradient of the clean model. Thus, the bubble was able to reattach quickly, which preserved the large leading-edge suction peak of the clean model, where most of the lift was generated. When the ice shape was located downstream of the suction peak of the clean model, the ice shape, and the resulting separation bubble, were located in an adverse pressure gradient. This resulted in a much longer separation bubble, which eliminated the strong leading-edge suction peak found on the clean model. When the ice shape was placed further downstream, the leading-edge suction peak started to grow, recovering some of the lost lift. When the ice shape was located near 10% chord, a very long separation bubble formed because it was in an adverse pressure gradient. However, it was also close enough to the leading edge that very little of the leading edge suction peak had recovered. Fig. 4.42 shows the surface pressure distribution at α = 8°. It shows that the flow downstream of the ice shape had separated at all ice shape locations except for the leading-edge case.

Figures 4.40 and 4.41 also showed why there was no classically defined $C_{l,max}$ present when the ridge ice was located between x/c = 0.12 and 0.30. When the ridge was located downstream of x/c = 0.30, a significant suction peak existed upstream of the ice shape. This grew with increasing angle of attack even though the flow downstream of the ice shape was completely separated, increasing the lift. The maximum lift was achieved

only when the flow separated upstream of the ice shape, eliminating the suction peak. When the ridge ice was located between x/c = 0.12 and 0.30, the suction peak upstream of the ice shape was not large enough to significantly contribute to lift. Because of this, increasing the angle of attack did not significantly increase lift and a maximum lift value was not observed.

Figures 4.43 to 4.45 show the pressure distribution as the angle of attack was increased from 0° to past stall with the simulated ridge ice at fixed locations. This showed the similarities and differences in the development of the separation bubble and the stall process when the ridge ice was at different locations. Figure 4.43 shows the development of the boundary layer with the ridge ice at x/c = 0.02. It shows that the C_p value in the constant pressure region of the separation bubble decreased when the angle of attack was increased from 0° to 4°. The growth of the separation bubble was also relatively small in this a range. However, at α = 5°, the C_p value in the constant pressure region of the bubble started to increase and the bubble started to grow rapidly. This was approximately the angle of attack at which the lift curve (Fig. 4.31a) started to "flatten" out and become nonlinear. At α = 12°, the flow behind the ice ridge was completely separated, as indicated by nearly constant C_p between the ice ridge to the trailing edge. There was no lift generated ahead of the ice ridge because it was so close to the leading edge.

Figure 4.44 shows the development of the pressure distribution with the ridge ice at x/c = 0.10. It shows that the C_p in the constant pressure region of the bubble increased with angle of attack starting at α = 0°. The separation bubble reattachment point rapidly moved downstream with increasing angle of attack (from x/c = 0.65 at α = 0° to x/c = 0.90 at α = 2°). There was a small suction peak ahead of the bubble that grew slightly with increasing angle of attack.

Figure 4.45 shows the surface pressure distributions with the ridge ice at x/c = 0.20. It shows that the C_p value of the constant pressure region of the bubble did not vary with angle of attack between α = 0° and 2°. However, the location of the bubble reattachment increased from x/c = 0.72 at α = 0° to x/c = 0.85 at α = 2°. The C_p value in the constant pressure region of the bubble started to increase with angle of attack at α = 3°. There was a significant suction peak ahead of the ridge ice that grew with increasing angle of attack. This suction peak continued to grow even after the flow downstream of

the ridge ice was completely separated. It was due to this suction peak that the lift continued to increase even after the bubble failed to reattach (as shown in Fig. 4.31c).

4.4.3 Ice-Ridge Height

Figures 4.46 to 4.49 show the effect of the simulated ridge-ice height on the integrated aerodynamic coefficients of the NACA 23012m. Again, the forward-facing quarter round was used. Three simulated ice shape-heights were tested: 0.10", 0.15", and 0.25" (k/c = 0.056, 0.0833, and 0.0139). As before, the boundary layer was tripped for the cases with the simulated ridge ice located at, and downstream of x/c = 0.04.

Figure 4.46 shows the lift coefficients with the simulated ice ridge shapes on the airfoil surface at x/c = 0.00, 0.02, 0.10, and 0.20. Figure 4.46a shows that when the simulated ridge ice was located at x/c = 0.00, increasing the ridge height from 0.15" to 0.25" had little effect on the lift curve. In fact, the 0.10" and 0.15" cases had nearly identical lift curves with $C_{l,max}$ of 1.00 at $\alpha = 12°$. The 0.25" case had a slightly lower $C_{l,max}$ of 0.94 at $\alpha = 11°$. The ice-ridge size had a much more significant effect when it was located at x/c = 0.02, as Fig. 4.46b shows. When the ice-ridge height was 0.10", the $C_{l,max}$ was 0.88 and occurred at $\alpha = 10°$. At 0.15" ice-ridge height, the $C_{l,max}$ was 0.74 at $\alpha = 8°$. Finally, at 0.25" ice-ridge height, the $C_{l,max}$ was 0.58 at $\alpha = 7°$. Thus, increasing the ice ridge height decreased the $C_{l,max}$ and $\alpha_{Cl,max}$. Figure 4.46c shows similar results when the simulated ice ridge was located at x/c = 0.10. The maximum lift was less well-defined than when the ice shape was located at $x/c < 0.10$. For the k/c = 0.25" lift curve reached a plateau instead of reaching a clearly defined $C_{l,max}$. As before, the angles of attack at which the lift curve became nonlinear and at which the maximum lift occurred decreased with increasing ridge height. Figure 4.46d shows lift curves when the ice ridge was located at x/c = 0.20. Again, it showed decreasing lift values with increasing ice-ridge size. The 0.10" and 0.15" cases showed clearly defined $C_{l,max}$. However, the 0.25" case did not exhibit a clearly defined $C_{l,max}$. Jacobs[28] and Kim and Bragg[30] showed similar results for the NACA 0012 (Fig. 2.5) and NLF 0414 airfoils (Figs. 2.7 - 2.9). When the protuberance was located at the leading edge, the lift curve was relatively insensitive to the protuberance height. However, when the protuberance was located away from the leading edge, the maximum lift decreased with increasing height. The

angles of attack at which the onset of nonlinearity and stall occurred also decreased with increasing protuberance height.

Figure 4.47 shows the effect of the simulated ridge-ice height on drag. When the ice ridge was located at the leading edge, the effect of the ridge-ice height when it was varied from 0.10" to 0.25" was minimal, as Fig. 4.47a shows. Increasing the ice shape height only slightly increased the drag. However, Fig. 4.47b shows that when the simulated ice shape was located at $x/c = 0.02$, increasing the simulated ice shape height resulted in a much more significant increases in drag. Figures 4.47c and 4.47d show that when the ice shape location was moved downstream to $x/c = 0.10$ and 0.20, increasing the height resulted in even higher increases in drag.

Figure 4.48 shows the effect of the simulated ridge-ice height on the pitching moment. Figure 4.48a shows that when the simulated ice shape was located at the leading edge, the effect of the ice-shape height on the pitching moment was minimal. The break in the pitching moment of all three iced cases occurred at $\alpha = 12°$. Before this break, the pitching moment curves of all three cases appeared nearly identical. Figure 4.48b shows that when the simulated ice shape was located at $x/c = 0.02$, increasing the ice-shape height had a significant effect on the pitching moment. As the ice shape height was increased from 0.10" to 0.25", the angle of attack at which the pitching moment started to rapidly become more negative decreased from 9° to 5°. Similar trends were observed when the ice shape was located at $x/c = 0.10$ and 0.20, as Figs. 4.48c and 4.48d show.

Figure 4.49 shows the effect of the simulated ridge-ice height on the flap hinge moment. The results were very similar to that of the pitching moment. Figure 4.49a shows that when the simulated ice shape was located at the leading edge, the effect of the ice-shape height on the flap-hinge moment was minimal. The pitching moment curves of all three iced cases appeared nearly identical, with the break in the hinge moment at $\alpha = 10°$. Figure 4.49b shows that when the simulated ice shape was located at $x/c = 0.02$, increasing the ice-shape height had a significant effect on the hinge moment. As the ice shape height was increased from 0.10" to 0.25", the angle of attack at which the pitching moment started to rapidly become more negative decreased from 8° to 5°. Similar trends were observed when the ice shape was located at $x/c = 0.10$ and 0.20, as Figs. 4.65c and

4.49d show. Again, Bragg and Kim[30] found similar results with simulated glaze ice as Figs. 2.7b and 2.8b show.

Figure 4.50 shows a summary of the $C_{l,max}$ as a function of the ridge-ice location for the three sizes tested. Also shown on the plot is the effect of 0.025" roughness grit (as described in Section 3.7) location on maximum lift. When the k = 0.25" shape was tested, a classically defined $C_{l,max}$ existed only when the ice shape was located at and upstream of x/c = 0.12. However, for the two smaller shapes (k = 0.10 and 0.15), $C_{l,max}$ existed at all chordwise locations tested. Figure 4.50 clearly shows that for these three ridge heights, the most critical ice-shape location (in terms of losses in $C_{l,max}$) was not the leading edge of the airfoil. Instead, it is the region around the 10% chord. Also, when the ice shape was located at the leading edge, increasing the height from 0.10" to 0.25" did not significantly affect the $C_{l,max}$, which was approximately 1.0. This was the only chordwise location at which this was observed. When the much smaller roughness grit was tested, the most critical location was between the leading edge and x/c = 0.02. This was because the roughness had an effect that was quite different than that of the ridge ice. The ridge ice induced early stall through the formation of a separation bubble that grew rapidly. The roughness induced early stall by inducing early boundary-layer transition. Because of this, the largest loss in momentum occurred when the roughness was located at the leading edge (which coincided with the lowest $C_{l,max}$). However, when the roughness and the three ridge-ice shapes were located at the leading edge, nearly identical $C_{l,max}$ (approximately 1.0) resulted. This indicated that when the ridge ice was located at the leading edge, the stall process was similar to that of an airfoil with a leading edge roughness. The early stall was initiated not by the rapidly growing separation bubble, but by early transition. This was because the pressure gradient was so favorable at the leading edge, the separation bubble remained very small at did not grow significantly with angle of attack (at least not to the point where it had a global effect on the airfoil pressure distribution). Thus, the only significant effect of the bubble was transitioning the boundary layer at the leading edge. This was the reason why the maximum lift was relatively insensitive to the ridge-ice height at the leading edge.

Figure 4.51 shows the summary of $C_{l,max}$ as a function of the ice-ridge height at various ice-shape locations. Figure 4.51a shows the absolute values of the maximum lift, and Fig. 4.51b shows the percentage reduction in the maximum lift, similar to

Brumby's[27] plot (Fig. 2.3). It shows that increasing the ice-ridge height decreased the $C_{l,max}$ at all chordwise location except at the leading edge where the $C_{l,max}$ was relatively insensitive to the ice shape height. This compared very favorably to the results of Jacobs[28] (Fig. 2.5) and Kim and Bragg[30] (Fig. 2.9). Unlike in Brumby's plot, moving the ice shape closer to the leading edge did not increase the reduction in maximum lift. Of the locations shown, the maximum reduction in lift occurred when the ice shape was located at $x/c = 0.10$.

The reason for this behavior is that as the simulated ice shape height was increased, the separation bubble became larger in chordwise extent. This can be seen in the surface pressure plots of Figs. 4.52 to 4.55. Figure 4.52a shows the pressure distributions at $\alpha = 0°$ when the simulated ridge ice was located at the leading edge. It shows that the three ice shapes had a minimal effect on the pressure distribution, as they were located in an extremely favorable pressure gradient. The separation bubbles that formed downstream of the ice shapes were able to reattach quickly, resulting in minimal disturbances to the pressure distribution. Figure 4.52b shows the pressure distributions with the simulated ice shapes at the same location but at $\alpha = 5°$. The simulated ice shapes altered the pressure distribution slightly more at this angle of attack. Increasing the ice-shape height increased the C_p value at the suction peak that formed around 6% chord. Suction peaks were also observed near 2% chord for the iced cases. These were the separation bubbles that formed downstream of the ice shapes. The similarities in the pressure distributions with the three ice shape heights explains why increasing the ice-shape height from 0.10" to 0.25" did not significantly decrease the maximum lift when it was located at the leading edge.

Figure 4.53 shows the pressure distribution plots when the simulated ridge ice was located at $x/c = 0.02$. Figure 4.53a shows that increasing the ice ridge height resulted in significant changes in the pressure distribution even at $\alpha = 0°$. Increasing the ice shape height from 0.10" to 0.25" increased the separation bubble reattachment location from x/c = 0.06 to 0.12. The C_p in the separation bubble also decreased from -0.92 to -1.16 as the flow acceleration increased over the larger ice shape. Figure 4.53b shows the pressure distributions at $\alpha = 5°$. As before, increasing the ice-shape height increased the length of the separation bubble that formed downstream of the ice shape. However, the C_p downstream of the ice shapes increased with increasing ice-shape height as the large

bubble exerted a global effect on the pressure distribution. The larger bubble extracted more momentum from the flow and the reduced pressure recovery can be seen in the trailing edge pressure, which became more negative with increasing ice-shape height.

Figures 4.54 and 4.55 show the pressure distribution plots with the simulated ice ridge located at x/c = 0.10 and 0.20, respectively. The trends were very similar to that shown in Fig. 4.53. Increasing the ice-shape height increased the size of the separation bubble. Also, the C_p increased downstream of the ice shape and decreased at the trailing edge as more momentum was extracted from the flow. This also caused the local suction peak upstream of the ice shape to be smaller. The differences shown in the aerodynamic coefficient plots of Figs. 4.46 to 4.49 were attributed to the longer separation bubble that formed when the ice-shape height was increased. The longer separation bubble resulted in earlier stall, higher drag, and an earlier divergence of the pitching and the flap-hinge moments from the clean values.

4.4.4 Ice-Ridge Geometry

The effects of the simulated ice shape geometry on airfoil aerodynamics were also studied in order to understand what the critical features were. Figures 4.56 to 4.58 show the effect of various geometries (as shown in Fig. 3.11) on integrated aerodynamic coefficients. All of the simulations shown in Figs. 4.56 to 4.58 had a height of 0.25". Figure 4.56 shows the effect of the ice-shape geometry when the simulated ice shape was located at x/c = 0.02. Figure 4.56a shows that the forward-facing quarter round had a $C_{l,max}$ of 0.56 while the backward facing quarter round had a $C_{l,max}$ of 0.63. The backward facing quarter round had only a slightly less severe effect on lift than the forward-facing quarter round even though the side facing the flow was much more streamlined. The half round had a significantly higher $C_{l,max}$ (0.73) than the backward-facing quarter round even though they had an identical forward face exposed to the flow. Thus, the geometry of the downstream side had a significant effect on lift. However, this was the case only when the face exposed to the flow is streamlined (such as with the backward facing quarter round and the half round). Figure 4.56a shows that the forward-facing quarter round and the ramp shape had nearly identical lift curves even though they

had very different downstream sides. Thus, for the two shapes with very blunt forward faces, the shape of the backward face was not as important (for the shapes tested).

Figure 4.56b shows the effect of the simulated ice-shape geometry on drag. It shows that the forward facing quarter round and the ramp shape had nearly identical drag polars. Of the simulated iced cases, the half round had the least drag, followed by the backward-facing quarter round. This was consistent with the drag of these geometries as two-dimensional bodies in isolation (with the geometry mirrored in the surface plane),[60] as shown on Table 4.11. The half-cylinder with the blunt side facing the flow (C_D = 1.7) corresponded to the forward-facing quarter round, the half-cylinder with the rounded side facing the flow (C_D = 1.2) corresponded to the backward-facing quarter round, a wedge with the blunt side facing the flow (C_D = 2.0) corresponded to the ramp shape, and a circular cylinder (C_D = 1.2) corresponded to the half round. The maximum lift values, however, did not correspond as well.

Table 4.11: Lift and drag with various simulated ridge-ice geometry and drag of equivalent isolated geometry. NACA 23012m, ridge-ice at x/c = 0.02.

Ridge-Ice Geometry	$C_{l\,.max}$	C_{d0}	Equivalent Isolated Geometry	C_D
Forward-facing quarter round	0.56	0.0170	Half cylinder w/blunt side facing the flow	1.7
Forward-facing ramp	0.54	0.0179	Wedge with blunt side facing the flow	2.0
Backward-facing quarter round	0.64	0.0167	Half cylinder w/round side facing the flow	1.2
Half round	0.76	0.0167	Full cylinder	1.2

Similar effects were observed for the pitching and flap-hinge moments, as shown in Figs. 4.56c and 4.56d. They show that the backward-facing quarter round experienced C_m and C_h divergence at a higher α than the forward-facing quarter round (at 6° and 7° compared to 5° and 6°), respectively. The half round, in turn, had the divergences at significantly higher α's (8° and 9°) than the backward-facing quarter round. Finally, the forward-facing quarter round and the ramp shape had nearly identical pitching moment and flap-hinge moment curves.

The effect of the ice-shape geometry on the aerodynamic coefficients when the ice shape was located at x/c = 0.10 and 0.20 is shown on Fig. 4.57 and 4.58, respectively.

The results were very similar to that when the ice shape was located at x/c = 0.02 (Fig. 4.53). The forward facing quarter round and the ramp shapes had nearly identical effect on the aerodynamic coefficients. They also had the most severe effect, in terms of altering the aerodynamic coefficients. The half round had the least severe effect, with the backward-facing quarter round falling somewhere in between.

The effect of the ice-shape geometry on the pressure distribution is shown in Fig. 4.59. Figure 4.59a shows that at $\alpha = 0°$, the forward-facing quarter round and the ramp shape (which had nearly identical pressure distribution) resulted in the longest separation bubble, with the reattachment at x/c = 0.60. The backward-facing quarter round had reattachment at x/c = 0.50, and the half round had reattachment at x/c = 0.30. The half round had the lowest C_p values in the constant pressure region of the separation bubble as well as at the local suction peak just ahead of the ice shape. This indicated that it resulted in the least momentum loss (therefore lowest drag), as Fig. 4.57b shows. The backward-facing quarter round and the ramp shape had the highest C_p values in the constant pressure region of the bubble, as well as at the local suction peak just ahead of the ice shape location, indicating the largest momentum loss. Similar results were observed at α = 5°, as Fig. 4.59b shows.

4.4.5 Effect of Roughness Near Ice Shape

SLD icing flight tests have shown the presence of roughness-type accretions upstream and downstream of the spanwise ice shape. Thus, it was important to understand the effect of the roughness-type accretion on the iced-airfoil aerodynamics. The roughness-type accretion was simulated using 16-grit roughness tape (with k = 0.025", k/c = 0.0014, density = 30%) extending upstream and downstream from the simulated ice shape. Here, the density referred to the percentage of the surface area covered by the roughness grit. Figure 4.60a shows the result of the roughness on lift. In all of the cases, a 0.25" forward-facing quarter round was used at x/c = 0.10. Unlike the other cases, the boundary layer on the upper surface was not tripped, as the roughness was expected to trip the flow. The various extents of the roughness that were tested did produce large relative changes in lift, but they were not large in an absolute sense since the C_l values were so low. Figure 4.60a shows that the lowest $C_{l,max}$ (0.31) resulted

when the roughness extended 0.5" in front of the ice shape. When the chordwise roughness extent was smaller than 0.25", most or all of the roughness was located inside the separation bubble that formed upstream of the ice shape, lessening its effect ($C_{l,max}$ = 0.34). When the roughness extent was increased from 0.5" to 2", the $C_{l,max}$ increased from 0.31 to 0.37. This may have happened because the roughness decreased the effective height of the ice shape by displacing the boundary layer upwards. Figure 4.60a also shows that when the 2" chordwise extent roughness was placed immediately downstream of the roughness in addition to the 1" extent upstream, the resulting $C_{l,max}$ was 0.32. This was slightly lower than the case with only the 1" extent upstream roughness ($C_{l,max}$ = 0.34). Thus the roughness downstream of the ice shape had a measurable effect on lift even though it was completely submerged within the long separation bubble that formed downstream of the ice shape.

The effect of the surface roughness on drag is shown on Fig. 4.60b. It shows that the surface roughness extent did have measurable effects on drag although they were not large. Of the cases tested, the 2" roughness extent had the least drag. Figures. 4.60c and 4.60d show the effects of surface roughness extent on the pitching and flap hinge moments. Again, they show that the surface roughness extent did not have a large effect on C_m and C_h. However, as before, the 2" roughness extent had the least aerodynamic degradation, as the C_m and C_h curves diverged from the clean case at a higher α than the other cases tested.

Figure 4.61 shows the effect of the surface roughness on the pressure distribution. Figure 4.61a shows that at $\alpha = 0°$, there was very little change in C_p due to variations in the roughness extent. All of the cases with the roughness, however, resembled the no-roughness case without the trip. There was more variations in the pressure distribution at $\alpha = 5°$, as Fig. 4.61b shows. The 0.5" upstream and the 1" unpstream/2" downstream cases had the least amount of pressure recovery (as indicated by the highest value of C_p in the constant pressure region of the bubble). This resulted in the lowest $C_{l,max}$, as Fig. 4.60a showed. A not of interest was that all of the roughness C_p's appeared to be bounded by the tripped and untripped cases.

4.4.6 Effects of Spanwise Gap

In SLD aircraft icing tests,[8,9] the spanwise ice accretions were observed to partially shed, leaving spanwise gaps. This causes the ice accretion and the associated flowfield to be strongly three-dimensional. Because of this, cases were run in order to simulate the ice accretion after partial shedding. The baseline 0.25" forward facing quarter round was tested with nominal spanwise gaps of 2.5" and 5". The simulated ice accretion span was kept at 6". The schematics of the spanwise gaps are shown in Fig. 4.62. The model on the left has 2.5" spanwise gaps and the model on the right has 5" spanwise gaps. The direction of the flow is from the left to the right. This particular arrangement was chosen in order to keep one of the simulated ice shape spans over the model's surface taps.

Figure 4.63 shows the effects of spanwise gaps on the aerodynamic coefficients. All of the data shown in this figure were derived from the force balance measurements because the pressure measurements cannot capture spanwise variations in highly 3-D flow. Figure 4.63a shows that the presence of the spanwise gaps significantly increased the lift in the non-linear range when compared to the full-span simulated ice case. However, the lift curves became non-linear at nearly the same angle of attack (3°). Also, there was not a large difference in the lift curve between the 2.5" and 5" gap cases (the 5" gap case had slightly higher lift and slightly lower drag). Figure 4.63b shows the effect of spanwise gaps on drag. Again, it shows that the spanwise gaps significantly reduced drag when compared to the full-span case. The 5" gap case had less drag than the 2.5" case because it had less flow blockage.

Figures 4.63c and 4.63d show the effect of the spanwise gaps on pitching and flap hinge moments. The gaps significantly delayed the onset of the divergence of C_m and C_h from the clean model values. The divergence in C_m (for both 2.5" and 5" gap cases) occurred at α = 4°, instead of α = 0° for the full span case. The divergence in C_h occurred at α = 4°, instead of α = 1°.

4.4.7 Lower Surface Ice

In a typical icing encounter, ice accretes on the lower surface as well as the upper surface. Thus, the NACA 23012m was tested with the baseline 0.25" quarter round on the upper and lower surface. Figure 4.64 shows the integrated aerodynamic coefficients with the simulated ice shape placed at x/c = 0.10 on the upper and lower surfaces. The boundary layer was tripped on both upper and lower surfaces. The lift and pitching moment data shown were derived from the force balance measurements. This was because when the simulated ice shape was located at x/c = 0.10 on the lower surface, there were not enough pressure taps left available on the lower surface to accurately generate lift and pitching moment (due to sparse pressure tap distribution on the lower surface). The drag data, however, was still derived from the wake pressure measurements.

Figure 4.64a shows that when the simulated ice shape was located only on the lower surface, its effect on lift was much less severe than when it was located only on the upper surface. The $C_{l,max}$ when the simulated ice accretion was placed only on the lower surface was 1.26. This was much greater than the $C_{l,max}$ of 0.27 when the simulated ice shape was located on the upper surface only. The worst lift degradation occurred when the simulated ice accretion was located on both the upper and the lower surface, with a $C_{l,max}$ of 0.21. However, the lift curve was very similar to the case where the simulated ice accretion was located only on the upper surface. The simulated ice shape on the lower surface did not have a large effect on lift because at positive angles of attack, the pressure gradient on the lower surface was very favorable. Thus, the separation bubble due to the simulated ice shape was much smaller than that on the upper surface.

Figure 4.64b shows the effect of the lower surface simulated ice accretion on drag. It shows that when the simulated ice accretion was located only on the upper surface, it produced large increases in drag only at positive lift (i.e. positive α). When the simulated ice accretion was located only on the lower surface, large increases in drag were observed only at negative lift. When the simulated ice shape was located at both the upper and lower surfaces, large increases in drag were observed at both negative and positive lift (and were close to the sum of the upper-only and lower-only cases).

Figure 4.64c and 4.64d show the effect of the lower surface ice accretion on pitching and flap hinge moments. It shows that when the simulated ice accretion was located only on the lower surface, the C_m and C_h curves were very similar to that of the clean model case. When the simulated ice accretion was located on both the upper and lower surfaces, the C_m and C_h curves were very similar to that of the case where the simulated ice accretion was located only on the upper surface.

4.4.8 Reynolds Number Effect

As stated in Section 2.4, when the Reynolds number of a clean airfoil is increased, the $C_{l,max}$ typically increases as well. However, on an airfoil with surface contamination, this does not occur once a critical Reynolds number is reached, as $C_{l,max}$ becomes relatively insensitive to increases in the Reynolds number, as discussed in Section 2.4. It is important to note that when the Reynolds number was varied in the University of Illinois Subsonic Wind Tunnel, there was also a variation in the Mach number as well, which may have influenced the results. However, the highest Mach number tested was 0.18 and the airfoils tested were not of the high lift type (with very negative C_p at the suction peak). Thus, while the author was aware of possible influences of Mach number variations, it was thought not to be large.

Figures 4.65 to 4.68 show the same results for the simulated ridge ice on the NACA 23012m when the Reynolds number was increased from 1 to 1.8 million. Figure 4.65 shows the effect of increasing the Reynolds number when the simulated ridge ice was located at the leading edge. The $C_{l,max}$ of the clean model increased from 1.38 to 1.50 as the Reynolds number was increased from 1 to 1.8 million. However, the aerodynamic coefficients of the ice airfoil were relatively insensitive to the changes in the Reynolds number in this range. The iced-airfoil $C_{l,max}$ was identical for both of the Reynolds number, with nearly identical lift curves. The Re = 1.8 million case did, however, have slightly higher C_l in the nonlinear region before stall. Figure 4.65b shows that there was not a significant Reynolds number effect on drag either. The Re = 1.8 million case did have slightly lower drag, which was similar to that observed for the clean model. Figures 4.65c and 4.65d show the effect of Reynolds number on pitching moment and hinge moment. Again, the effects were almost negligible. The break in the C_m and

C_h occurred at the same angle of attack (12° for C_m and C_h) for both Reynolds number. However, before the break, C_m and C_h for the Re = 1.8 million case were slightly higher than the Re = 1 million case.

Fig. 4.66 shows the effect of Reynolds number when the simulated ridge ice was located at x/c = 0.02. Again, increasing the Reynolds number from 1 to 1.8 million had negligible effect on iced-airfoil aerodynamics. Figure 4.67 shows the Reynolds number effect when the ridge ice was located at x/c = 0.10. The Reynolds number effect was more significant at this ice shape location. Increasing the Reynolds number reduced the $C_{l,max}$ from 0.29 to 0.27 and increased drag at all angles of attack. This was opposite of what was observed on the clean model. There were also larger differences in the C_m and C_h. However, increasing the Reynolds number did not changed the angle of attack at which C_m and C_h broke. Figure 4.68 shows the Reynolds number effect when the simulated ridge ice was located at x/c = 0.20. The results were very similar to that when the ice shape was located at x/c = 0.10. Increasing the Reynolds number resulted in slightly lower C_l and higher C_d at nearly all angles of attack. The changes in the C_m and C_h were similar as well. Although increasing the Reynolds number from 1 to 1.8 million had measurable effects on the ice-aerodynamic coefficients, they were very small when compared to that of the ice-shape size, geometry, and location.

An implication of the insensitivity of the 2-D iced-airfoil to the increases in the Reynolds number is that the wind-tunnel data generated at relatively low Reynolds number (less than 2 million) can be applied to flight Reynolds number (over 6 million) since the results will not vary significantly. This was consistent with findings of Hoerner[33] and Morgan, Ferris, and McGhee.[34] Also, this indicates that when the full size ice shape/airfoil is to be scaled down to be tested using a smaller airfoil at lower Reynolds number, the proper ice shape scaling is the k/c (geometric scaling) and not one based on the local boundary-layer thickness (k/δ). As the Reynolds number was varied, k/δ varied as well since the local boundary thickness varies with Reynolds number. If maintaining k/δ value had been critical, there would have been a very large variation in aerodynamic coefficients. Maintaining the k/c value was extremely important because as shown in Section 4.4.3, variations in k/c had a large effect on iced-airfoil aerodynamics.

4.4.9 Flap Deflection

Figure 4.69 shows the effects of the flap deflection on integrated aerodynamic coefficients. Figure 4.69a shows that flap deflection did not significantly alter the lift characteristics of the airfoil with simulated ice (x/c = 0.10, k = 0.25"). All three flap deflection cases show a very gradual stall characteristic of thin-airfoil stall, with the lift curve becoming nonlinear at $\alpha = 2°$. Also, as the flap deflection was increased, the linear region of the iced cases became increasingly shifted vertically from the clean cases (i.e. reduced lift at a given α). This occurred because increasing the flap-deflection angle increased the decambering effect of the ice shape. At δ_f = -5°, there was almost no vertical shift in the lift curve, indicating that the ice shape did not significantly decamber the airfoil. However, at δ_f = 5°, there was a 0.08 shift in between the iced and the clean cases, indicating that the ice shape had caused a significant decambering of the airfoil.

Figure 4.69b shows the effect of flap deflection on drag. On the clean model, the varying the flap deflection did not change the drag polars by a large amount. However, increasing the flap deflection did significantly decrease the drag at matched lift coefficients for the case with simulated ice accretion.

Figures 4.69c and 4.69d show the effect of flap deflection on the pitching and flap hinge moments. Increasing the flap deflection from -5° to 5° did not change where the breaks in the C_m curves (with simulated ice shapes) occurred, as it occurred at α = -1° for all three flap deflections. Varying the flap deflection from -5° to 5° decreased the angle of attack at which the C_h curves broke from 2° to 0°. Increasing the flap deflection also increased the differences in C_m and C_h between the clean and the iced case at negative angles of attack. This was similar to the vertical shift in the linear regions of the lift curve (Fig. 4.69a).

Figure 4.70 shows the plot of lift verses the flap deflection angle at constant angles of attack. This is a plot of the flap effectiveness as it shows how effective the flap is in changing lift. It shows that at α = -2° and 0°, the simulated ice shape did not greatly decrease the flap effectiveness. At α = -2°, the $C_{l,\delta f}$ was 5.17/rad for the clean case and 4.71/rad for the simulated ice case, a 9% reduction in flap effectiveness. However, at α = 2° and 4°, there were very large reductions in the flap effectiveness. On the clean model (at $\alpha = 4°$), the $C_{l,\delta f}$ was 5.17/rad while on the simulated ice case, the $C_{l,\delta f}$ was 2.87/rad,

a 44% reduction. Thus, in the linear range of the lift curve, the simulated ice shape did not significantly alter the flap effectiveness. However, in the nonlinear regions, the flap effectiveness was cut almost in half.

Fig. 4.71 shows the effect of flap deflection on the pitching moment at constant angles of attack. It shows that the simulated ice shape caused large changes in C_m, as much as 0.09 in the range of α's shown. However, it did not affect $C_{m,\delta f}$ as much as $C_{l,\delta f}$. In the worst case, the simulated ice shapes altered $C_{m,\delta f}$ by only 18%.

4.5 NLF 0414 Results

The importance of airfoil geometry on iced-airfoil aerodynamics was investigated by testing the simulated ice shapes on the NLF 0414 airfoil, which has aerodynamic characteristics quite different from the NACA 23012m. Studying the effect of simulated ice shapes on two very different airfoils provided a clearer explanation of the aerodynamic factors that determine the critical ice shape location.

4.5.1 Comparison of Clean Models

Large differences in the iced-airfoil aerodynamics between the NACA 23012m and the NLF 0414 were observed. This was because these two airfoils have very different geometry and aerodynamic characteristics. Figure 4.72 shows the comparisons between the NACA 23012m and the NLF 0414 geometry. NACA 23012m was designed to provide low pitching moment by generating most of the lift near the leading edge. NLF 0414, however, was designed to achieve laminar flow over the airfoil by distributing the load over a large portion of the chord and delaying the onset of pressure recovery and the accompanying large adverse pressure gradient (where transition occurs) until around 70% chord.

The different aerodynamic characteristics are quite apparent in the measured clean-model surface pressure of Fig. 4.73 (Re = 1.8 million, M = 0.18). In this figure, the surface pressures are compared at nearly identical lift coefficients. However, because the NLF 0414 is highly cambered, it's α was much lower than that of NACA 23012m. On the NACA 23012m, there was a strong suction peak centered at x/c = 0.08, followed by an adverse pressure gradient that extended to the trailing edge. On the NLF 0414, a

leading-edge suction peak was not present. Instead, after the initial acceleration around the leading edge to x/c = 0.02, the surface pressure was nearly constant ($C_p \approx$ -0.8) to x/c = 0.73. The pressure recovery process began at this point and the adverse pressure gradient extended from here to the trailing edge. Since the flow around the nose on the NACA 23012m accelerated to a $C_{p,min}$ = -1.7 versus only -0.9 for the NLF 0414, much more pressure recovery was required on the NACA 23012m airfoil.

4.5.2 Effect of Ice-Shape Locations

All of the results in this section were with the 0.25" forward-facing quarter round ice shape simulation. The boundary layer was tripped at x/c = 0.02 on the upper surface and x/c = 0.05 on the lower surface. The boundary layer was not tripped for the clean model or when the ice shape was located at $x/c \leq$ 0.02. The Reynolds number was 1.8 million, and the Mach number was 0.18.

The differences in the airfoil geometry (and the resulting clean-airfoil aerodynamic characteristics) between the NACA 23012m and NLF 0414 led to large differences in behavior with simulated ice shapes. Figure 4.74a shows the effect of simulated ice shape on the lift of the NACA 23012m. Varying the ice shape location from x/c = 0.02 to 0.20 had large effects on the lift of the NACA 23012m. The loss in lift was most severe when the ice shape was located at x/c = 0.10 (with $C_{l,max}$ = 0.27). When the ice shape was located at x/c = 0.02, the $C_{l,max}$ was approximately doubled to 0.57.

Figure 4.74b shows the effect of simulated ice on the lift of the NLF 0414. There was not a large difference in the lift curve when the ice shape location was varied from x/c = 0.02 to 0.20, with only slight changes in the $C_{l,max}$ and $\alpha_{c_\ell,max}$. When the ice shape was located at x/c = 0.02, the $C_{l,max}$ was 0.74 at α = 5°. When the ice shape was located at x/c = 0.20, the $C_{l,max}$ was 0.71 at α = 7°. These maximum lift values were much higher than on the NACA 23012m. It will be shown later that when the ice shape was located downstream of x/c = 0.20, significant changes occurred in the lift.

Figure 4.75 shows the effect of the ridge-ice location on drag on the two airfoils. It shows that generally, drag was lower on the NLF 0414 at comparable lift values. There

was more variation in drag with varying ice-shape locations (when compared to lift), with increasing drag as the ice shape was moved downstream.

Figure 4.76 shows the effect of ridge-ice location on the pitching moment. Figure 4.76a shows that on the NACA 23012, the angle of attack at which the C_m started to decrease quickly (due to rapid bubble growth) decreased from $\alpha = 5°$ to $\alpha = -3°$ when the ridge ice was moved from $x/c = 0.02$ to 0.20. The NLF 0414 was much less sensitive to the changes in the ice-shape location. Although moving the ice shape downstream from $x/c = 0.02$ to 0.20 decreased the C_m value before the onset of rapid bubble growth, the angle of attack at which this occurred remained constant at $\alpha = 5°$.

The effect of the ridge-ice location on hinge moment is shown on Fig. 4.77. Figure 4.77a shows that on the NACA 23012m, there was a sharp break in the C_h-α slope when the separation bubble reached the flap. This occurred at $\alpha = 6°$ when the ice shape was located at $x/c = 0.02$ and at $\alpha = 1°$ when the ice shape was located at $x/c = 0.10$ and 0.20. On the NLF 0414, the presence of ice shape did not have a large effect on the C_h. This was because the flow over the flap on the clean model was separated.

Figures 4.78 to 4.81 shows the effect of ridge-ice location on the NLF 0414 by itself in more detail, with several more ice shape locations. Figure 4.78 shows the effect of ridge-ice location on lift. There was a large difference in lift curve when the ice-shape location was varied from the leading edge to $x/c = 0.02$, with the $C_{l,max}$ decreasing from 1.05 to 0.72. However, when the simulated ice shape location was varied from $x/c = 0.02$ to 0.20, the lift curves did not vary significantly, with only slight changes in the $C_{l,max}$ and $\alpha_{Cl,max}$. The maximum lift was also much higher than on the NACA 23012m, with a typical value of 0.70. When the ice shape was located at $x/c = 0.30$, the lift curve started to change significantly, with $C_{l,max}$ reduced to 0.58. When the ice shape was located at $x/c = 0.40$, the lift curve appeared very different as it did not have a clearly defined $C_{l,max}$. Instead, there was an inflection in the lift curve at $\alpha = 0°$ due to the separation of the flow downstream of the simulated ice shape. These variations were due to the proximity of the ice shape to the trailing edge pressure recovery region where the severe adverse pressure gradient (as shown on Fig. 4.73) was present. This will be explained in more detail when the flowfield is diuscussed.

Figure 4.79 shows the effect of ice-shape location on the drag polars. The drag on the NLF 0414 generally increased as the ice shape was moved downstream. However,

when the ice shape was located between x/c = 0.06 and 0.20, the change in drag was small, with very similar polars. Large changes in the drag polars were once again observed when the ice shape was moved from x/c = 0.20 to 0.30 due to increased separation bubble size. When the ice shape was located at x/c = 0.40 and 0.50, there was a break in the drag polar (at C_d = 0.14 for x/c = 0.40 and at C_d = 0.07 for x/c = 0.50), where the lift increased without large increases in drag. This occurred because the ice shape was located so far aft that even after the flow had completely separated downstream of the ice shape, significant lift was still being generated upstream of the ice shape in the leading-edge suction region. Increasing the angle of attack did not increase drag by a large amount (in the order of an airfoil undergoing stall) because the flow behind the ice shape was already fully separated. However, lift continued to increase because the flow upstream of the ice shape was still attached.

The effect of the ice-shape location on the pitching moment is shown in Fig. 4.80. Generally, as the simulated ice shape was moved downstream, the break in the pitching moment occurred at lower angles of attack and was more gradual. As with lift and drag, the pitching moment curves appeared very similar when the ice shape was located between x/c = 0.06 and 0.20. The angle of attack at which the pitching moment started to break in changed only from 5° to 4° as the ice shape was moved from x/c = 0.06 to 0.20. This was much smaller that what was observed on the NACA 23012m (Fig. 4.33). However, when the ice shape was located at x/c = 0.30, the pitching moment curve appeared very different, with no distinct negative break in the slope. This lack of break was observed at other ice shape locations downstream of x/c = 0.30.

Figure 4.81 shows the effect of ice shape location on the flap hinge moment. The ice shape did not produce significant changes in the C_h values for the NLF 0414 when its location was varied between x/c = 0.02 and 0.20. The slope $C_{h,\alpha}$ started to break and become more negative at about α = 5°, where the airfoil was stalling. When the ice shape was at x/c = 0.30, the angle of attack at which $C_{h,\alpha}$ broke decreased to 1° because the bubble reached the flap at a lower angle of attack. As the ice shape was moved further downstream, the angle of attack at which $C_{h,\alpha}$ broke decreased further.

The large differences between the NACA 23012m and NLF 0414 airfoils can also be seen in Fig. 4.82, a summary of $C_{l,max}$ as a function of ice-shape location. On the NACA 23012m, there was a dramatic drop in $C_{l,max}$ as the ice shape location was varied

from x/c = 0.00 to 0.10. However, Fig. 4.82 shows that on the NLF 0414, the variations in the ice-shape location did not have a large effect on $C_{l,max}$ between x/c = 0.02 and x/c = 0.20. The $C_{l,max}$ varied only between 0.68 and 0.79 when the ice shape was located in this region. The only significant change took place when the ice shape was moved from the leading edge to x/c = 0.02, which decreased the $C_{l,max}$ from 1.08 to 0.76. When the simulated ice shape was located at x/c = 0.30, the $C_{l,max}$ dropped to 0.58 and then to 0.26 at x/c = 0.35. When the ice shape was located downstream of this location, the lift curves did not have a true $C_{l,max}$ in the classical sense. Instead, only an inflection in the lift curve was observed where the flow downstream of the simulated ice shape had failed to reattach. Generally the $C_{l,max}$ values for the NLF 0414 were much higher than those observed for the NACA 23012m.

Figure 4.83 shows the lift loss ΔC_l (when compared to the clean airfoil) due to the 0.25" ice shape simulation on the NLF 0414. On the NACA 23012m (Fig. 4.36) the most critical location of the simulated ice shape (in terms of lift loss) was between x/c = 0.10 and 0.12 and did not vary significantly with angle of attack. This was the same location that resulted in the lowest $C_{l,max}$, as shown in Fig. 4.82. The most critical location was situated between the locations of the maximum local air velocity and the maximum adverse pressure gradient. Thus, it did appear that the most critical ice-shape location was related to these flow features.

The lift loss behavior of the NLF 0414 airfoil, as shown in Fig. 4.83, was quite different from that of NACA 23012m. Figure 4.83 shows that when the ice shape was placed between x/c = 0.02 and 0.20, there was not a large variation in the lift loss. This was similar to what was observed in the $C_{l,max}$ plot of Fig. 4.82. It was only when the ice shape was located downstream of x/c = 0.30, and closer to the adverse pressure gradient at the trailing-edge pressure recovery that a much larger increase in the lift loss was observed. This was even the cases at $\alpha > 3°$ where the adverse pressure gradient associated with the leading-edge suction peak was more severe than the trailing-edge pressure recovery.

Figure 4.84 shows ΔC_d, the drag increase due to the ice shape when compared to the clean airfoil, for the 0.25" ice shape. Figure 4.36 shows the drag increase on the NACA 23012m. It shows that the most critical location of the simulated ice shape (in terms of ΔC_d) moved upstream with increasing angles of attack and closely coincided

with the location of the maximum local air velocity. Fig. 4.84 shows the drag increase on the NLF 0414. At angles of attack of -3° and 0°, a leading-edge suction peak was not observed. Instead, the highest local air velocity occurred near midchord at x/c = 0.55 (for α = -3°) and 0.45 (for α = 0°). The location of maximum adverse pressure gradient was located at the trailing edge pressure recovery near x/c = 0.75. Because the simulated ice shape was not tested at x/c > 0.50, some of these points described above are not shown in Fig. 4.84. At angles of attack of 3° and 5°, a leading-edge suction peak was present, with the location of the $C_{p,min}$ at x/c = 0.01. The location of the maximum adverse pressure gradient was located immediately downstream of the $C_{p,min}$ and not at the trailing edge pressure recovery. At angles of attack of -3° to 0° (where there was no leading-edge suction peak on the clean model), there was a gradual increase in ΔC_d as the ice shape was moved downstream from the leading edge to x/c = 0.30. As the ice shape was moved further downstream, ΔC_d increased at a much faster rate. At angles of attack of 3° and 5°, ΔC_d was relatively constant between x/c = 0.02 and x/c = 0.20, after which ΔC_d started to increase rapidly. The ΔC_d values eventually reached a maximum (at x/c = 0.4 for α = 3° and at x/c = 0.35 for α = 5°) after which they decreased. Unlike the NACA 23012m, the location of the maximum local air velocity was not a good indicator of the most critical simulated ice-shape location.

Figures 4.85 and 4.86 shows ΔC_m, and $\Delta C_{h,}$ respectively on the NLF 0414. At α = -3°, the highest value of ΔC_m was observed when the simulated ice shape was located at x/c = 0.40. As the angle of attack was increased, this location moved upstream, reaching x/c = 0.10 at α = 8°, which was well past stall. Similar trends were observed for ΔC_h as well, as Fig. 4.86 shows. At α = -3°, the most critical location was at x/c = 0.50 (most likely even further downstream, but ice shapes were not tested there). As the angle of attack was increased, the most critical location started to move upstream. However, instead of there being a single, most critical location, there was a region of ice shape location that had nearly the same ΔC_h values. For example, at α = 4°, the most critical location was the region between x/c = 0.35 and 0.50. As the angle of attack was increased, the chordwise location where this constant region started moved upstream.

4.5.3 Flowfield Comparisons

The flowfield of the NLF 0414 airfoils will be discussed and compared to the NACA 23012m in order to provide an explanation to the performance data of the previous section.

Figure 4.87 shows the surface pressure distribution on the NLF 0414 model with the ice-shape simulation at various chordwise locations. The angle of attack was 1°, where the clean airfoil had a C_l similar to the NACA 23012m at $\alpha = 5°$. When the ice shape was located at and between x/c = 0.02 and 0.20, the suction region (due to separation) had similar C_p values (-1.3) and the separation length did not vary as much as it did for the NACA 23012m. The bubble length varied from 18% chord for x/c = 0.02 case to 28% chord for the x/c = 0.20 case. After the flow had reattached, the C_p on all three cases dropped to approximately 0.50 and remained fairly constant until the pressure recovery over the flap occurred.

When the ice shape was located at x/c = 0.40, the surface pressure distribution looked significantly different. Also, based on the low trailing-edge pressures and flow visualization, the separation bubble was determined to not to have reattached, resulting in a separation length of 60% chord.

The reason for the similarities in the x/c = 0.02 to 0.20 cases was that the ice shape and the resulting separation bubble was located in a region of relatively constant pressure (on the clean model). Thus, the separation bubbles in the three cases above were all allowed to reattach in a similar pressure gradient (which happened to be nearly zero in this case). The resulting separation bubbles all appeared similar, with relatively similar suction regions and separation lengths because the ice shape was in a similar flowfield. The slight variation in the separation length may be due to the thicker boundary layer the ice shape encountered as it was moved downstream. The similarities ended when the ice shape was located at x/c = 0.40. Although the ice shape itself was in the region of constant pressure, it was located close to the clean model pressure recovery region (where there was a strong adverse pressure gradient). Thus, the separation bubble was forced to reattach in an adverse pressure gradient, resulting in a trailing-edge separation.

4.5.4 Summary of NLF 0414 Results

The simulated ice shape in the range of $0 \leq x/c \leq 0.20$ affected the NACA 23012m and the NLF 0414 very differently due to the differences in their geometries and clean-airfoil aerodynamics. The NACA 23012m was a much more forward-loaded airfoil, which resulted in a very severe adverse pressure recovery downstream of a large, near-leading-edge suction peak. Thus, the separation bubble that forms downstream of the simulated ice shape had to reattach in a very adverse pressure gradient. This resulted in very long separation bubbles with severe performance degradations. On the other hand, the NLF 0414 had a much more aft-loaded pressure distribution. The separation bubbles that formed downstream of the simulated ice shape attached much quicker, which resulted in much less severe performance degradation. This is shown on Fig. 4.88. It shows the separation bubble reattachment location as a function of angle of attack for the two airfoils tested. The results for the NACA 23012m were obtained from surface fluorescent oil flow visualization. The results for the NLF 0414 were obtained from the surface pressure measurements because flow visualization data were not available for this airfoil. Because of this, the reattachment location was not shown up to stall because at $\alpha > 4°$, the bubble was so large that the reattachment location could not be determined from the pressure measurements.

The results obtained on the NACA 23012m and the NLF 0414 suggest techniques for the design airfoils that are less sensitive to SLD ice accretion. The start of the pressure recovery (and the associated adverse pressure gradient) should be downstream of the impingement limit of the SLD accretion. This means that the location of the $C_{p,min}$ should also be downstream of the likely SLD accretion. Thus, a very front-loaded lift distribution typically employed for low C_m is not desirable, because the $C_{p,min}$ would be very close to the leading edge, ahead of the likely location of the SLD accretion. For existing airfoils, if the $C_{p,min}$ is upstream of the impingement limit of SLD icing, then the deicing system should be far downstream enough to remove all of the icing.

Chapter 5

Summary, Conclusions, and Recommendations

An experimental study was conducted at the University of Illinois in order to understand the effect of supercooled large droplet (SLD) ice accretion on airfoil aerodynamics. The study consisted of a sensitivity analysis of airfoil lift, drag, pitching moment, and hinge moment to different chordwise locations, sizes, and shape of the ridge-ice simulations. This was used to identify location, size, and geometry of ridge ice that results in the most severe performance and control degradation and determine why these are most severe. The effect of SLD icing on flap effectiveness was also investigated. The importance of airfoil geometry on the sensitivity to SLD icing was studied by testing two airfoils (NACA 23012m and NLF 0414) with very different aerodynamic characteristics.

The following is a summary of the results and conclusions of this investigation:

- The forward-facing quarter round used as SLD ridge-ice simulation severely altered the flowfield around the two airfoils tested. A small separation bubble formed upstream of the ice-shape simulation, and a much larger separation bubble formed downstream of the ice-shape simulation. The bubble upstream of the ice shape did not grow significantly with increasing angle of attack. The separation bubble that formed downstream of the bubble grew rapidly with increasing angle of attack. The bubble separated completely off the model at an angle of attack much lower than that at which the clean airfoil stalled. This led to severe reduction in maximum lift and a

large increase in drag. The pitching and hinge moments were severely altered as well.

- The most critical ice-shape location on the NACA 23012m was around x/c = 0.10. This corresponded to the location of the maximum adverse pressure gradient of the clean airfoil, just aft of the large leading-edge pressure peak where most of the lift was generated. When the ice shape was located in this region, the bubble that formed downstream had to reattach in a very adverse pressure gradient. This led to a very large bubble and a severely altered pressure distribution, with the elimination of the leading-edge suction peak. This caused a substantial reduction in lift since the suction peak generated most of the lift. When the ice shape was moved forward of this location, the pressure gradient was more favorable, which resulted in shorter bubble length. The leading-edge suction peak was largely intact as well, resulting in less lift loss. When the ice shape was located downstream of x/c = 0.10, the separation bubble was still very large. However, there was enough distance between the leading edge of the airfoil and the ice shape for the leading-edge suction to start growing and generating lift.

- The effects of simulated ice shape on the NLF 0414 were quite different from the NACA 23012m. There was little variation in lift when the simulated ice-shape location was varied from x/c = 0.02 to 0.20. This was because the pressure gradient of the clean airfoil was nearly zero between the leading edge and x/c = 0.75. When the ice shape was located upstream of x/c = 0.20, the separation bubble was relatively short, and the lift loss was not severe. The large losses in lift occurred when the ice shape was located downstream of x/c = 0.30 and the separation bubble formed over the adverse pressure gradient which started at x/c = 0.75. The effect of the ice shape (at the locations that SLD accretion is likely to form) on the NLF 0414 was not as severe as on the NACA 23012m. This was because the lift pressure recovery on the NLF 0414 occurs well downstream of the likely SLD accretion.

- Increasing the ice-shape height from 0.10” to 0.25” decreased maximum lift and the stall angle of attack. The drag was also increased. This occurred because as the ice-

shape height was increased, the separation-bubble length increased as well. However, when the ice shape was located at the leading edge, increasing the ice shape height had very little effect on lift. The separation bubble that formed downstream of the ridge ice at the leading edge was very small and acted more like a transition strip than an ice accretion.

- Streamlining the ice shape decreased the performance loss of the airfoil. This occurred because streamlining the ice shape shortened the separation bubble

- The presence of surface roughness in the vicinity of the shape did not have large effects on lift, drag, pitching moment, and hinge moment. The ice shape itself remained the dominant feature, and the surrounding roughness did not have a significant impact.

- The presence of gaps in the spanwise ridge-ice simulation significantly increased maximum lift when compared to the full span case. The drag was also decreased.

- The presence of ice shape on the lower surface of the airfoil model (in addition to the one on the upper surface) did not significantly degrade the performance. This was because at positive angles of attack, the pressure gradient on the lower surface was very favorable, resulting in a very small bubble.

- There was little effect on ice-airfoil aerodynamics as the Reynolds number was varied from 1 to 1.8 million. This was consistent with findings of other studies.

- The simulated ice shape did not significantly degrade the flap effectiveness in the linear regions of the lift curve. However, the flap effectiveness was severely degraded in the non-linear region of the lift curve.

The following are recommendations for further study in this area:

- A further analysis of the results with the flap deflected. Determine the effect of flap deflection on critical ice-shape location.

- Determine if there are any robust methods for determining the reattachment location for large bubbles from surface pressure measurements. This will lessen the dependence on time-consuming flow visualization, which is currently required to determine the exact reattachment location for large bubbles.

- Study SLD ice shapes on other airfoils. Only two airfoils were tested in this experiment. Studying more airfoils will further increase the understanding of the effect of airfoil geometry on iced airfoil aerodynamic. It will also provide more validation data for further CFD studies.

- Conduct tests at higher Reynolds number to verify that the results obtained at Re = 1.8 million are applicable to more realistic flight Reynolds number of approximately 6 million.

- Study the effect of Mach number variation. In this study, the Mach number could not be controlled because the wind tunnel was not pressurized. Although one would not expect significant Mach number effects at the speeds of interest with the airfoils used in this test, a test to verify this would be useful.

- Study effects of sidewall boundary-layer control. The flow visualization results showed that there were significant spanwise variations in the flow near the model-wall junction. A sidewall boundary layer control system would reduce these variations and make the flow more two-dimensional.

- A detailed flowfield study of the large separation bubble that formed downstream of the ice shape using split film anemometer. A preliminary attempt was made during this study, but publishable results were not obtained. Determine if there was any change in the bubble characteristics as it grew rapidly. This will increase the understanding of the mechanism that leads to a rapid bubble growth on an iced airfoil.

Figures

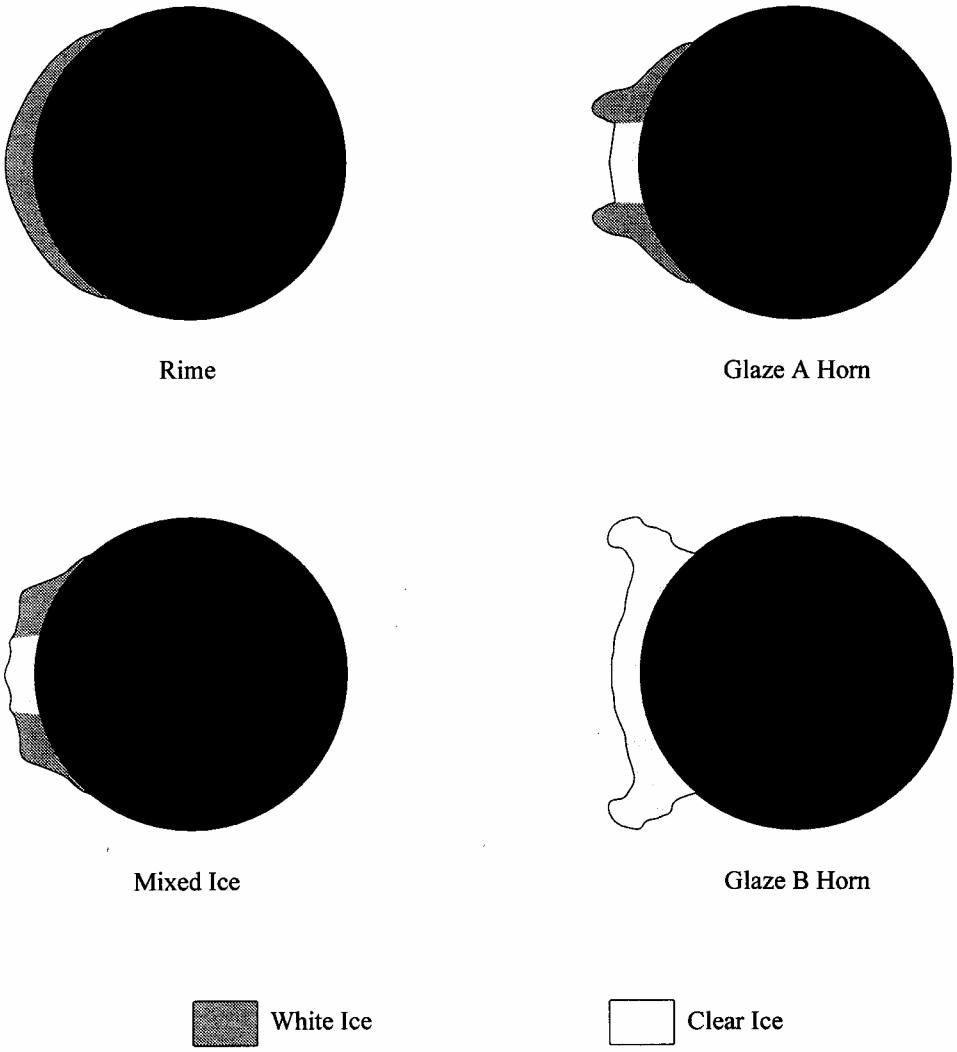

Fig. 1.1: Ice-accretion types observed by Hansman.[4]

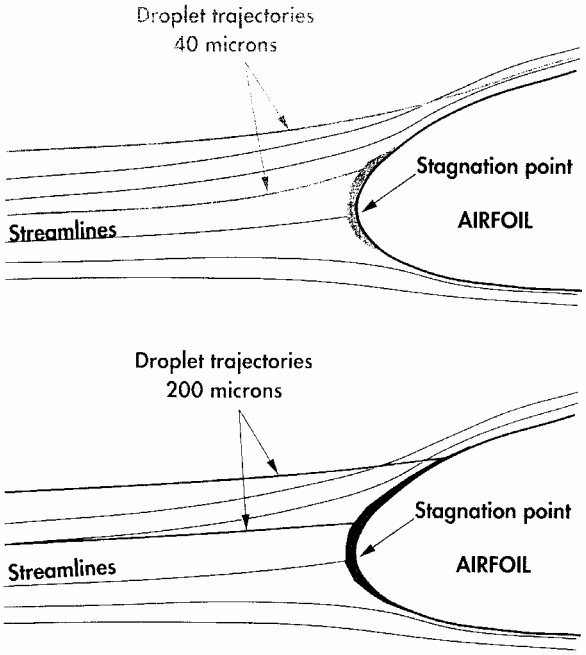

Fig. 1.2: Comparison of trajectories of large and small droplets.[9]

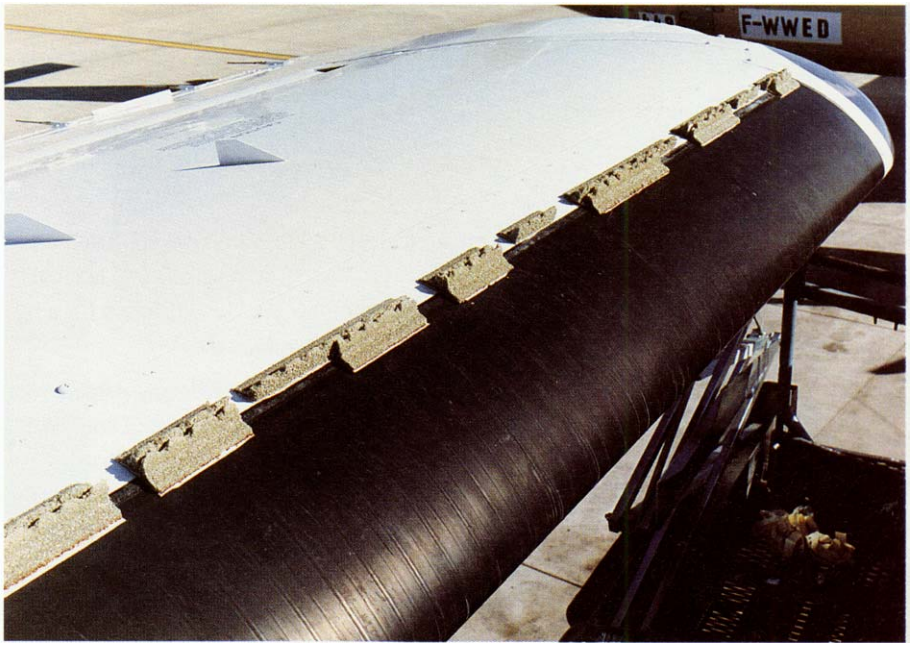

Fig. 1.3: Simulated SLD ice shapes on ATR-72 wing.[9]

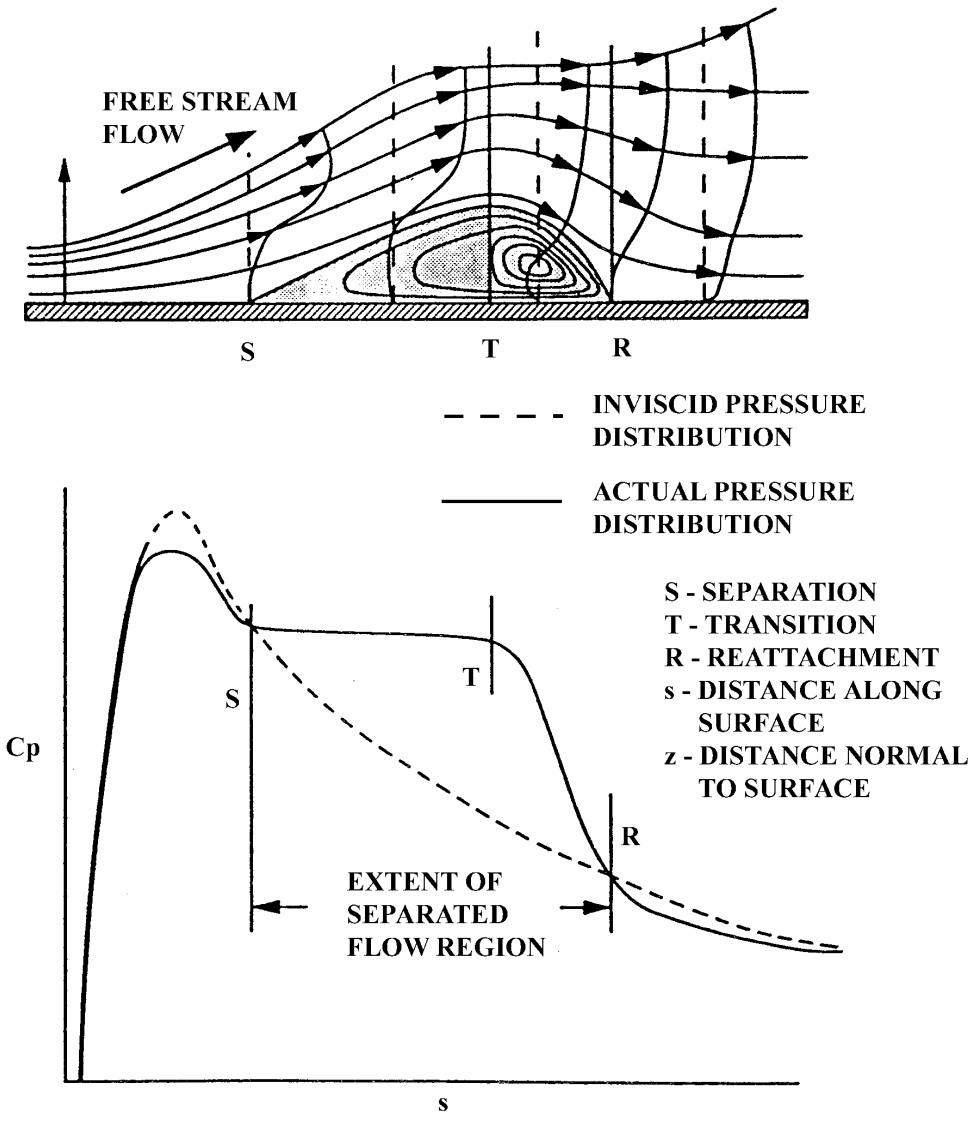

Fig. 2.1: Laminar separation bubble on clean airfoil.[24]

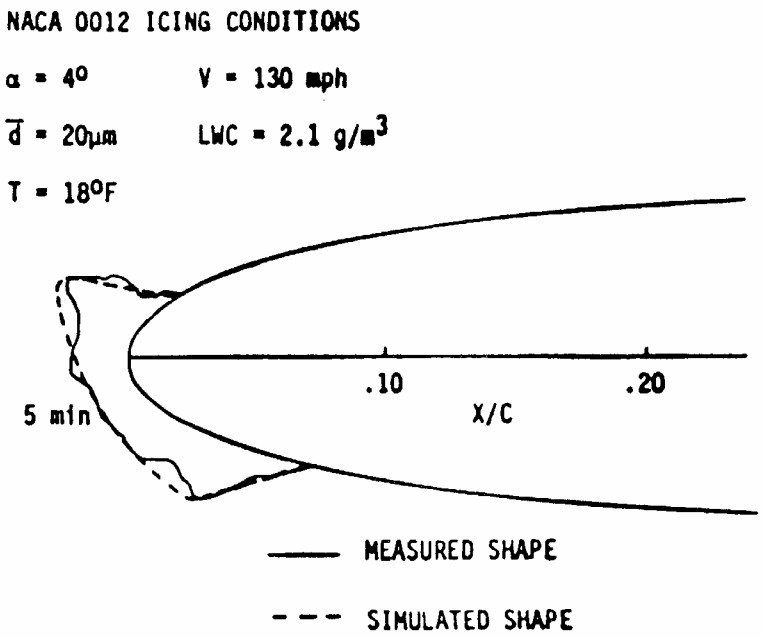

Fig. 2.2a) Glaze-ice simulation

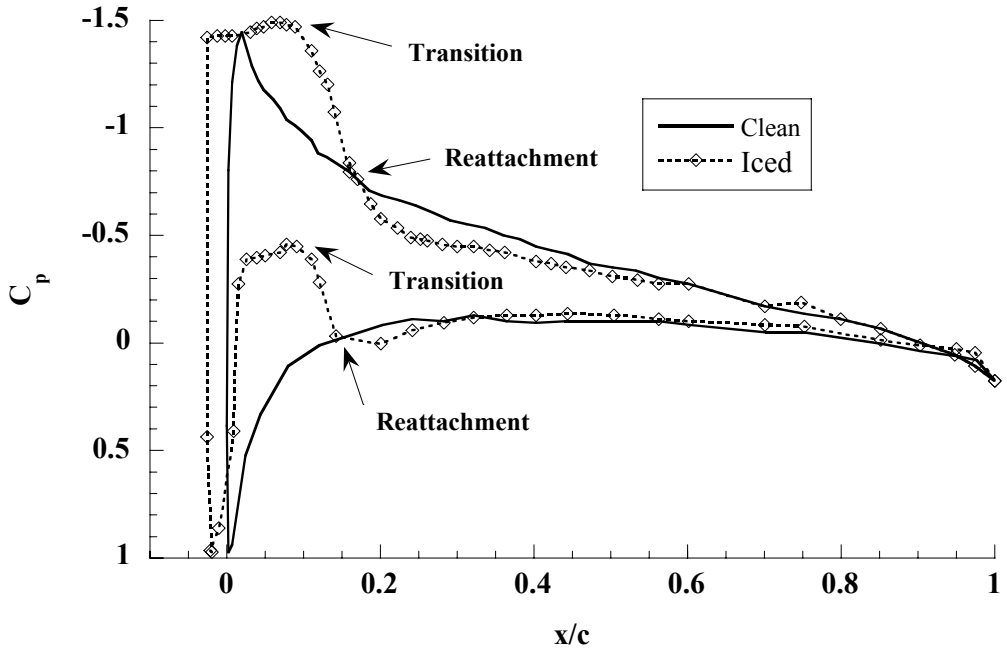

Fig. 2.2b) Pressure distribution

Fig. 2.2: Surface pressure distribution on an airfoil with simulated glaze ice accretion. NACA 0012, *Re* = 1.5 million.[26]

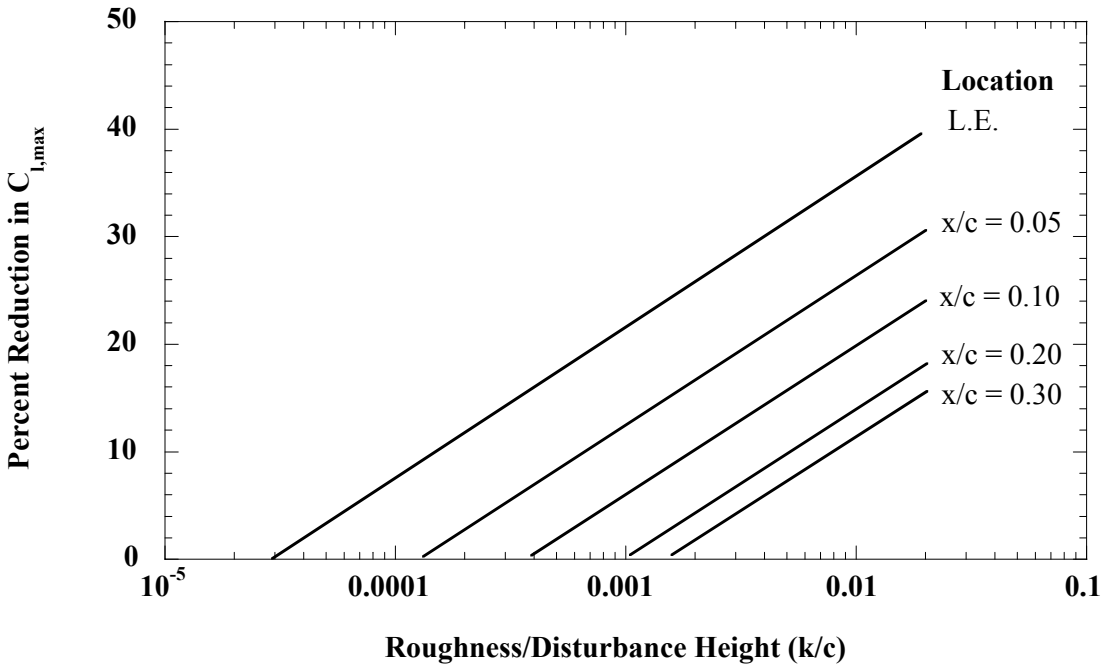

Fig. 2.3: Effect of disturbance height and location on maximum lift.[27]

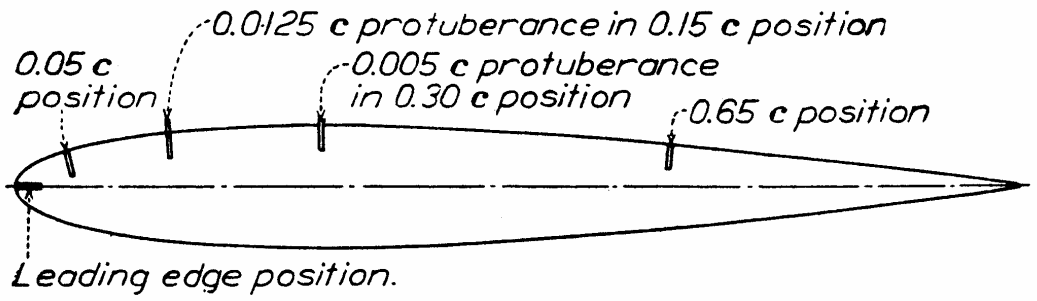

Fig. 2.4: NACA 0012 airfoil and spanwise protuberance geometry used by Jacobs.[28]

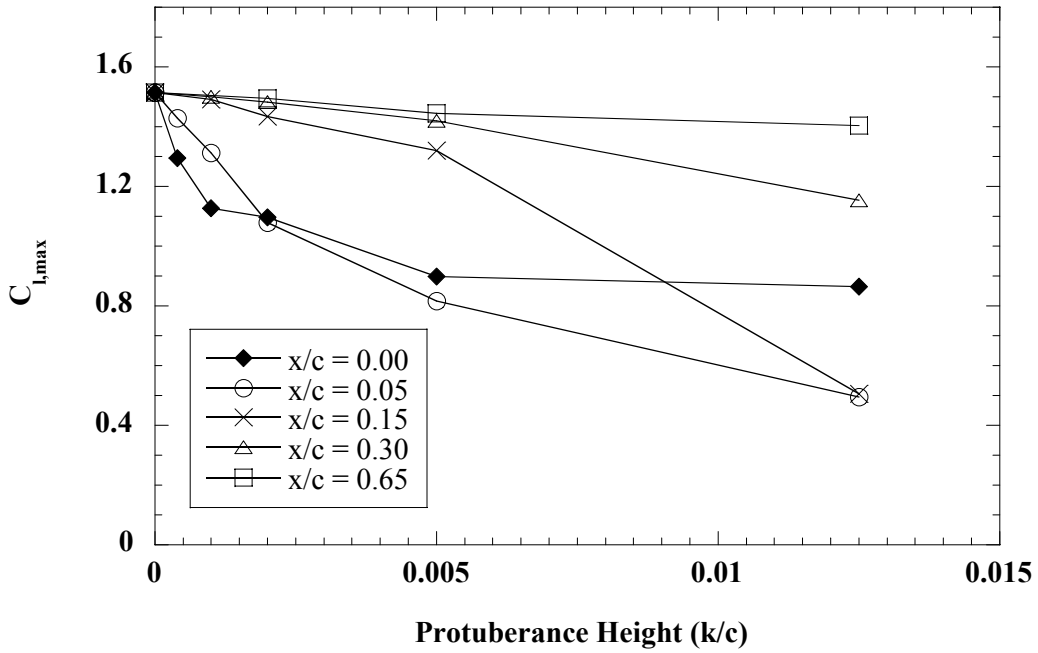

Fig. 2.5: Variation of maximum lift with spanwise protuberance height on NACA 0012; $Re = 3.1 \times 10^6$; Jacobs[28]

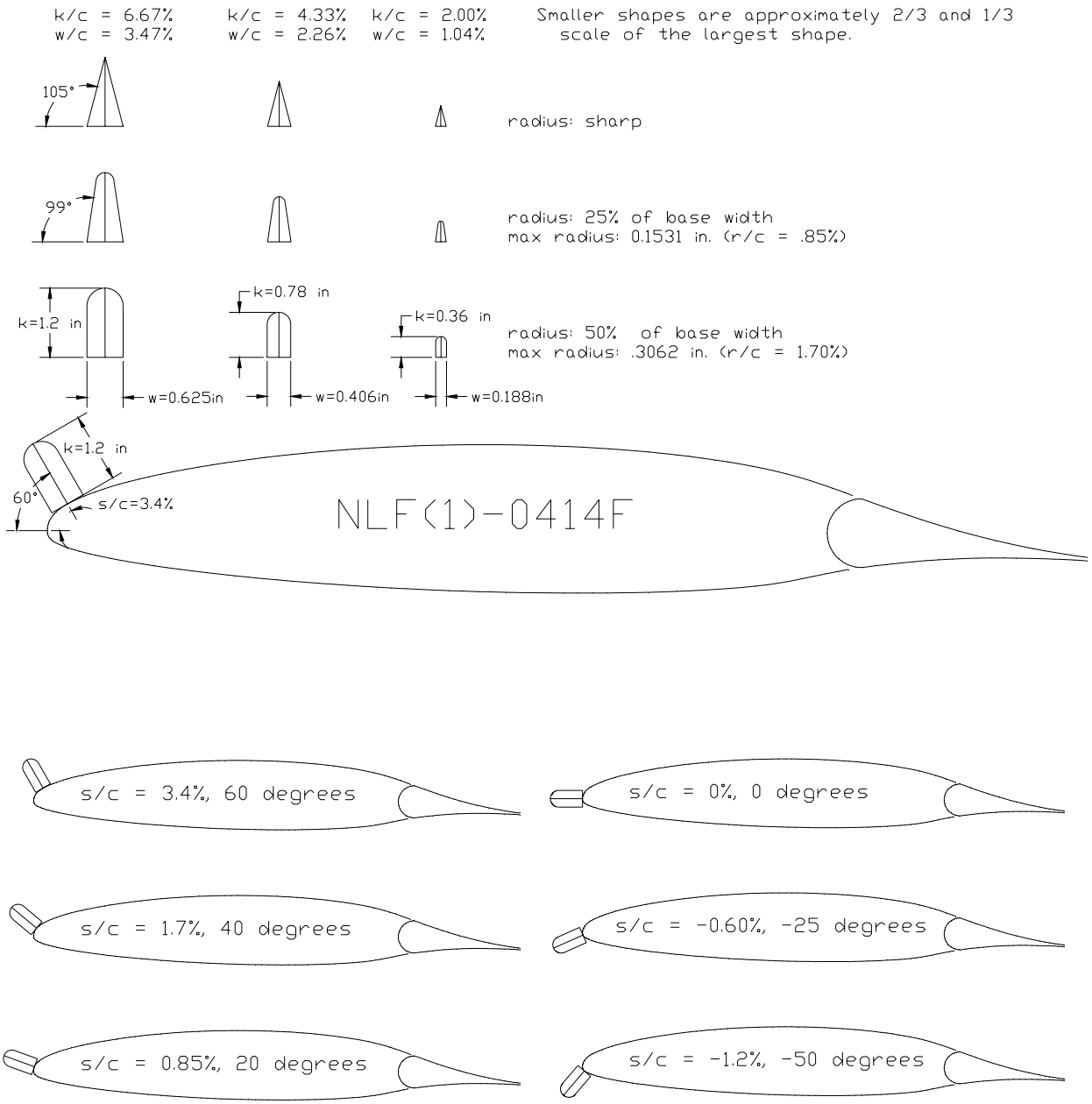

Fig. 2.6: Simulated glaze ice shapes and NLF-0414 model used by Kim and Bragg.[30]

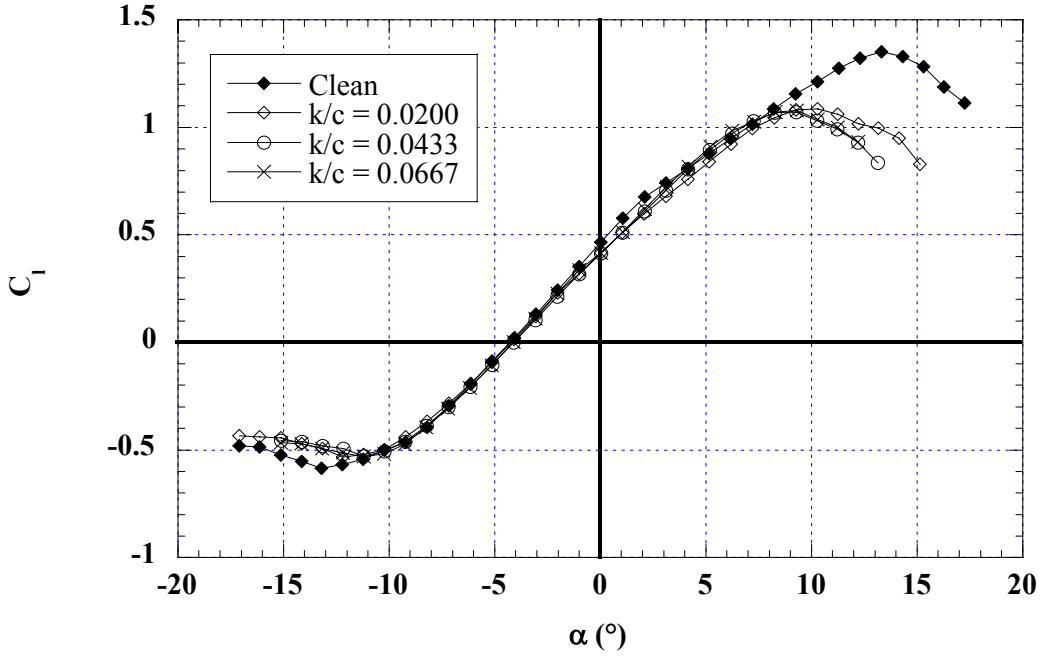

Fig. 2.7a) Lift

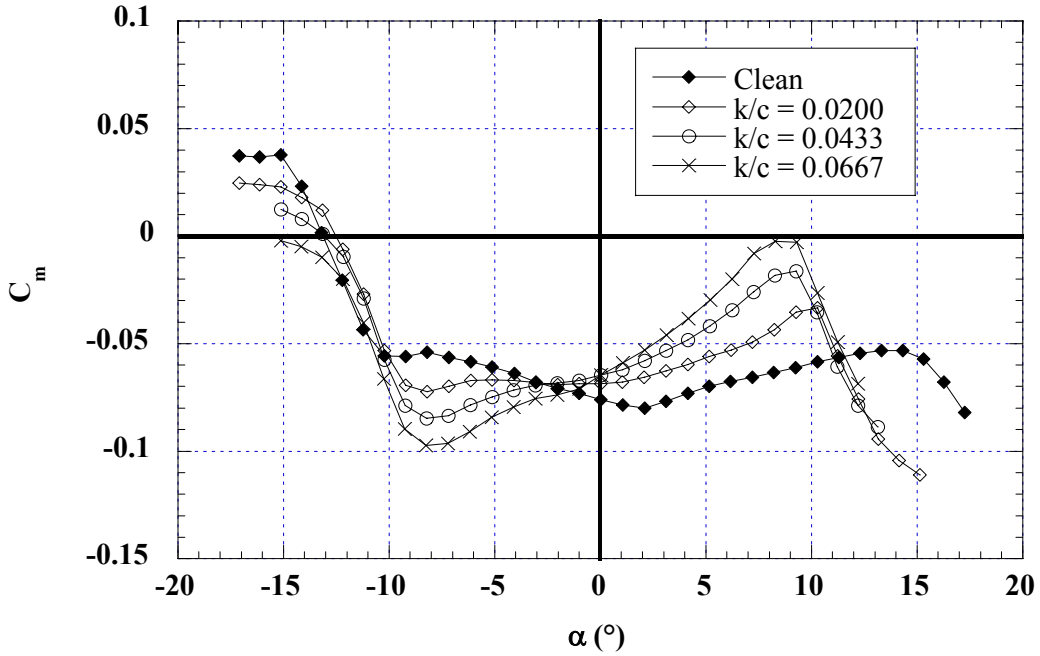

Fig. 2.7b) Pitching Moment

Fig. 2.7: Glaze ice simulation height effects on NLF 0414. s/c = 0.00; Re = 1.8x10^6. Kim and Bragg.[30]

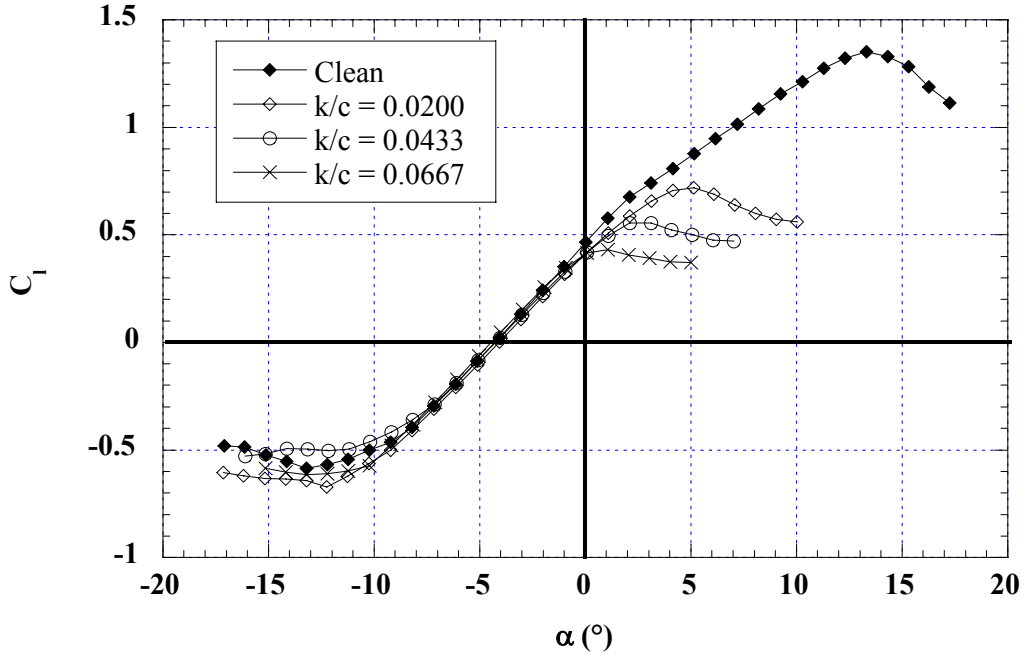

Fig. 2.8a) Lift

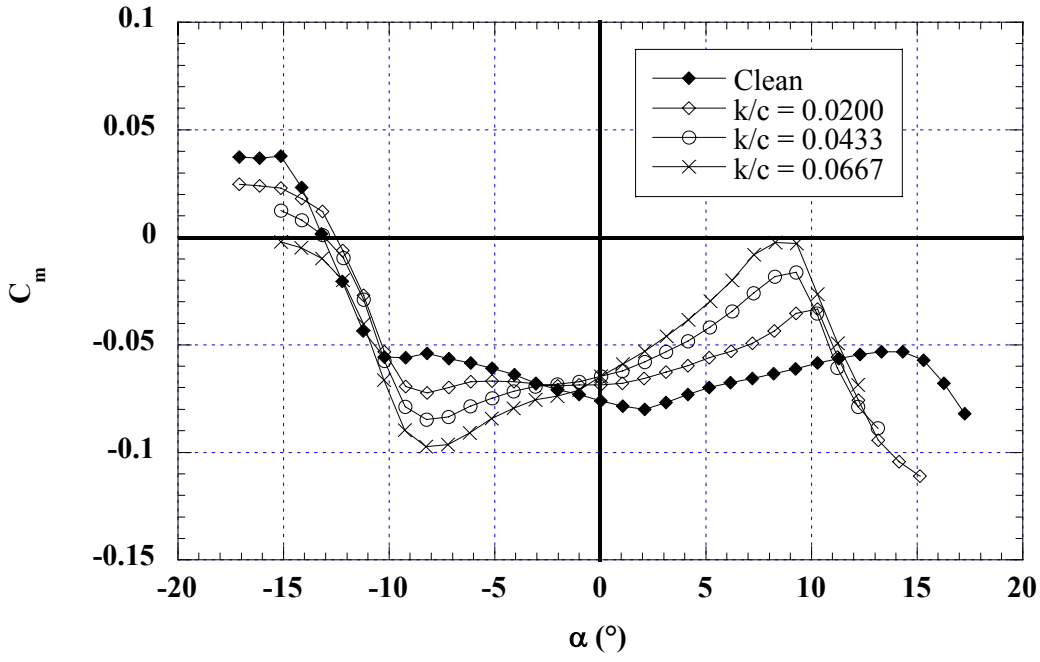

Fig. 2.8b) Pitching Moment

Fig. 2.8: Glaze-ice simulation height effects on NLF 0414; s/c = 0.034; Re = 1.8x10^6. Kim and Bragg.[30]

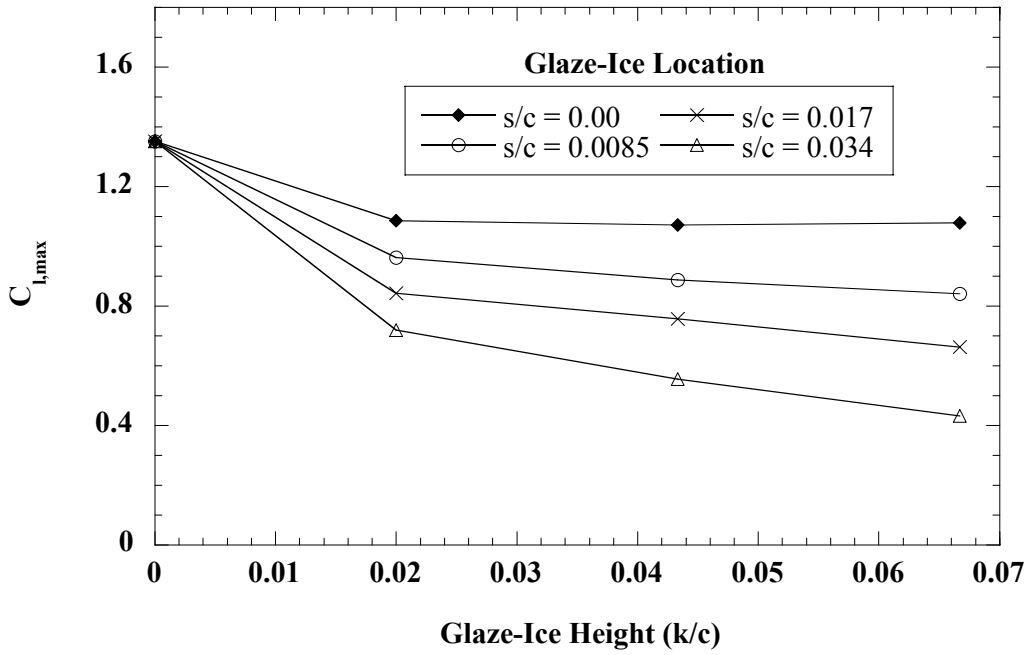

Fig. 2.9: Variation of maximum lift with simulated glaze-ice height on NLF 0414; *Re* = 1.8×10^6, Kim and Bragg.[30]

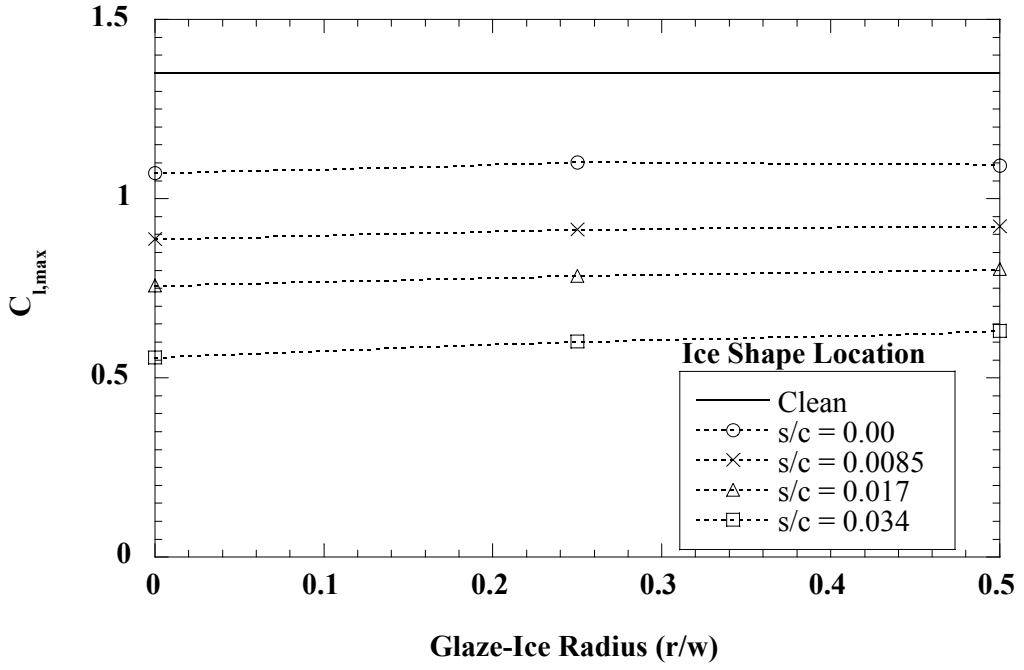

Fig. 2.10: Glaze-ice simulation horn radius effects on NLF 0414; k/c = 0.0433; Re = 1.8x10^6, Kim and Bragg.[30]

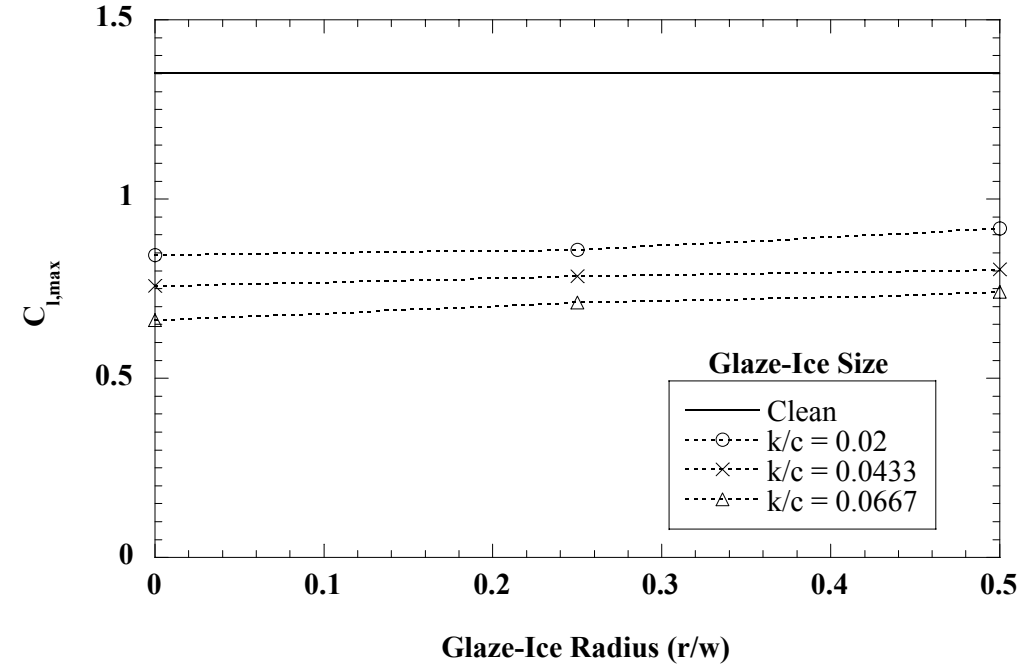

Fig. 2.11: Glaze-ice simulation horn radius effects on NLF 0414; s/c = 0.017; Re = 1.8x10^6, Kim and Bragg.[30]

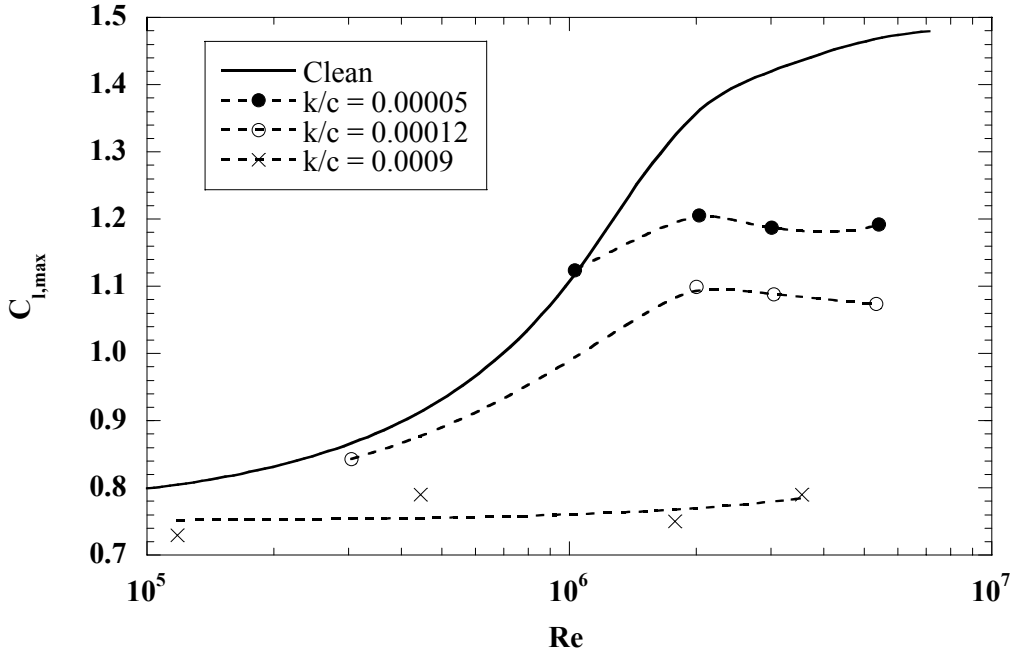

Fig. 2.12: Effect of Reynolds number on maximum lift on the NACA 0012 airfoil with leading-edge roughness; Hoerner.[33]

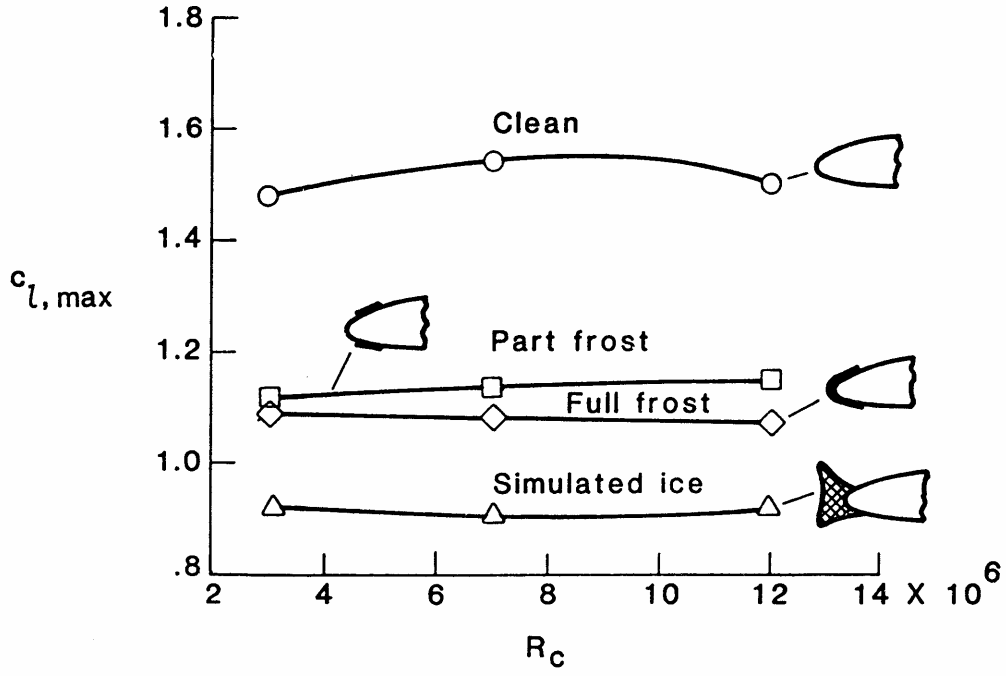

Fig. 2.13: Effect of Reynolds number on maximum lift of clean and iced airfoils. M = 0.20, Morgan, Ferris, McGhee[34]

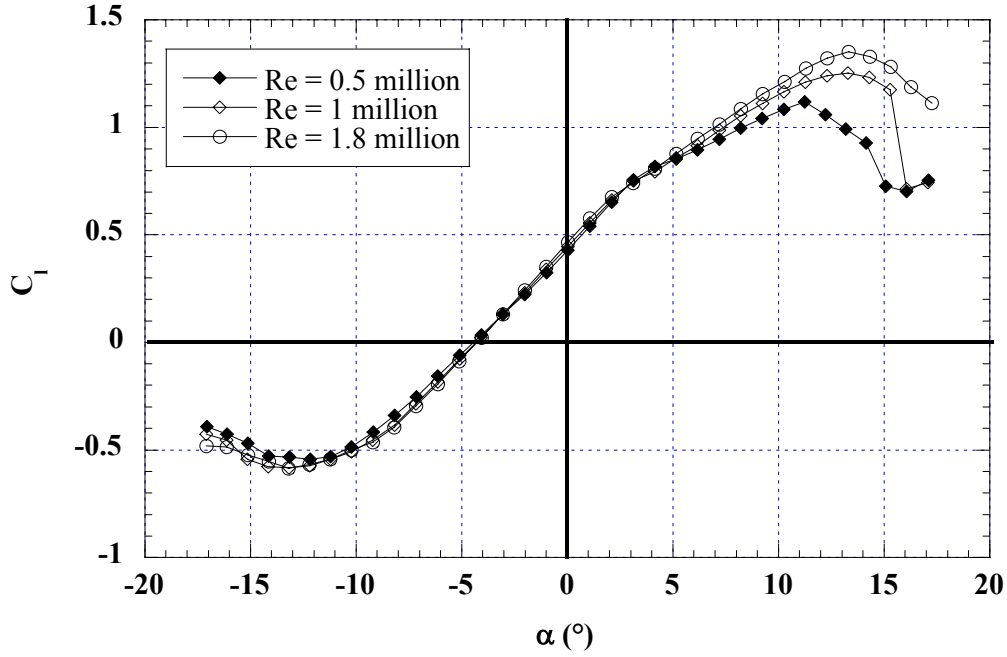

Fig. 2.14a) Lift

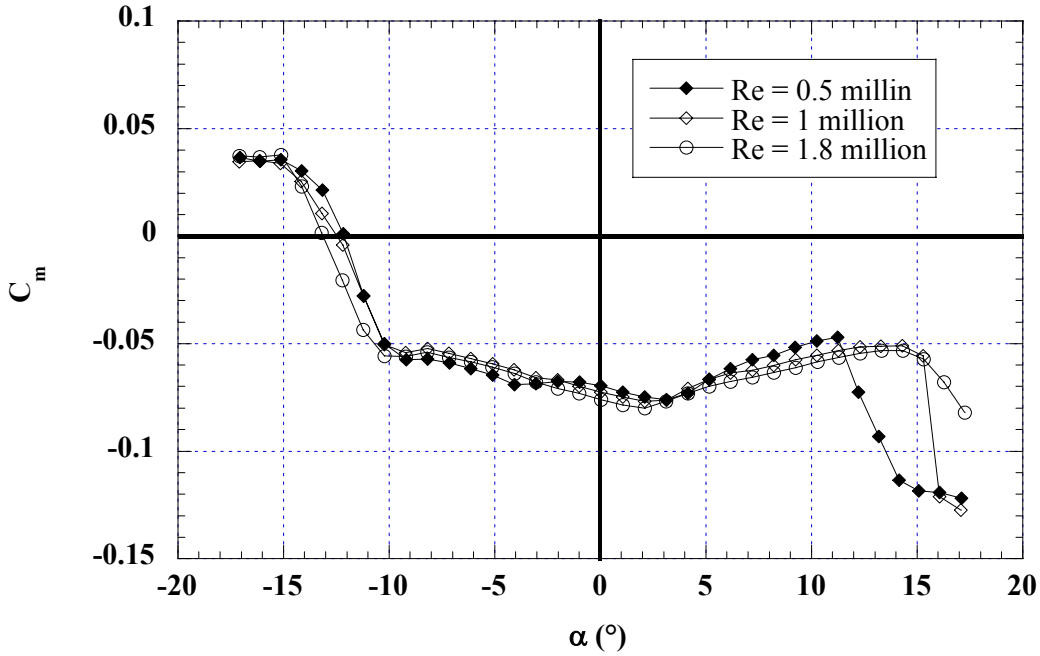

Fig. 2.14b) Pitching Moment

Fig. 2.14: NLF 0414 clean-airfoil data at 3 Reynolds numbers. NLF 0414; Kim and Bragg.[30]

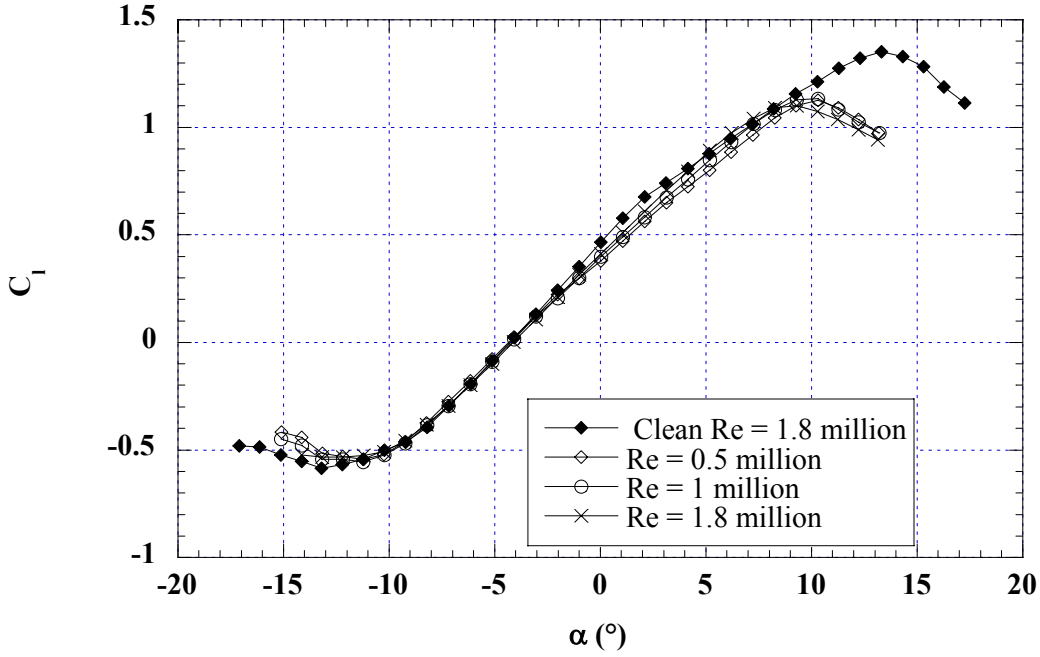

Fig. 2.15a) Lift

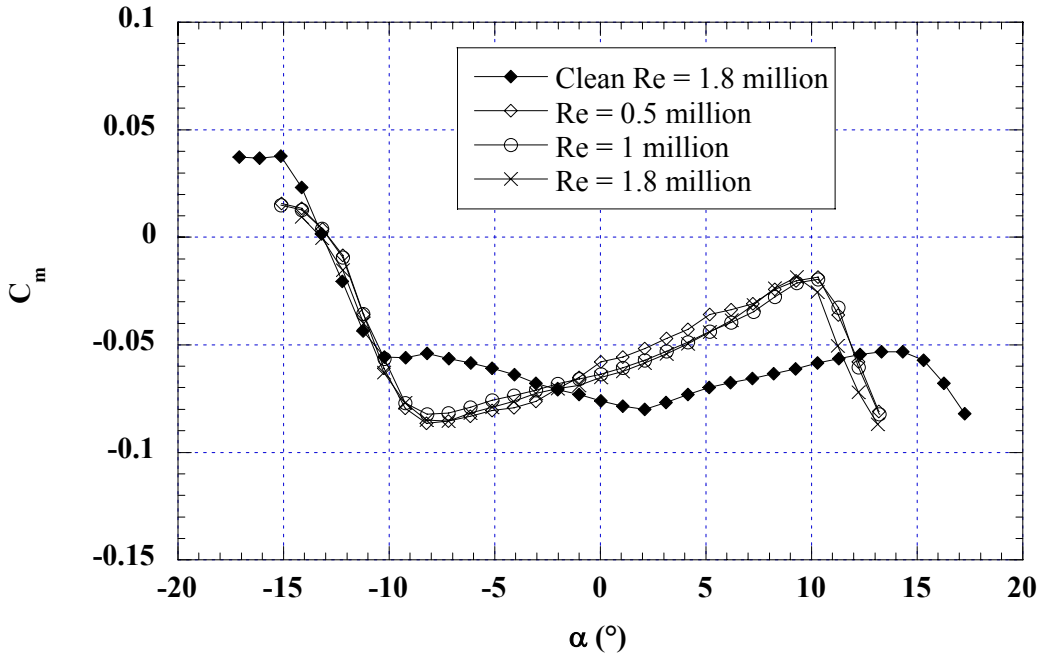

Fig. 2.15b) Pitching Moment

Fig. 2.15: Reynolds number effects for simulated glaze ice on NLF 0414; $r/w = 0.5$, $s/c = 0.0$ and $k/c = 0.0433$, Kim and Bragg.[30]

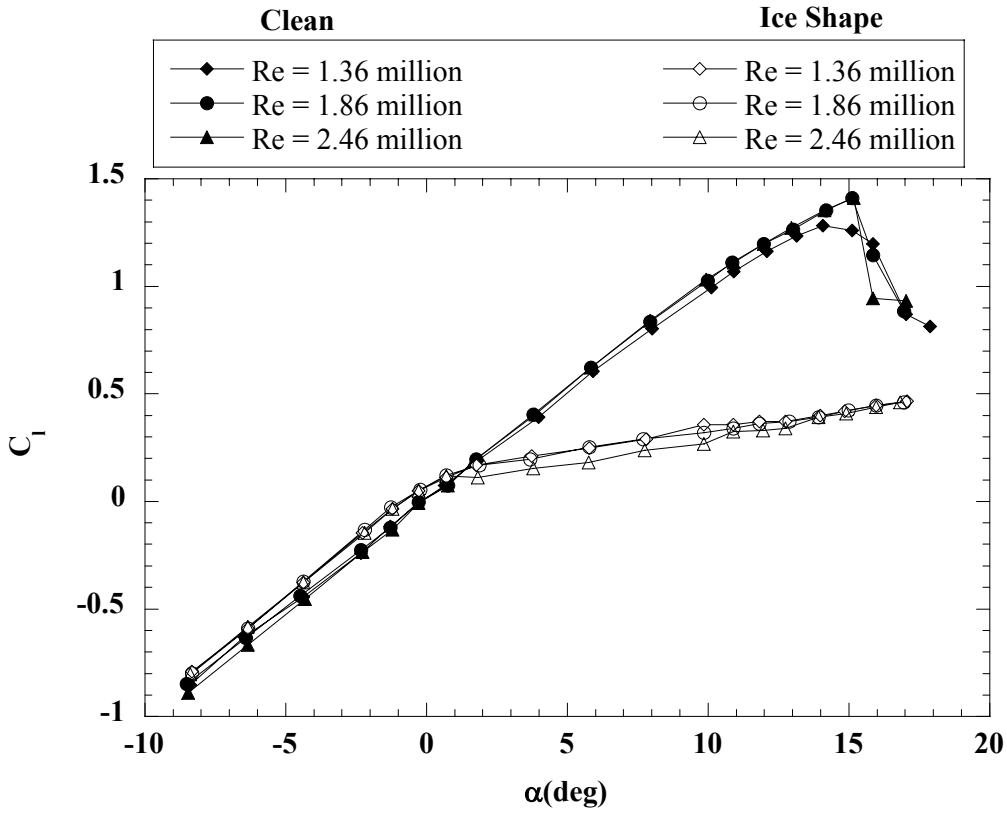

Fig. 2.16: Reynolds number effect on lift; NACA 0011; $k/c = 0.0625$; Papadakis.[29]

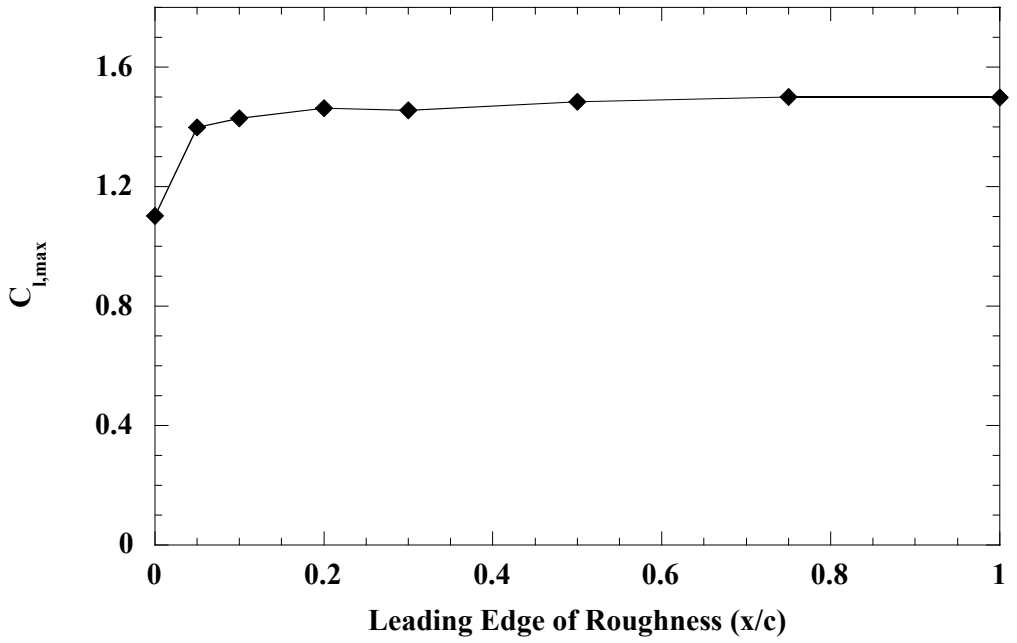

Fig. 2.17: Effect of roughness location on maximum lift. NACA 0012; $Re = 2.88 \times 10^6$; $k/c = 0.004$; Gregory.[35]

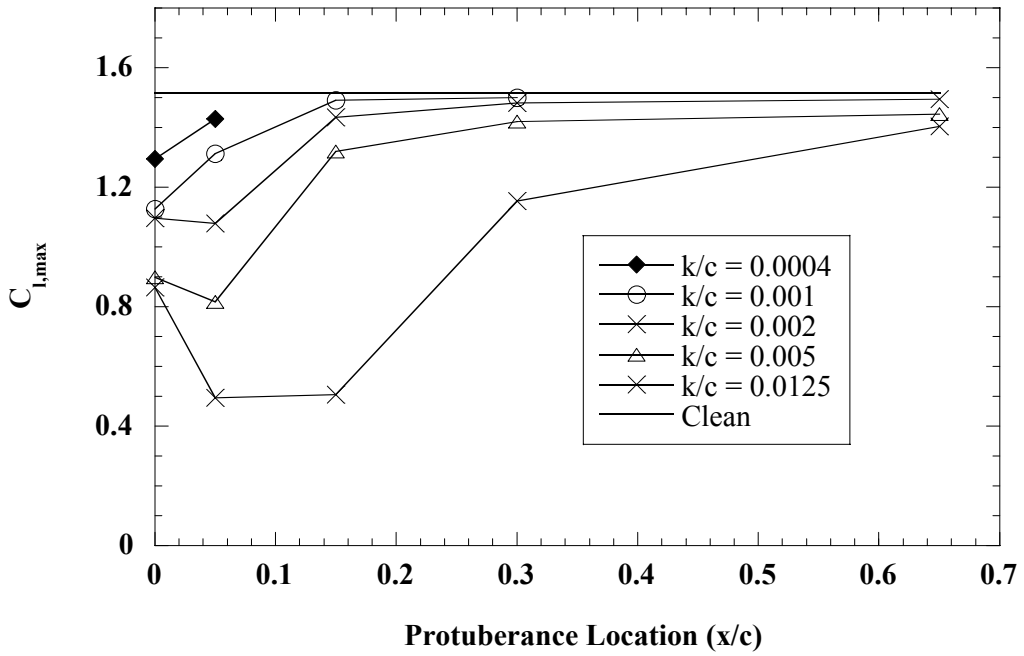

Fig. 2.18: Summary of maximum lift with spanwise protuberances of various heights Jacobs,[28] NACA 0012; $Re = 3.1 \times 10^6$.

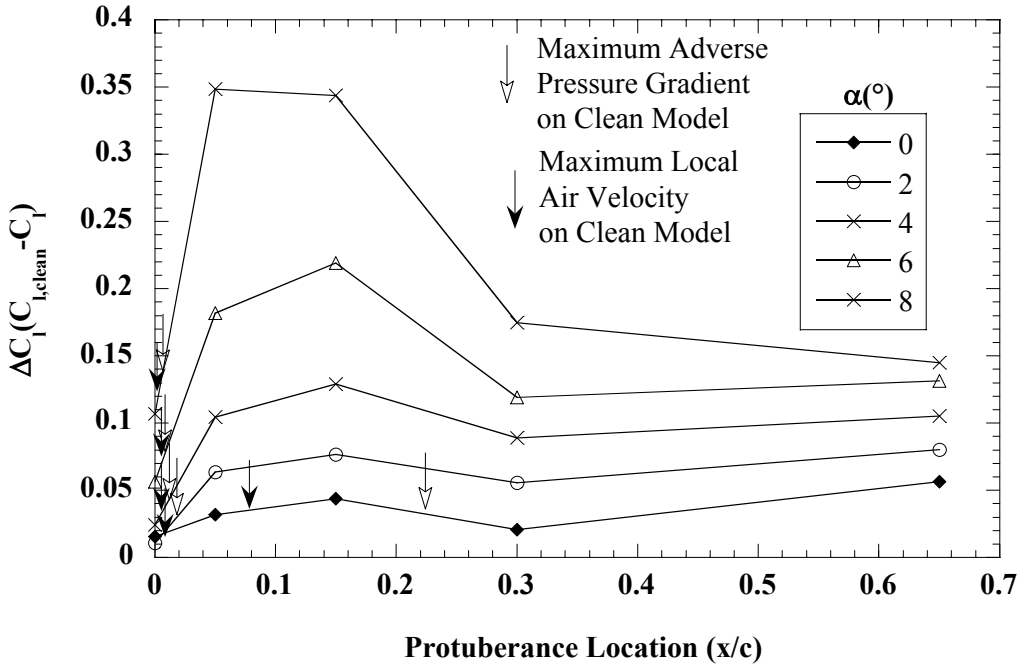

Fig. 2.19: Lift loss due to spanwise protuberance. Jacobs[28], NACA 0012, $Re = 3.1 \times 10^6$, $k/c = 0.0125$.

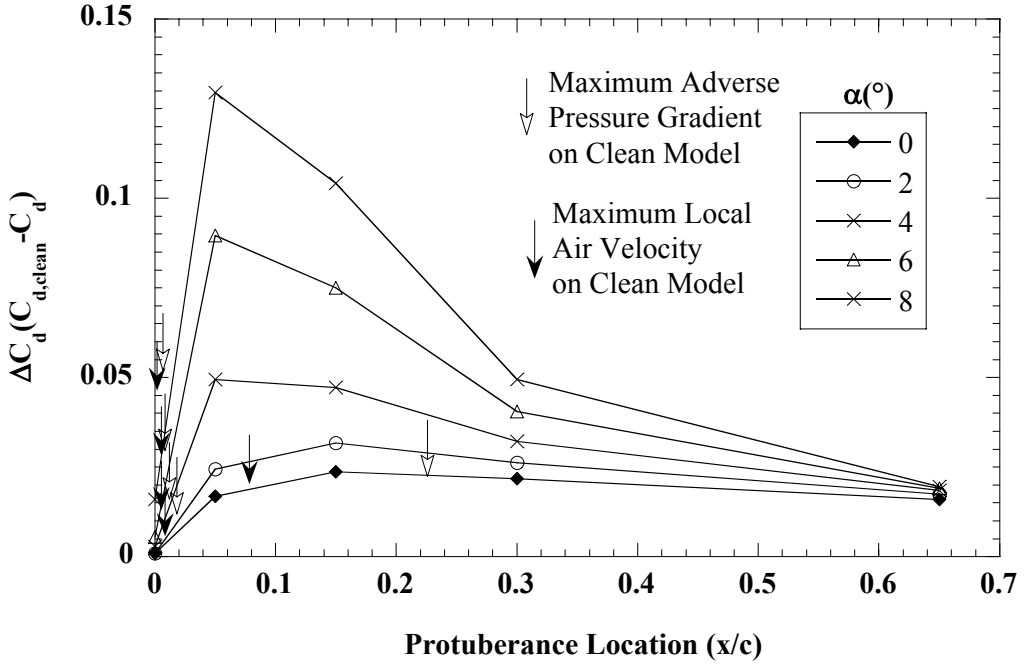

Fig. 2.20: Drag increase due to spanwise protuberance. Jacobs[28], NACA 0012, $Re = 3.1 \times 10^6$, $k/c = 0.0125$.

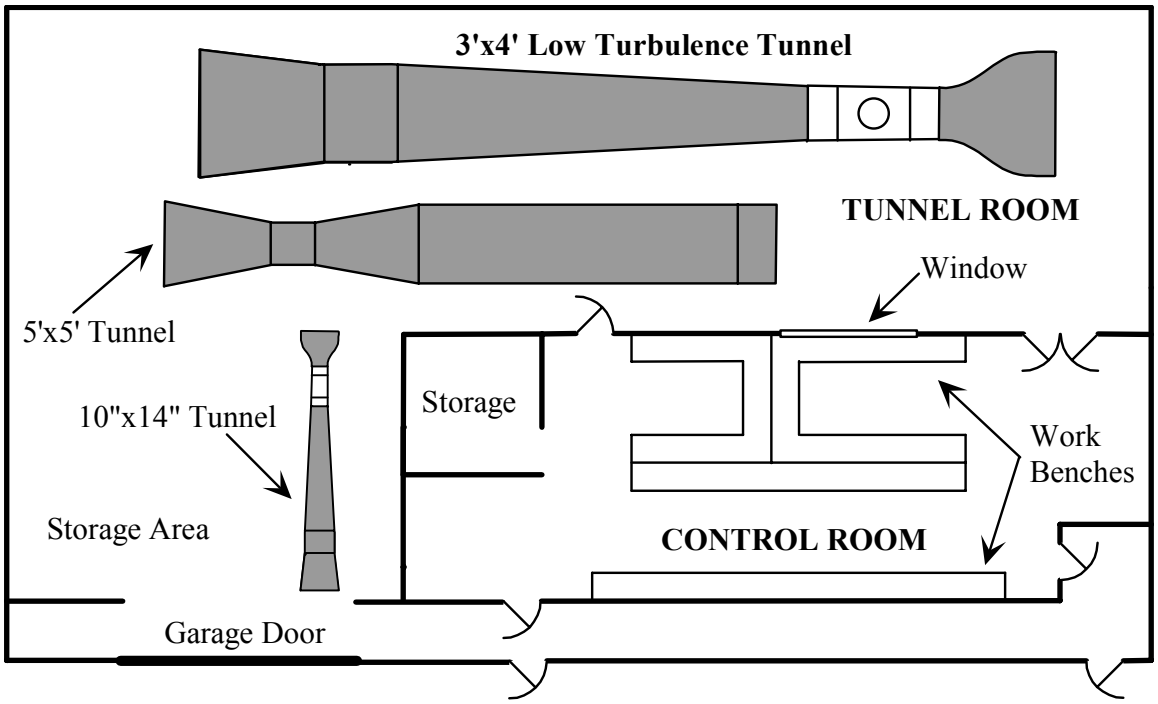

Fig. 3.1: General layout of the Subsonic Aerodynamics Laboratory at the University of Illinois at Urbana-Champaign.

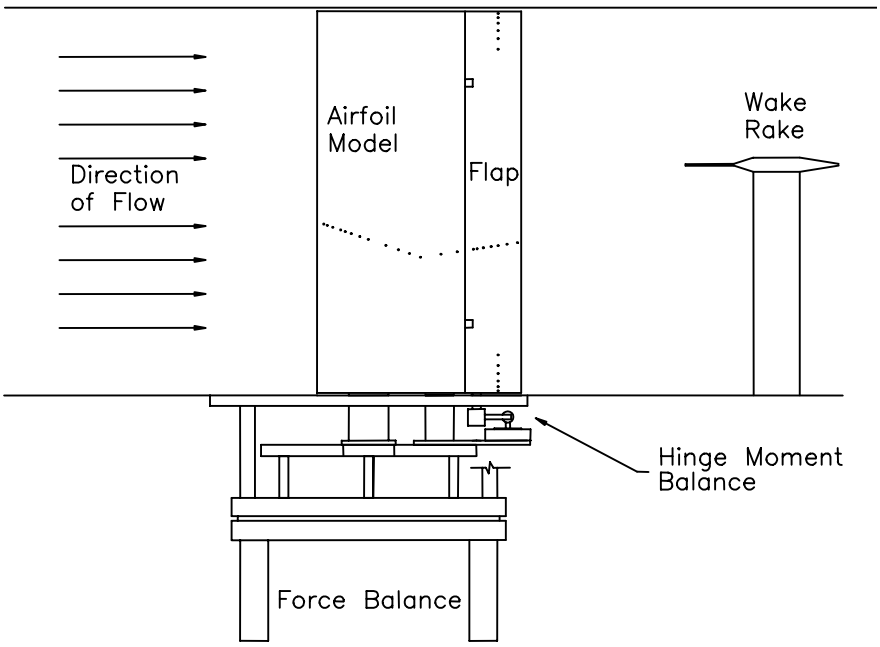

Fig. 3.2: Schematic of the experimental setup (test section).

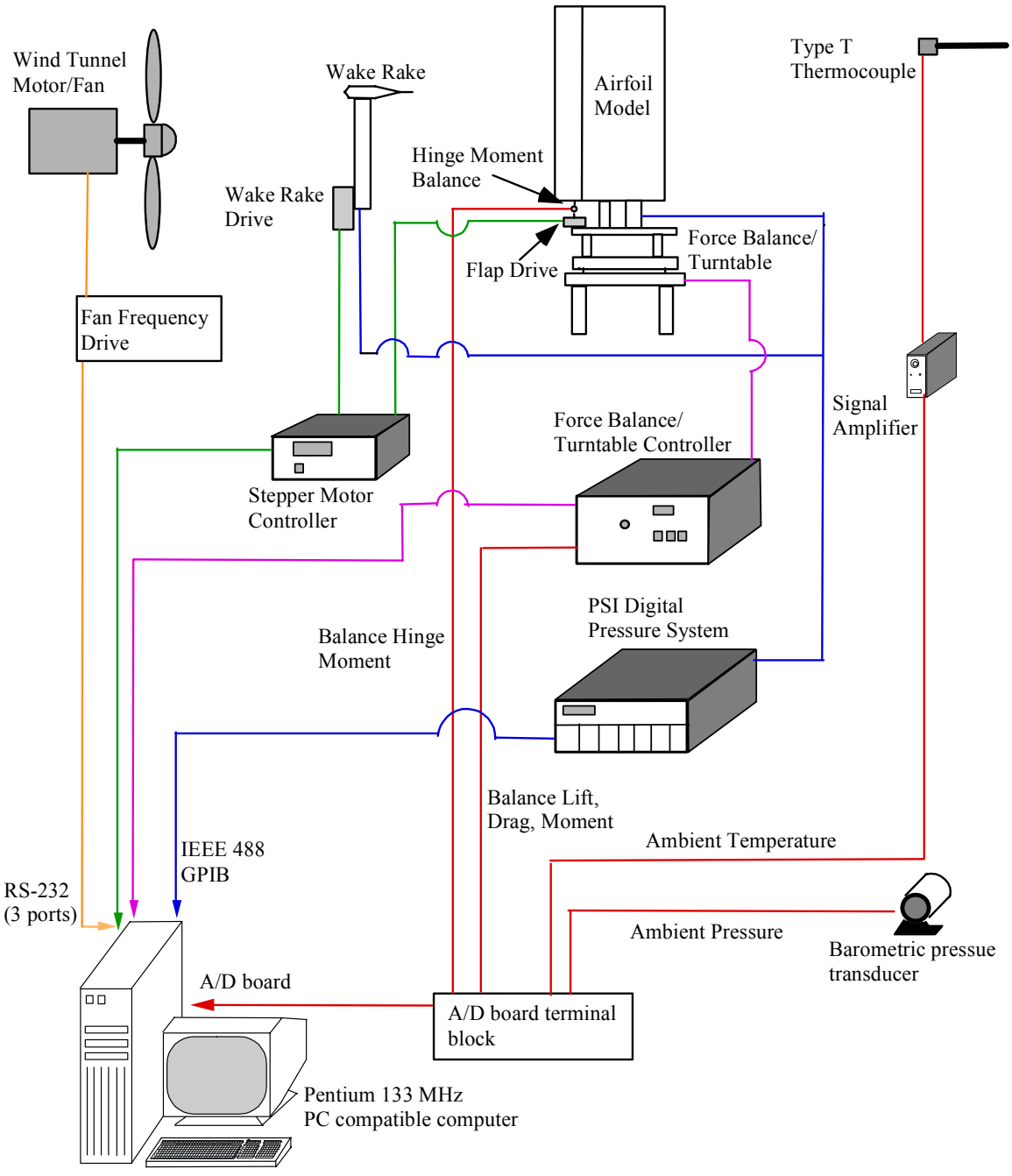

Fig. 3.3: Schematic of the experimental setup.

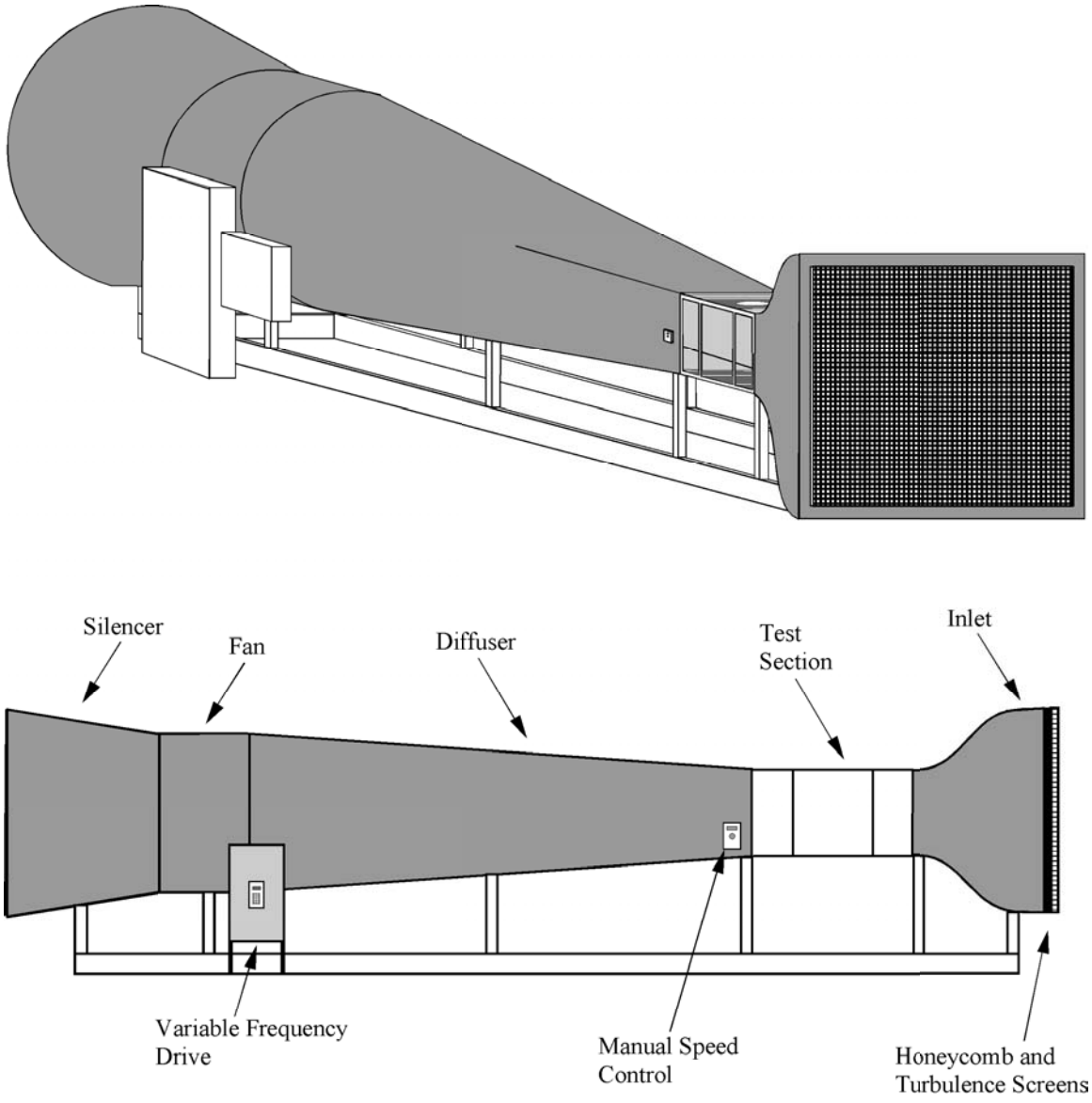

Fig. 3.4: University of Illinois 3'x4' Subsonic Wind Tunnel

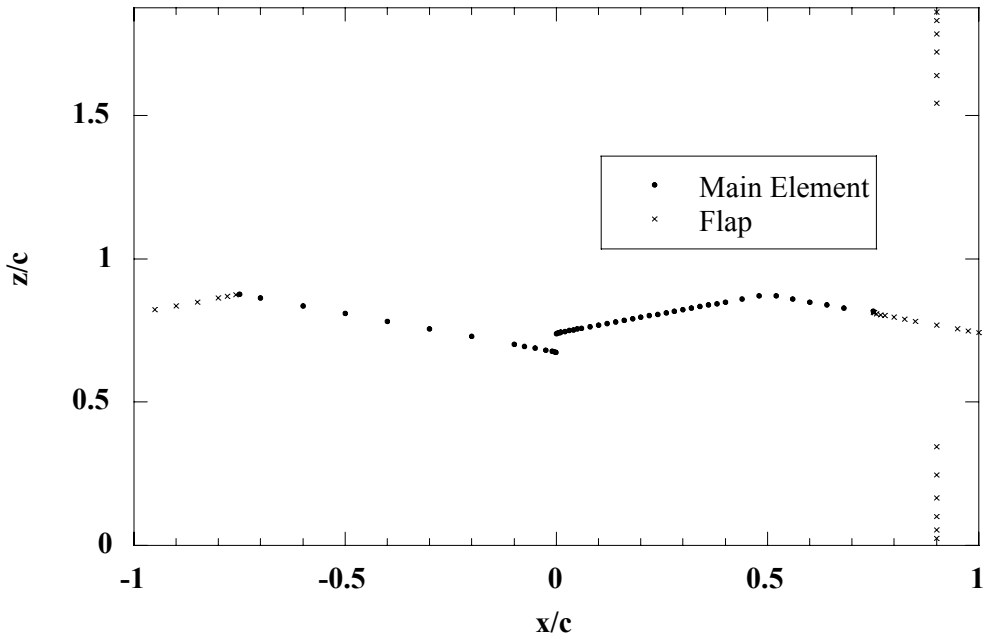

Fig. 3.5a) NACA 23012m

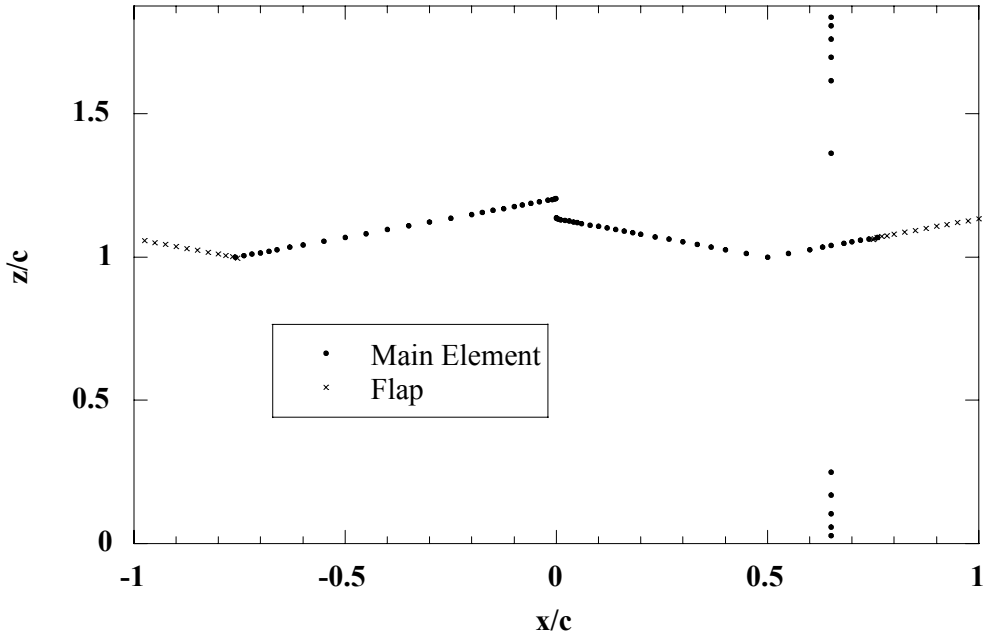

Fig. 3.5b) NLF 0414

Fig. 3.5: Surface pressure-tap locations for the NACA 23012m and NLF 0414 airfoil models. Negative chordwise locations indicate lower surface.

Fig. 3.6: Aerotech three-component force balance.

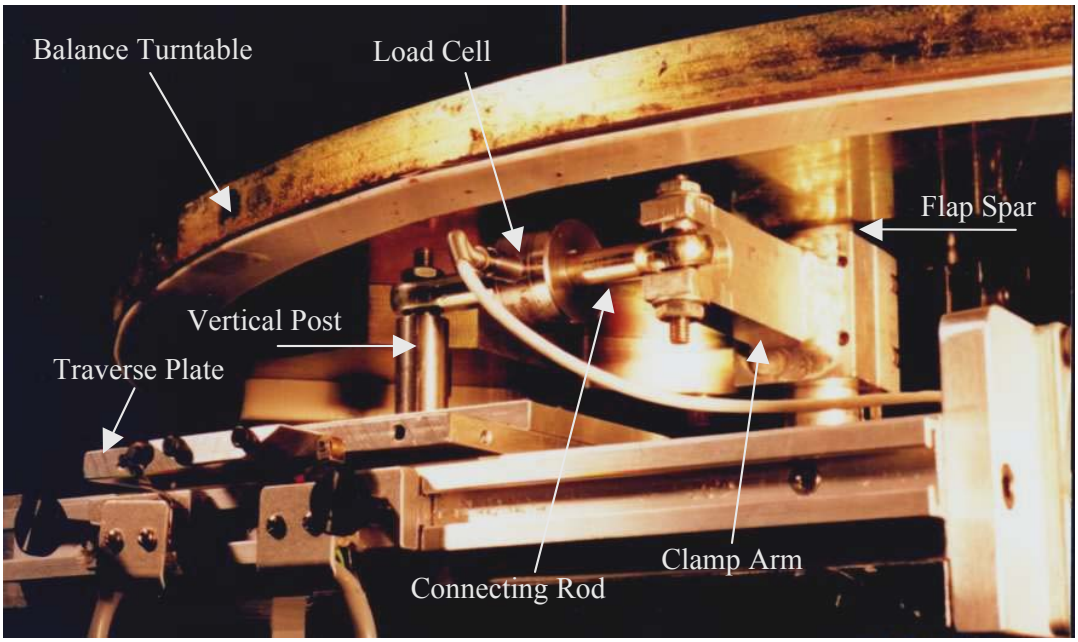

Fig. 3.7: Flap hinge-moment balance.

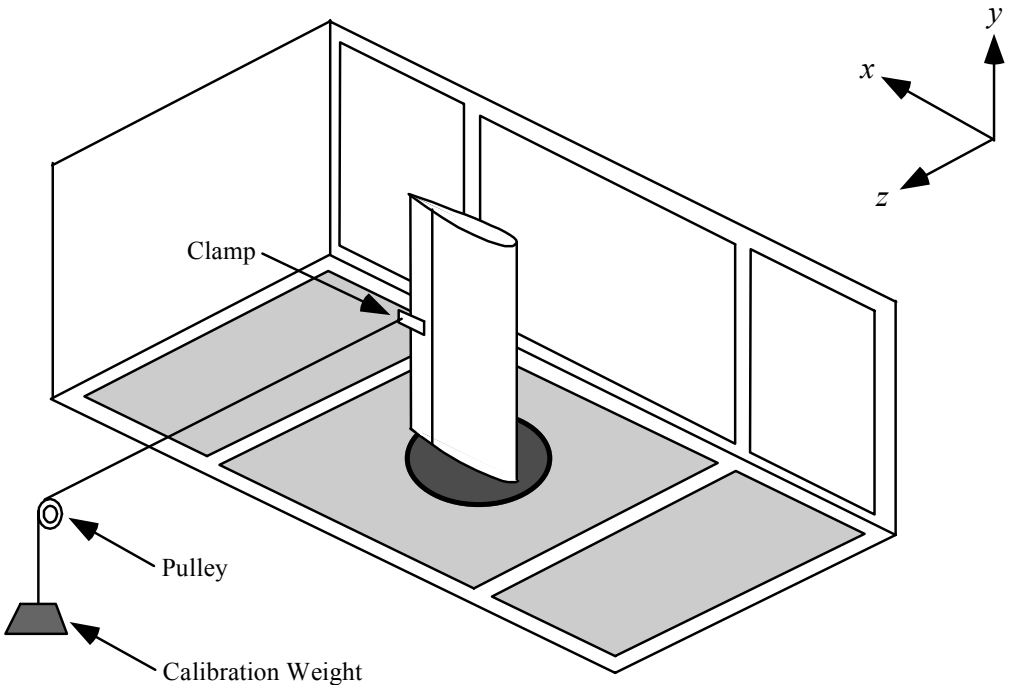

Fig. 3.8: Flap hinge-moment balance calibration setup.

Fig. 3.9: Wake rake.

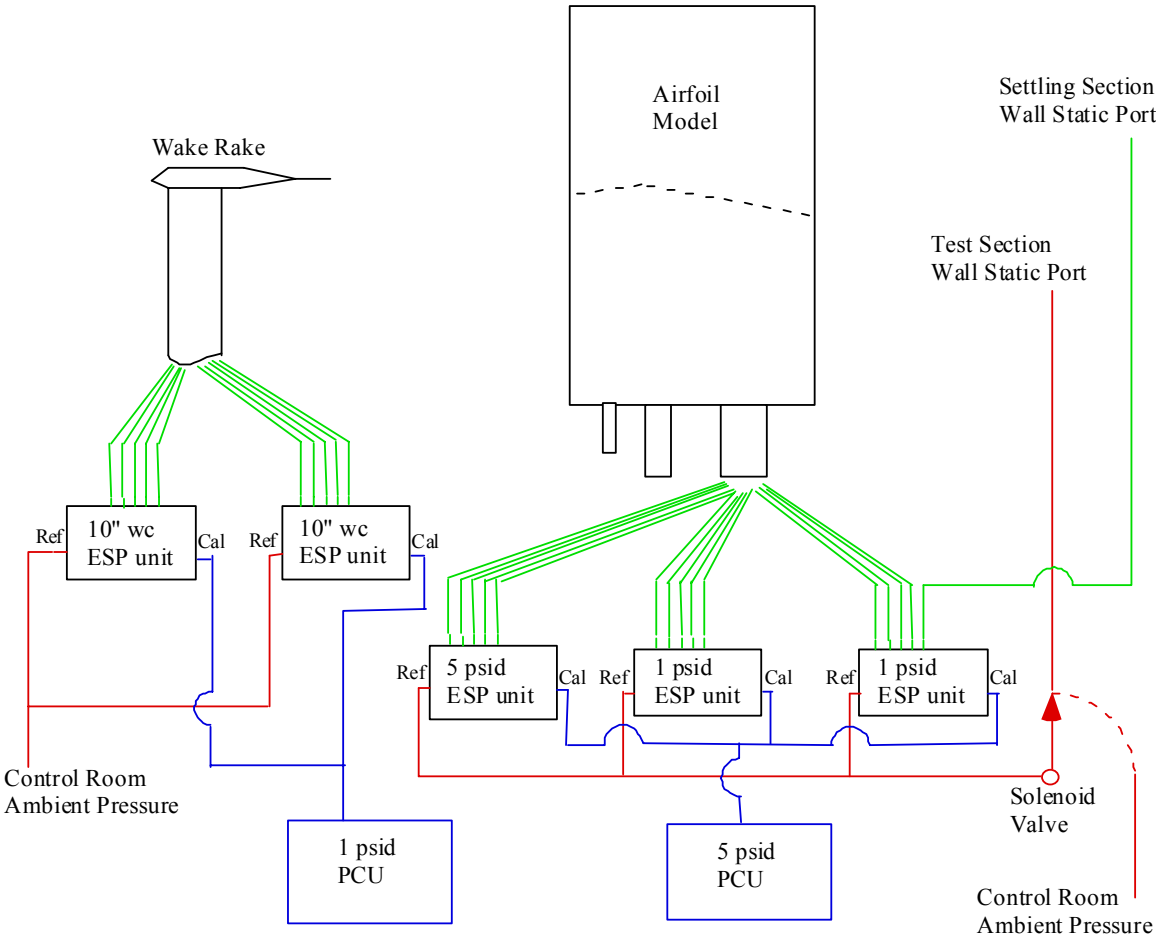

Fig. 3.10: Pressure measurement system schematics.

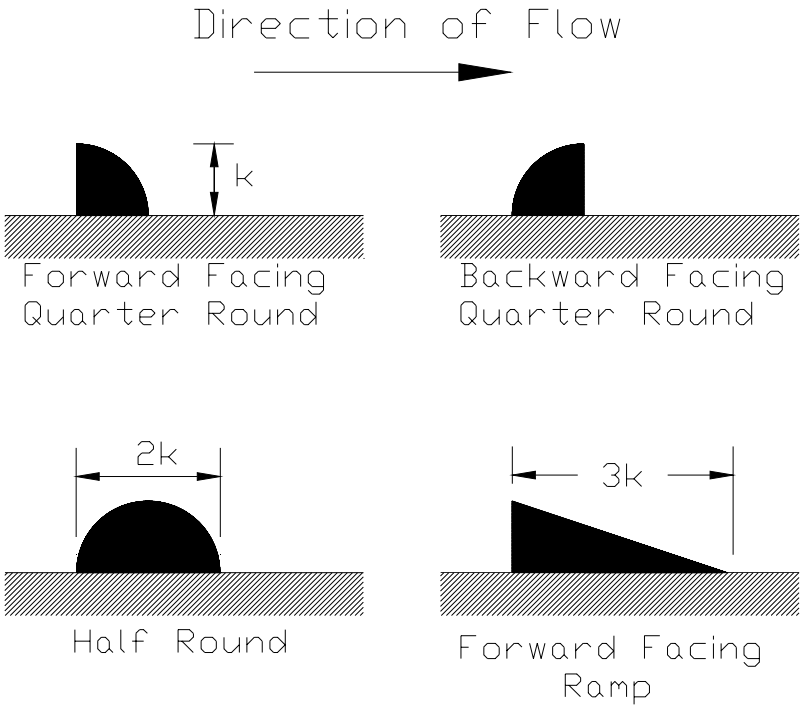

Fig. 3.11: Ice-shape simulation geometry.

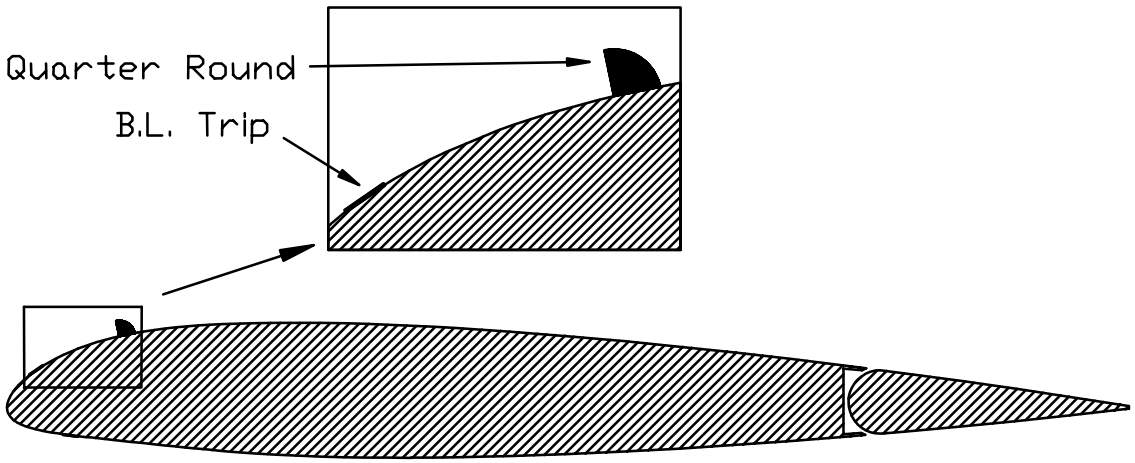

Fig. 3.12: NACA 23012m model with quarter round ice simulation. (0.25" quarter round at x/c = 0.10 shown)

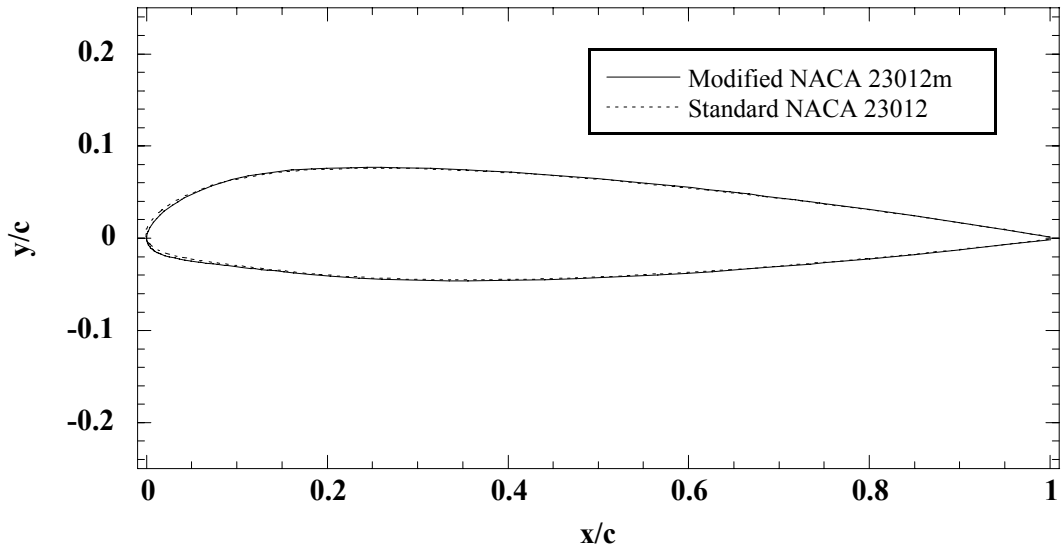

Fig. 4.1a) Entire model

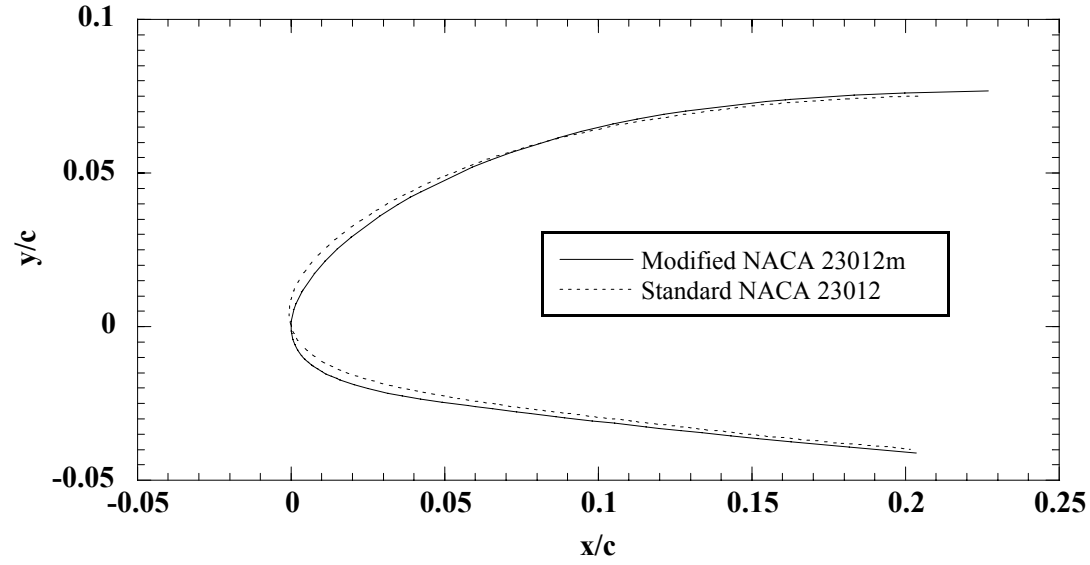

Fig. 4.1b) Leading edge

Fig. 4.1: Geometry comparison between modified NACA 23012m used in this study and standard NACA 23012

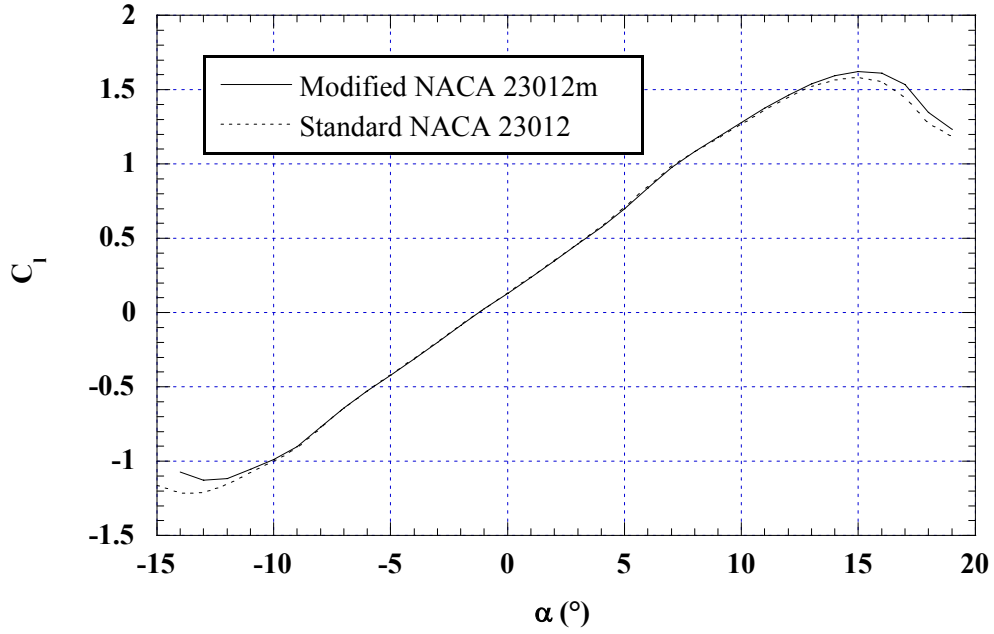

4.2a) Lift

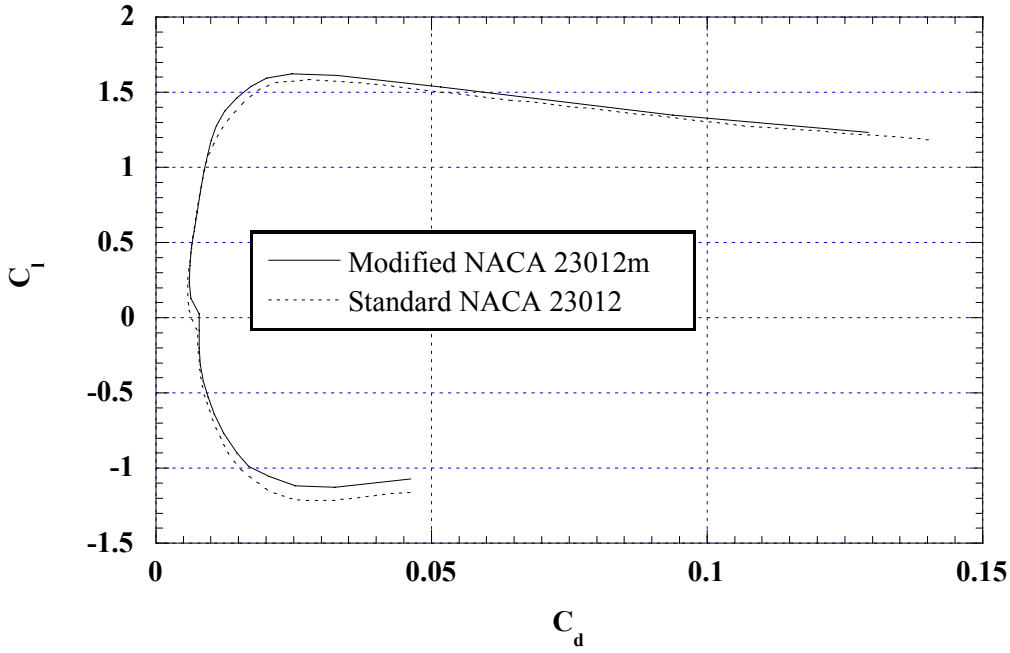

4.2b) Drag

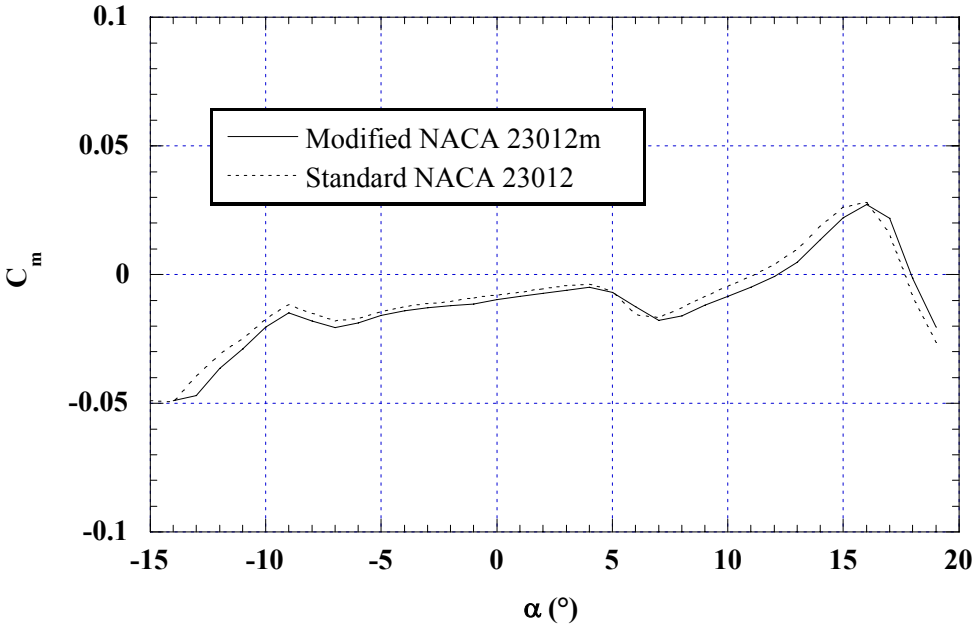

4.2c) Pitching Moment

Fig. 4.2: Aerodynamic coefficient comparison between modified NACA 23012m used in this study and standard NACA 23012; results from XFOIL, M = 0.20, Re = 1.8×10^6.

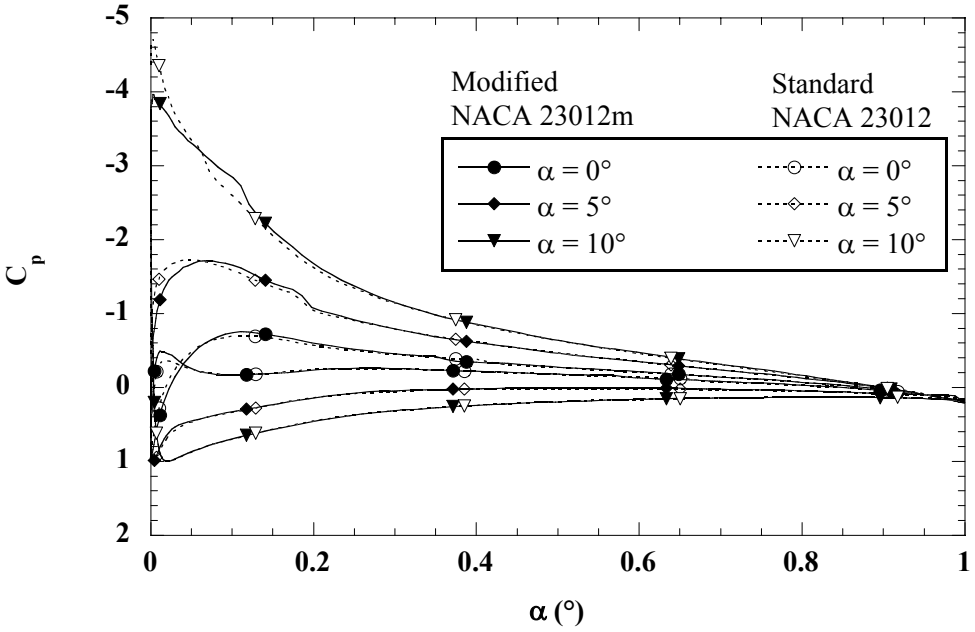

Fig. 4.3: Surface-pressure comparison between modified NACA 23012m used in this study and standard NACA 23012; results from XFOIL, Re = 1.8×10^6

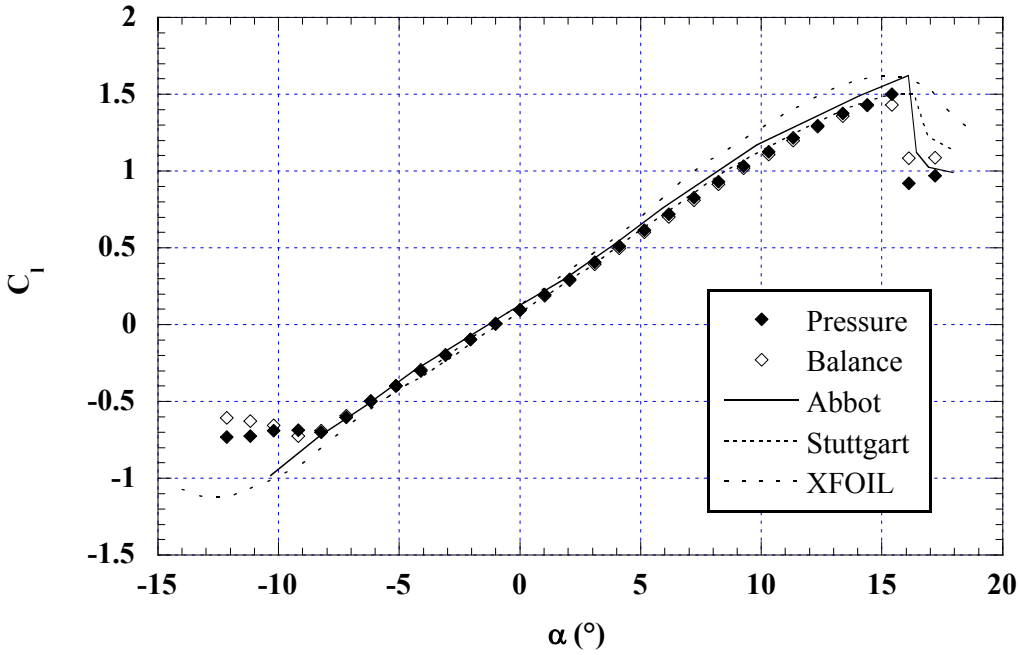

Fig4.4a) Lift

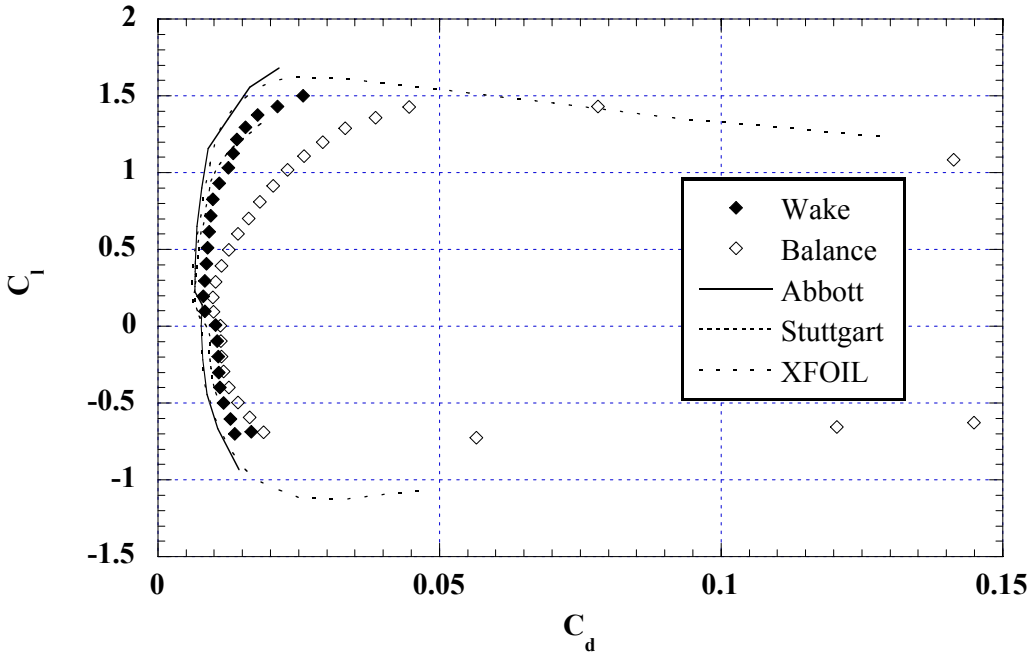

Fig. 4.4b) Drag

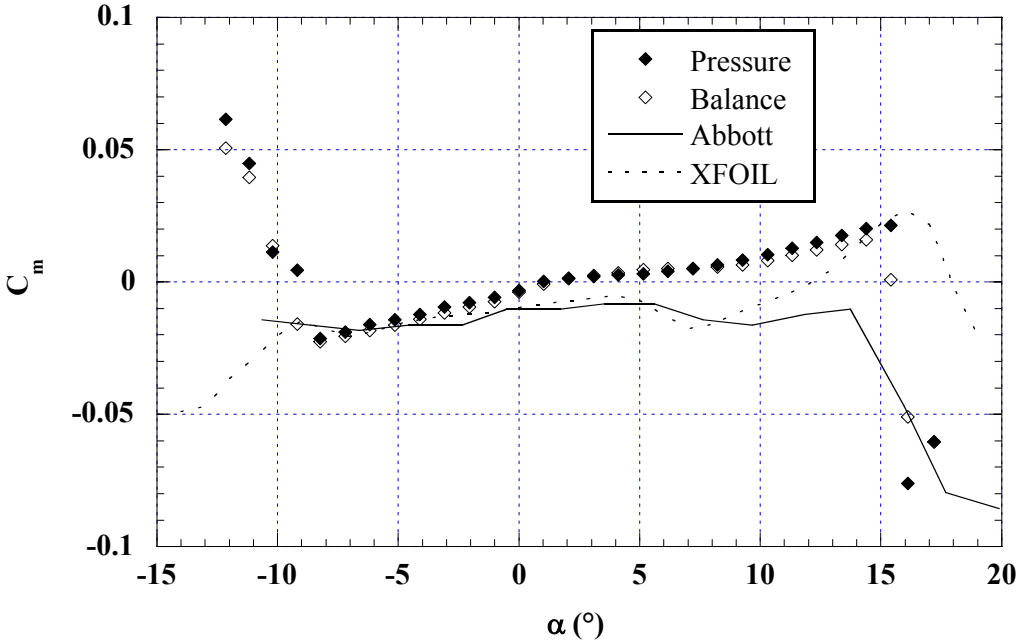

Fig. 4.4c) Pitching moment

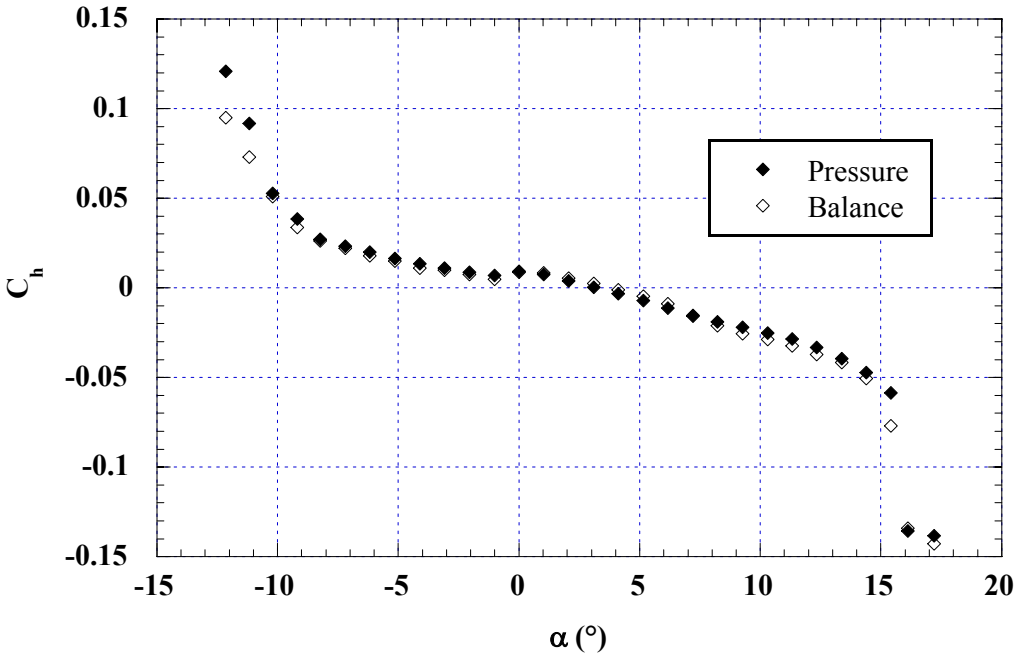

Fig. 4.4d) Flap hinge moment

Fig. 4.4: Aerodynamic coefficients of the clean NACA 23012m airfoil. Comparisons of present Illinois data with existing data and XFOIL numerical results. (Illinois, XFOIL $Re = 1.8 \times 10^6$; Abbot $Re = 3 \times 10^6$, Stuttgart $Re = 2 \times 10^6$)

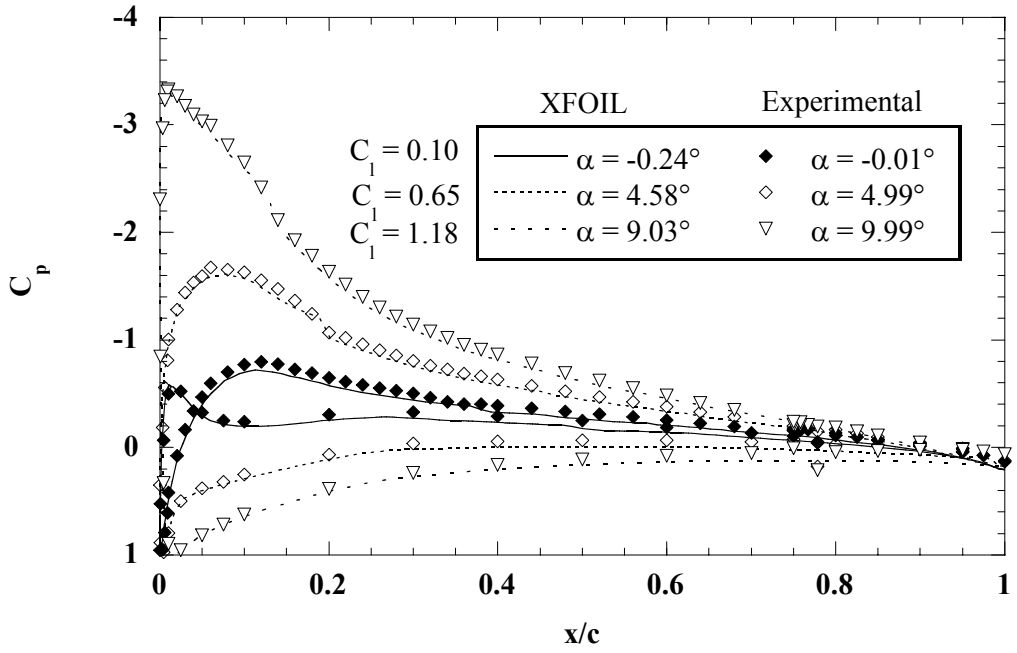

Fig. 4.5a)

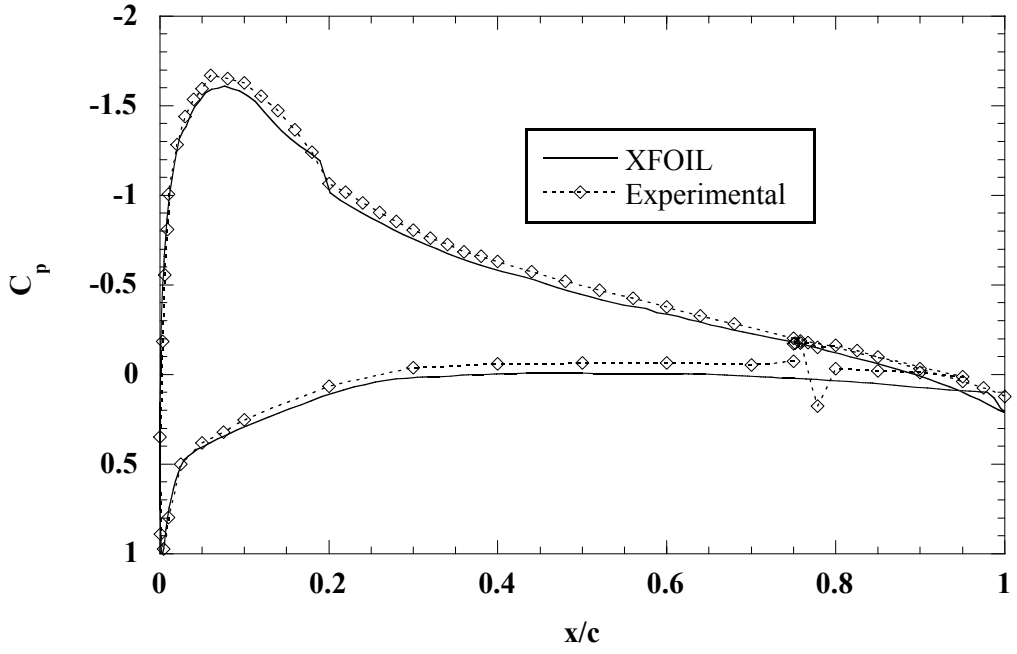

Fig. 4.5b) $C_l = 0.62$

Fig. 4.5: Surface pressure of the clean NACA 23012m airfoil. Comparisons of experimental data and XFOIL at matched lift coefficients; *Re* = 1.8 million.

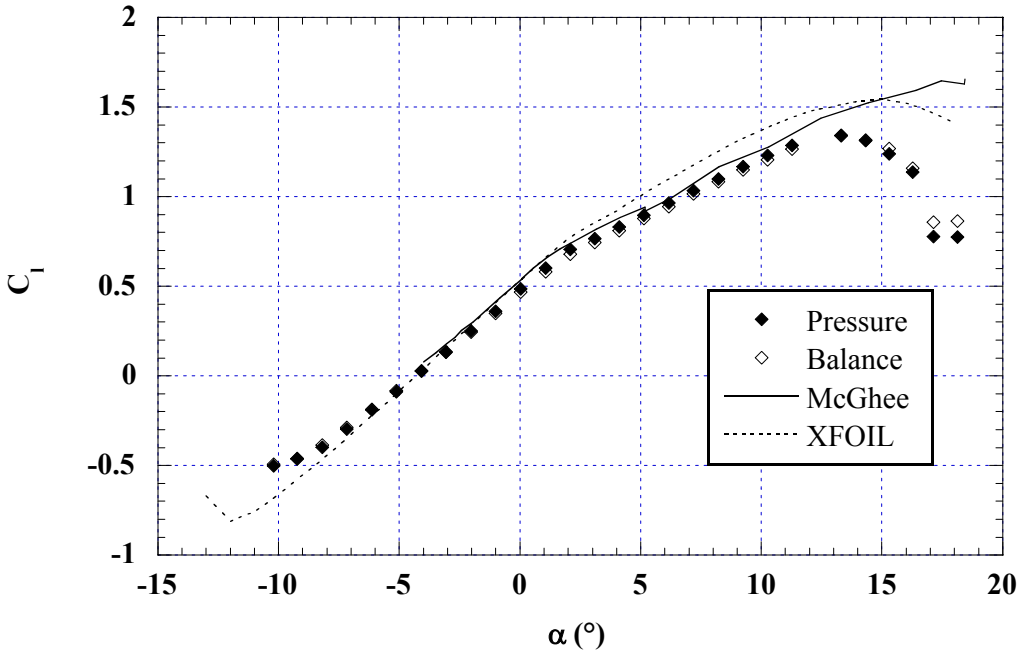

Fig. 4.6a) Lift

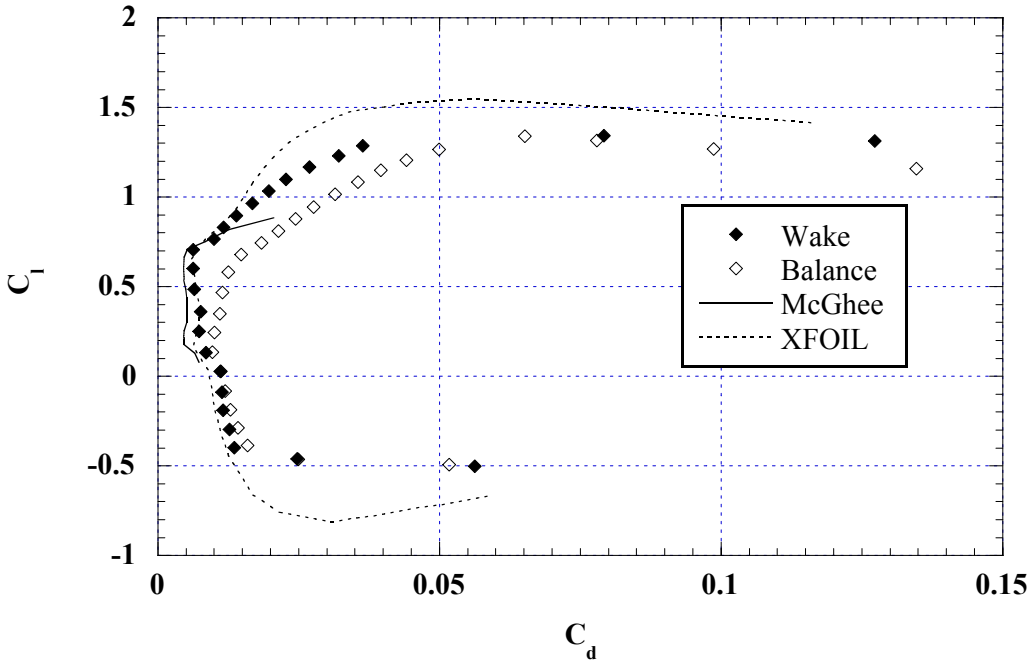

Fig. 4.6b) Drag

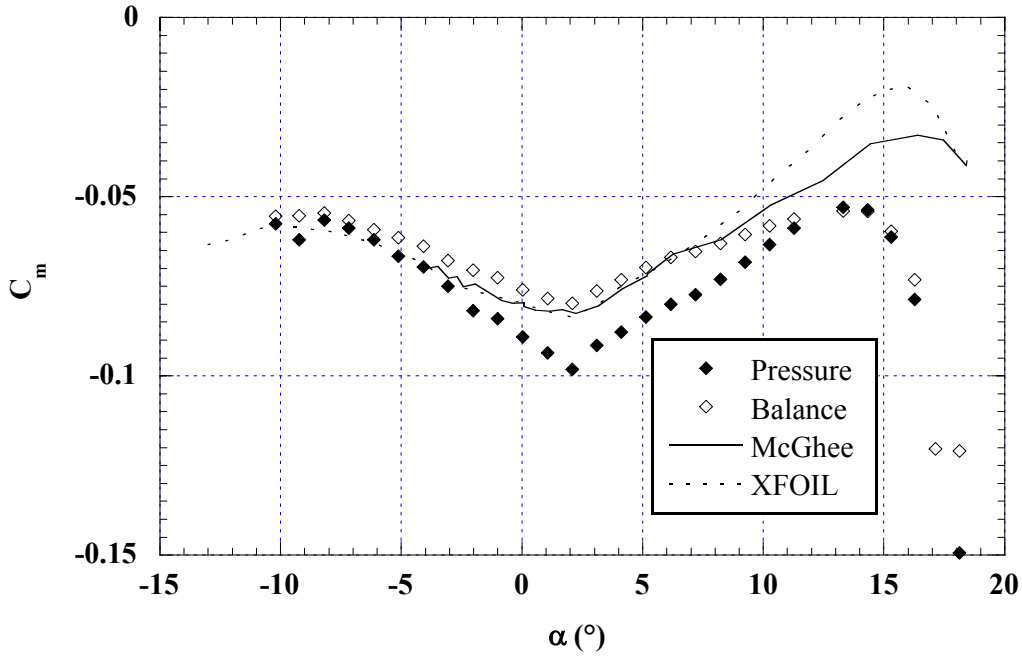

Fig 4.6c) Pitching Moment

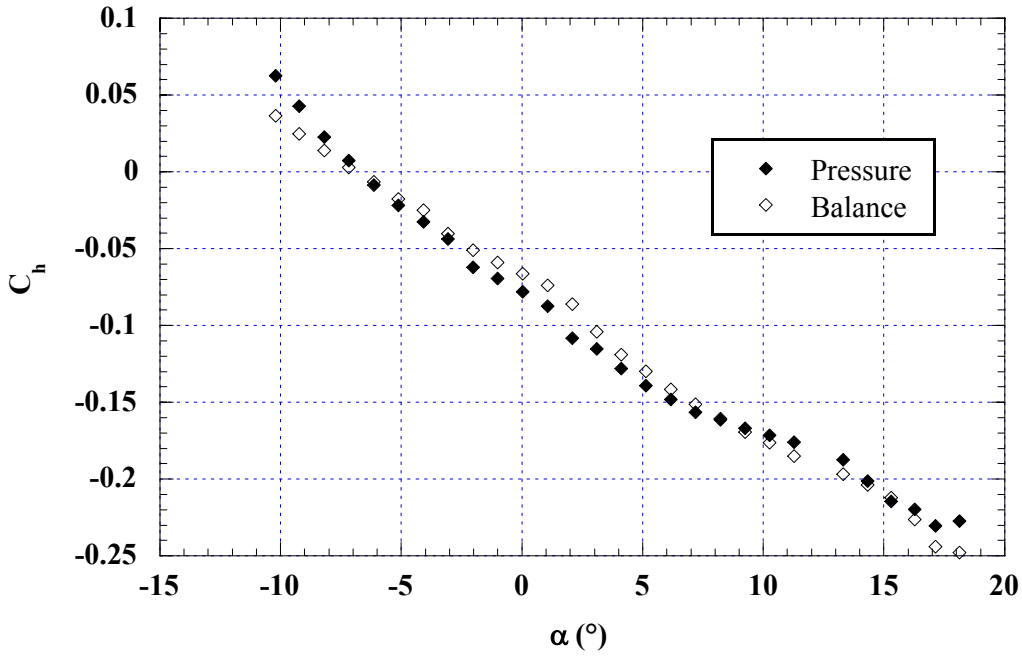

Fig. 4.6d) Flap hinge moment

Fig. 4.6: Aerodynamic coefficients of the clean NLF 0414 airfoil. Comparisons of present Illinois data with existing data and XFOIL numerical results. (Illinois, XFOIL Re = 1.8×10^6; McGhee Re = 3×10^6).

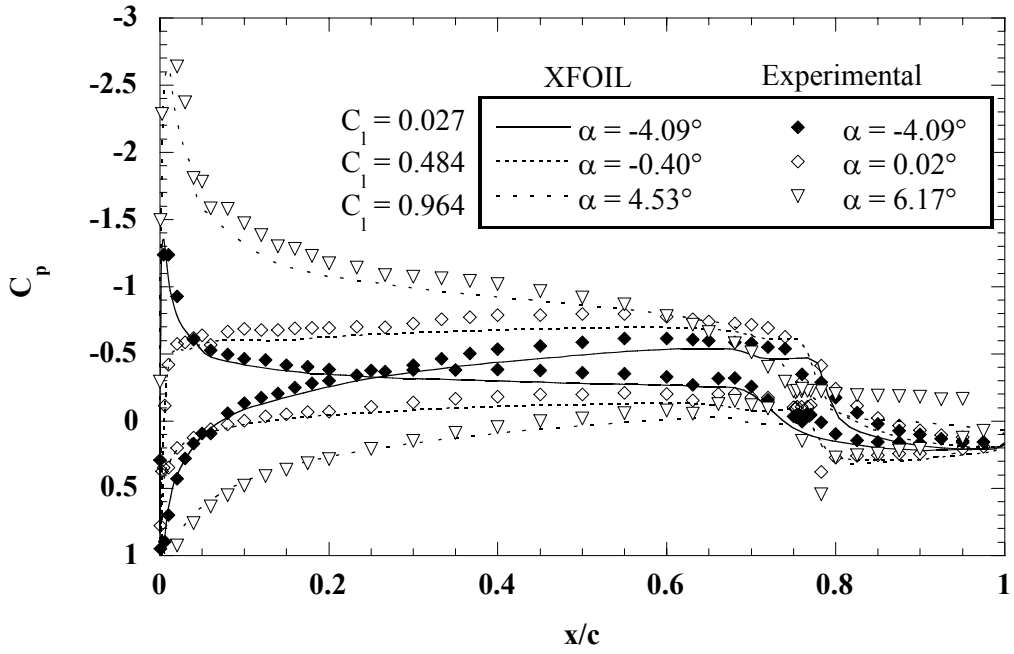

Fig. 4.7: Surface pressure of the clean NLF 0414 airfoil. Comparisons of experimental data and XFOIL at matched lift coefficients.

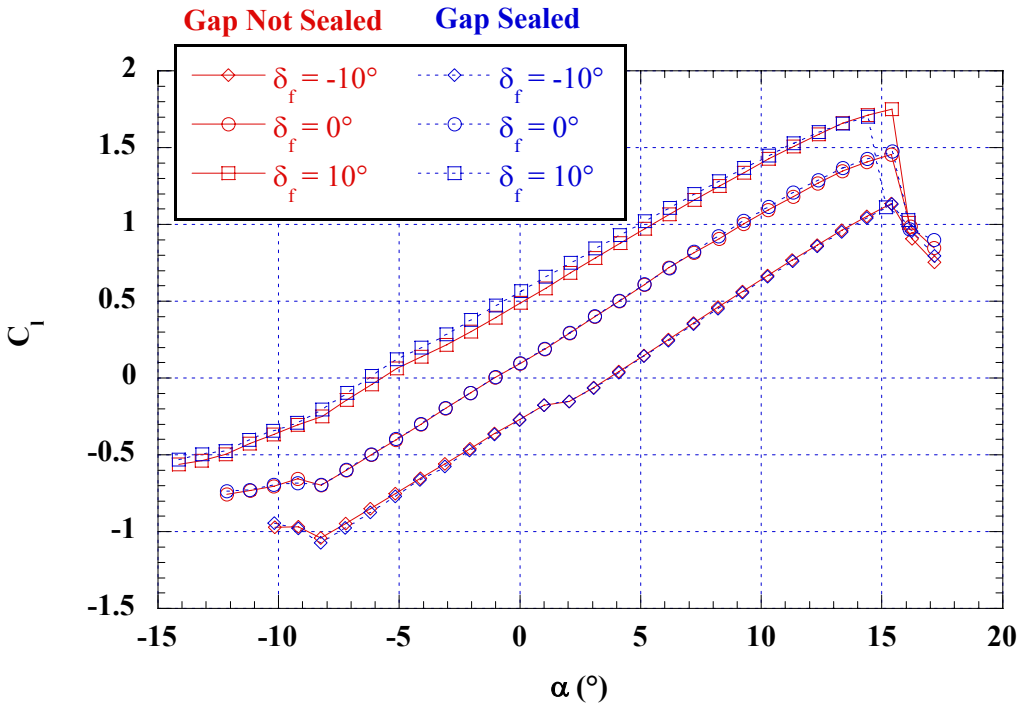

Fig. 4.8a) Lift

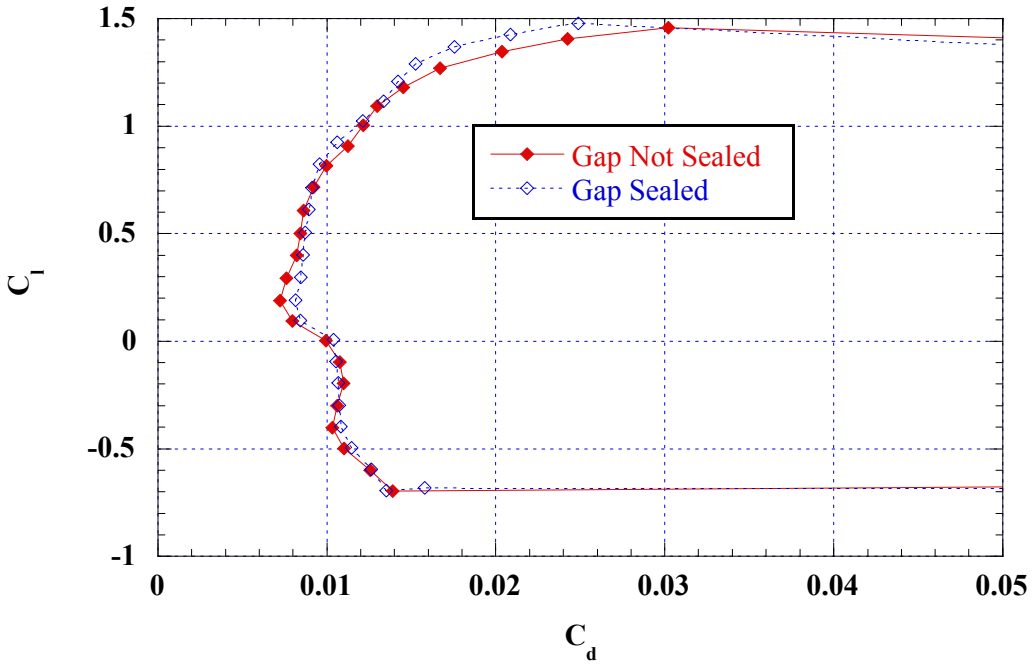

Fig. 4.8b) Drag, $\delta_f = 0°$

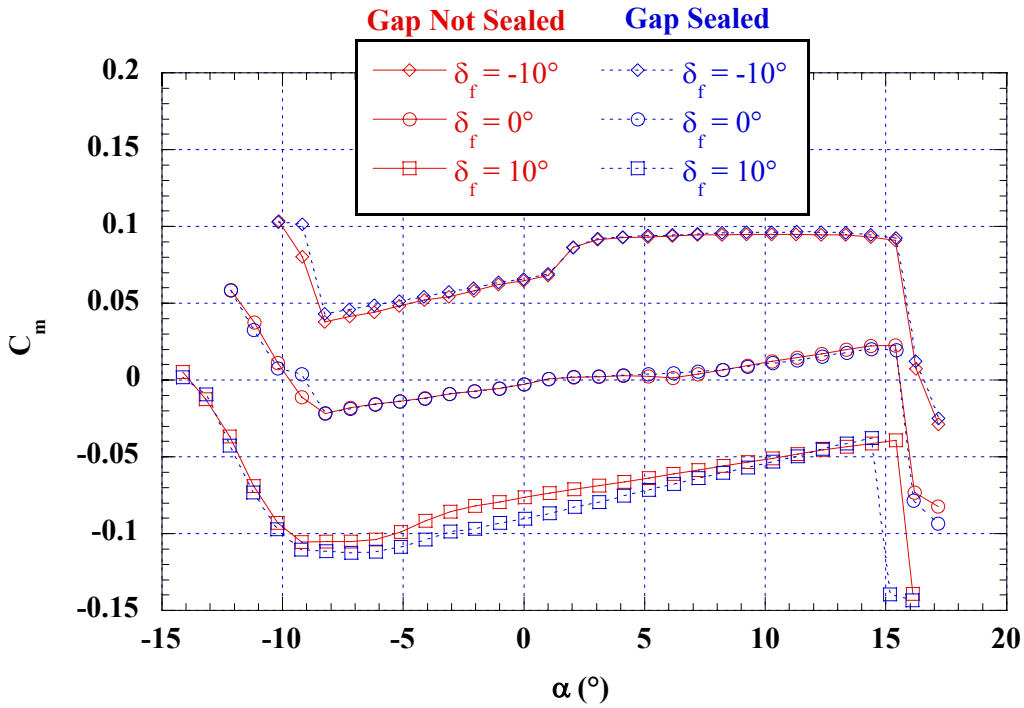

Fig. 4.8c) Pitching Moment

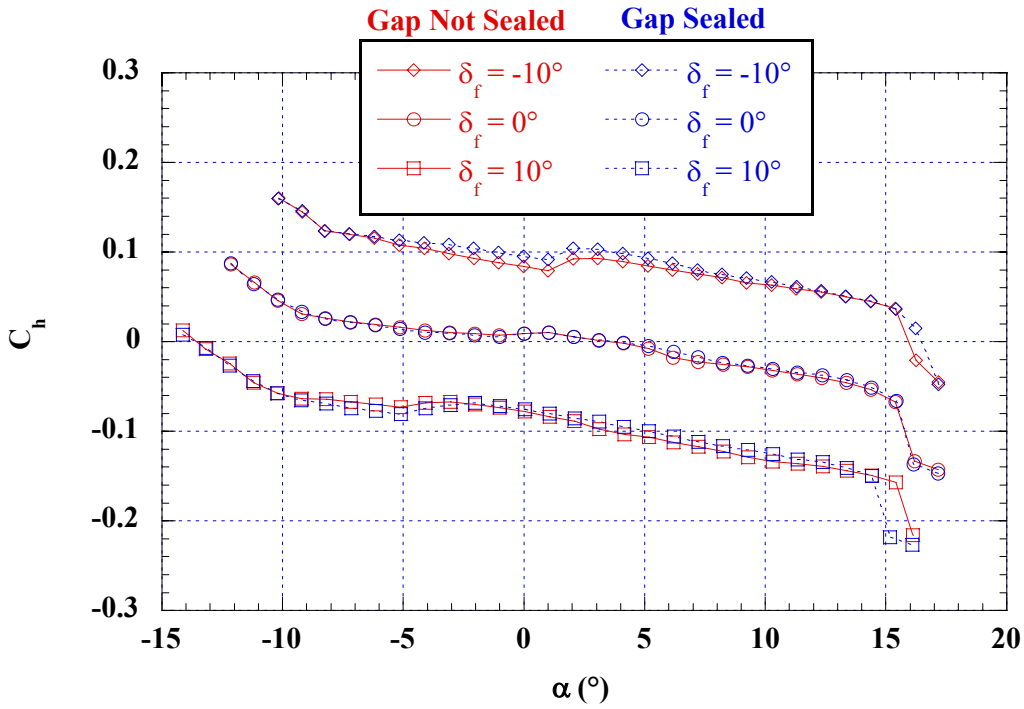

Fig. 4.8d) Flap hinge moment

Fig. 4.8: Effect of flap-gap seal on clean-model aerodynamics. NACA 23012m, *Re* = 1.8×10^6.

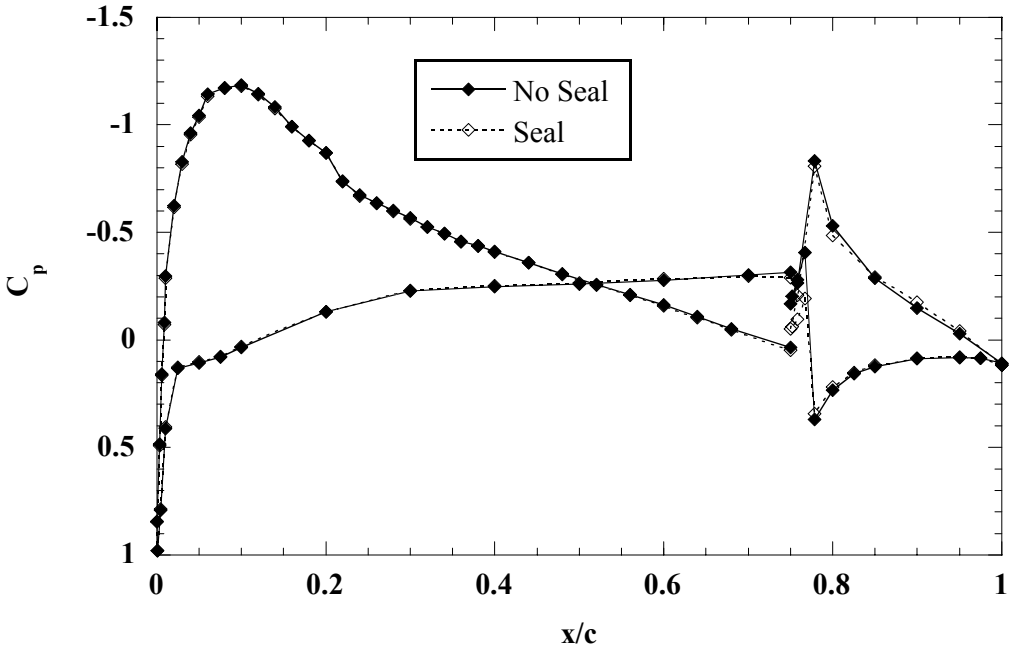

Fig 4.9a) $\delta_f = -10°$

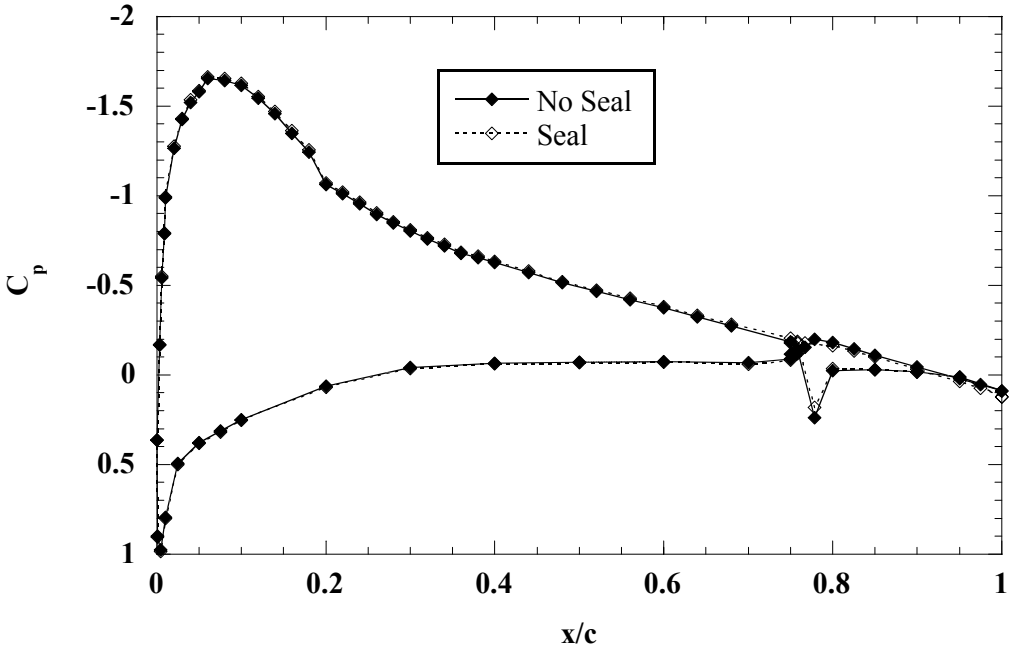

Fig 4.9b) $\delta_f = 0°$

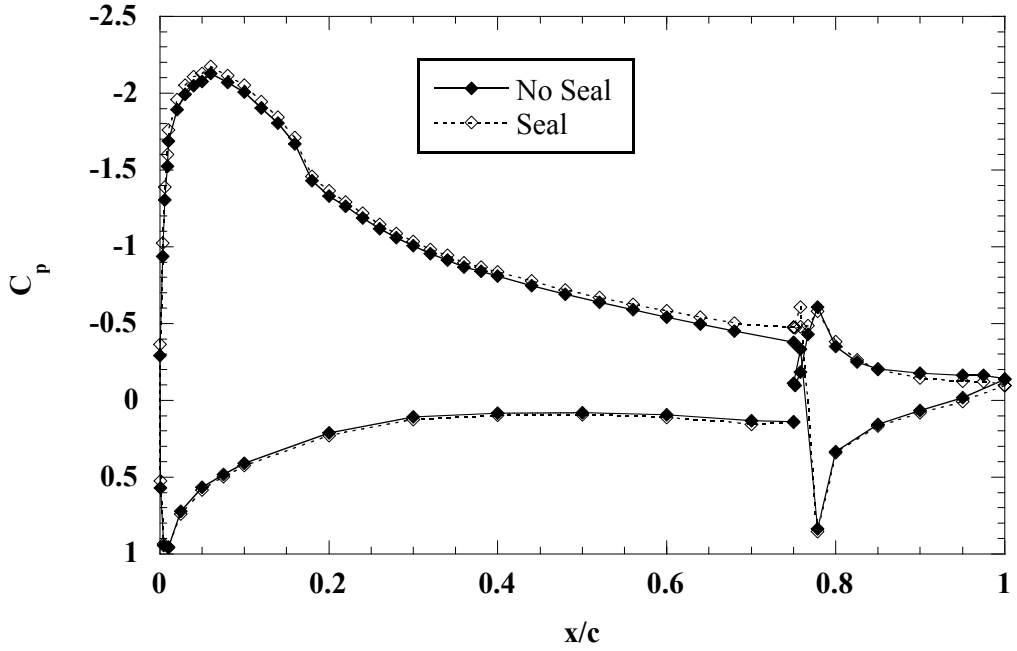

Fig 4.9c) $\delta_f = 10°$

Fig. 4.9: Effect of flap-gap seal on the surface pressure distribution. NACA 23012m, $Re = 1.8 \times 10^6$, $\alpha = 5°$.

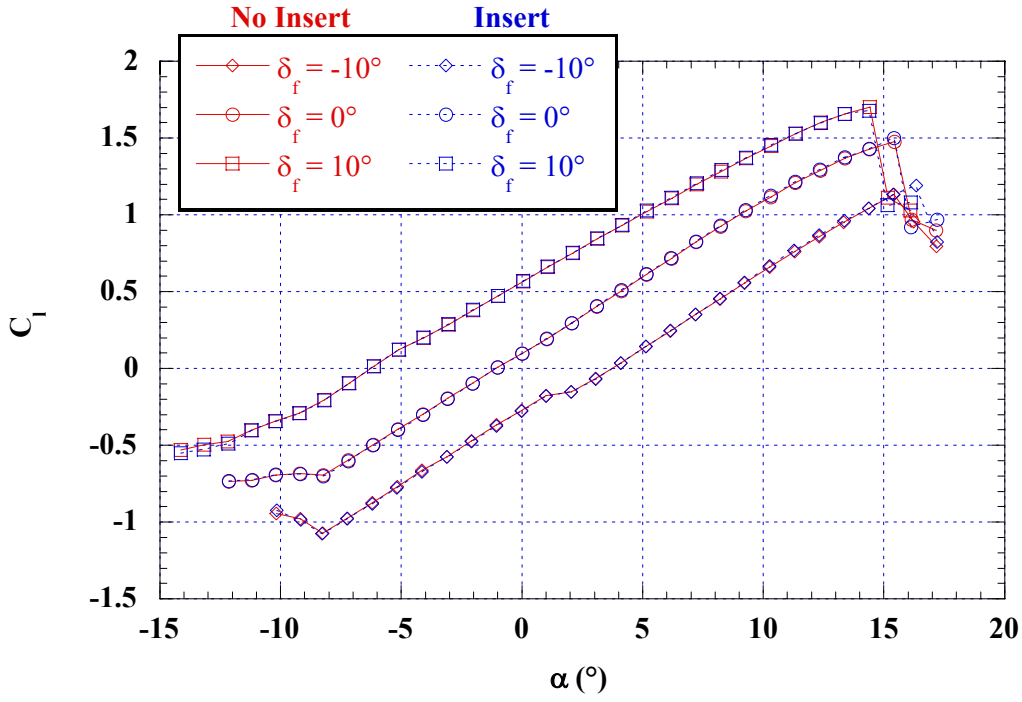

Fig. 4.10: Effect of spanwise-gap insert on the lift curve. NACA 23012m, $Re = 1.8 \times 10^6$.

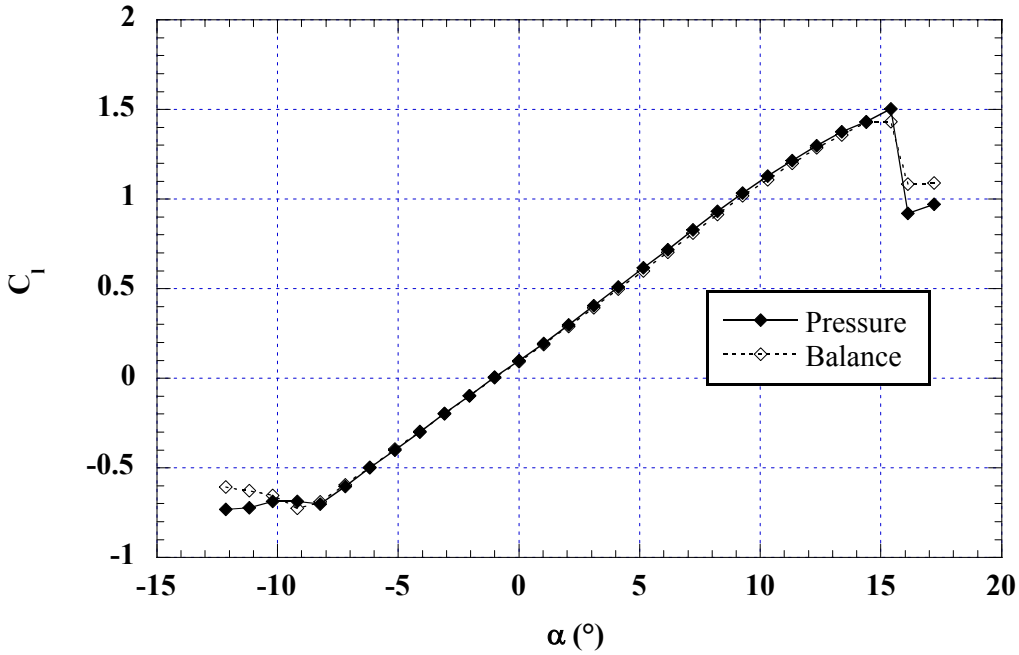

Fig. 4.11a) Lift

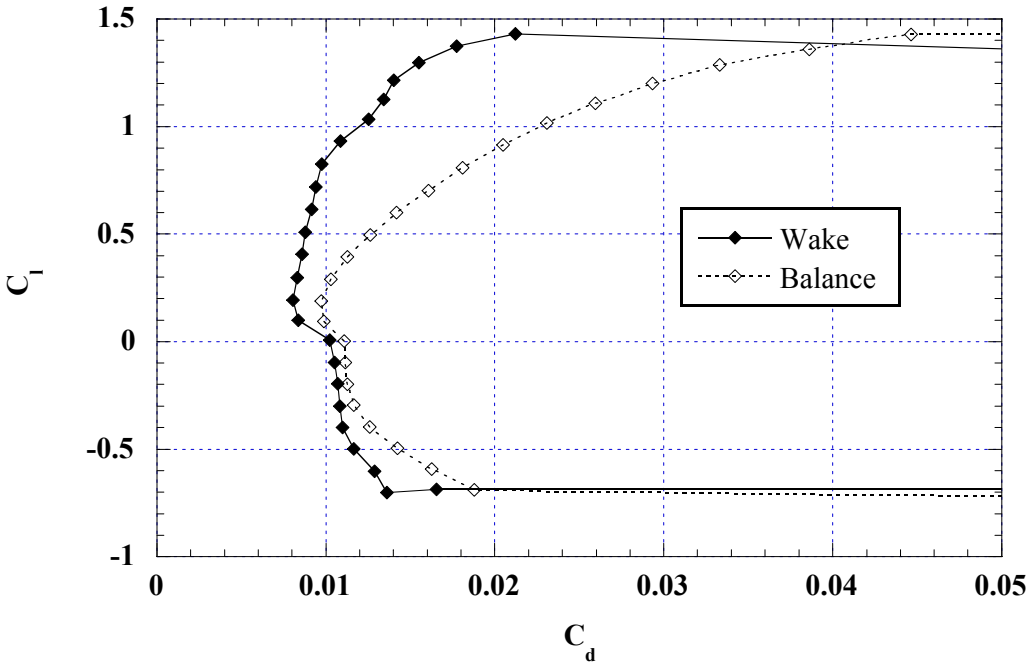

Fig. 4.11b) Drag

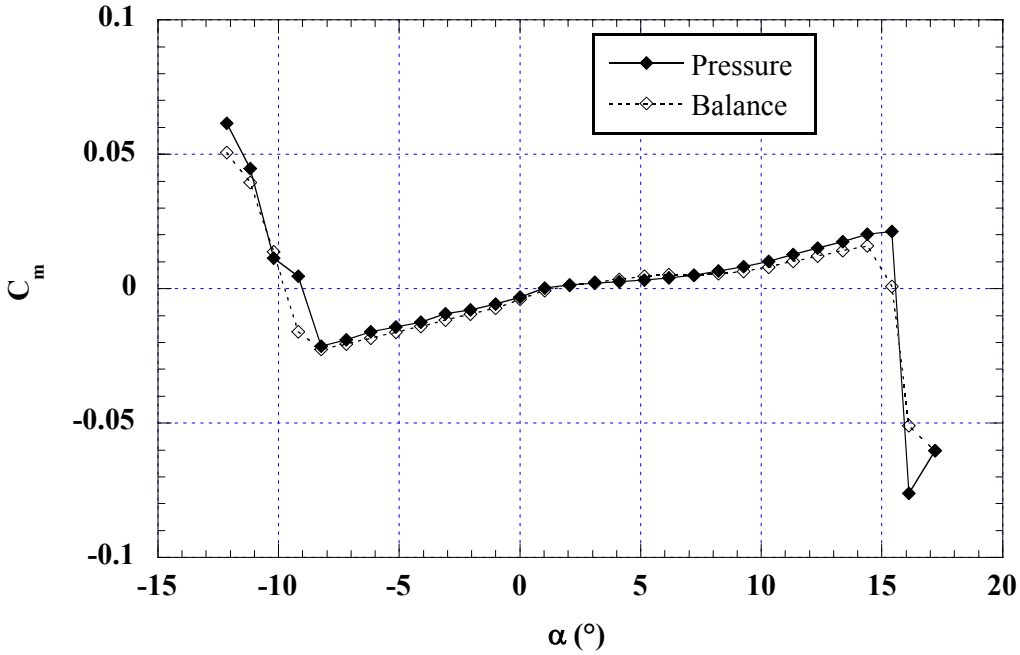

Fig. 4.11c) Pitching moment

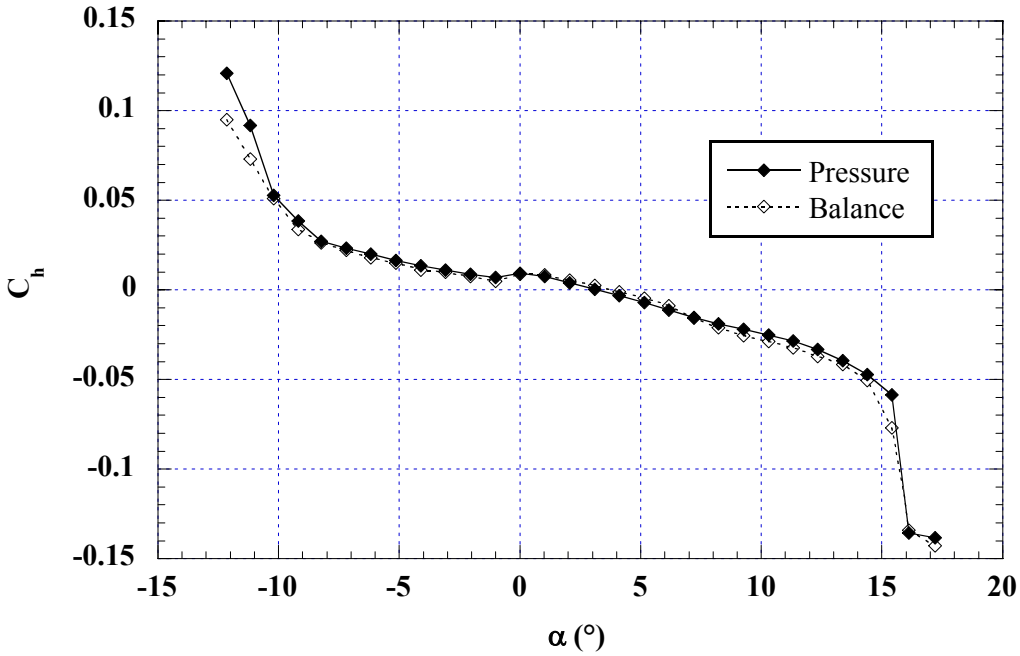

Fig. 4.11d) Flap hinge moment

Fig. 4.11: Baseline NACA 23012m aerodynamic coefficients. Clean model, *Re* = 1.8 million, $\delta_f = 0°$.

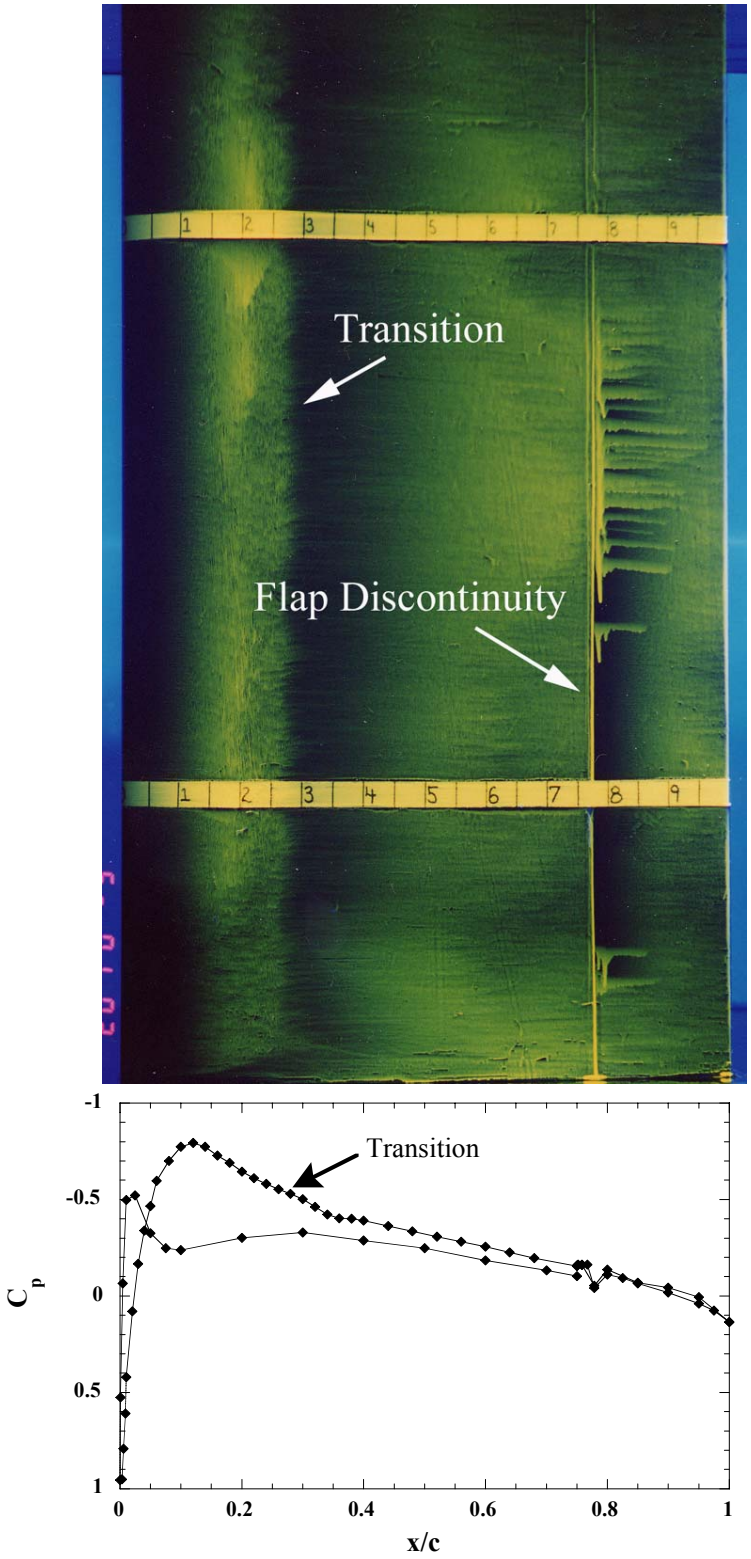

Fig. 4.12a) $\alpha = 0°$

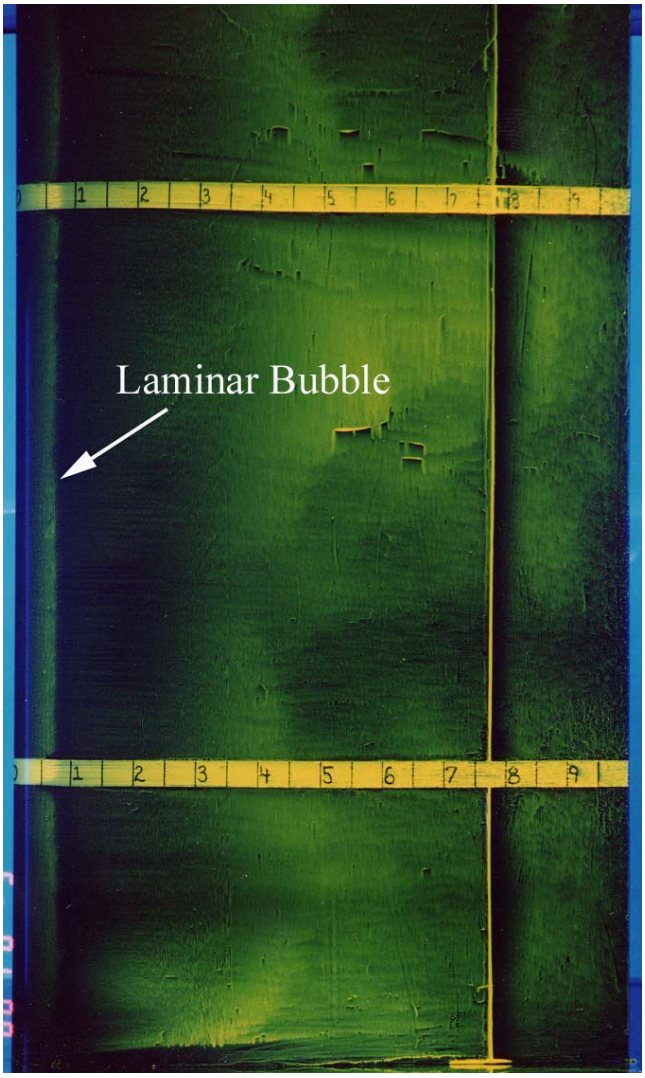

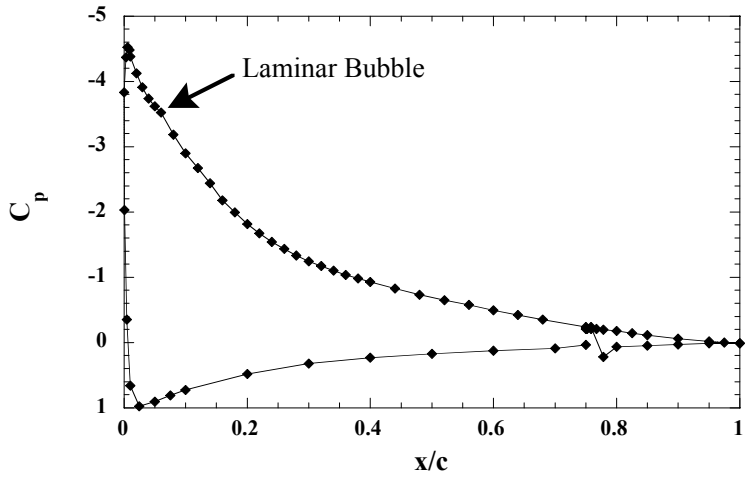

Fig. 4.12b) $\alpha = 5°$

Fig. 4.12: Baseline NACA 23012m surface flow visualization and pressure distribution. Clean model, Re = 1.8 million, $\delta_f = 0°$.

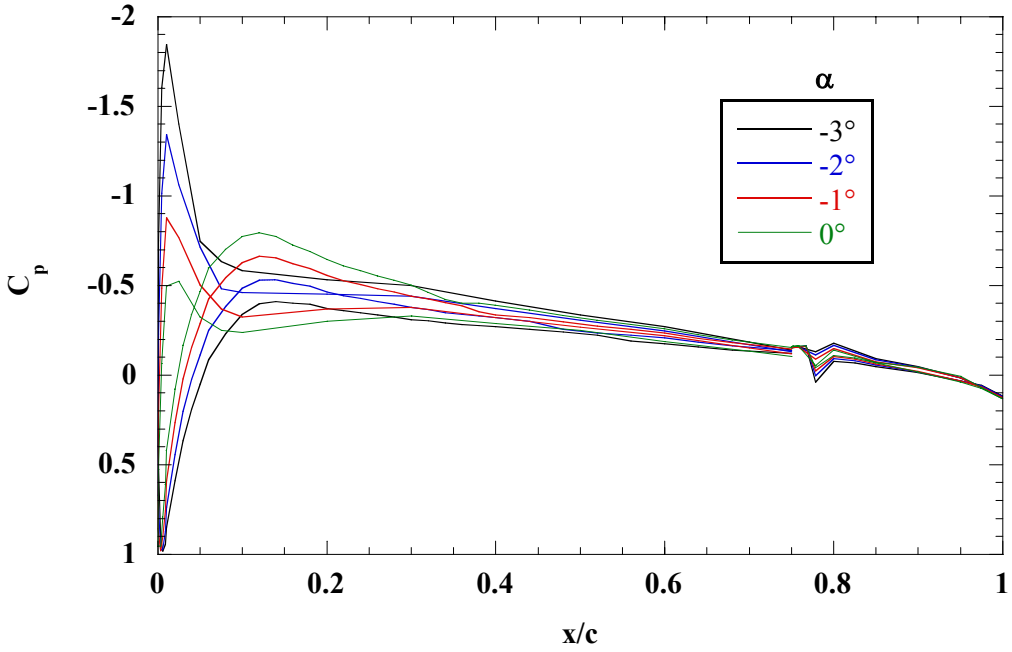

Fig. 4.13α) α = -3° to 0°

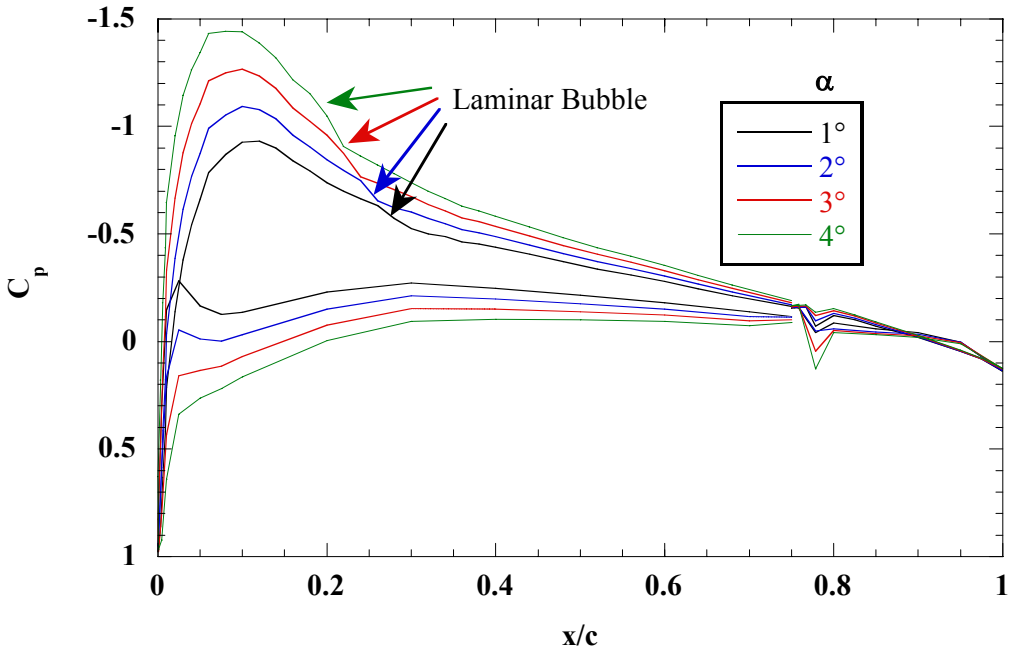

Fig. 4.13b) α = 1° to 4°

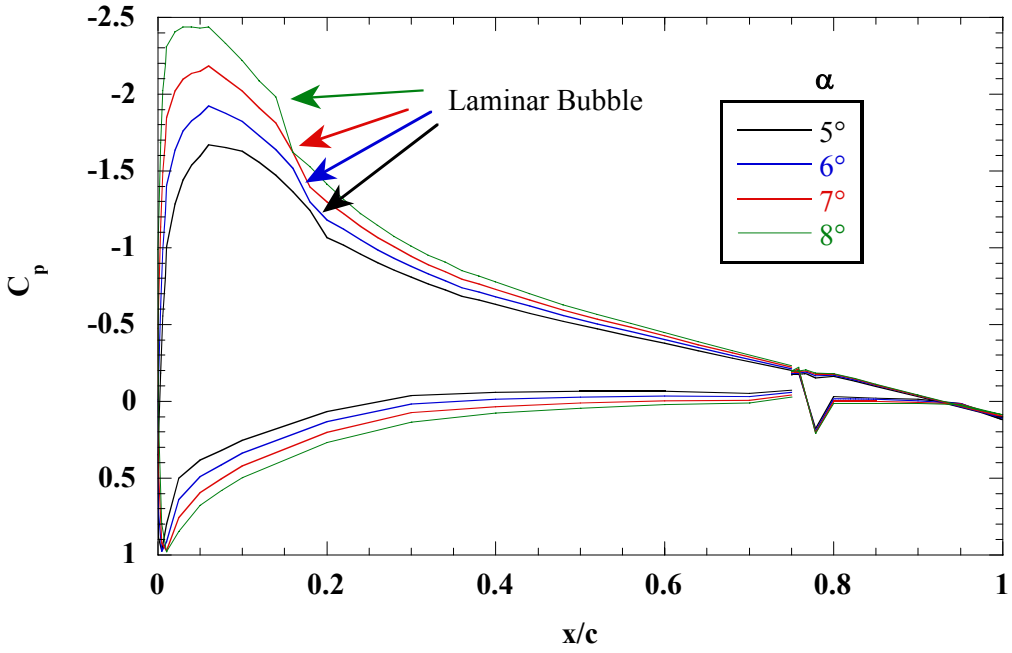

Fig. 4.13c) $\alpha = 5°$ to $8°$

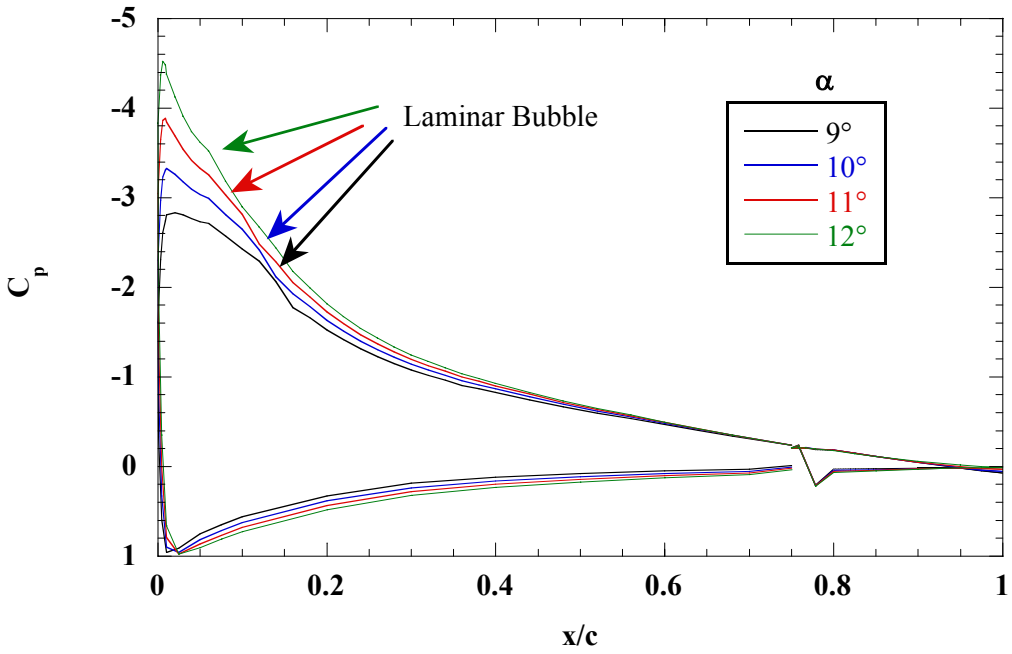

Fig. 4.13d) $\alpha = 9°$ to $12°$

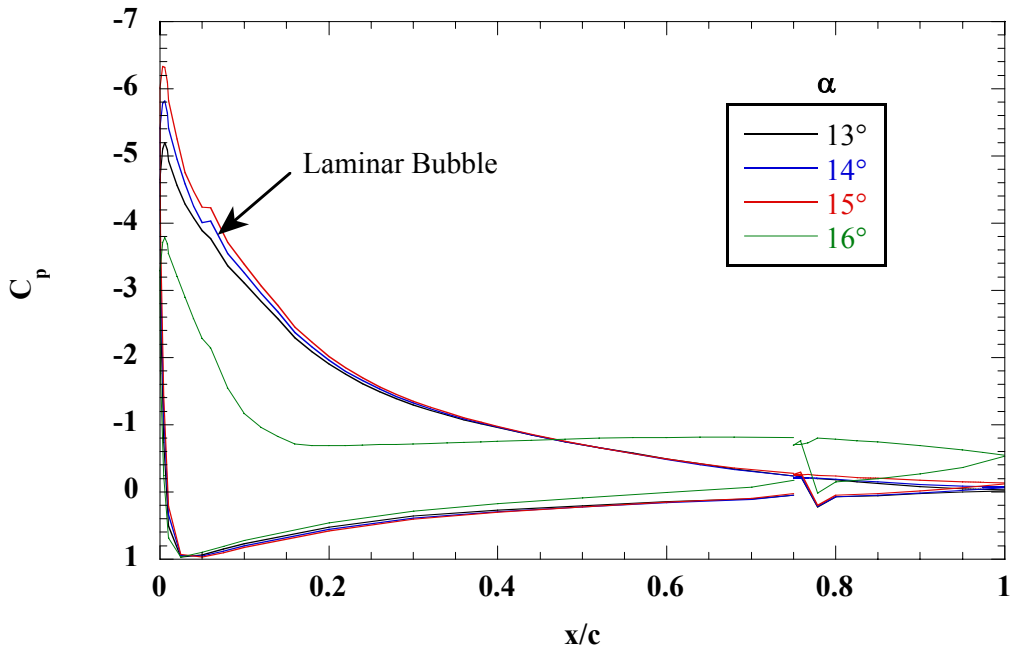

Fig. 4.13e) α = 13° to 16°

Fig. 4.13: Baseline NACA 23012m pressure distributions. Clean model, *Re* = 1.8 million, $\delta_f = 0°$.

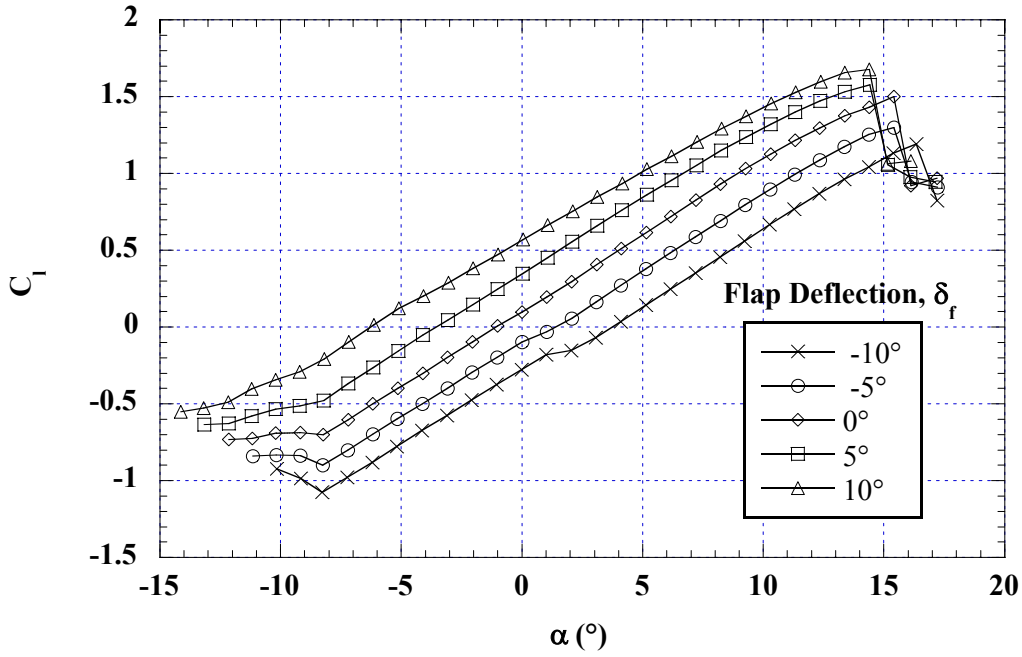

Fig. 4.14a) Lift

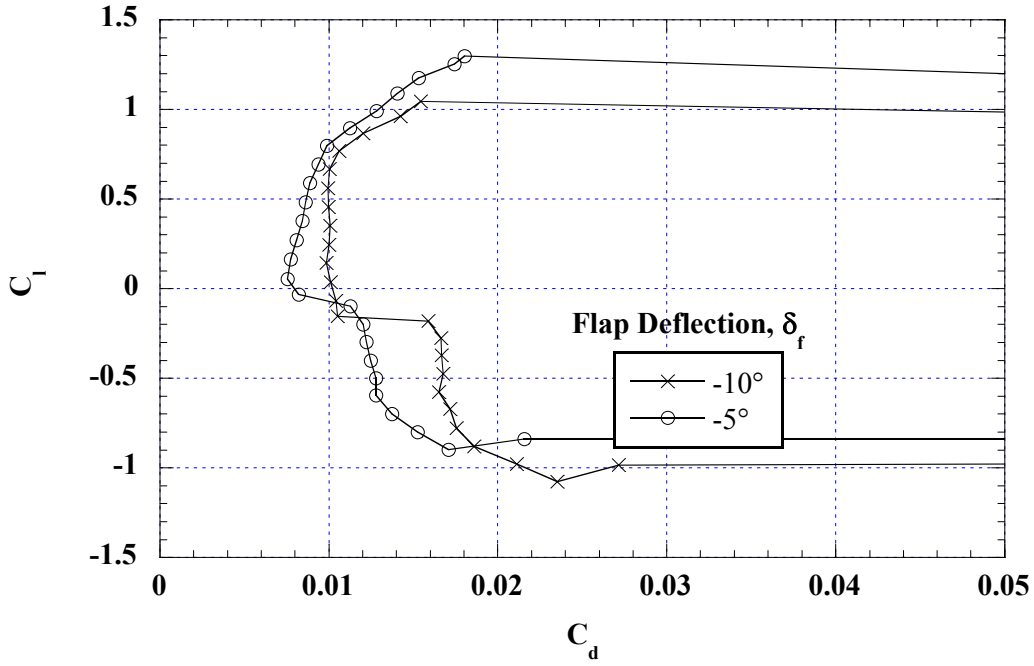

Fig. 4.14b) Drag, δ_f = -10° and -5°

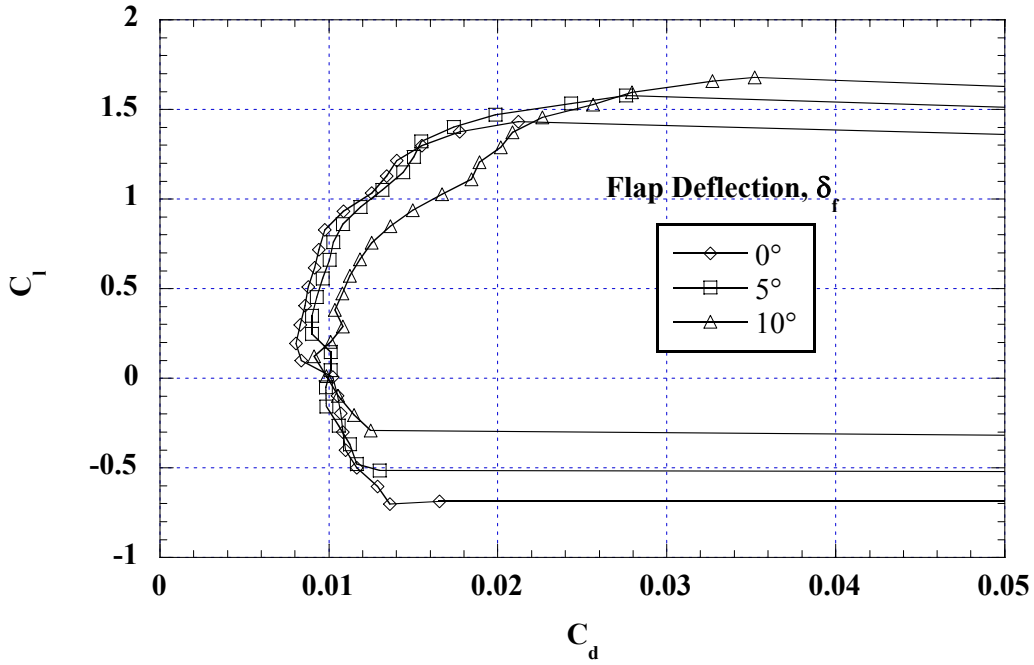

Fig. 4.14c) Drag, $\delta_f = 0°$ to $10°$

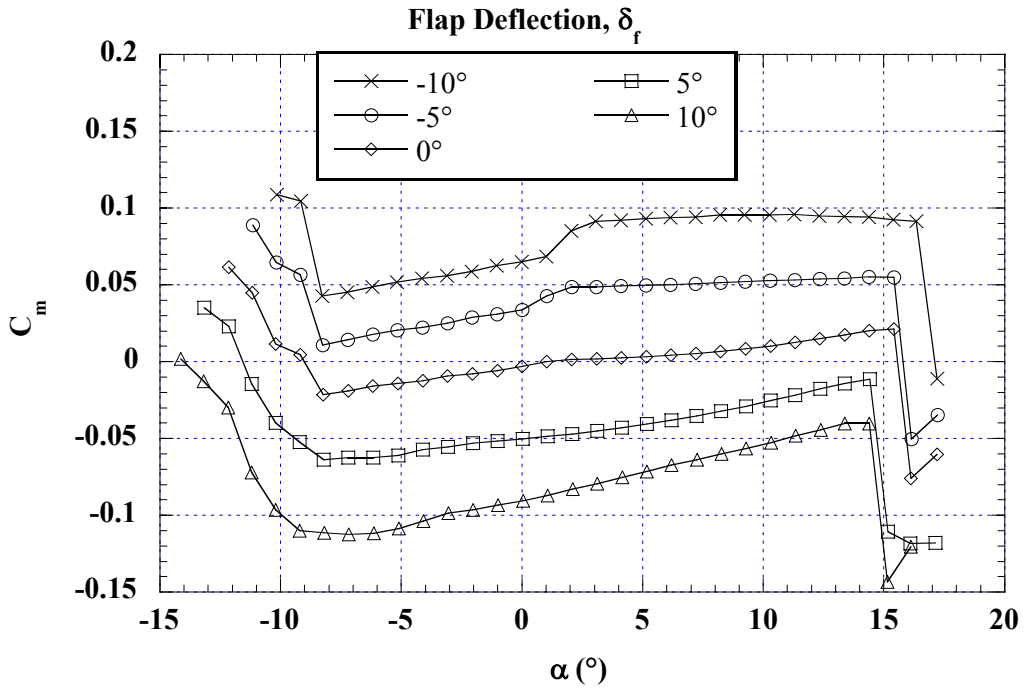

Fig. 4.14d) Pitching moment

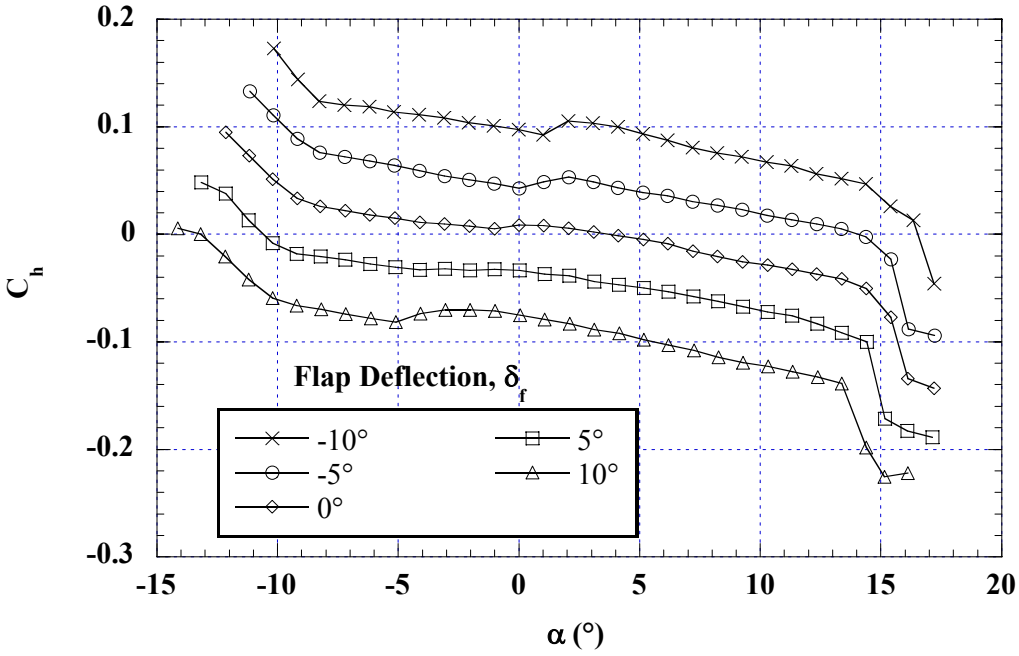

Fig. 4.14e) Flap hinge moment

Fig. 4.14: Effect of flap deflection on aerodynamic coefficients. NACA 23012m, clean model, *Re* = 1.8 million.

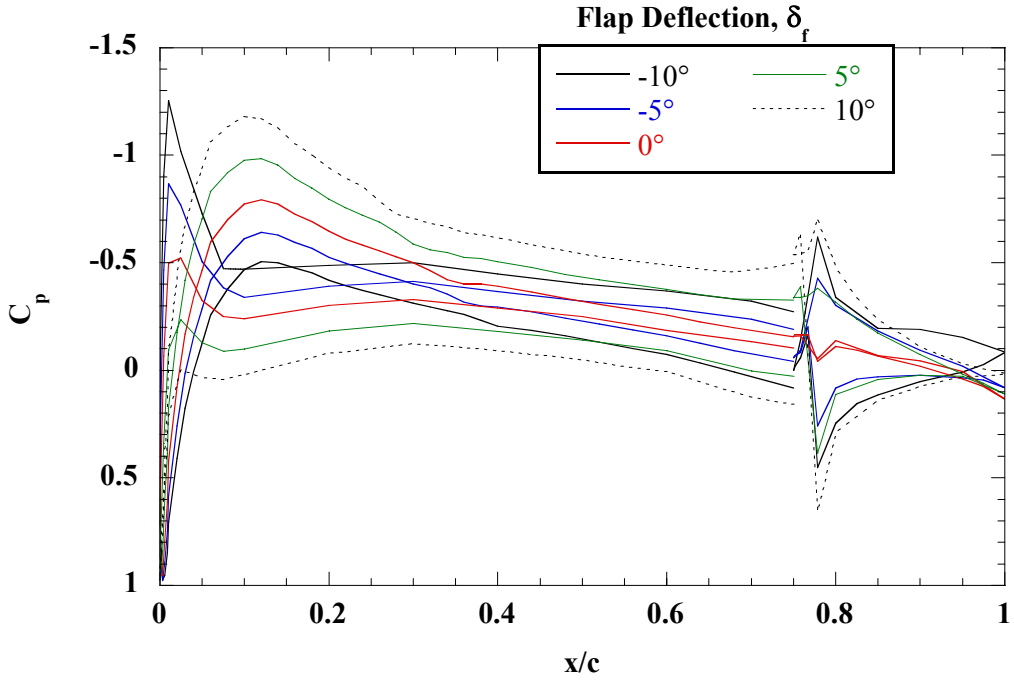

Fig. 4.15a) $\alpha = 0°$.

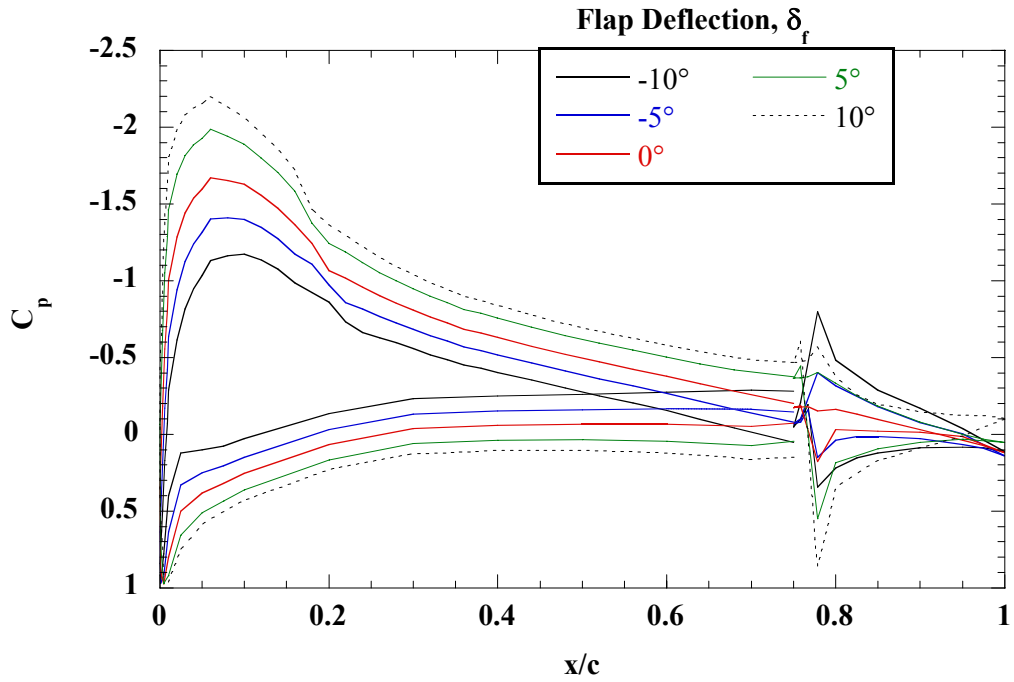

Fig. 4.15b) $\alpha = 5°$.

Fig. 4.15: Effect of flap deflection on surface pressure distribution. NACA 23012m, clean model, Re = 1.8 million.

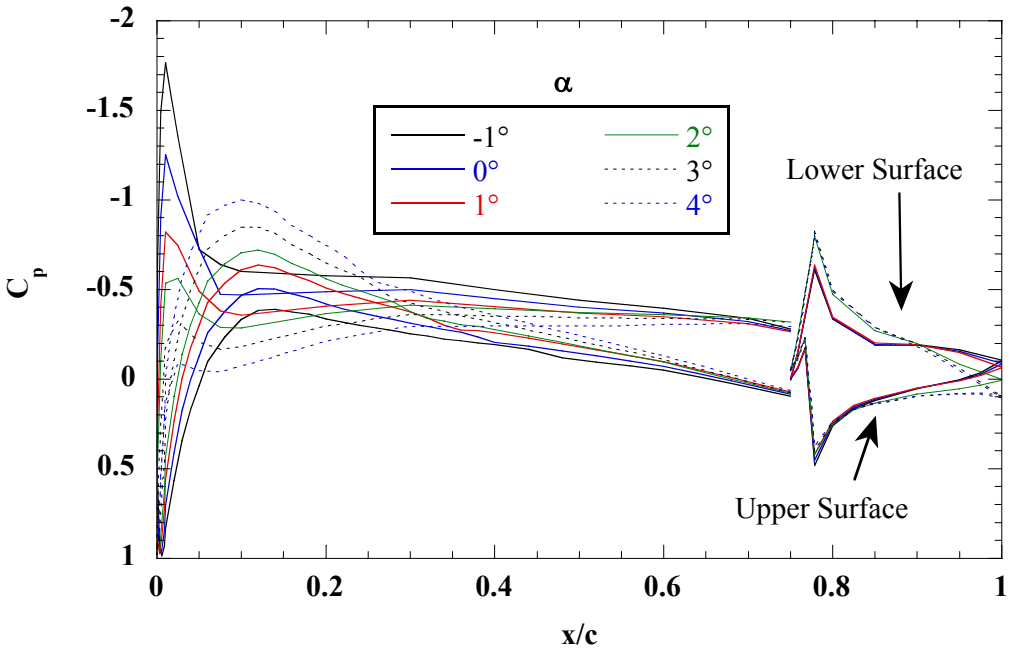

Fig. 4.16: Surface pressure distribution. NACA 23012m, Re = 1.8 million, δ_f = -10°.

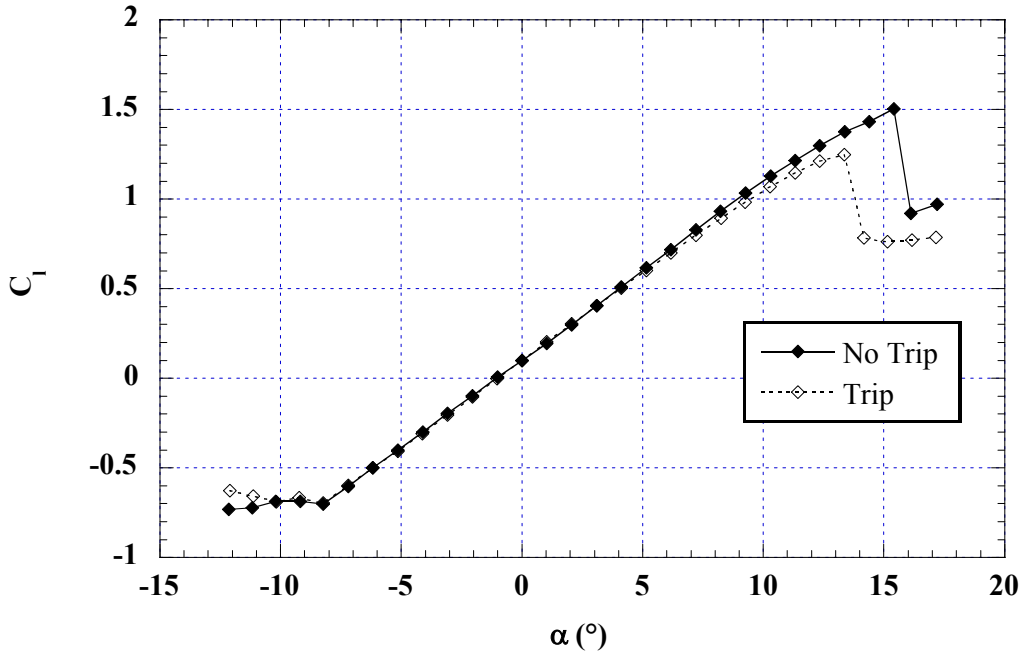

Fig. 4.17a) Lift

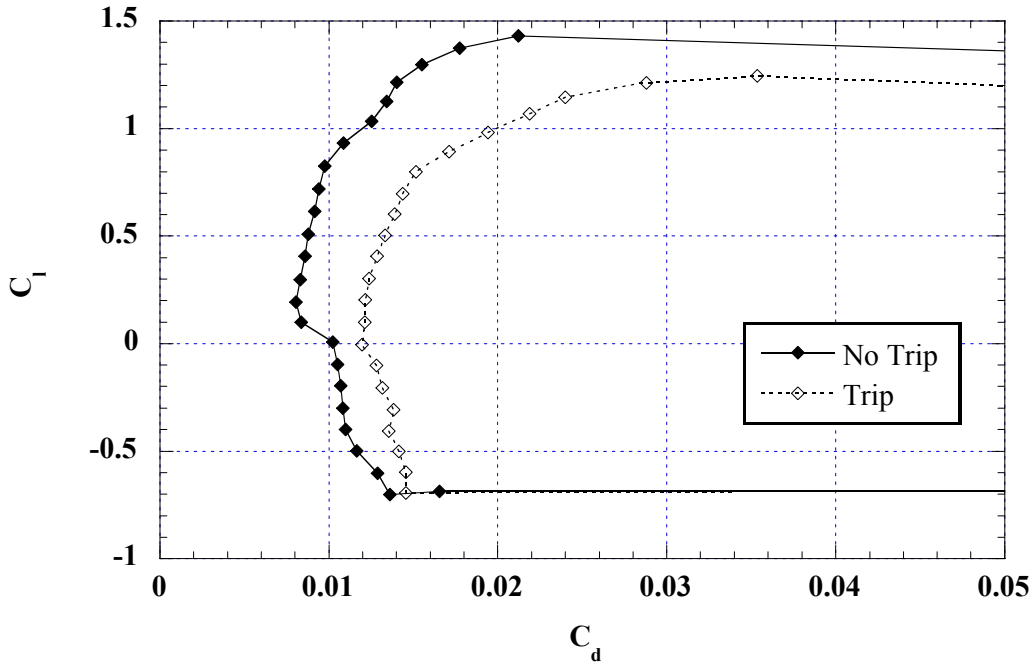

Fig. 4.17b) Drag

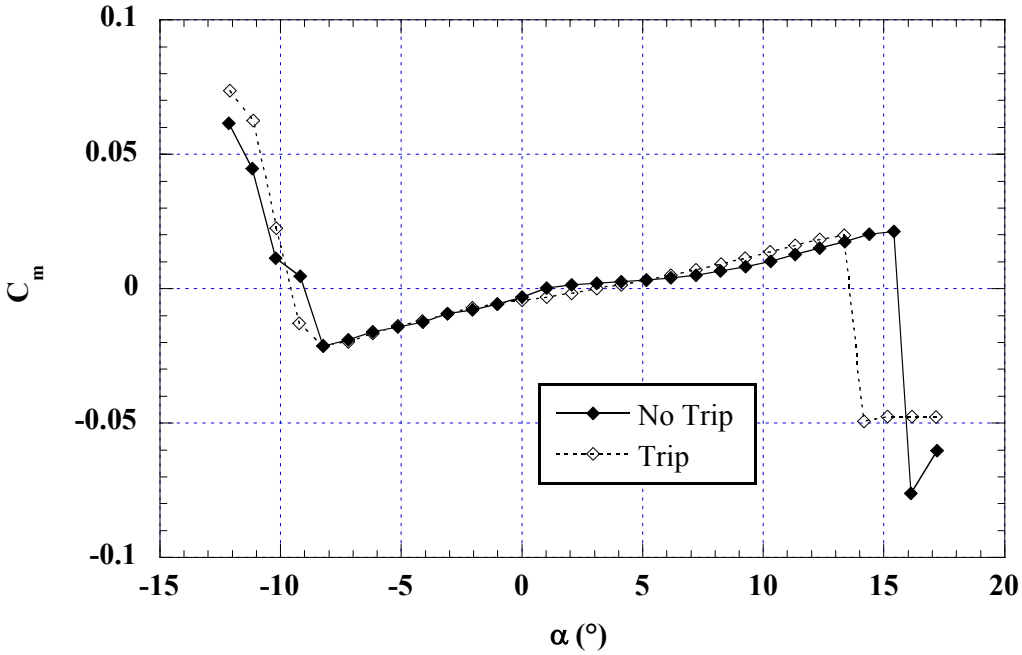

Fig. 4.17c) Pitching moment

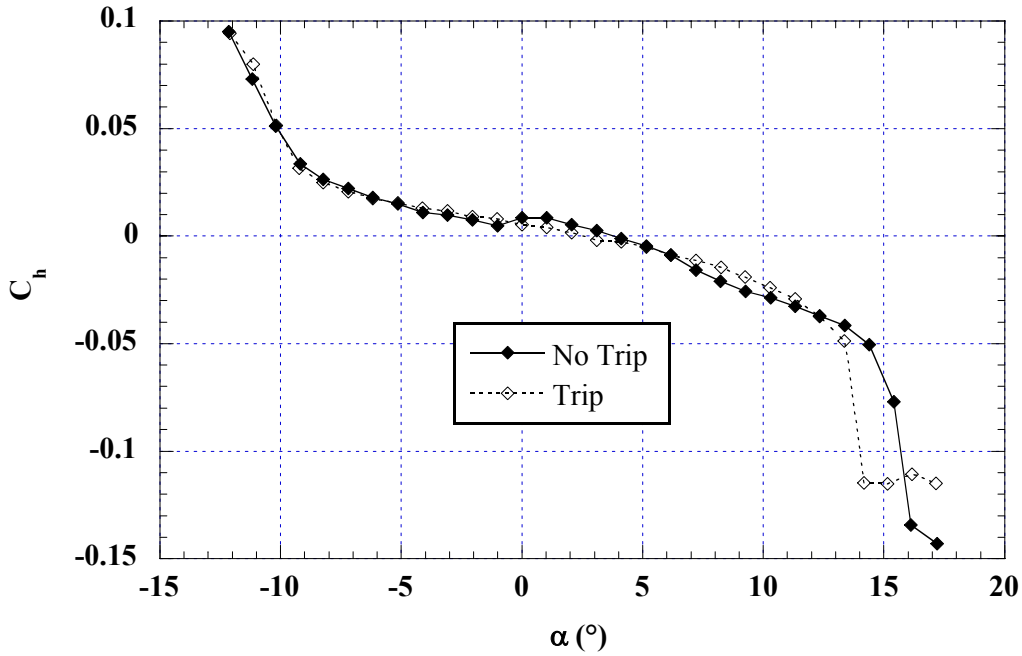

Fig 4.17d) Flap hinge moment

Fig. 4.17: Effect of boundary-layer trip on aerodynamic coefficients. NACA 23012m, *Re* = 1.8 million, trip at *x*/*c* = 0.02 upper and 0.05 lower surfaces.

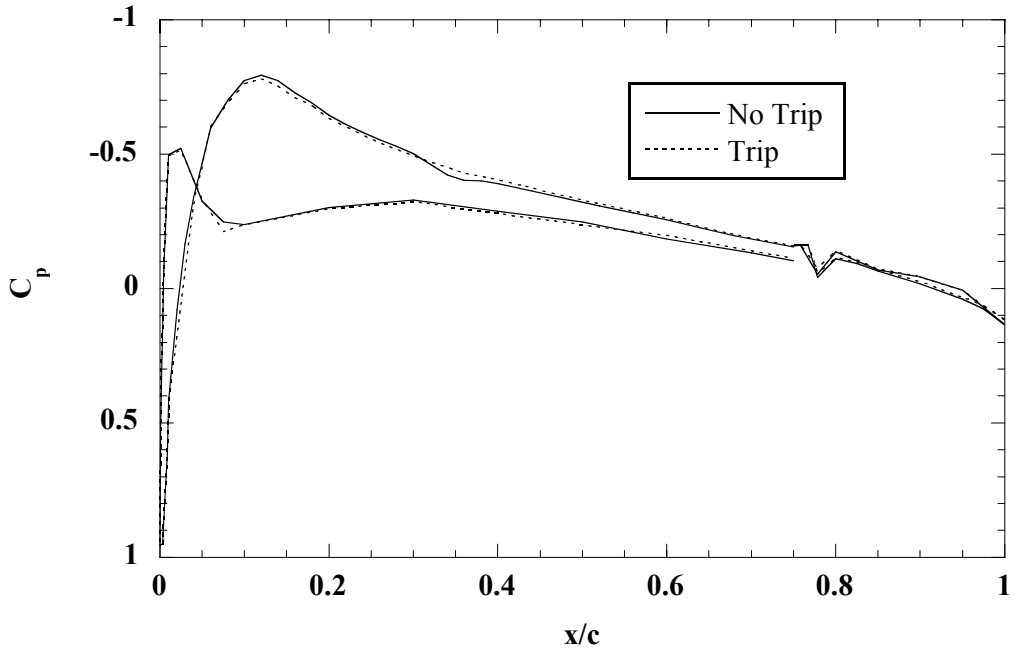

Fig. 4.18a) $\alpha = 0°$.

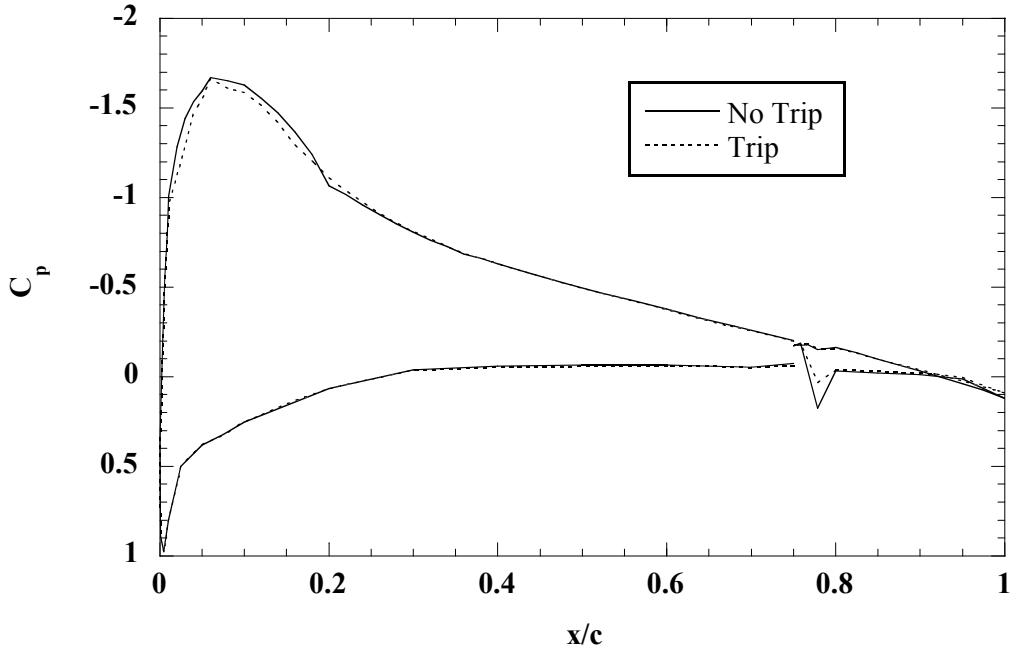

Fig. 4.18b) $\alpha = 5°$.

Fig. 4.18: Effect of boundary layer trip on surface pressure distribution. NACA 23012m, *Re* = 1.8 million, trip at *x*/*c* = 0.02 upper and 0.05 lower surfaces.

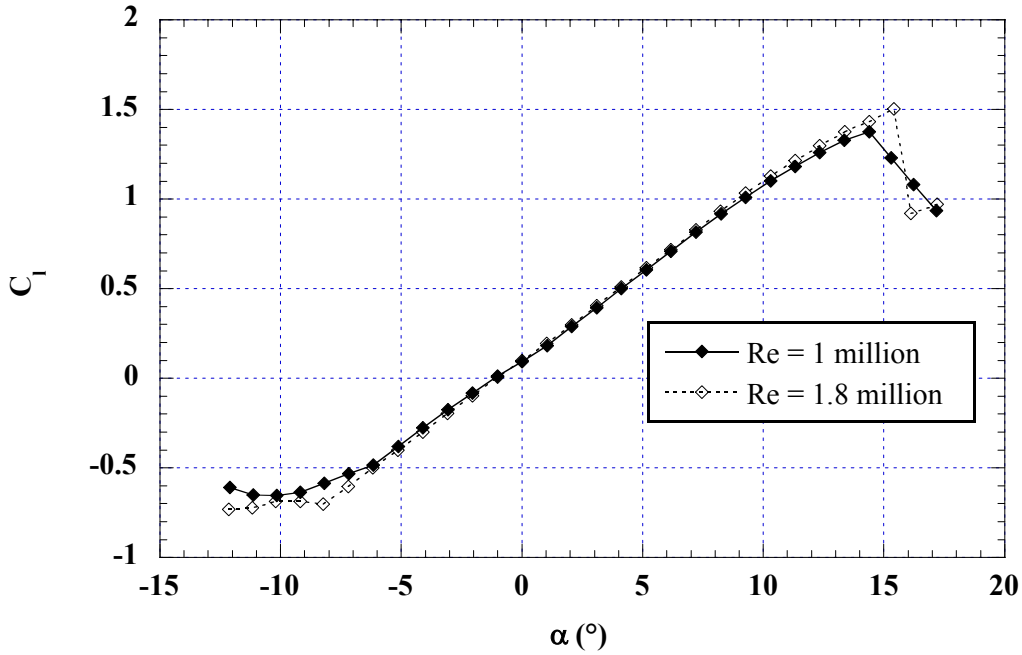

Fig. 4.19a) Lift

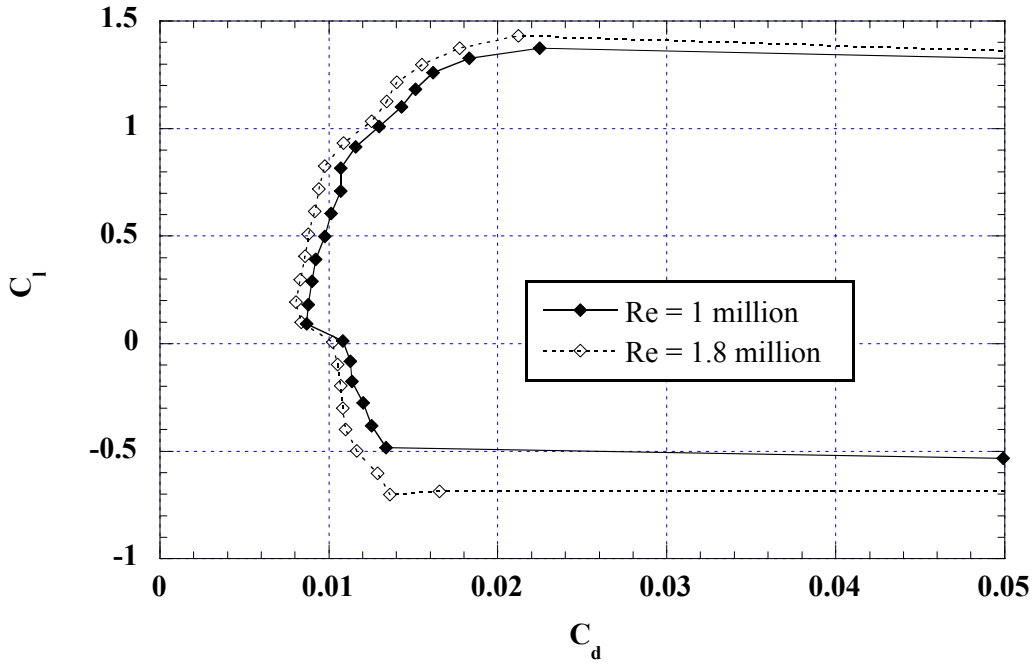

Fig. 4.19b) Drag

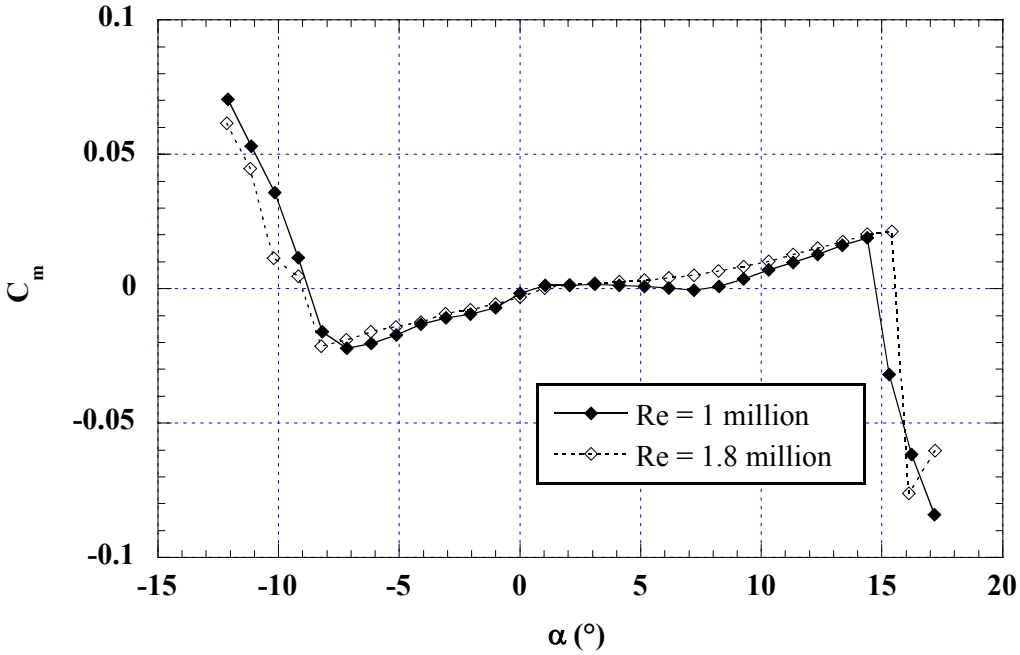

Fig. 4.19c) Pitching moment

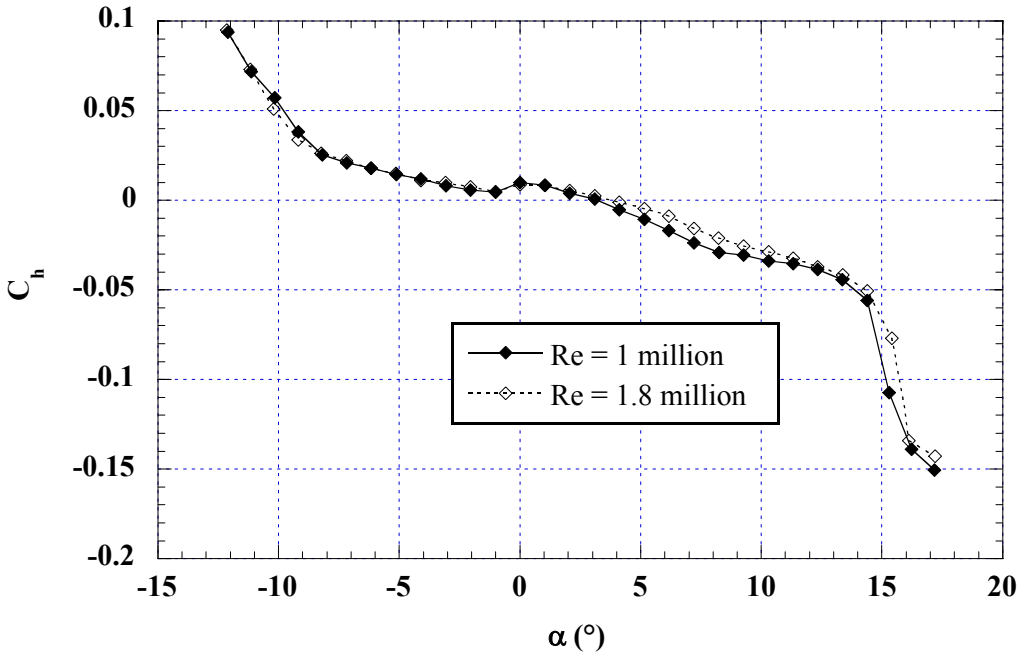

Fig .4.19d) Flap hinge moment

Fig. 4.19: Effect of Reynolds number on aerodynamic coefficients. NACA 23012m, clean model.

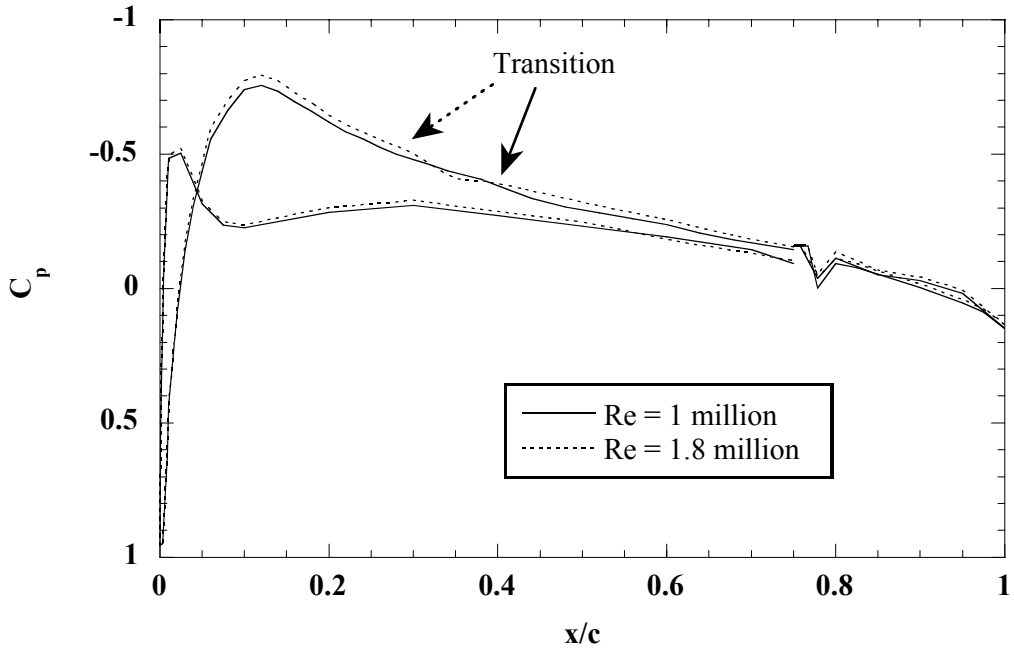

Fig. 4.20a) $\alpha = 0°$

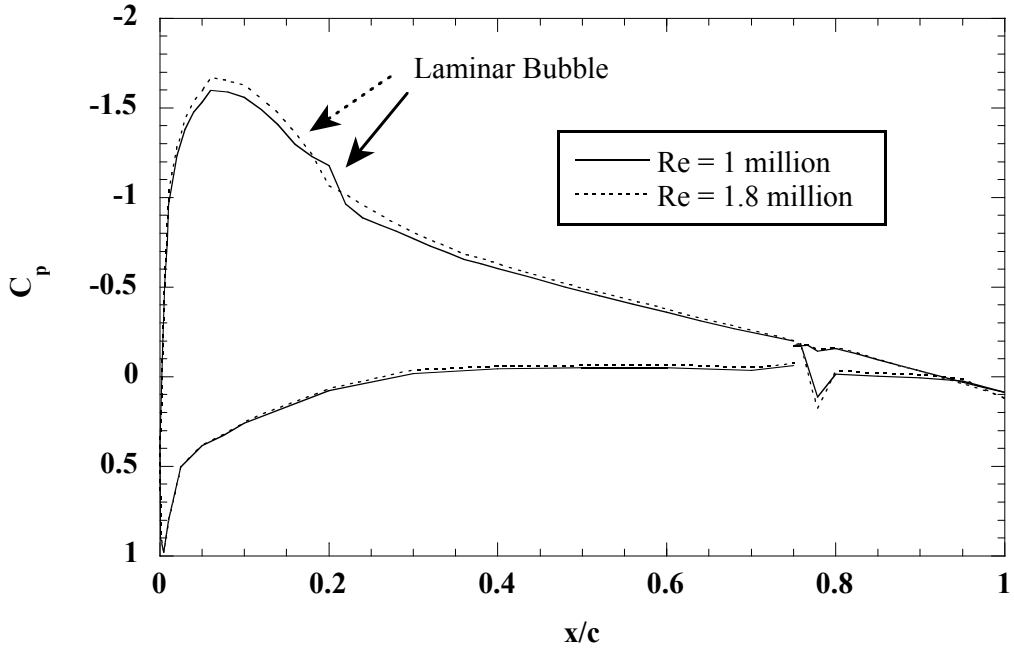

Fig. 4.20b) $\alpha = 5°$

Fig. 4.20: Effect of Reynolds number on surface-pressure distribution. NACA 23012m, clean model.

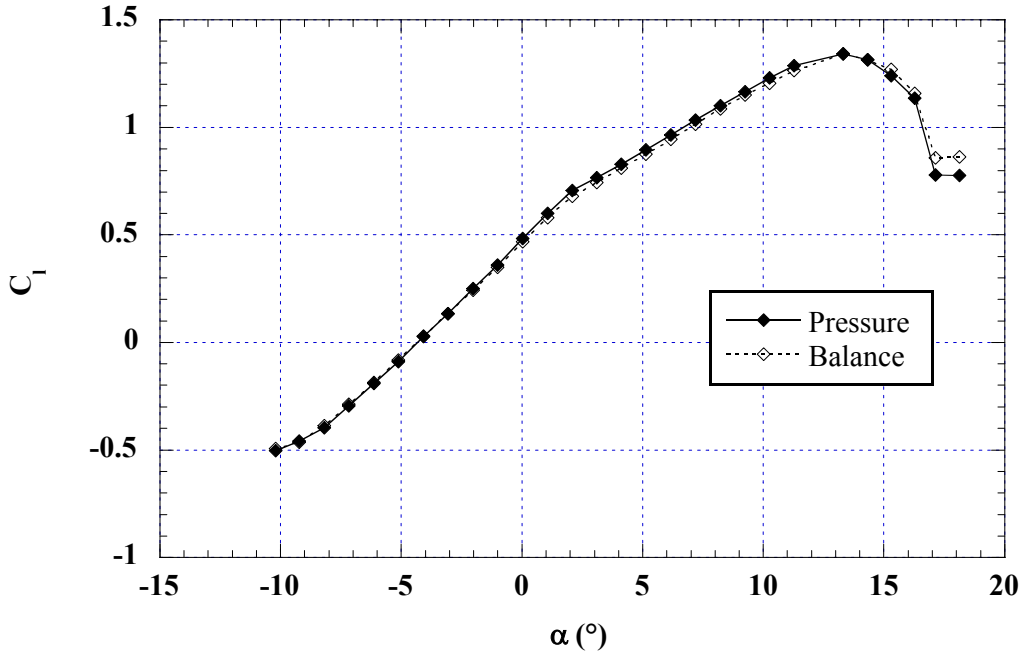

Fig. 4.21a) Lift

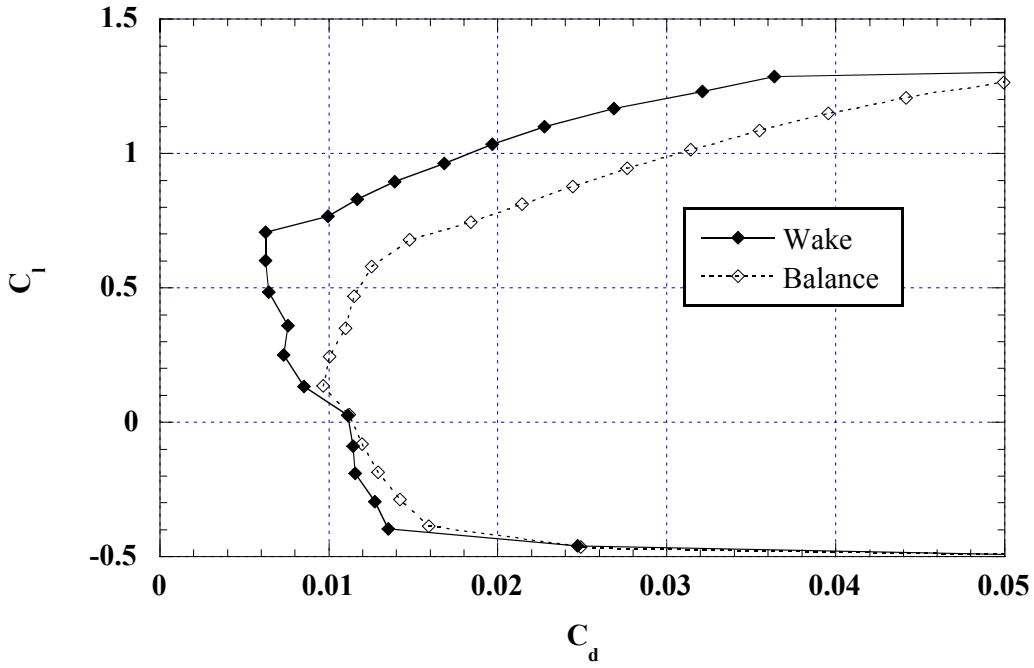

Fig. 4.21b) Drag

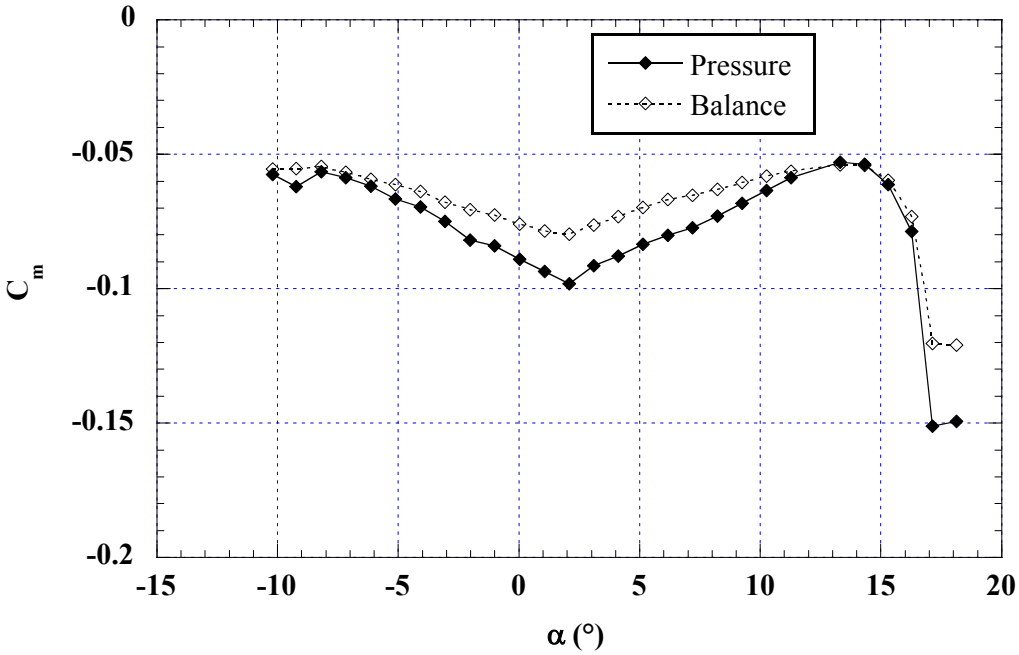

Fig. 4.21c) Pitching moment

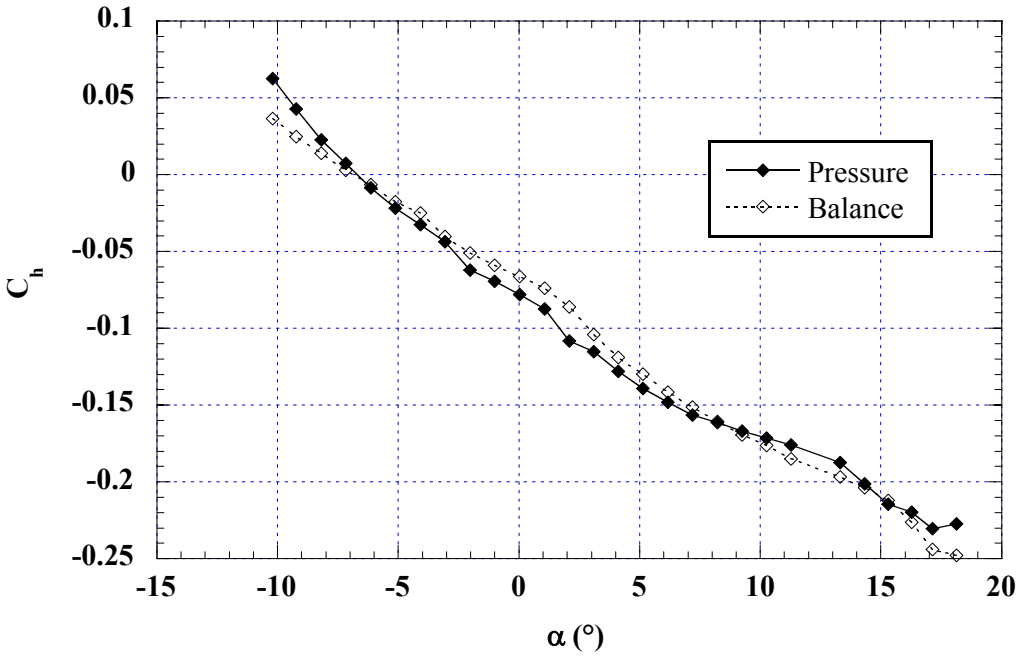

Fig. 4.21d) Flap hinge moment

Fig. 4.21: Baseline NLF 0414 aerodynamic coefficients. Clean model, *Re* = 1.8 million, $\delta_f = 0°$.

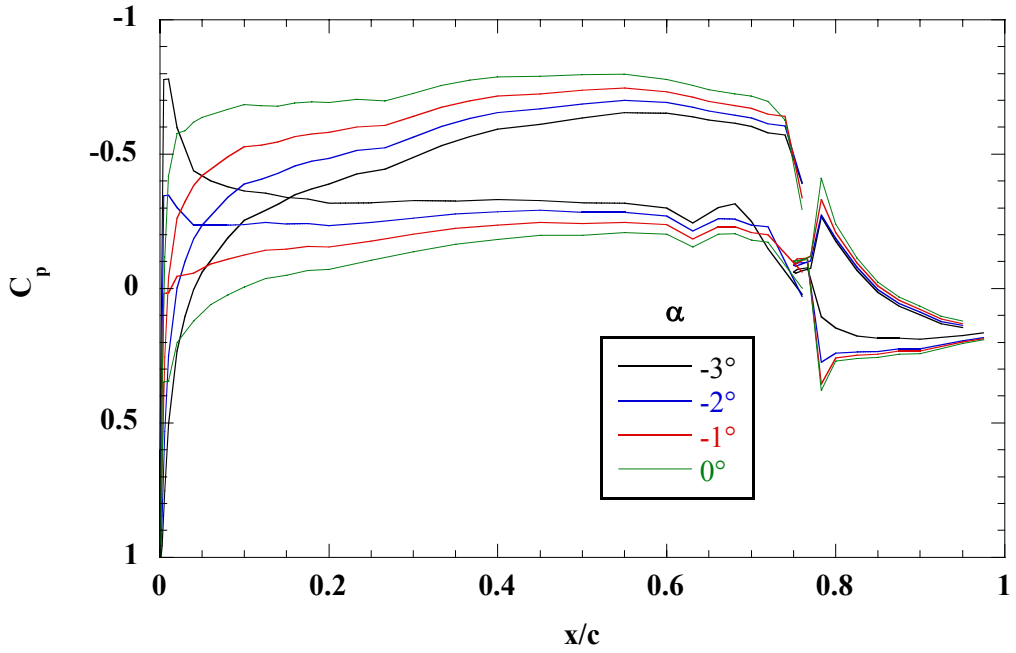

Fig. 4.22a) α = -3° to 0°

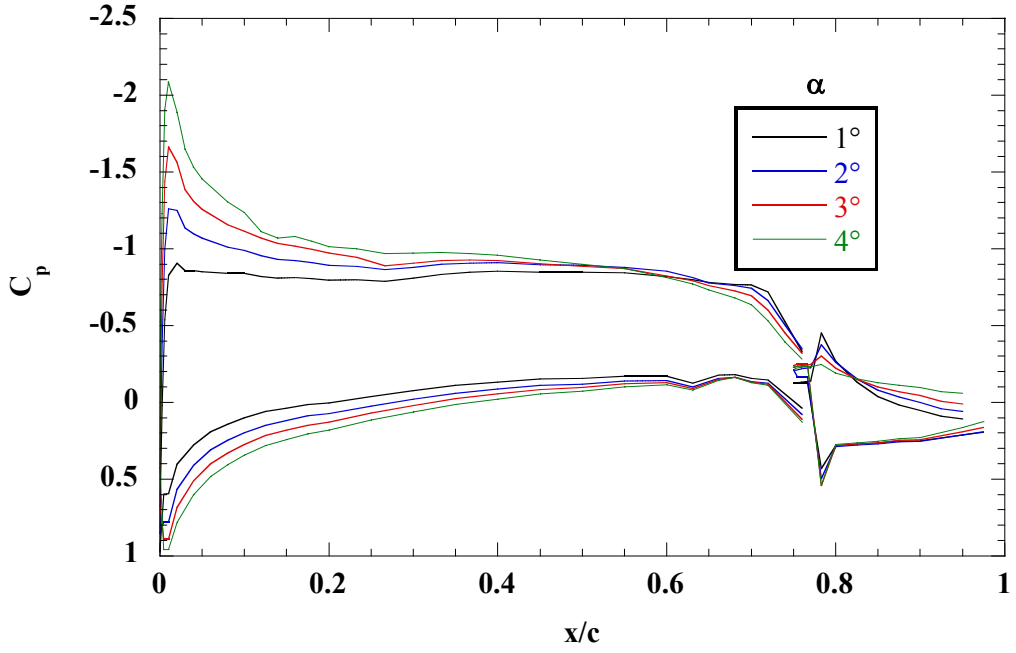

Fig. 4.22b) α = 1° to 4°

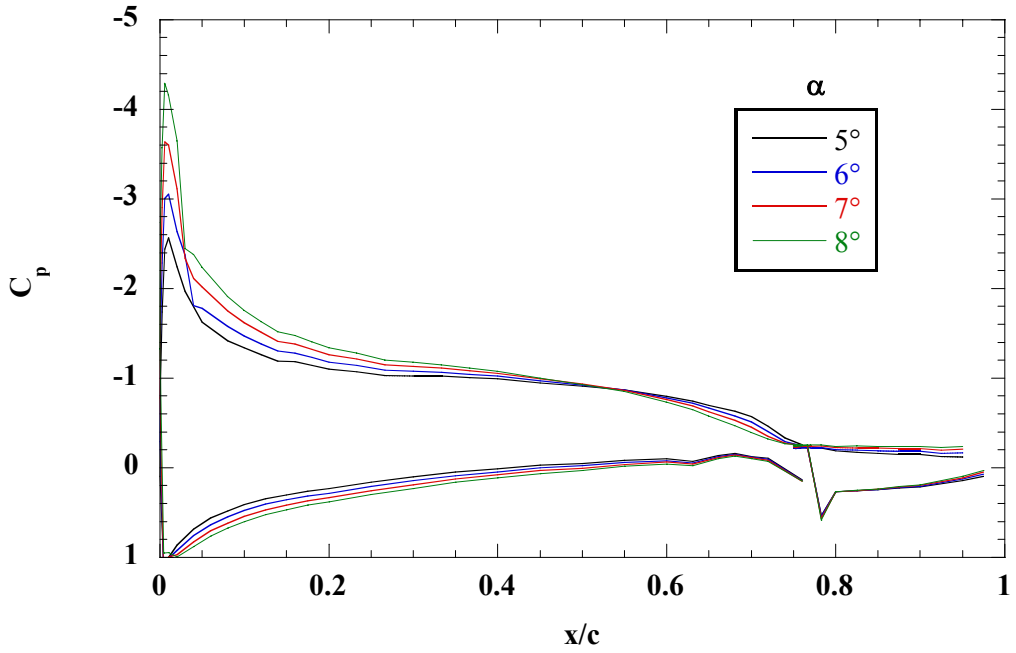

Fig. 4.22c) $\alpha = 5°$ to $8°$

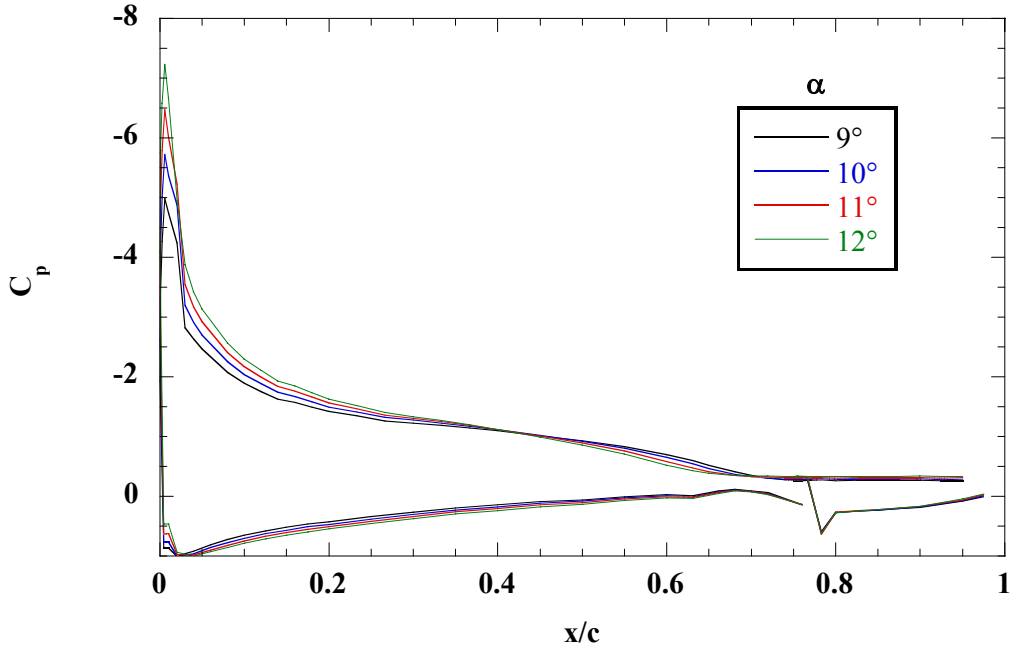

Fig. 4.22d) $\alpha = 9°$ to $12°$

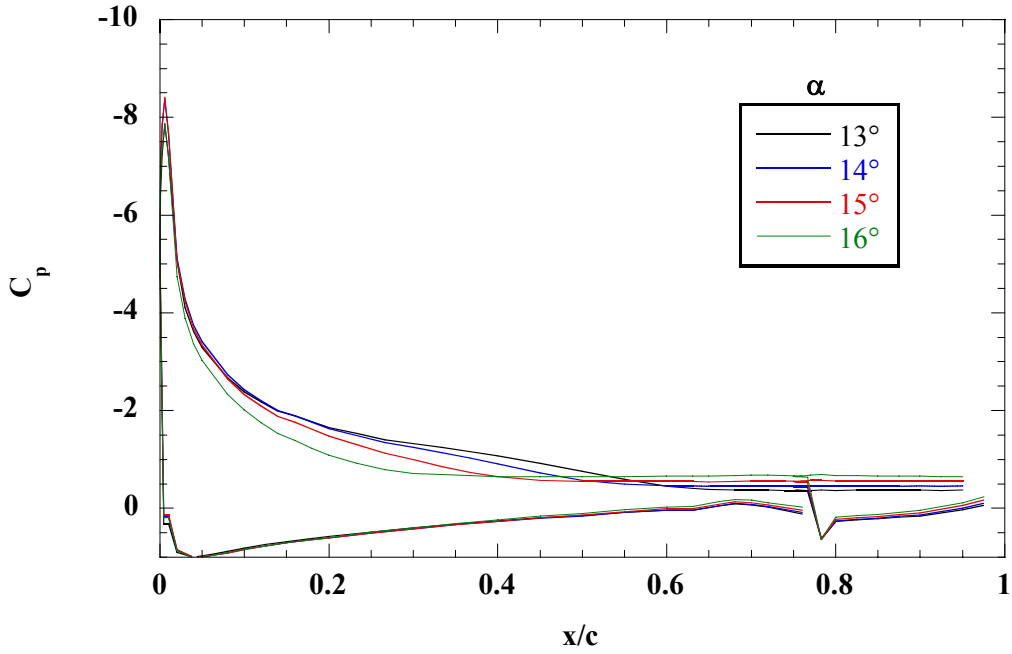

Fig. 4.22e) $\alpha = 13°$ to $16°$

Fig. 4.22: Baseline NLF 0414 pressure distributions. Clean model, Re = 1.8 million, $\delta_f = 0°$.

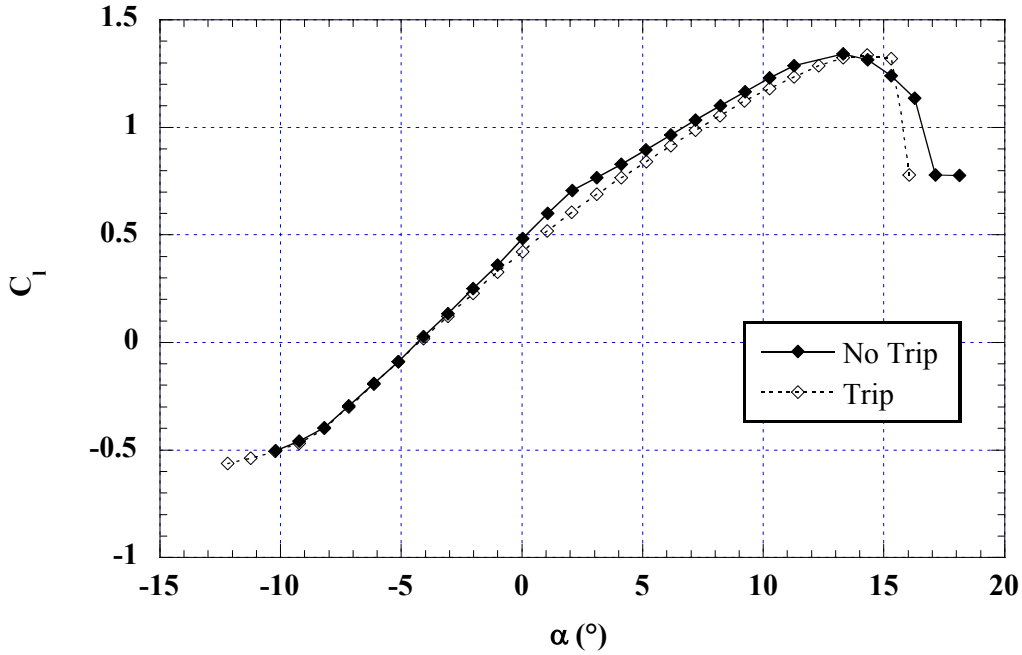

Fig. 4.23a) Lift

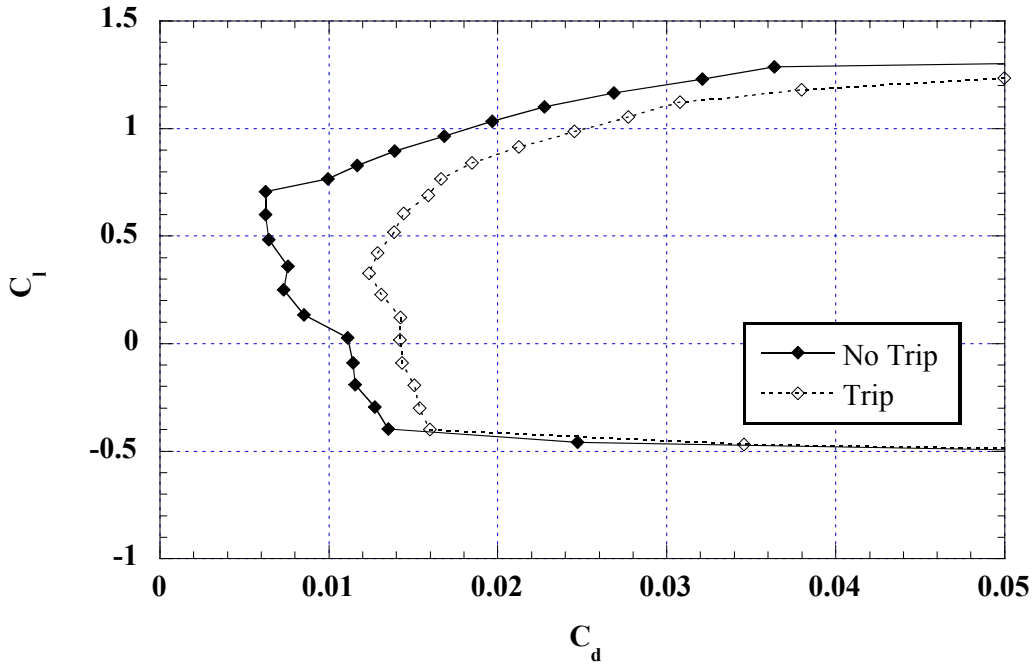

Fig. 4.23b) Drag

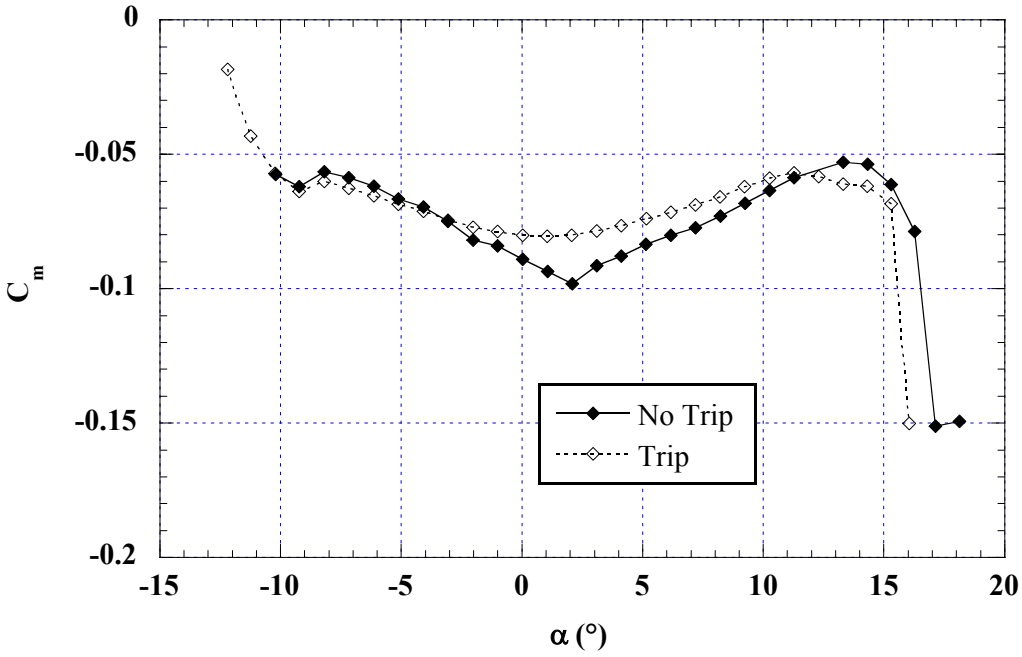

Fig. 4.23c) Pitching moment

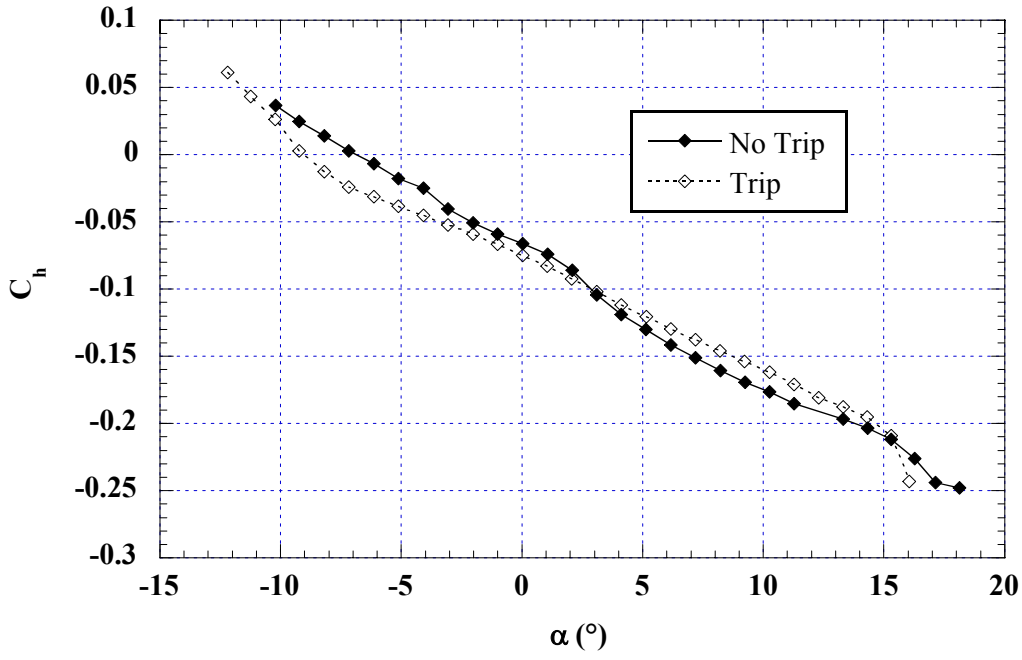

Fig. 4.23d) Flap hinge moment

Fig. 4.23: Effect of boundary layer trip on aerodynamic coefficients. NLF 0414, *Re* = 1.8 million, trip at *x*/*c* = 0.02 upper and 0.05 lower surfaces.

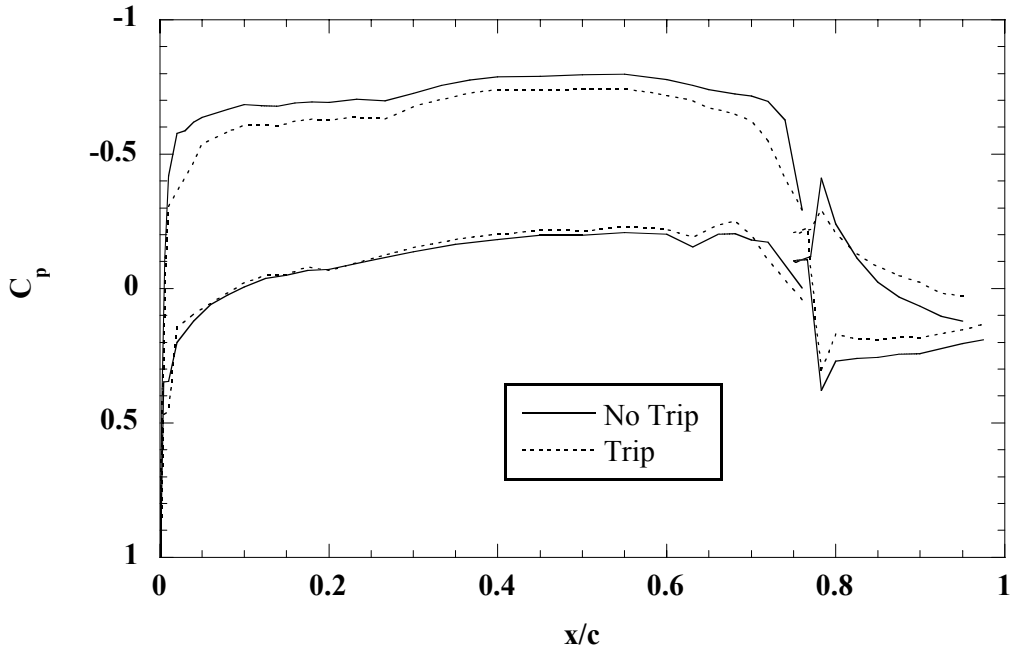

Fig. 4.24a) $\alpha = 0°$

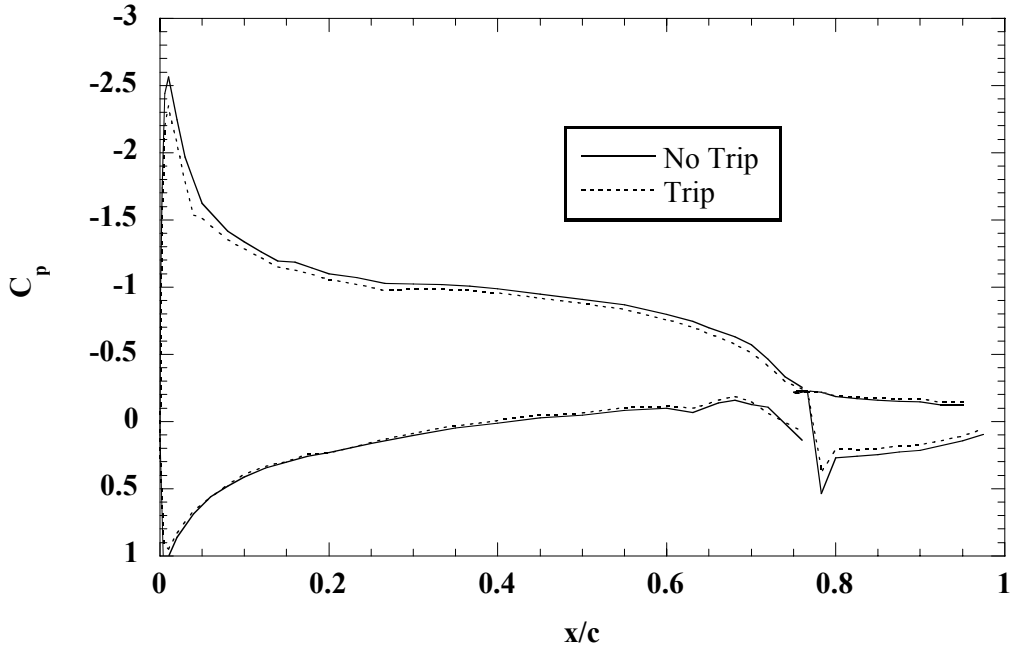

Fig. 4.24b) $\alpha = 5°$

Fig. 4.24: Effect of boundary layer trip on surface pressure distribution. NLF 0414, *Re* = 1.8 million, trip at *x*/*c* = 0.02 upper and 0.05 lower surfaces.

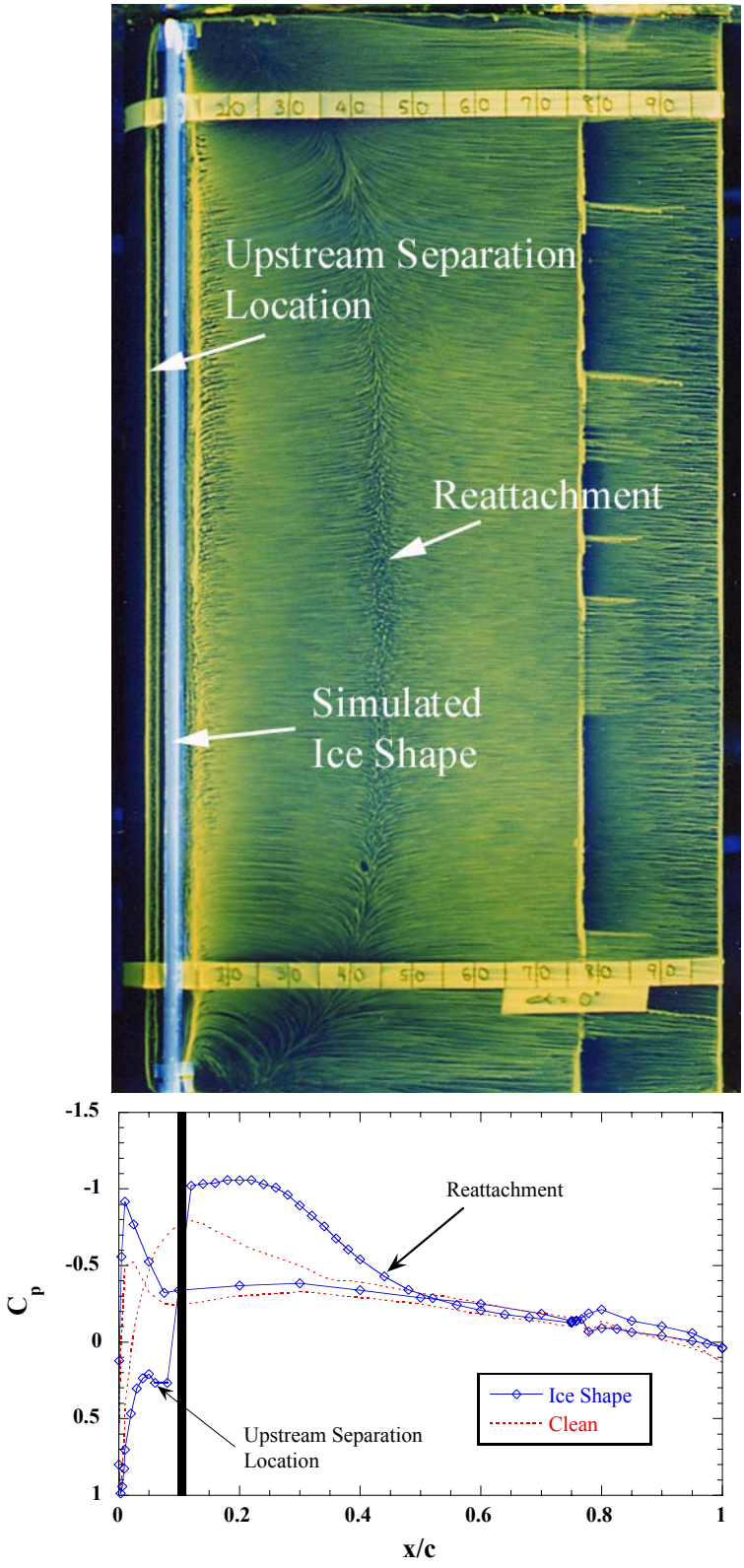

Fig. 4.25: Fluorescent oil flow visualization and surface pressure distribution. NACA 23012m; forward-facing quarter round. $\alpha = 0°$; boundary layer not tripped; *Re* = 1.8 million.

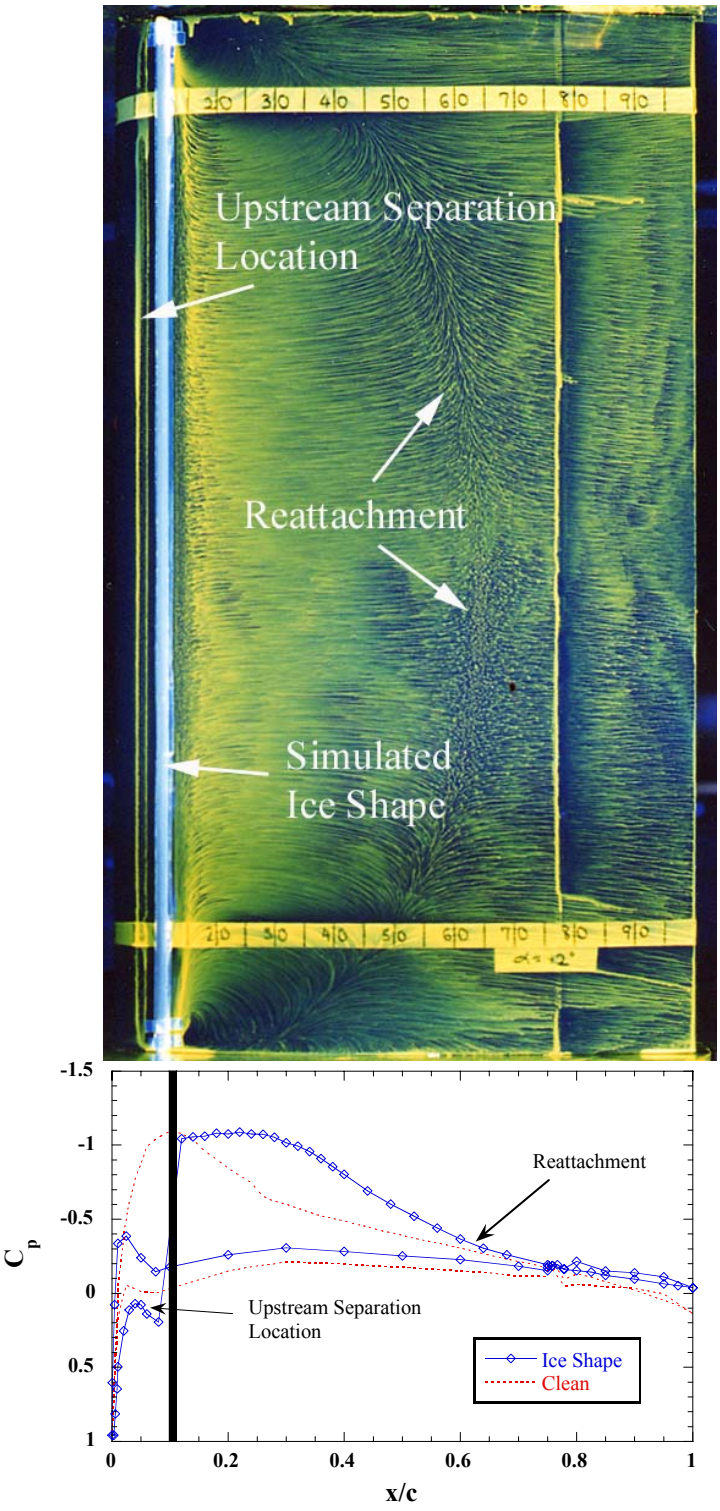

Fig. 4.26: Fluorescent oil flow visualization and surface pressure distribution. NACA 23012m; forward-facing quarter round. $\alpha = 2°$; boundary layer not tripped; *Re* = 1.8 million.

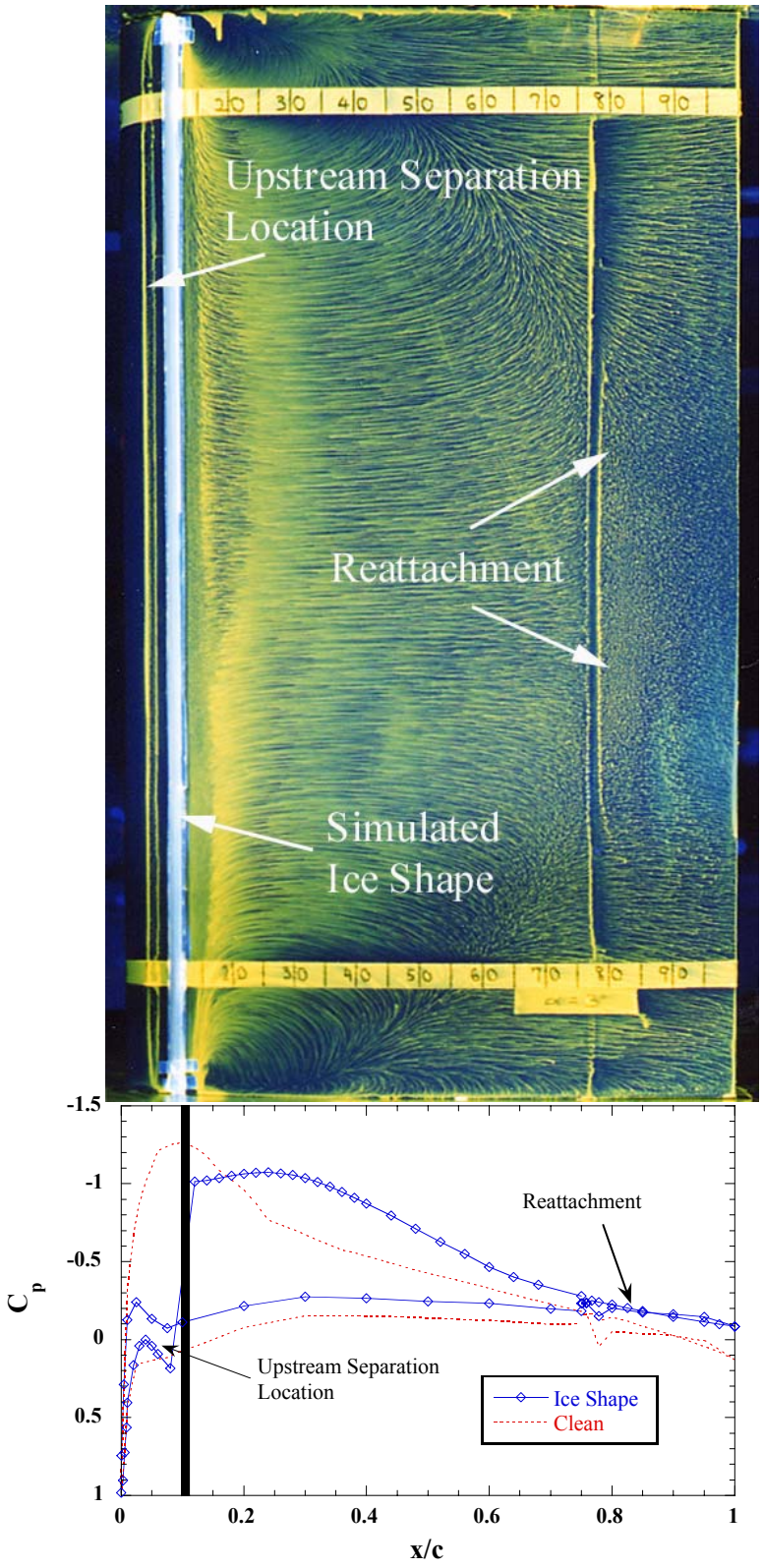

Fig. 4.27: Fluorescent oil flow visualization and surface pressure distribution. NACA 23012m; forward-facing quarter round. $\alpha = 3°$; boundary layer not tripped; Re = 1.8 million.

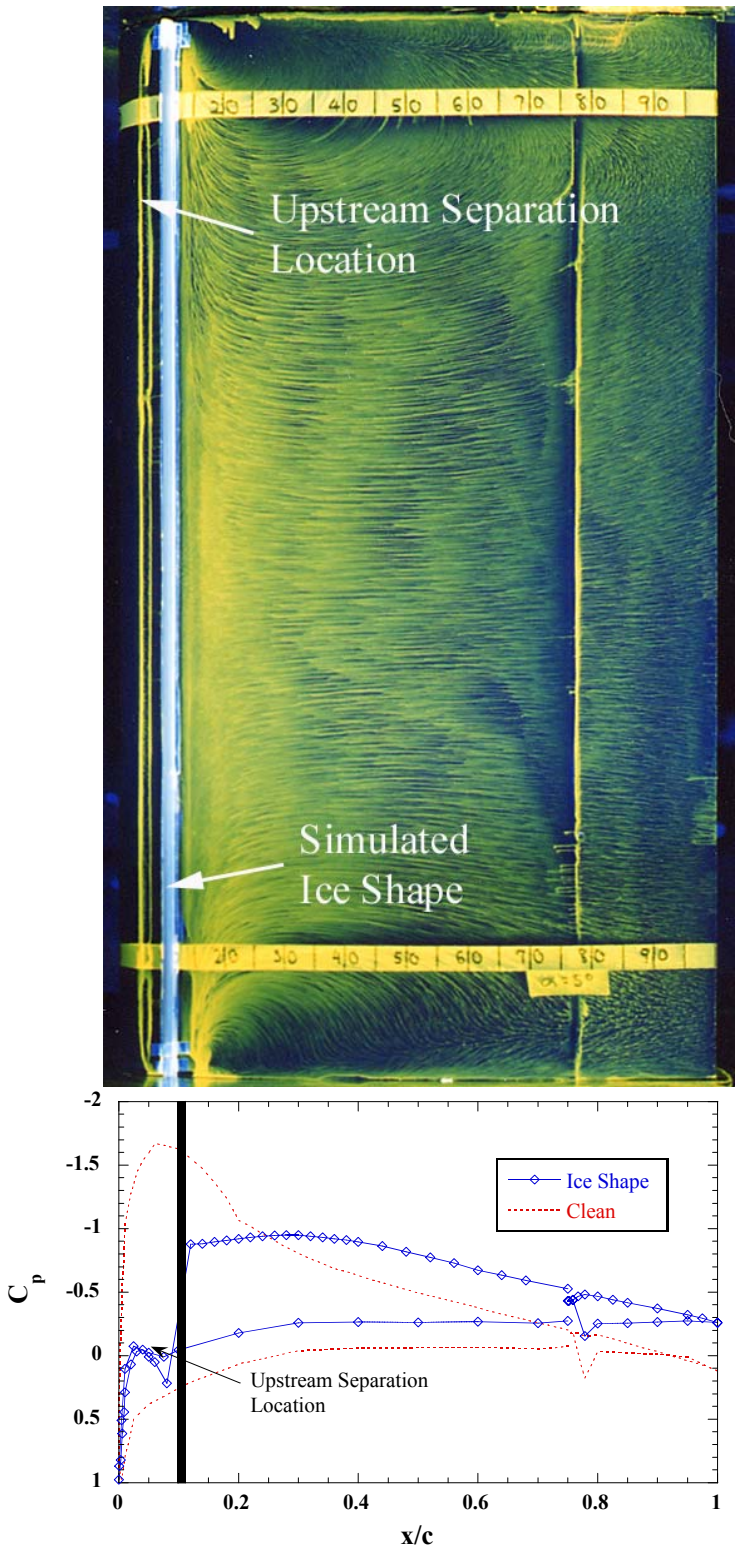

Fig. 4.28: Fluorescent oil flow visualization and surface pressure distribution. NACA 23012m; forward-facing quarter round. $\alpha = 5°$; boundary layer not tripped; *Re* = 1.8 million.

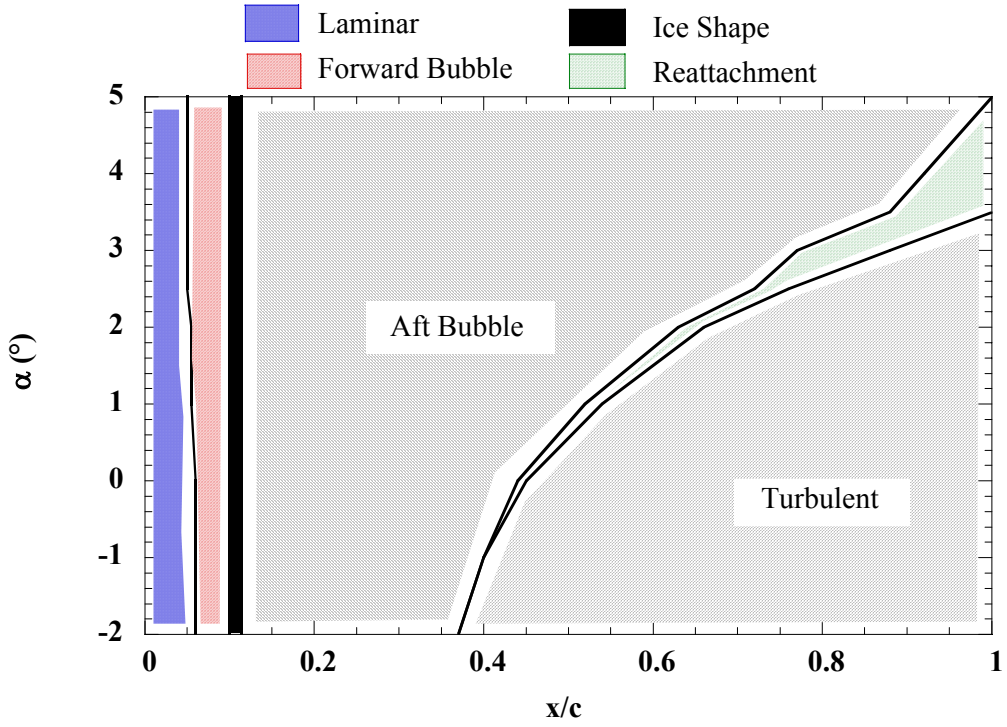

Fig. 4.29: Summary of boundary-layer state with the simulated ice at x/c = 0.10. NACA 23012m. Forward-facing quarter round. Boundary layer not tripped. Re = 1.8 million.

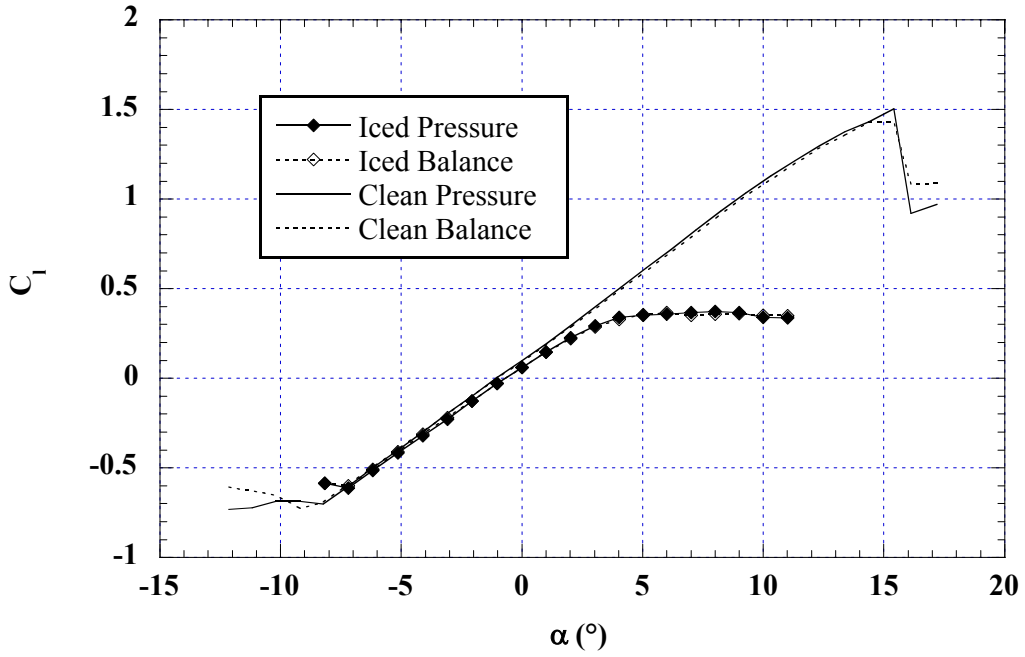

Fig. 4.30a) Lift

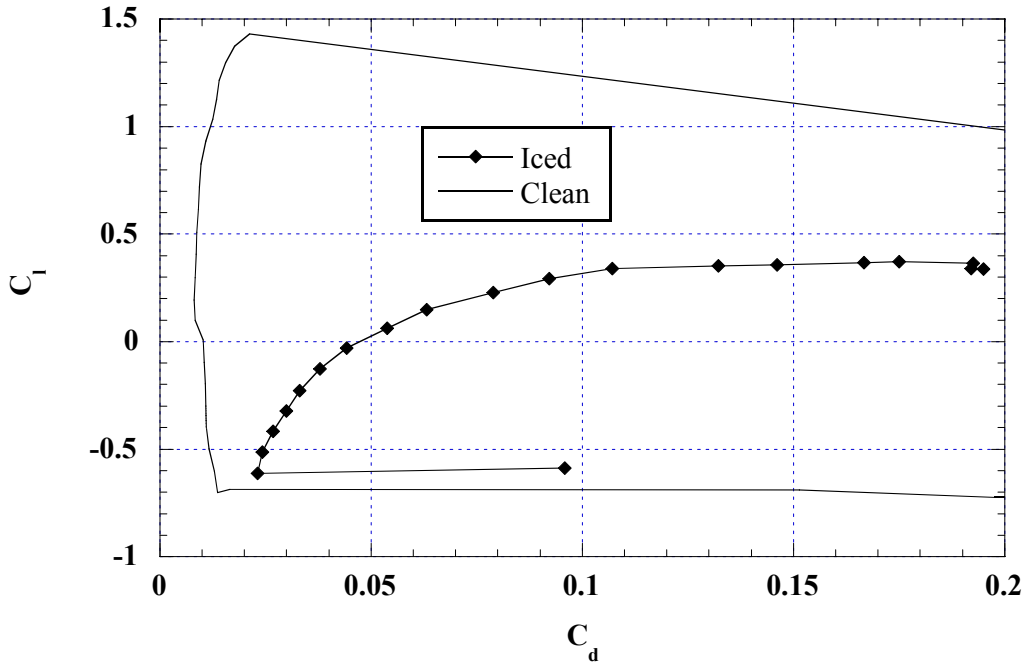

Fig. 4.30b) Drag

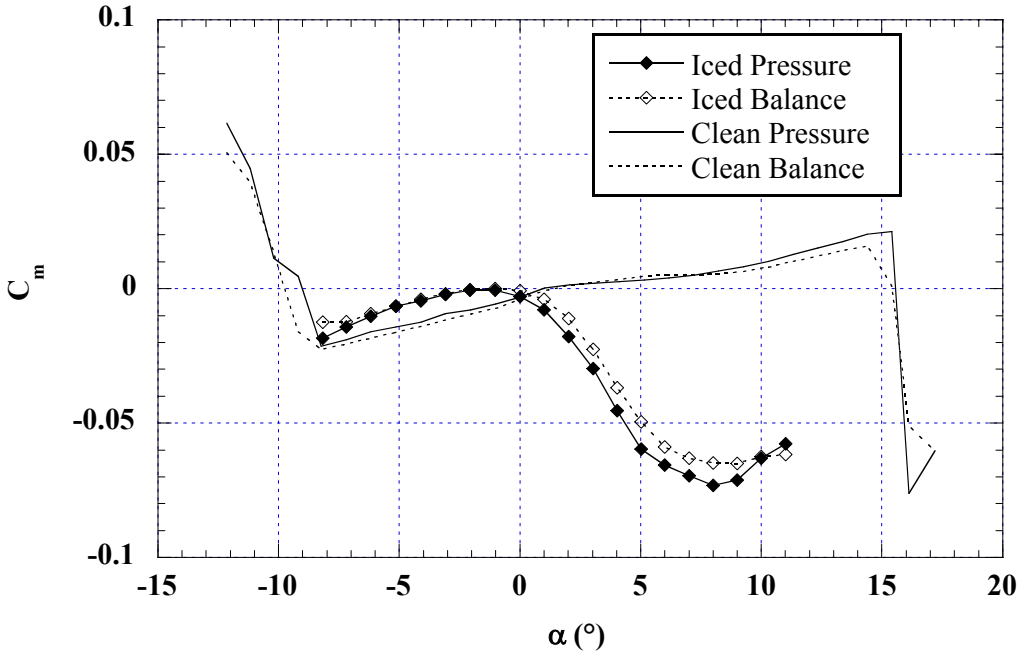

Fig. 4.30c) Pitching Moment

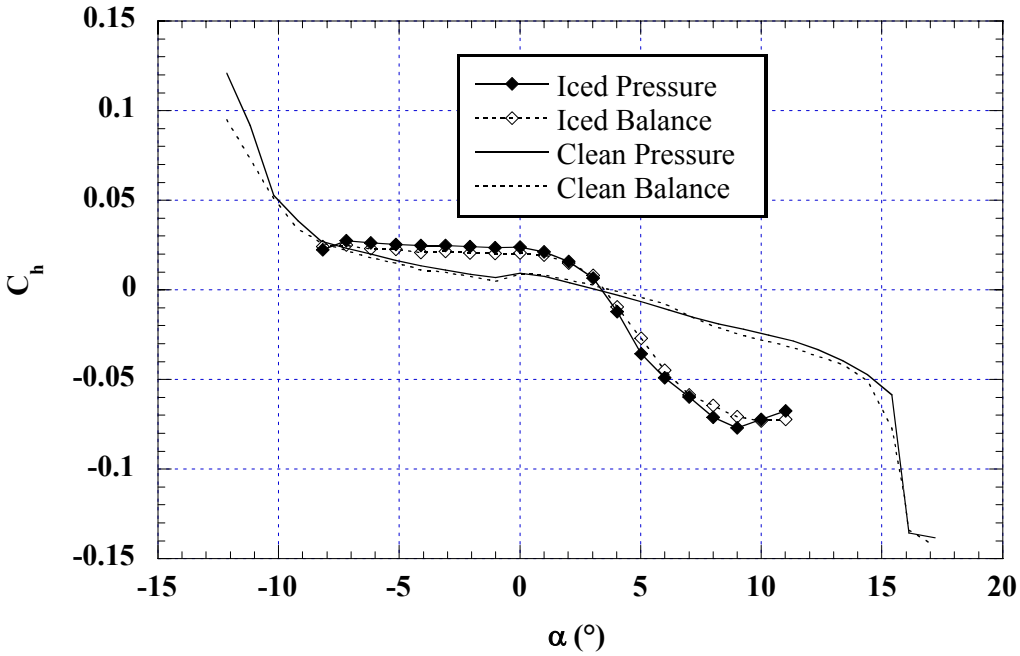

Fig. 4.30d) Flap-hinge moment

Fig. 4.30: Aerodynamic coefficients with k = 0.25" forward-facing quarter round at x/c = 0.10; NACA 23012m; boundary layer not tripped. Re = 1.8 million.

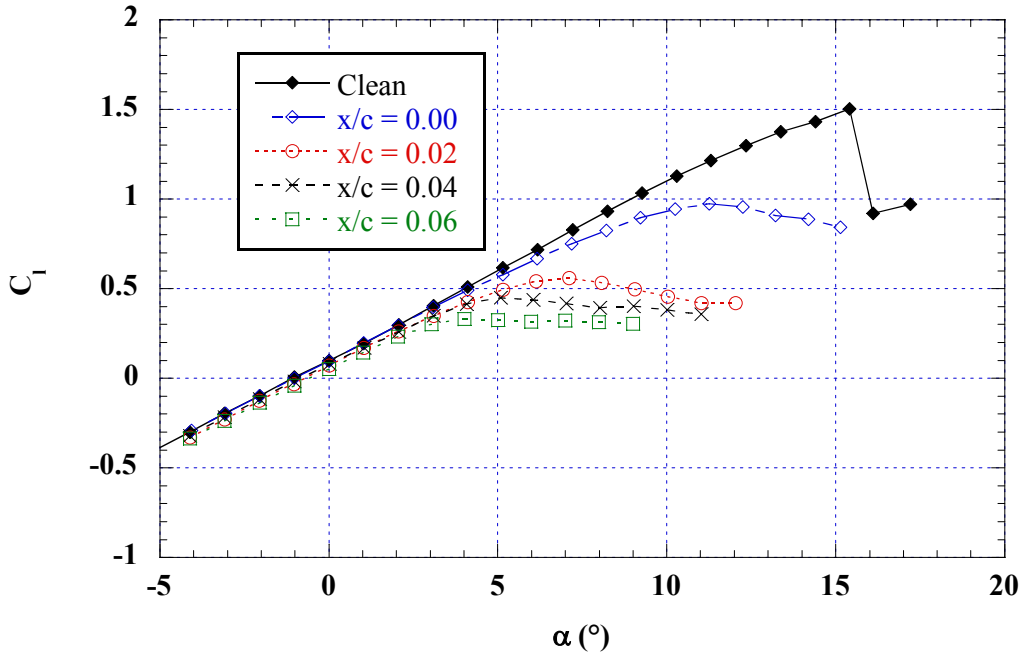

Fig. 4.31a) x/c = 0.00 to 0.06

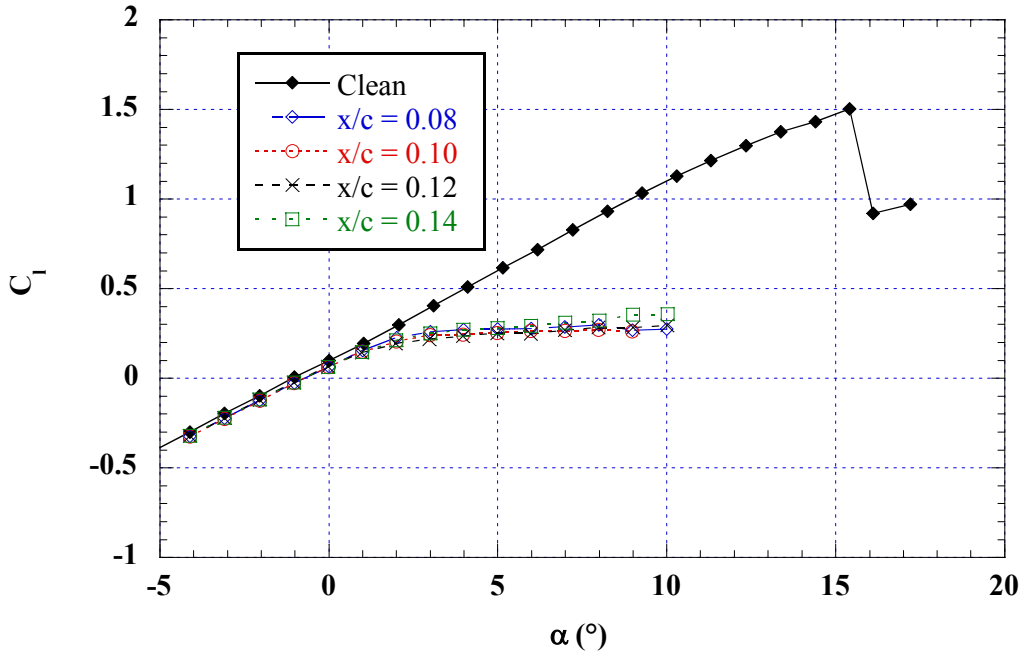

Fig. 4.31b) x/c = 0.08 to 0.14

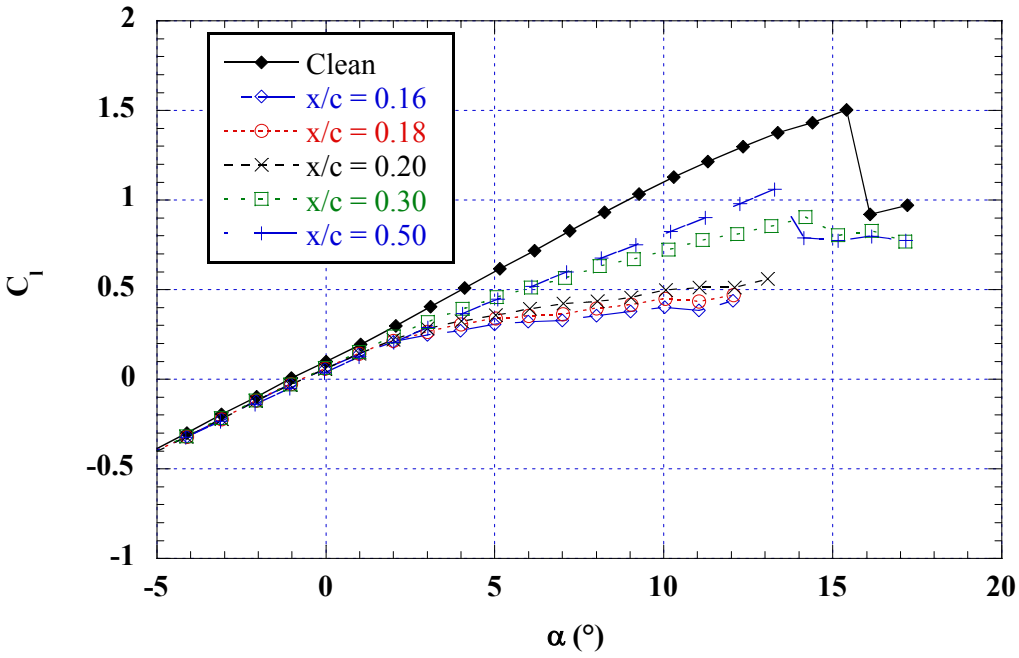

Fig. 4.31c) x/c = 0.16 to 0.50

Fig. 4.31: Effect of simulated ice ridge location on lift; NACA 23012m; forward-facing quarter round; k = 0.25"; α = 5°; Re = 1.8 million; boundary layer tripped (except for x/c = 0.00 and 0.02 cases).

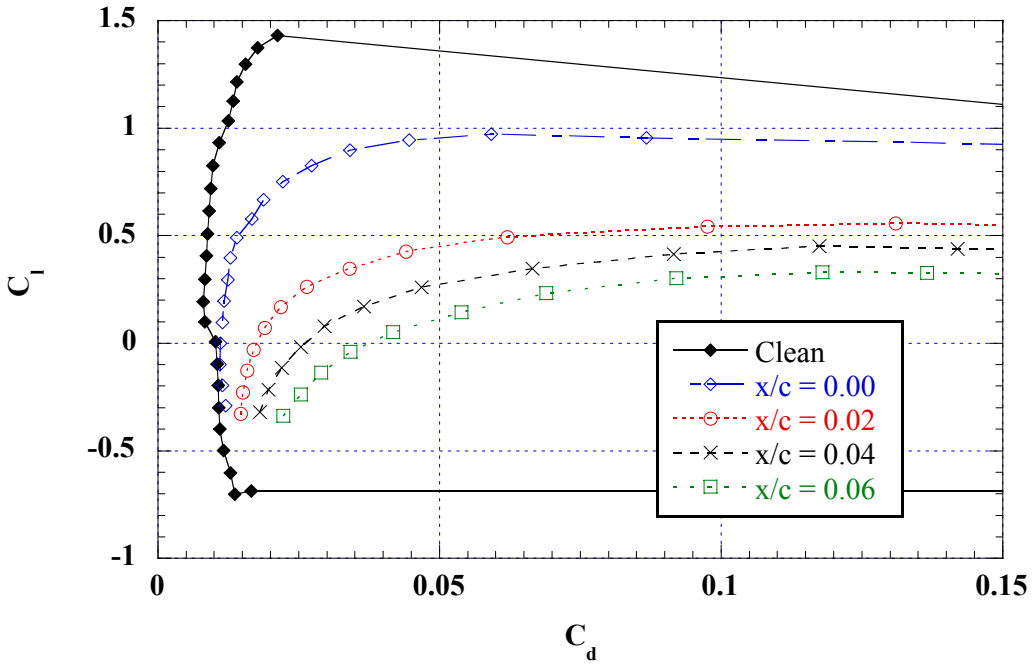

Fig. 4.32a) x/c = 0.00 to 0.06

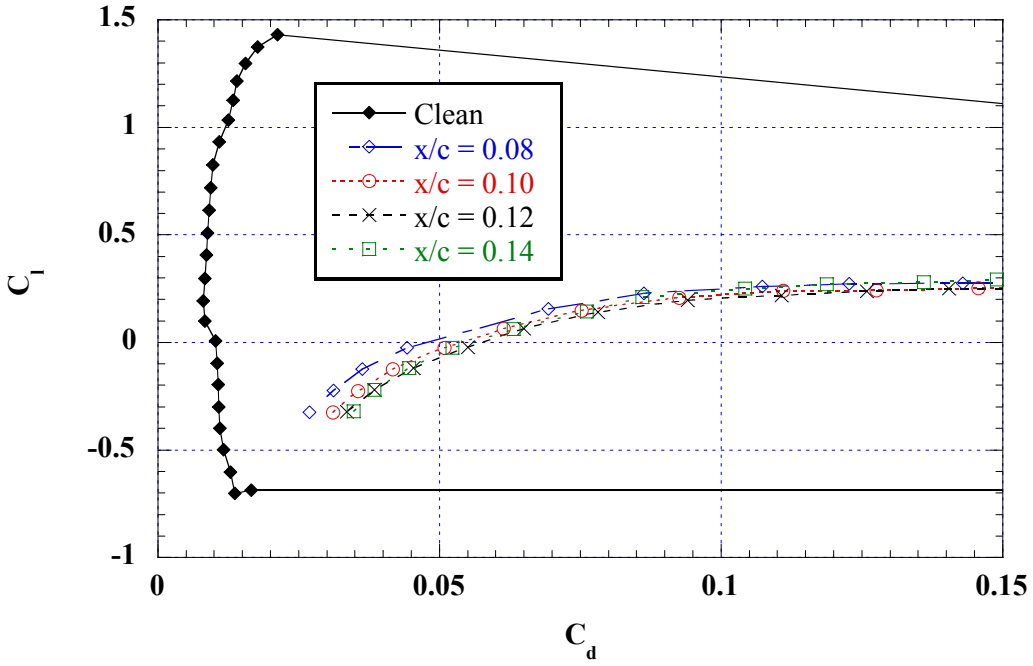

Fig. 4.32b) x/c = 0.08 to 0.14

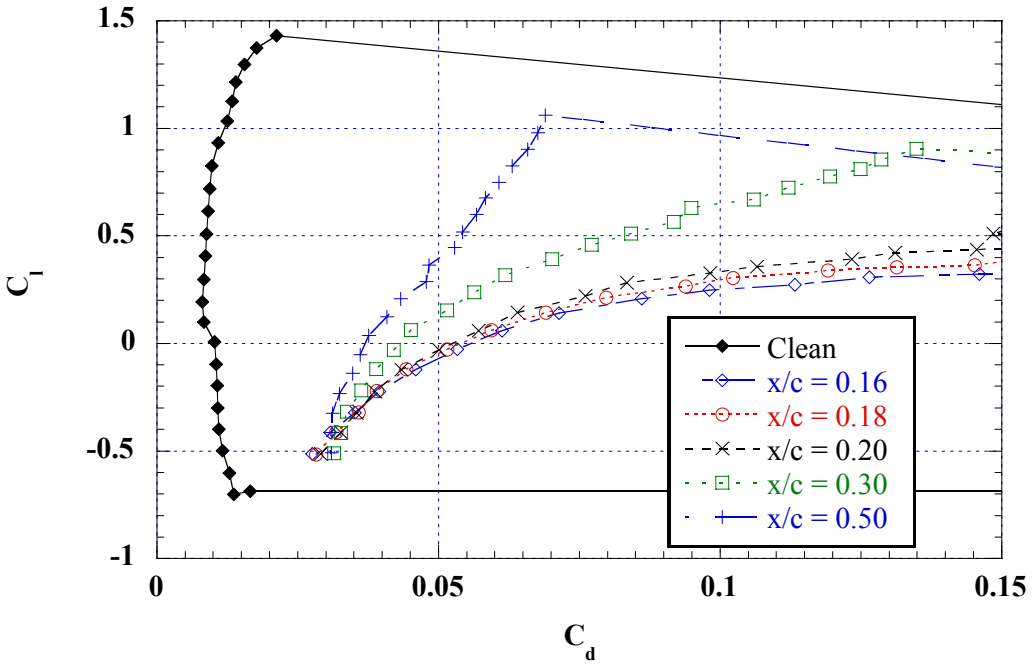

Fig. 4.32c) x/c = 0.16 to 0.50

Fig. 4.32: Effect of simulated ice ridge location on drag; NACA 23012m; forward-facing quarter round; k = 0.25"; α = 5°; boundary layer tripped (except for x/c = 0.00 and 0.02 cases); Re = 1.8 million.

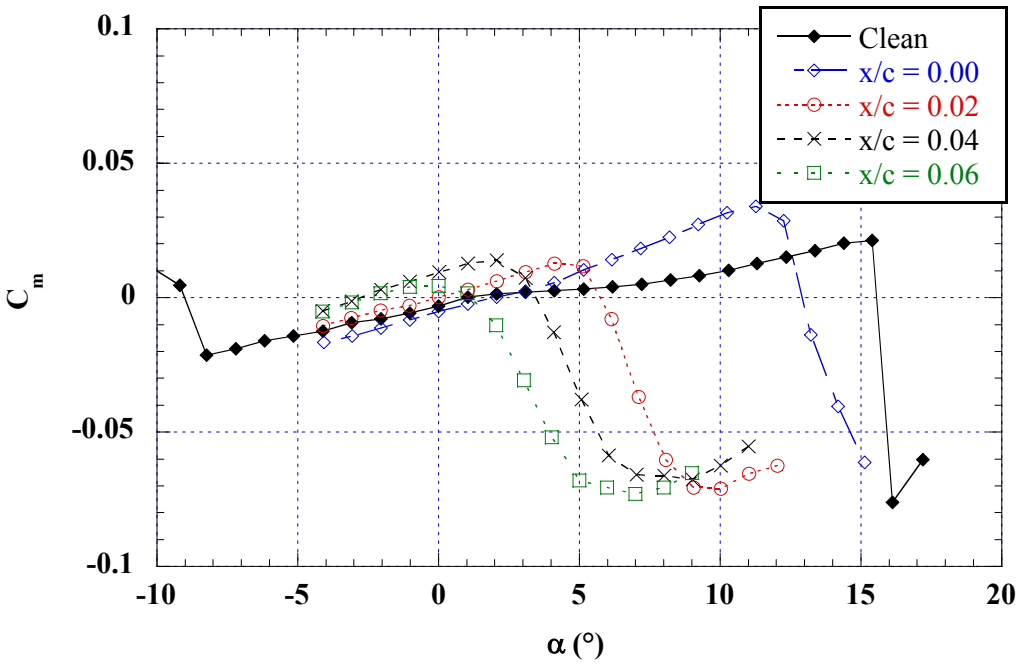

Fig. 4.33a) x/c = 0.00 to 0.06

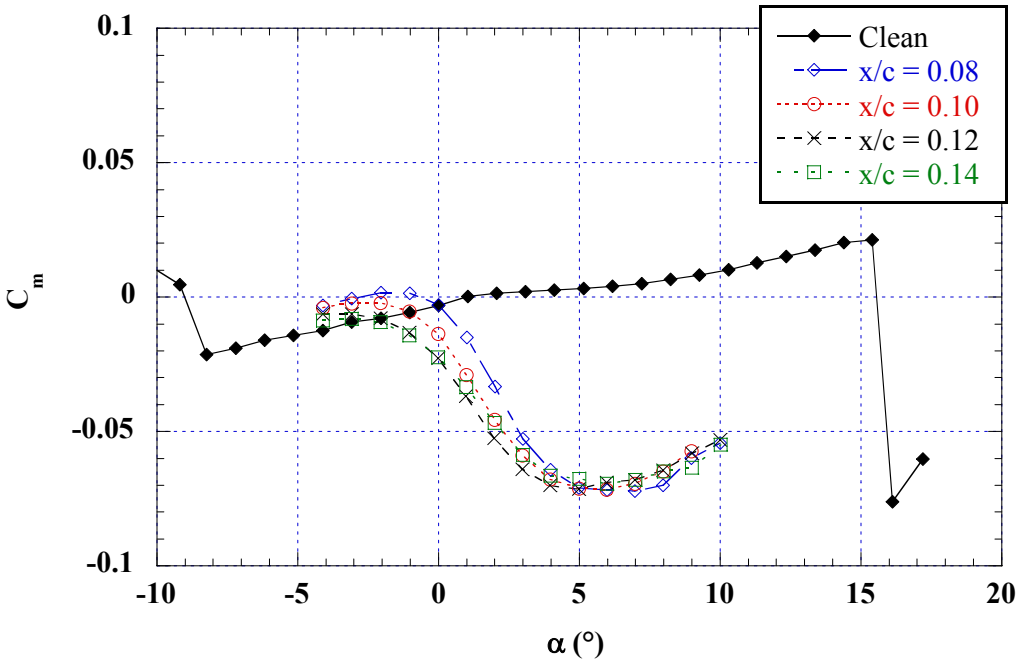

Fig. 4.33b) x/c = 0.08 to 0.14

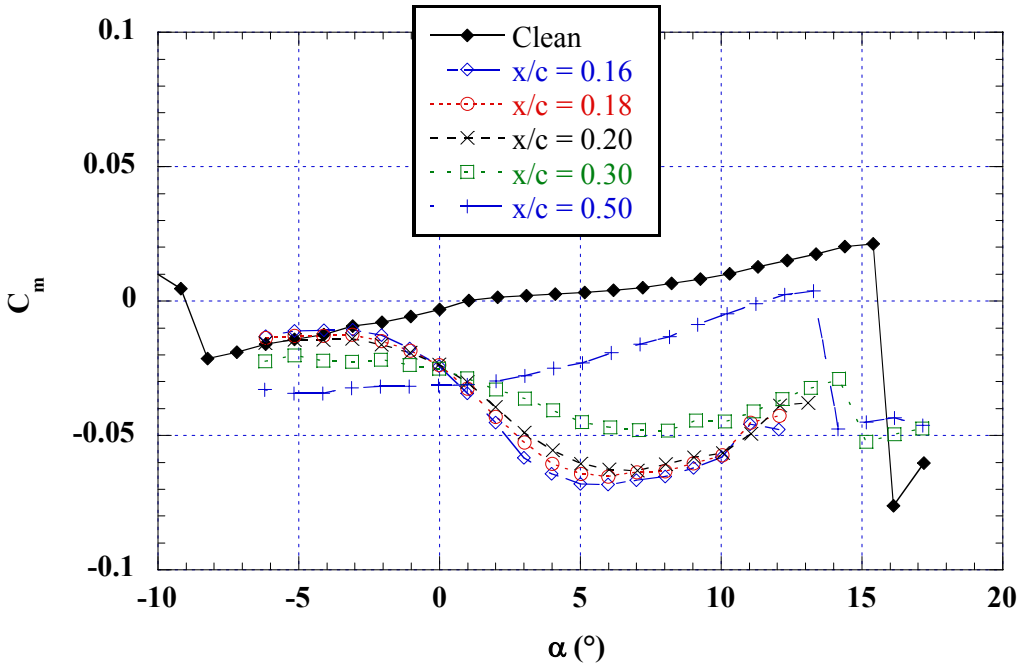

Fig. 4.33c) x/c = 0.16 to 0.50

Fig. 4.33: Effect of simulated ice ridge location on pitching moment; NACA 23012m; forward-facing quarter round; k = 0.25"; α = 5°; boundary layer tripped (except for x/c = 0.00 and 0.02 cases); Re = 1.8 million.

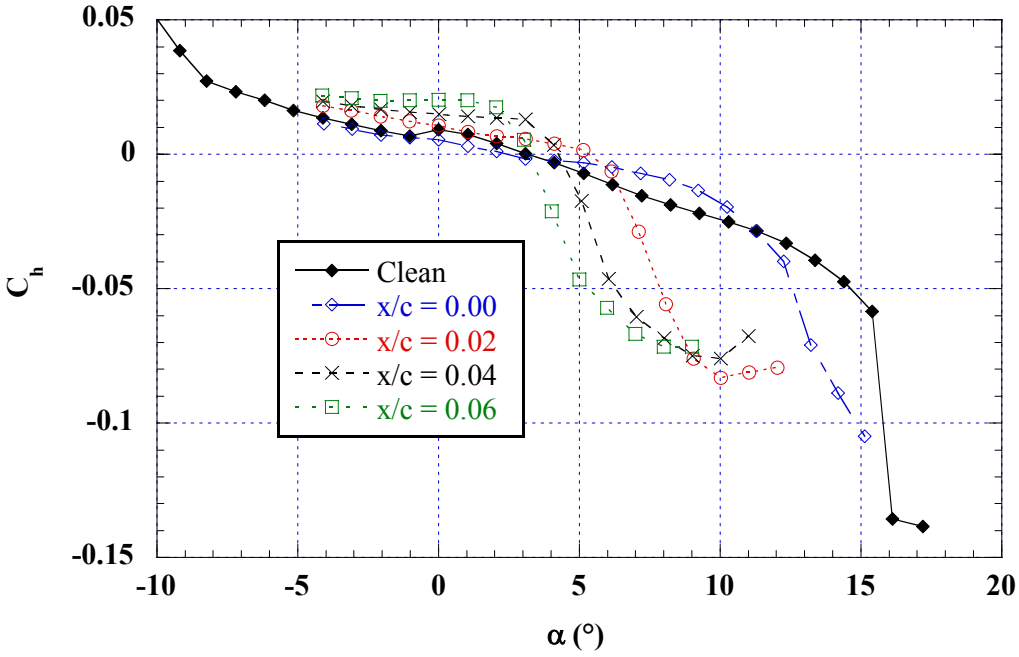

Fig. 4.34a) x/c = 0.00 to 0.06

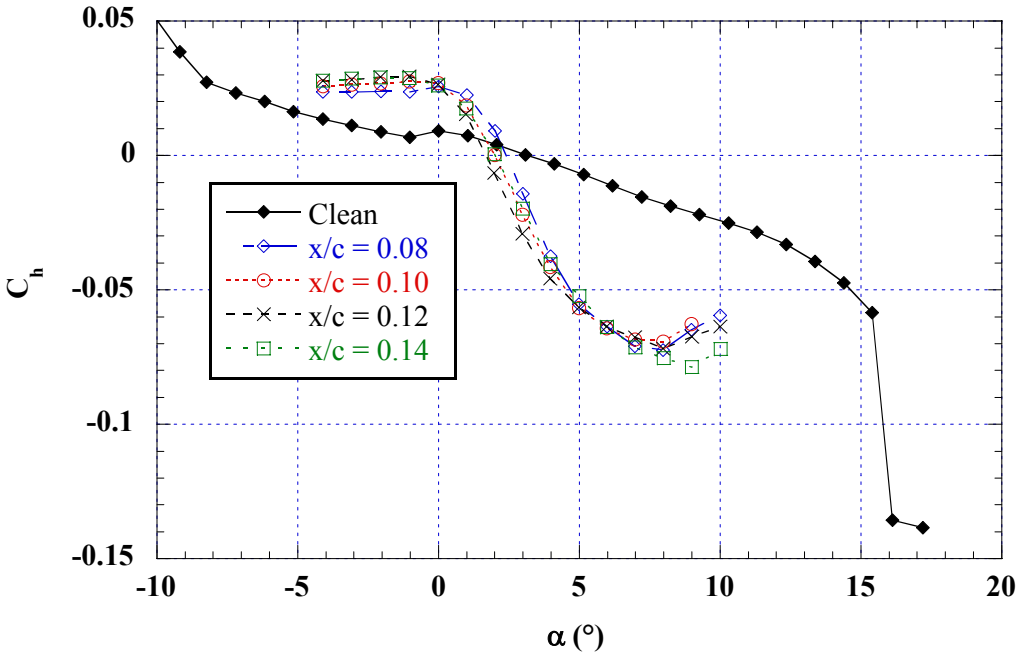

Fig. 4.34b) x/c = 0.08 to 0.14

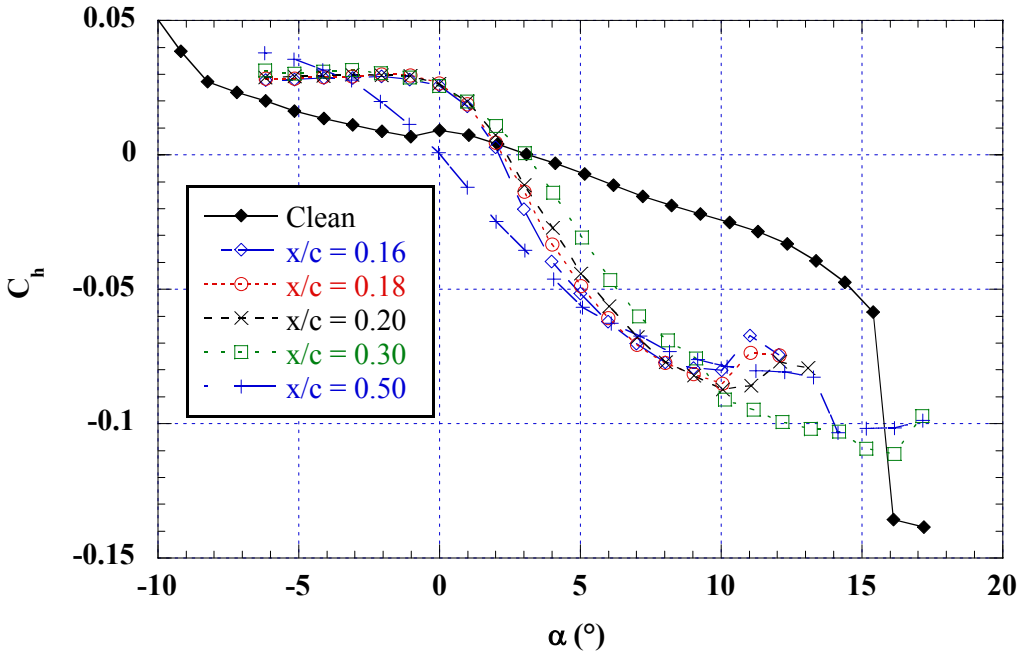

Fig. 4.34c) x/c = 0.16 to 0.50

Fig. 4.34: Effect of simulated ice ridge location on flap hinge moment; NACA 23012m; forward-facing quarter round; k = 0.25"; α = 5°; boundary layer tripped (except for x/c = 0.00 and 0.02 cases); Re = 1.8 million.

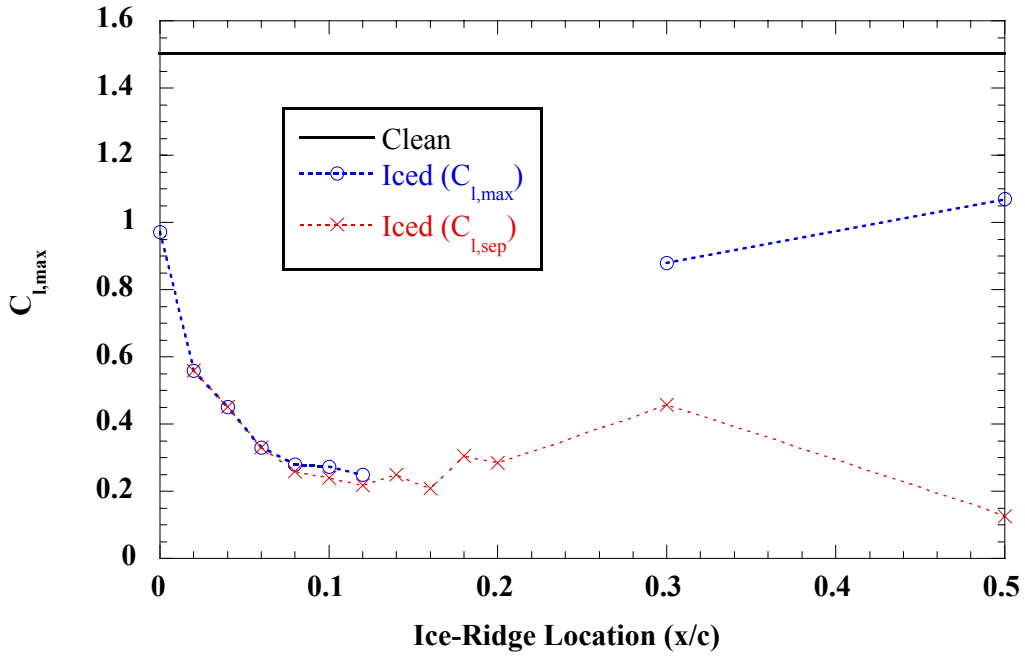

Fig. 4.35: Effect of simulated ice ridge location on maximum lift; NACA 23012m; forward-facing quarter round; k = 0.25”; boundary layer tripped (except for x/c = 0.00 and 0.02 cases); Re = 1.8 million.

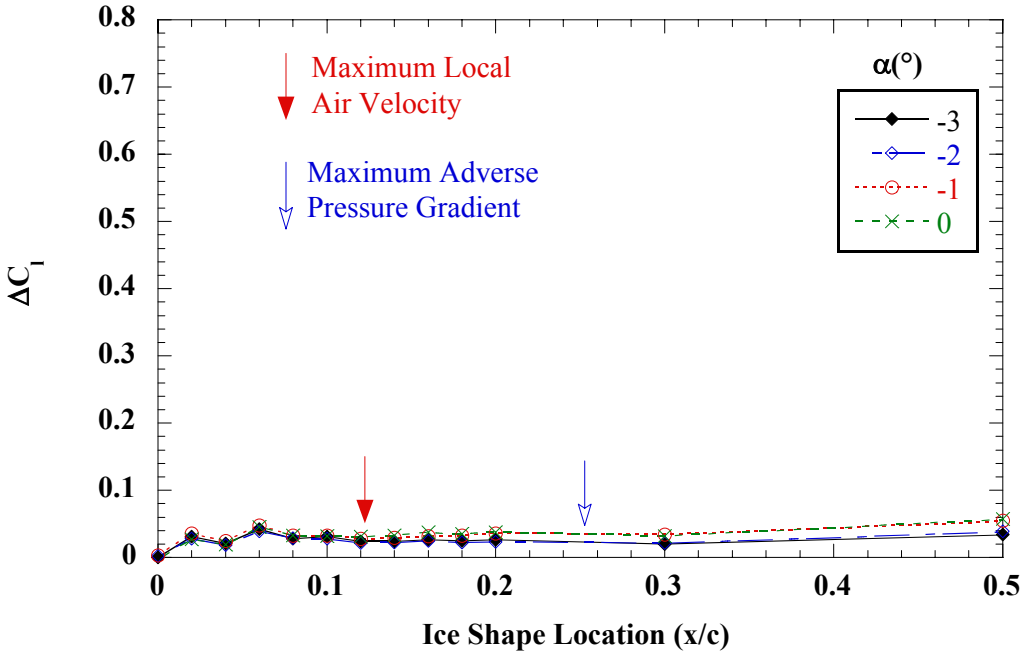

Fig. 4.36a) α = -3° to 0°

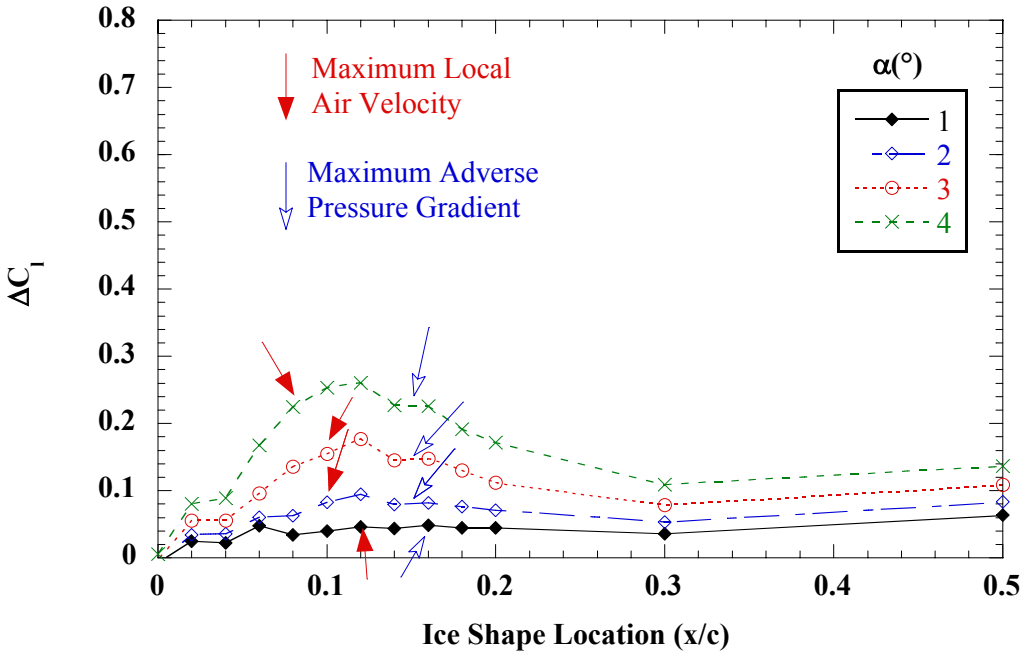

Fig. 4.36b) α = 1° to 4°

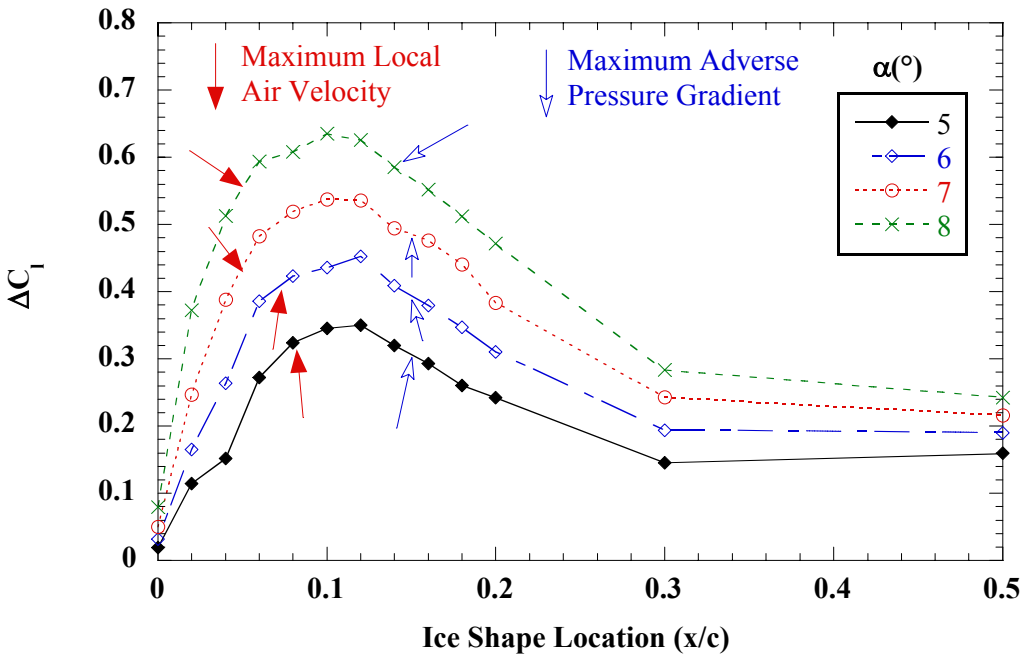

Fig. 4.36c) $\alpha = 5°$ to 8°

Fig. 4.36: Effect of simulated ice ridge location on lift loss; NACA 23012m; forward-facing quarter round; k = 0.25"; boundary layer tripped (except for x/c = 0.00 and 0.02 cases); Re = 1.8 million.

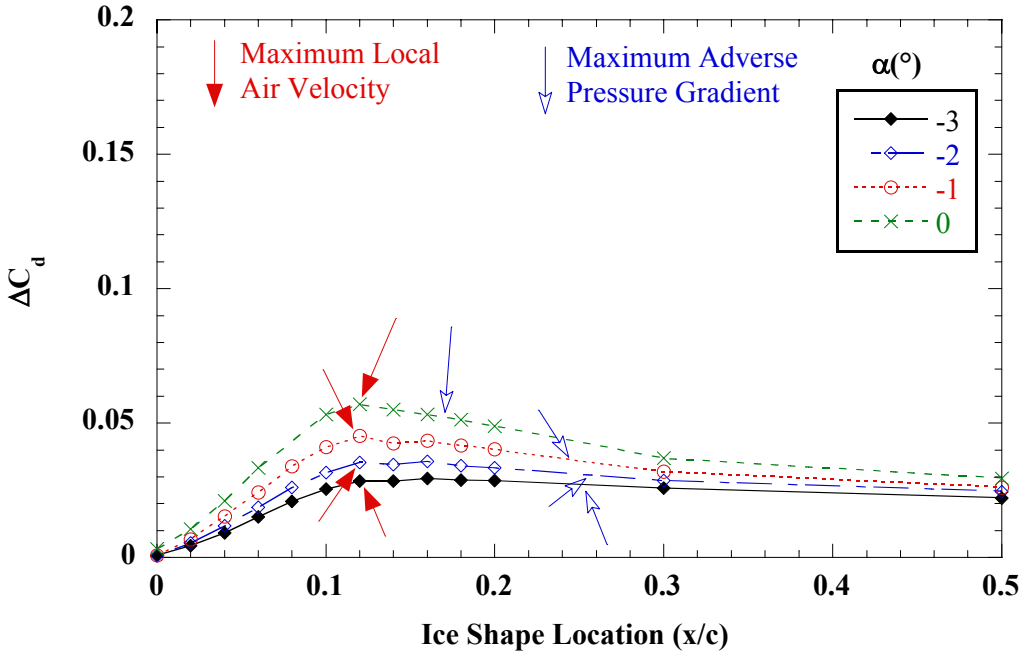

Fig. 4.37a) α = -3° to 0°

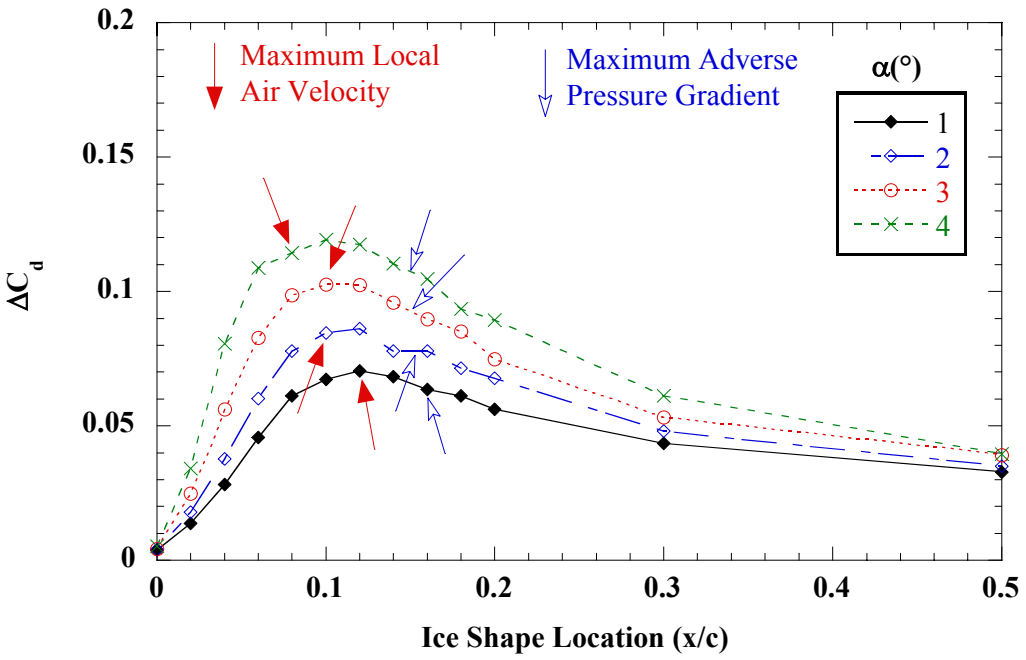

Fig. 4.37b) α = 1° to 4°

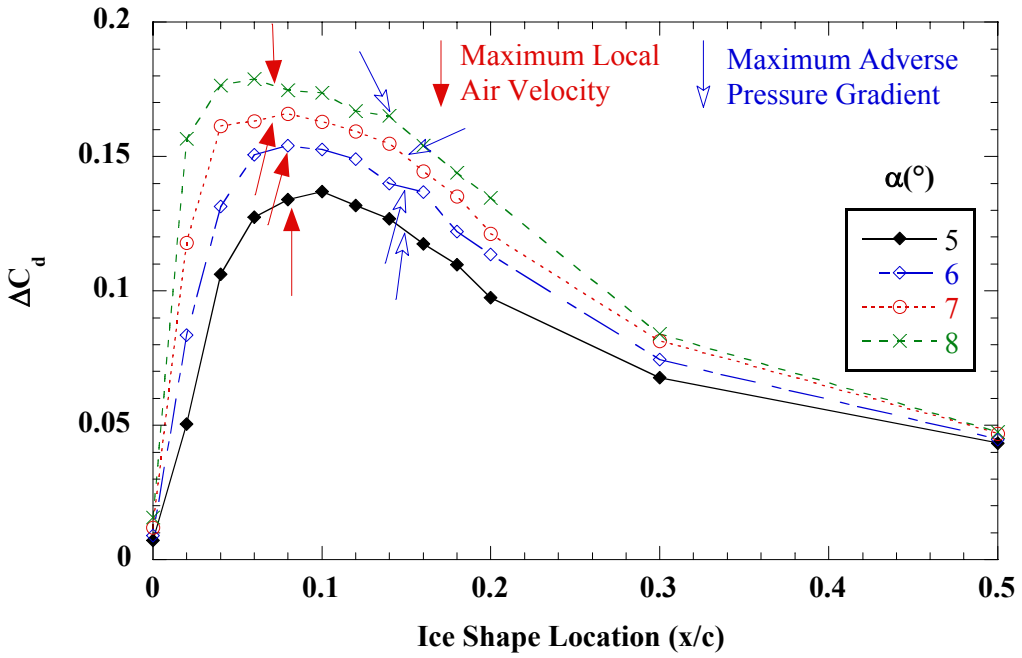

Fig. 4.37c) $\alpha = 5°$ to $8°$

Fig. 4.37: Effect of simulated ice ridge location on drag increase; NACA 23012m; forward-facing quarter round; k = 0.25"; boundary layer tripped (except for x/c = 0.00 and 0.02 cases); Re = 1.8 million.

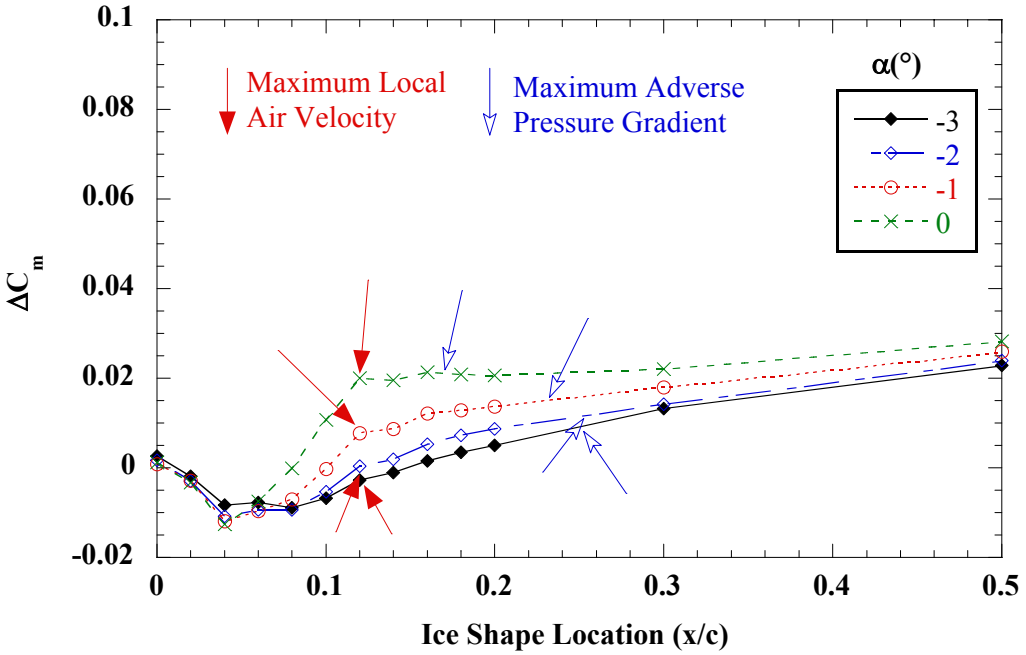

Fig. 4.38a) α = -3° to 0°

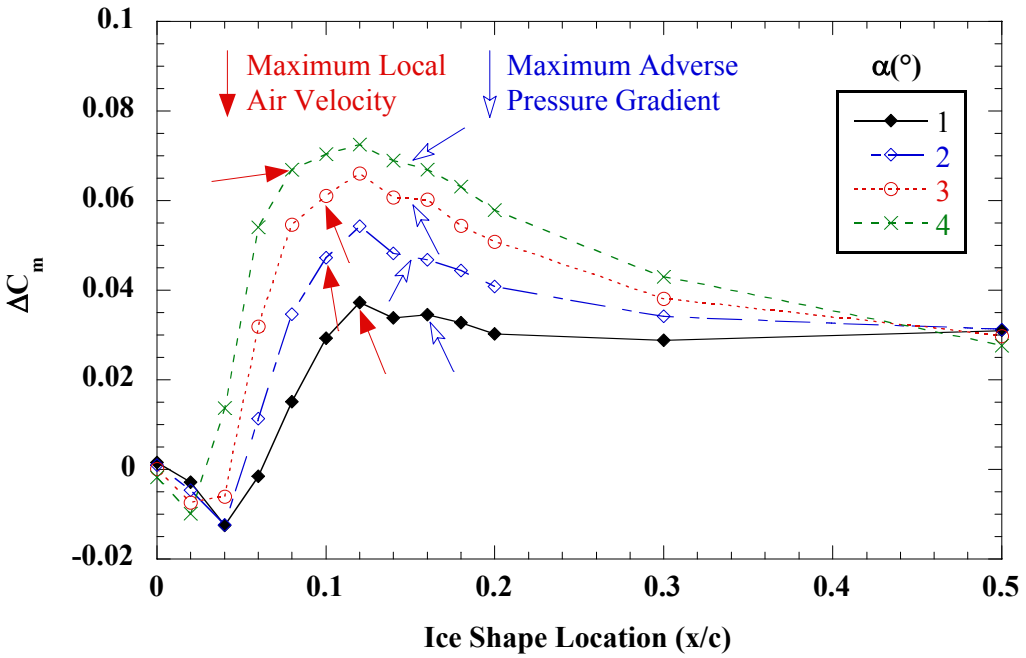

Fig. 4.38b) α = 1° to 4°

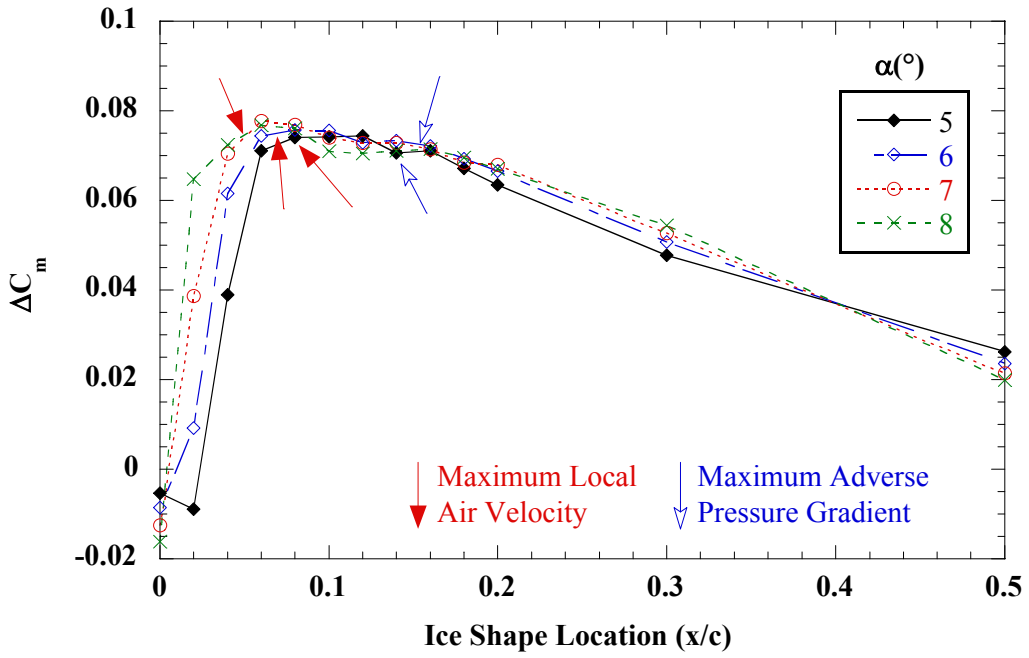

Fig. 4.38c) $\alpha = 5°$ to $8°$

Fig. 4.38: Effect of simulated ice ridge location on pitching moment change; NACA 23012m; forward-facing quarter round; k = 0.25"; boundary layer tripped (except for x/c = 0.00 and 0.02 cases); Re = 1.8 million.

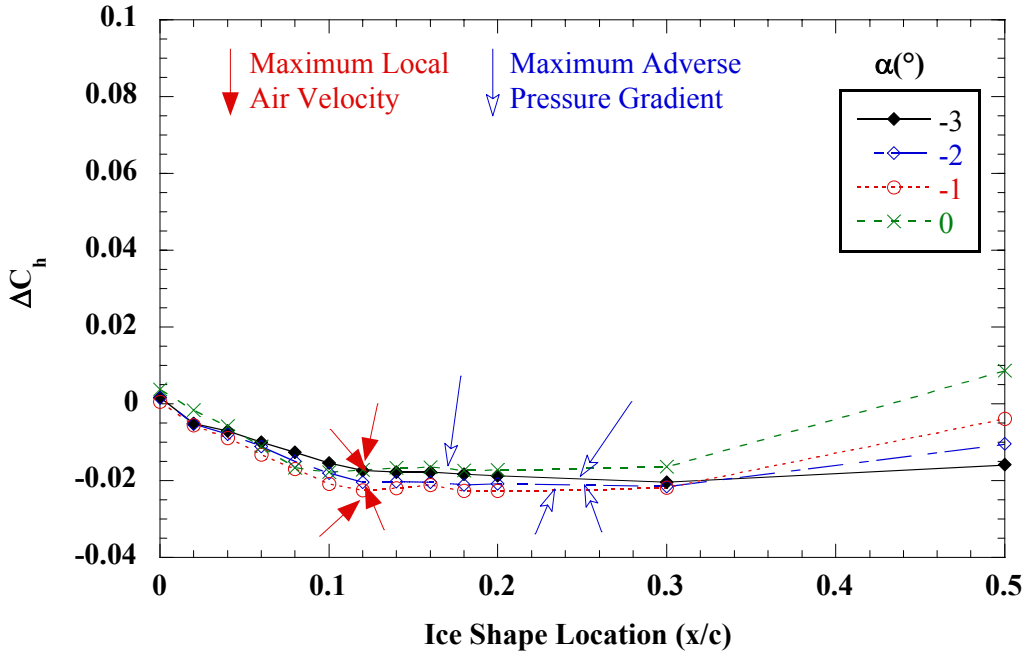

Fig. 4.39a) α = -3° to 0°

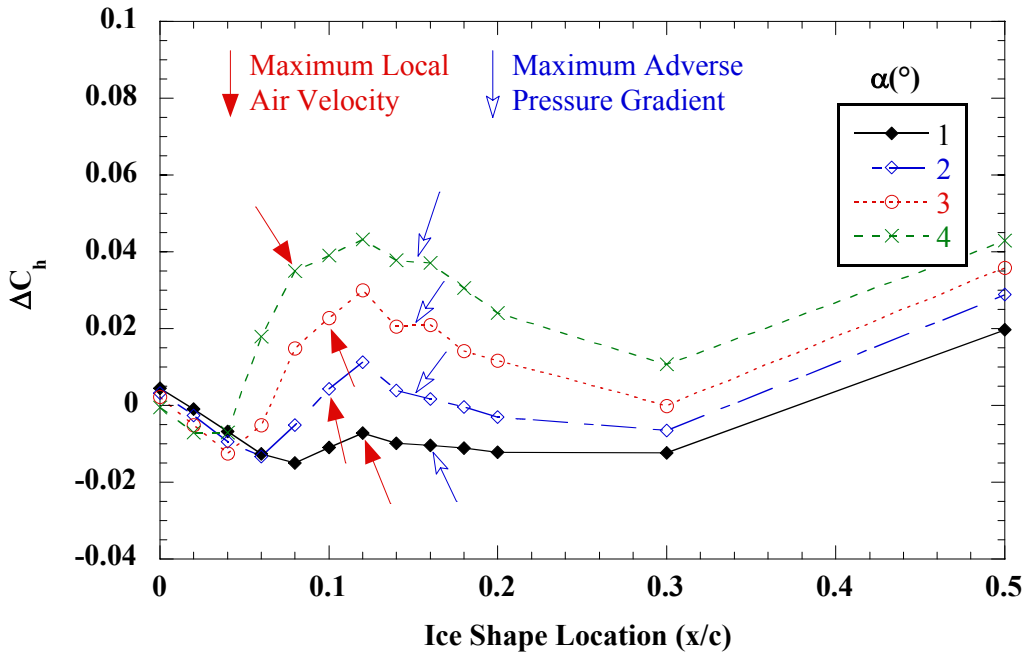

Fig. 4.39b) α = 1° to 4°

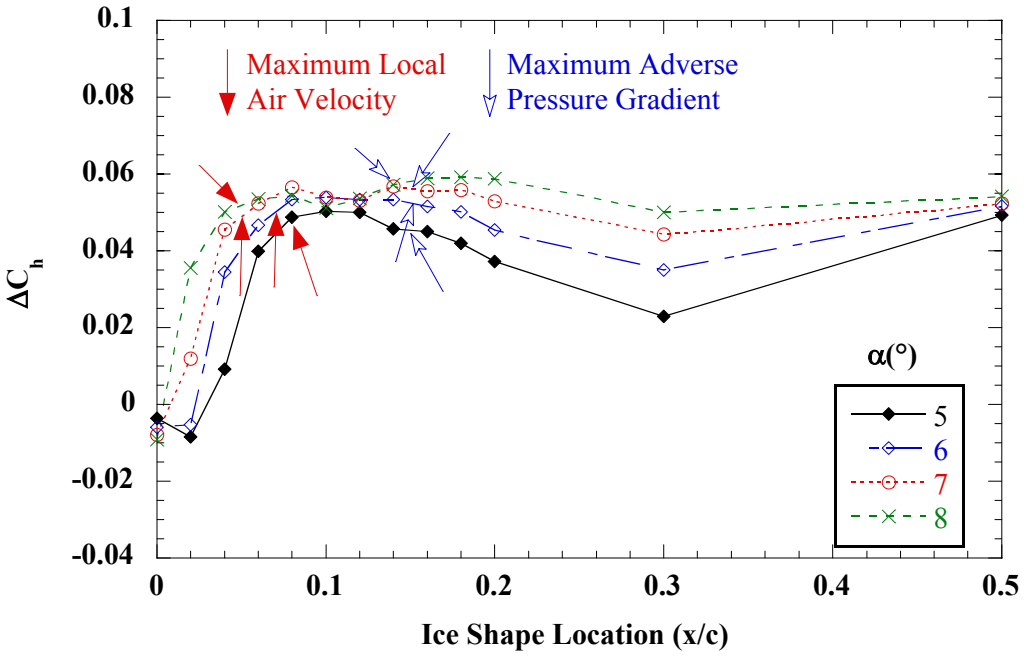

Fig. 4.39c) $\alpha = 5°$ to 8°

Fig. 4.39: Effect of simulated ice ridge location on flap hinge moment change; NACA 23012m; forward-facing quarter round; k = 0.25"; boundary layer tripped (except for x/c = 0.00 and 0.02 cases); Re = 1.8 million.

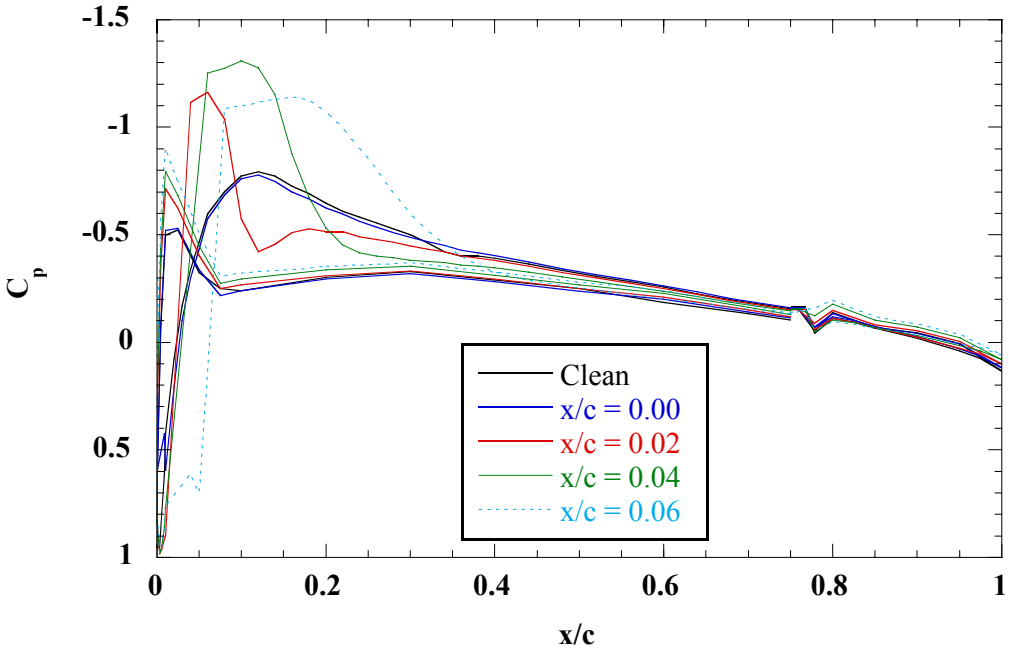

Fig. 4.40a) x/c = 0.00 to 0.06

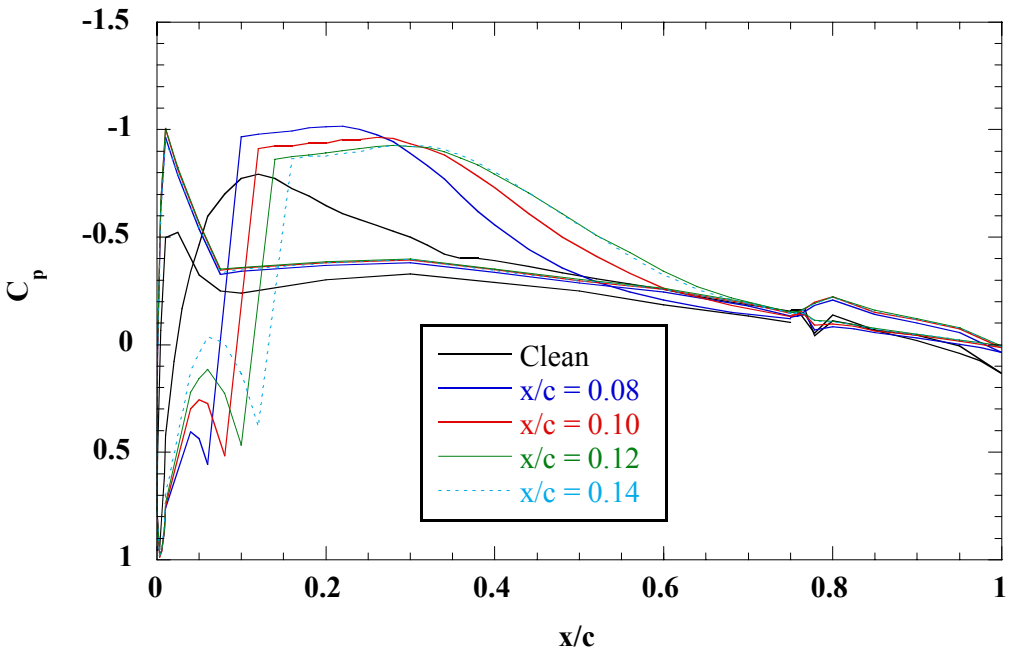

Fig. 4.40b) x/c = 0.08 to 0.14

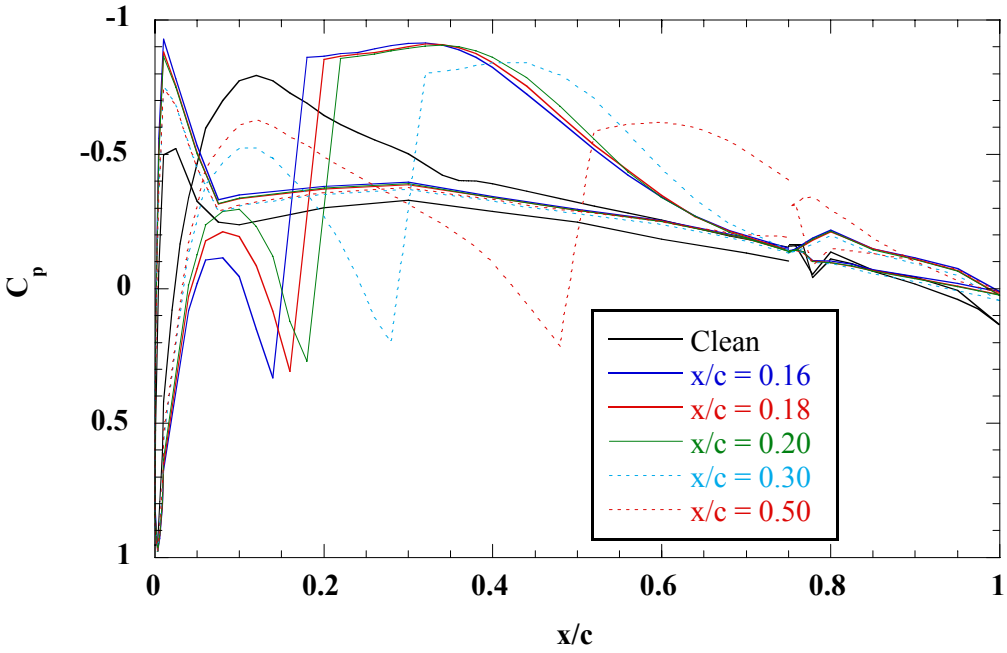

Fig. 4.40c) x/c = 0.16 to 0.50

Fig. 4.40: Effect of simulated ice ridge location on flap hinge moment change; NACA 23012m; forward-facing quarter round; α = 0°; k = 0.25"; boundary layer tripped (except for x/c = 0.00 and 0.02 cases); Re = 1.8 million.

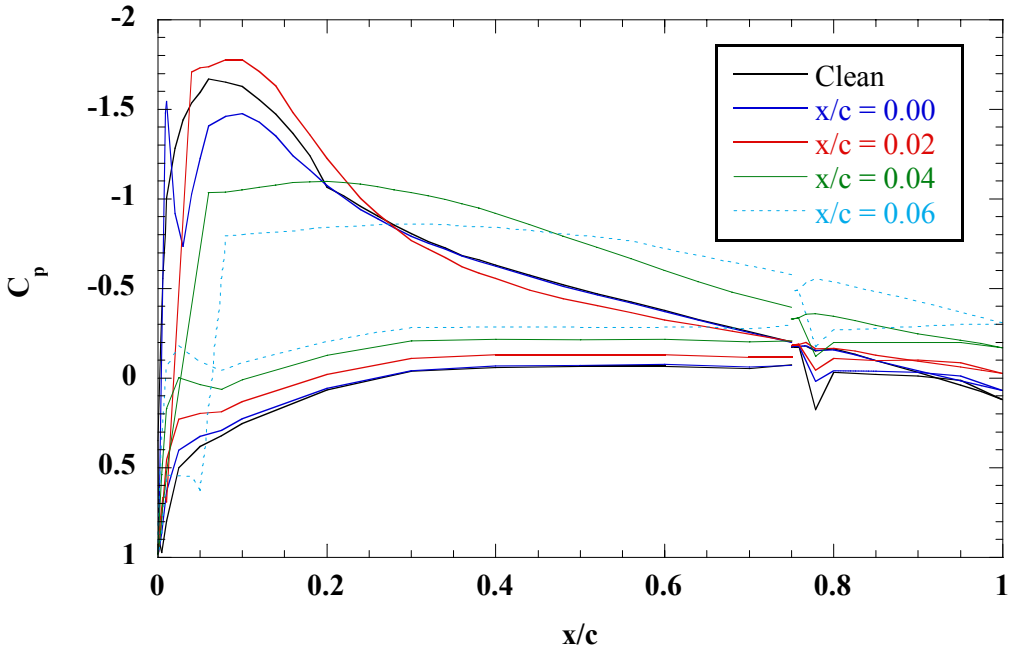

Fig. 4.41a) x/c = 0.00 to 0.06

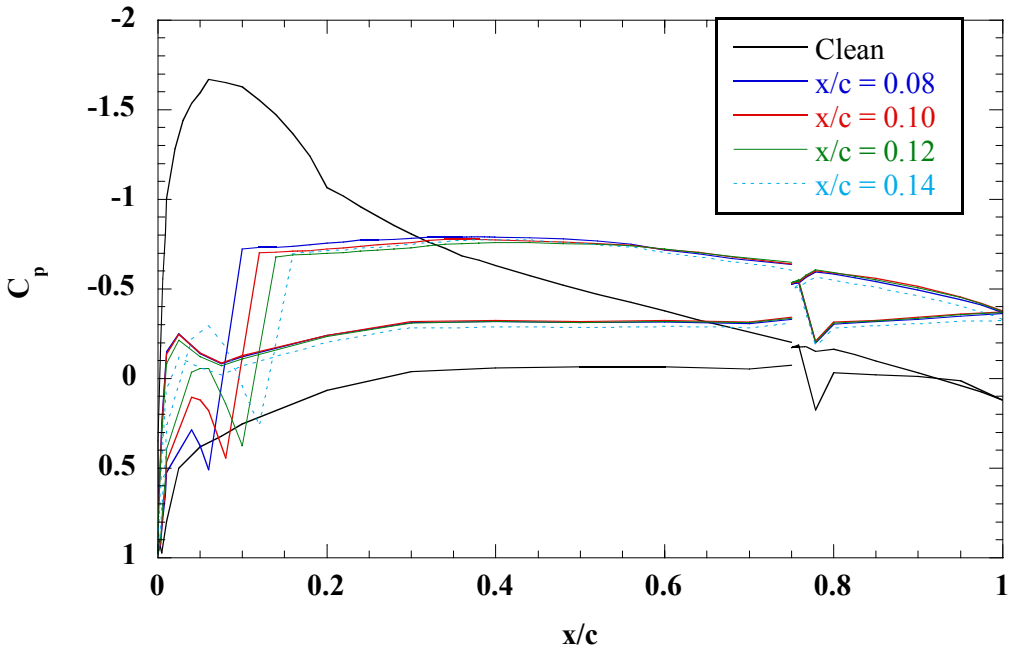

Fig. 4.41b) x/c = 0.08 to 0.14

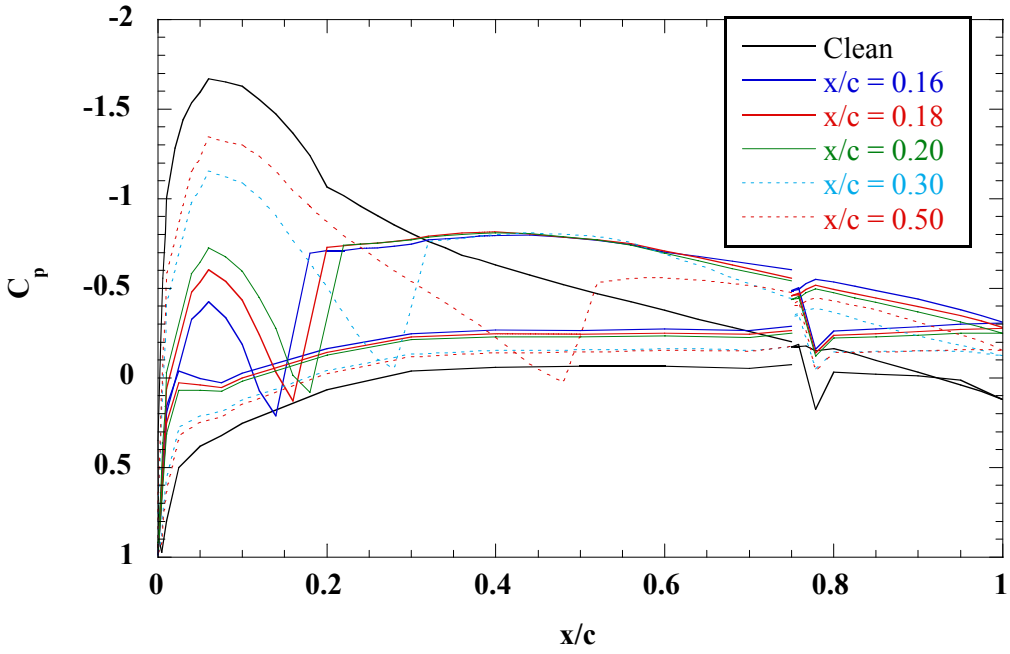

Fig. 4.41c) x/c = 0.16 to 0.50

Fig. 4.41: Effect of simulated ice ridge location on flap hinge moment change; NACA 23012m; forward-facing quarter round; α = 5°; k = 0.25"; boundary layer tripped (except for x/c = 0.00 and 0.02 cases); Re = 1.8 million.

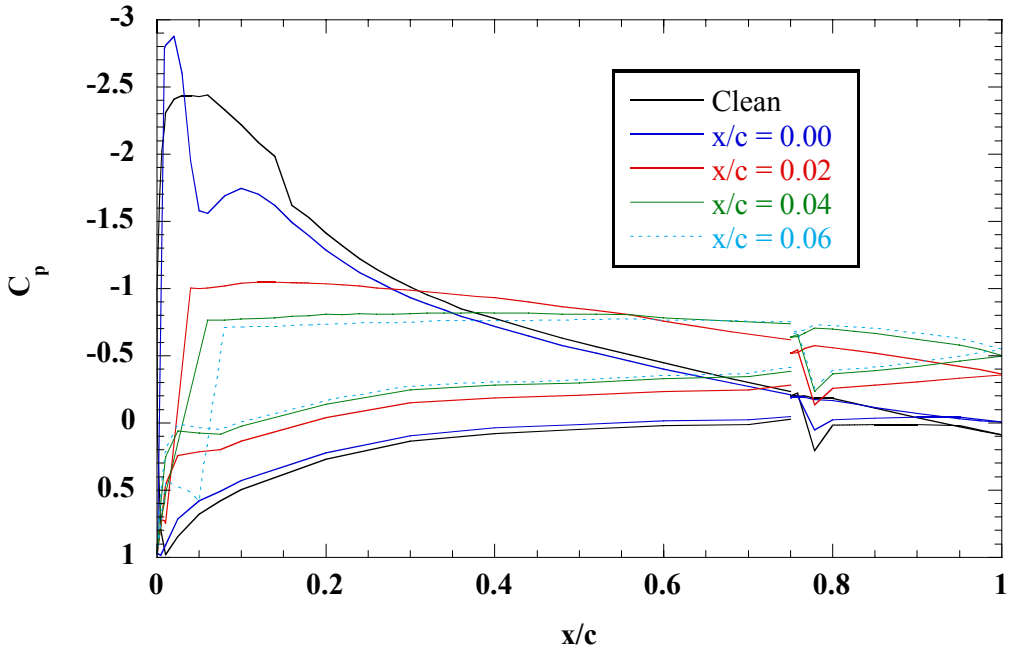

Fig. 4.42a) x/c = 0.00 to 0.06

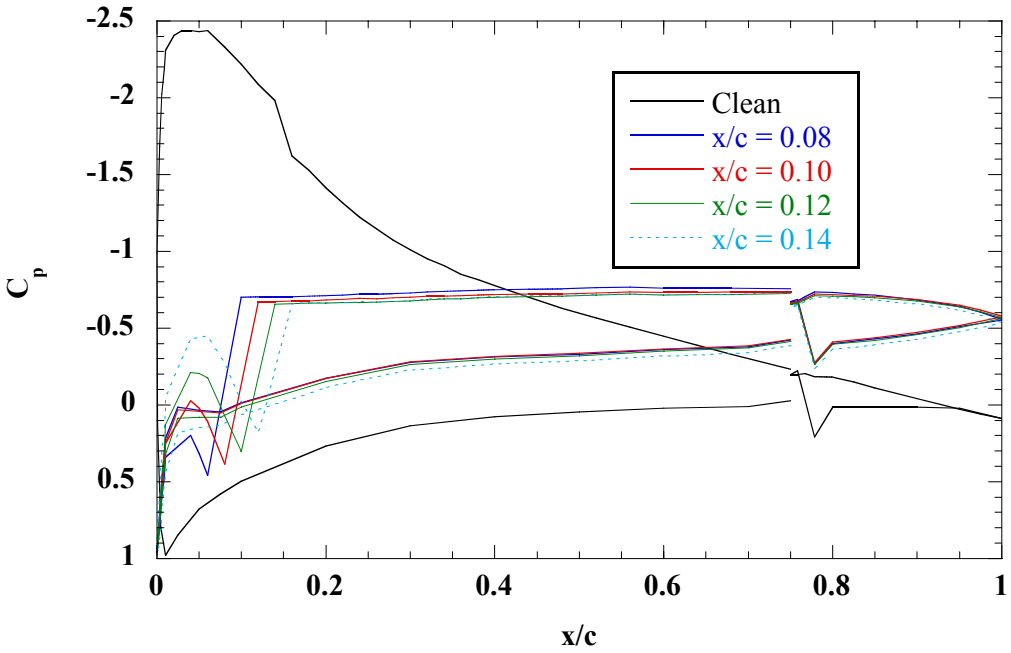

Fig. 4.42b) x/c = 0.08 to 0.14

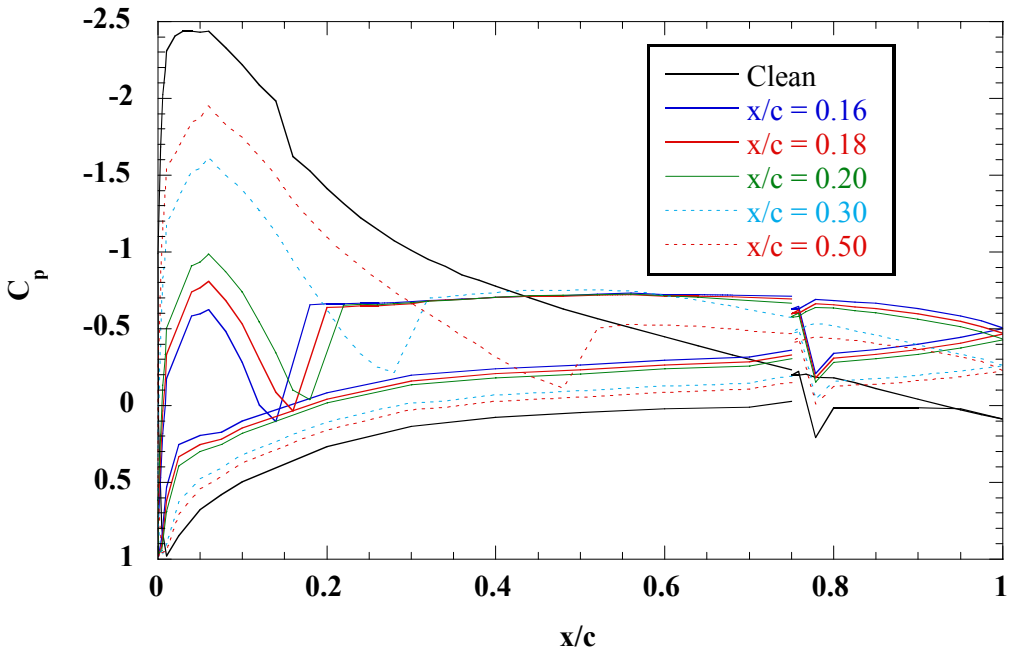

Fig. 4.42c) x/c = 0.16 to 0.50

Fig. 4.42: Effect of simulated ice ridge location on flap hinge moment change; NACA 23012m; forward-facing quarter round; α = 8°; k = 0.25"; boundary layer tripped (except for x/c = 0.00 and 0.02 cases); Re = 1.8 million.

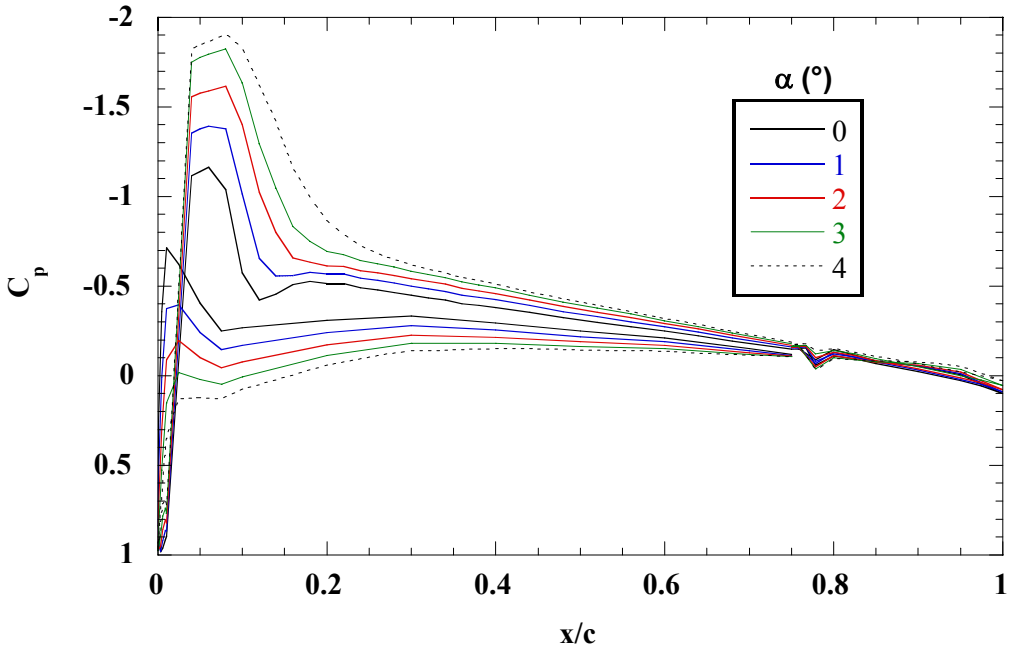

Fig. 4.43a) α = 0° to 4°

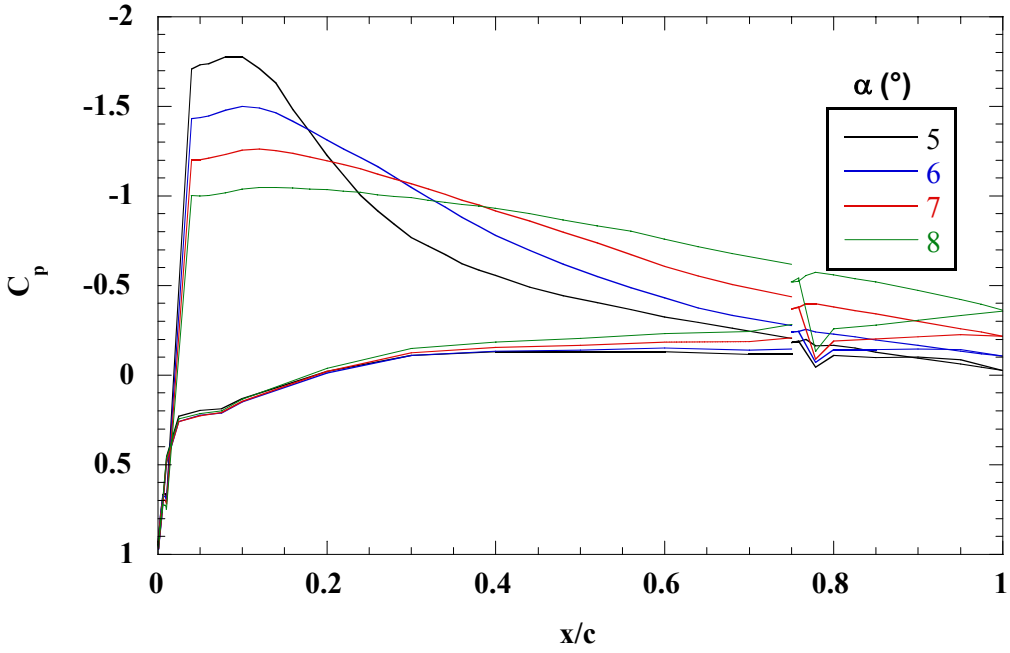

Fig. 4.43b) α = 5° to 8°

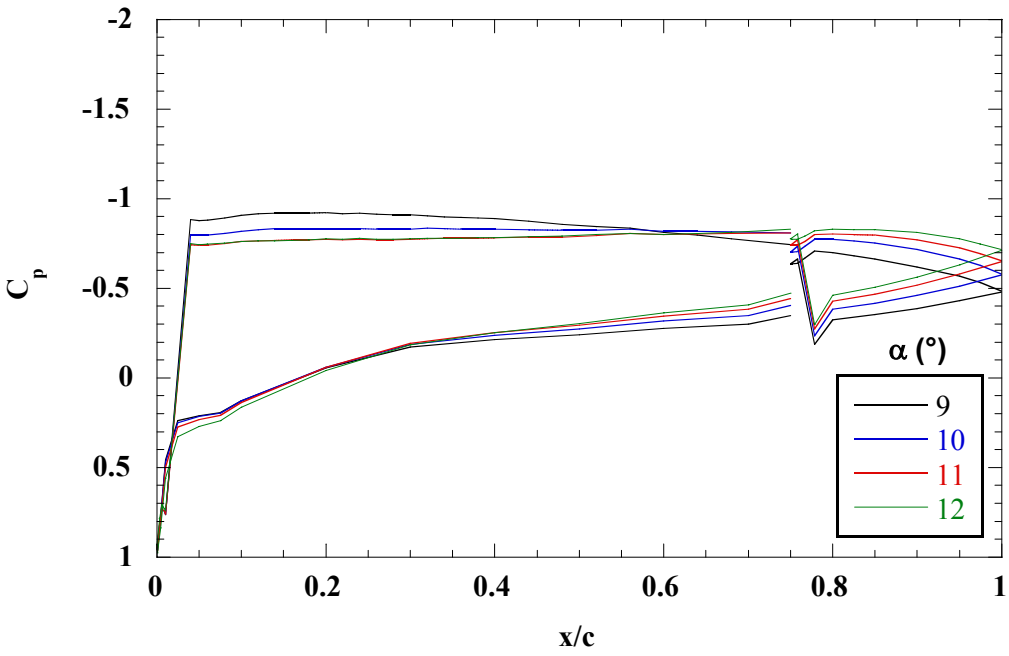

Fig. 4.43c) α = 9° to 12°

Fig. 4.43: Effect of simulated ridge ice on pressure distribution; NACA 23012m; forward-facing quarter round at x/c = 0.02; k = 0.25"; boundary layer not tripped, Re = 1.8 million.

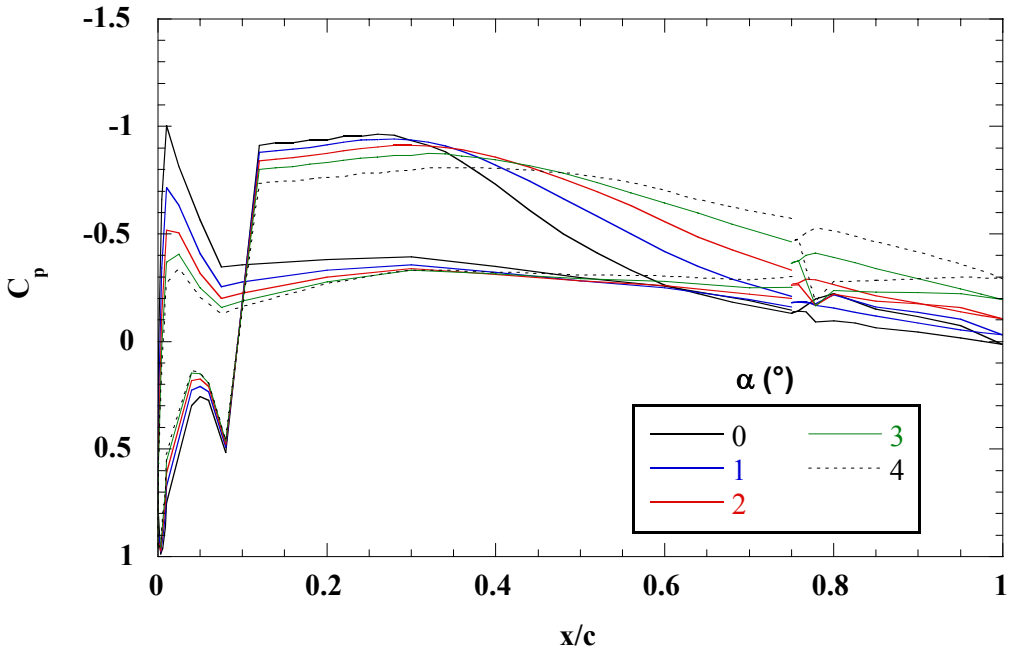

Fig. 4.44a) α = 0° to 4°

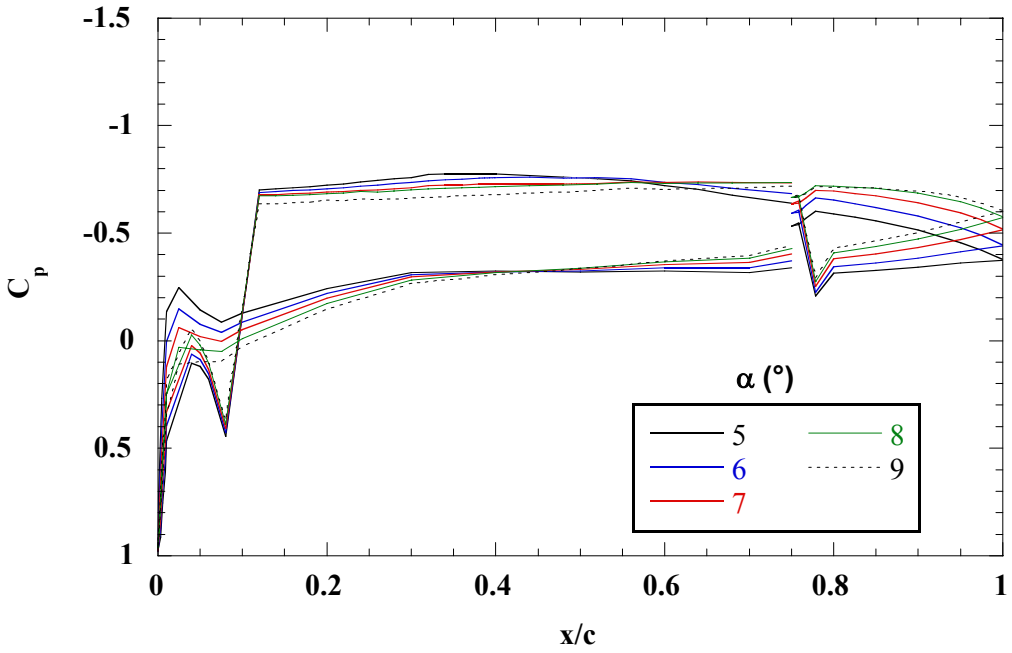

Fig. 4.44b) α = 5° to 9°

Fig. 4.44: Effect of simulated ridge ice on pressure distribution; NACA 23012m; forward-facing quarter round at x/c = 0.10; k = 0.25"; boundary layer not tripped, Re = 1.8 million.

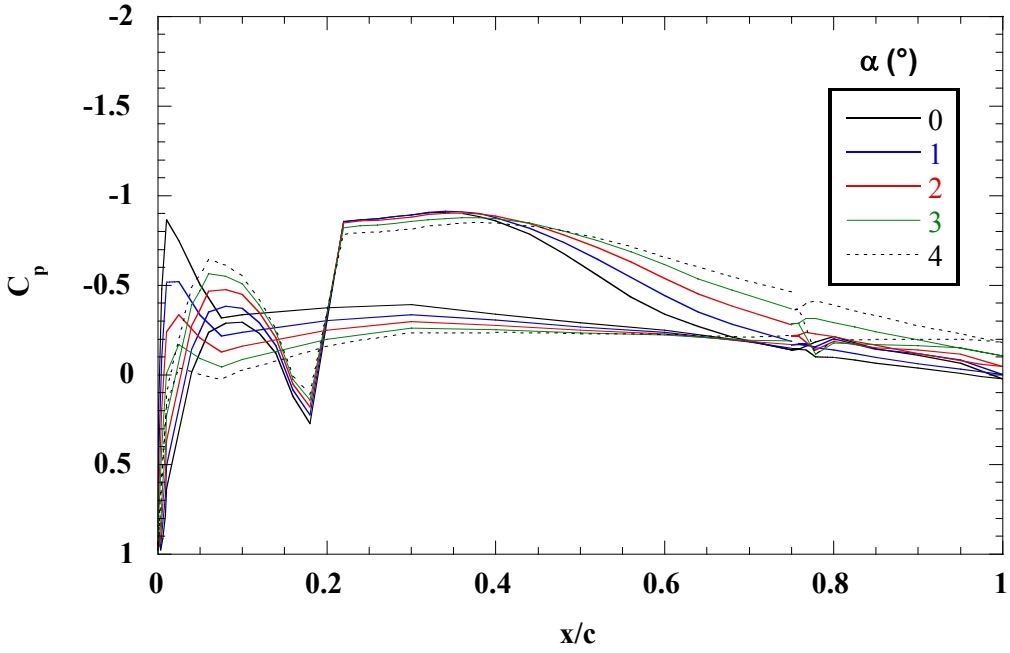

Fig. 4.45a) α = 0° to 4°

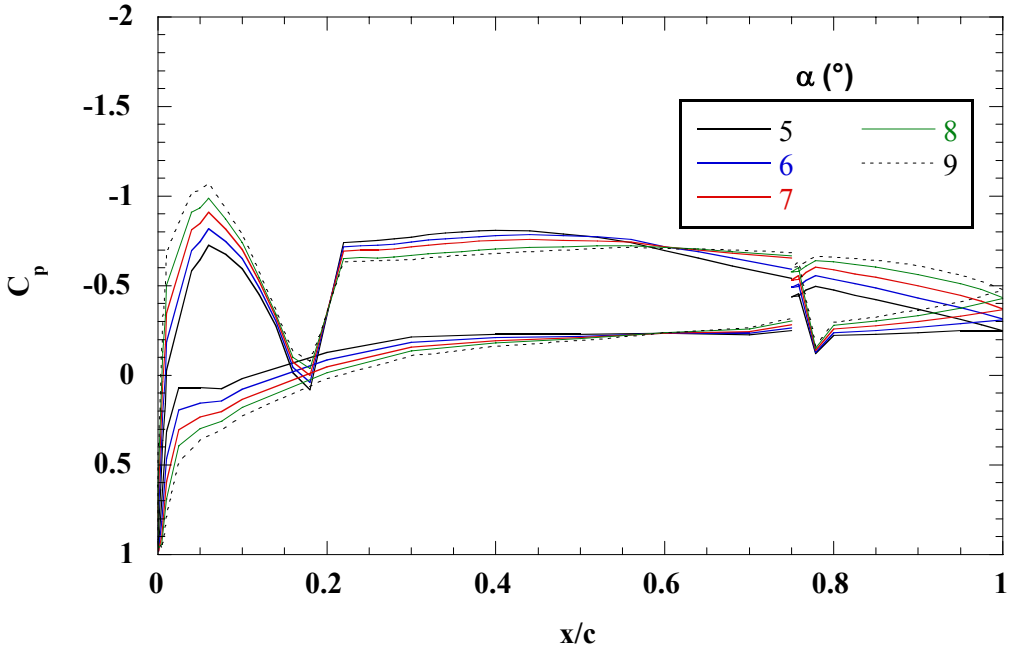

Fig. 4.45b) α = 5° to 9°

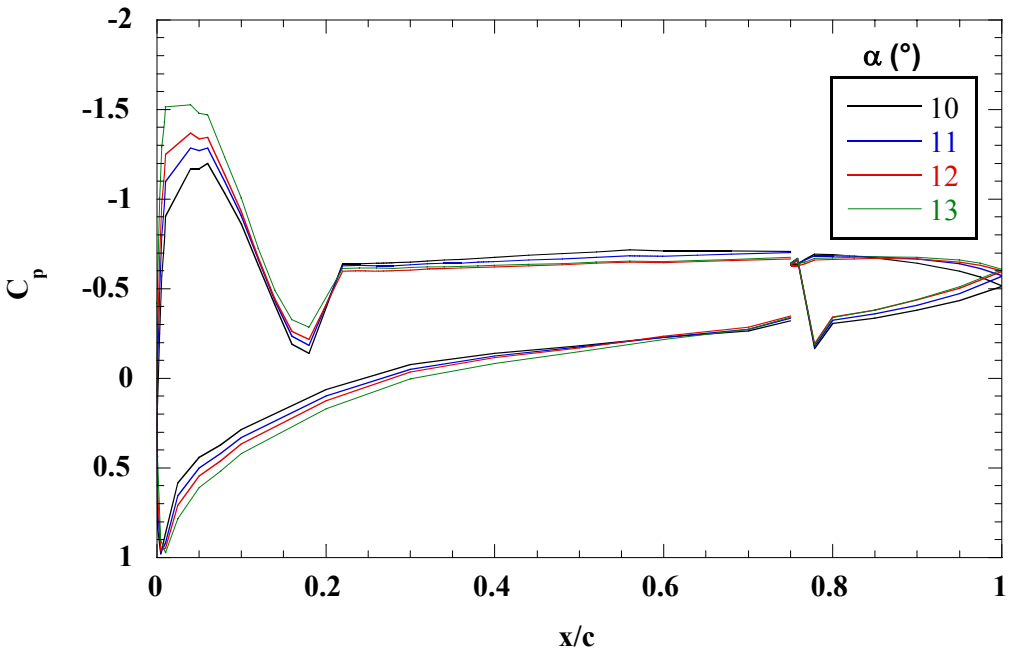

Fig. 4.45c) α = 10° to 13°

Fig. 4.45: Effect of simulated ridge ice on pressure distribution; NACA 23012m; forward-facing quarter round at x/c = 0.20; k = 0.25"; boundary layer not tripped, Re = 1.8 million.

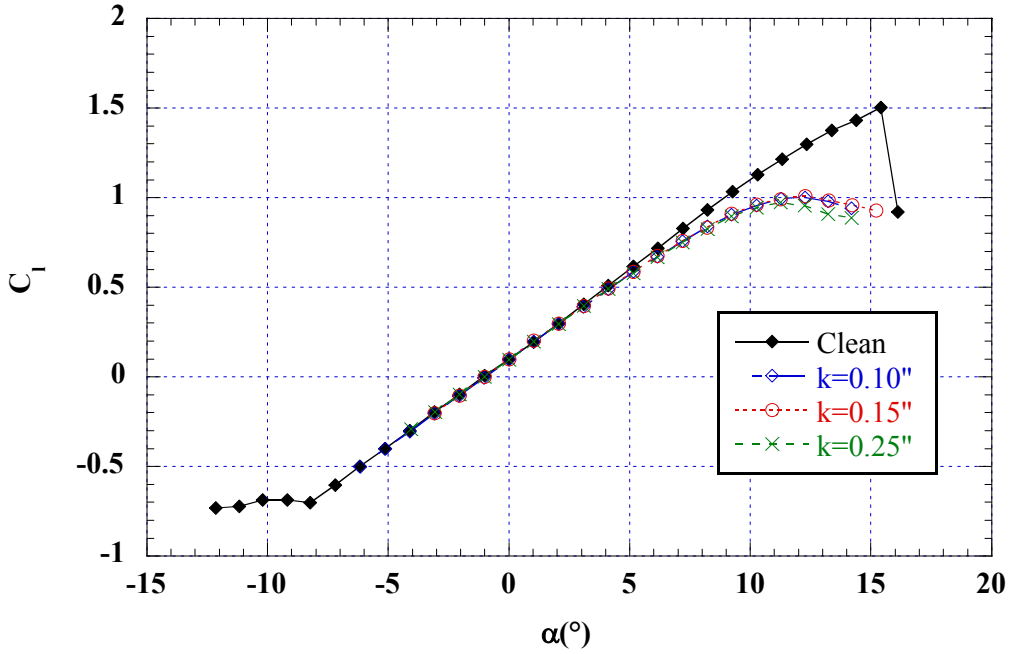

Fig. 4.46a) $x/c = 0.00$

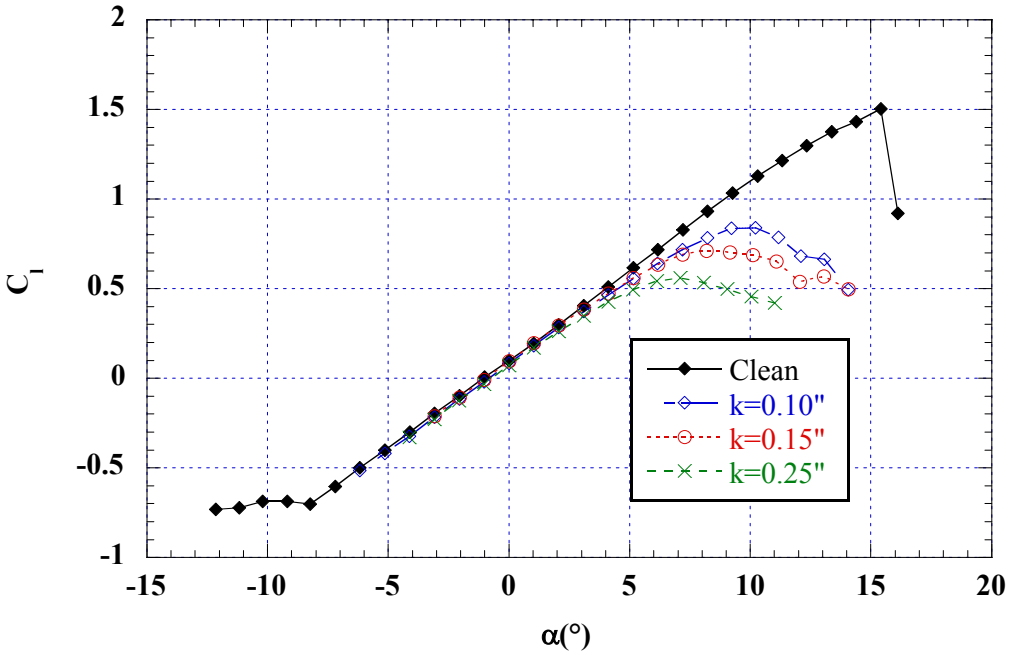

Fig. 4.46b) $x/c = 0.02$

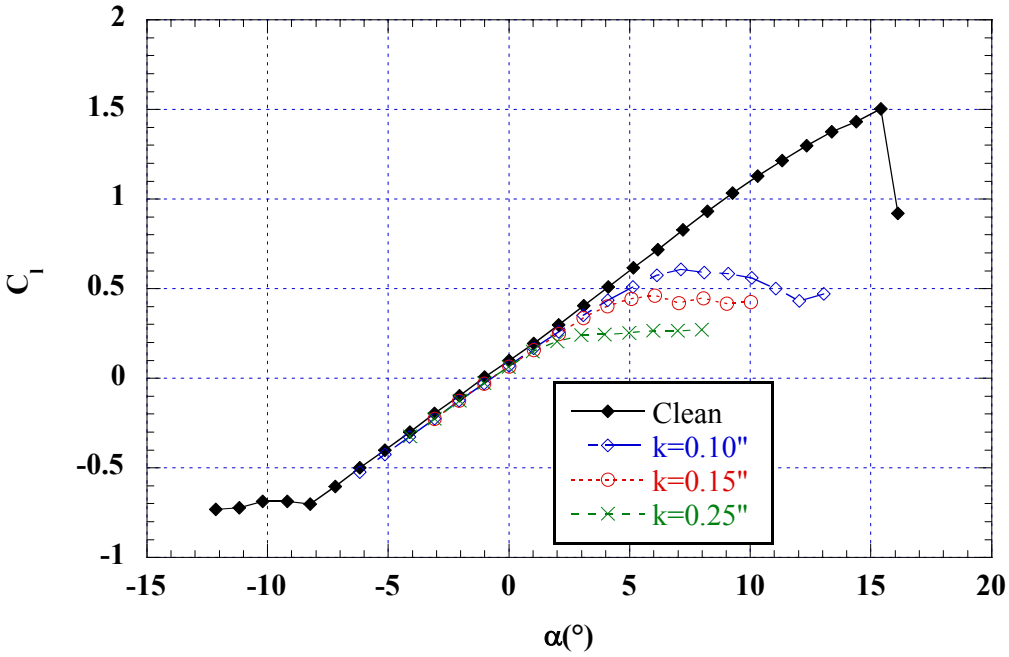

Fig. 4.46c) $x/c = 0.10$

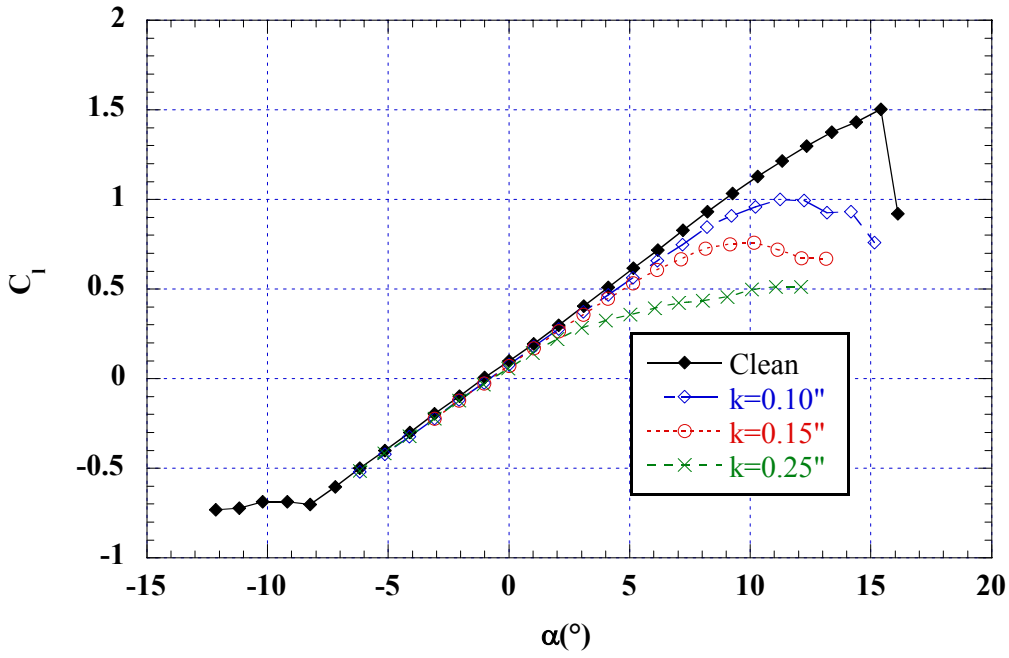

Fig. 4.46d) $x/c = 0.20$

Fig. 4.46: Effect of simulated ridge-ice height on lift; NACA 23012m; forward-facing quarter round; boundary layer tripped (except for $x/c = 0.00$ and 0.02 cases); $Re = 1.8$ million.

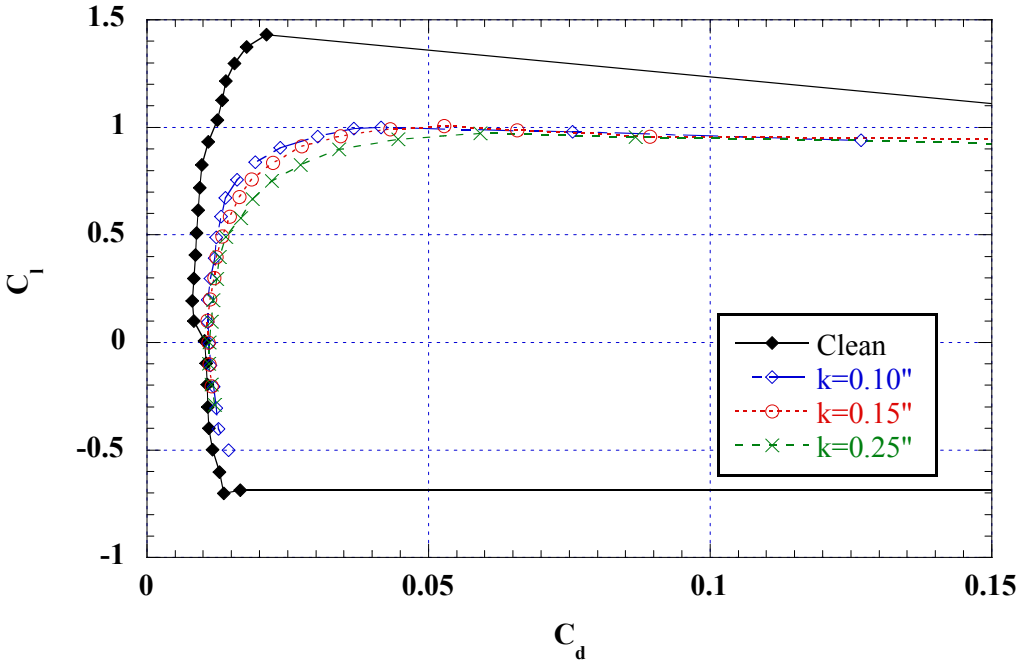

Fig. 4.47a) $x/c = 0.00$

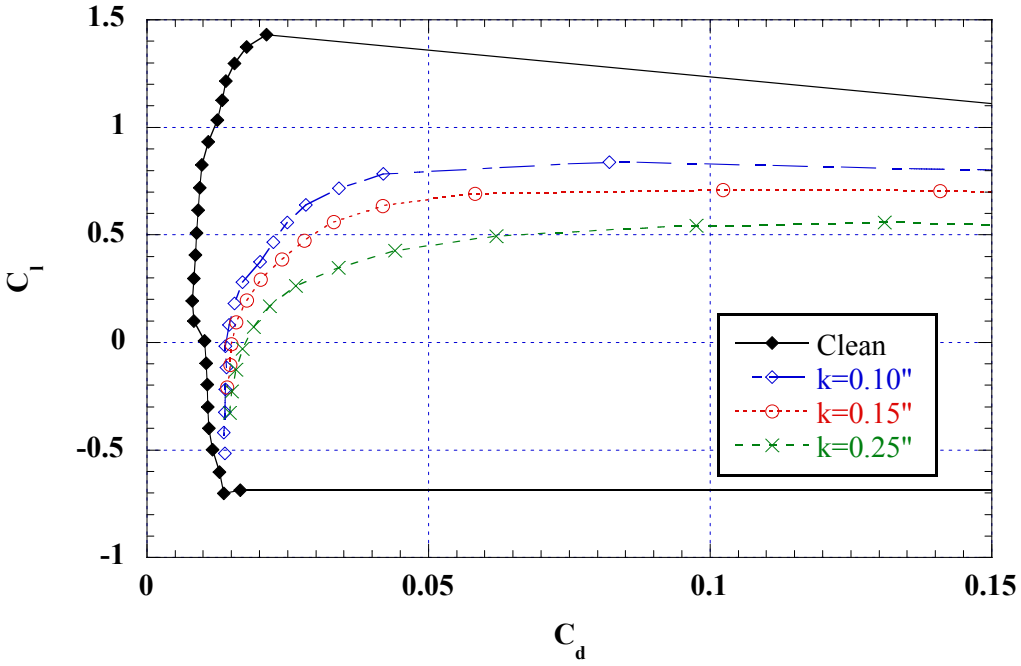

Fig. 4.47b) $x/c = 0.02$

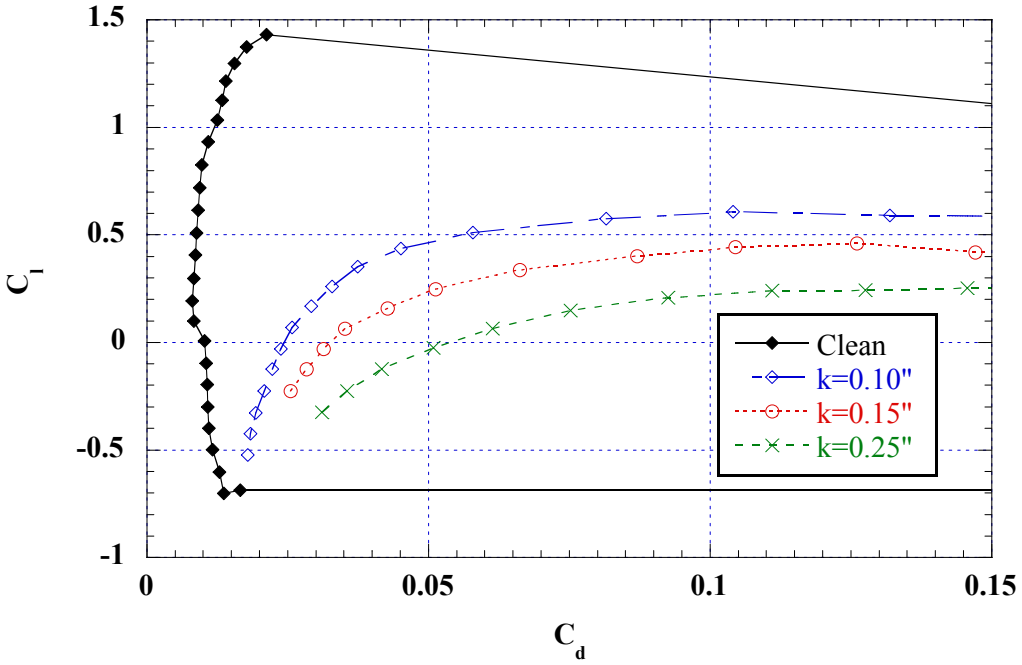

Fig. 4.47c) x/c = 0.10

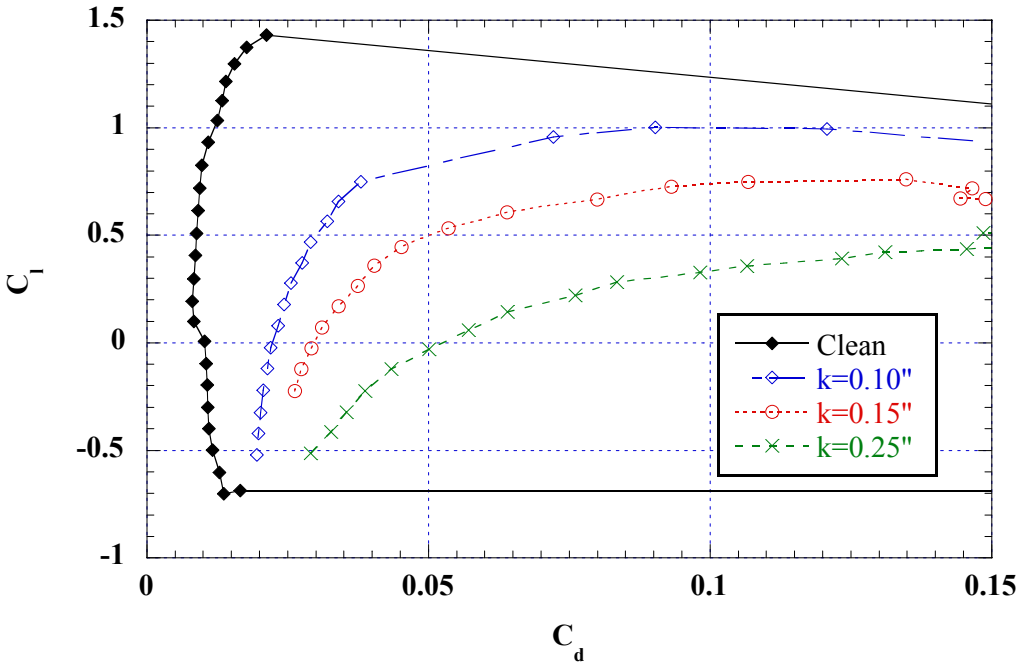

Fig. 4.47d) x/c = 0.20

Fig. 4.47: Effect of simulated ridge-ice height on drag; NACA 23012m; forward-facing quarter round; boundary layer tripped (except for x/c = 0.00 and 0.02 cases); Re = 1.8 million.

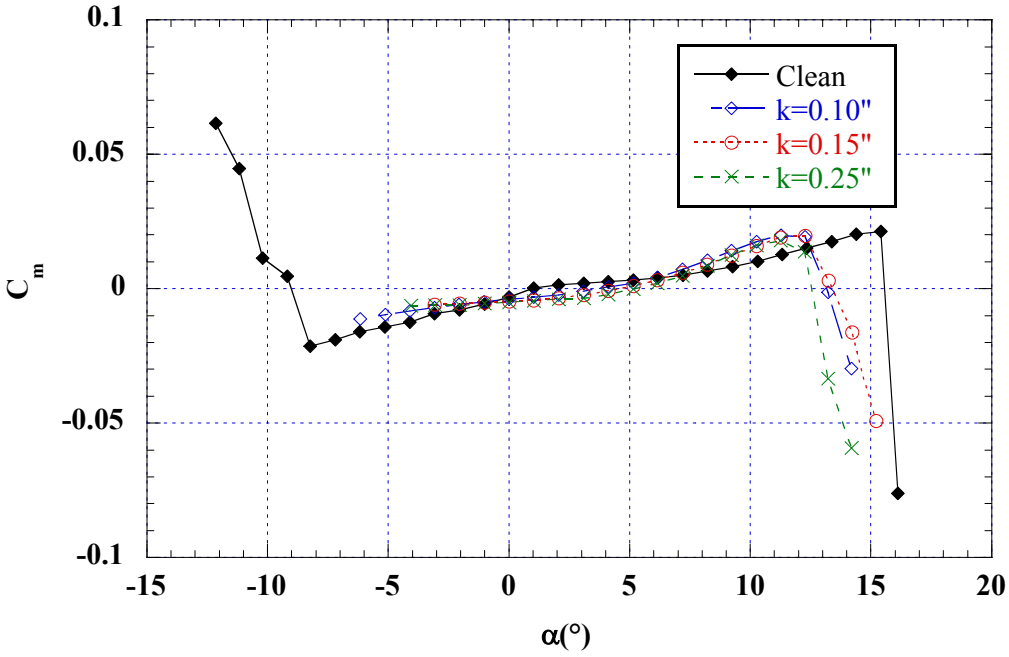

Fig. 4.48a) $x/c = 0.00$

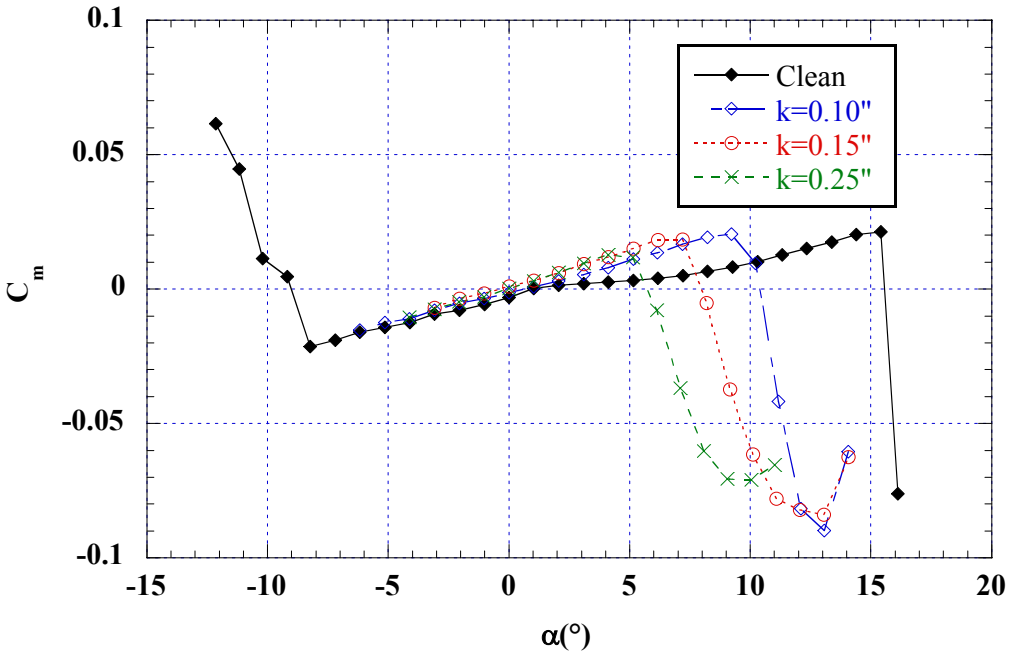

Fig. 4.48b) $x/c = 0.02$

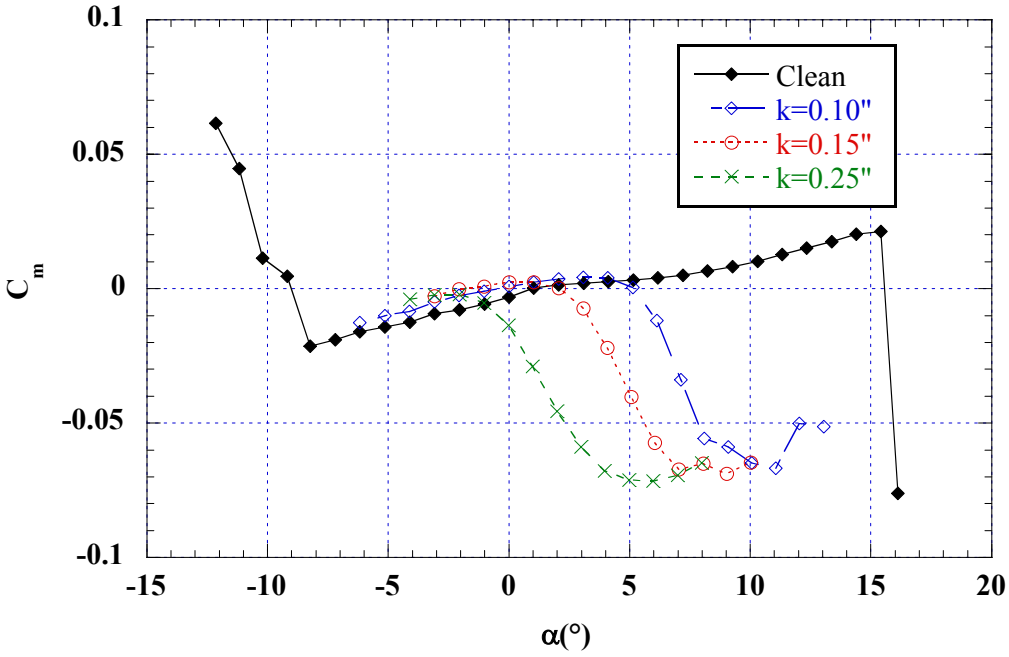

Fig. 4.48c) x/c = 0.10

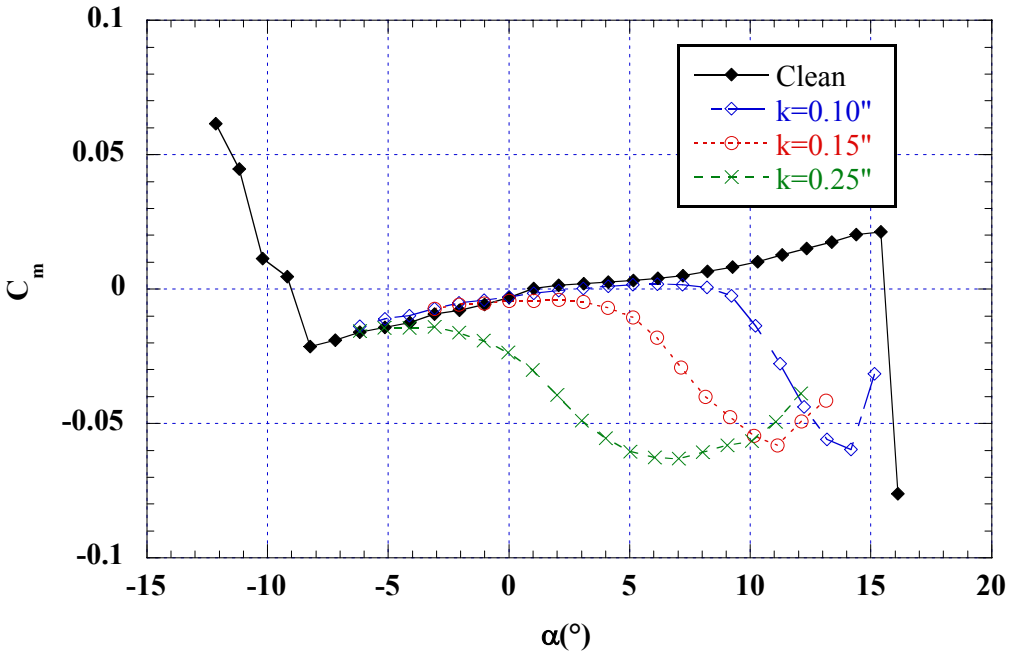

Fig. 4.48d) x/c = 0.20

Fig. 4.48: Effect of simulated ridge-ice height on pitching moment; NACA 23012m; forward-facing quarter round; boundary layer tripped (except for x/c = 0.00 and 0.02 cases); Re = 1.8 million.

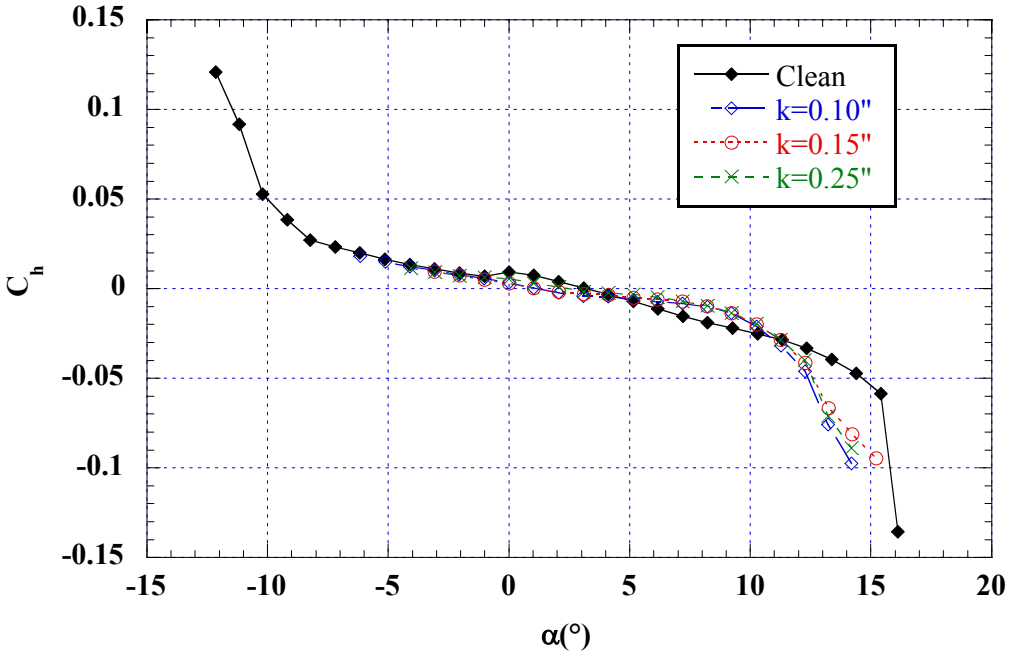

Fig. 4.49a) $x/c = 0.00$

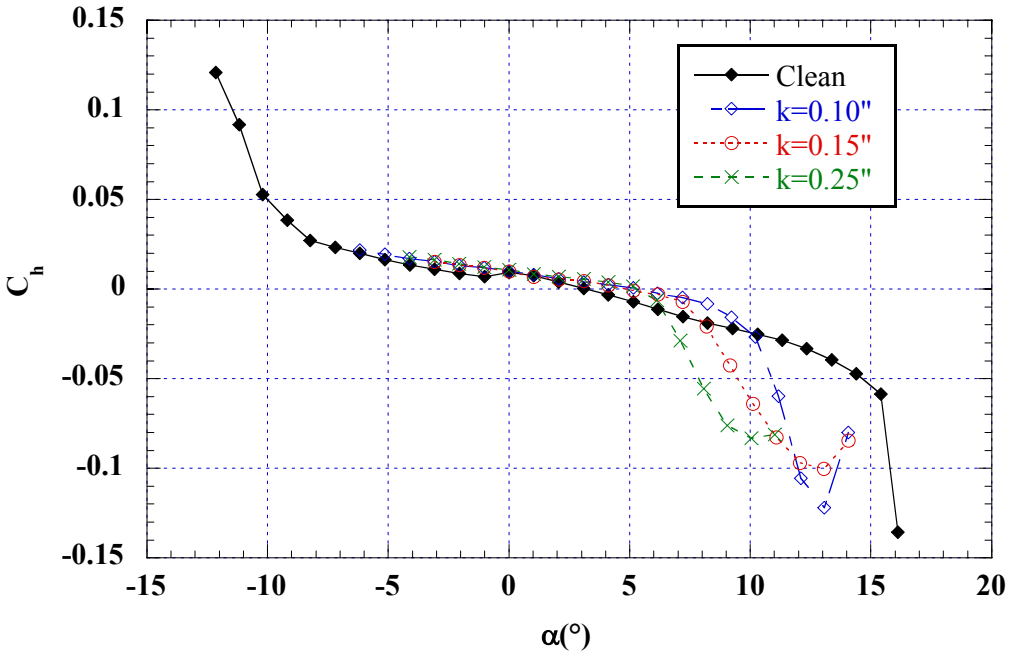

Fig. 4.49b) $x/c = 0.02$

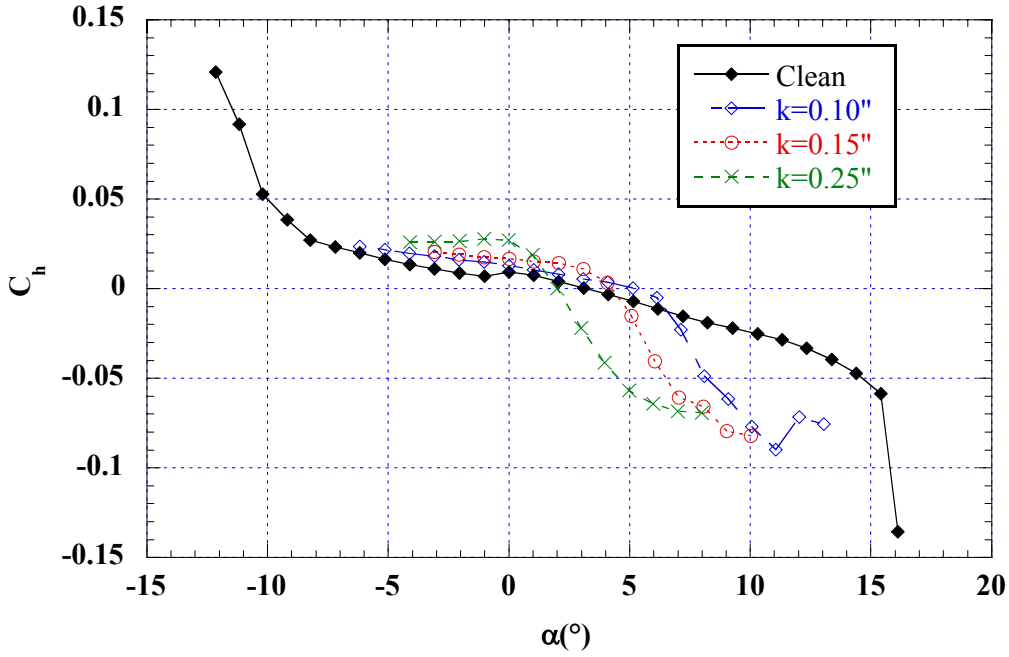

Fig. 4.49c) x/c = 0.10

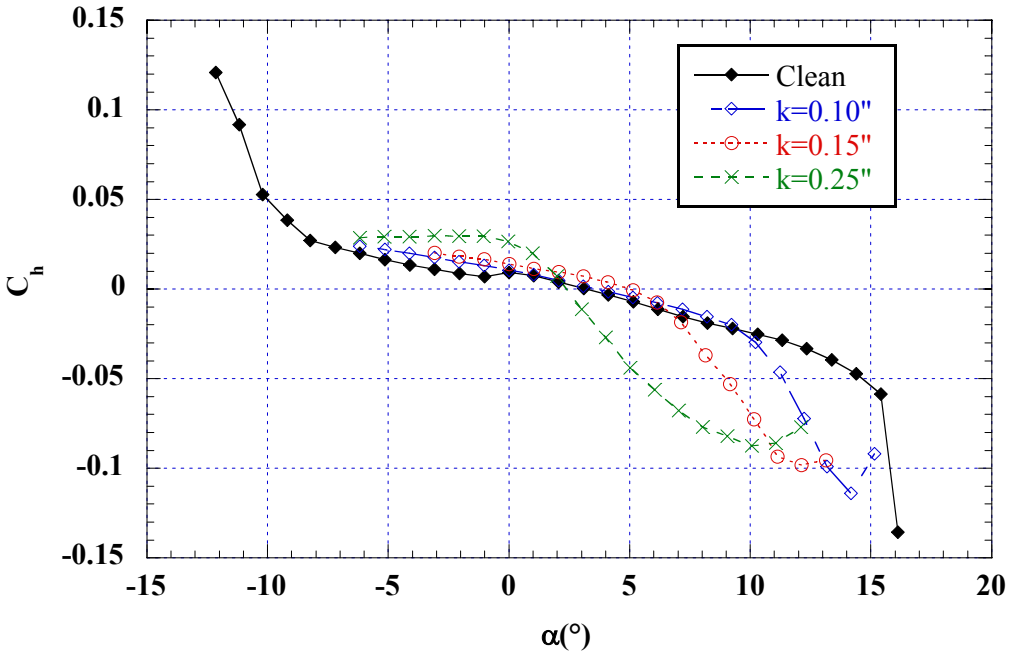

Fig. 4.49d) x/c = 0.20

Fig. 4.49: Effect of simulated ridge-ice height on flap hinge moment; NACA 23012m; forward-facing quarter round; boundary layer tripped (except for x/c = 0.00 and 0.02 cases); Re = 1.8 million.

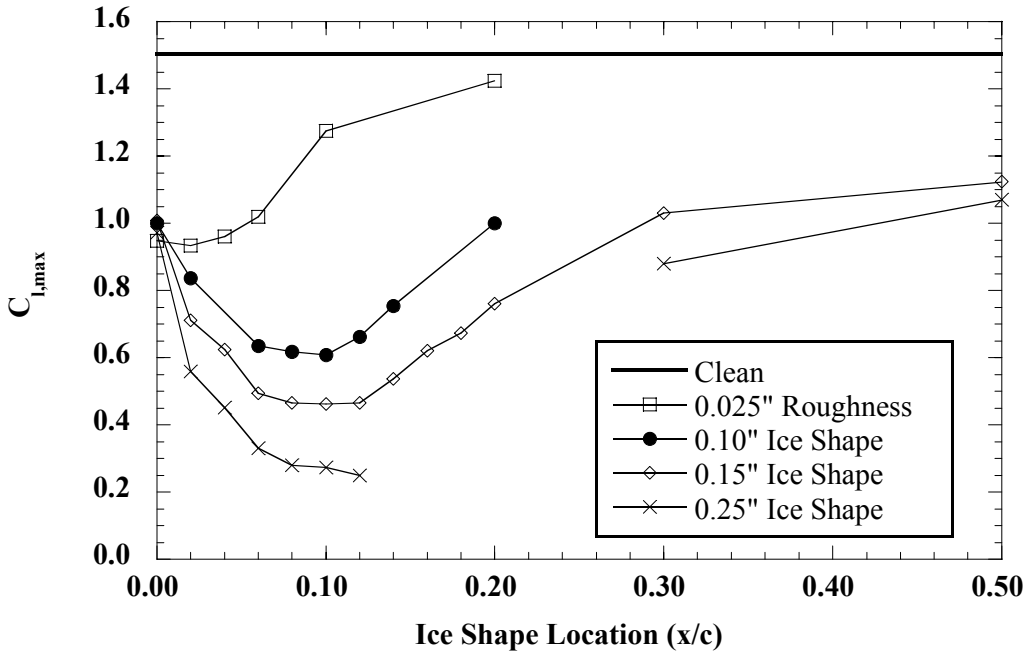

Fig. 4.50: Effect of simulated ridge-ice height on maximum lift as a function of location; NACA 23012m; forward-facing quarter round; boundary layer tripped (except for x/c = 0.00 and 0.02 cases); Re = 1.8 million.

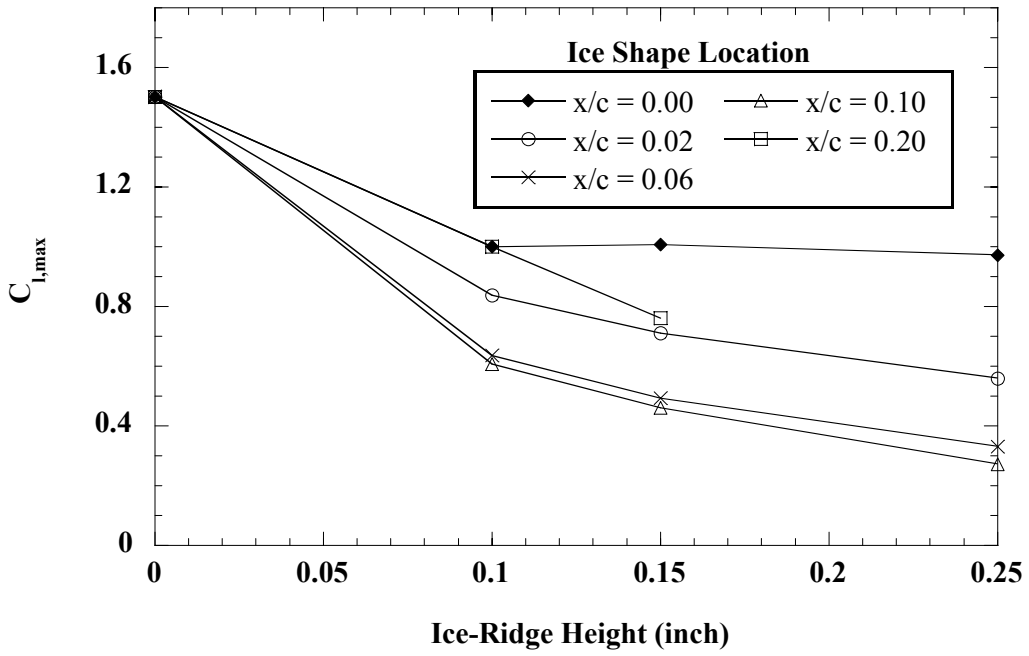

Fig. 4.51a) Maximum lift

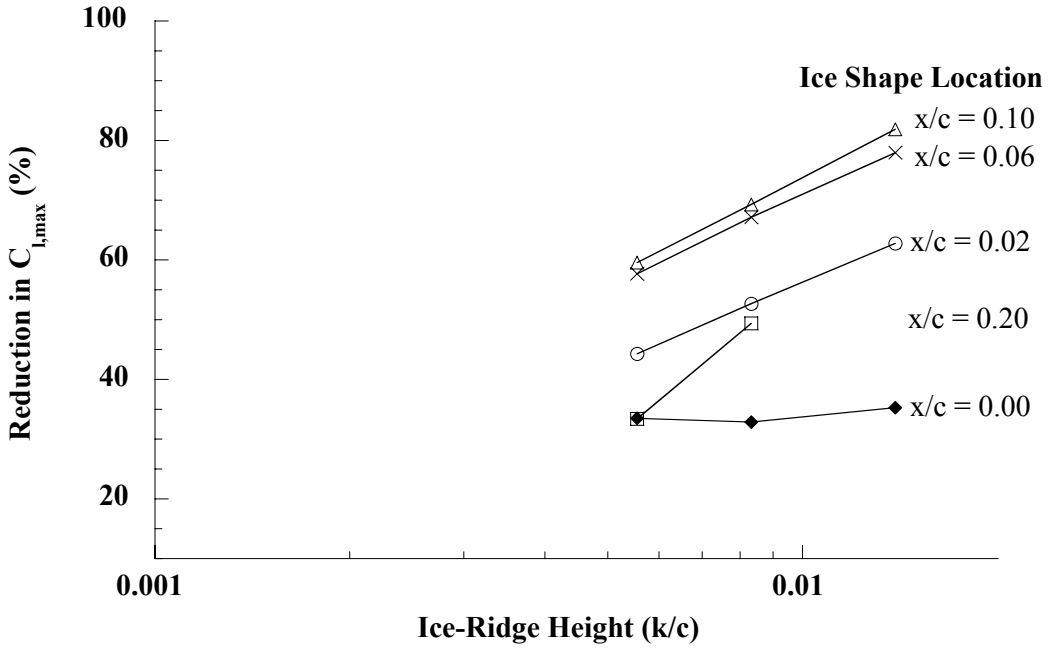

Fig. 4.51b) Maximum lift reduction

Fig. 4.51: Effect of simulated ice-ridge location on maximum lift as a function of height; NACA 23012m; forward-facing quarter round; boundary layer tripped (except for x/c = 0.00 and 0.02 cases); Re = 1.8 million.

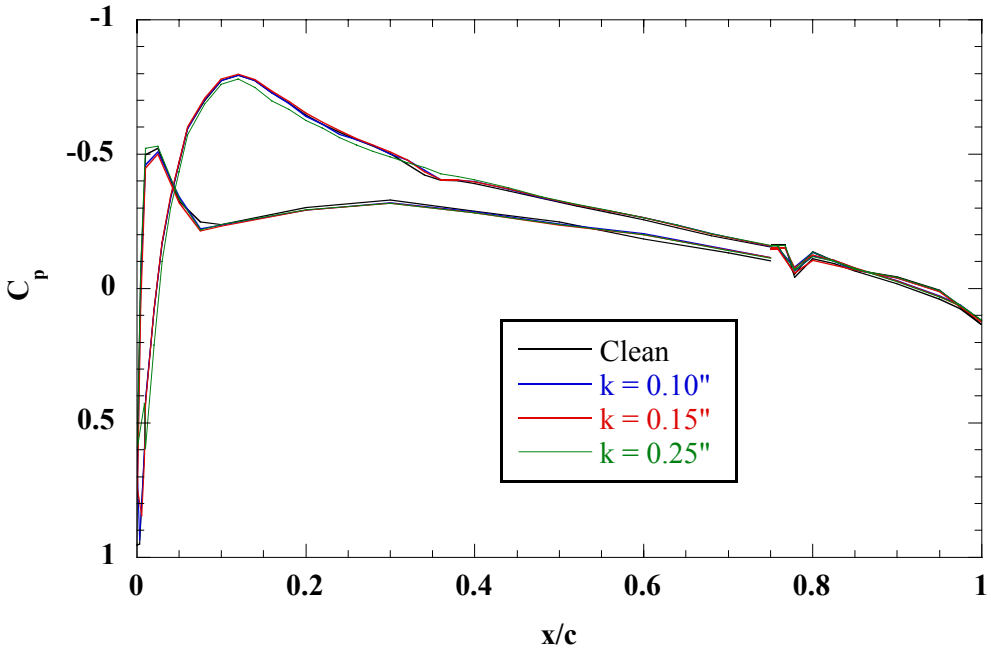

Fig. 4.52a) $\alpha = 0°$

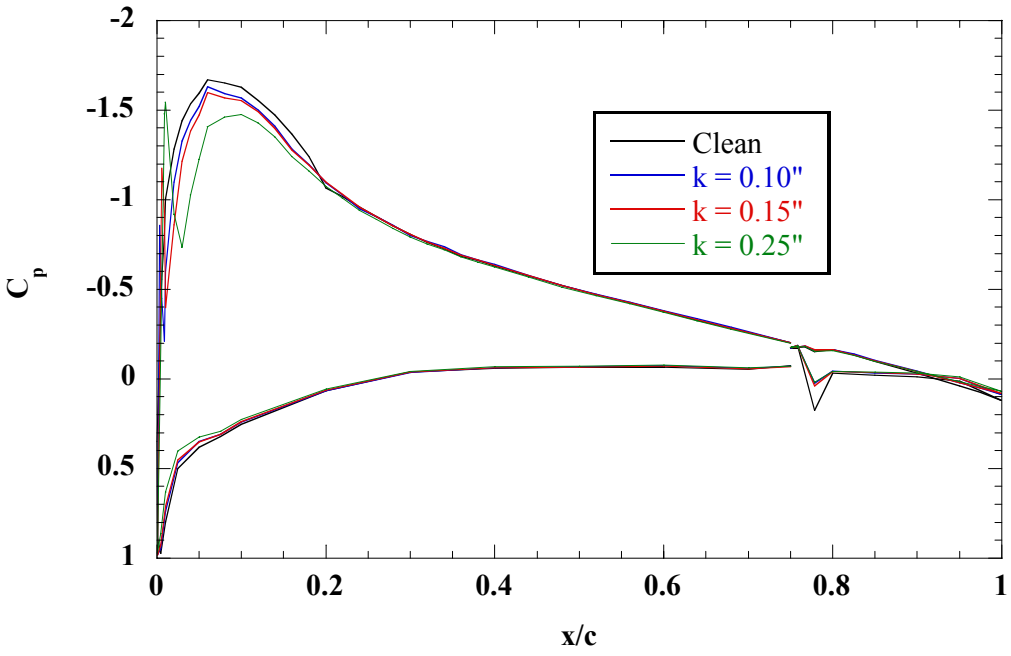

Fig. 4.52b) $\alpha = 5°$

Fig. 4.52: Effect of simulated ridge-ice height on surface-pressure distribution; NACA 23012m; forward-facing quarter round at x/c = 0.00; boundary layer not tripped; Re = 1.8 million.

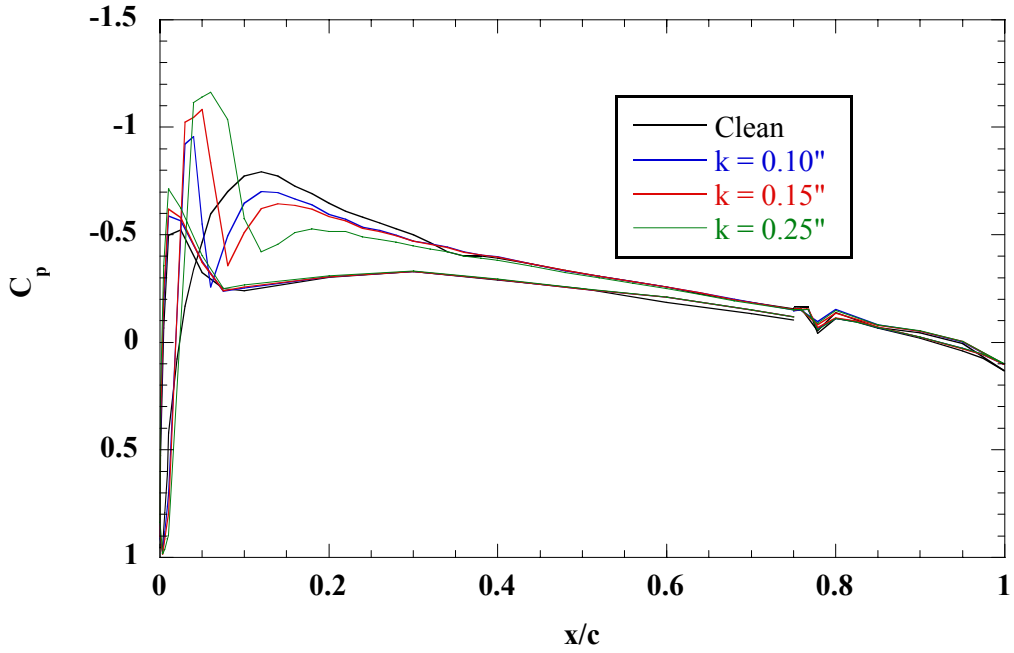

Fig. 4.53c) $\alpha = 0°$

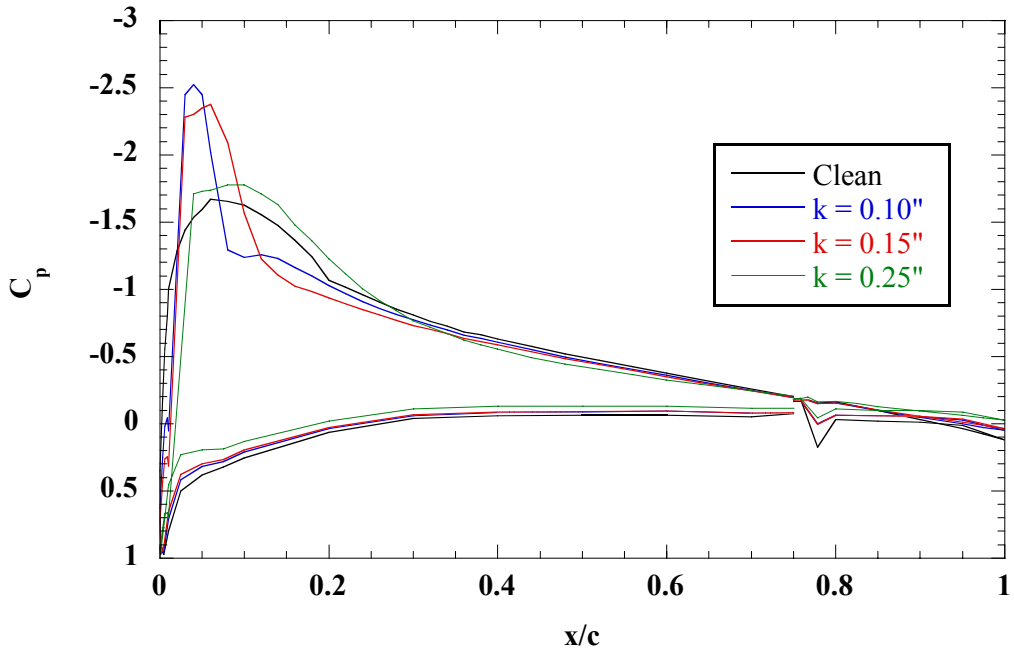

Fig. 4.53d) $\alpha = 5°$

Fig. 4.53: Effect of simulated ridge-ice height on surface-pressure distribution; NACA 23012m; forward-facing quarter round at x/c = 0.02; boundary layer not tripped; Re = 1.8 million.

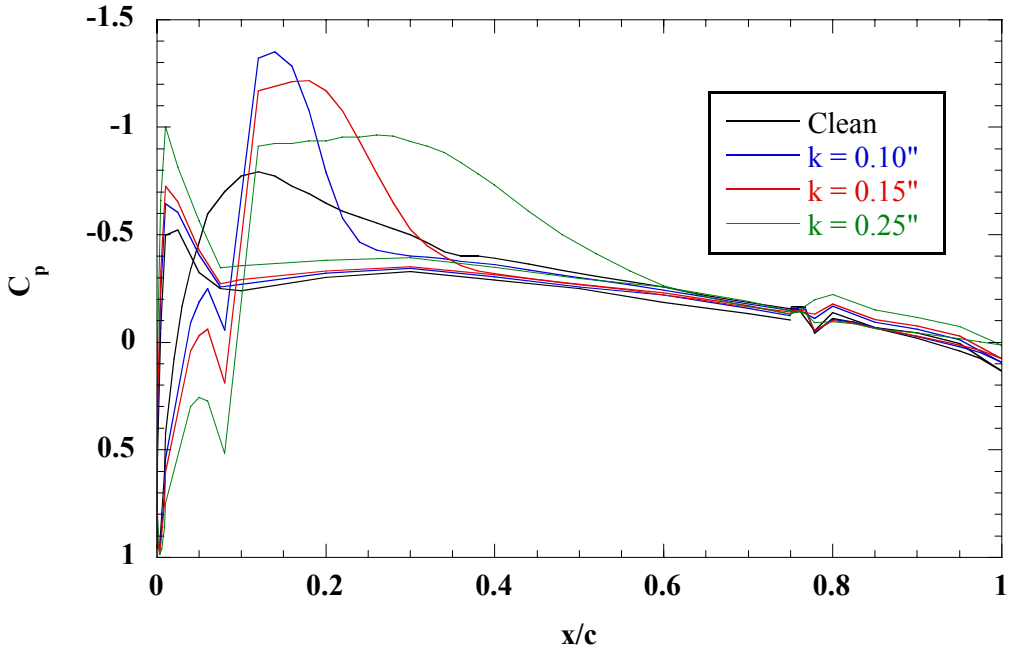

Fig. 4.54a) $\alpha = 0°$

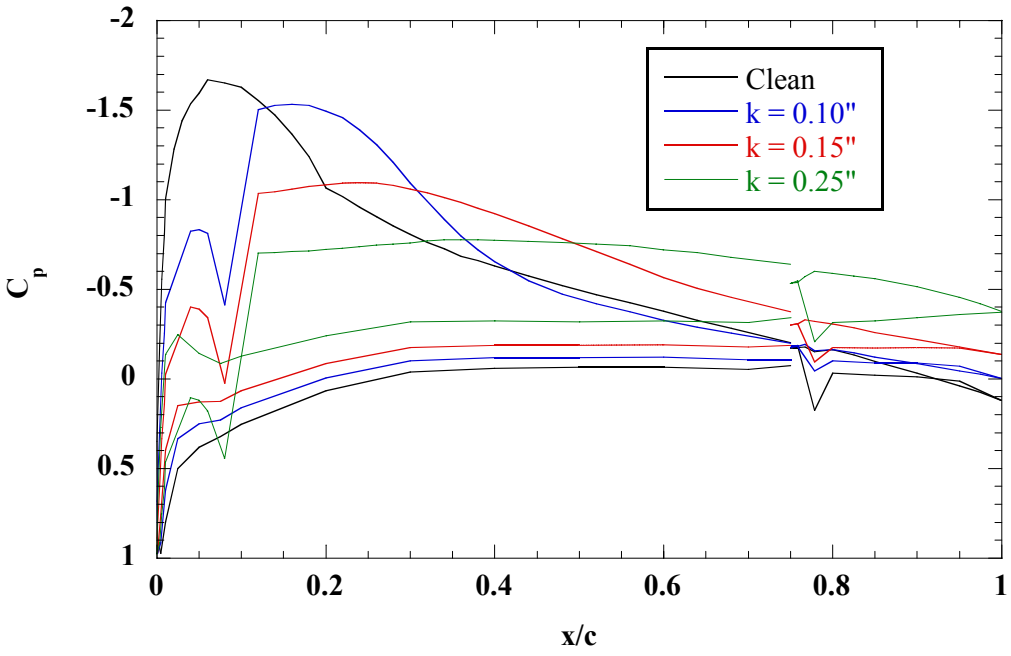

Fig. 4.54b) $\alpha = 5°$

Fig. 4.54: Effect of simulated ridge-ice height on surface-pressure distribution; NACA 23012m; forward-facing quarter round at x/c = 0.10; boundary layer tripped; Re = 1.8 million.

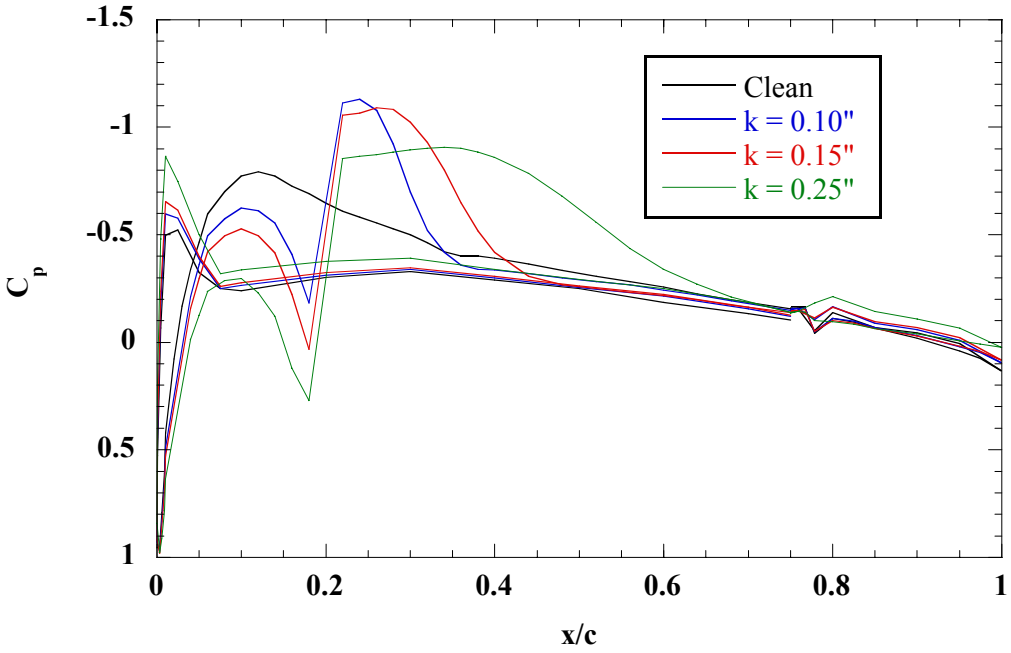

Fig. 4.55c) $\alpha = 0°$

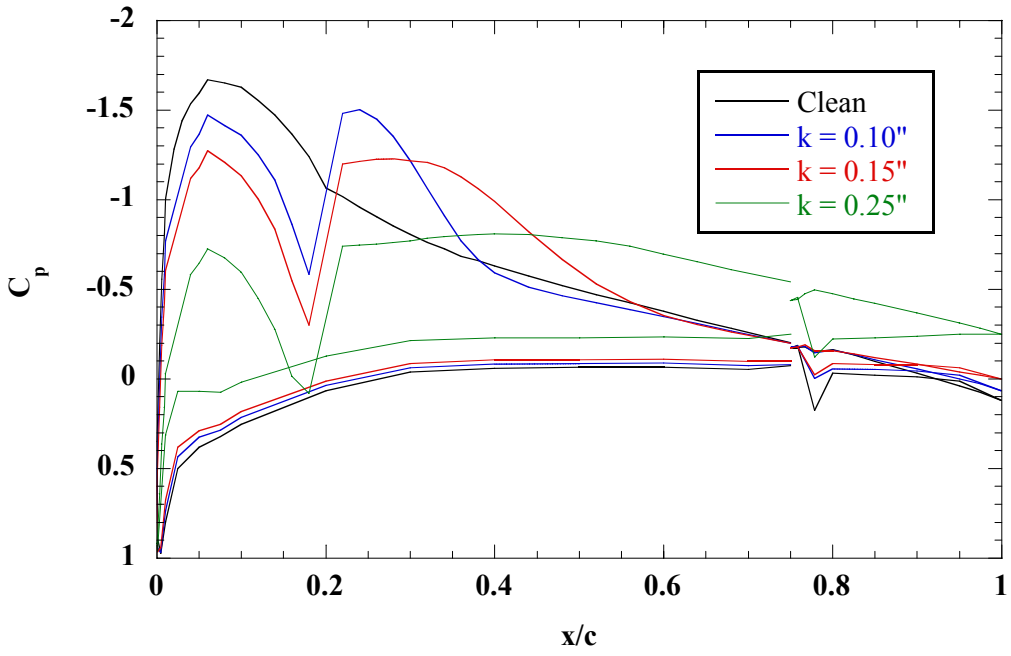

Fig. 4.55d) $\alpha = 5°$

Fig. 4.55: Effect of simulated ridge-ice height on surface-pressure distribution; NACA 23012m; forward-facing quarter round at x/c = 0.20; boundary layer tripped; Re = 1.8 million.

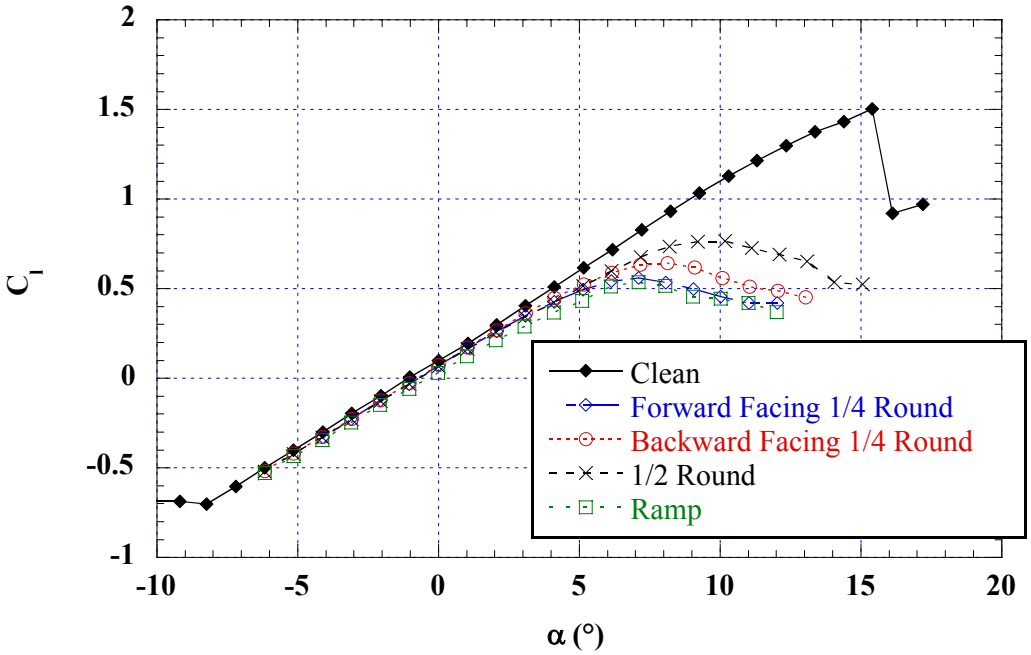

Fig. 4.56a) Lift

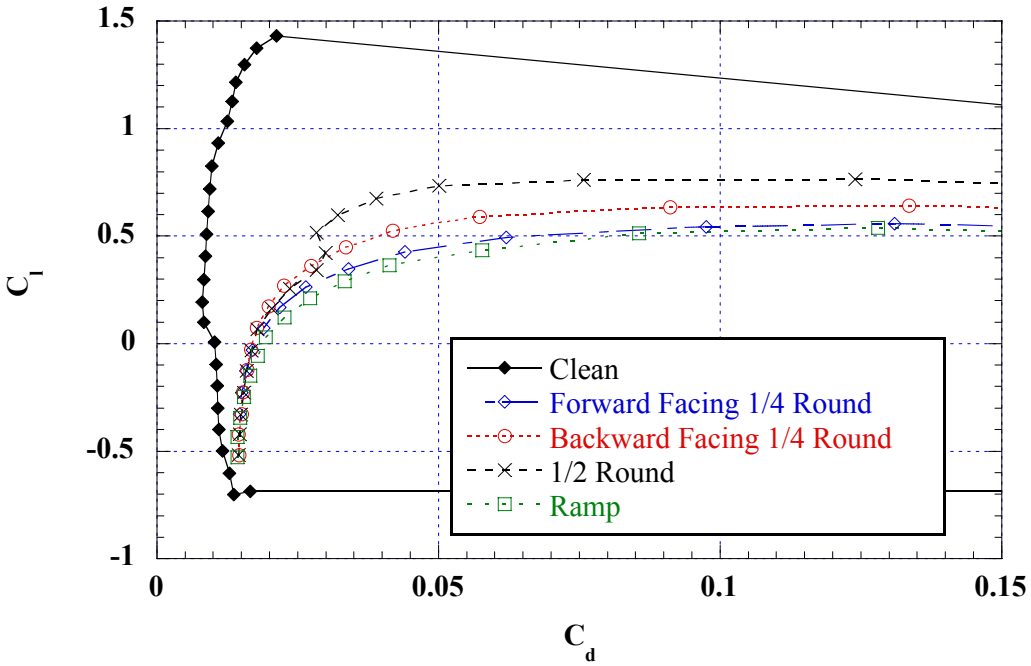

Fig. 4.56b) Drag

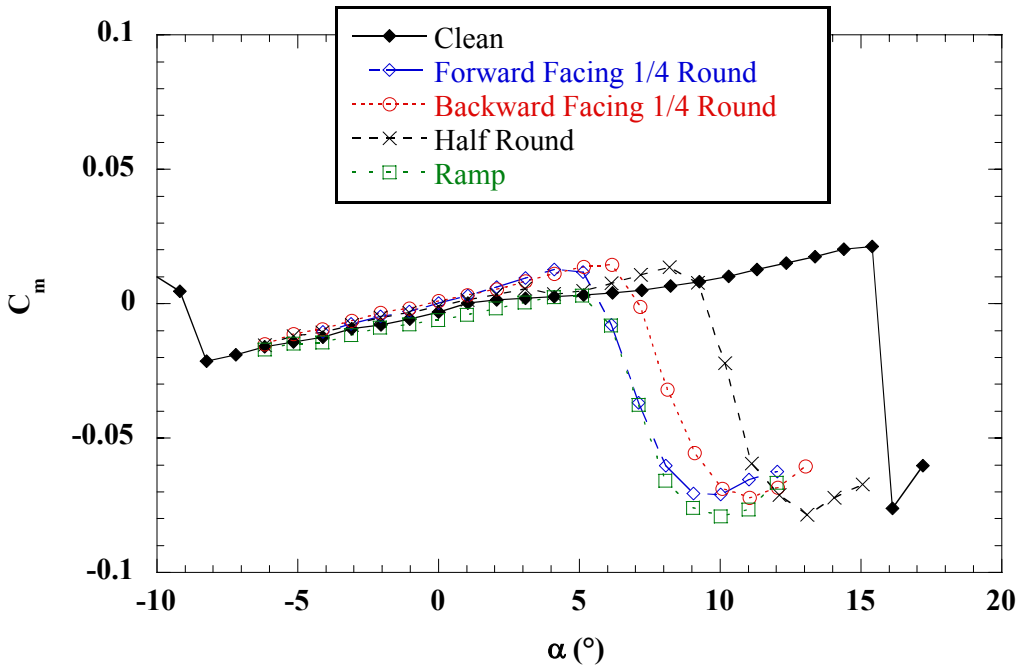

Fig. 4.56c) Pitching Moment

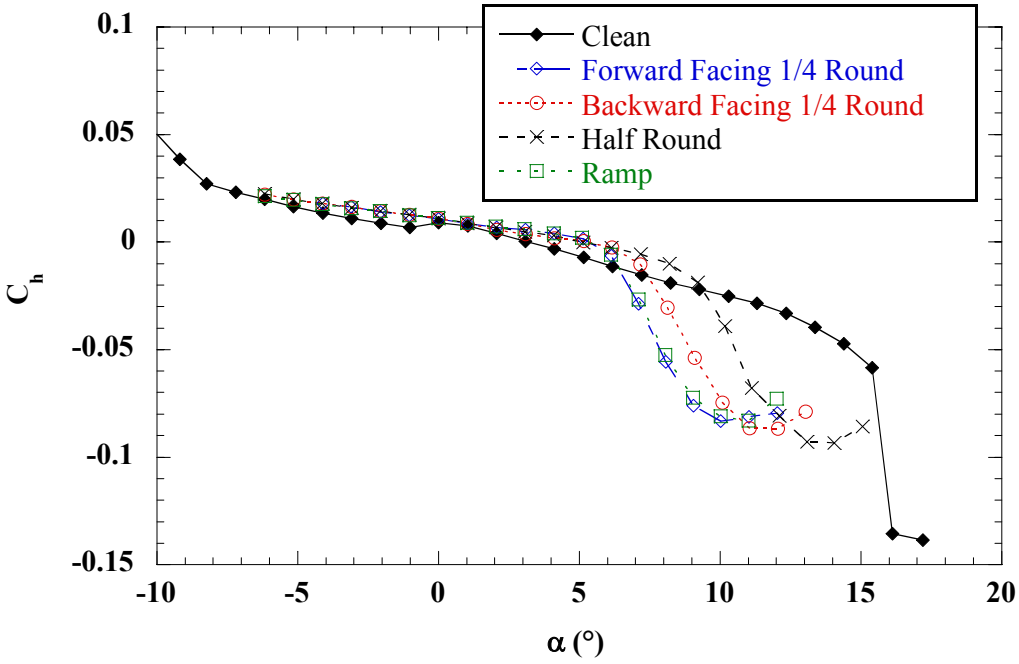

Fig. 4.56d) Flap hinge moment

Fig. 4.56: Effect of simulated ice-shape geometry on aerodynamic coefficients; NACA 23012m; k = 0.25”; ice shapes at x/c = 0.02; boundary layer not tripped; Re = 1.8 million.

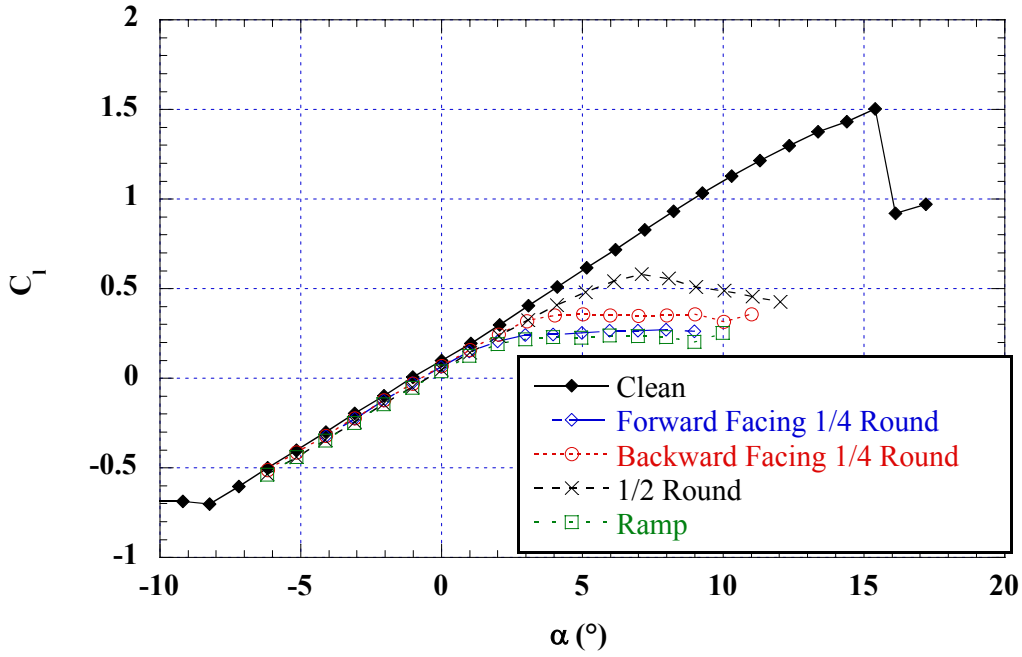

Fig. 4.57a) Lift

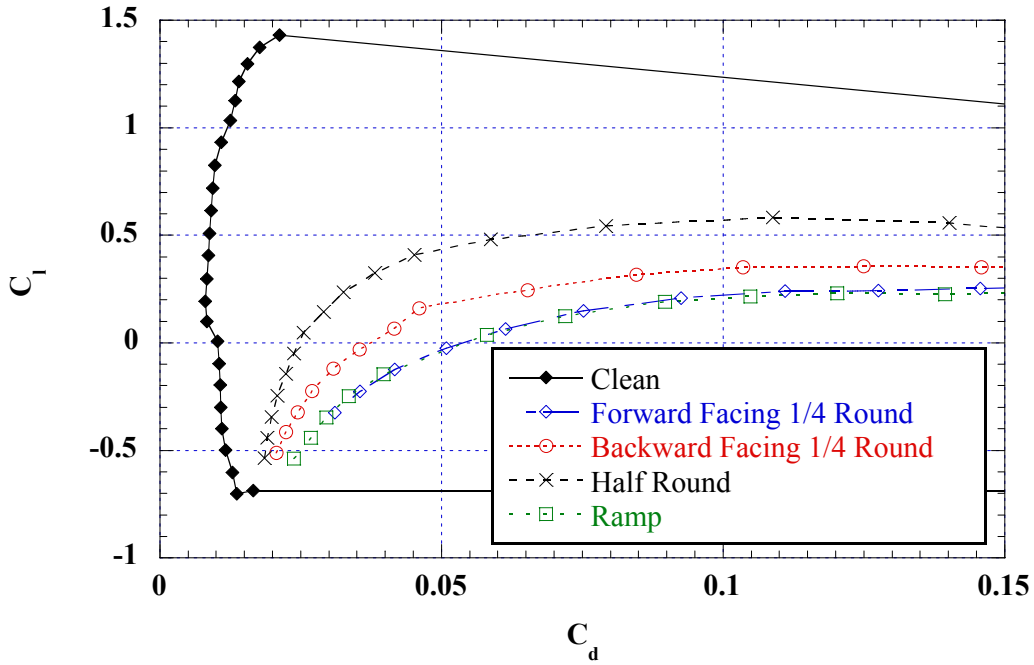

Fig. 4.57b) Drag

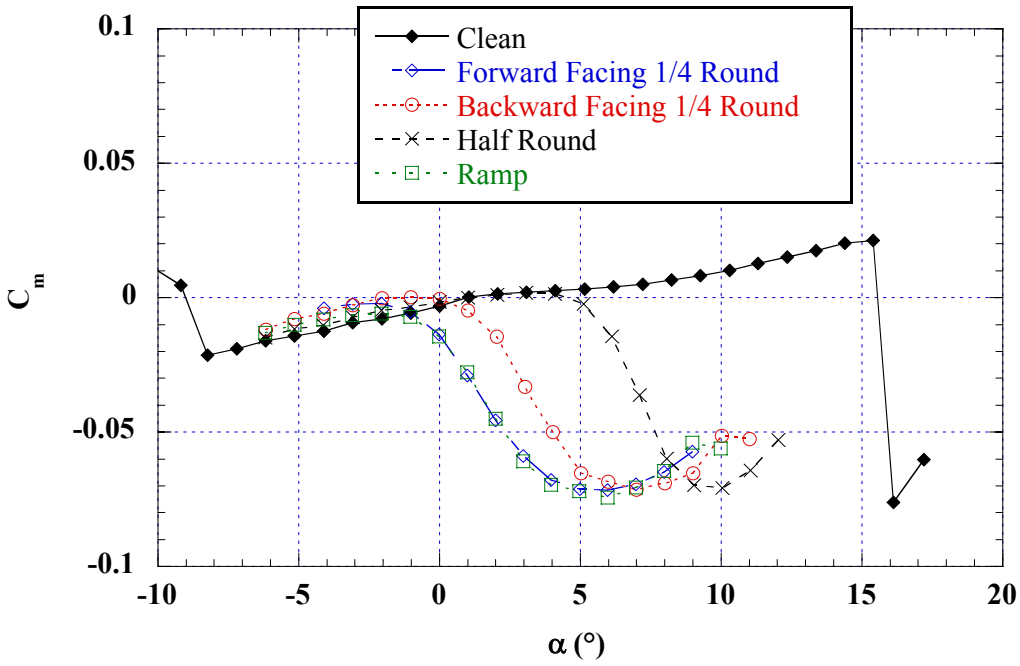

Fig. 4.57c) Pitching moment

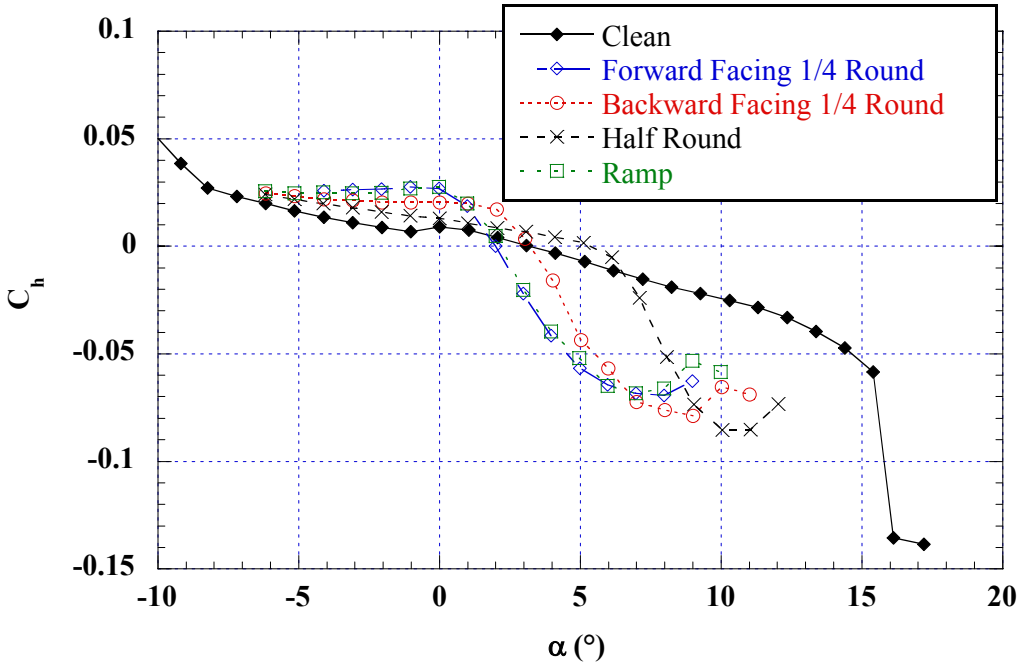

Fig. 4.57d) Flap hinge moment

Fig. 4.57: Effect of simulated ice-shape geometry on aerodynamic coefficients; NACA 23012m; k = 0.25"; ice shapes at x/c = 0.10; boundary layer tripped; Re = 1.8 million.

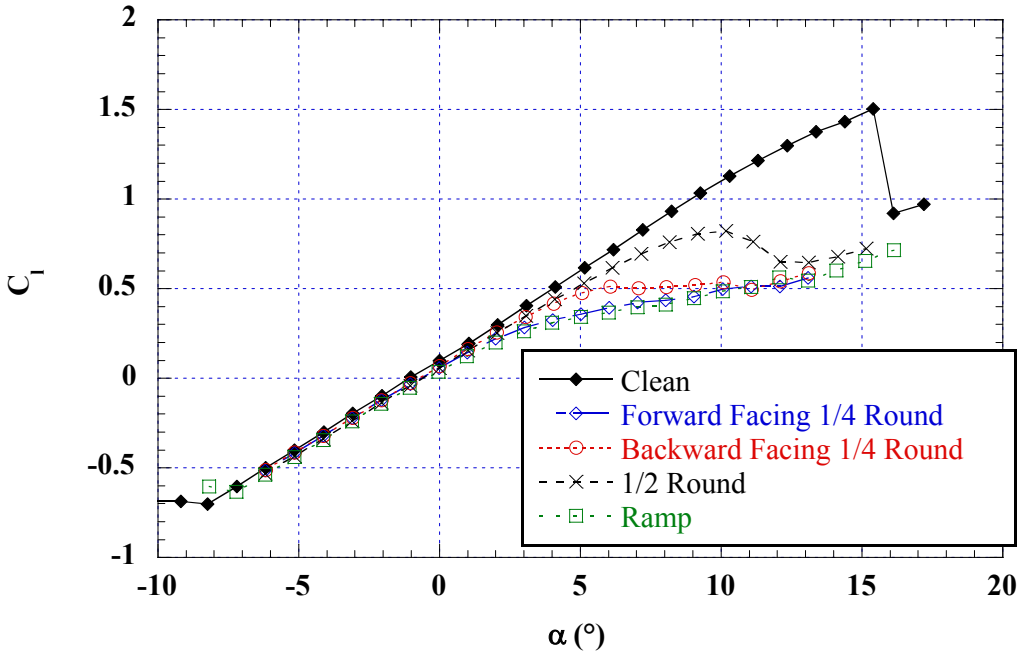

Fig. 4.58a) Lift

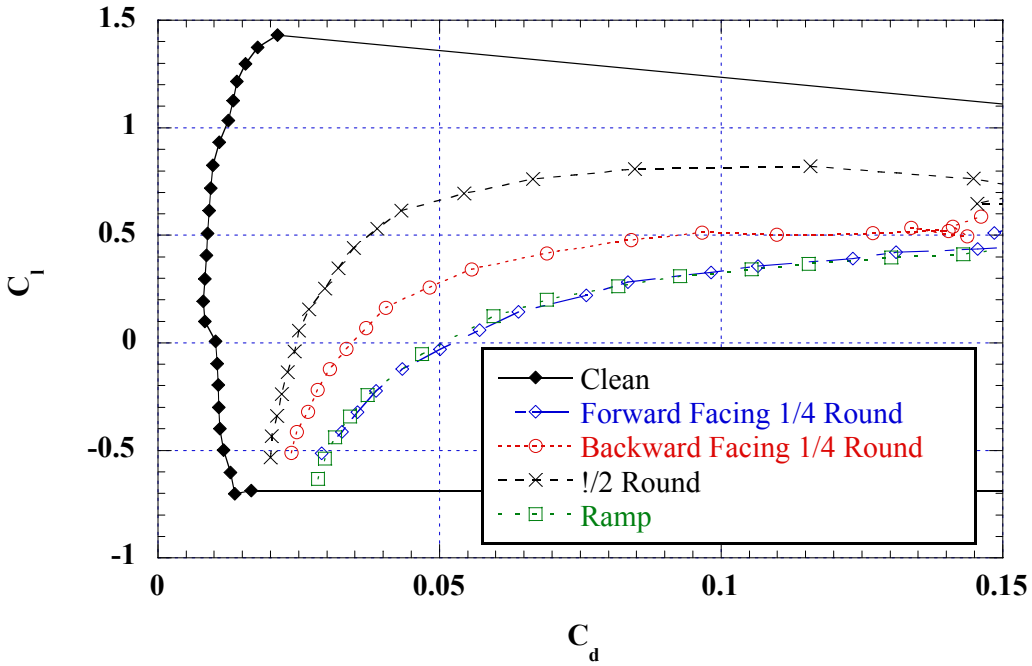

Fig. 4.58b) Drag

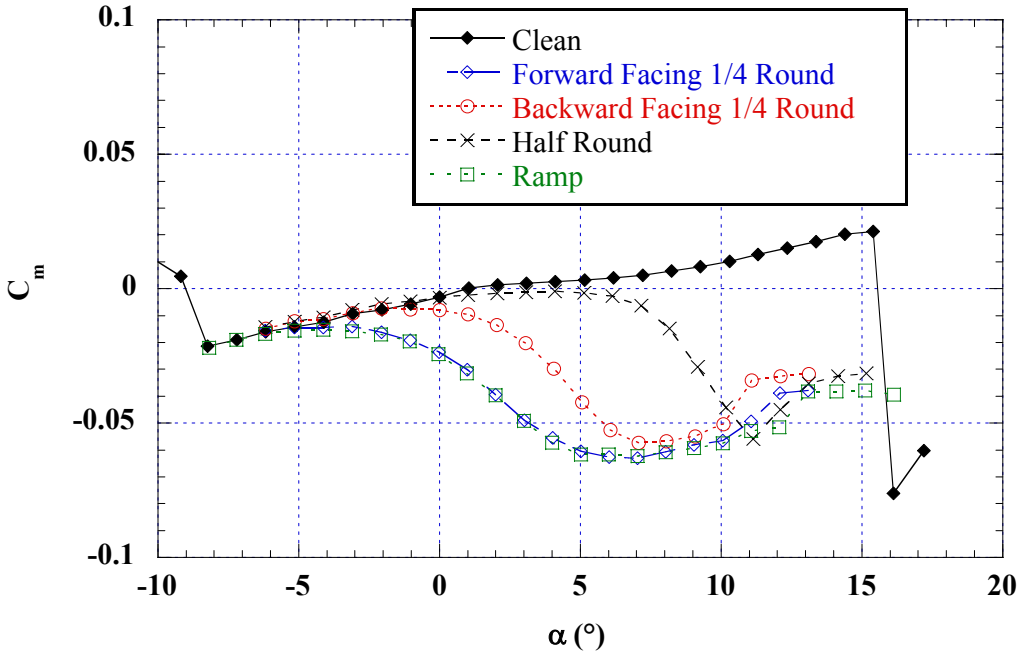

Fig. 4.58c) Pitching moment

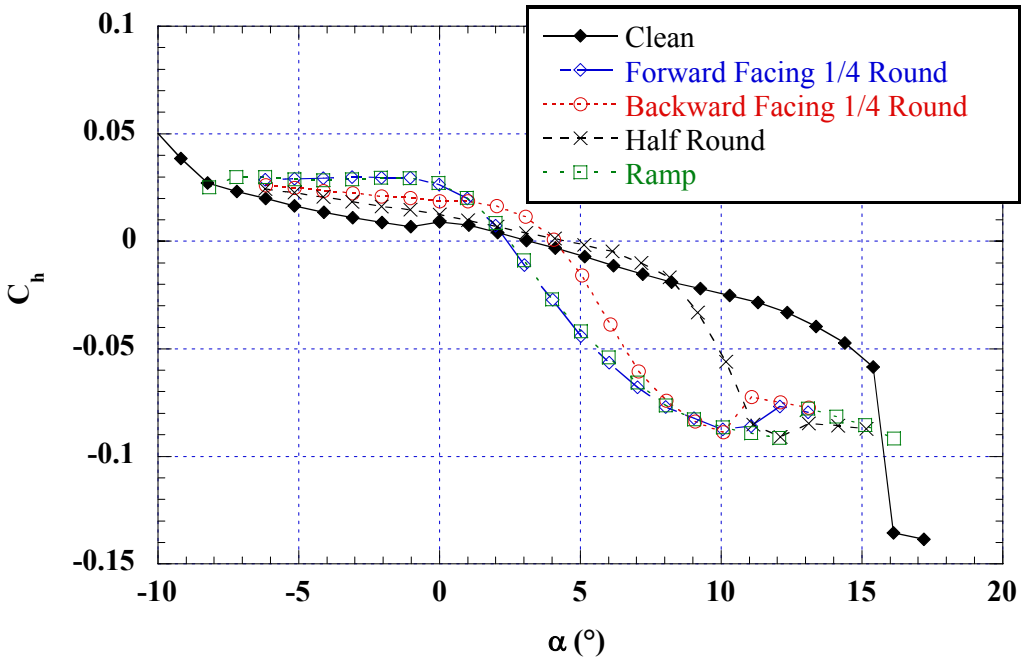

Fig. 4.58d) Flap hinge moment

Fig. 4.58: Effect of simulated ice-shape geometry on aerodynamic coefficients; NACA 23012m; k = 0.25"; ice shapes at x/c = 0.20; boundary layer tripped; Re = 1.8 million.

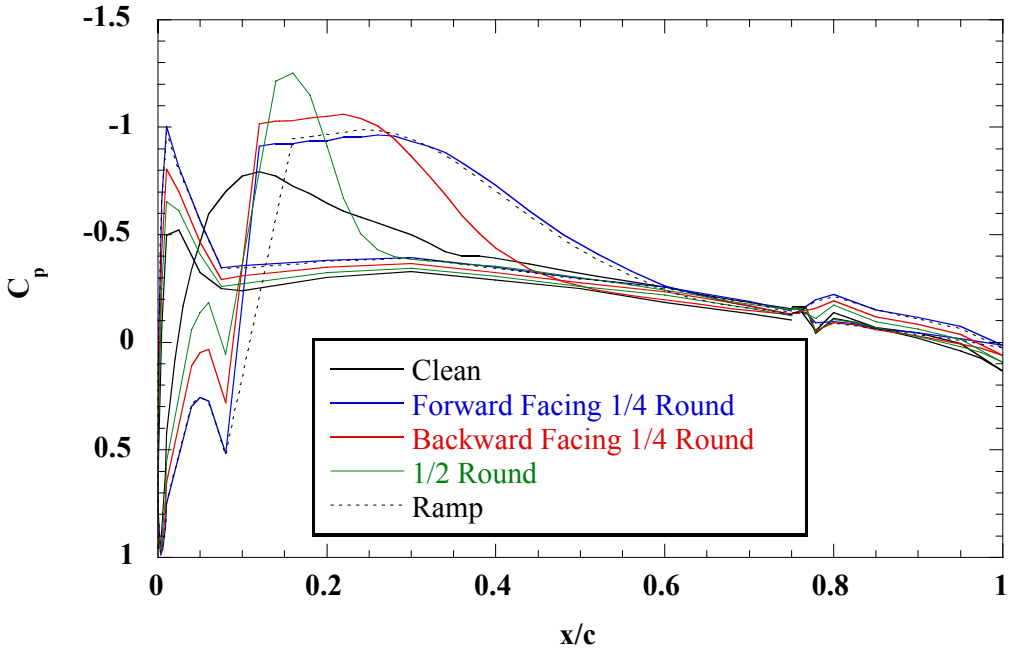

Fig. 4.59a) $\alpha = 0°$

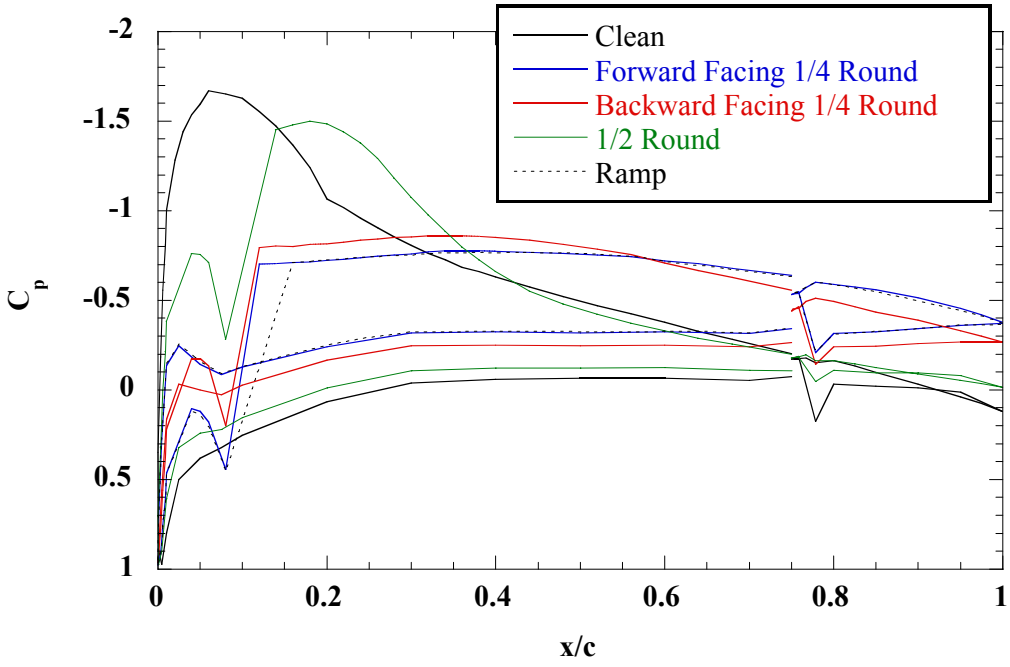

Fig. 4.59b) $\alpha = 5°$

Fig. 4.59: Effect of simulated ice-shape geometry on surface pressure distribution; NACA 23012m; k = 0.25"; ice shapes at x/c = 0.10; boundary layer tripped; Re = 1.8 million.

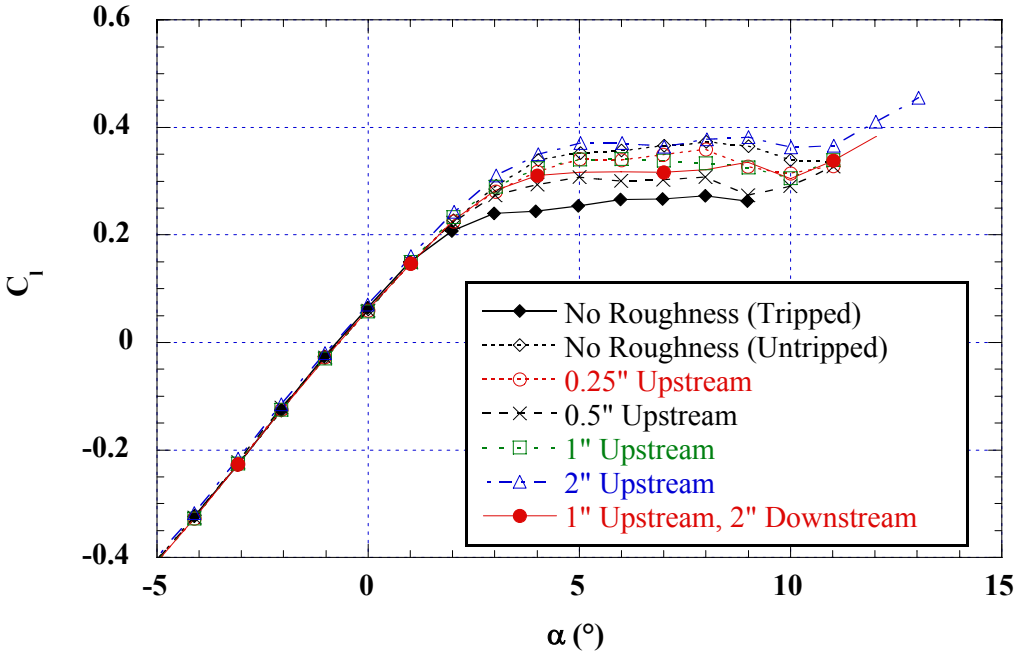

Fig. 4.60a) Lift

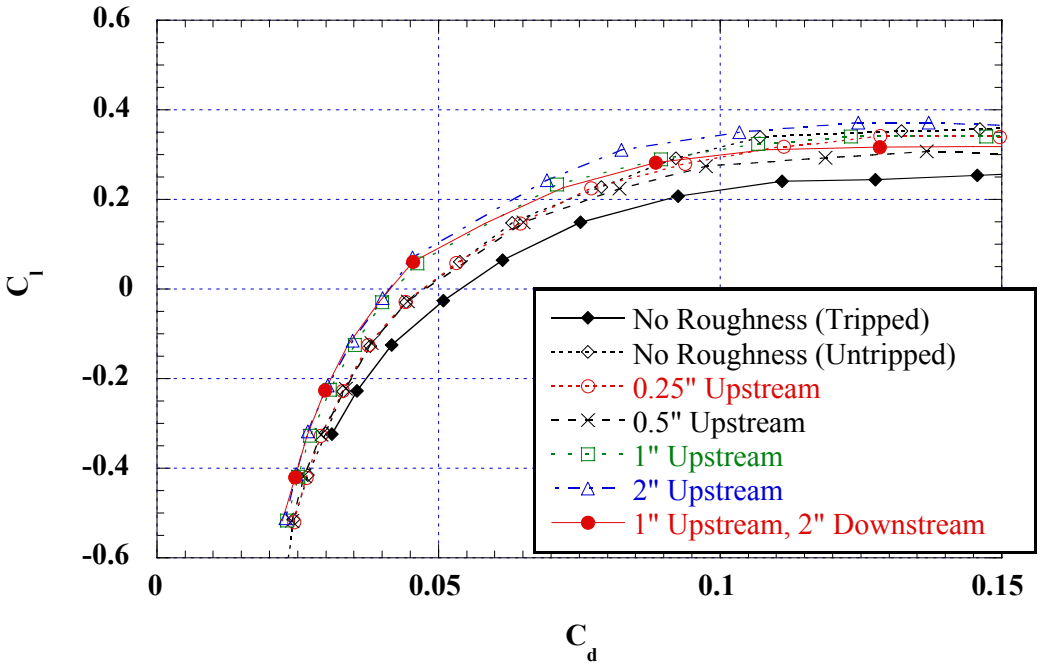

Fig. 4.60b) Drag

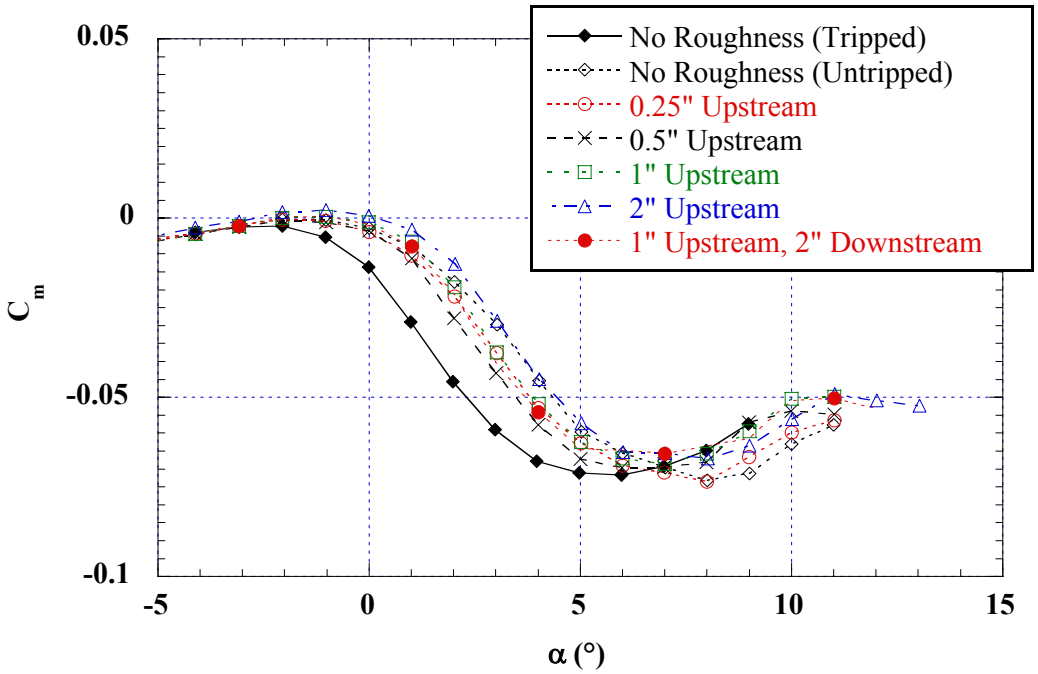

Fig. 4.60c) Pitching moment

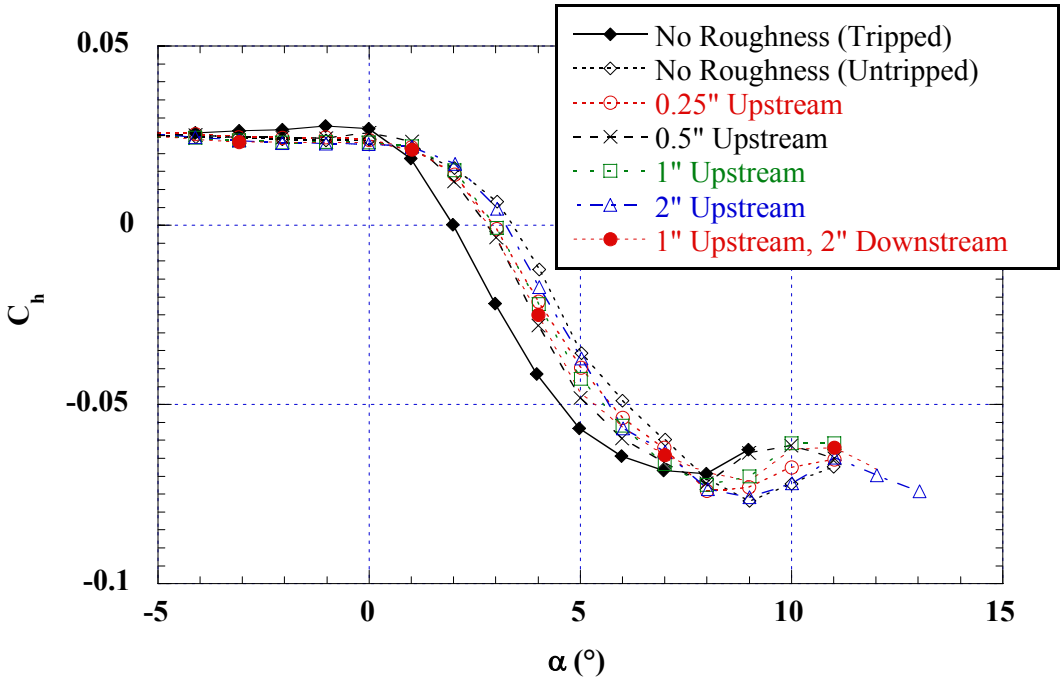

Fig. 4.60d) Flap hinge moment

Fig. 4.60: Effect of roughness in vicinity of ice shape on aerodynamic coefficients; NACA 23012m; k = 0.25" forward facing quarter round at x/c = 0.10; Re = 1.8 million.

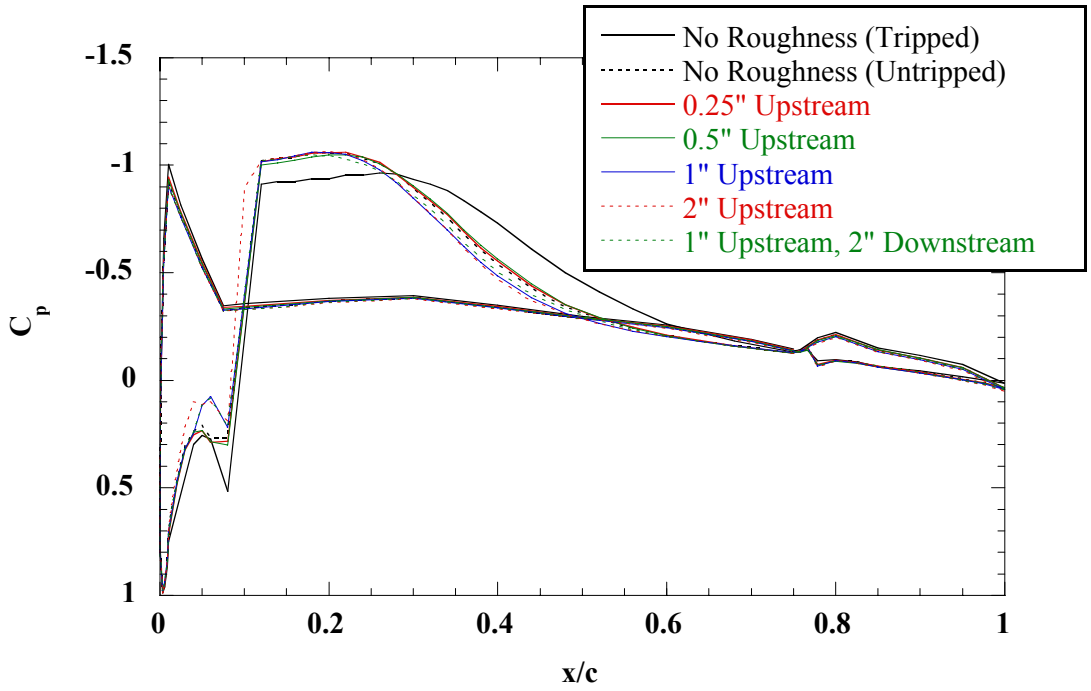

Fig. 4.61a) $a = 0°$

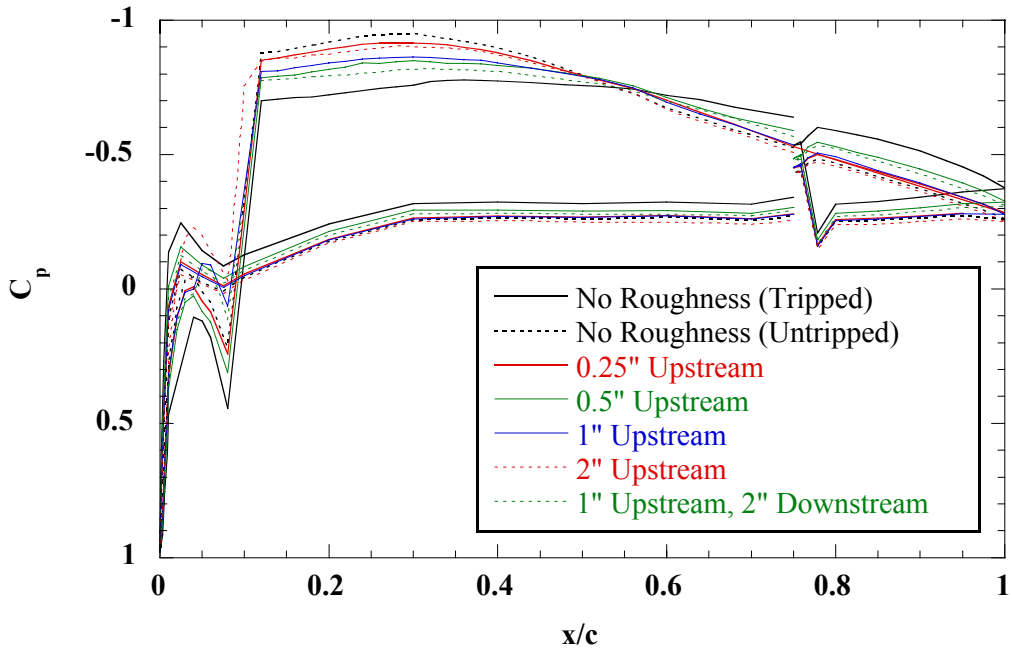

Fig. 4.61b) $a = 5°$

Fig. 4.61: Effect of roughness in vicinity of ice shape on pressure distribution; NACA 23012m; k = 0.25" forward facing quarter round at x/c = 0.10; Re = 1.8 million.

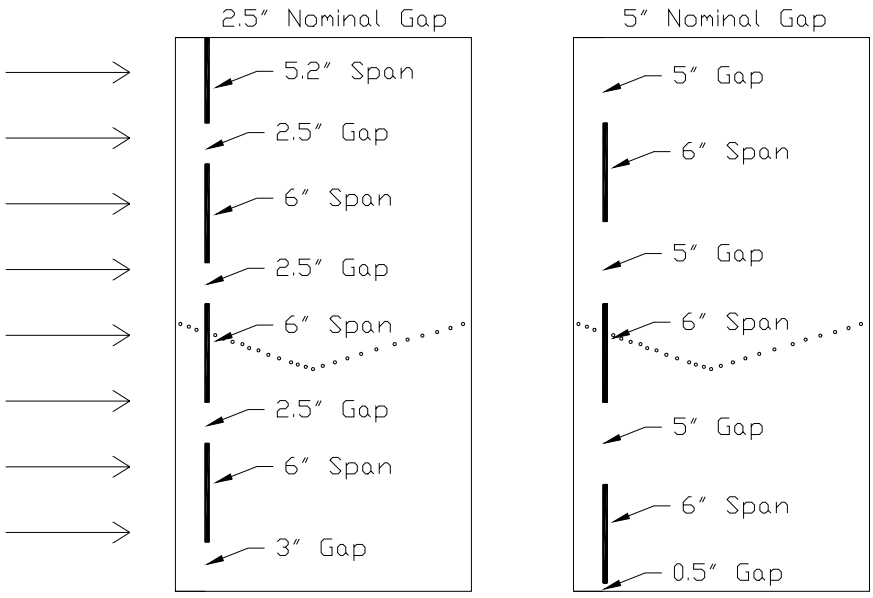

Fig. 4.62: Spanwise gaps tested on the NACA 23012m; k = 0.25” forward facing quarter round at x/c = 0.10.

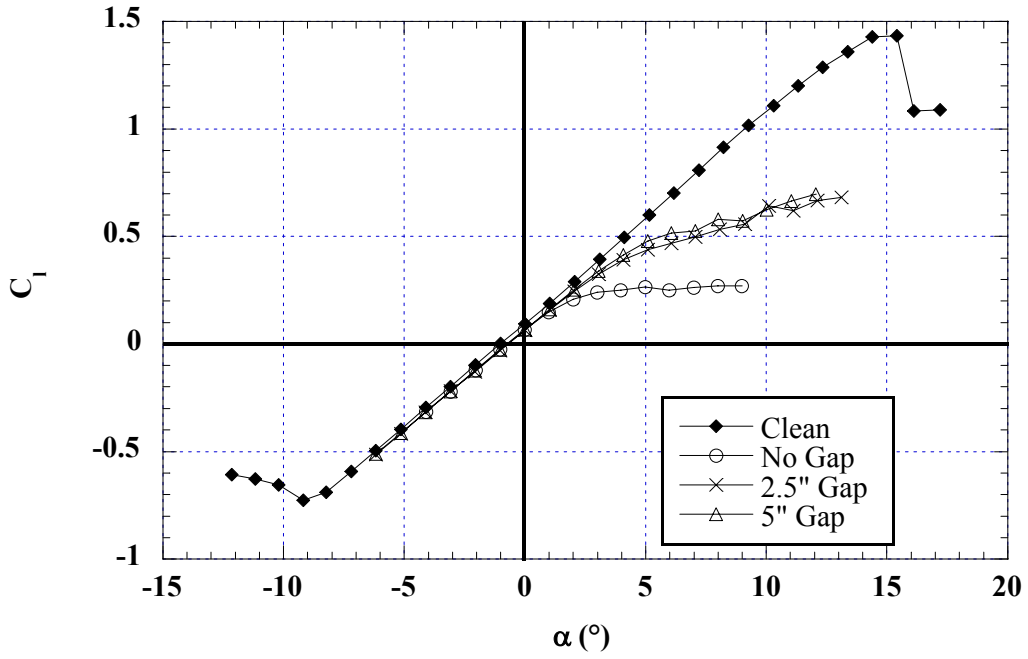

Fig. 4.63a) Lift

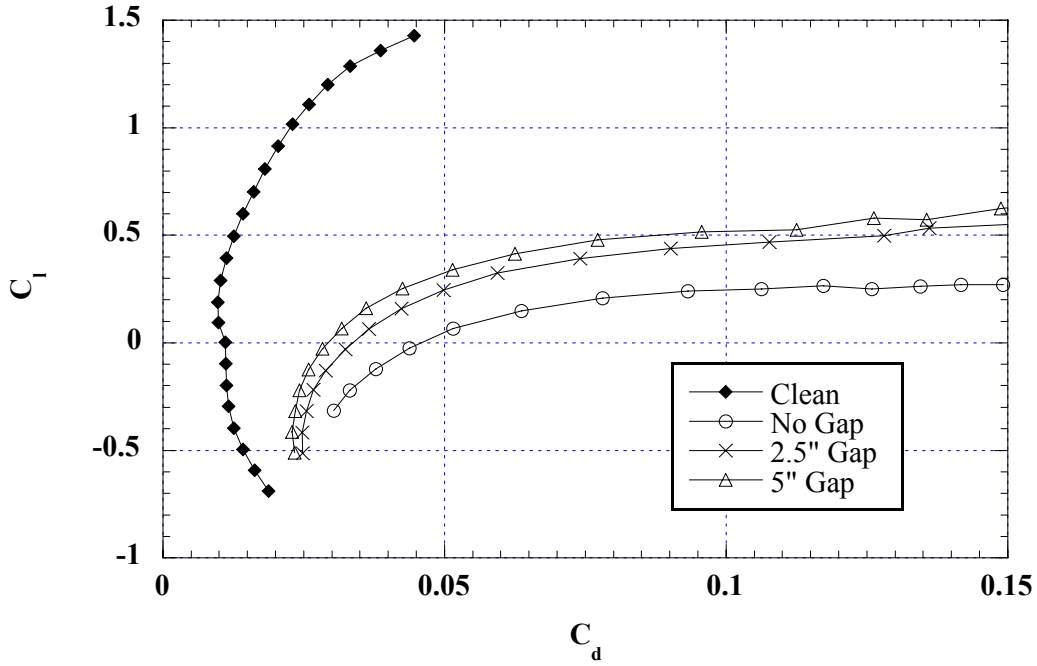

Fig. 4.63b) Drag

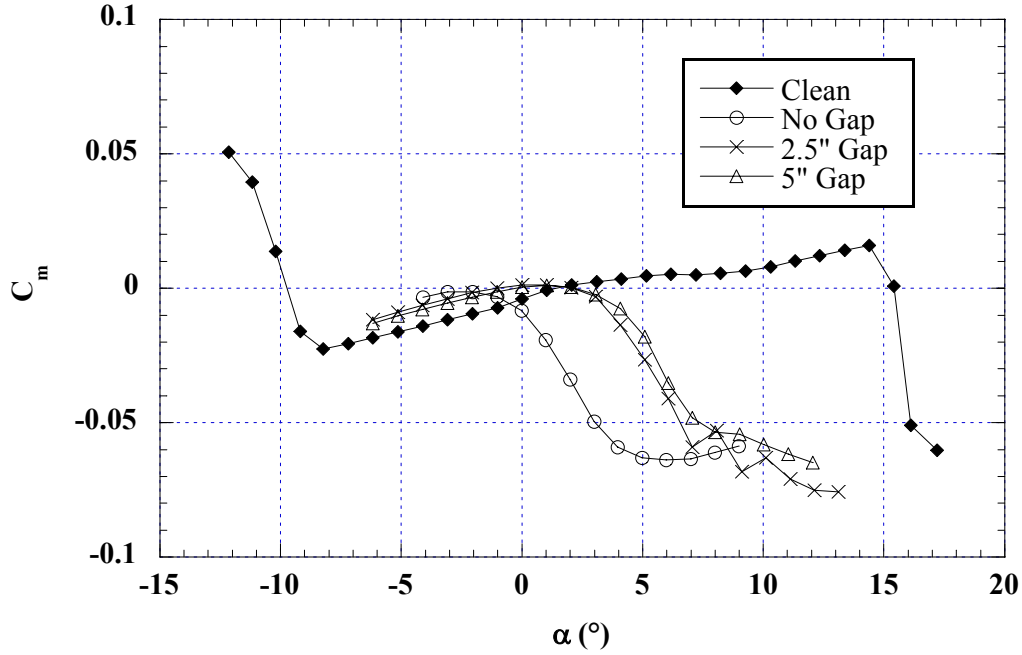

Fig. 4.63c) Pitching moment

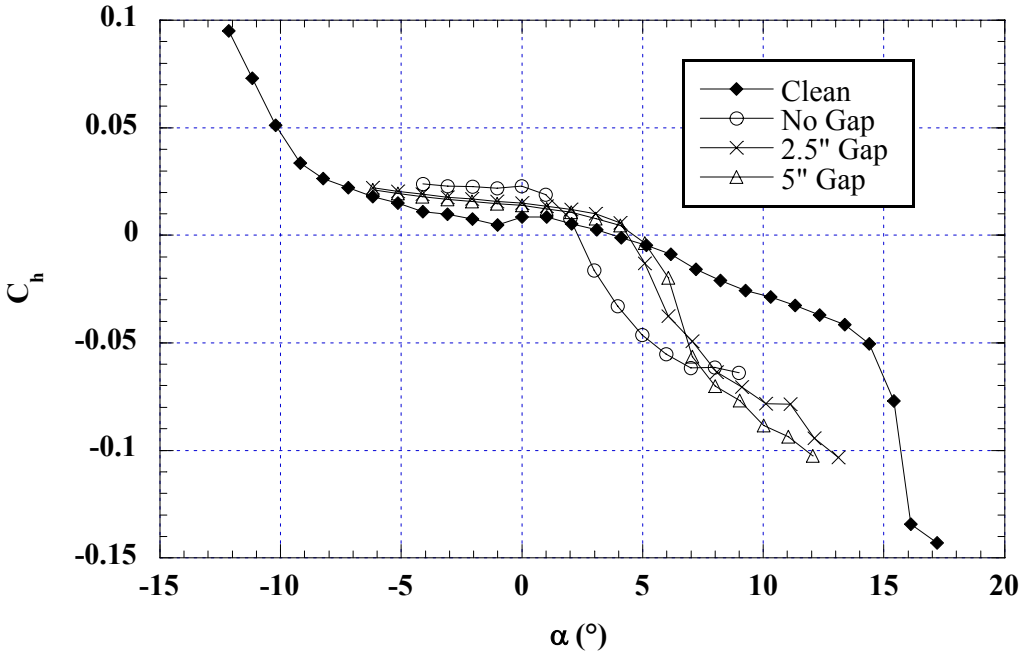

Fig. 4.63c) Flap hinge moment

Fig. 4.63: Effect of spanwise gaps on aerodynamic coefficients; NACA 23012m; k = 0.25” forward facing quarter round at x/c = 0.10; boundary layer tripped; Re = 1.8 million.

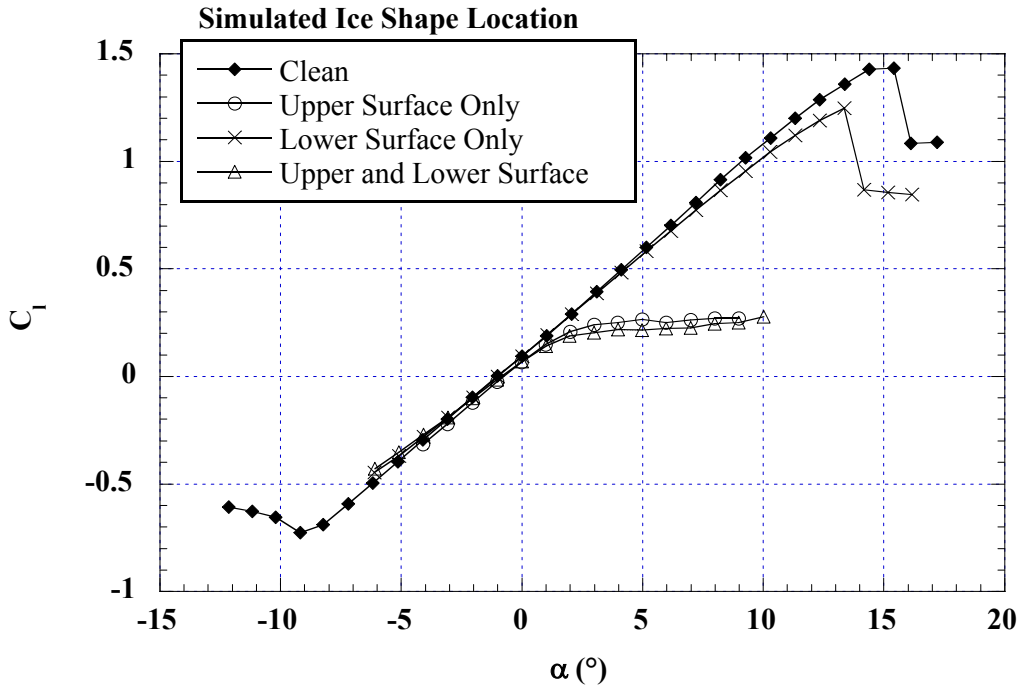

Fig. 4.64a) Lift

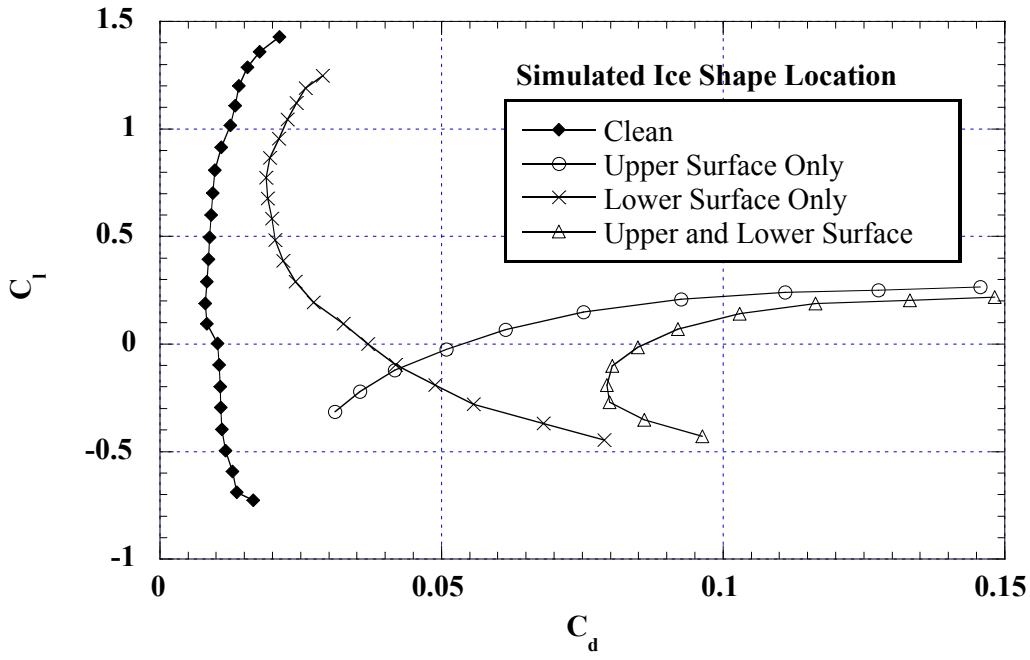

Fig. 4.64b) Drag

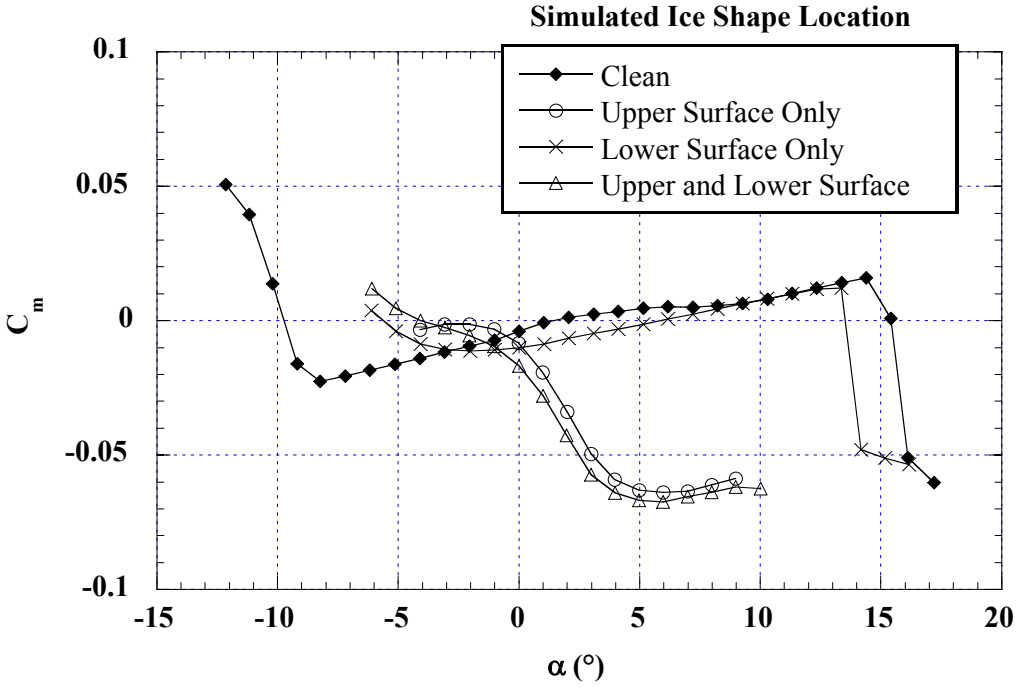

Fig. 4.64c) Pitching moment

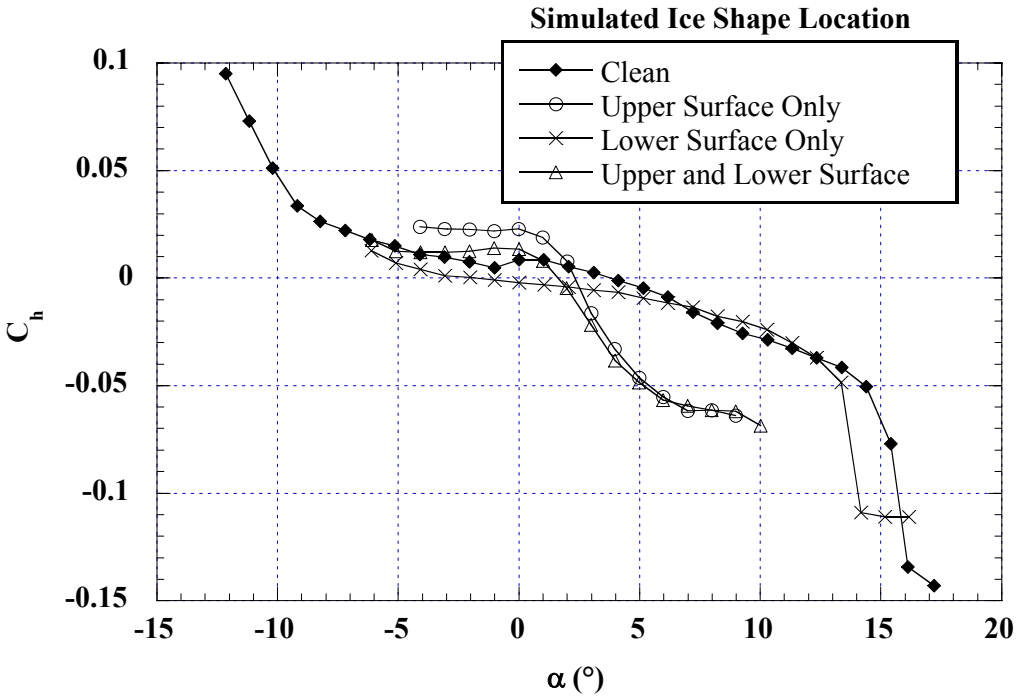

Fig. 4.64d) Flap hinge moment

Fig. 4.64: Effect of lower surface ice shapes on aerodynamic coefficients; NACA 23012m; k = 0.25" forward facing quarter round at x/c = 0.10 on both upper and lower surface; boundary layer tripped; Re = 1.8 million.

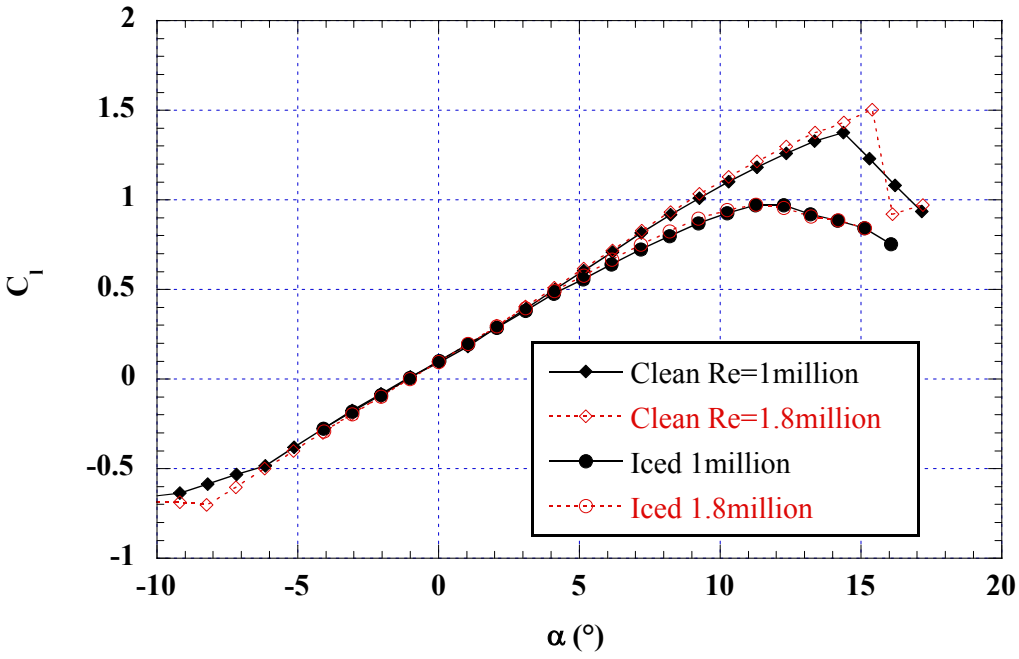

Fig. 4.65a) Lift

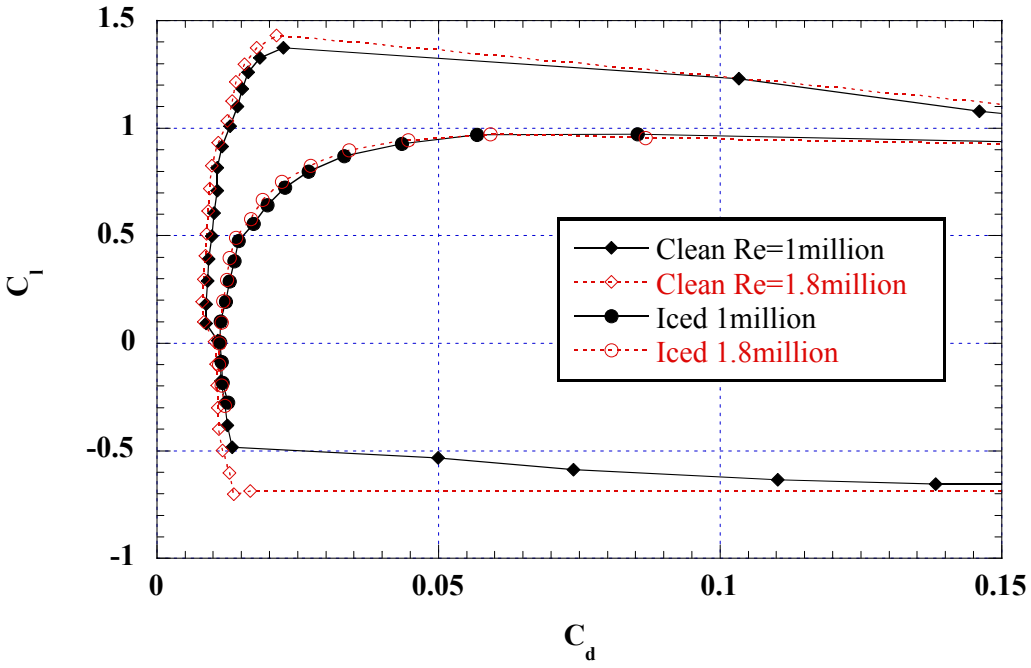

Fig. 4.65b) Drag

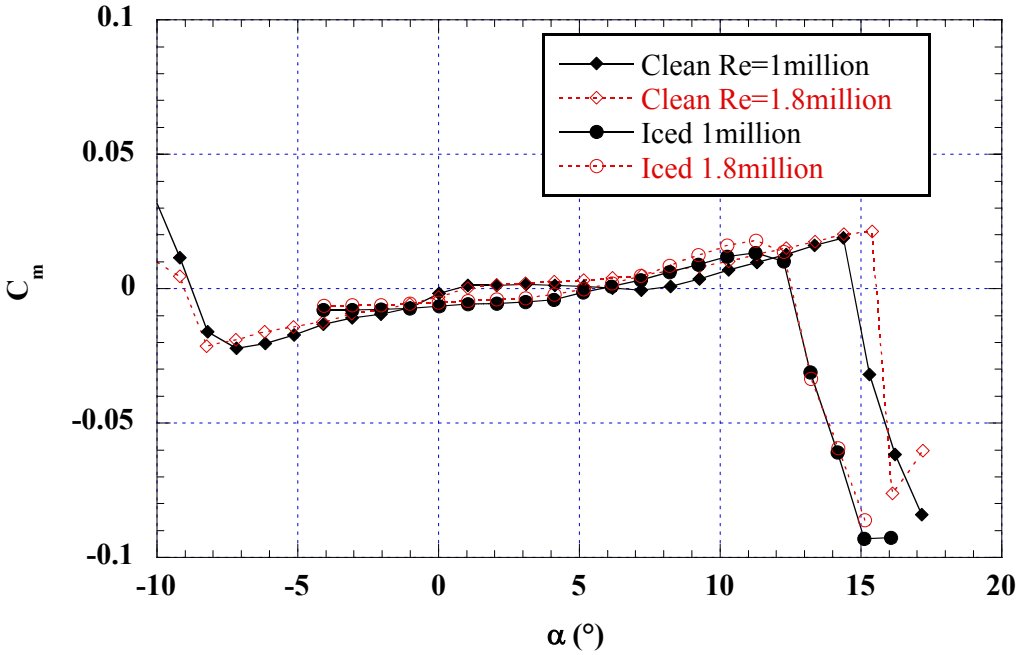

Fig. 4.65c) Pitching moment

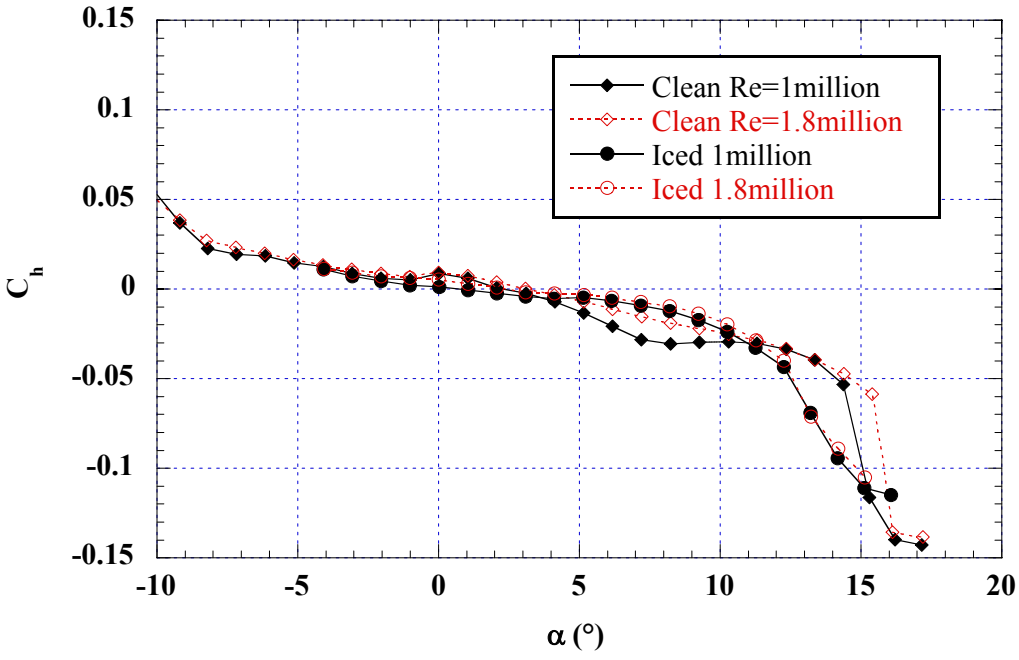

Fig. 4.65d) Flap hinge moment

Fig. 4.65: Effect of Reynolds number on aerodynamic coefficients; NACA 23012m; k = 0.25” forward facing quarter round at x/c = 0.00; boundary layer not tripped.

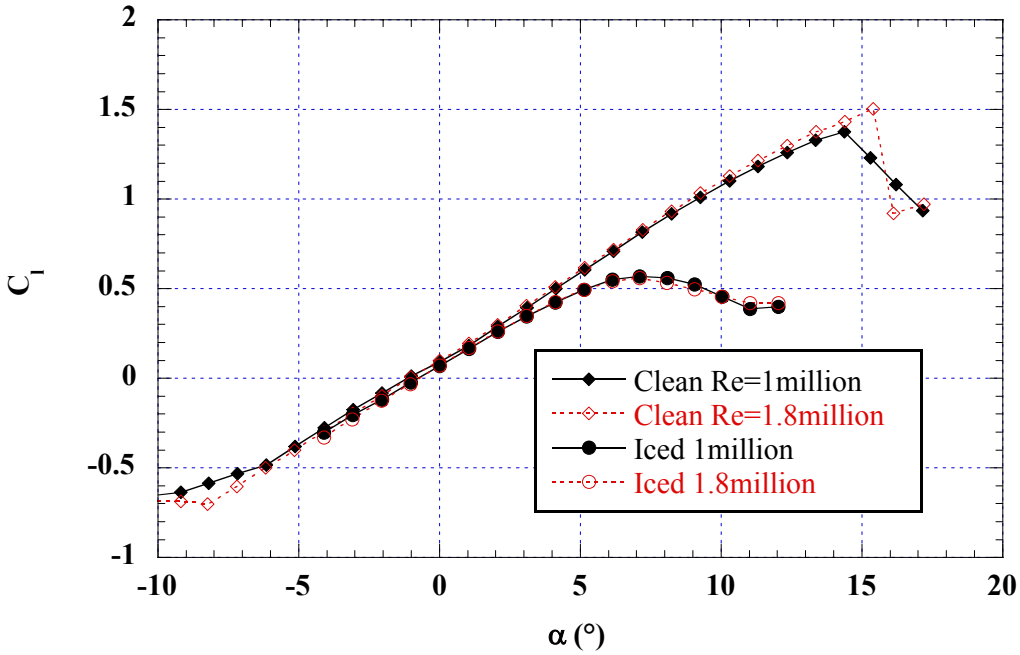

Fig. 4.66a) Lift

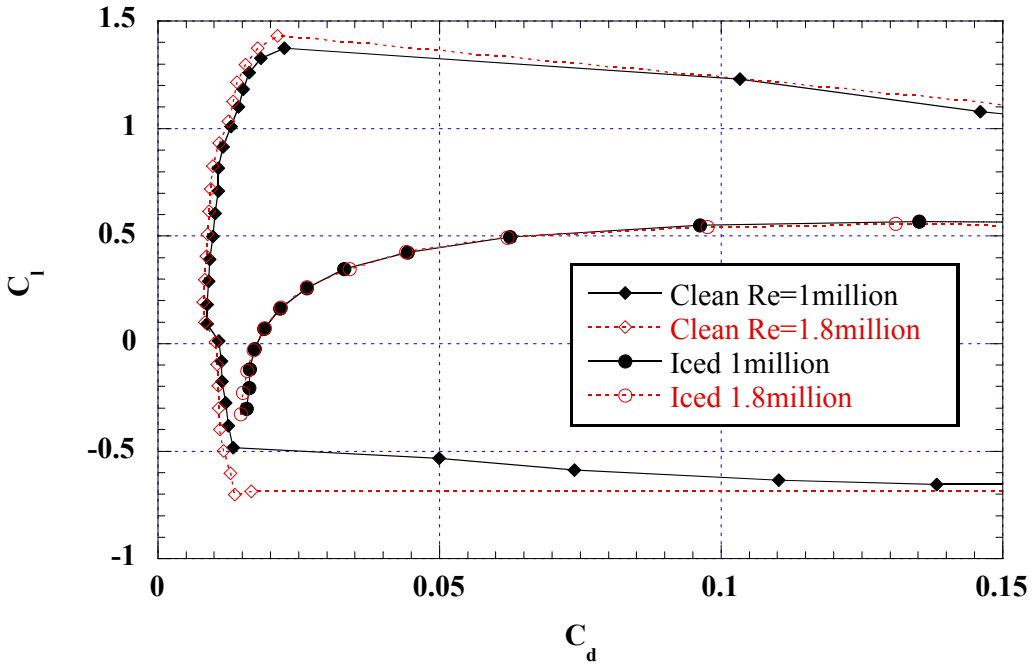

Fig. 4.66b) Drag

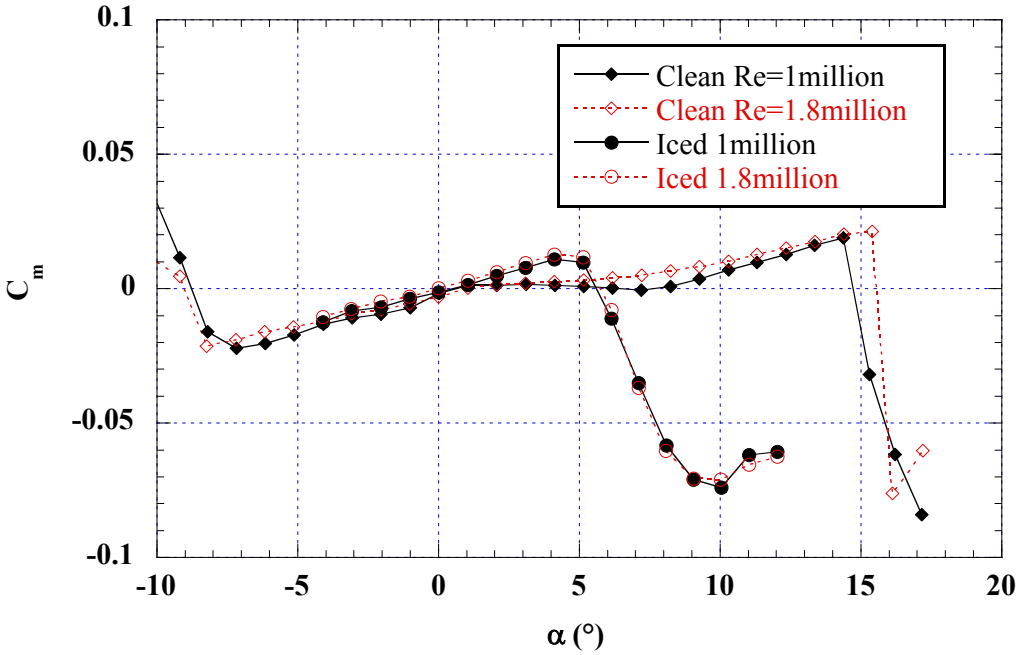

Fig. 4.66c) Pitching moment

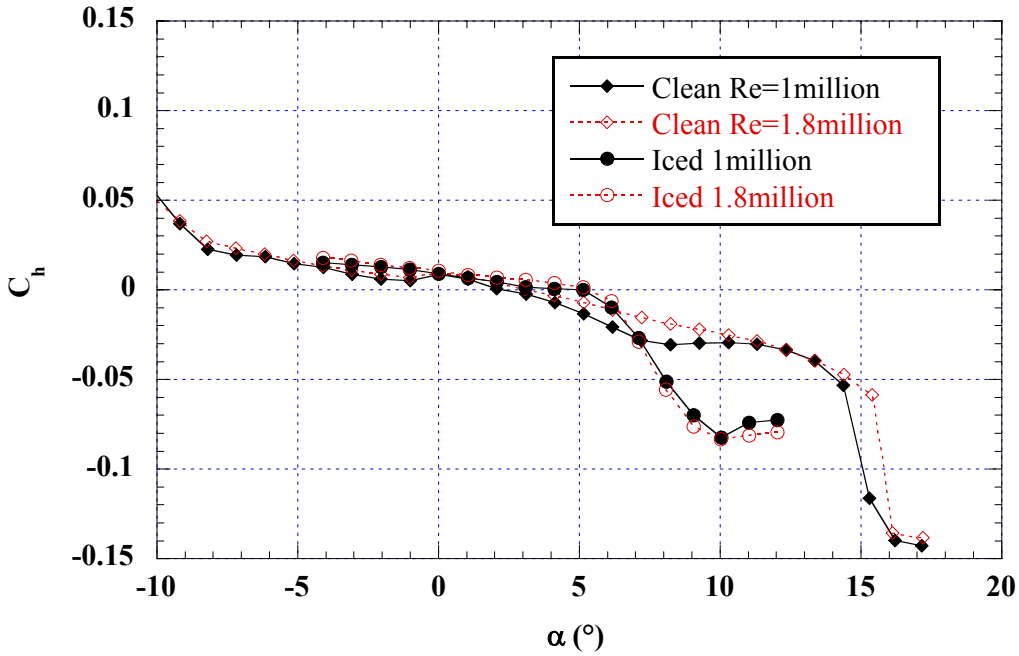

Fig. 4.66d) Flap hinge moment

Fig. 4.66: Effect of Reynolds number on aerodynamic coefficients; NACA 23012m; k = 0.25" forward facing quarter round at x/c = 0.02; boundary layer not tripped.

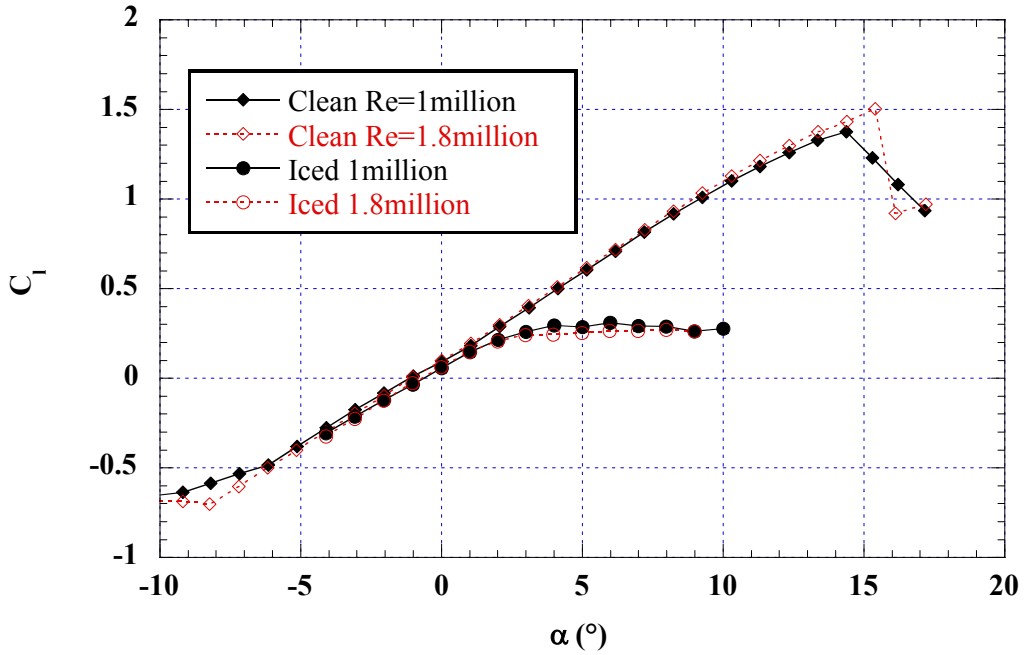

Fig. 4.67a) Lift

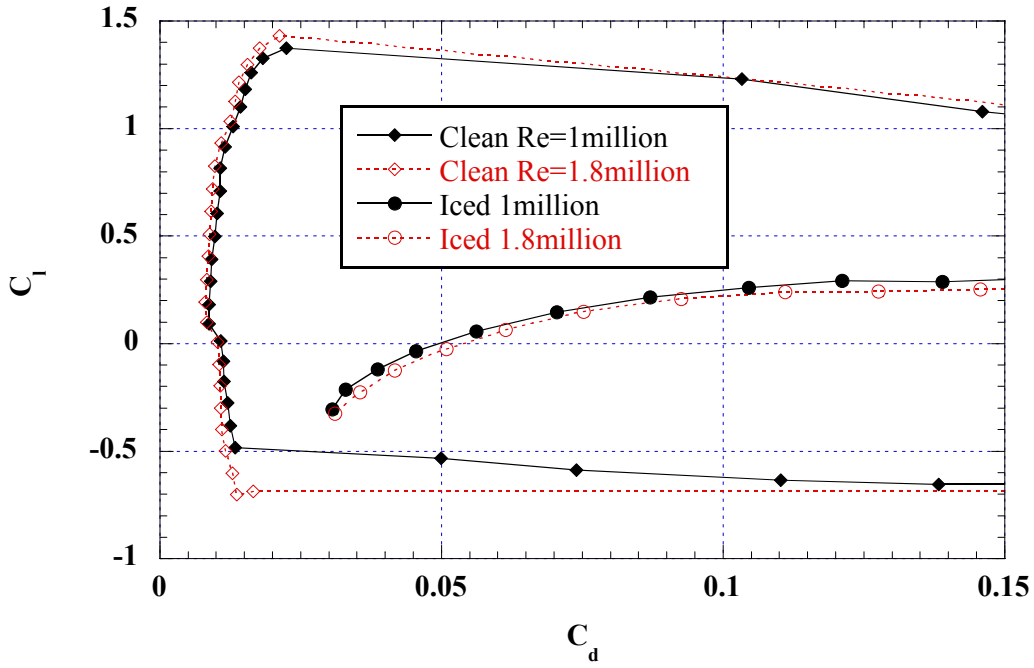

Fig. 4.67b) Drag

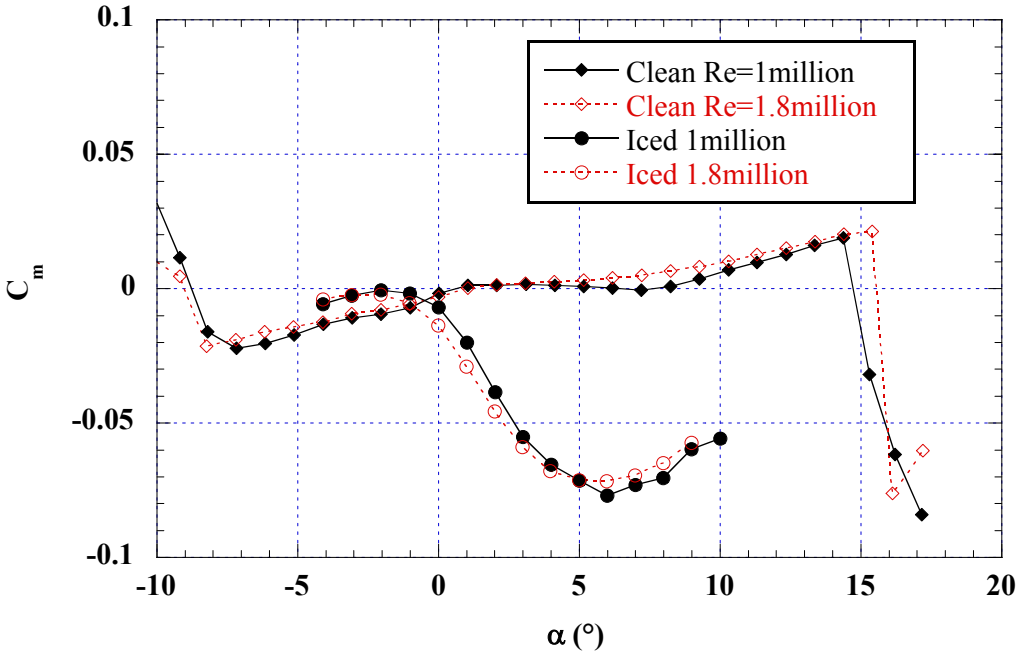

Fig. 4.67c) Pitching moment

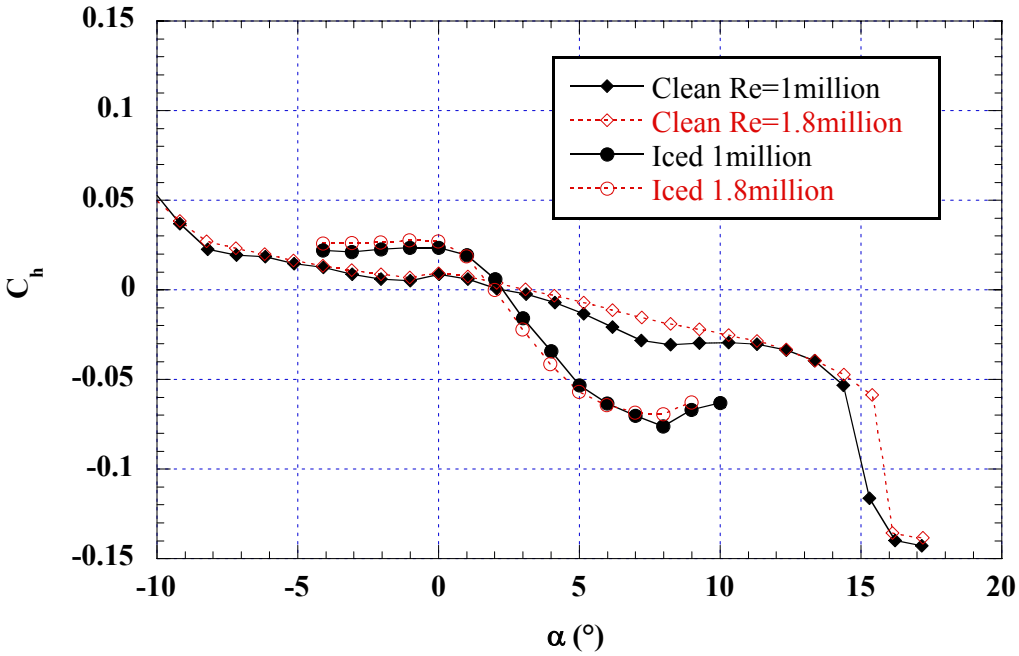

Fig. 4.67d) Flap hinge moment

Fig. 4.67: Effect of Reynolds number on aerodynamic coefficients; NACA 23012m; k = 0.25" forward facing quarter round at x/c = 0.10; boundary layer tripped.

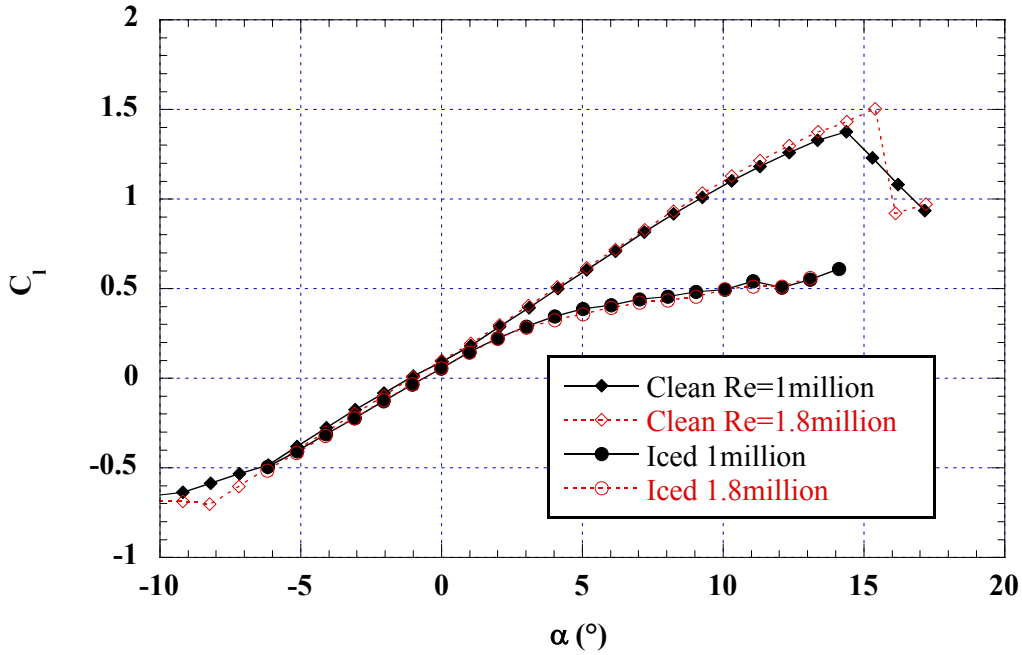

Fig. 4.68a) Lift

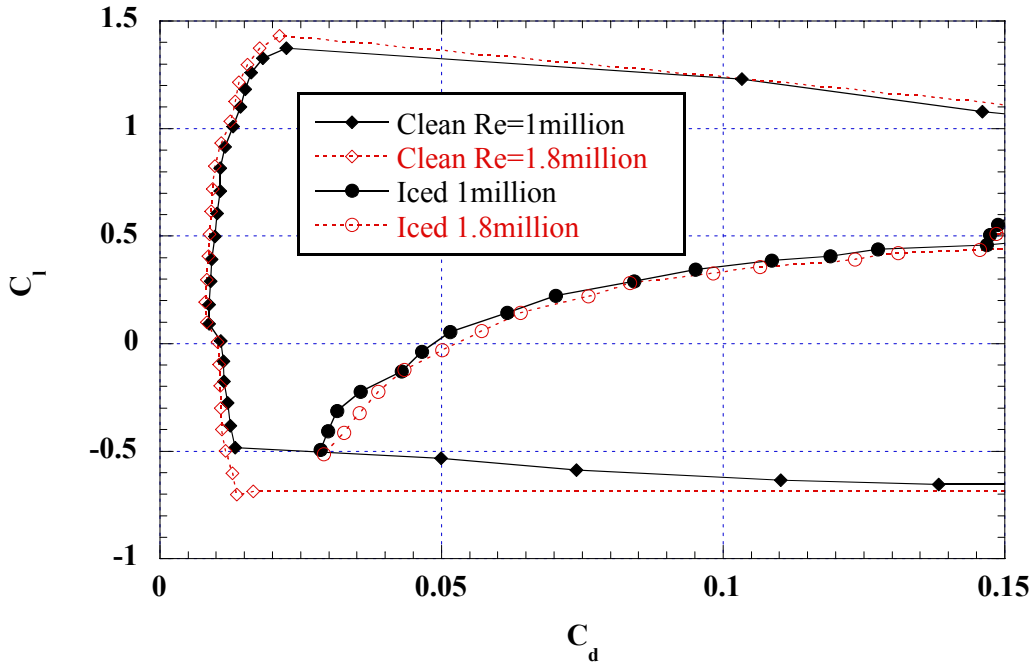

Fig. 4.68b) Drag

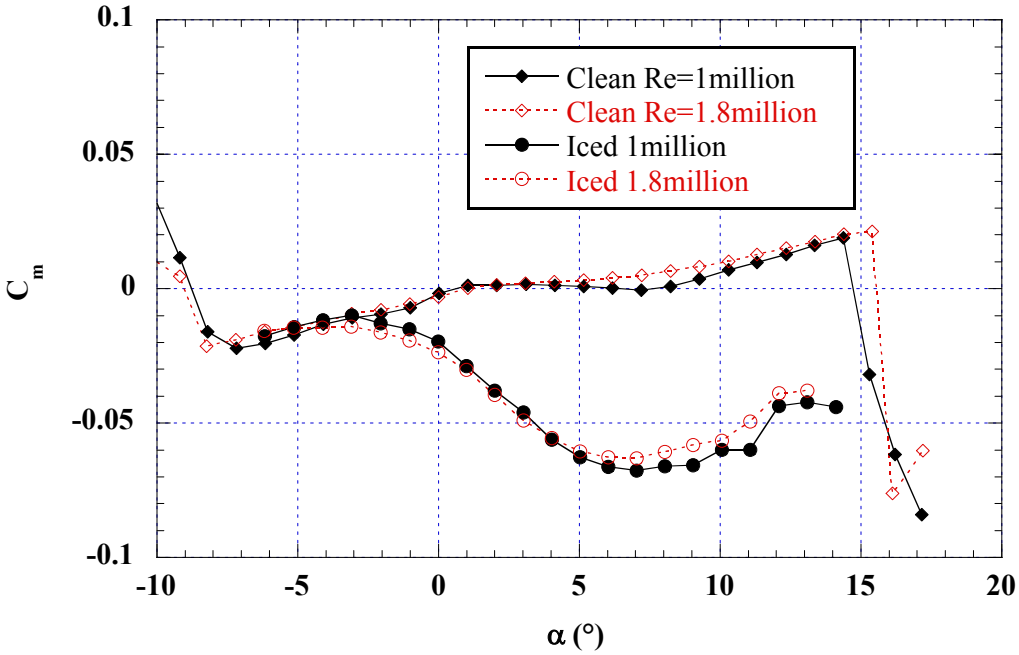

Fig. 4.68c) Pitching moment

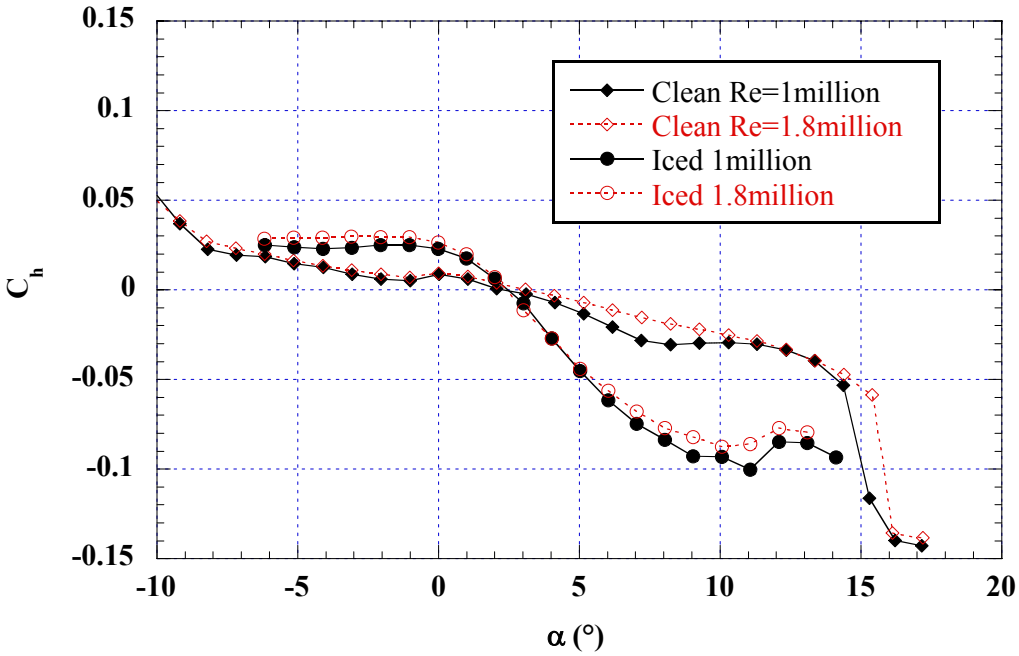

Fig. 4.68a) Flap hinge moment

Fig. 4.68: Effect of Reynolds number on aerodynamic coefficients; NACA 23012m; k = 0.25" forward facing quarter round at x/c = 0.20; boundary layer tripped.

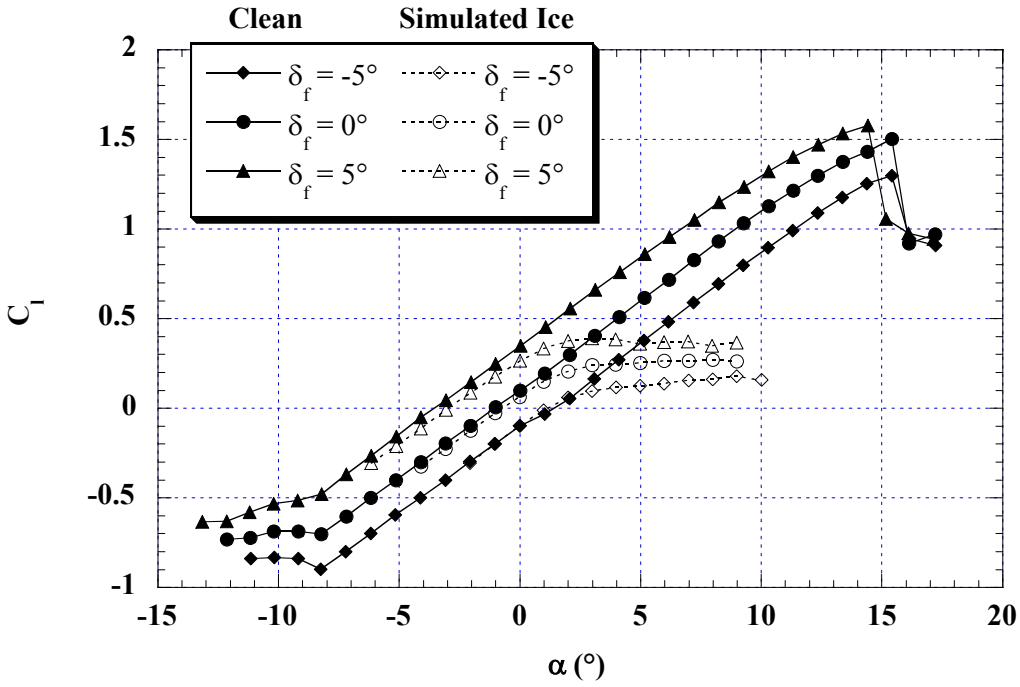

Fig. 4.69a) Lift

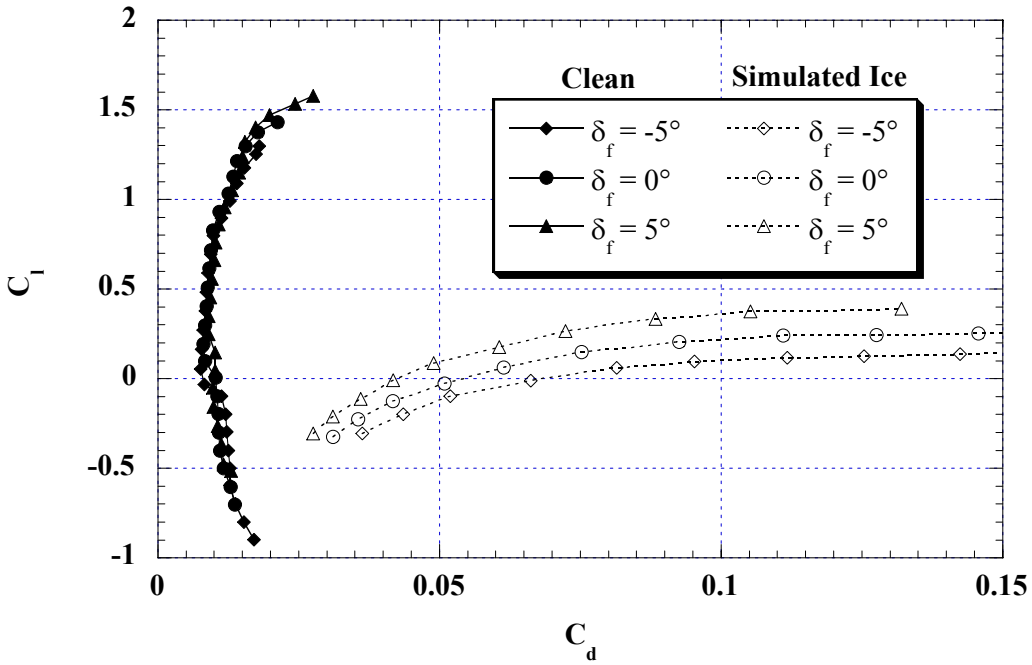

Fig. 4.69b) Drag

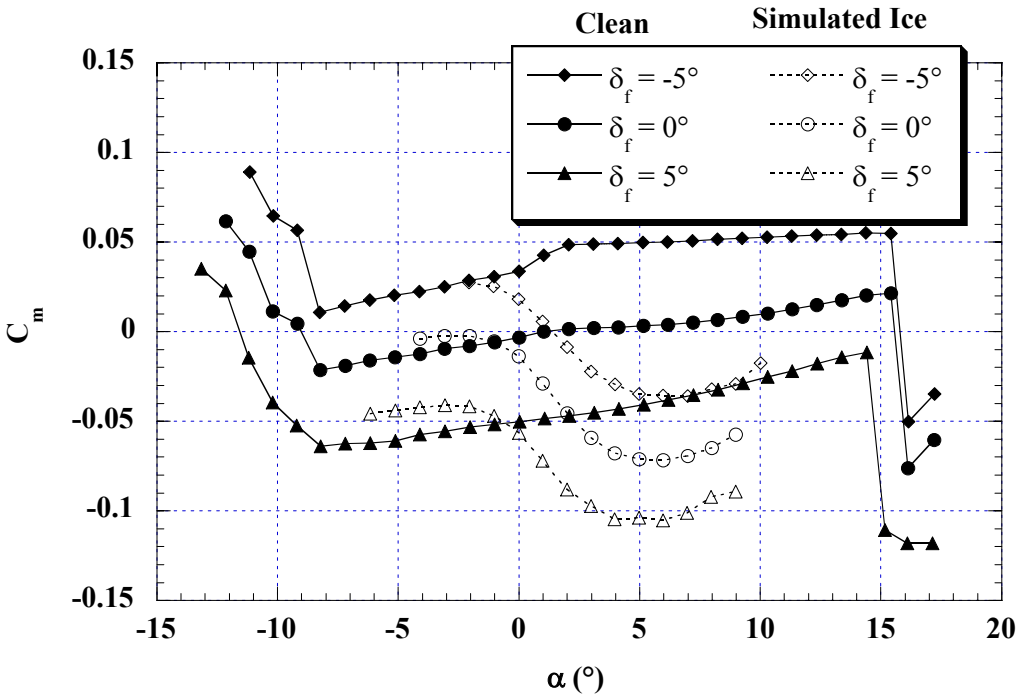

Fig. 4.69c) Pitching moment

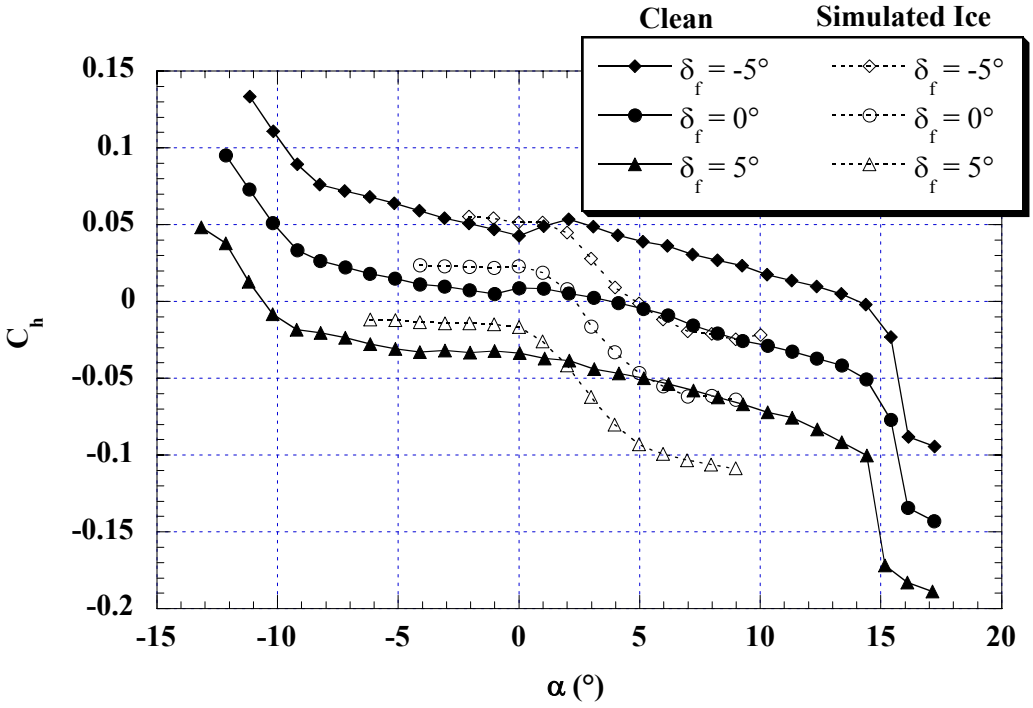

Fig. 4.69d) Flap hinge moment

Fig. 4.69: Effect of flap deflection on iced-airfoil aerodynamic coefficients; NACA 23012m; k = 0.25" forward facing quarter round at x/c = 0.10; boundary layer tripped.

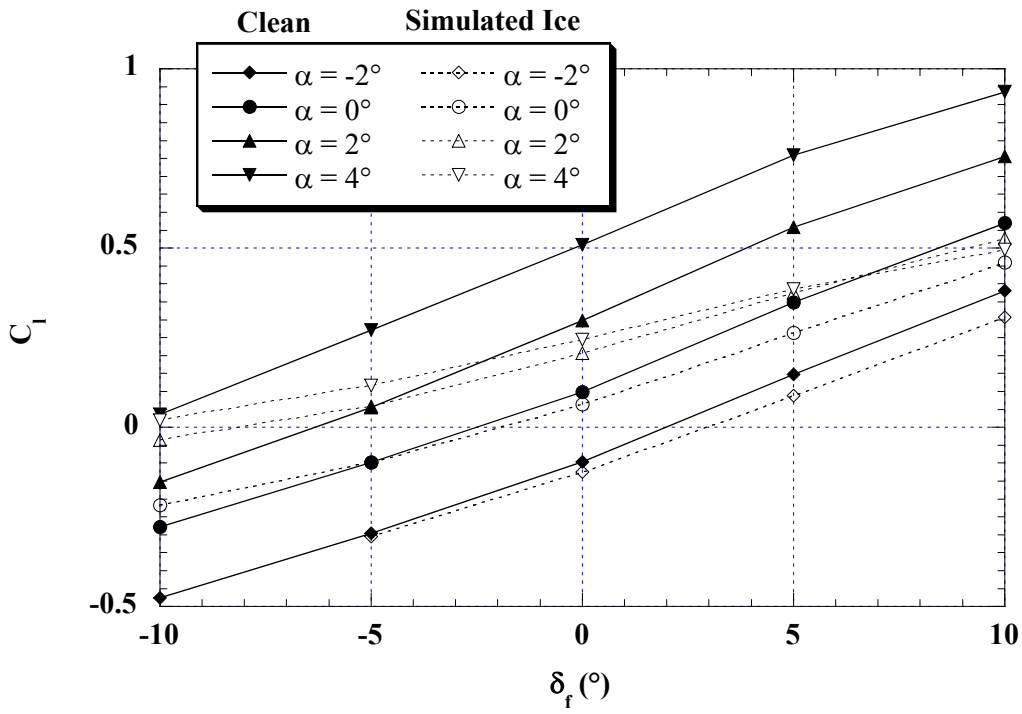

Fig. 4.70: Effect of simulated ridge ice on flap effectiveness; NACA 23012m; k = 0.25" forward facing quarter round at x/c = 0.10; boundary layer tripped.

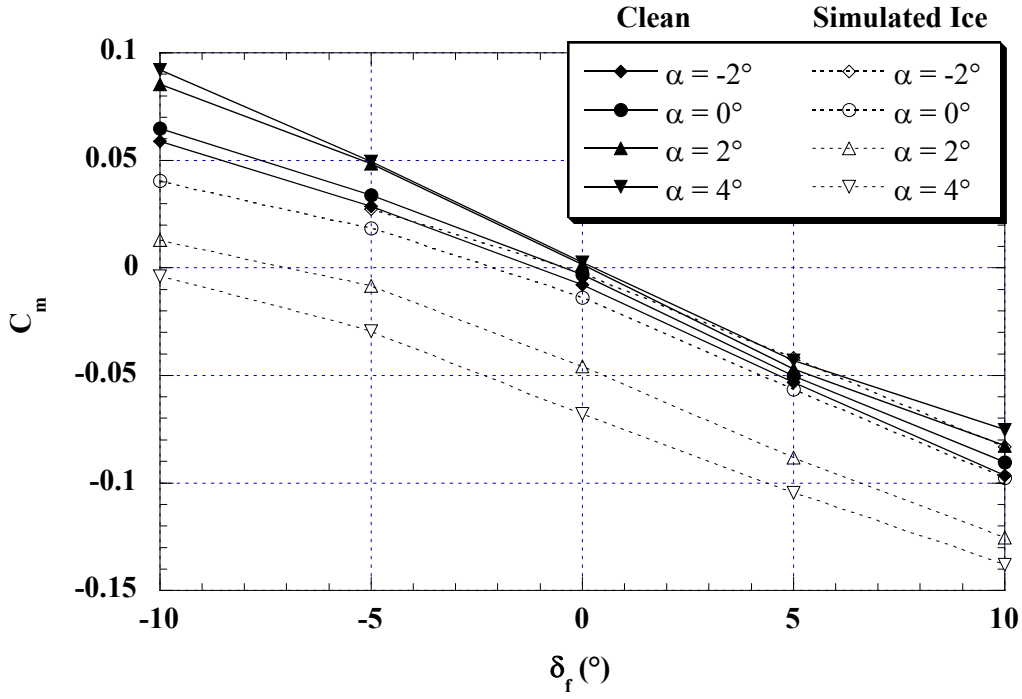

Fig. 4.71: Effect of simulated ridge ice on flap effectiveness; NACA 23012m; k = 0.25" forward facing quarter round at x/c = 0.10; boundary layer tripped.

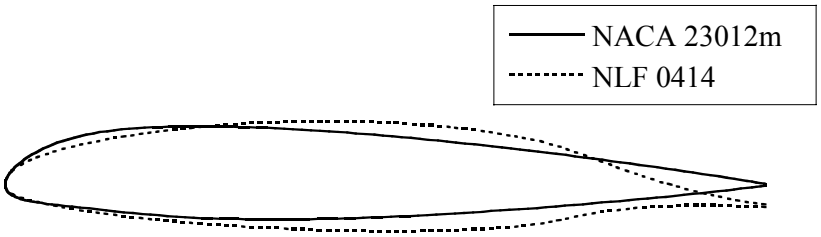

Fig. 4.72: Airfoil-geometry comparison.

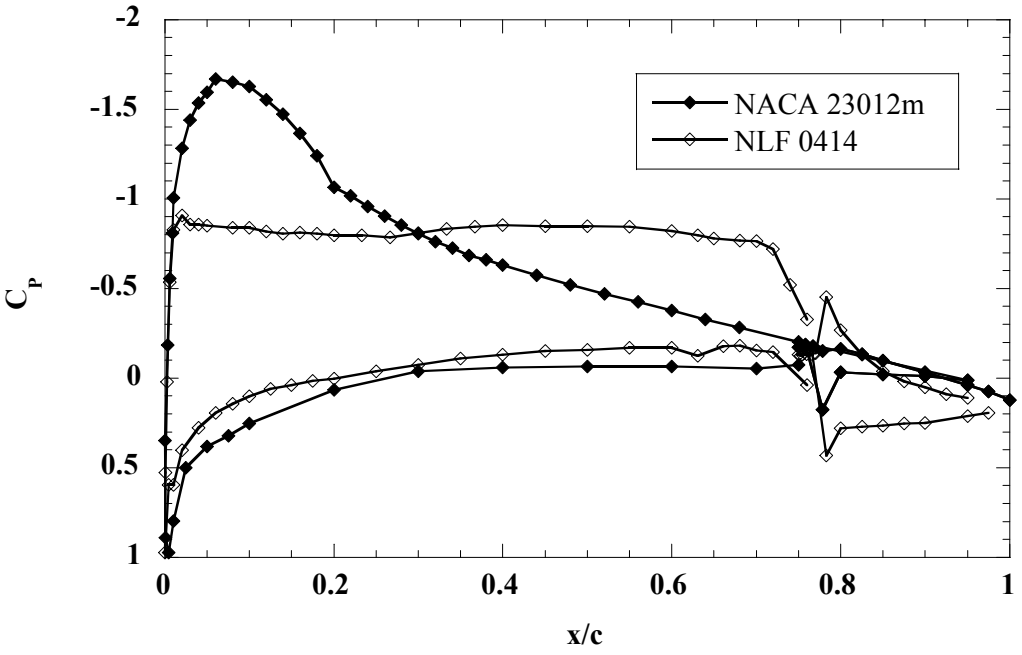

Fig. 4.73: Comparison of clean-model pressure distribution at matched lift coefficient; $C_l = 0.60$; $Re = 1.8$ million; (NACA 23012m $\alpha = 5.15°$; NLF 0414 $\alpha = 1.06°$).

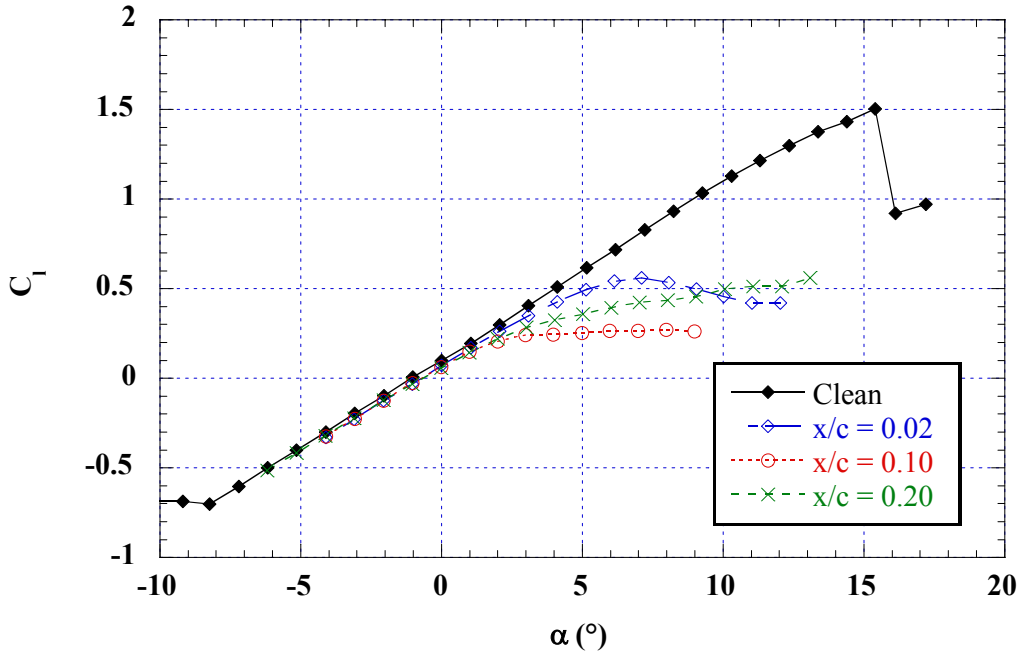

Fig. 4.74a) NACA 23012m

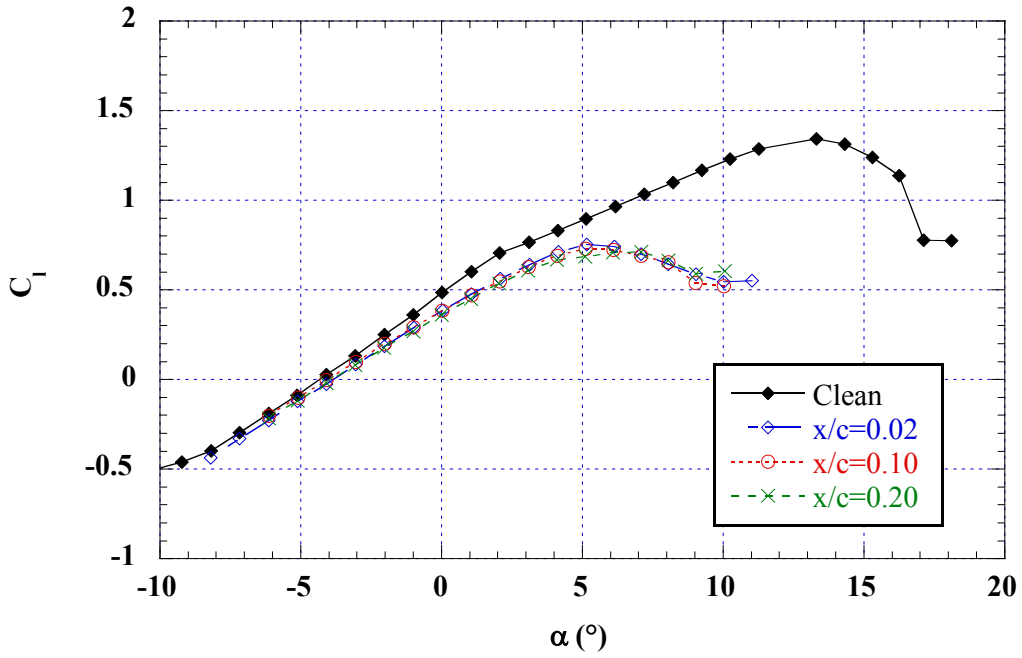

Fig. 4.74b) NLF 0414

Fig. 4.74: Effect of ridge-ice location on lift. *Re* = 1.8 million; forward-facing quarter round; $k = 0.25$".

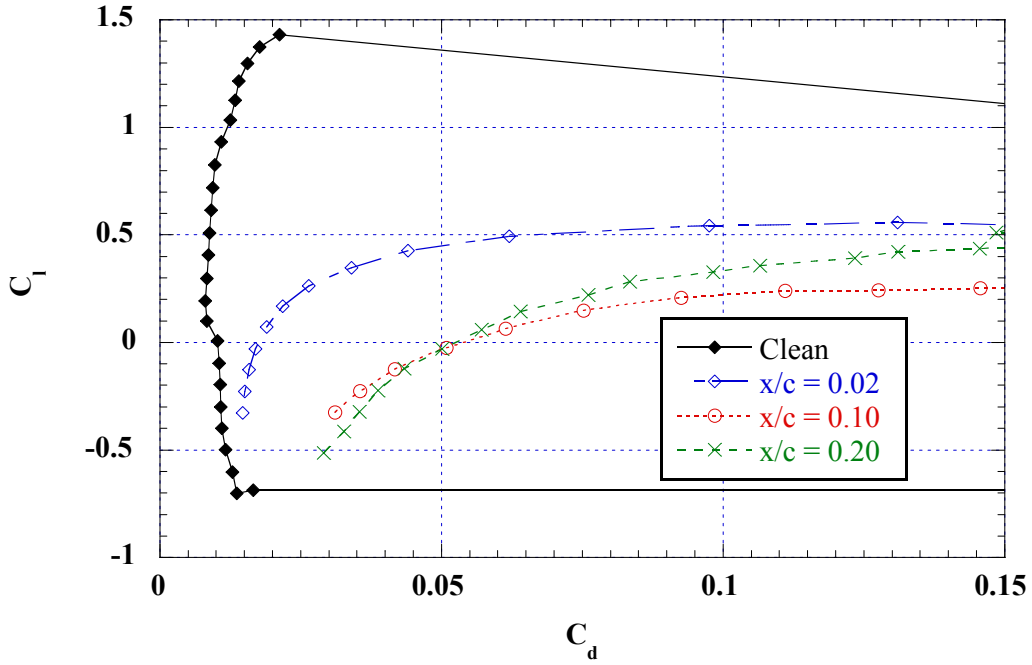

Fig. 4.75a) NACA 23012m

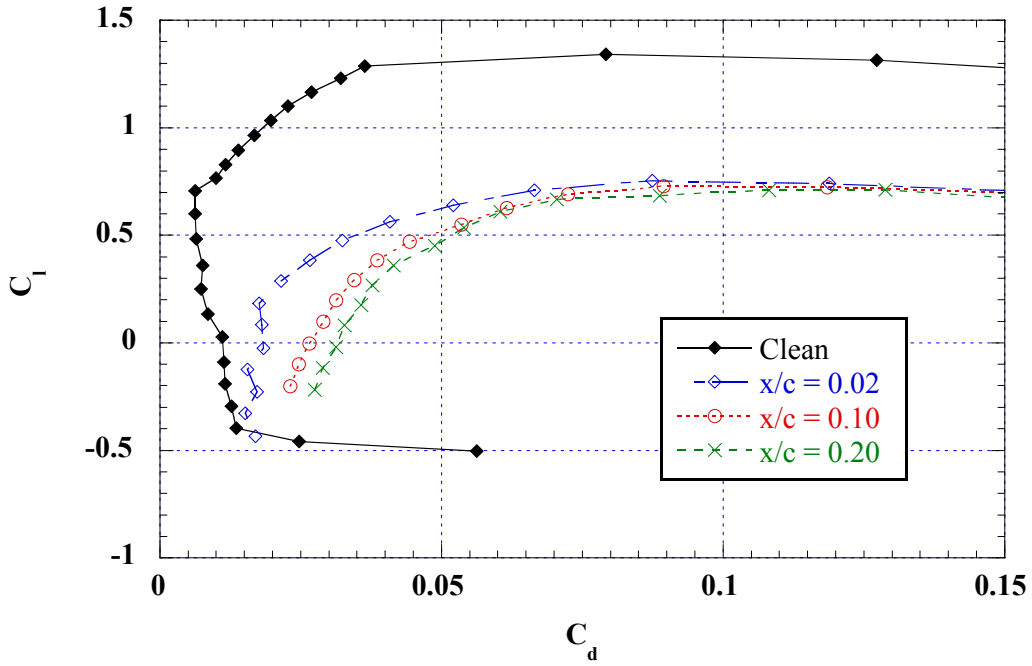

Fig. 4.75b) NLF 0414

Fig. 4.75: Effect of ridge-ice location on drag. *Re* = 1.8 million; forward-facing quarter round; $k = 0.25$".

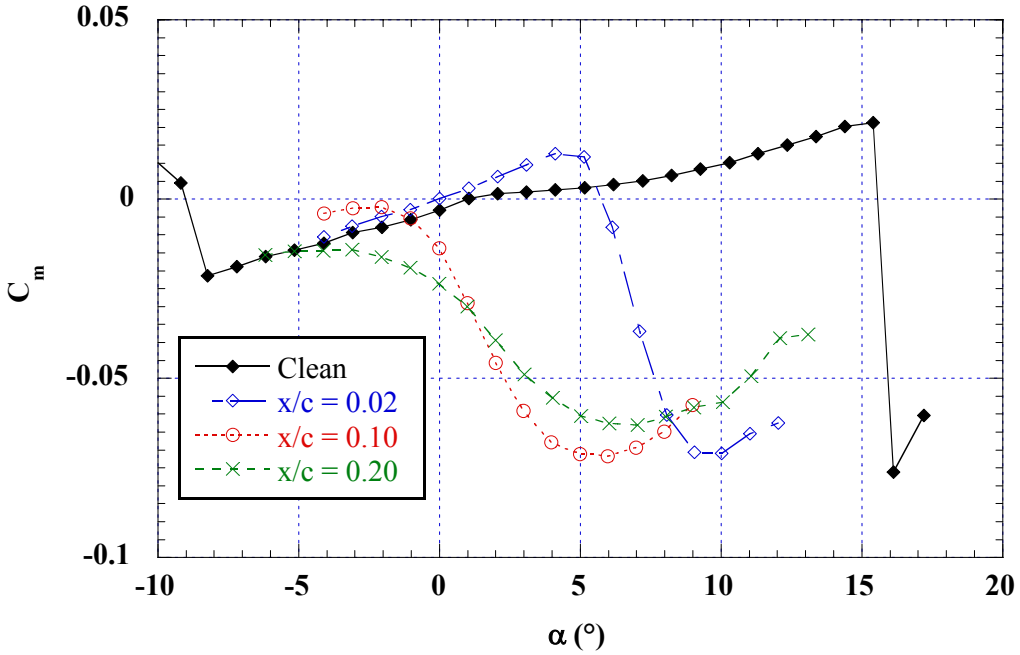

Fig. 4.76a) NACA 23012m

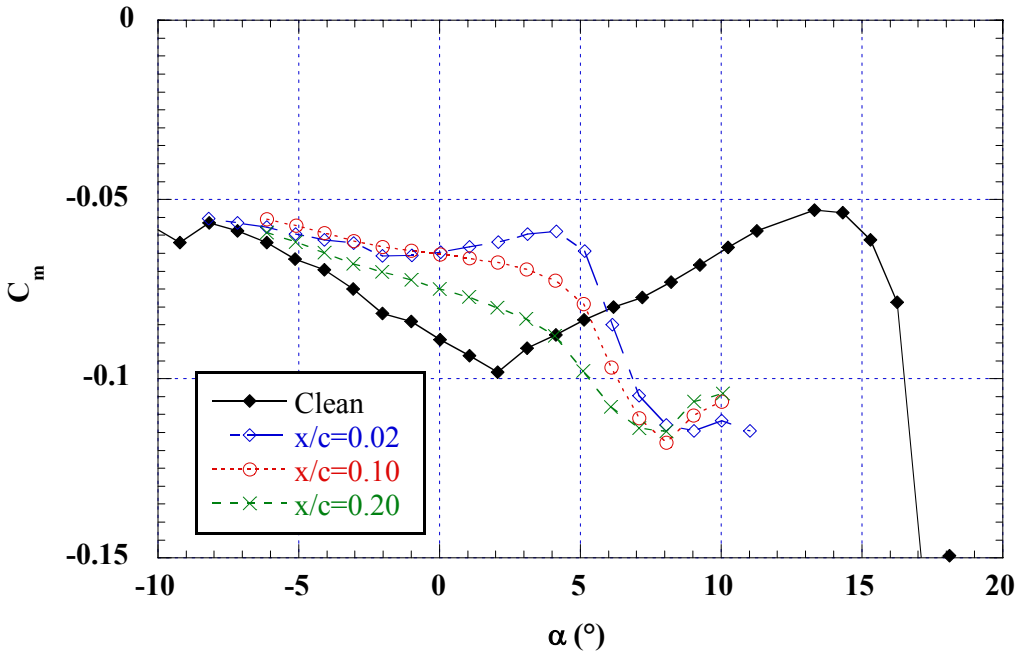

Fig. 4.76b) NLF 0414

Fig. 4.76: Effect of ridge-ice location on pitching moment. *Re* = 1.8 million; forward-facing quarter round; *k* = 0.25".

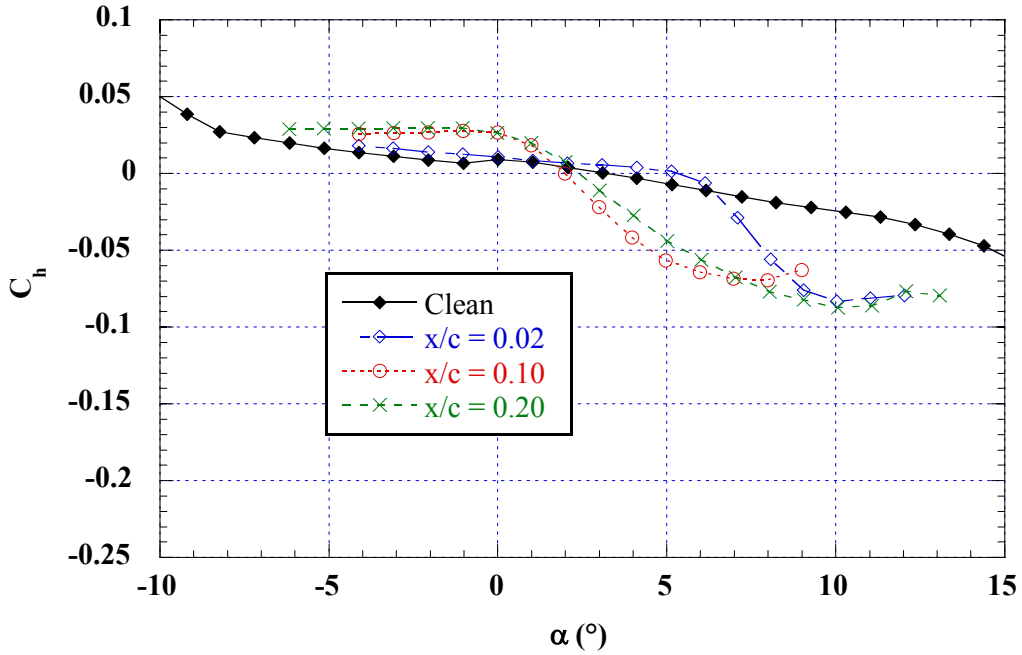

Fig. 4.77a) NACA 23012m

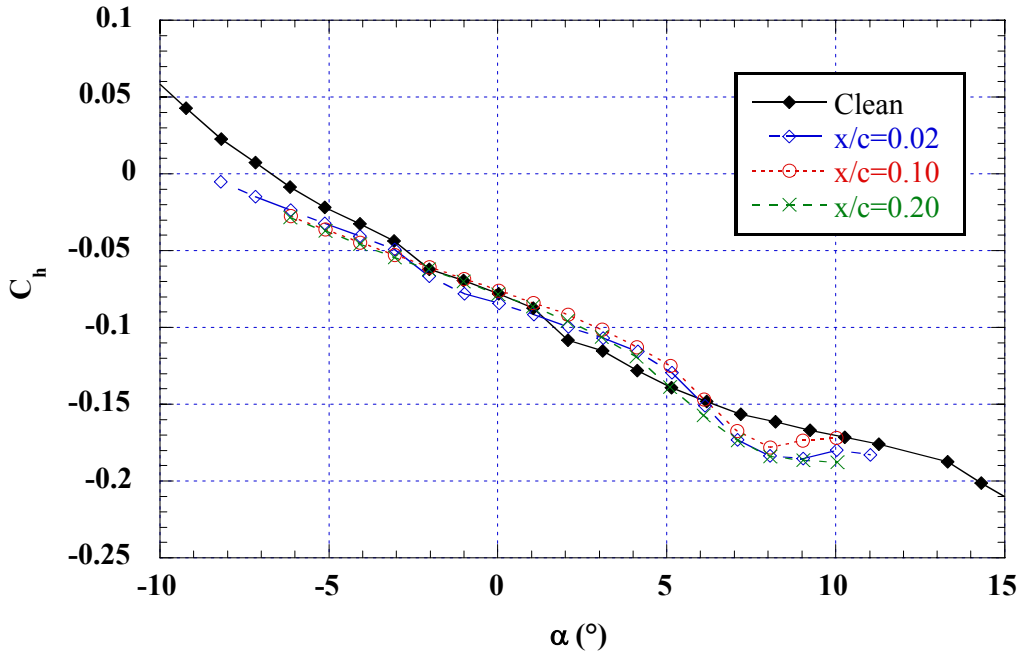

Fig. 4.77b) NLF 0414

Fig. 4.77: Effect of ridge-ice location on flap-hinge moment. *Re* = 1.8 million; forward-facing quarter round; $k = 0.25$".

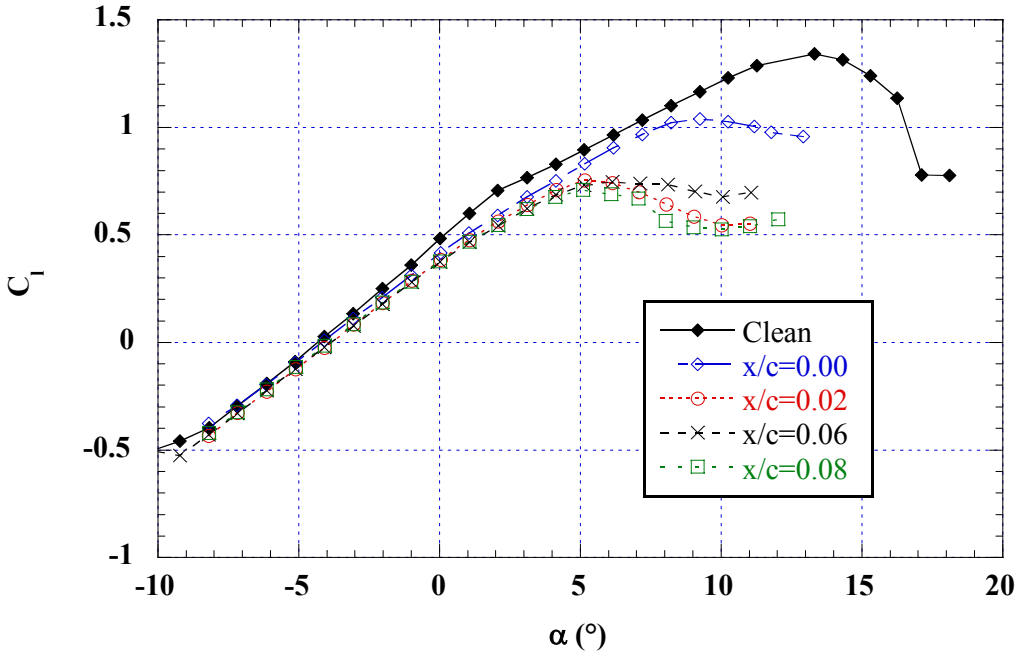

Fig. 4.78a) x/c = 0.00 to 0.08

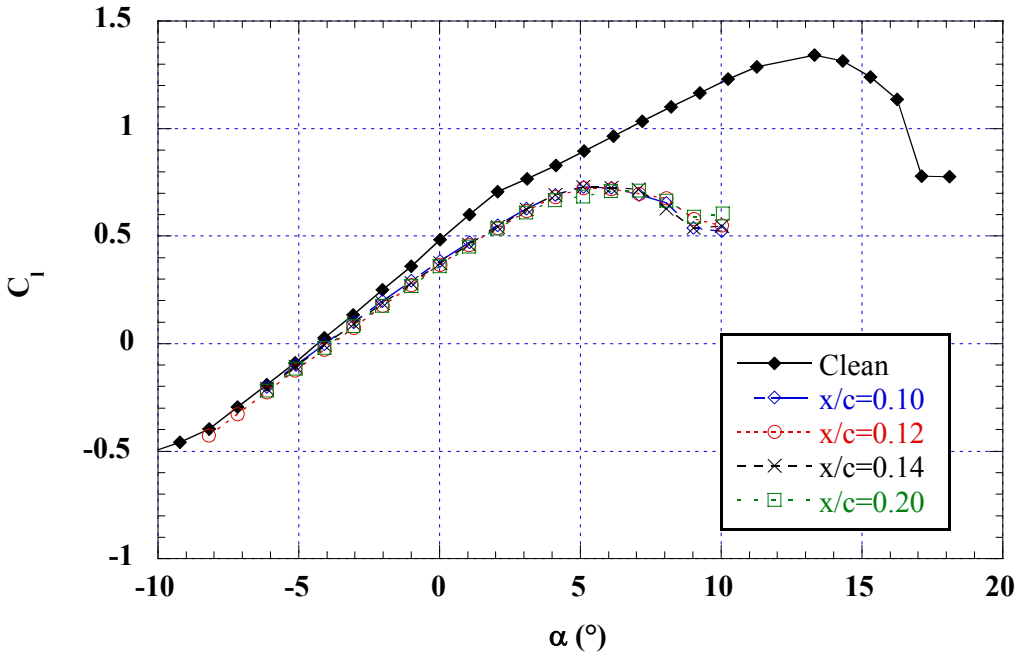

Fig. 4.78b) x/c = 0.10 to 0.20

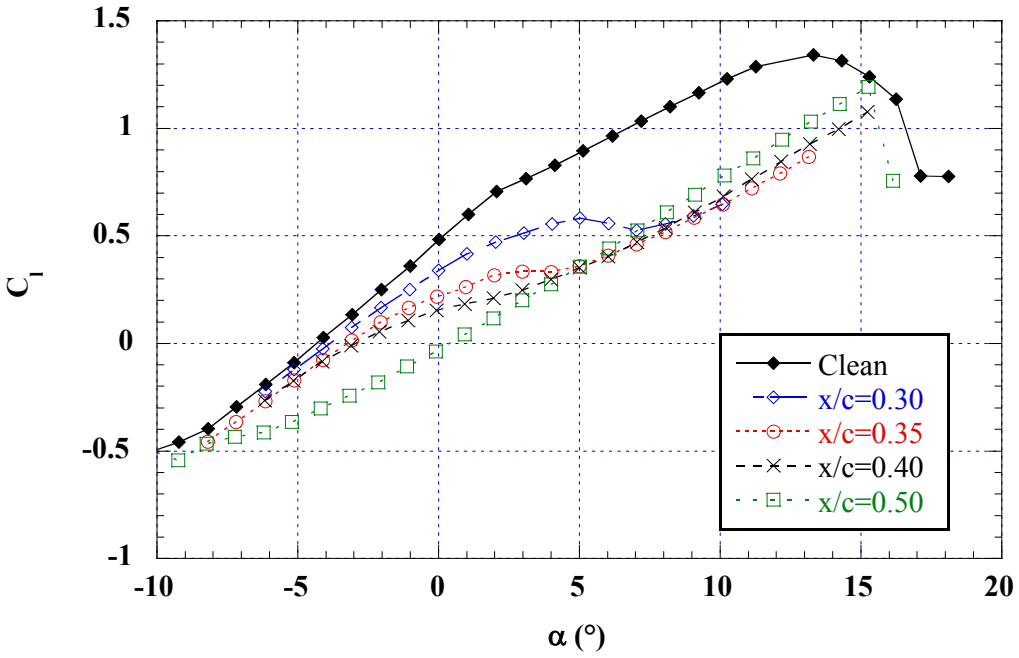

Fig. 4.78c) x/c = 0.30 to 0.50

Fig. 4.78: Effect of simulated ridge-ice location on lift on NLF 0414; k = 0.25" forward-facing quarter round; boundary layer tripped; Re = 1.8 million.

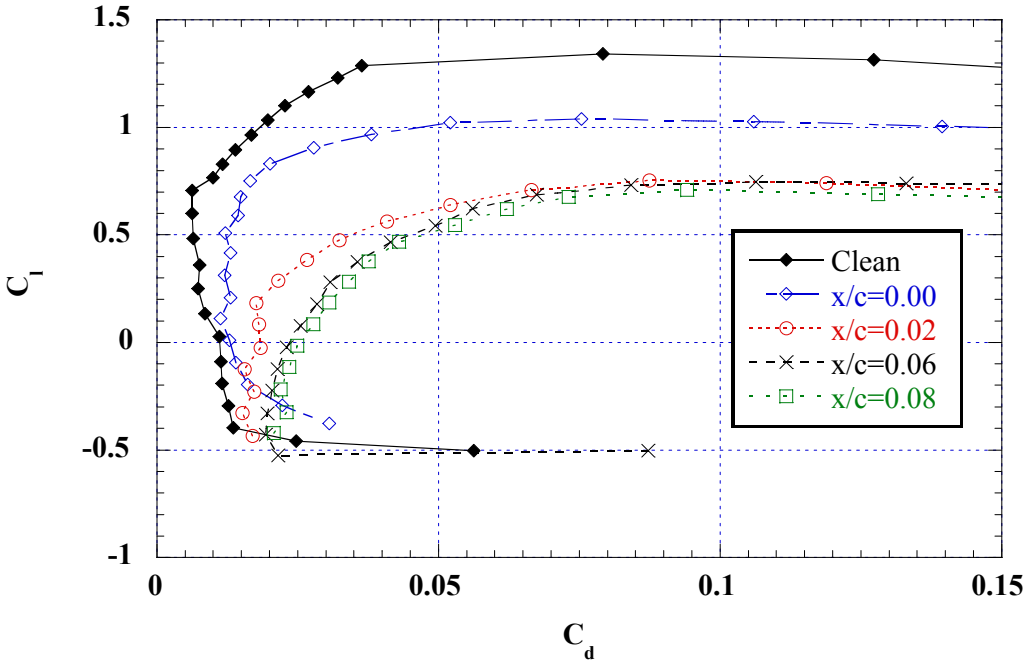

Fig. 4.79a) x/c = 0.00 to 0.08

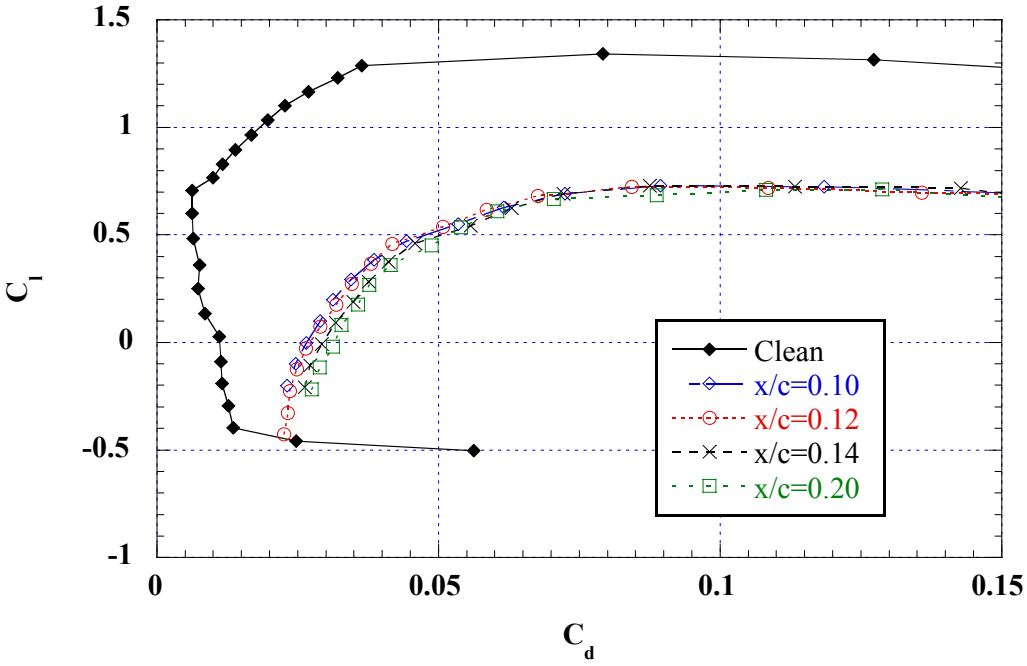

Fig. 4.79b) x/c = 0.10 to 0.20

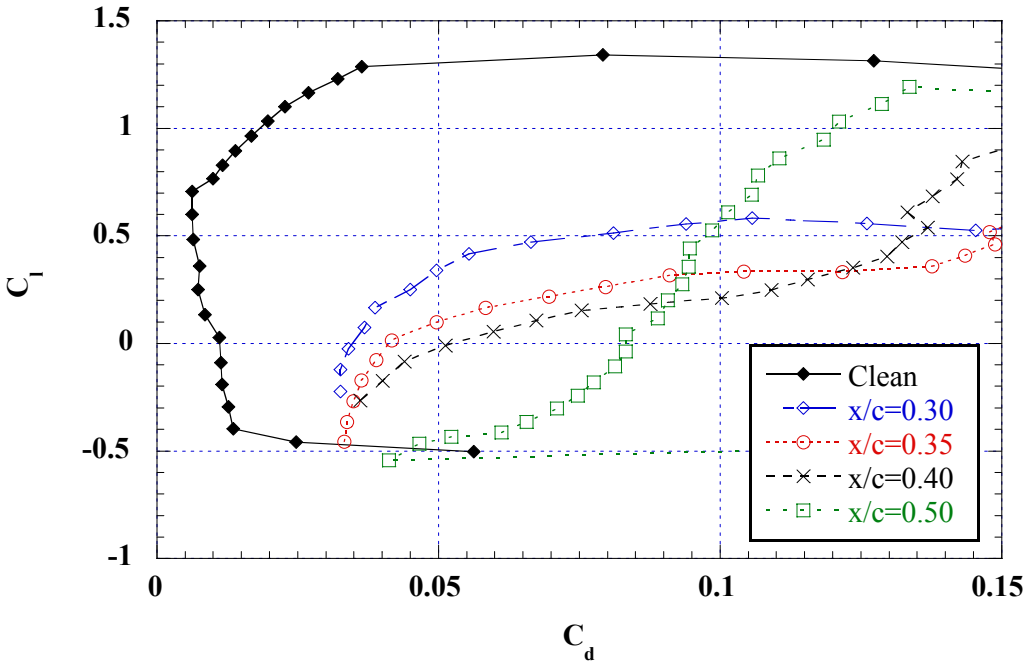

Fig. 4.79c) x/c = 0.30 to 0.50

Fig. 4.79: Effect of simulated ridge-ice location on drag on NLF 0414; k = 0.25" forward-facing quarter round; boundary layer tripped; Re = 1.8 million.

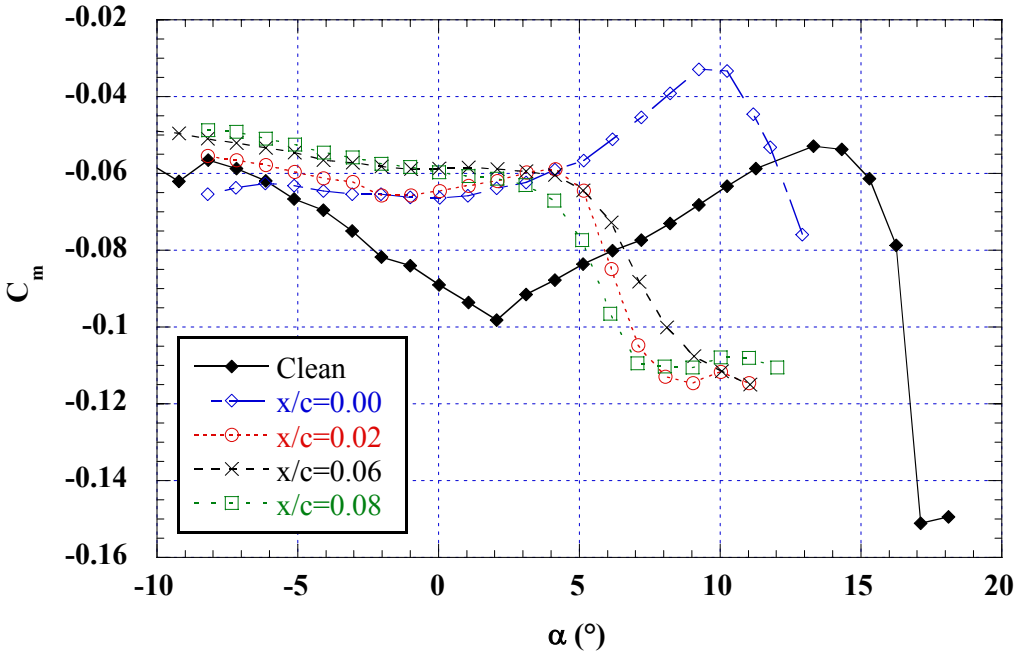

Fig. 4.80a) x/c = 0.00 to 0.08

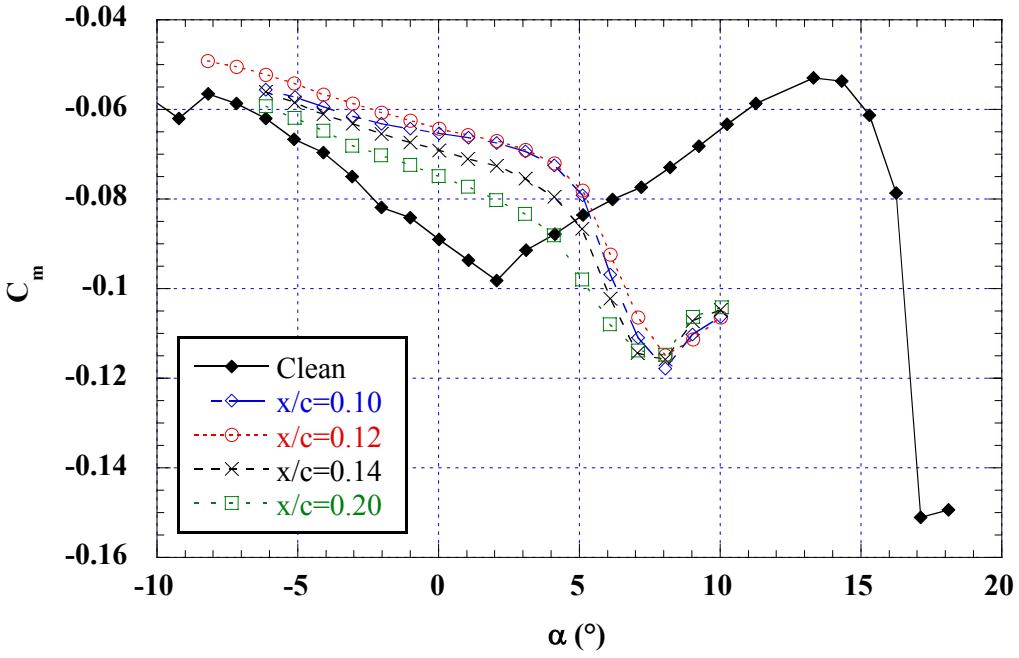

Fig. 4.80b) x/c = 0.10 to 0.20

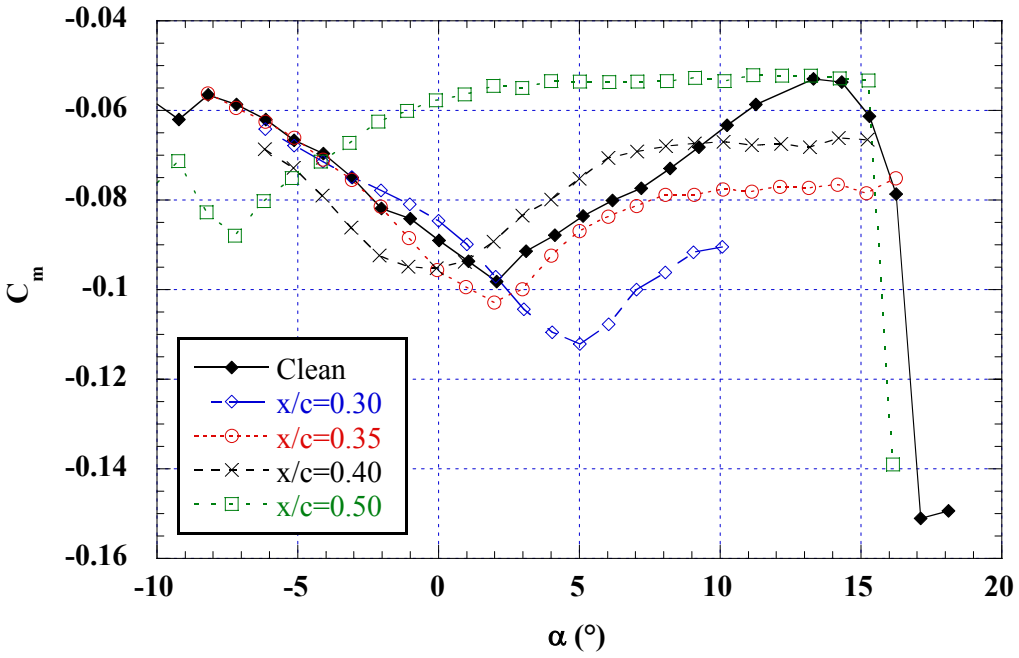

Fig. 4.80c) x/c = 0.30 to 0.50

Fig. 4.80: Effect of simulated ridge-ice location on pitching moment on NLF 0414; k = 0.25" forward-facing quarter round; boundary layer tripped; Re = 1.8 million.

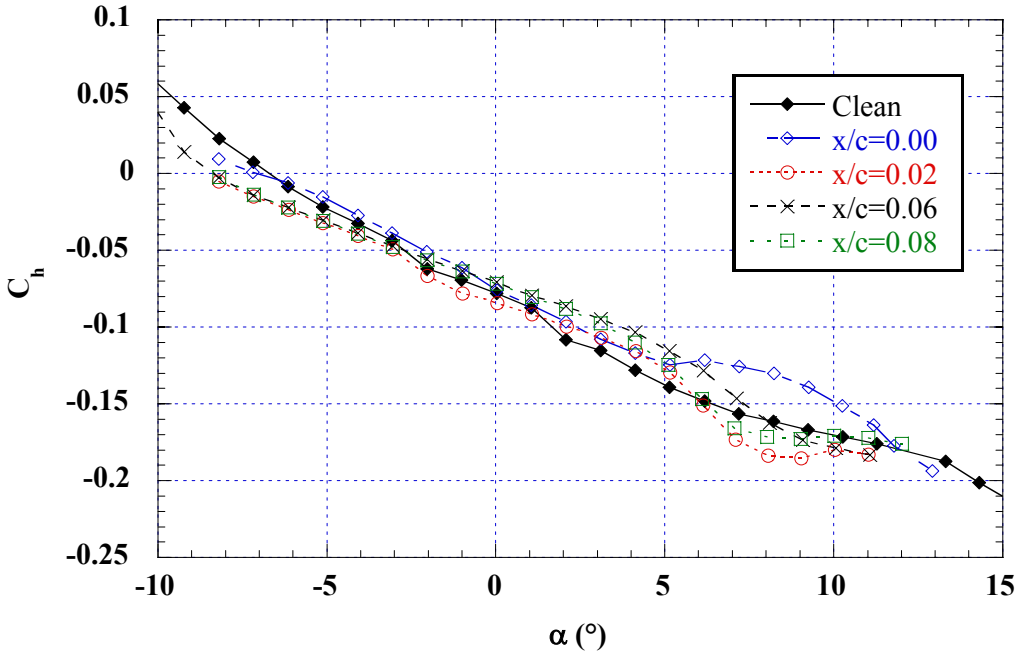

Fig. 4.81a) x/c = 0.00 to 0.08

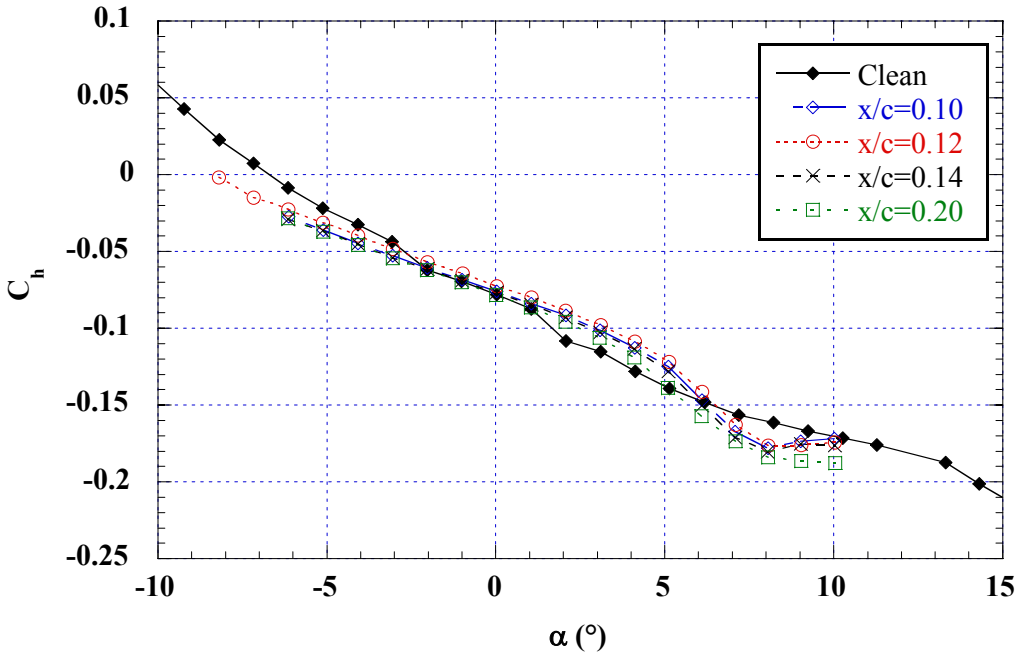

Fig. 4.81b) x/c = 0.10 to 0.20

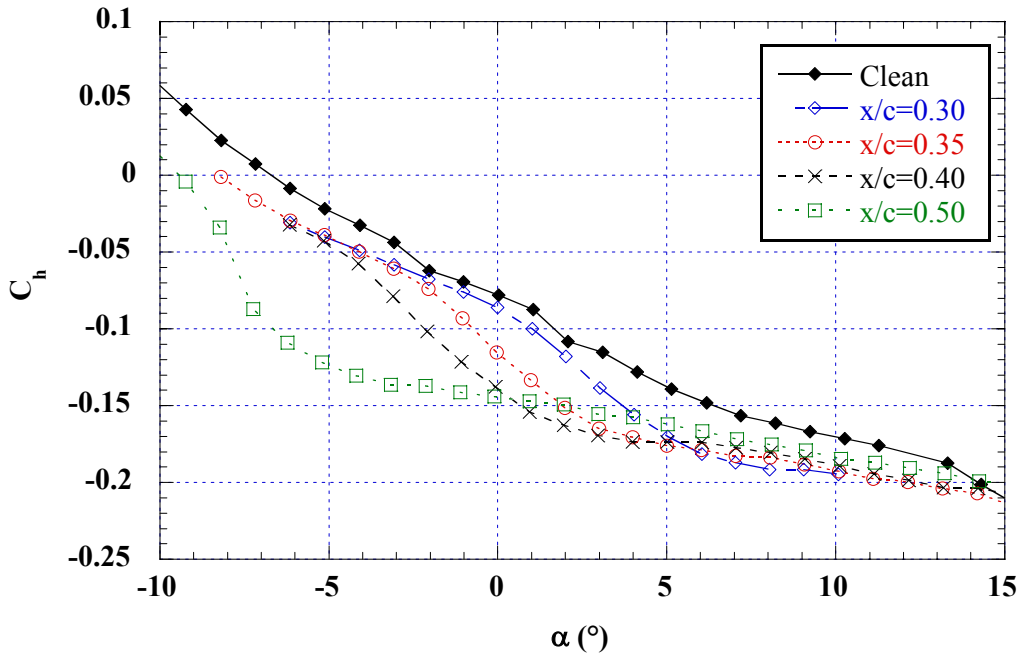

Fig. 4.81c) x/c = 0.30 to 0.50

Fig. 4.81: Effect of simulated ridge-ice location on flap hinge moment on NLF 0414; k = 0.25" forward-facing quarter round; boundary layer tripped; Re = 1.8 million.

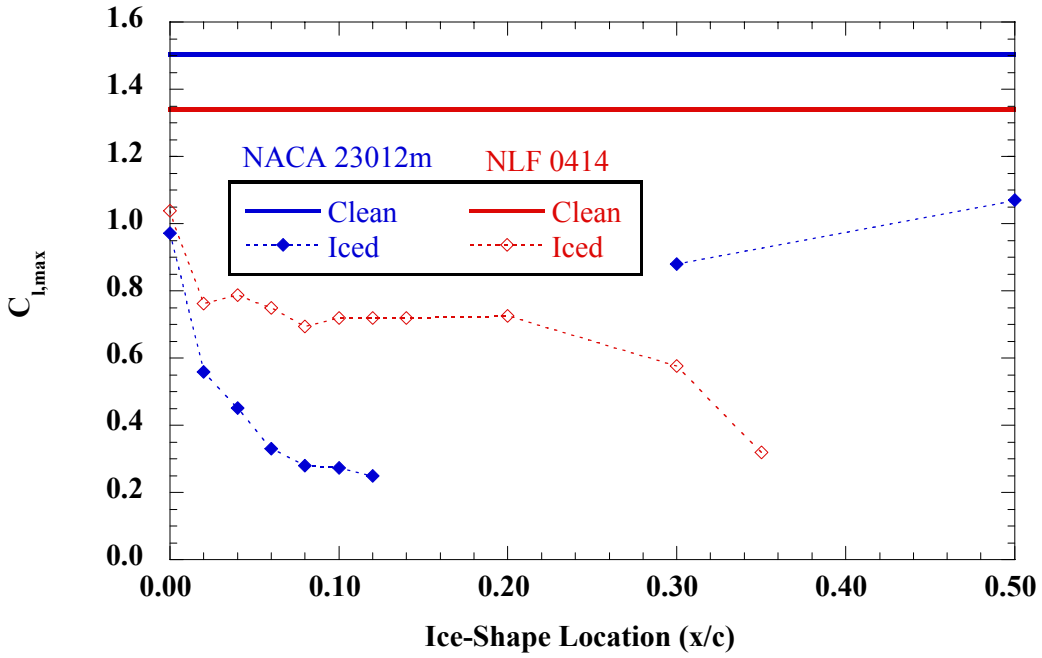

Fig. 4.82: Effect of simulated ridge-ice location on maximum on NACA 23012m and NLF 0414; $k = 0.25$" forward-facing quarter round; boundary layer tripped; *Re* = 1.8 million.

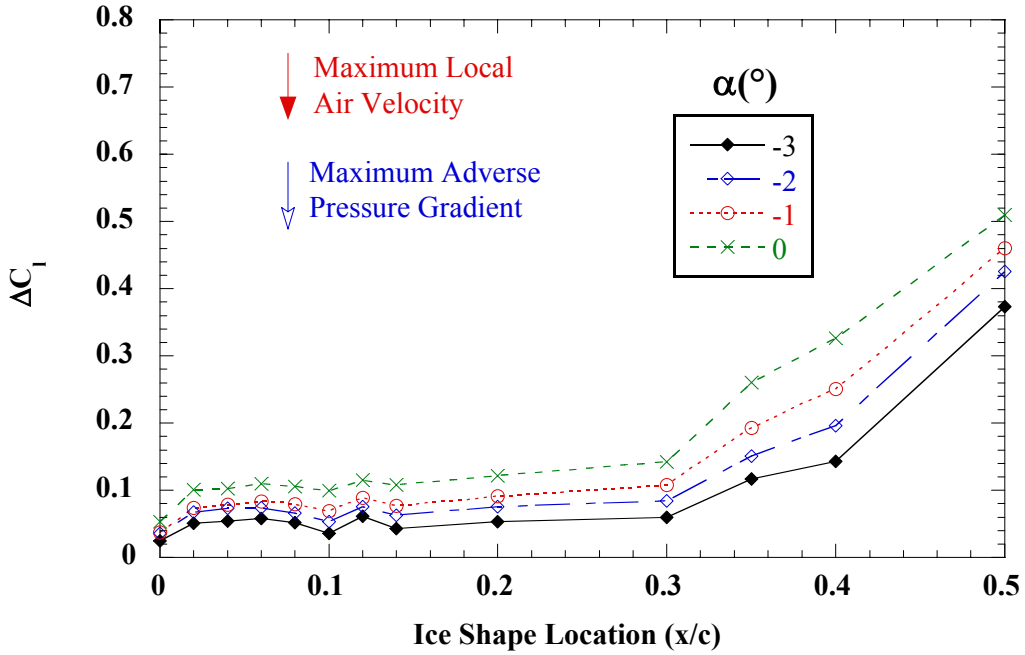

Fig. 4.83a) α = -3° to 0°

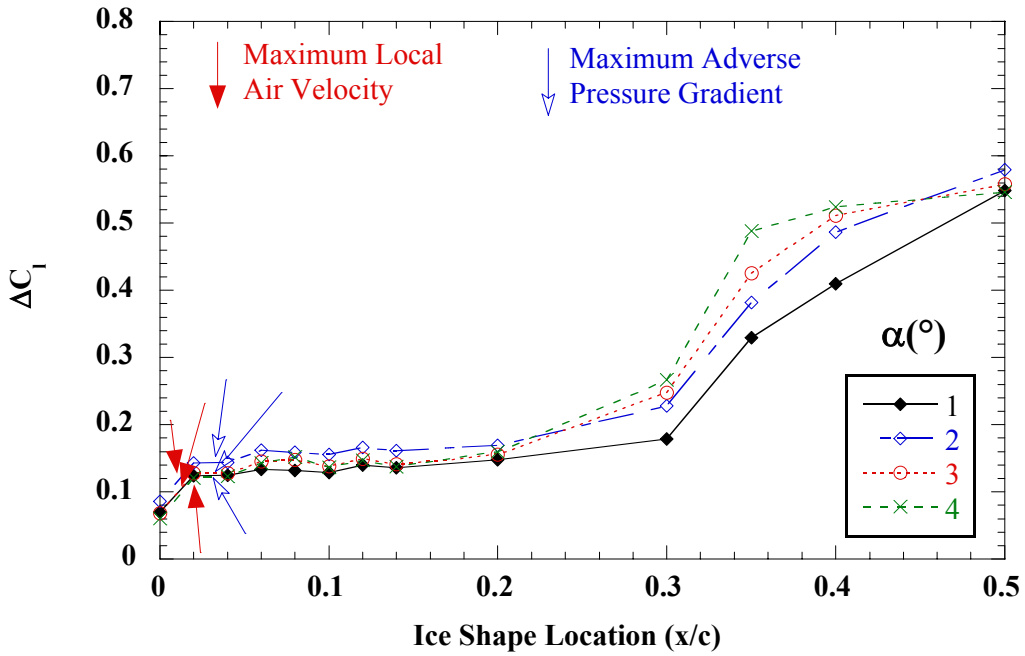

Fig. 4.83b) α = 1° to 4°

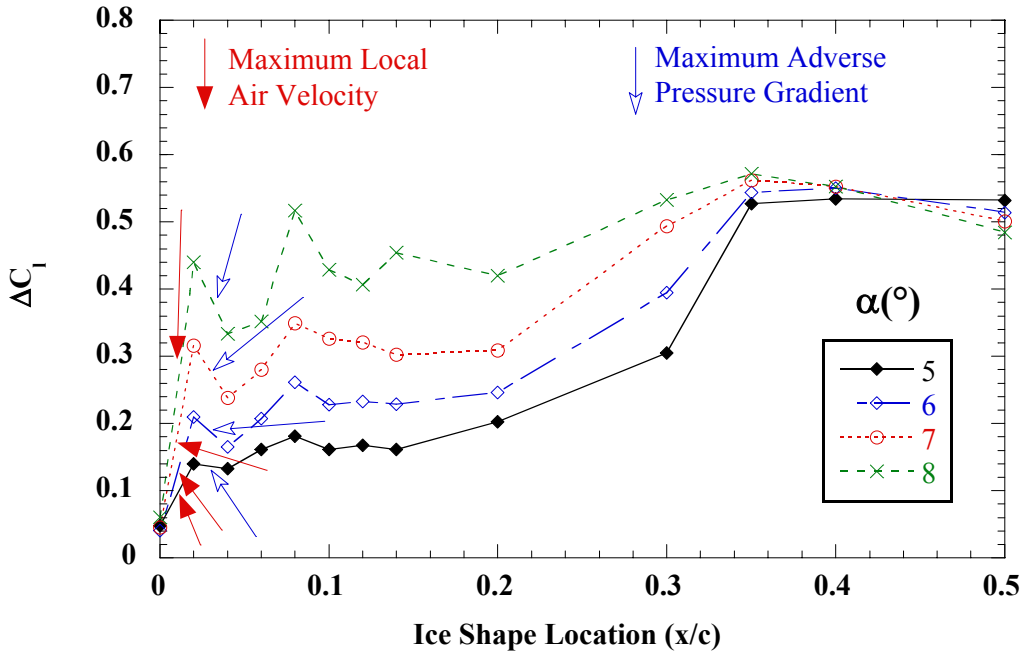

Fig. 4.83c) $\alpha = 5°$ to $8°$

Fig. 4.83: Effect of simulated ridge-ice location on lift loss on NLF 0414; k = 0.25" forward-facing quarter round; boundary layer tripped; Re = 1.8 million.

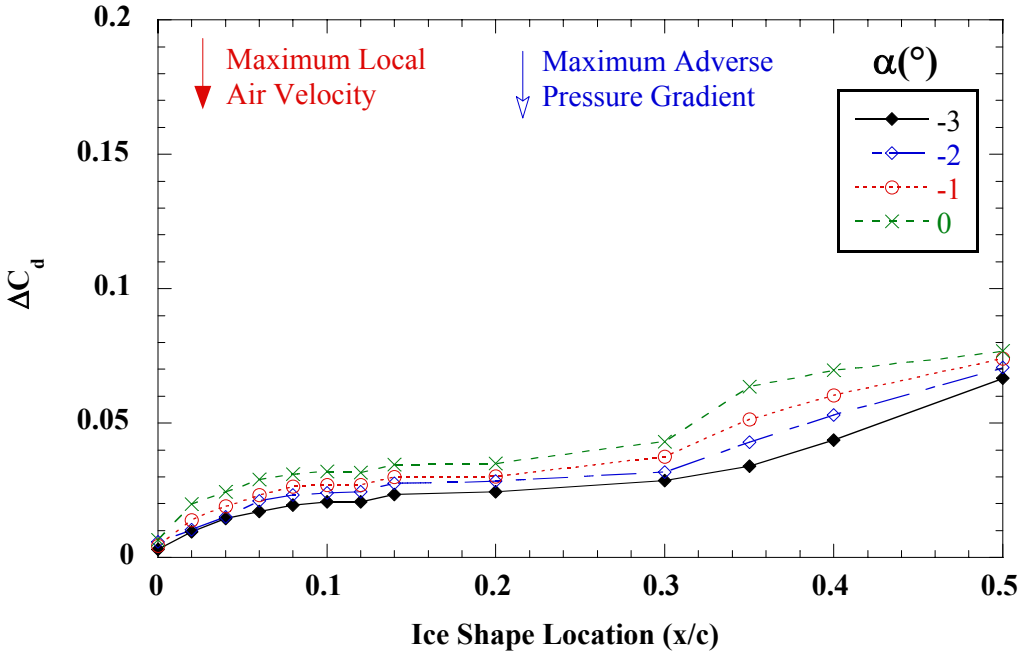

Fig. 4.84a) α = -3° to 0°

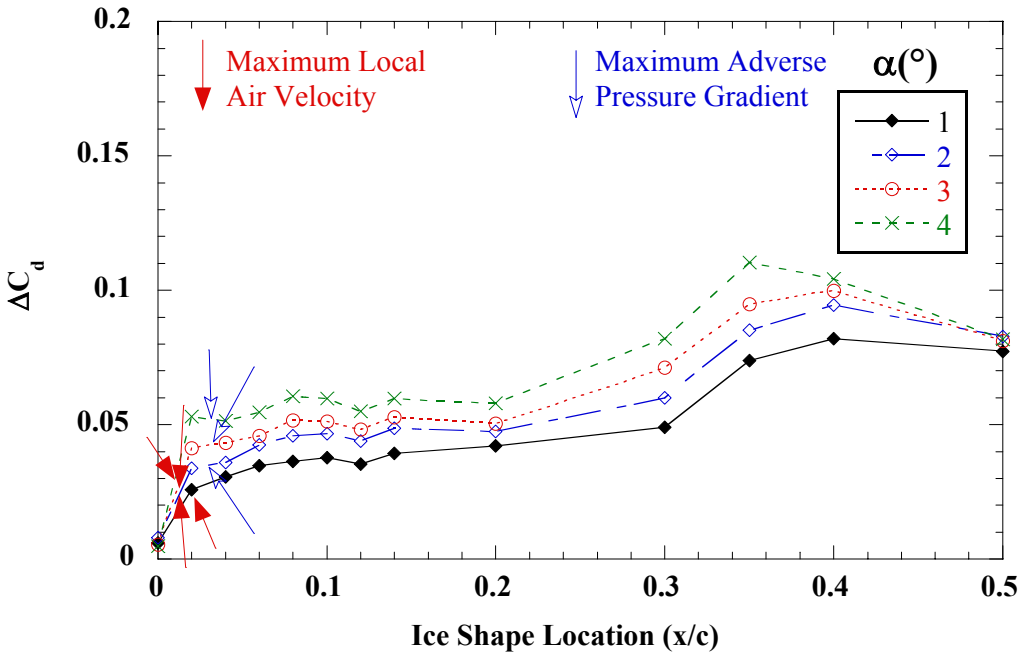

Fig. 4.84b) α = 1° to 4°

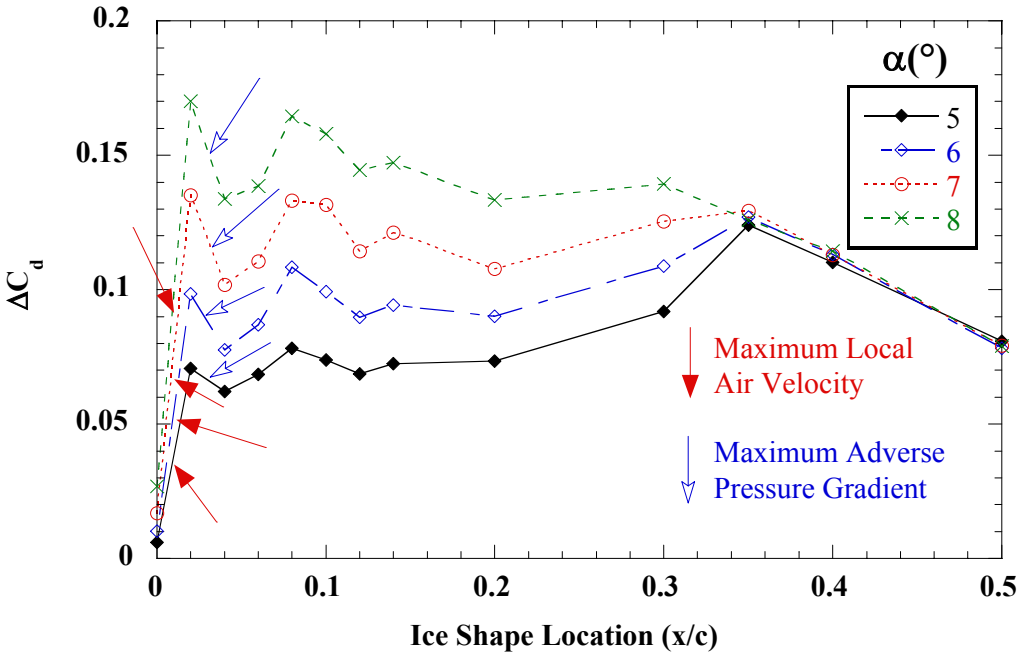

Fig. 4.84c) $\alpha = 5°$ to $8°$

Fig. 4.84: Effect of simulated ridge-ice location on drag increase on NLF 0414; k = 0.25" forward-facing quarter round; boundary layer tripped; Re = 1.8 million.

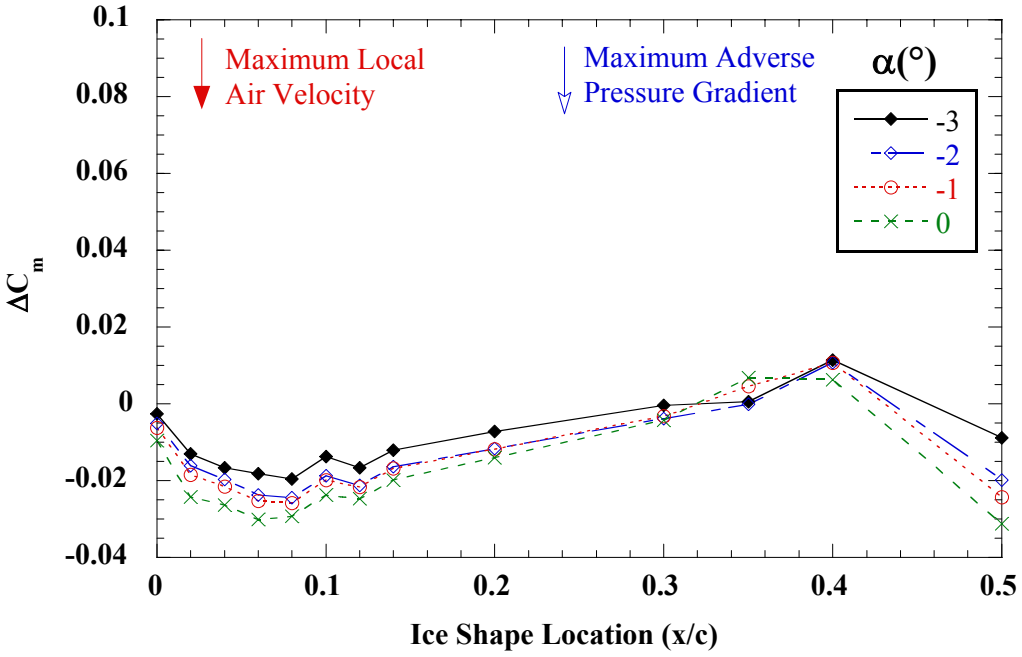

Fig. 4.85a) α = -3° to 0°

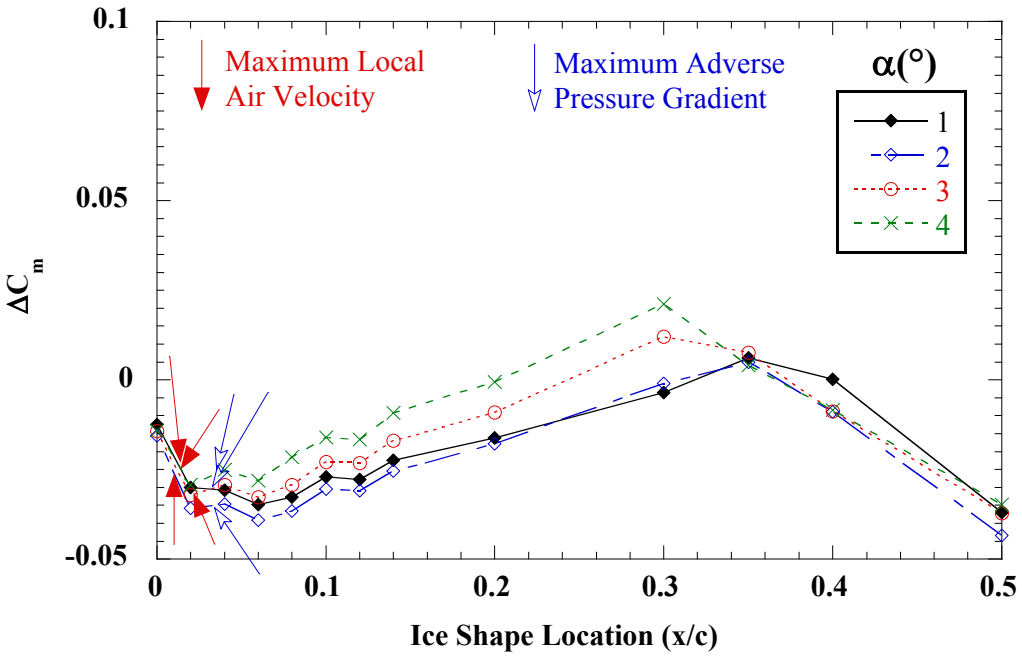

Fig. 4.85b) α = 1° to 4°

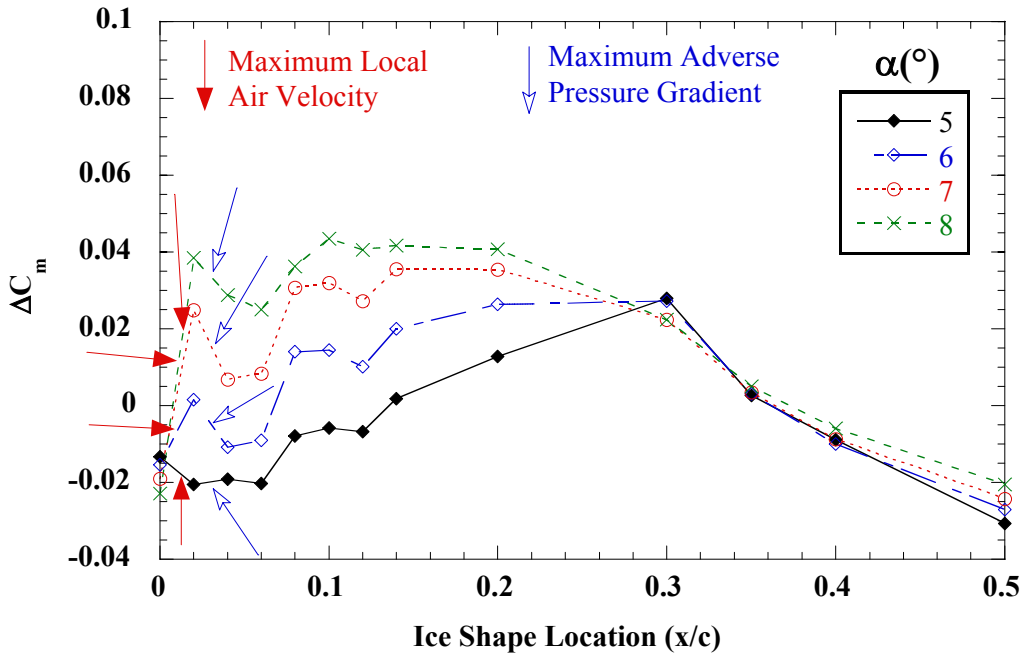

Fig. 4.85c) $\alpha = 5°$ to $8°$

Fig. 4.85: Effect of simulated ridge-ice location on pitching moment alteration on NLF 0414; k = 0.25" forward-facing quarter round; boundary layer tripped; Re = 1.8 million.

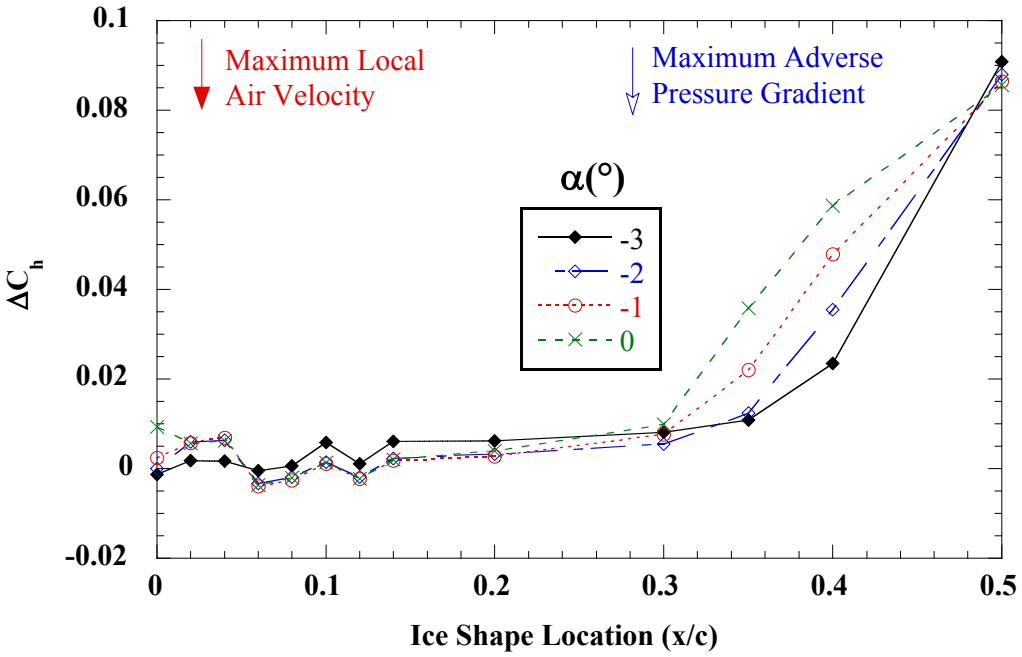

Fig. 4.86a) α = -3° to 0°

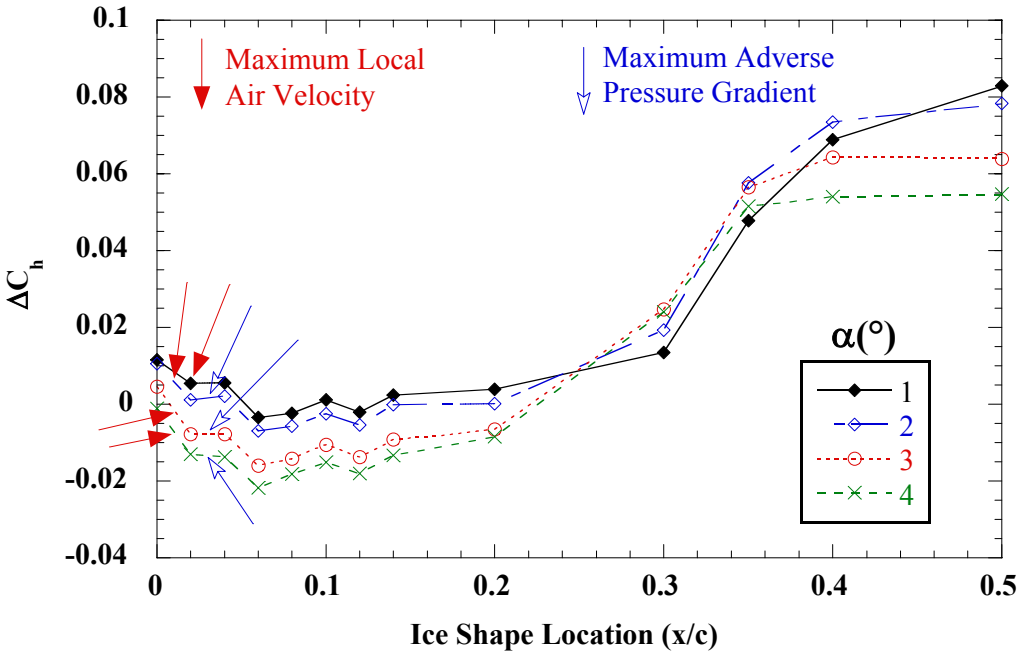

Fig. 4.86b) α = 1° to 4°

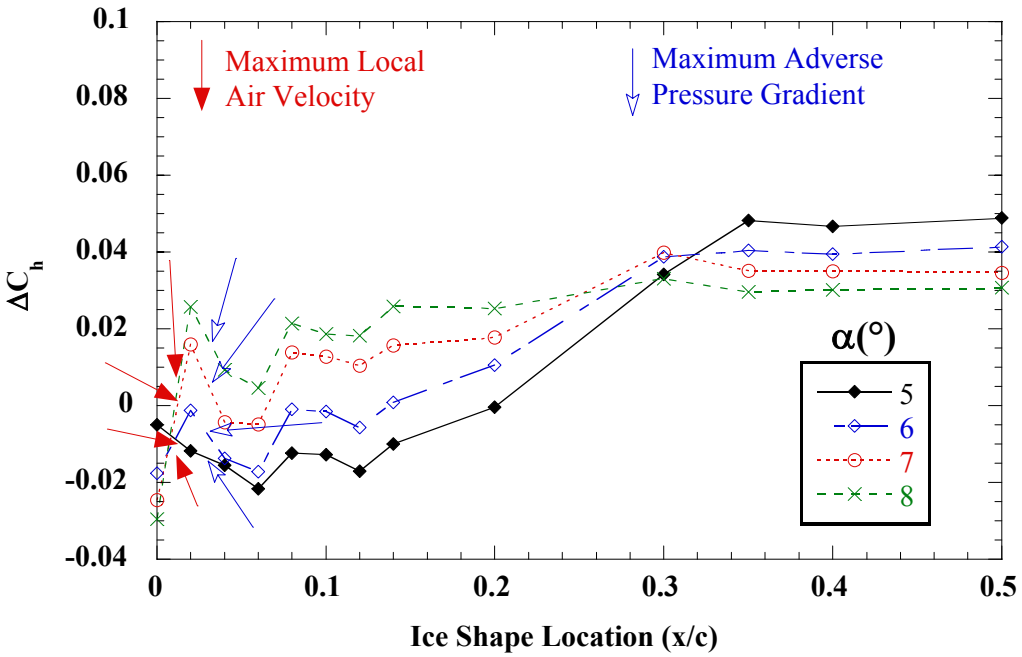

Fig. 4.86c) $\alpha = 5°$ to $8°$

Fig. 4.86: Effect of simulated ridge-ice location on flap hinge moment alteration on NLF 0414; k = 0.25" forward-facing quarter round; boundary layer tripped; Re = 1.8 million.

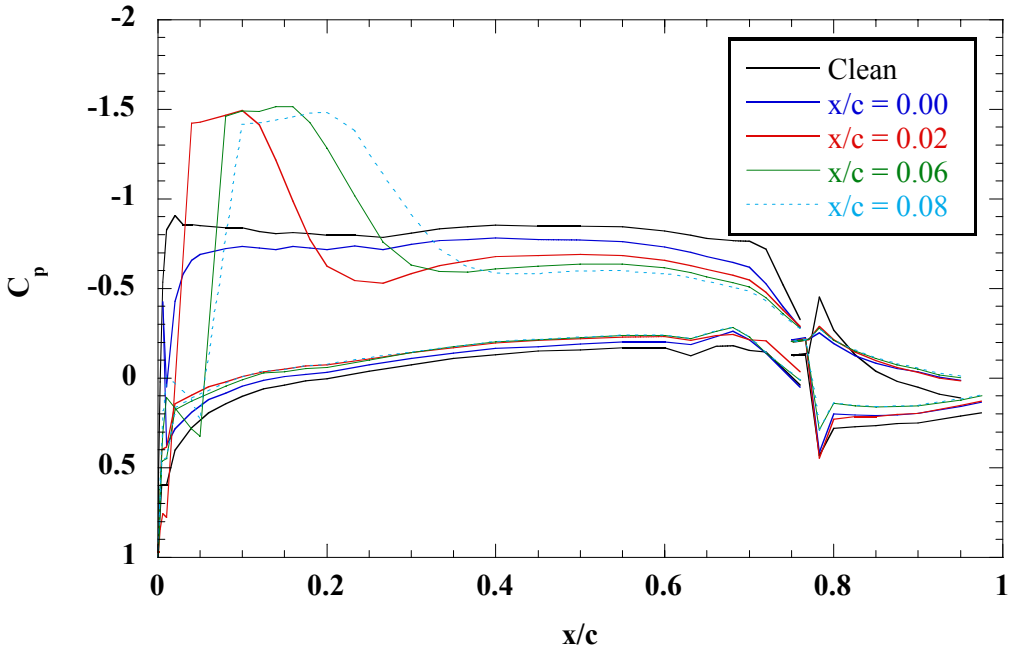

Fig. 4.87a) x/c = 0.00 to 0.08

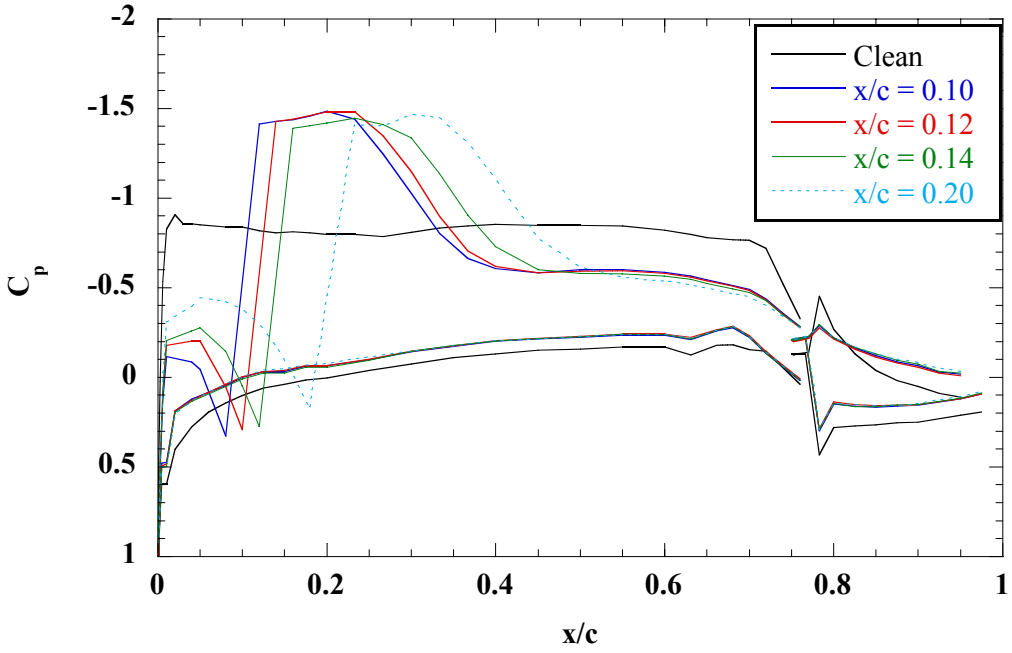

Fig. 4.87b) x/c = 0.10 to 0.20

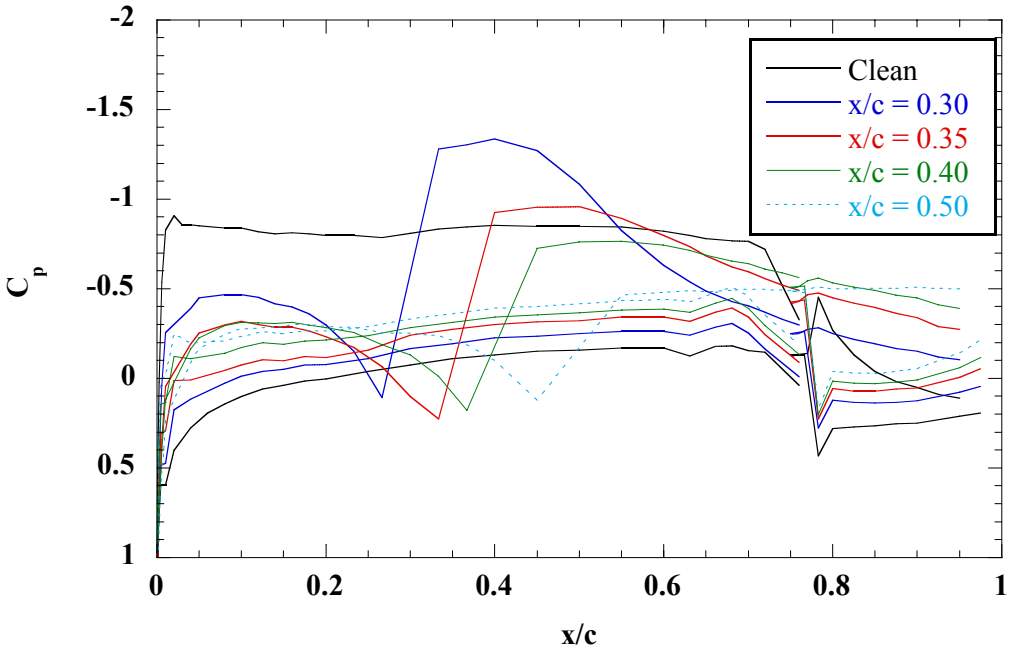

Fig. 4.87c) x/c = 0.30 to 0.50

Fig. 4.87: Effect of simulated ridge-ice location on pressure distribution on NLF 0414; k = 0.25" forward-facing quarter round; boundary layer tripped; α = 1°; Re = 1.8 million.

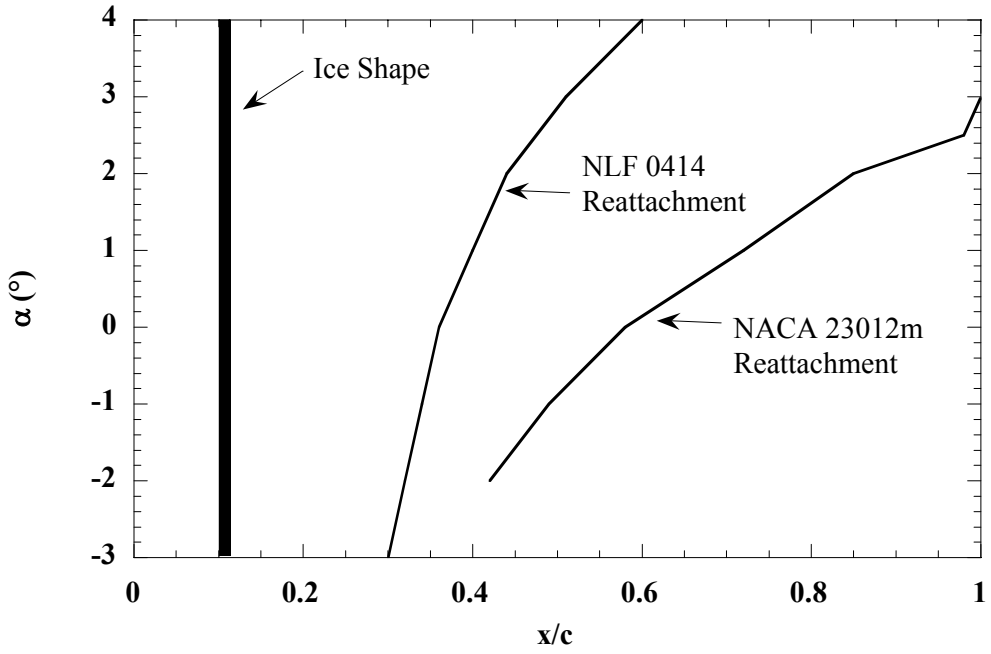

Fig. 4.88: Reattachment location of the separation bubble that formed downstream of the simulated ridge ice; k = 0.25" forward-facing quarter round at x/c = 0.10; boundary layer tripped; NACA 23012m results obtained from flow visualization; NLF 0414 results obtained from surface pressures; Re = 1.8 million.

Appendix A

Airfoil Stall Types

There are three types of airfoil stall at low speeds: trailing-edge stall, leading-edge stall, and thin-airfoil stall. The type of stall an airfoil experiences is dependent on the where the boundary layer first separates and how the separated flow grows. This, in turn, is dependent primarily on the airfoil geometry, Reynolds number, surface roughness, and free-stream turbulence. McCullough and Gault[61] provide a detailed explanation of the three types of airfoil stall.

The trailing-edge stall occurs when the flow separation starts from the trailing edge of the airfoil, and the separation point progresses upstream as the angle of attack is increased. This stall type is usually associated with thick airfoils with thickness ratio greater than 0.15. An example of an airfoil that has a trailing edge stall is the NACA 63_3-018. The lift curve of this airfoil is shown on Fig. A1.[61] It shows a smooth and gradual stall, with a round peak in the lift curve. The lift curve became nonlinear at $\alpha = 10°$. This coincided with the angle of attack at which the flow started to separate at the trailing edge. The lift curve slope continued to decrease as the separation propagated upstream. The $C_{l,max}$ occurred when the flow was separated over half of the airfoil.

The leading-edge stall is typically found on airfoils with moderate thickness ratios (between 0.09 and 0.15). The NACA 63_3-012 is an example of this. On these types of airfoils, a small laminar separation bubble usually forms at moderate angles of attack just downstream of the suction peak (where the boundary layer transitions). As the angle of attack is increased, the laminar separation bubble moves upstream. As the angle of attack is further increased, the bubble rapidly burst (fails to reattach), leading to a sudden stall. The result of this is a very abrupt discontinuity in the lift curve at stall, as shown in Fig. A1. Another example of an airfoil that has a leading-edge stall is the NACA 23012m, which was used in this study.

The thin-airfoil stall occurs on all sharp-edge airfoils and some thin airfoils (with thickness ratio less than 0.09). The double wedge airfoil shown on Fig. A1 is an example of this. The thin airfoil stall is characterized by a flow separation that forms on the leading edge of the airfoil that grows downstream with increasing angle of attack. This growth in the separation bubble is much more gradual than the sudden bubble burst that occurs on the leading-edge stall, resulting in a much more gradual stall. A "kink" in the lift curve is often observed when the leading-edge bubble starts to grow rapidly. On the double-wedge airfoil, this occurs at $\alpha = 2°$. The lift reaches a maximum when the bubble fails to reattach. The top of the curve is relatively flat with little lift loss after stall.

An airfoil can also have stall characteristics that are a combination of two of the types described above. An example of this is the combination of the thin-airfoil and the trailing-edge stall. Flow separation can form both at the leading and the trailing edge. As the angle of attack is increased, the separation will grow until the two bubbles join at stall.

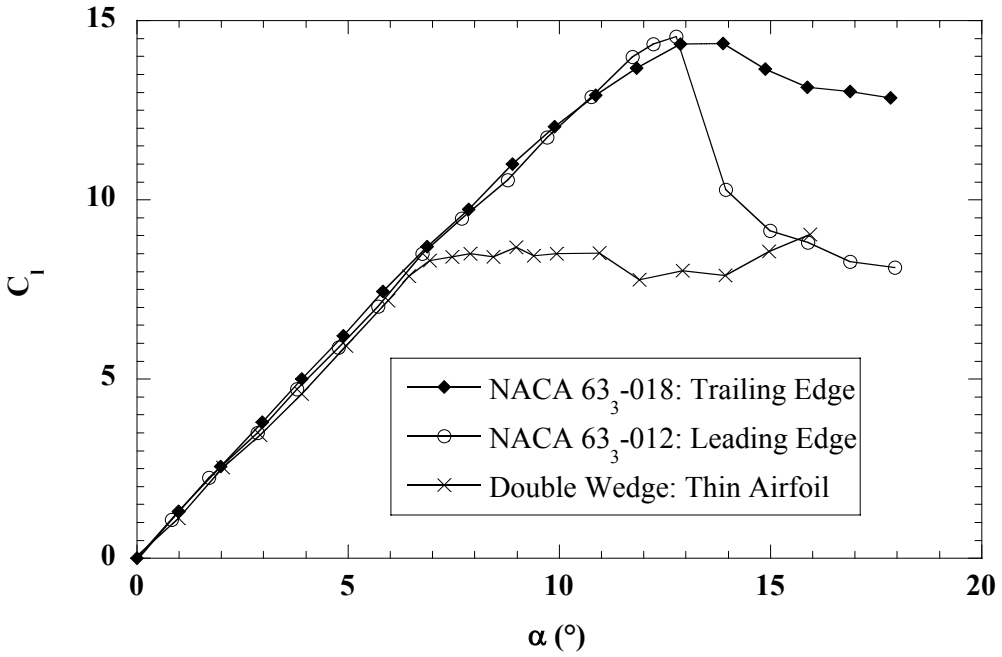

Fig. A1: Lift characteristics of the three airfoil stall types.

Appendix B

Trailing-Edge Pressure as Separation Indicator

In many of the iced cases tested in this study, it was desirable to know at what angle of attack the bubble that formed downstream of the ice shape reached the trailing edge. The most certain way to obtain this was through the use of fluorescent oil flow visualization (as described in Section 3.9). However, because flow visualization was extremely time consuming (1 day for an α sweep for a single flap setting compared to 30 minutes for pressure and balance measurements), it was impractical to obtain flow visualization for every case tested. Therefore, it was necessary to correlate the pressure data to the flow visualization results in order to obtain separation information for cases where flow visualization was not available. A logical choice was to look at the pressure form the trailing edge pressure tap since that was the location of interest.

Figure B1a shows the change in the trailing-edge pressure coefficient with the angle of attack for one of the cases tested. Figure B1b shows the corresponding change in the separation bubble reattachment location (x_r/c) with angle of attack from flow visualization. Note that there are two lines at $\alpha > 5°$ because the reattachment location started to be less clearly defined due to unsteadiness. It shows that the pressure coefficient remained constant between $-4° \leq \alpha \leq -1°$. At $\alpha = 0°$, the C_p started in increase as the separation bubble started to grow. As the bubble grew in length, more momentum was extracted from the boundary layer, leading to decreased trailing-edge pressure recovery. Between $-1° \leq \alpha \leq 8°$, there was an increase in the rate at which the trailing edge pressure decreased. This was due to an increase in the rate at which the separation bubble grew, as Fig. B1b shows. At $\alpha = 8°$, there was a decrease in the rate at which the trailing edge pressure decreased, leading to an inflection in the curve. This corresponded well with the flow visualization results, which showed that the bubble reached the trailing edge between $\alpha = 7°$ and 8°.

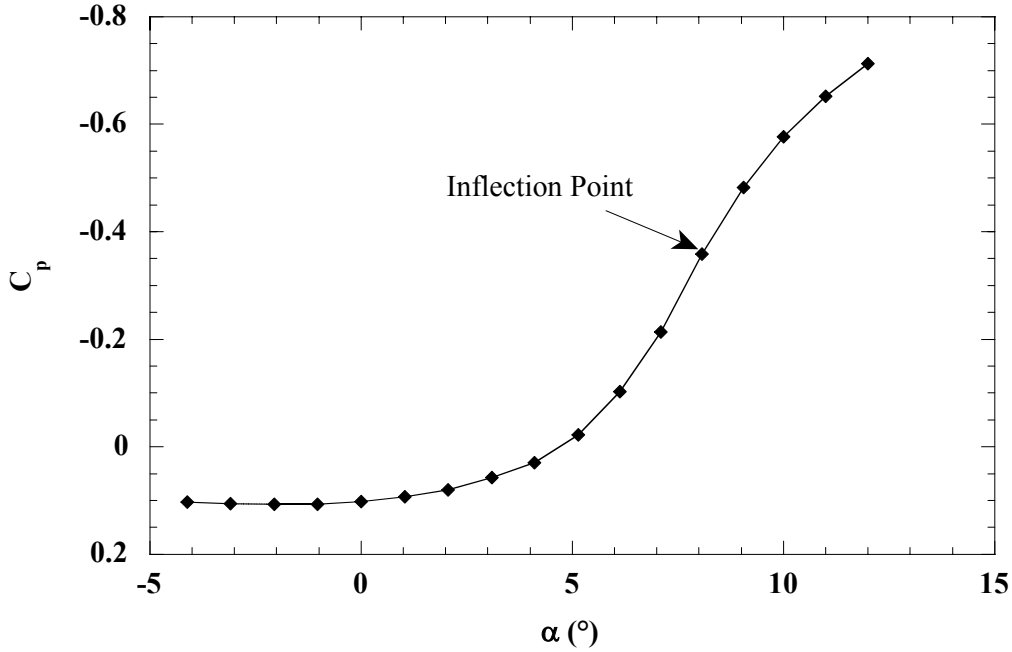

Fig. B1a) Trailing-edge pressure coefficient

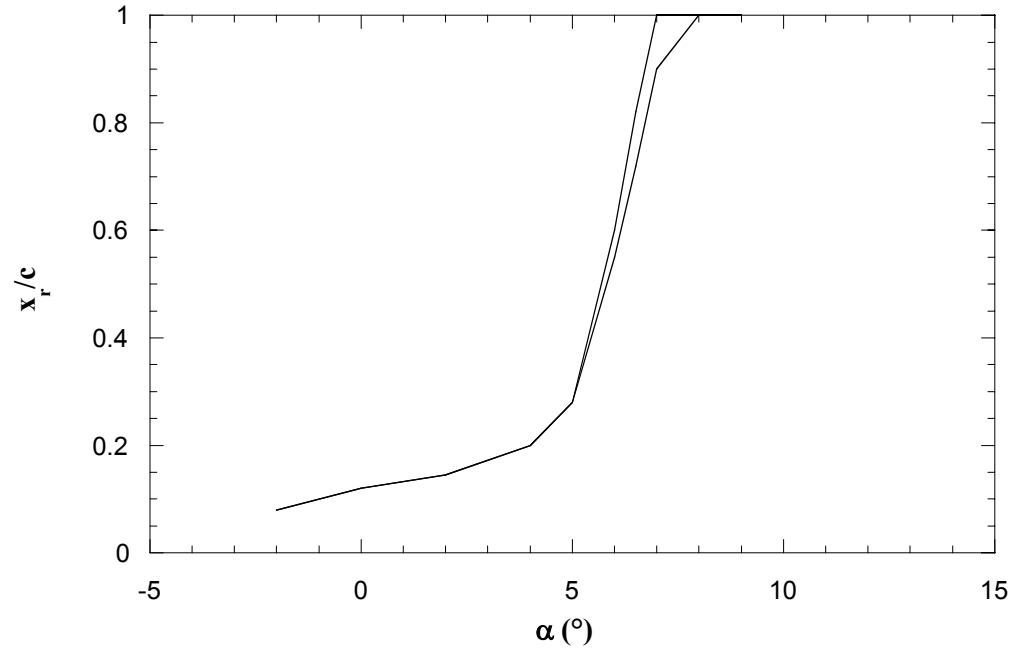

Fig. B1b) Separation-bubble reattachment location

Fig. B1: Trailing-edge pressure coefficient and bubble reattachment location as a function of angle of attack. NACA 20312m; 0.25" forward facing quarter round at x/c = 0.02, Re = 1.8 million; M = 0.18; boundary layer not tripped.

Tables B1 to B3 show the comparison between the angle of attack at which the inflection point in the trailing edge C_p occurred and at which the separation bubble reached the trailing edge. All of the cases (including the tripped cases) show good agreement. It is important to note that this method only worked for cases where the boundary layer at the trailing edge did not separate before the bubble reached the trailing edge. Thus, this method could not be used for NLF 0414 or the NACA 23012m with the flap deflected.

Table B1: Comparison of trailing edge pressure coefficient inflection angle and separation angle. NACA 23012m, 0.25" forward facing quarter round; *Re* = 1.8 million, *M* = 0.18, boundary layer not tripped.

Ice-Ridge Location (x/c)	α Inflection (°)	α Separation (°)
0.02	8	7.5
0.10	5	4.5
0.20	2	2

Table B2: Comparison of trailing edge pressure coefficient inflection angle and separation angle. NACA 23012m, 0.25" forward facing quarter round; *Re* = 1.8 million, *M* = 0.18, boundary layer tripped.

Ice-Ridge Location (x/c)	α Inflection (°)	α Separation (°)
0.10	3	2.5
0.20	4	3.5

Table B3: Comparison of trailing edge pressure coefficient inflection angle and separation angle. NACA 23012m, 0.25" forward facing quarter round; *Re* = 1.0 million, *M* = 0.10, boundary layer tripped.

Ice-Ridge Location (x/c)	α Inflection (°)	α Separation (°)
0.02	7	7.5
0.10	4	3.5
0.20	4	3.5

References

[1] Cole, J. and Sand, W., "Statistical Study of Aircraft Icing Accidents," AIAA Paper 91-0558, Jan. 1991.

[2] Shifrin, Carole A., "FAA Establishes Focused Safety Agenda," *Aviation Week & Space Technology*, April 20, 1998, pp. 38-39.

[3] Messinger, B.L., "Equilibrium Temperature of an Unheated Icing Surface as a Function of Air Speed," *Journal of Aeronautical Sciences*, Vol. 20., No. 1, Jan. 1953.

[4] Hansman, R.J., Breuer, K.S., Hazan, D, Reehorst, A., and Vargas, M., "Close-Up Analysis of Aircraft Ice Accretion," AIAA Paper 93-0029, Jan. 1993.

[5] Sand, W.R, and Biter, C.J., "Meteorology Surrounding the Roselawn Accident," AIAA Paper 99-0496, Jan. 1999.

[6] Brahimi, M.T., Tran, P., Chocron, D., Tezok, F., and Paraschiviu, I., "Effect of Supercooled Large Droplets on Ice Accretion Characteristics," AIAA Paper 97-0306, Jan. 1997.

[7] Perkins, P.J., Dow, J.P., Sweet, D., "Survey of Ice Accretions Formed in Freezing Drizzle Under Natural Icing and Simulated Icing Behind the United States Air Force Tanker and in the NASA-Lewis Icing Research Tunnel," unpublished report, 1997.

[8] National Transportation Safety Board, "Icing Tanker Test Factual Report," Docket No: SA-512, Exhibit No: 13B, DCA95MA001, Washington D.C., Feb. 16, 1995.

[9] "Freezing Drizzle: Towards a Better Knowledge and Better Prediction," published by Avions de Transport Regional, Nov. 5, 1995.

[10] Johnson, C.L., "Wing Loading, Icing and Associated Aspects of Modern Transport Design," Journal of Aeronautical Sciences, Vol. 8, No. 2, Dec. 1940, pp. 43-54.

[11] Morris, D.E., "Designing to Avoid Dangerous Behavior of an Aircraft due to the Effects on Control Hinge Moments of Ice on the Leading Edge of the Fixed Surface," A.R.C. Technical Report 10670, 1952.

[12] Ashenden, R. and Marwitz, J., "Turboprop Aircraft Performance Response To Various Environmental Conditions," AIAA Paper 97-0305, *Journal of Aircraft,* Vol 34, no. 3, May-June 1997, pp. 278-287.

[13] Ashenden, R., Lindberg, W. and Marwitz, J., "Two-Dimensional NACA 23012 Airfoil Performance Degradation by Super Cooled Cloud, Drizzle, and Rain Drop Icing," AIAA 34th Aerospace Sciences Meeting, Reno, NV, January 15-18, 1996.

[14] Bernstein, B.C., Ratvasky, T.P., Miller, D.R., and McDonough, F., "Freezing Rain as an In-Flight Hazard," NASA TM 2000-210058, June 2000.

[15] Cook, D.E., "Unusual Natural Icing Encounters During Boeing 777 Flight Tests," AIAA Paper 97-0304, AIAA 35th Aerospace Sciences Meeting, Reno, NV, January 6-10, 1997.

[16] Bragg, M.B., "Aircraft Aerodynamic Effects Due To Large Droplet Ice Accretions," AIAA Paper No. 96-0932, AIAA 34th Aerospace Sciences Meeting, Reno, NV, January 15-18, 1996.

[17] Bragg, M.B., "Aerodynamics of Supercooled-Large-Droplet Ice Accretion and the Effect on Aircraft Control," *Proceedings of the FAA International Conference on Aircraft Inflight Icing*, Volume II, DOT/FAA/AR-96/81,II, August 1996, pp. 387-399.

[18] Lee, S., T. Dunn, H.M. Gurbacki, M.B. Bragg and E. Loth, "An Experimental and Computational Investigation of Spanwise-Step-Ice Shapes On Airfoil Aerodynamics," AIAA Paper No. 98-0490, Reno, NV, January 12-15, 1998

[19] Lee, S., M.B. Bragg, "Effects of Simulated-Spanwise-Ice Shapes on Airfoils: Experimental Investigation," AIAA Paper No. 99-0092, Reno, NV, January 11-14, 1999.

[20] Lee, S., Kim, H.S., and Bragg, M.B., "Investigation of Factors that Influence Iced-Airfoil Aerodynamics," AIAA Paper No. 2000-0099, 38th Aerospace Sciences Meeting and Exhibit, Reno NV, January 10-13, 2000

[21] Lee, S. and Bragg, M.B., "An Experimental Investigation of Simulated Large-Droplet Ice shapes on Airfoil Aerodynamics," *Journal of Aircraft*, Vol. 36, No. 5, Sept.-Oct. 1999, pp. 844-850

[22] Dunn, T.A., "Prediction of Ice-Airfoil Aerodynamics," M.S. Thesis, University of Illinois at Urbana-Champaign, Urbana, IL, 1998.

[23] Dunn, T.A., Loth, E., and Bragg, M.B., "A Computational Investigation of Simulated Large-Droplet Ice shapes on Airfoil Aerodynamics," *Journal of Aircraft*, Vol. 36, No. 5, Sept.-Oct. 1999, pp. 836-843.

[24] Tani, I., "Low-Speed Flows Involving Bubble Separations," *Progress in Aeronautical Sciences*, Vol. 5, MacMillian, New York, 1964.

[25] Khodadoust, A., “An Experimental Study of the Flowfield on a Semispan Rectangular Wing with a Simulated Glaze Ice Accretion,” Ph.D. Dissertation, University of Illinois at Urbana-Champaign, Urbana, IL, 1993.

[26] Bragg, M.B., Khodadoust, A. and Spring, S.A., "Measurements in a Leading-Edge Separation Bubble due to a Simulated Airfoil Ice Accretion," *AIAA Journal*, Vol. 30, No. 6, June 1992.

[27] Brumby, R.E., “Wing Surface Roughness – Cause & Effect,” *D.C. Flight Approach*, Jan. 1979, pp. 2-7.

[28] Jacobs, E. N., “Airfoil Section Characteristics as Affected by Protuberances,” NACA Report No. 446, 1932.

[29] Papadakis, M., Alansatan, S., and Seltman, M., “Experimental Study of Simulated Ice Shapes on a NACA 0011 Airfoil,” AIAA Paper 99-0096, 37th Aerospace Sciences Meeting & Exhibit, Reno, NV 1999.

[30] Kim, H.S., and Bragg, M.B., “Effects of Leading-Edge Ice Accretion Geometry on Airfoil Performance,” AIAA Paper 99-3150, 17th Applied Aerodynamics Conference, Norfolk, VA, June 28-July 1, 1999.

[31] Trunov, O.K. and Ingelman-Sundberg, M., “On the Problem of Horizontal Tail Stall Due to Ice,” The Swedish-Soviet Working Group on Scientific-Technical Cooperation in the Field of Flight Safety, Report No. JR-3, 1985.

[32] Wright, W.B. and Chung, J.K., “Correlation Between Geometric Similarity of Ice Shapes and the Resulting Aerodynamic Performance Degradation - A Preliminary Investigation Using WIND,” AIAA Paper 2000-0097, Jan. 2000.

[33] Hoerner, S.F., *Fluid-Dynamic Lift*, Hoerner Fluid Dynamics, Brick Town, NJ, 1975, p4-19.

[34] Morgan, H.L., Ferris, J.C., and McGhee, R.J., “A Study of High-Lift Airfoils at HIgh Reynolds Number in the Langley Low-Turbulence Pressure Tunnel,” NASA TM-89125, July 1987.

[35] Gregory, N. and O’Reilly, C.L., “Low-Speed Aerodynamic Characteristics of NACA 0012 Aerofoil Section, including the Effects of Upper-Surface Roughness Simulating Hoar Frost,” ARC R&M 3726, Jan. 1970.

[36] Calay, R.K., Holdù, A.E. and Mayman, P., “Experimental Simulation of Runback Ice,” *Journal of Aircraft*, Vol. 34, No, 2, March - April, 1997, pp. 206-212.

[37] Bowden, D.T., "Effect of Pneumatic De-Icers and Ice Formations on Aerodynamic Character of an Airfoil," NACA Technical Note 3564, February, 1956.

[38] Foss Van Zante, J. and Ratvasky, T.P., "Investigation of Dynamic Flight Maneuvers With an Iced Tailplane," AIAA Paper 99-0371, Jan. 1999.

[39] Ratvasky, T.P. and Foss Van Zante, J., "In-Flight Aerodynamic Measurements of an Iced Horizontal Tailplane," AIAA Paper 99-0638, Jan. 1999.

[40] Kuehn, D.M., "Effects of Adverse Pressure Gradient on the Incompressible Reattaching Flow over a Rearward-Facing Step," AIAA Journal, Vol. 19, No. 3, March 1980, pp343-344.

[41] Driver, D.M, Seegmiller, H.L., "Features of a Reattaching Turbulent Shear Layer in Divergent Channel Flow," AIAA Journal, Vol. 23, No. 2, Feb. 1985, pp 163-171.

[42] Eaton, J.K., Johnston, J.P., and Jeans, A.H., "Measurements in a Reattaching Turbulent Shear Layer," Porceedings of the 2nd Symposium on Turbulent Shear Flows," London, 1979.

[43] Adams, E.W. and Johnston, J.P., "Effects of the Separating Shear Layer on the Reattachment Flow Structure Part 2: Reattachment Length and Wall Shear Stress," Experiments in Fluids, vol. 6, no. 7, 1988, pp 493-499.

[44] Yoo, J.Y and Baik, S.J., "Redeveloping Turbulent Boundary Layer in the Backward-Facing Step Flow," Transactions of the ASME, vol. 114, Dec. 1992, pp. 522-529.

[45] Kerho, M.F., "Effect of Large Distributed Roughness Near an AIrfoil Leading Edge on Boundary-Layer Development and Transition," Ph.D. Dissertation, University of Illinois at Urbana-Champaign, Urbana, IL, 1995.

[46] Jackson, D.G., *Effect of Simulated Ice and Residual Ice Roughness on the Performance of a Natural Laminar Flow Airfoil, M.S. Thesis*, University of Illinois, Urbana, IL, 2000.

[47] Noe, S., "Force Balance Measurements of Wind-Turbine Airfoil Performance with Simulated Leading-Edge Ice Accretions," M.S. Thesis, University of Illinois at Urbana-Champaign, Urbana, IL, 1996

[48] Lambert, M., ed., *Jane's All the World's Aircraft 1990-1991*, Jane's Information Group, Inc., 1990.

[49] Winkler, J.F., **"**Local Flowfield about Large Distributed Roughness Elements in a Laminar Boundary Layer**"**, Ph.D. Thesis, University of Illinois at Urbana-Champaign, Urbana, IL, 1996.

[50] Rae, W.H. and Pope, A., *Low-Speed Wind Tunnel Testing*, John Wiley & Sons, New York, 1984.

[51] Jones, B.M., "The Measurement of Profile Drag by Pitot Traverse Method," Aeronautical Research Council, R&M 1688, 1936.

[52] Coleman, H.W. and Steel, W.G. Jr., *Experimentation and Uncertainty Analysis for Engineers*, John Wiley & Sons, Inc., New York, 1989.

[53] Wright, W.B., "User Manual for the NASA Glenn Ice Accretion Code LEWICE: Version 2.0," NASA CR-1999-209409, Sept., 1999.

[54] Althaus, D. and Wortmann, F. "Experimental Results from the Laminar Wind Tunnel of the Institute for Aerodynamic and Gasdynamics - The University of Stuttgart" published by Princeton University, Department of Mechanical and Aerospace Engineering, 1979.

[55] Abbott, I.H. and von Doenhoff, A.E., *Theory of Wing Sections*, Dover Press, 1959.

[56] Broeren, A.P., *An Experimental Study of Unsteady Flow Over Airfoils Near Stall, Ph.D Dissertation*, University of Illinois, Urbana, IL, Jan. 2000.

[57] McGhee, R.J., Viken, J.K., Pfenninger, W., Beasley, W.D., Harvey, W.D., "Experimental Results for a Flapped Natural-Laminar-Flow Airfoil with High Lift/Drag Ratio," NASA TM-85788, 1984.

[58] Winkelmann, A., "Flow Field Studies Behind a Wing at Low Reynolds Numbers", AIAA Paper 90-1471, June 1990.

[59] Menna, J.D. and Pierce, F.J., "The Mean Flow Structure Around and Within a Turbulent Junction or Horseshoe Vortex-Part I: The Upstream and Surrounding Three Dimensional Boundary Layer," *Journal of Fluids Engineering*, Vol. 110, pp. 406-414, December 1988.

[60] White, F.M., *Fluid* Mechanic, *Second Edition*, McGraw-Hill, New York, 1986, p. 418.

[61] McCullough, G.B. and Gault. D.E., "Examples of Three Representative Types of Airfoil-Section Stall at Low Speed," NASA TN-2502, Sept. 1951.

Vita

Sam Lee was born on June 12, 1971 in Taegu, South Korea. He was the middle of 3 children of David and Yon Lee. He was raised in South Korea until the age of eight, when he and his family immigrated to the United States and settled in Portland, Oregon. He attended Sunset High School in Beaverton, Oregon and graduated in June 1990. Upon graduation, Mr. Lee enrolled in Cornell University in Ithaca, New York where he majored in mechanical engineering. He graduated with B.S. degree in May 1994. Mr. Lee wanted to further his education in aeronautical engineering so he enrolled in the Department of Aeronautical and Astronautical Engineering at the University of Illinois in the fall of 1994. He has worked as a Graduate Research Assistant at the Subsonic Aerodynamics Laboratory under Professor Michael Bragg since his arrival at the University of Illinois. He received a M.S. degree in Aeronautical and Astronautical Engineering in January 1997 and continued on at the University of Illinois to pursue a doctoral degree.